EVALUATION OF THE 4-KM COUPLED MM5/TOPLATS/SSATS MODELING SYSTEM FOR THE AUGUST 1998 HOUSTON-GALVESTON AREA OZONE EXCEEDANCE EPISODE

Final Report

TNRCC Work Order Number 31985-05

Prepared for

Texas Natural Resource Conservation Commission
Mr. Bob Cameron, Project Officer
Building E
12100 Park 35 Circle
Austin, TX 78753

Prepared by

John N. McHenry, Research Meteorologist
MCNC Environmental Modeling Center
3021 Cornwallis Road, PO Box 12889
Research Triangle Park, NC 27709-2889

and

Christa D. Peters-Lidard*, Assistant Professor
School of Civil and Environmental Engineering
Georgia Institute of Technology
Atlanta, GA 30332-0355

Under subcontract to

Sonoma Technology, Inc.
Work Plan STI-900550-2056-WP

October 7, 2002

***Current Affiliation*: Research Scientist, Hydrological Sciences Branch**
NASA-GSFC Code 974, Greenbelt, MD 20771

Acknowledgments

The authors would like to thank Bob Cameron of TNRCC, the TNRCC, and the U.S. EPA for supporting this research. The authors thank Drs. Carlie Coats and Atanas Trayanov of the Environmental Modeling Center at MCNC for their important contributions to the model coupling software and engineering, and Mr. Don Olerud for his insightful handling of the MM5 output data and production of evaluation statistics and figures. Ms. Stacy Bergendahl provided significant help with graphical editing, Ms. Jeanne Eichenger contributed her truly artful editing, and Mr. Neil Wheeler of Sonoma Technology, Inc. provided untiring encouragement and enthusiasm.

TABLE OF CONTENTS

Section **Page**

TABLE OF CONTENTS (continued)

Section **Page**

TABLE OF CONTENTS (concluded)

LIST OF FIGURES

LIST OF FIGURES (Continued)

LIST OF FIGURES (Continued)

LIST OF FIGURES (Continued)

LIST OF FIGURES (Continued)

LIST OF FIGURES (Continued)

LIST OF FIGURES (Continued)

LIST OF FIGURES (Continued)

LIST OF FIGURES (Continued)

LIST OF FIGURES (Continued)

LIST OF FIGURES (Continued)

LIST OF FIGURES (Continued)

LIST OF FIGURES (Continued)

LIST OF FIGURES (Concluded)

LIST OF TABLES

1. Introduction

1.1 Purpose and Objective

In June 1998, TNRCC expressed initial interest in expanding a preliminary version of a coupled meteorological-hydrological-emission-air quality modeling system, the Advanced Texas Air Quality Model (ATAQM), then under development at MCNC (McHenry et al., 1999). During the spring of 1999, project plans were formalized and MCNC embarked on a Phase 1 Demonstration Case utilizing a standard version of the MM5 Mesoscale Meteorological Model (V2.12, Gre11 et al., 1995), the SMOKE emissions processing system, and MCNC's MAQSIP Air Quality Model.

Having successfully produced the base case using these standard models, Phase 2 was proposed to bring in the fully-distributed hydrological component, the TOPMODEL-based Land-Atmosphere Transfer Scheme (TOPLATS, Famiglietti and Wood, 1994; Peters-Lidard et al., 1997). A companion sea-surface transfer scheme designed by MCNC and Georgia Institute of Technology (Georgia Tech), the Sea-Surface Atmosphere Transfer Scheme (SSATS) was added to the system during Phase 2. Following development and implementation of hydrological and sea-surface temperature databases (Peters-Lidard, 2001a, b, c, d, e), the now coupled MM5/TOPLATS/SSATS system was to be tested and then applied to a case study of interest to TNRCC. Following that, case evaluation was to be undertaken without the emission and air quality components of ATAQM. In this report, ATAQM refers only to the meteorological/hydrological components of the system.

This report describes the successful application of the MM5/TOPLATS/SSATS modeling system to an ozone exceedance event that occurred in August 1998, completing the Phase 2 work. Head-to-head evaluation with an identical uncoupled version of the modeling system ranks the coupled system higher in both quantitative and qualitative metrics. For convenience, all Phase 2 work that was performed after August 31, 2001, is referred to as Phase 2b in this report, whereas work performed before that date is referred to as "original" or "initial" Phase 2 work.

1.2 Rationale for Model Formulation

Since a land-surface model (LSM) is integrated into Version 3.4 of the MM5 modeling system, it is reasonable to ask why MM5 V3.4 is not used instead of TOPLATS. The TOPLATS model has been re-designed by MCNC and Georgia Tech to run as an offline hydrological/surface-flux model driven by observational data (satellite-derived downward solar radiation, and remotely-sensed, gauge corrected precipitation). Both of these primary surface driving-variables are suspect in meteorological models, and the LSM is not configured to use any remotely sensed data. Further, using MM5 with LSM "as is" is problematic because there are rarely well-distributed, vertically discrete soil moisture data available for initialization. TOPLATS avoids this problem by spinning up the model using seven months of observational data. Such a spin-up run can execute in

just a few hours on the TNRCC typhoon computer, once the data have been quality assured.

Other schemes exist within MM5 that couldn't be fully coupled with TOPLATS for this project, but could be coupled in the future. Two in particular are the Mid-range Forecast (MRF) model, a boundary layer parameterization scheme, and the Rapid-Radiative Transfer Model (RRTM), a longwave radiation parameterization scheme. The Blackadar-based high-resolution PBL scheme (HIRPBL, Grell et al., 1995) for planetary boundary layer (PBL) processes was used instead of the MRF model because applications at MCNC showed that PBL heights were often too high in MRF-based runs, and that the sea breeze was often too strong. This could have detrimental effects on photochemical simulations. Because the RRTM was released too late in the project to develop the coupling interface, the Dudhia LWRAD scheme (Dudhia, 1989) was used for longwave coupling.

The results presented here suggest that the MM5/TOPLATS/SSATS system is ready for application as a photochemical model driver, having achieved demonstrable improvements over its uncoupled counterpart, MM5. Additional benefits could be gained by applying and evaluating the model for a case that features an intensive field program; this would allow exploration and validation of the many qualitative advantages discussed herein.

In the rest of this document, references to MM5 refer to V3.4 of the modeling system and its pre- and post-processing programs. Further, "outer domain" refers to the two-grid 36 km-12 km MM5 simulations and "inner domain" refers to the single-grid 4-km simulations that use the boundary conditions from the 12-km outer domain grid.

1.3 Case Study: The August 1998 Houston-Galveston Ozone Exceedance Episode

The chosen episode occurred during the period August 25-31, 1998, in the Houston/Galveston (HGA) region proximate to Galveston Bay in southeastern Texas. Table 1.1 shows the hourly average ozone characteristics during that period.

The meteorological scenario for this episode was fairly typical, characterized by surface high pressure with only weak regional-scale meteorological disturbances creating day-to-day ozone concentration differences. On August 25, the day prior to the first exceedance day, there were surface Highs in western Wyoming, Nebraska, and northern Georgia. A thermal Low over the Mexican highlands helped create a synoptic-scale flow from the south-southeast, which favored a well-developed afternoon sea breeze. Low-level moisture was abundant, and as the sea-breeze front moved inland along the entire Texas Gulf-coast, convection began to form, with shallow cloud streets dominating most of central-eastern Texas. By 2000 UTC, numerous deep convective cells and clusters were well developed and moving northwestward along the leading edge of the sea-breeze front. The front continued to propagate inland more than 130 km before the convection began to dissipate near 2300 UTC, leaving trailing anvil plumes stretched out to the

Table 1.1. Houston ozone exceedances during the August 1998 episode.

Date	Highest Hourly Average Ozone (ppb)	Number of Stations Exceeding 124 ppb
August 25	98	0
August 26	150	1
August 27	203	4
August 28	146	2
August 29	206	5
August 30	162	3
August 31	82	0

Source: Texas Natural Resource Conservation Commission

southwest under weak northwesterly 300-mb flow. Figure 1.1 shows this regional pattern at 1800 UTC on August 25.

On August 26 (Figure 1.2), the high pressure had moved to the west and strengthened, weakening the gradient and cutting off the persistent southerly flow. This movement was partly due to the expansion of the High to the north and the approach of Hurricane Bonnie along the Carolina coast. Low-level moist flow from the Gulf was restricted to a band centered near Corpus Christi, Texas, where convection similar to that on the previous day developed between 1500 UTC and 2000 UTC. Farther north, from Palacios, Texas, north toward HGA and Beaumont-Port Arthur, Texas, (BPA) weak morning northwesterly flow was supplanted by a far weaker (than the day before) sea breeze by around 2000 UTC. In addition, the proximity of the High and its subsidence began to dry out the moist boundary layer from the previous day, suppressing cloud formation over the Gulf proximate to Houston, such that with the onset of the weak afternoon sea breeze, the sky cleared. Mid-afternoon temperatures were well into the low 90's on both days, but the weaker flow and stronger high pressure on August 26 ushered in the beginning of the episode.

On August 27 (Figures 1.3a and 1.3b), the High strengthened, moving farther to the west, with mid-afternoon temperatures reaching the mid-90's. The anti-cyclonic circulation of the High centered near Houston is evident in the curved cloud streets visible in the 1800 UTC satellite imagery (not shown). Houston Sugarland (SGA) reported 97°F at 1800 UTC. Cloud development was further suppressed, with no deep convection occurring anywhere in eastern Texas. Modest shallow convection had formed by 1800 UTC, but was more widely scattered than on the previous day. The sea breeze was not well organized, but by mid-afternoon a weak breeze had formed south of Palacios and gradually expanded northeast toward the Houston Gulf Coast. The strong high pressure, suppression of cloud formation, and weak daytime flow near Houston contributed to a maximum 1-hour ozone concentration of 203 ppb (at Continuous Air Monitoring Station—CAMS—35), with four monitors exceeding 124 ppb (CAMS 10, 34, 35, and 53). Figure 1.3c shows the locations of various CAMS monitors in the Houston area.

On August 28, a very weak, dry, surface trough approached from the northwest (Figures 1.4a,b), allowing a slightly more organized sea breeze to form from near Angleton/Lake Jackson, Texas, south along the Gulf Coast, although surface pressures remained high, near 1016 mb. Shallow clouds formed ahead of the sea breeze, with much of interior eastern Texas pockmarked by cloud streets moving northeastward in weak southwesterly flow near the top of the PBL, in association with the trough. The trough passage represented a modest change of air mass, with a stronger High to the northwest replacing the westernmost side of the eastern United States high as a controlling feature. This is likely the reason ozone levels were suppressed somewhat on August 28, despite abundant sunshine, weak winds, and afternoon high temperatures in the mid-90's.

August 29 was the most intriguing day of the episode. Overnight on August 28, the previous day's weak frontal boundary apparently propagated northward, becoming stationary along an east-west axis about 200 km north of the HGA. An area of mid-level clouds that developed overnight accompanied this boundary, contributing moisture to it. This boundary developed as the western edge of the Bermuda High, now recovering after the passage of Hurricane Bonnie, re-strengthened, while the southeastern edge of the Pacific High flattened, and a surface low began to develop in the south-central Gulf of Mexico (Figures 1.5a, b). The convection formed along the boundary, oriented southwest-northeast about 150 km to the north-northwest of the HGA. Because the surface boundary moved back to the north, it is likely that the HGA was again exposed to some of the same airmass that had been present on August 27, enabling development of the highest ozone values of the episode. Further, the presence of the deep convection proximate to, but not within, the HGA suppressed cloud formation, further enhancing the ozone production potential.

August 30 (Figure 1.6a) was the last exceedance day of the period, with the peak hourly average ozone concentration reported as 162 ppb (CAMS 26). Three monitors exceeded the 124-ppb hourly standard (CAMS 1, 8, and 26) on this day. The boundary between the two Highs became ill-defined over east-central Texas, with moisture remaining along the previous day's convergence zone to the north. The Gulf low strengthened somewhat, with pressures at the two central-Gulf offshore buoys depicted in Figures 1.5a and 1.6a falling about a millibar, and central-Gulf winds becoming more cyclonic and slightly stronger. Further, subtropical moisture, located southwest of the HGA, began moving northeastward from off the Mexican coast toward the HGA Gulf coast under the influence of weak southwesterly upper-level flow (Figure 1.6b). The weak high pressure near the HGA was "squeezed" between the previous day's convergence zone, the approaching subtropical moisture from the southwest, and the strengthening low in the central Gulf. By late in the day, precipitation had begun in and near the area. This was the only significant precipitation during the six-day episode, and it served to bring it to a close.

1.4 Background for Work Order 5, Phase 2b

Phase 2b of Work Order 5 includes all work conducted after August 31, 2001, that was necessary to complete the Phase 2 Work Plan. Though a version of the coupled model

system had been demonstrated and delivered as of that date, time constraints had not permitted the full integration of the satellite-derived downward solar radiation capability described in the Work Plan. During Phase 2b, this integration was completed by using GOES-derived downward surface radiation budget (SRB) data as forcing data for TOPLATS, in accordance with the Work Plan. Phase 2b also completed the model re-runs needed as a result of the new SRB capability, along with the evaluation of the coupled model system.

While development of the SRB capability was being completed, review of the initial Phase 2 MM5/TOPLATS coupled runs was undertaken in order to make additional system improvements. This review led to further refinements to the modeling protocol:

(1) The interior 4-km MM5 grid size was reduced slightly (from 100 x 100 grid points to 70 x 70 grid points) to fully fit within the TOPLATS watershed domain in order to eliminate spurious effects occurring at the (irregular) TOPLATS boundary.

(2) Two additional outer domain (36 km-12 km) MM5 runs were conducted due to the presence of anomalous parameterized convection near the 4-km boundaries in the original Phase 2 36 km-12 km simulation.

(3) Improvements to the one-way TOPLATS coupling methodology in MM5 were implemented to permit better internal miter-step computations in the Blackadar PBL scheme (Grell et al., 1995).

These improvements led to the construction of a matrix of nine runs used for inter-comparison. Three outer domain 36 km-12 km runs were separately used to drive both coupled and uncoupled 4-km runs, producing six 4-km runs. An additional three 4-km coupled runs were added using an improved u_* parameterization, for a total of nine 4-km runs. Each of the coupled runs utilized the results of TOPLATS re-runs which made use of the new remotely-sensed SRB data.

This document describes the Phase 2b activity, its results, and conclusions. This includes the evaluation of the results of the nine TOPLATS/MM5 runs using surface observations and satellite imagery, using both quantitative statistical and qualitative analysis techniques. The coupled model results discussed represent the state-of-the-science for the meteorological-hydrological component of the ATAQM.

1.5 Structure of the Report

This report is organized into eight sections and three appendices. Figures for each section or subsection can be found at the end of the section or subsection. Section 2 discusses the integration of GOES-derived SRB data into TOPLATS, including temporal interpolation, SRB data filters, and the SRB reader method developed in TOPLATS. Section 3 documents the TOPLATS results using the new SRB data and compares them to the results based on the original surface solar radiation measurements.

Section 4 describes the Phase 2b MM5 configuration, including the refinements to the 36 km-12 km MM5 outer domain runs and the rationale for using them, the model domains, and the additional preprocessing that was required. The MM5 physics and run-time configurations used for both the outer 36 km-12 km and inner 4-km domains are also described. Section 5 presents the MM5/TOPLATS/SSATS coupling strategy and variables.

Section 6 contains the model evaluation for the August 1998 episode. It describes in detail the nine 4-km runs used to evaluate the system, and the evaluation approach. Time-series statistics at individual surface observing stations (in order to measure performance at a sample of locations) and time-series aggregates averaged over all available stations in the domain (to look at domain-wide performance) are described. This section also presents episode mean statistics to assess gross model performance for the episode.

Following presentation of the quantitative statistics, Section 6 provides a qualitative comparison of uncoupled-versus-coupled results in order to develop better insight into the statistical results. First, the modeled surface sensible and latent heat fluxes are compared. The boundary-layer depth and evolution in the various 4-km simulations are then discussed and key similarities and differences are pointed out. Next, the models' representation of the sea breeze as depicted in satellite imagery and surface station data are evaluated because of the important role the sea breeze plays in HGA air quality. Further, a qualitative analysis of cloud representation in the various 4-km models that compares model results against satellite observations is provided. Qualitative comparisons are provided with a view toward the effects the various processes (surface fluxes, PBL, sea-bay-land breezes, and clouds) have on air quality and on air quality model simulations that would be driven by the 4-km runs. Upper-air winds from the Ellington Field (EFD) Radar Wind Profiler (RWP) were also used to qualitatively evaluate the model's performance.

Section 7 provides overall conclusions about the results of the runs, based on both the quantitative and qualitative analyses, and the authors' experience in developing and using meteorological models as drivers for air quality simulations. Section 8 provides references for the report. Appendix A provides a list of Phase 2b terrain names, Appendix B provides MM5 compile options, Appendix C provides the MM5 run-time namelist, and Appendix D contains enlarged plots from Figures 6.9.1 through 6.9.5—day-by-day comparison of the RWP data with the model predictions.

1.6 Figures for Section 1

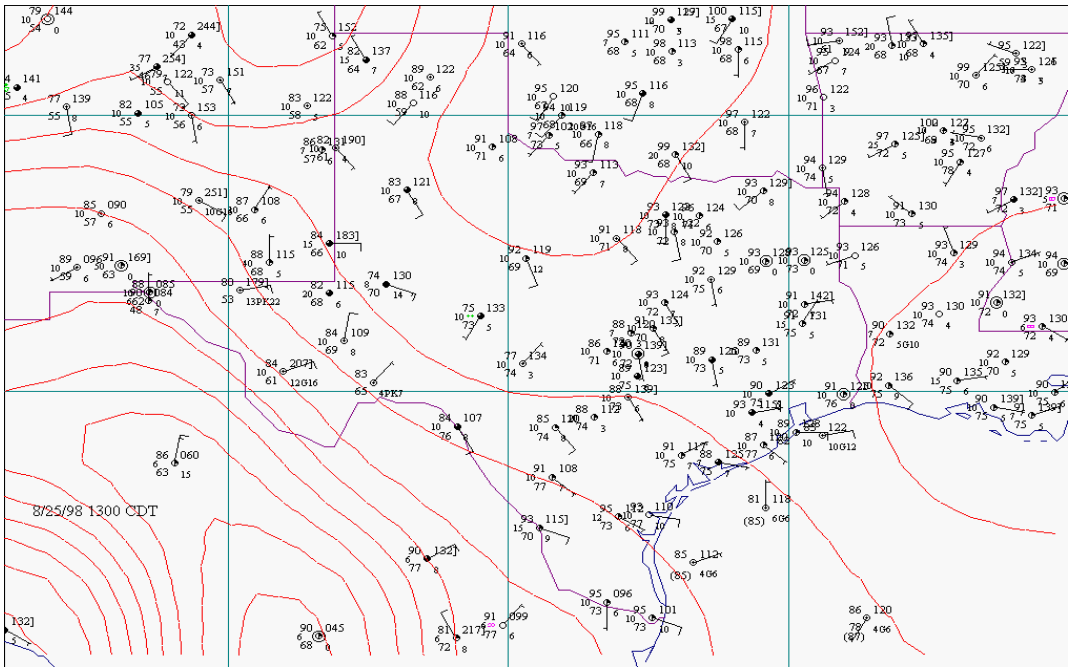

Figure 1.1. Regional surface weather map, 1800 UTC, August 25, 1998.

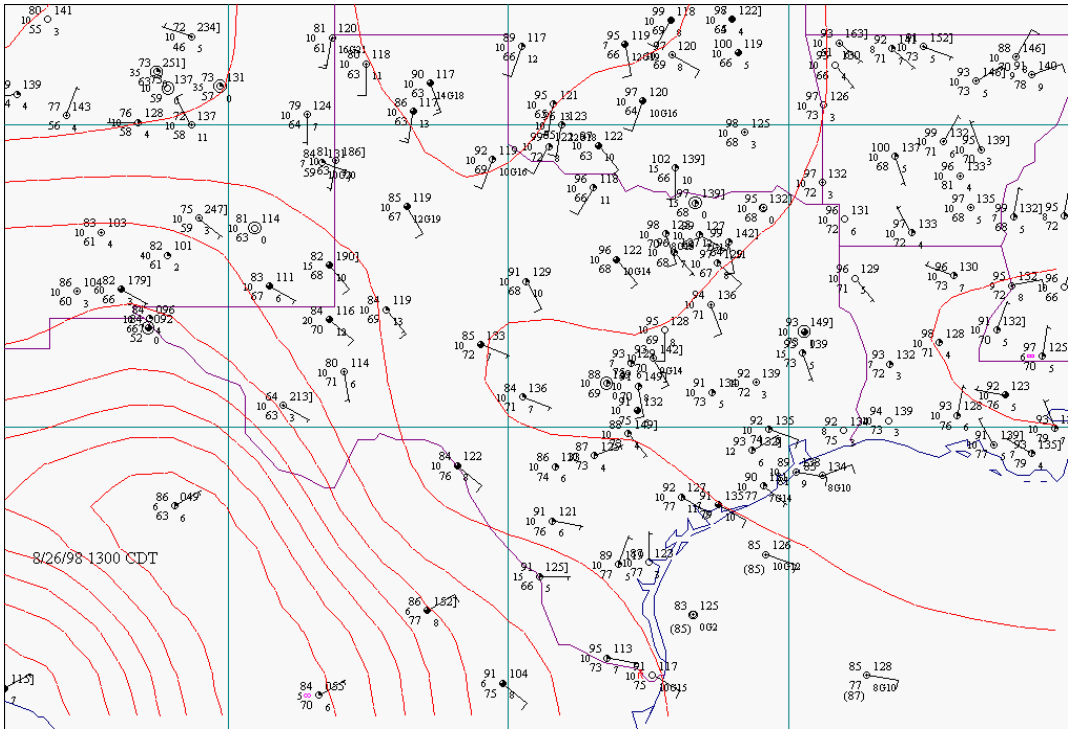

Figure 1.2. Regional surface weather map, 1800 UTC, August 26, 1998.

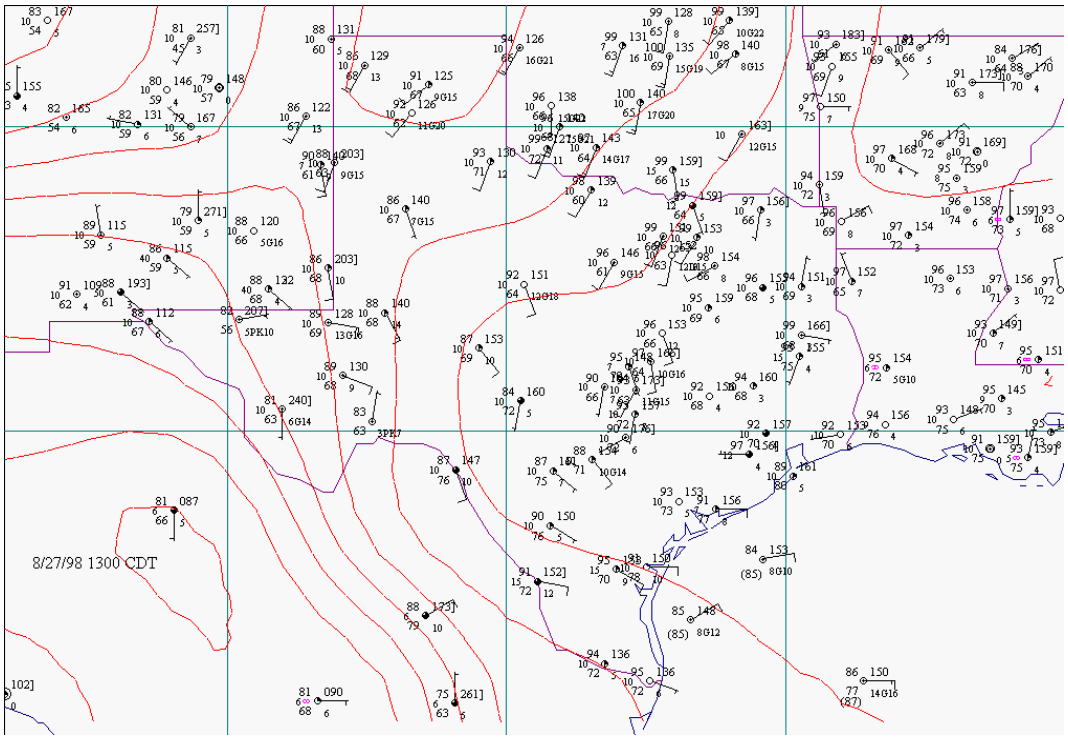

Figure 1.3a. Regional surface weather map, 1800 UTC, August 27, 1998.

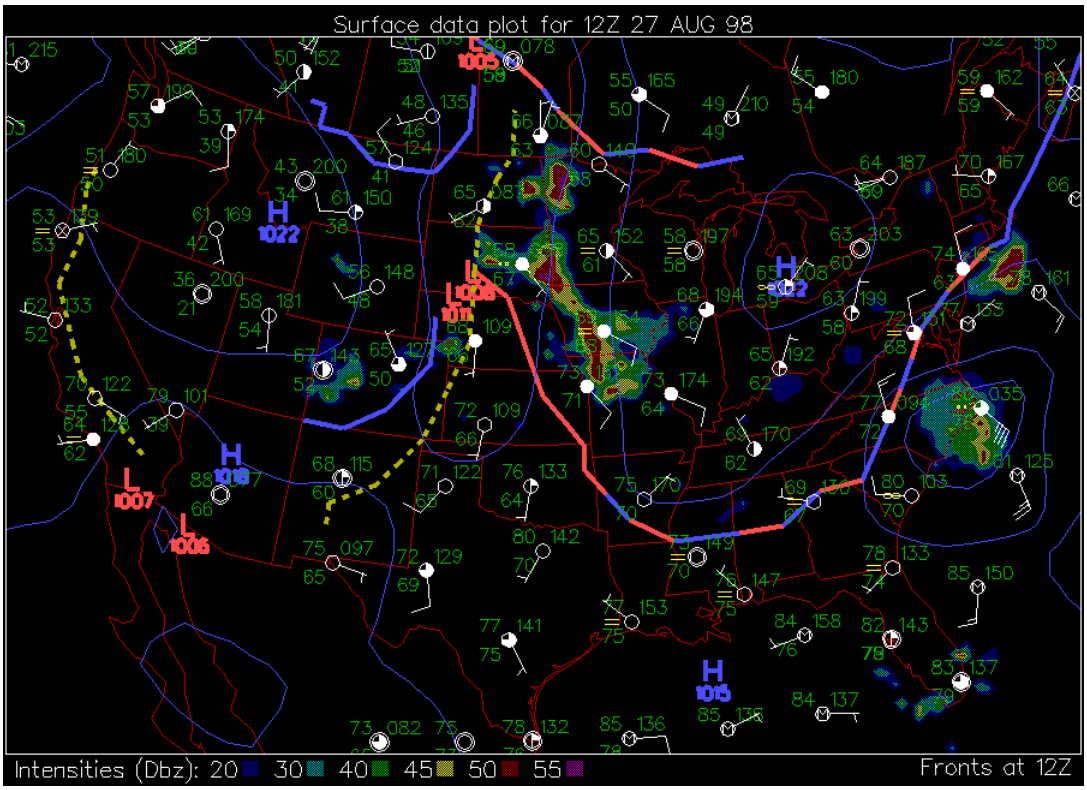

Figure 1.3b. Synoptic surface weather map, 1200 UTC, August 27, 1998.

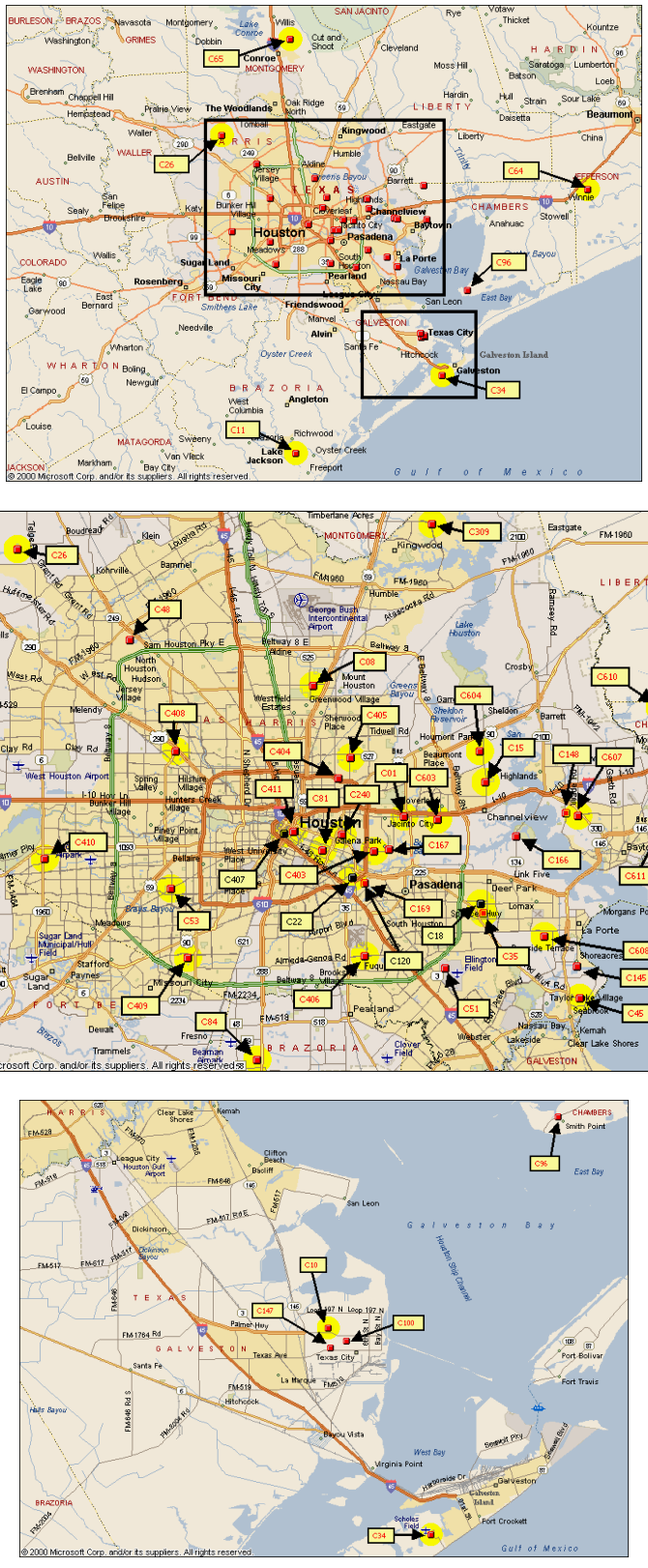

Figure 1.3c. Locations of various TNRCC CAMS monitoring stations.

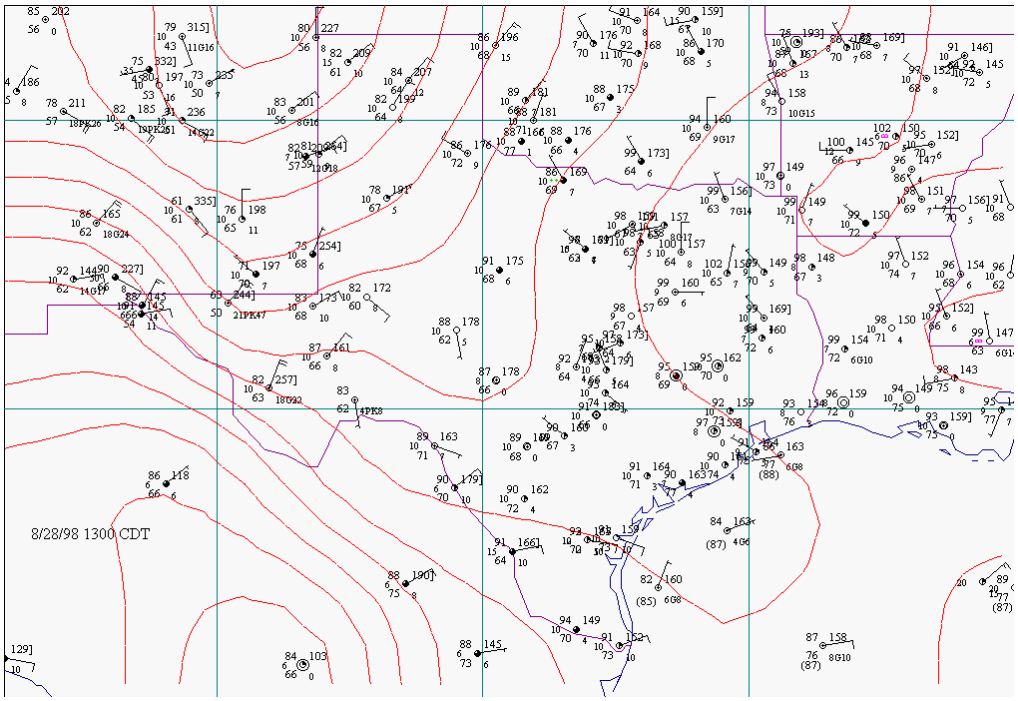

Figure 1.4a. Regional surface weather map, 1800 UTC, August 28, 1998.

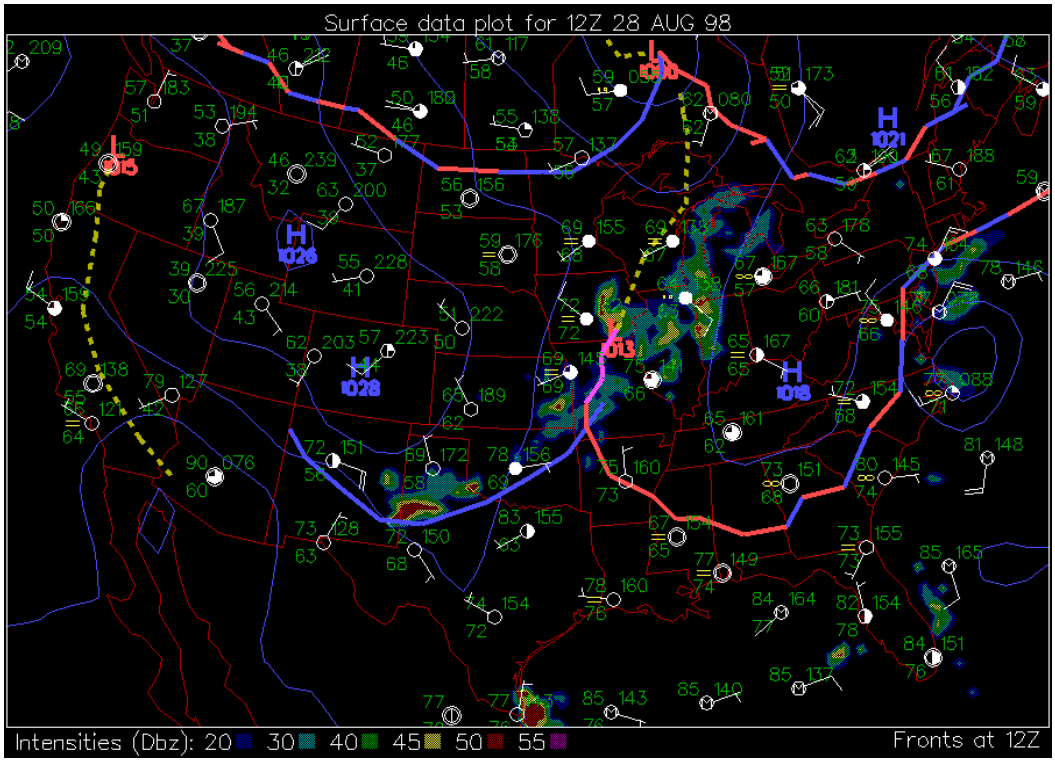

Figure 1.4b. Synoptic surface weather map, 1200 UTC, August 28, 1998.

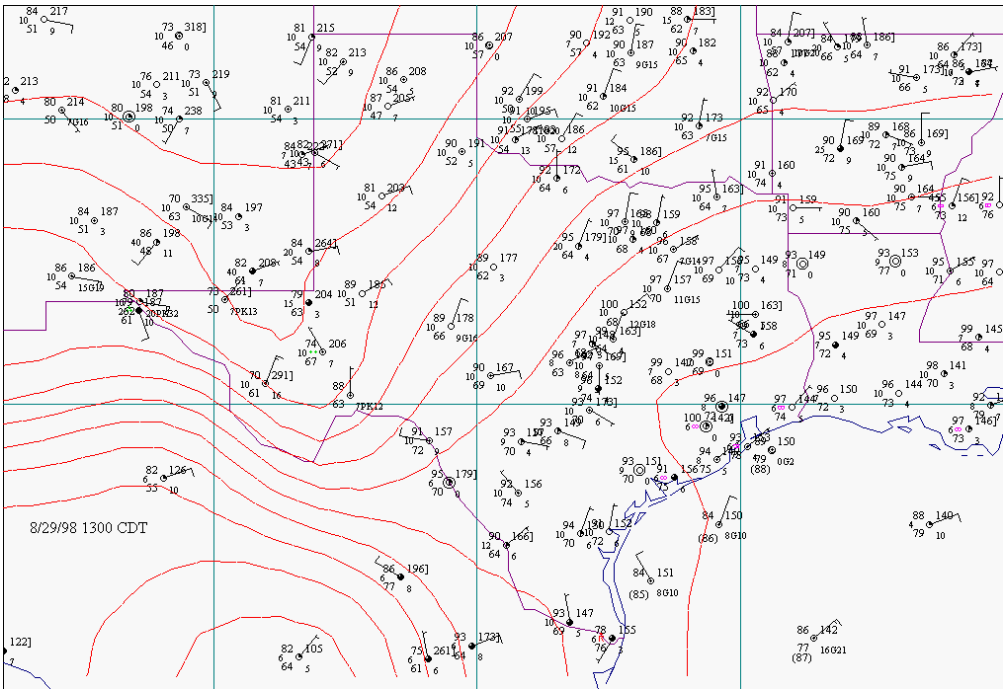

Figure 1.5a. Regional surface weather map, 1800 UTC, August 29, 1998.

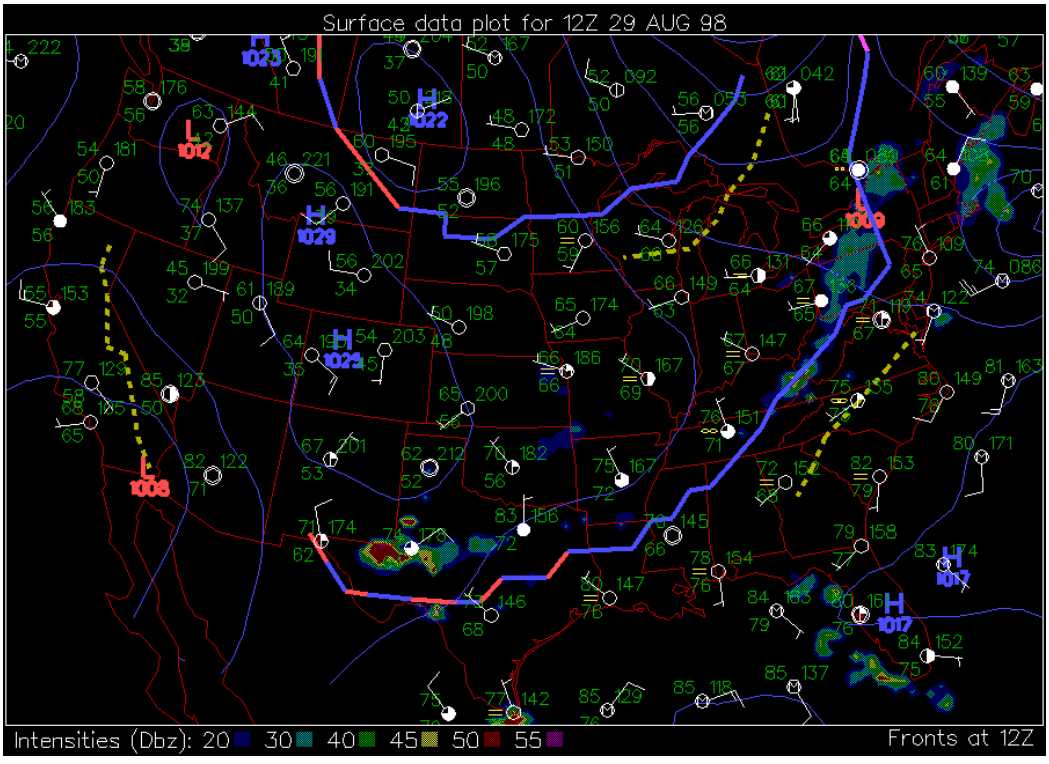

Figure 1.5b. Synoptic surface weather map, 1200 UTC, August 29, 1998.

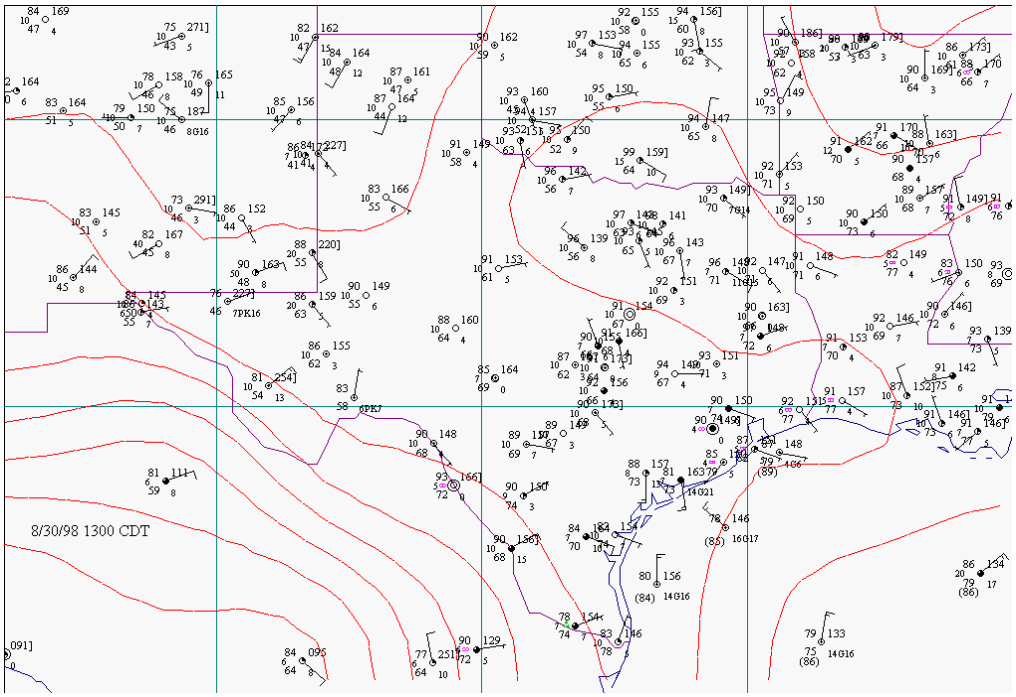

Figure 1.6a. Regional surface weather map, 1800 UTC, August 30, 1998.

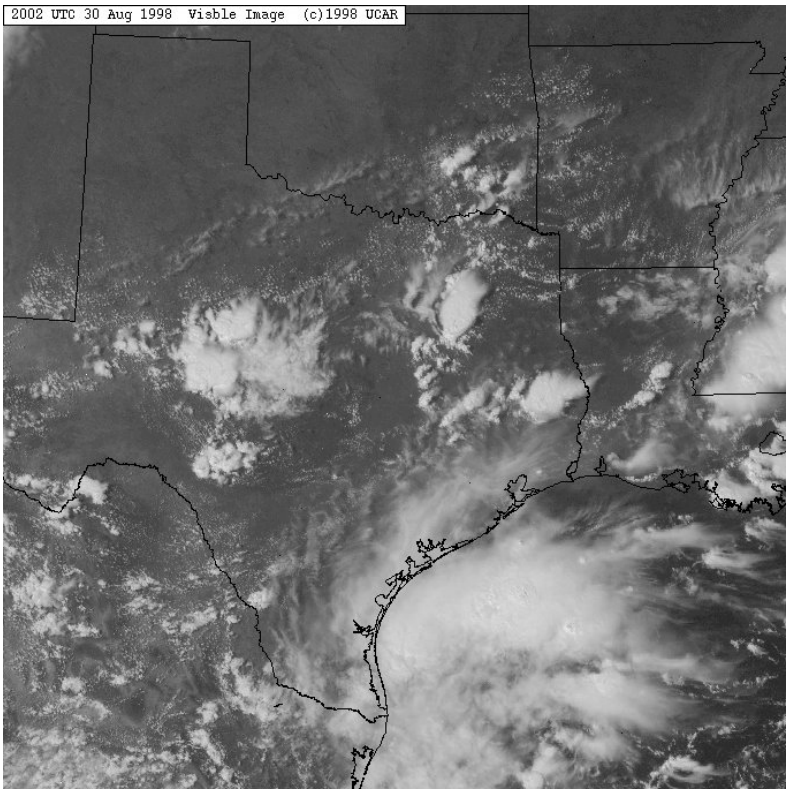

Figure 1.6b. Regional visible satellite image, 2000 UTC, August 30, 1998.

2. Integration of GOES-derived SRB Data into TOPLATS

Phase 2b undertook revisions to TOPLATS and development of "data filters," enabling the use of remotely sensed downward solar radiation data products. The products used are derived from GOES satellites by the Global Energy and Water Cycle Experiment (GEWEX) Continental Scale International Project (GCIP) and GEWEX Americas Prediction Project (GAPP) Surface Radiation Budget (SRB) project (Pinker and Lazslo, 1992; Pinker et al., 2001). According to the online documentation at <http://metosrv2.umd.edu/~srb/gcip>, these datasets have the following potential variables, with one variable and time period per file:

- Surface downward flux (denoted RSD in MM5 and TOPLATS)
- Surface downward photo-synthetically active radiation
- Top of atmosphere downward flux
- Top of atmosphere upward flux
- Cloud cover fraction
- Surface skin temperature
- Surface albedo

The following file types are generally available: instantaneous, hour-average, and daily. The instantaneous values at the instant of observation were not properly time-stepped, and would have required further processing to generate time-stepped output usable by TOPLATS. Daily average data were not useful for Phase 2b, although they might be useful for later analysis. The hourly average data were most appropriate, and can be time-stamped on the half-hour so that time-interpolation without phase error was possible.

Note also that this dataset contains at least two different grids. For Phase 2b, the pre-July 2001 grid definition was used.

2.1 Temporal Interpolation

MCNC learned that the hour-average data were constructed from the instantaneous satellite scan data by renormalizing RSD by the hour-mean cosine of the solar zenith angle (MUBAR; Pinker, 2001). However, the formula used was not strictly correct. When going from the instantaneous to the hour-average solar fluxes, the factor

$$mu(t) \,/\, \mathrm{MEAN}(\text{from } t=H \text{ to } t=H+1(mu(t)))$$

was applied, where $mu(t)$ is the cosine of the solar zenith angle at time t and H is hour. Negative values were replaced by a "missing"-flag value of -999.0. When this was done, cancellations in the computation of that mean for hours when *mu* takes on both positive and negative values (i.e., during hours that contain a sunrise or sunset) occurred, yielding unrecoverable underestimates of RSD for sunrise/sunset hours, an unacceptable situation

for high-resolution coupled modeling. Instead, the following factor should have been used:

$$mu(T) / \text{MEAN}(\text{from } t=H \text{ to } t=H+1 \ (\text{MAX}(mu(t), 0.0))$$

2.2 SRB Data Filters

Two data filters were developed to deal with the above problem as well as with the problem of missing and/or defective records in the input data (as determined by extensive manual quality assurance [QA] examination).

The first filter, SRB2IOAPI, reads potentially multiple SRB files for a common grid and time period, and merges them into a single gridded Models-3 input/output Application Program Interface (I/O API) file over that time period. MCNC's Package for Analysis and Visualization of Environmental Data (PAVE) is then used to analyze and QA the data. At this point, it is essential that the output of this filter undergo manual QA. For example, manual QA of the August 25-31, 1998, SRB data with PAVE shows that there are several missing daytime hours, as well as one hour that has clearly erroneous satellite-scan values. Once "missing" or "unacceptable" values were identified, they were removed by the second SRB filter program.

This second filter, GSW2SOLAR, reads the SRB/MUBAR data set produced by the SRB2IOAPI filter and then "zeros-out" RSD for a user-selected set of time steps that fail the manual QA step. Further, GSW2SOLAR "zeros-out" sunrise/sunset hours, where the existing renormalization is incorrect, as described above.

At each valid column, row, and hour, GSW2SOLAR calculates the variable SOLAR(c,r,h) = SRB(c,r,h)/MUBAR(c,r,h) that represents the solar radiation incident (SOLAR) on a zenith-normal plane; SOLAR(c,r,h) is initialized to zero elsewhere, where c = column number, r = row number, and h = hour. For each row and column in the grid, GSW2SOLAR fills in the holes in SOLAR by time interpolation from valid values in the interior of the time period, and by extension-by-constant for the initial and terminal segments—e.g., if h is the first hour for which SOLAR(c,r,h) > 0, all values from SOLAR(c,r,1) to SOLAR(c,r,h-1) were set to SOLAR(c,r,h).

Finally, GSW2SOLAR writes variable SOLAR out to a second gridded file, denoted SOLAR_CRO_2D, which is the final form used by the SRB readers. For this file, variable SOLAR is defined everywhere, and time interpolation is handled properly following the discussion above.

2.3 SRB Reader Method in TOPLATS

The implementation of SRB data within TOPLATS is accomplished in a manner similar to that for the Next-Generation Radar (NEXRAD) data: the SRB data may be selected as an input method at run-time as part of a list of reader methods in the TOPLATS run script.

The SRB reader method interpolates the value of SOLAR to the center of the current time step, calls a subroutine MUFACTOR (described below) to compute the correct time-step mean solar zenith angle cosine factor, MUFAC, and multiplies the two to arrive at current time-step mean values or RSD for the SRB grid. Note that since MUFACTOR correctly deals with sun-over-the-horizon effects, sunrise and sunset are resolved correctly even with very short TOPLATS time steps. The TOPLATS SRB reader then performs bilinear interpolation of the resulting RSD to the TOPLATS superpixel centroids in a manner similar to other reader methods.

Subroutine MUFACTOR calculates the gridded value of

$$\mathrm{MUFAC}(c,r,T,DT) = \mathrm{MEAN}(t=T\ t=T+DT\ (\mathrm{MAX}(mu(t), 0.0)))$$

(where c = column, r = row, T = time, and DT = time step) which has the property that $\mathrm{SOLAR}(c,r,T+DT/2)\cdot\mathrm{MUFAC}(c,r,T,DT)$ is the correctly normalized mean value of RSD for the time step from T to $T+DT$, where $\mathrm{SOLAR}(c,r,T+DT/2)$ is the time-interpolated value at the center of that time step. Figure 2.1 shows an example SRB image from the Houston/Galveston region.

2.4 Figures for Section 2

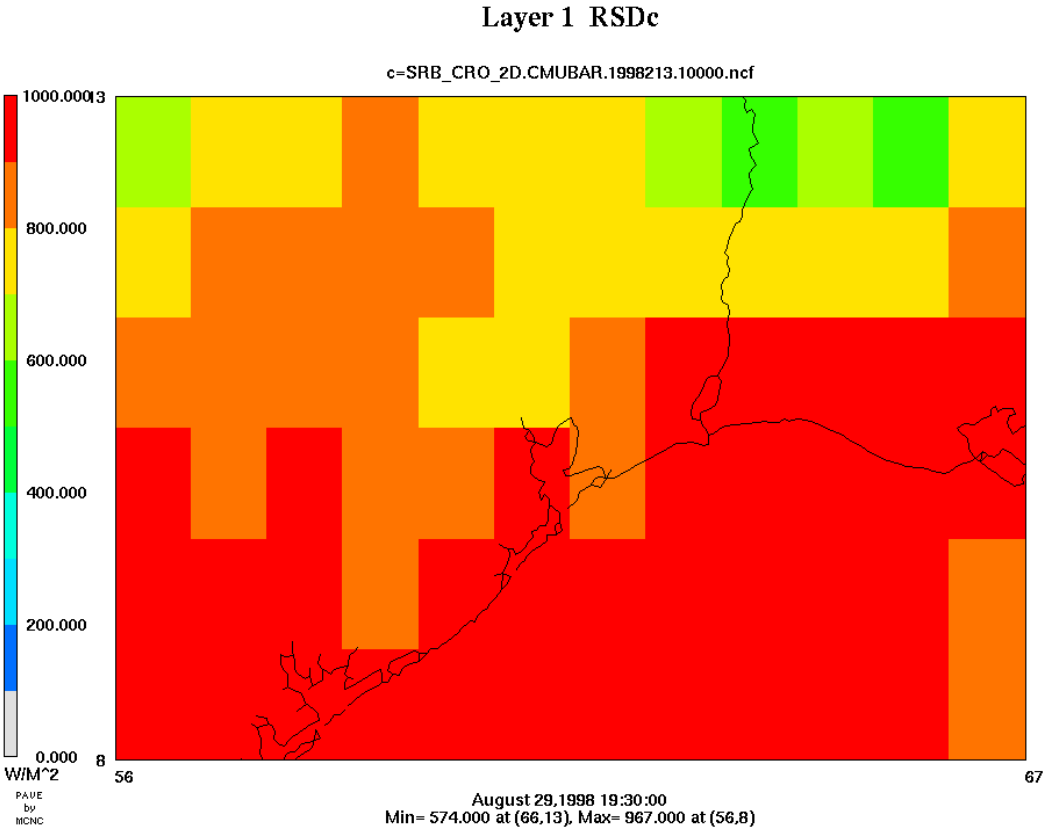

Figure 2.1. Example SRB downward solar radiation (RSD) image for the Houston/Galveston, Texas region.

3. Results of TOPLATS Reruns Using SRB Data

Because surface measurements of RSD were limited in the HGA, the use of RSD from SRB data was investigated. This section describes that investigation and its results.

3.1 SRB Data Example

Figure 3.1 shows RSD on August 29, 1998, at 1900 UTC from interpolated surface stations and as calculated by the uncoupled MM5 V3.4. The figure indicates upwards of 200 Wm^{-2} low biases in the station data in some locations. Overall, the scarcity of stations with RSD measurements in the HGA leads to a nearly uniform interpolated field at locations far away from the stations. The MM5-calculated values on the right side of the figure show significant areas of lower radiation values associated with spurious clouds produced by the simulation.

In contrast to Figure 3.1, Figure 3.2 shows RSD from the SRB data on August 29, 1998. Because the surface flux data are given as hourly averages, Figure 3.2 illustrates two time periods: from 1800-1900 UTC and from 1900-2000 UTC. A comparison of Figure 3.1 with Figure 3.2 illustrates the following general conclusions about the SRB data. First, the native spatial resolution of the SRB data (approximately 0.5 deg) is coarser than MM5's (4 km), but able to resolve much more spatial detail than interpolation of the available station data. Second, the values in and around Galveston Bay are generally 200-300 Wm^{-2} higher in the SRB data compared to the MM5 output due to the presence of spurious clouds in the MM5 simulation without TOPLATS. Finally, the low values observed at the station to the northwest of Houston are not verified by the SRB data.

Given that the SRB RSD values appear to be superior to interpolated station data, the following subsections describe the effects of these differences on TOPLATS-modeled surface fluxes.

3.2 Domain-averaged SRB Versus Station Data Comparisons

Consistent with the example presented in Section 3.1, the domain-averaged comparisons of SRB-based RSD and station data-based RSD confirm a low bias in the station data relative to the SRB data (Figure 3.3). The magnitude of this bias ranges from 0 to almost 200 Wm^{-2} (approximately 0-20%); however, it does not follow a clear pattern with time.

These differences have a large effect on the TOPLATS-modeled sensible heat flux (HFX), as shown in Figure 3.4. The magnitude of the HFX and the difference in HFX as reported using both SRB and station data grow during the episode. The physical process of soil dry-down, as modeled in TOPLATS, contributes to this growth. This dry-down is also reflected in the latent heat flux, which decreases over time, as shown in Figure 3.5. However, given that HFX is the primary determinant of PBL heights, it is important to

note that errors in RSD are primarily reflected in HFX rather than in latent heat flux. Thus, the negative impact of low-biased station-based RSD was reflected in unacceptably low PBL heights in the initial Phase 2 results.

3.3 Spatial SRB versus Station Data comparisons

Given that the domain-averaged solar radiation fluxes indicate substantial differences depending on the radiation data source, it is useful to explore the spatial patterns of these differences and their relation to the sensible heat flux pattern. Figure 3.6 illustrates differences in RSD and associated differences in HFX for August 25 at 1900 UTC (near solar noon). Similar results are obtained for the other days in the episode. For example, on August 27, the domain-averaged bias depicted in Figure 3.3 is small, but, as shown in Figure 3.7, differences near the stations are quite large, suggesting potential issues with the observations, especially since this was nearly a cloud-free day.

The end of the episode reflects the largest domain-averaged bias. Figure 3.8 illustrates this for August 29, 1998, at 1900 UTC. In this case, the convection mentioned above is brushing the northeastern part of the domain, but it is not reflected in the station data; all stations are in the Houston vicinity. Additionally, in the Houston/Galveston area and southwest, a consistent low bias in the station data relative to the SRB data is seen—hence the large domain-averaged bias, particularly in the morning hours. This bias would seriously degrade the ability to properly model the morning transition from stable to unstable PBL.

The preceding discussion indicates that there are substantial differences between the downward solar radiation forcing and associated sensible heat fluxes when using SRB products versus spatially interpolated station data. It should be noted that the SRB products are not error-free, and may not always represent "ground-truth." However, given that the spatial pattern of energy fluxes is critical for resolving circulations in a weakly forced environment typical of ozone exceedance episodes, the benefits of using the SRB data likely substantially outweigh the disadvantages.

3.4 Figures for Section 3

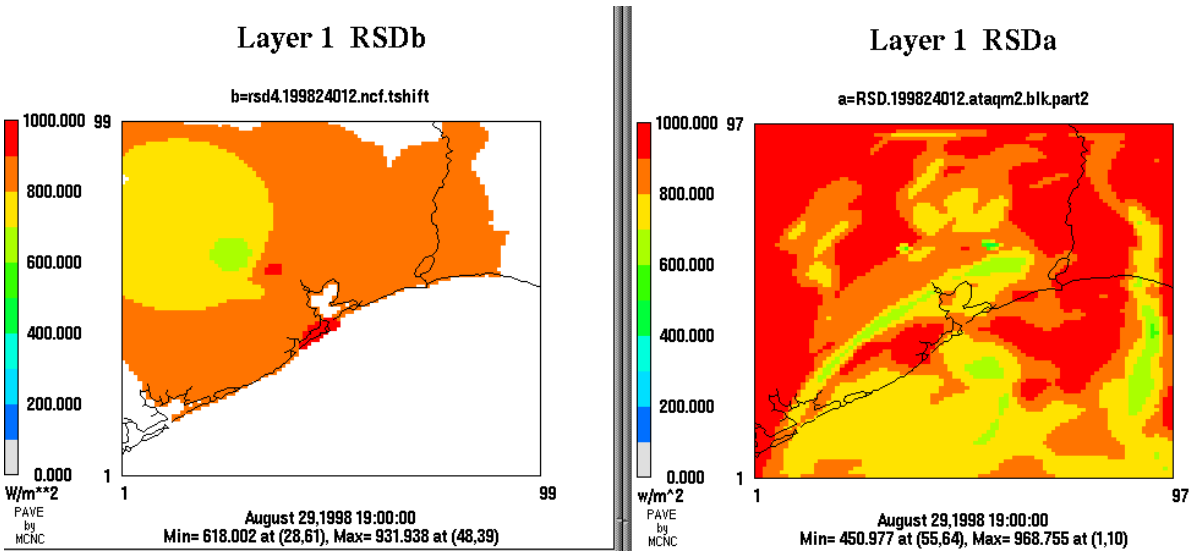

Figure 3.1. Downward surface flux of solar radiation (RSD) on August 29, 1998, at 1900 UTC from interpolated surface stations (left) and as calculated by MM5 V3.4 (right).

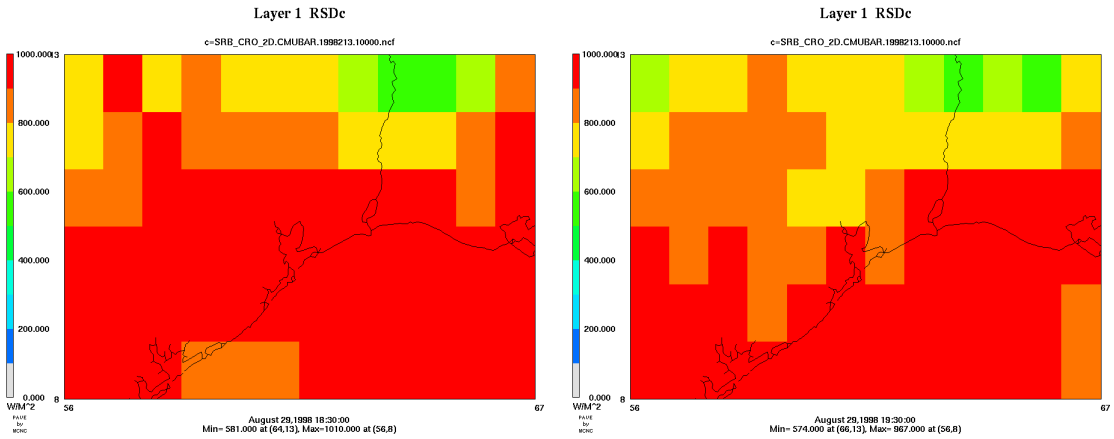

Figure 3.2. Downward surface flux of solar radiation (RSD) on August 29, 1998, from SRB data. The left panel shows hourly average RSD from 1800-1900 UTC, and the right panel shows hourly average RSD from 1900-2000 UTC. Comparison with Figure 3.1 demonstrates the potential for correcting surface flux biases caused by station data and/or MM5 internal calculations.

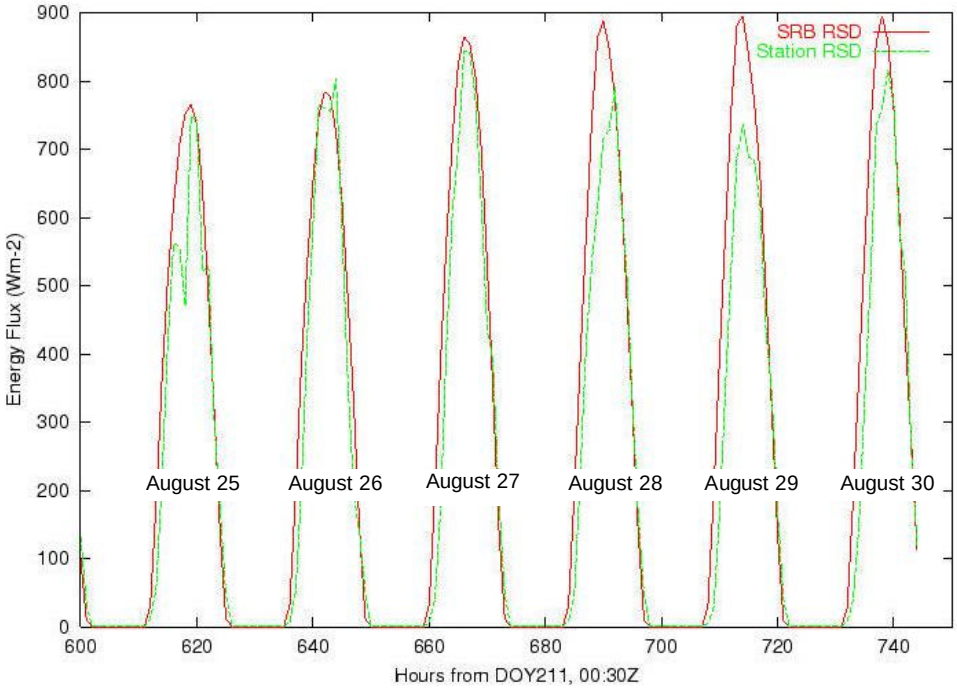

Figure 3.3. TOPLATS domain-averaged RSD using the SRB data versus that estimated by station data using inverse-distance weighting. The August 25-30, 1998, episode is depicted.

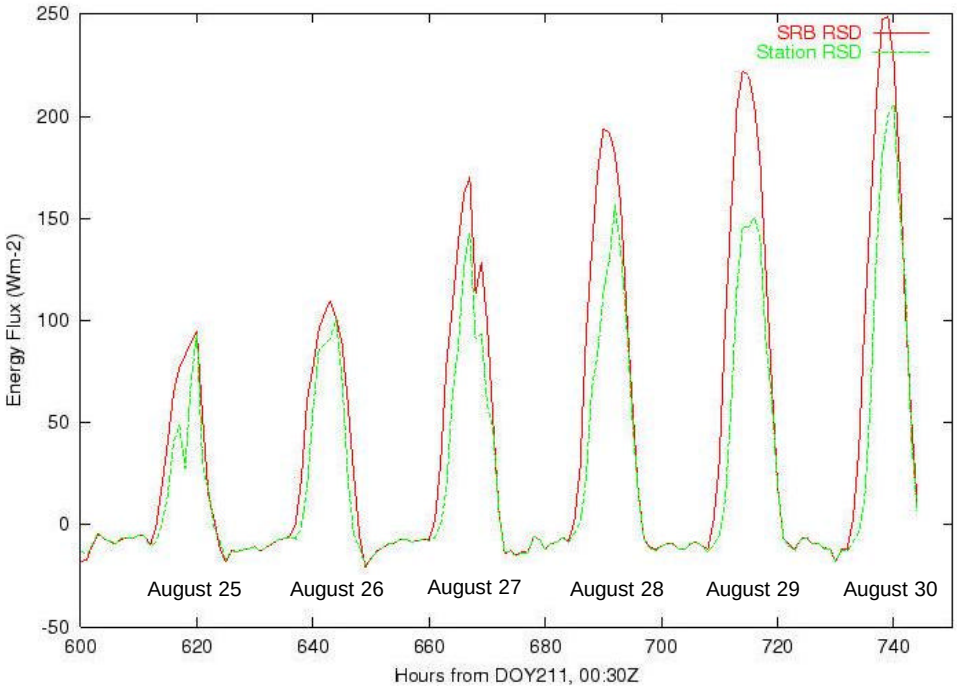

Figure 3.4. TOPLATS domain-averaged HFX using the SRB data versus that estimated by station data using inverse-distance weighting. The August 25-30, 1998, episode is depicted.

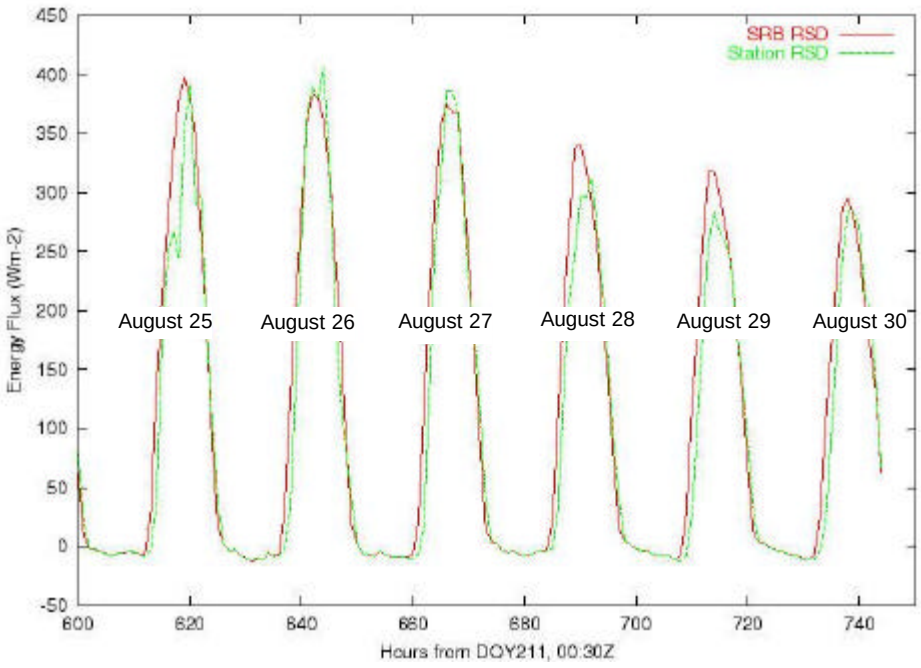

Figure 3.5. TOPLATS domain-averaged latent heat flux using the SRB data versus that estimated by station data using inverse-distance weighting. The August 25-30, 1998, episode is depicted.

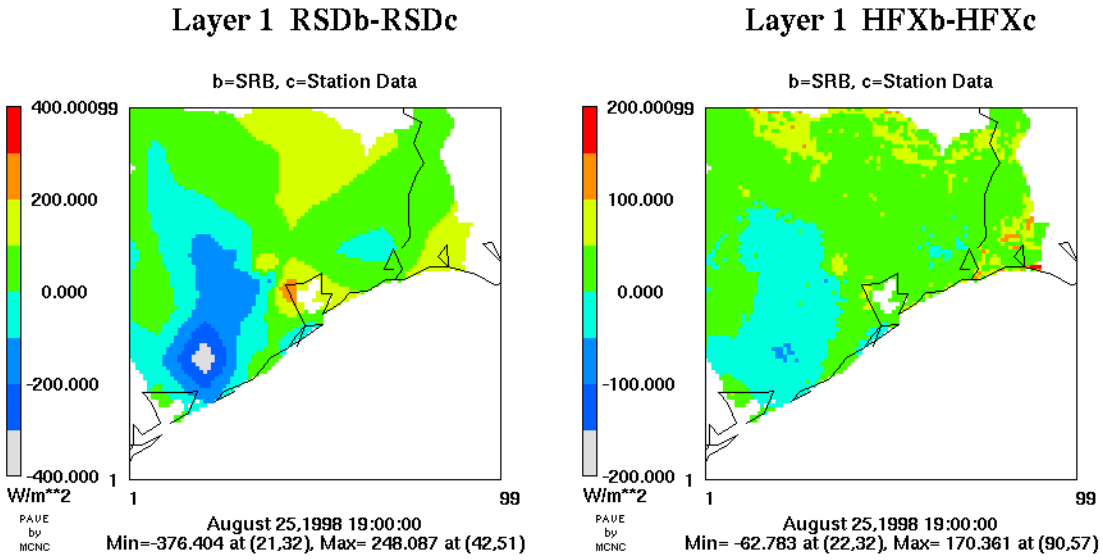

Figure 3.6. Differences in RSD and HFX for August 25, 1998, at 1900 UTC. These figures illustrate the presence of cloudy (gray-blue) and cloud-free (yellow-orange) areas that are resolved with the SRB data but not with the station data.

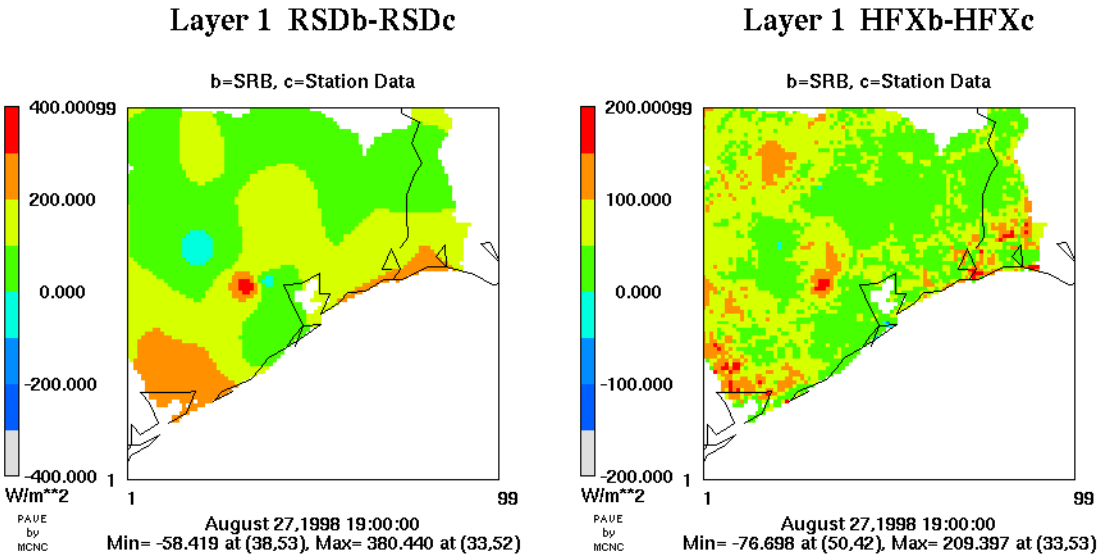

Figure 3.7. Differences in RSD and HFX for August 27, 1998, at 1900 UTC. These figures illustrate the presence of cloudy (gray-blue) and cloud-free (yellow-orange) areas that are resolved with the SRB data but not with the station data.

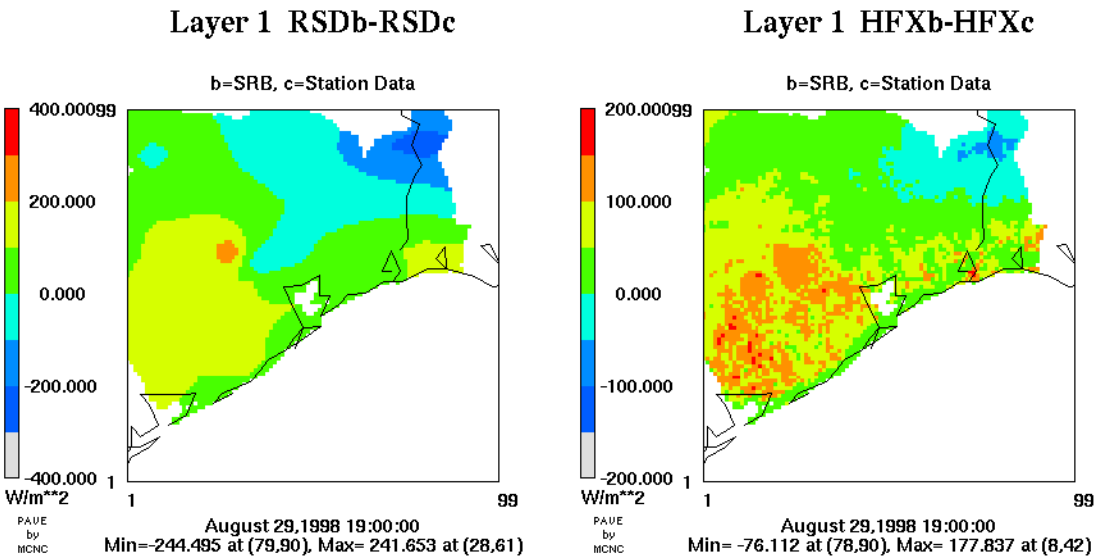

Figure 3.8. Differences in RSD and HFX for August 29, 1998, at 1900 UTC. These figures illustrate the presence of cloudy (gray-blue) and cloud-free (yellow-orange) areas that are resolved with the SRB data but not with the station data.

4. Phase 2b MM5 Configuration

As noted in Section 1, all MM5 preprocessing and model runs were performed with V3.4 of the modeling system. The episode was divided into two segments (S1 and S2), S1 consisting of the first 84 hours, and S2 consisting of the final 60 hours. Runs began at 0000 UTC on August 25 and ended at 0000 UTC on August 31. For S1, only Global Data Assimilation System (GDAS) data were available for initialization, boundary conditions, and nudging. For S2, archived Eta Data Assimilation System (EDAS) data were available.

4.1 Outer-Domain (36 km-12 km) MM5 refinements

In the initial Phase 2 effort, one outer-domain 36 km-12 km run was conducted (hereafter denoted case "van") using one-way nest interaction and the NESTDOWN program to produce 4-km initial and boundary conditions. However, analysis of that run showed the production of substantial spurious parameterized Kain-Fritsch (KF) convection (on August 25 and 29) near the 4-km domain boundary, resulting in undesirable advection effects. Figures 4.1 and 4.2 show examples from August 25 at 1600 UTC and August 29 at 2300 UTC, respectively. On August 25, the model output showed that convection began early in the day, just inland of the coast, while the satellite observed that convection began later in the day (along with the sea breeze) and propagated inland. This was not of major concern because the first exceedance did not occur until August 26.

On August 29, the effect was more serious. On this day, satellite and surface data indicated the formation of a cluster of convective clouds well north of Houston around 1900 UTC, propagating along a surface-convergence axis extending southwest-northeast. This convection was far enough away from HGA that its anvil-outflow-subsidence probably prevented cloud formation in the area during the latter half of the afternoon. Though the initial Phase 2 run does initiate some convection, the location (too near HGA) and evolution (separate "rings" of outflow-based convection propagating in opposite directions across the domain) of the convection is severely compromised. Figure 4.3 shows the effects of the August 29 spurious-convection event on the interior 4-km domain winds, where winds are strongly converging toward the domain interior from three directions (east, north, and west) in an unrealistic manner.

Sensitivity studies were run with the 36 km-12 km model to determine an appropriate approach to correcting the problem. Experience with the KF scheme suggested that the ring-like patterns shown in Figure 4.2 could be the result of the interaction of the default downdraft formulation and a weak synoptic environment. The default formulation forces the parameterized downdraft to detrain mass entirely within the lowest model level, which in the present 43-layer implementation, confines it to a layer about 35 meters thick. For strong storms whose downdraft equivalent potential temperature is significantly lower than their immediate environment, this might be realistic. But, in general, the downdraft is likely to entrain enough surrounding air to mix-out some of the initial

difference in density, effectively detraining itself as it subsides. By allowing it to detrain through a slightly deeper layer, in this case 50 mb, the "overactive" downdraft and its effects are suppressed. Simulations that used this formula were denoted "kf5.

Independently, the effect of two-way nesting was tested, because this had not been used in the initial Phase 2 configuration. Some modest improvements were noted (not shown). The most significant improvements were achieved by combining the downdraft modifications with two-way nesting (Figure 4.4). Denoted case "kf5.2w," it was chosen as a second outer-domain simulation.

Finally, a third simulation (denoted case "kf5.2w.c2") in which TOPLATS/SSATS one-way coupling to the 12-km domain was added to the "kf5.2w" configuration, was conducted. It too provided improvement (Figure 4.5). Since MM5 used the Rapid Radiation Transfer Model (RRTM) for all 36 km-12 km runs (but not the 4-km runs), TOPLATS coupling to longwave radiation was turned off for case "kf5.2w.c2". The potential inconsistency in longwave parameterizations between the outer 36 km-12 km model (using RRTM) and the inner 4-km model (using LWRAD) would be expected to produce only slight nocturnal near-surface boundary condition effects. Thus, these effects were ignored for this study.

Table 4.1 summarizes the overall strategy used to produce the outer-domain runs, their differences, and their associated naming conventions. As discussed, the two 36 km-12 km runs added for Phase 2b utilized two-way nesting as opposed to one-way nesting in the original run. Since two-way nesting provides an interactive feedback mechanism in the grid interior, FDDA was not used on the 12-km grid for these two runs. Further, analysis nudging is suspect at the finer scales because it may result in suppression of fine-scale structure; that is, the analyses themselves are provided on relatively coarse grids, and the nudging in the model is a relatively strong constraint, so that matching of the spatial/temporal scales of the analyses and the simulation is an important consideration. Though no formal data quality analysis was conducted on the analysis fields used for FDDA, they were from the best available archived NCEP analyses. The procedures used to process these data are discussed in Section 4.3.

Table 4.1. MM5 V3.4 36 km-12 km runs.

Case	Nest Strategy	KF Convective Cloud Formulation	FDDA Strategy	Coupling Strategy
"van" (Original Phase 2)	One-way	Standard	GRID-nudging, both 36-km and 12-km grids	Uncoupled
"kf5.2w"	Two-way	Downdraft modified to detrain over 50-mb deep level	GRID nudging on 36-km grid only	Uncoupled
"kf5.2w.c2"	Two-way	Downdraft modified to detrain over 50-mb deep level	GRID nudging on 36-km grid only	One-way coupled on 12-km domain, longwave radiation not coupled

4.2 Phase 2b Modeling Domains

The Phase 2b four-nest configuration of MM5 V3.4 is shown in Figure 4.6. The map projection is Lambert-conformal with central latitude/longitude at 39°N/98°W. The outer, 36-km domain has 112 x 140 grid points, and the inner, 12-km domain has 121 x 121 grid points. The 4-km domain has 70 x 70 grid points. A fourth, very-high-resolution 1.33-km domain was configured but not used. The TERRAIN program namelist defining all of the domains and input data is provided in Appendix A. Terrain and U.S. Geological Survey (USGS) 24-category land-use datasets available from the National Center for Atmospheric Research (NCAR) were used for the outer domains.

4.3 Phase 2b Preprocessing

The MM5 modeling system includes a series of preprocessors that are used to prepare the input files needed to run the MM5 meteorological model. This section describes the preprocessing performed. The names of the preprocessor programs are listed below along with a description of their function.

- TERRAIN - domain configuration, create terrestrial fields
- REGRID - create first-guess meteorological fields on MM5 grid
- RAWINS - perform objective analysis (add observations to the first-guess)
- INTERPF - interpolate pressure-level data to model coordinate
- NESTDOWN - create one-way nest or nested model input
- INTERPB - interpolate model sigma-level data to pressure levels

A particular dataset issue relevant to MM5 was the lack of availability of EDAS analysis fields for the first part of the episode, August 25-28, 1998. Therefore, as indicated previously, the episode was run as two segments.

For S1, the analysis fields were only available at 12-hour intervals. Thus, the 36 km-12 km grids (two-way nesting) were run twice. The first pass used analysis nudging at 12-hour intervals. In the second pass, these results were fed into the INTERPB program to produce 3-hour fields. These fields were fed back through the RAWINS and INTERPF programs, and the results were used to nudge MM5 with 3-hour analysis fields. For S2, the EDAS analysis fields were fed into REGRID, then RAWINS, INTERPF, and finally MM5.

Reconfiguration of the 4-km domain between Phase 2 and Phase 2b led to the need for additional processing with the TERRAIN and NESTDOWN programs. TERRAIN was configured as described in Section 4.2 and re-run in order to supply all of the uncoupled simulations with appropriate lower boundary land-use data and supply all of the runs with modified 4-km terrain data. NESTDOWN was run using the original 36 km-12 km "van" runs to produce new boundary condition data for the new "van" 4-km runs. Additional NESTDOWN runs were conducted to extract boundary condition data for the "kf5.2w" and "kf5.2w.c2" sets of 4-km runs. Since the reconfigured 4-km domain was designed to completely cover all of the TOPLATS/SSATS geographic extent (Figures 5.1 and 5.2),

every MM5 grid cell was coupled to the independent land- and sea-surface flux models, providing for complete consistency within the 4-km domain.

4.4 Phase 2b MM5 Physics Configuration

MM5 physics options are configured at compile time using the configure.user file. The relevant portions of the 36 km-12 km configure.user file for the coupled model are presented in Appendix B. This configuration was used for the uncoupled model as well. In the uncoupled case, libiocpl.a is simply not utilized. Table 4.2 shows the major physics options used in the outer domain runs.

Table 4.2. Major physics options used in 36 km-12 km MM5 simulations.

Parameterization	Process Represented	Scheme Used
Explicit Moisture	Grid-scale Clouds and Precipitation	Reisner-1
Convection	Convective Clouds and Precipitation	Kain-Fritsch
Boundary Layer	PBL Mixing Effects	Blackadar with SMRAQ Modifications
Longwave Radiation	Thermal Radiative Emission	Rapid Radiative Transfer Model
Shortwave Radiation	Solar Radiative Input	Dudhia (Grell et al., 1995)
Soil	Land-Surface Atmosphere Interaction	Five-layer for Uncoupled Runs; TOPLATS (12 km only) for coupled runs
Shallow Convection	Shallow Convective Cloud Mixing	None

Minor changes were made to the model configuration prior to making the 4-km runs. The Dudhia Longwave Radiation Scheme (LWRAD) replaced the RRTM scheme for terrestrial radiation, since TOPLATS is coupled with LWRAD. Further, no convective parameterization was used. That is, KF was turned off, allowing the Reisner mixed phase explicit moisture scheme (Reisner et al., 1998) to produce all clouds at the grid scale. This change, necessitated by the change in grid scale, plays an important role in the relative success of fine-scale runs at grid resolutions of 4 km or less. In both cases, the Blackadar-based HIRPBL—with Seasonal Model for Regional Air Quality (SMRAQ) modifications—was used since it, too, couples with TOPLATS. TOPLATS itself replaced the five-layer soil model for coupled runs.

The SMRAQ modifications to HIRPBL were introduced by MCNC during the SMRAQ project (http://www.emc.mcnc.org/SMRAQ) in order to improve deficiencies in the default version contained in MM5, which tended to produce too-rapid late-afternoon collapses in PBL height, and caused other problems.

The approach proposed by Holtslag (1990) is implemented in the revision. Here, the Bulk Richardson (BR) number is calculated for every model level starting from the lowest. Then, the vertical level for which the BR number exceeds the Critical Richardson number (=0.25) is determined. For example, if the BR number for levels 15 and 16 is respectively 0.31 and 0.18, then the PBL top lies in between the heights of those two levels, and can be estimated by linearly interpolating to a height at which the BR number is exactly 0.25. This linearly interpolated height is considered to be the height of the PBL above ground level.

Figure 4.7 shows a comparison of the difference between the default scheme and the SMRAQ-modified scheme for a reference simulation conducted as part of the SMRAQ project. The figure depicts a 66-hour section of a 5-day run that clearly shows improvements in the behavior of the calculated PBL depth at a grid cell in far SW Louisiana, representative of typical HGA conditions. The modifications result in smoother PBL growth and decay along with a longer-lasting daytime mixed layer.

In addition to these major parameterizations, MM5 was configured with 43 vertical layers. These are described by McHenry et al., 2001, and are not repeated here.

4.5 Phase 2b MM5 Run-Time Configuration

There are numerous run-time switches, generally input as namelist variables, with which to turn on or off various features of MM5 V3.4. In Appendix C, the namelist portion of the job-deck shows the options used for the 36 km-12 km domain. For the 4-km domain, the three-dimensional Coriolis force, nest feedback, and FDDA options were turned off. Otherwise, the run-time switches were identical for the outer and inner domains.

The three-dimensional Coriolis terms were neglected in the 4-km domain because it was decided that differences between the coupled and uncoupled model results would be easier to physically interpret if the standard horizontal Coriolis approximation was used. In the standard approximation, terms in the cross product of the Earth's rotation vector and the three-dimensional wind vector, which either contain the vertical velocity, w, or are directed in the vertical direction of the unit vector k, are neglected. These terms involve the cosine of the latitude and so increase in magnitude toward 2Ω from pole to equator. For horizontal motions, they lead to small upward or downward accelerations proportional to the grid-scale vertical velocity, which is typically one to two orders of magnitude smaller than the horizontal wind. For vertical motions, they lead to small westward or eastward accelerations. The standard approximation neglects these vertical terms because they are mostly small compared to other terms in the respective horizontal and vertical momentum equations.

Since the inertial period, given as 24-hours/2sinφ, is approximately 1 day at 30^0N latitude (approximately the latitude of the HGA), large-scale inertial oscillations--induced by both diurnal frictional differences and unequal heating effects in the presence of a weak synoptic pressure gradient--are typically in-phase with the diurnal cycle. Neilson-

Gammon (2001a, 2001b) notes that preliminary analyses of data from the Texas Air Quality Study-2000 (TXAQS-2000) indicate evidence of such oscillations and that the two causes mentioned may have been contributing factors, thereby playing a role in determining the evolution of the surface and aloft winds during that study.

The scale of the inertial oscillations observed during TXAQS-2000 are similar to the type reported in Moore (2002), who describes them in relationship to the evolution of low-level jets. Moore notes that in the south-central Midwest, a nocturnal inversion wind maximum forms during the late spring-summer months at the top of the *nocturnal* inversion under synoptically quiescent conditions, reaching maximum intensity around 1-3 a.m. This feature may be manifested as "adverse wind shear" during the following morning, in which the low-level jet mixes down to the surface after PBL growth has begun but before it has entrained (from aloft) air with much less (synoptic-scale) momentum, resulting in a stronger morning surface wind. Moore (2002) shows how, under these circumstances, such a frictional decoupling will lead to an inertial oscillation of the wind vector as the momentum attempts to regain geostrophic balance. This is shown in Figure 4.8.

Variations upon this general theory exist, some of which are cited in Moore (2002) and in Neilson-Gammon (2001a, 2001b), but none make reference to the vertical Coriolis terms, no doubt for the same scaling reasons cited above. Thus, neglect of these terms in the 4-km domain simulations was deemed unlikely to affect MM5's ability to simulate the dynamic effects resulting from heterogeneous frictional and thermal surface forcing.

4.6 Figures for Section 4

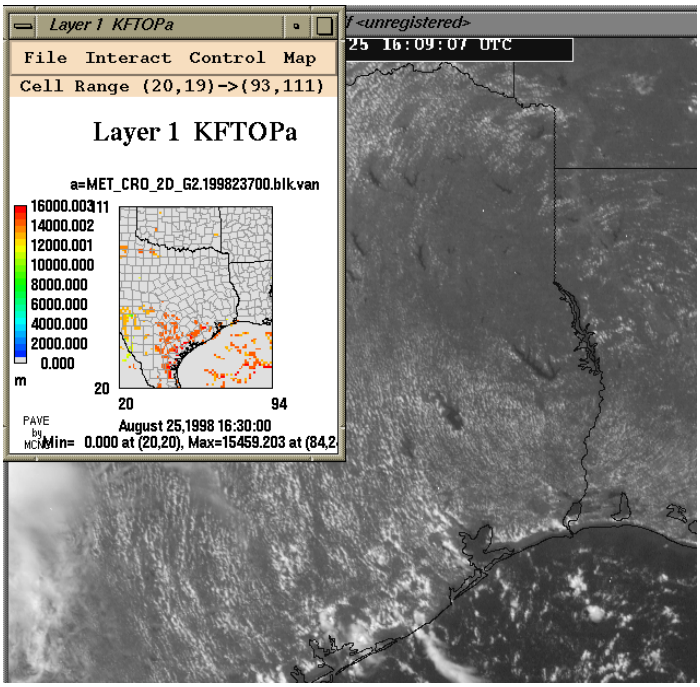

Figure 4.1. Spurious KF 12-km convection on August 25, 1998, for case "van" for the hour beginning 1600 UTC.

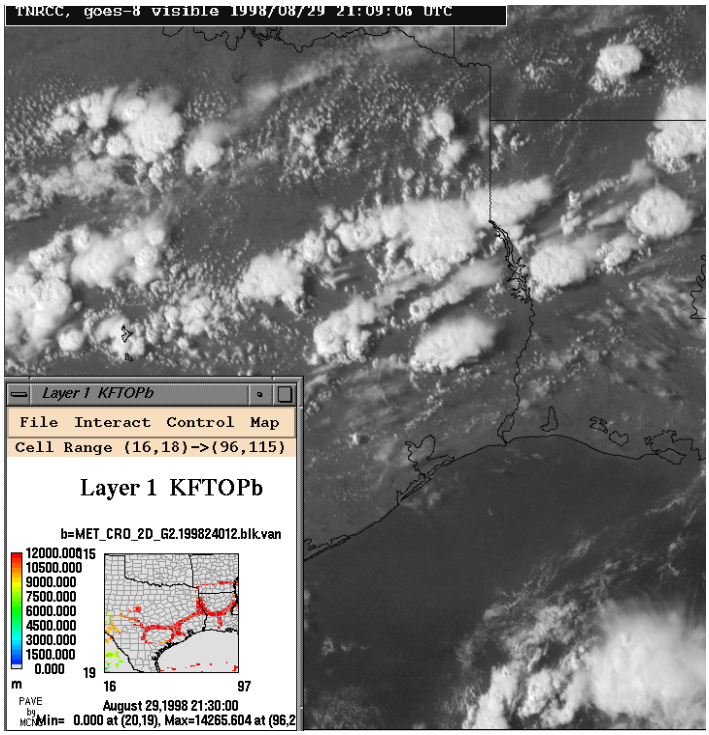

Figure 4.2. Poorly-represented 12-km KF convection on August 29, 1998, for case "van" for the hour beginning 2300 UTC.

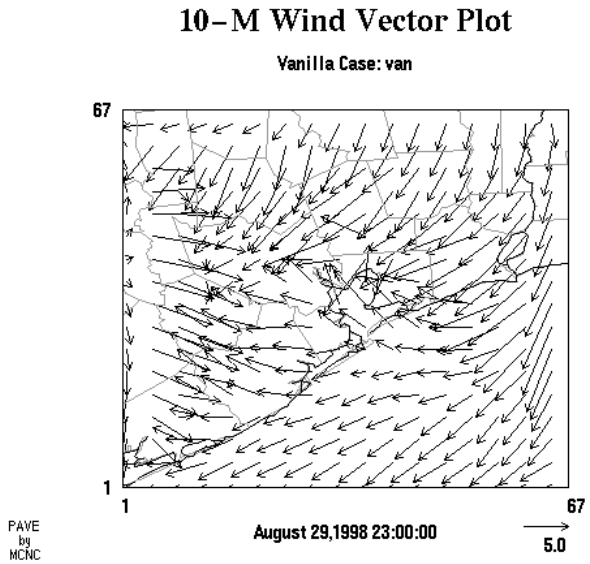

Figure 4.3. Effects of oppositely-propagating, spurious rings of KF-based 12-km convection on 4-km winds on August 29 at about 2300 UTC.

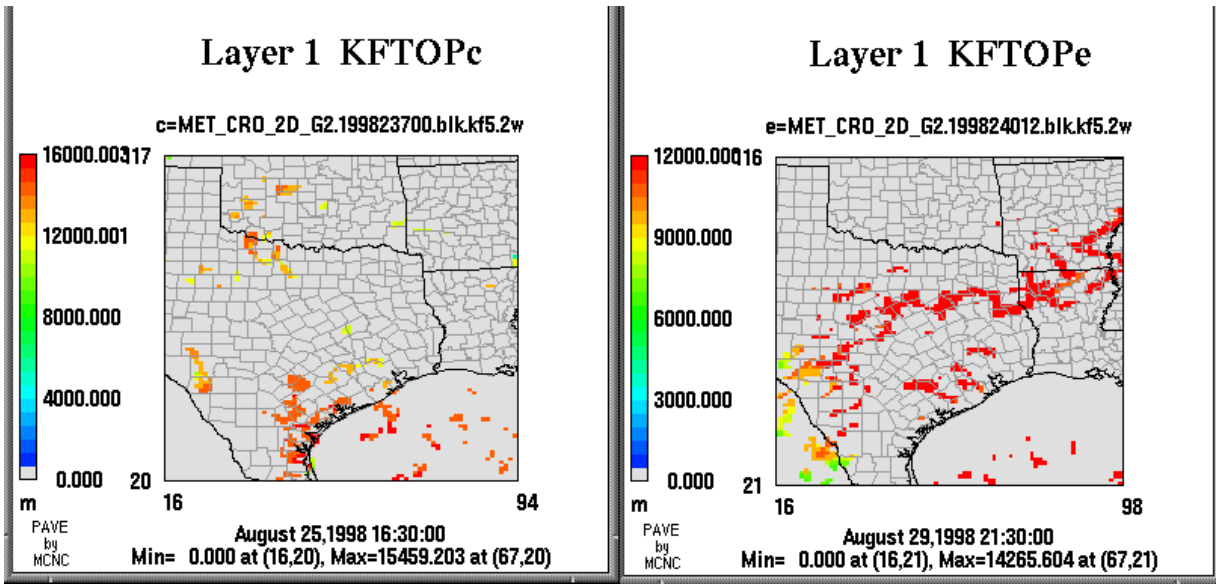

Figure 4.4. Re-run 36 km-12 km uncoupled case "kf5.2w" depicting the location and intensity of modeled KF convection on August 25 (left) and August 29 (right). This shows significant improvement over the structure, timing, and evolution of the convection compared to earlier model runs depicted in Figures 4.1 and 4.2.

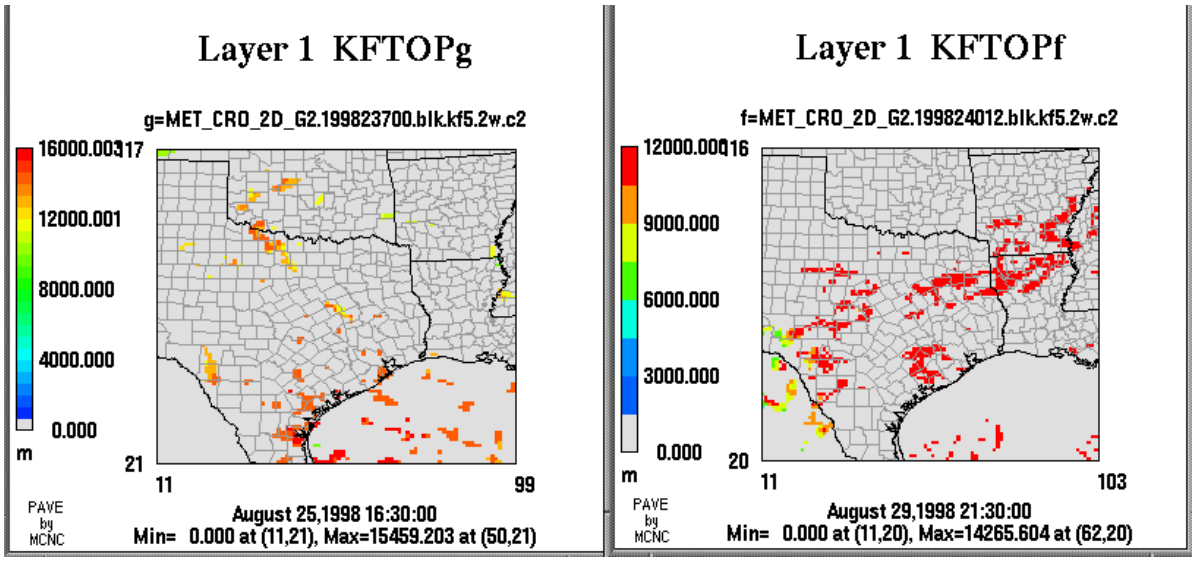

Figure 4.5. Re-run 36 km-12 km uncoupled case "kf5.2w.c2" depicting the location and intensity of modeled KF convection on August 25 (left) and August 29 (right). This shows significant improvement over the structure, timing, and evolution of the convection compared to earlier model runs depicted in Figures 4.1, 4.2, and 4.4.

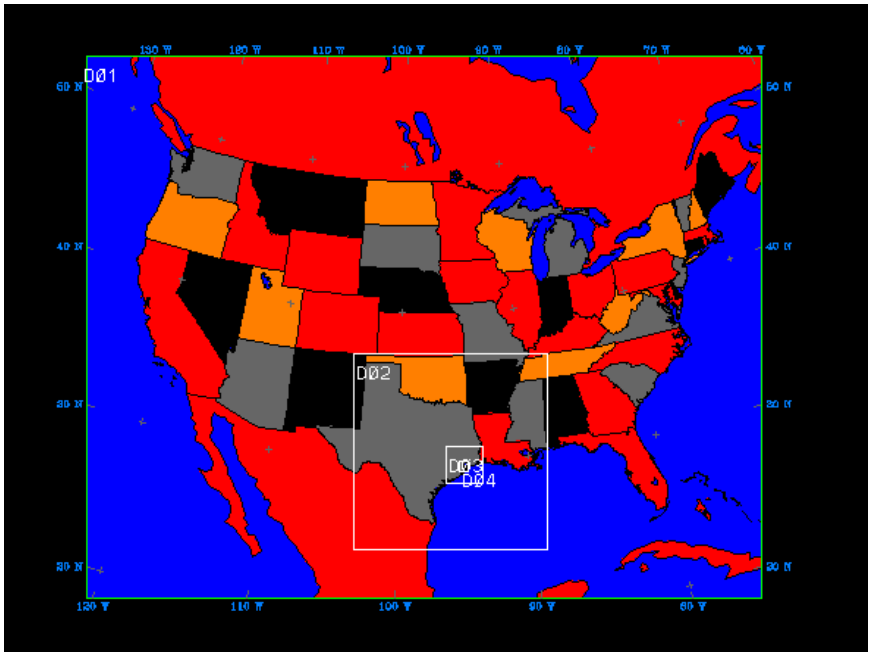

Figure 4.6. ATAQM Phase 2b MM5 36-km (D01), 12-km (D02), and 4-km (D03) domains. The 1-km domain (D04) was not used.

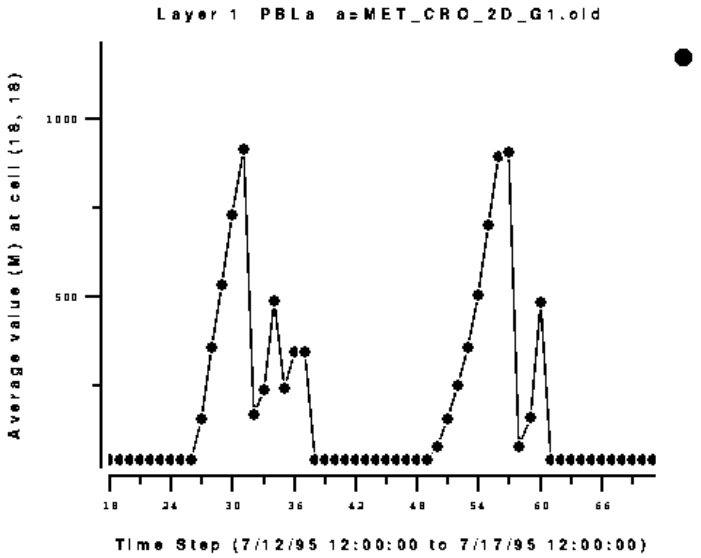

Old Scheme

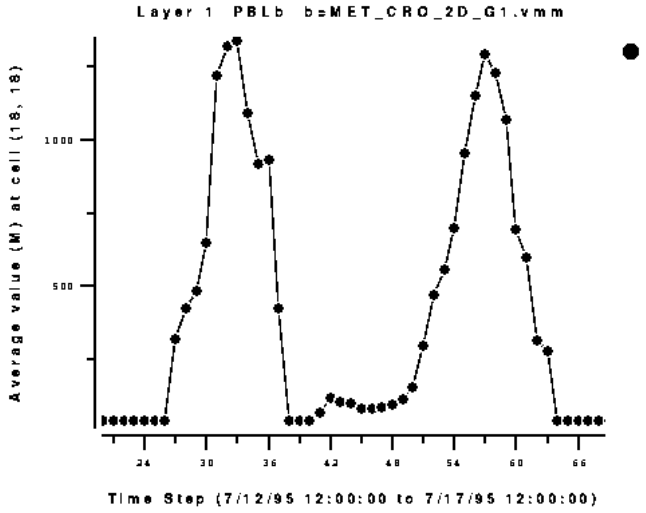

New Scheme

Figure 4.7. Depth of HIRPBL-calculated PBL height for an example grid cell in extreme SW Louisiana from a retrospective July 1995 simulation, run during the SMRAQ project. The top figure shows results using the default scheme and the bottom figure shows results using the MCNC-modified version, based on the Holtslag (1990) method.

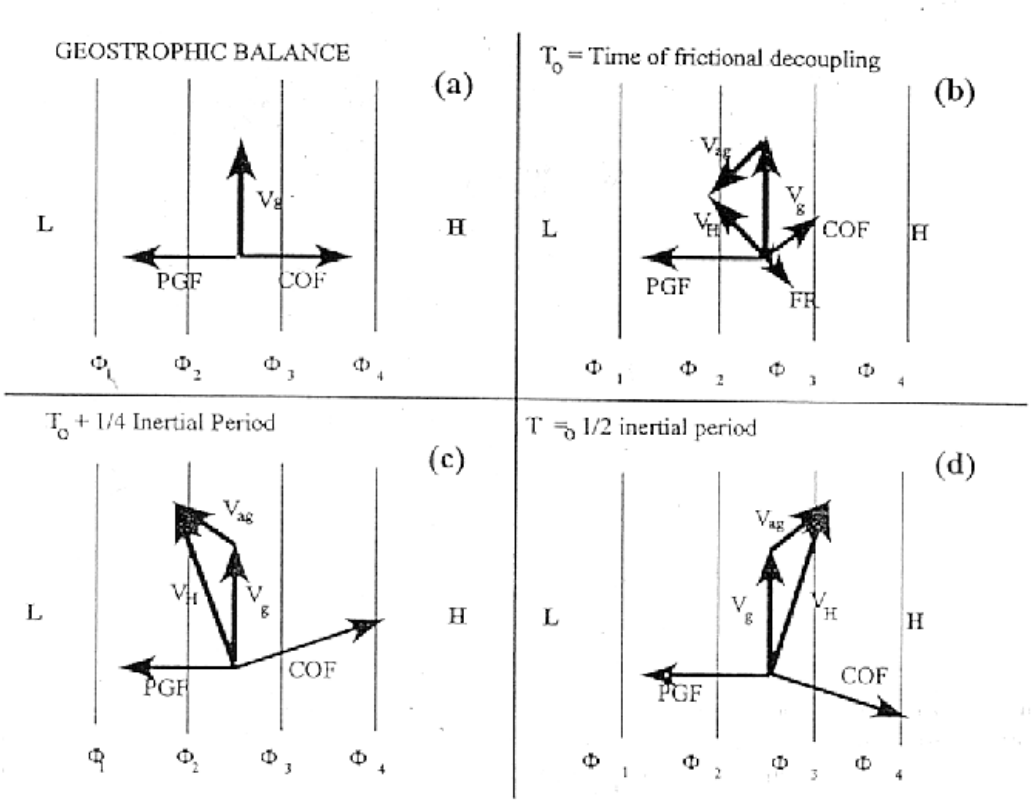

Figure 4.8. Theoretical diagram of the inertial oscillation (using an idealized Ekman-layer) of the ageostrophic wind vector about a constant geostrophic wind. Vg is the geostrophic wind, VH is the actual wind, and V_{ag} is the ageostrophic component. In panel (b), the ageostrophic component results from frictional retardation acting opposite to the mean surface wind. Upon decoupling, the wind, no longer feeling the retarding effects of friction, accelerates (at the top of the nocturnal inversion) and begins to swing back toward a geostrophic force balance (c) and then overshoots (d). From Moore, 2002.

5. MM5/TOPLATS/SSATS Coupling Strategy and Variables

5.1 Strategy

In the ATAQM, TOPLATS and SSATS are both one-way coupled with MM5 V3.4. In one-way coupling, TOPLATS and SSATS are run offline first, and flux data from them are fed into MM5. Figure 5.1 shows the combined coverage fractions of TOPLATS/SSATS in relationship to the Phase 2b 4-km MM5 domain, portraying the geographic extent of the earth-surface models that are one-way coupled with MM5. With the domain refinements described above, the combined coverage fraction is 100%.

The one-way coupling strategy permits the use of observational meteorological data to drive the earth-surface models, which in turn solve for the surface "skin" temperature and soil moisture. Since SSATS provides observed sea-surface temperatures (SSTs), the energy balance does not need to be calculated. Given the observations, both TOPLATS and SSATS calculate surface sensible and latent heat fluxes, which can then be ingested by MM5's surface physics routines.

5.2 Variables

Table 5.1 depicts the coupled variables and the MM5 routines in which the coupling occurs. Variables are interpolated from synchronized TOPLATS output to the MM5 advection time-step in all routines. The run-scripts may be used to decouple or couple any one of the variables listed, permitting sensitivity studies. A brief discussion of each coupling variable follows the table.

Table 5.1. TOPLATS and SSATS coupling variables and associated MM5 physics routines.

Variable	Units	Definition	Subroutine ingested within MM5	Function within MM5
XLEACT	W/m^2	Actual latent heat flux	HIRPBL	Used with XLEPET to estimate "moisture availability" for internal mitering calculation
XLEPET	W/m^2	Potential latent heat flux	HIRPBL	Used with XLEACT to estimate "moisture availability" for internal mitering calculation
HACT	W/m^2	Actual sensible heat flux	HIRPBL	Bottom sensible flux boundary condition
QFX	$kg/s/m^2$	Kinematic latent heat flux	HIRPBL	Bottom latent flux boundary condition
RNACT	W/m^2	Net radiation at the surface	SLAB	Echo values from TOPLATS to output files
TKACT	K	Skin temperature	SLAB	Replaces MM5 skin temperature at coupled cells
EMISG	None	Earth surface emissivity	LWRAD	Replaces emissivity within MM5; used to calculate upward-reflected component of downward longwave flux
RLU_EARTH_ ACT	W/m^2	Earth upward grey-body longwave radiation flux	LWRAD	Replaces earth upward grey-body longwave flux

XLEACT and XLEPET. TOPLATS' ratio of the actual to the potential evapotranspiration is expected to be a better measure of the soil moisture availability (MAVAIL) than the default MAVAIL values provided with MM5. In Phase 2b, this ratio is used to calculate the "internal" latent-flux "kernel." This kernel is used to help estimate the number of mitering steps (sub-time-steps) needed by HIRPBL. The equations are somewhat complex and so are not shown here, but the internal kernel is closely related to the MM5 User's Guide (Grell et al., 1995) equation 5.4.3.15. In addition, the ground virtual potential temperature is decoupled to more faithfully represent evaporative processes taking place at the surface.

HACT. TOPLATS' surface sensible heat flux is ingested by HIRPBL, replacing its native calculation at all coupled cells. This flux is used to solve for the surface-layer temperature tendency in the PBL. Positive fluxes provide a heat source, during periods when the surface is heating more rapidly than the surface-layer atmosphere. Negative fluxes provide a heat sink. Nonlocal mixing during the rapid daytime surface-layer heating results in PBL growth.

QFX. TOPLATS' surface latent flux is ingested by HIRPBL, providing a moisture source (positive flux) or sink (negative flux) for the surface layer. The 0.0 floor on QFX has been removed in HIRPBL for coupled runs, since TOPLATS provides for dew

formation. Again, daytime nonlocal mixing efficiently transports surface-based moisture throughout the PBL.

RNACT. This TOPLATS net radiation term is ingested for QA purposes.

TKACT. TOPLATS' surface temperature is ingested into the SLAB multi-layer soil model, for all coupled cells. Within SLAB, the internal MM5 energy balance calculation is ignored. TKACT replaces MM5's T_g, and is used in HIRPBL, most importantly to determine the Bulk Richardson number (BRNUM) of the surface layer. This, in turn, is used to determine the stability class, stability functions, and, ultimately, u_*, which affects the momentum fluxes. (Currently, TOPLATS is not used to couple the momentum terms directly, for theoretical reasons.) Once u_* is determined, the surface momentum fluxes are calculated. In HIRPBL, the following relation is used to solve for u_*:

$$u_* = k \times \frac{MAX\left(\langle U \rangle, 1.0\right)}{\left(\log\left(Z_a / Z_0\right) - y_m\right)},$$

where k is Von Karman's constant, $\langle U \rangle$ is the magnitude of the wind, Z_a is the layer-1 half-sigma height in m, Z_0 is the roughness length, and y_m is the stability function for momentum. In the standard MM5, the *MAX* function is apparently implemented to prevent the momentum fluxes, equal to $r\, u_*\, u_*$, from becoming small. However, during the transition from nighttime to daytime, too large a value for u_* can prevent the wind from initially accelerating under the influence of land-surface-based heating, because of the delicate balance between and interdependence among the variables in the above equation (the denominator becomes smaller with increasing instability). Once the instability is large, frictional dissipation remains large and PBL winds may not accelerate, even with downward mixing of momentum. Thus, the lighter the nocturnal surface winds, the more likely a problem is to occur with the *MAX* function implemented as above. Figure 5.2 shows a comparison of the uncoupled models' and coupled models' u_* with overlaid wind vectors at 1250 UTC on August 25, illustrating the morning transition issue.

The lack of daytime wind acceleration problem occurred repeatedly in the initial set of Phase 2b 4-km coupled runs, no matter which set of boundary conditions was used ("van," "kf5.2w," or "kf5.2w.c2"). Removing the *MAX* function corrected the problem, by allowing u_* to scale appropriately, as it should, with light morning winds.

This lack of daytime wind acceleration effect has also been observed with the standard uncoupled Gayno-Seaman PBL (GSPBL) scheme at 4 km, and it is believed to be caused by the same problem. As a result, three additional 4-km runs were added using the corrected formulation, denoted by adding the acronym "wspd" (for wind speed) to this set of 4-km runs. The run naming convention is presented in Table 6.1 in the following section.

EMISG. TOPLATS' aggregated surface emissivity is used in place of the MM5 value, in order to fully replace MM5's land surface. It is used in LWRAD, together with RLU_EARTH_ACT, to estimate the gross upward longwave radiation.

RLU_EARTH_ACT. This is TOPLATS' estimate of the earth-upward grey-body longwave radiative flux. Together with *EMISG*, it is used to calculate the longwave heating tendency resulting from land-surface properties.

Note that no shortwave coupling is necessary because in MM5 V3.4 outgoing shortwave radiation is lost to space.

5.3 Figures for Section 5

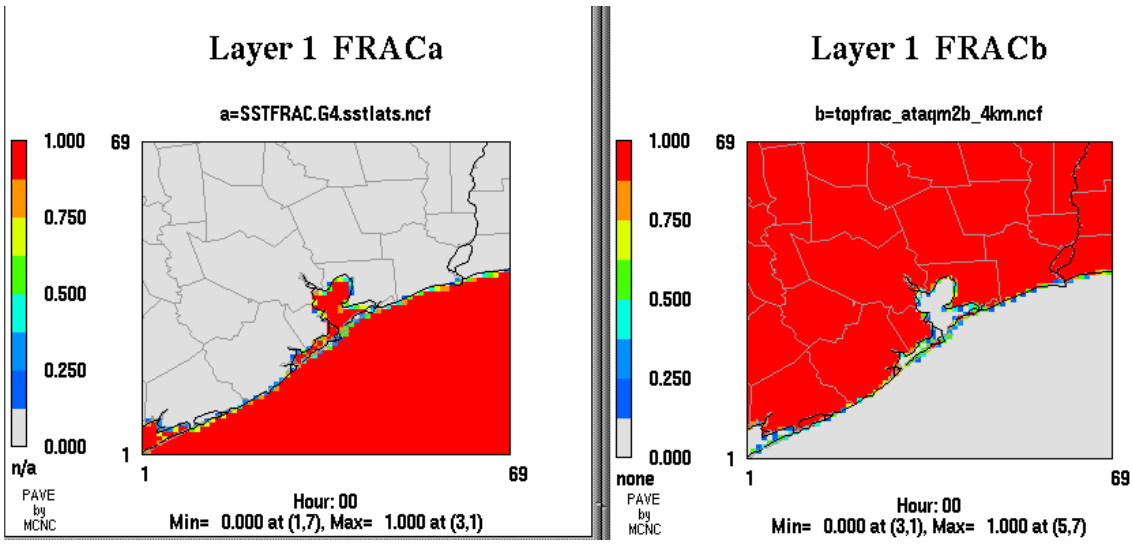

Figure 5.1. SSATS (left) and TOPLATS (right) coverage fractions in the Phase 2b HGA 4-km domain.

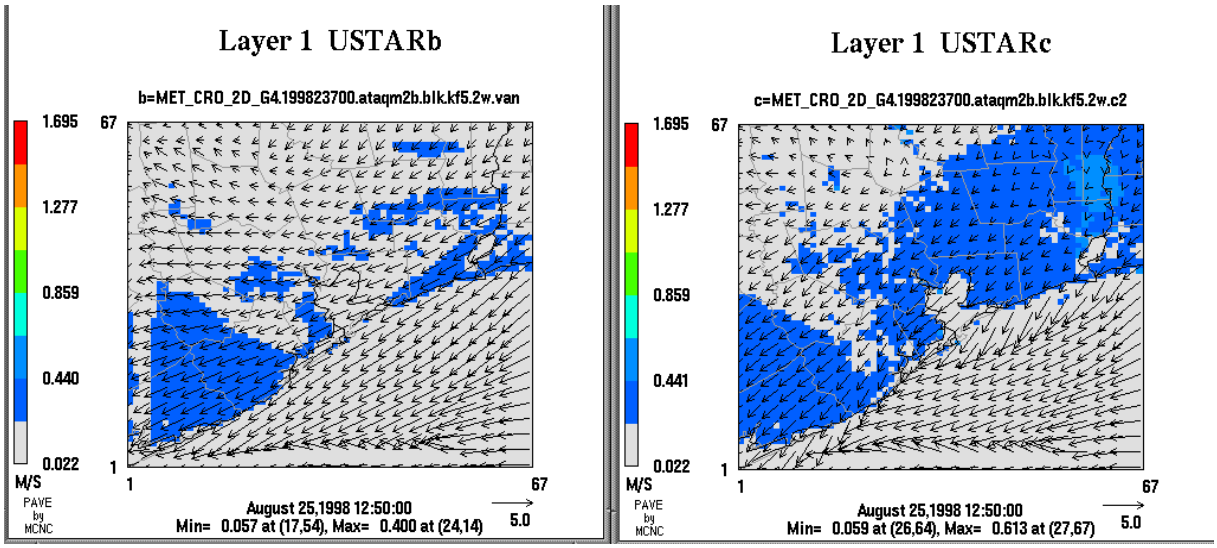

Figure 5.2. Uncoupled (left) and coupled (right) plots of the magnitude of u_* with wind vectors overlaid during the morning transition. The right-hand frame depicts an area of large u_* values in the northeast quadrant, associated with an area of light winds. If u_* values are not allowed to scale appropriately with the light winds, daytime PBL wind acceleration may not occur appropriately, and daytime wind speeds may be biased low over land.

6. MM5 4-km Uncoupled and Coupled Run Evaluation

6.1 Evaluation Approach

The evaluation of the coupled versus the uncoupled runs is broken down into quantitative (first) and qualitative (second) sections. It is important to conduct both because standard statistics do not always accurately reflect model performance, particularly since minor spatial-temporal phase errors create poor point-location statistics. Also, station data are typically sparse and not fully representative of surface conditions throughout an entire modeling domain. Finally, factors that are important to air quality simulations—the timing and location of clouds, the evolution and depth of the boundary layer, the diurnal surface flux pattern, and the cycling of the sea breeze—may not be reflected in standard statistics.

The motivation for conducting the three outer-domain 36 km-12 km runs with which to drive the interior, 4-km domain runs is described in Section 1.4. By using NESTDOWN to produce 4-km boundary conditions, the effects of the larger-scale domains on the 4-km domain were isolated.

Table 6.1 provides the 4-km run naming conventions and descriptions. As noted in Section 5.2, the wind-speed related u* problem created the need to conduct two sets of coupled runs. In all cases, run names that end with ".c2" are coupled and run names that end in ".van" are uncoupled. The prefixes describe the 36 km-12 km "parent" run. The suffix "c2" was chosen because other sets of coupled runs, using various coupling strategies, were also tried. The "c2" runs provided the best theoretical combination of coupling variables and best overall coupling results to date. The acronym "wspd" is added to designate the corrected u* formulation and the additional identifier "blk" is added to denote the use of the Blackadar-based HIRPBL in the runs. The 4-km run suffixes are highlighted in bold lettering in Table 6.1. An alternate designation for the "wspd" coupled runs is included to clarify some of the figure labels in the sections that follow.

A large number of different data types were considered for objective use in either the modeling or evaluation parts of the project. Though a complete list is provided in McHenry et al. (2001), the part of this list relevant to evaluating the 4-km runs is presented in Table 6.2.

Table 6.1. MM5 V3.4 4-km run naming conventions and descriptions.

36 km-12 km Parent Run Prefix (see Table 4.1)	4-km Full Run Designation	Coupled at 4-km (Y/N)	Comments
"van"	"blk.van.**van**"	N	
"van"	"blk.van.**c2**"	Y	
"van"	"blk.van.**wspd.c2**" *alternatively* "blk.wspd.van.c2"	Y	Removes wspd MAX function
"kf5.2w"	"blk.kf5.2w.**van**"	N	
"kf5.2w"	"blk.kf5.2w.**c2**"	Y	
"kf5.2w"	"blk.kf5.2w.**wspd.c2**" *alternatively* "blk.wspd.kf5.2w.c2"	Y	Removes wspd MAX function
"kf5.2w.c2"	"blk.kf5.2w.c2.**van**"	N	
"kf5.2w.c2"	"blk.kf5.2w.c2.**c2**"	Y	
"kf5.2w.c2"	"blk.kf5.2w.c2.**wspd.c2**" *alternatively* "blk.wspd.kf5.2w.c2.c2"	Y	Removes wspd MAX function

Table 6.2. Objective data sources and their dispositions.

Objective Data Type/Source/Comments	Use in Evaluation of 4-km Runs and Other Comments on Disposition
DS353.4: NCEP Global Upper-air Observations, Aug 1998; Y46895 (12- and 6-hourly)	Used for creating objective analyses for MM5 initial and boundary conditions and for upper-air FDDA. *Not used in 4-km evaluation.*
DS464.0 NCEP Global Surface Observations: Y46892 and Y46893 (land 6- and 3-hourly)	Used for creating objective analyses for MM5 initial and boundary conditions. Not used for nudging since no surface nudging was performed. *Not used in 4-km evaluation.*
DS464.0 NCEP Global Surface Observations: Y46894 (all ship)	Used for creating objective analyses for MM5 initial and boundary conditions. Not used for nudging since no surface nudging was performed. *Not used in 4-km evaluation.*
DS083.0 NCEP Global tropospheric analyses: Y46505, August 1998	(GDAS) Used as first guess field for segment S1 objective analyses. *Not used in 4-km evaluation.*
Eta EDAS Analysis Data	(EDAS) Used as first guess field for segment S2 objective analyses. *Not used in 4-km evaluation.*
Raw Hourly Surface Station Observations (ds472.0; dataset hrel199808-asc.Z) from NOAA Techniques Development Lab (TDL)	Station data was used for 4-km model surface evaluation.
US EPA "Aerometric Information Retrieval System (AIRS) datasets: 1 per episode-day	Not used. Some redundancy over Techniques Development Laboratory data. *Not used in 4-km evaluation.*

Table 6.2. Objective data sources and their dispositions.

Objective Data Type/Source/Comments	Use in Evaluation of 4-km Runs and Other Comments on Disposition
NEXRAD Stage IV Precipitation Data	Used for driving TOPLATS. *Not used in 4-km evaluation.*
TNRCC Radar Wind Profiler Data	Used for low-level upper-air wind evaluation.
NOAA Radar Wind Profiler Data	None located. See http://www-dd.fsl.noaa.gov/online.html
TNRCC Sounding Acoustic Radar (SODAR) Data	Considered for low-level upper-air wind evaluation, but *not used due to limited vertical extent.*
TNRCC Continuous Air Monitoring Station (CAMS) Data; 5-minute intervals	Considered for surface evaluation, but *not used due to uncertain shelter conditions*.
Houston Regional Monitoring (HRM) Network Data	Considered for surface evaluation, but *not used due to uncertain shelter conditions.*
Land-Surface Data a. 4-km Skin Temperature	None available.
b. 1-km Skin Temperature	None available.
c. Surface Heat Flux Data	None available.
d. Surface Radiation Budget Data	Incorporated to drive TOPLATS. *Not used in 4-km evaluation.*
Cloud Drift Winds	None located.
DMSP SSM/I low level winds	Speed only, no direction, elevation 19.5 m. Not obtained. See: http://wwwo2c.nesdis.noaa.gov/owinds/winds_info_framed.htm
DMSP ERS-2 Active Microwave-derived Ocean Surface Winds	None obtained. See http://wwwo2c.nesdis.noaa.gov/owinds/winds_info_framed.htm
DMSP QuickSCAT Derived Ocean Surface Winds	None obtained. See http://wwwo2c.nesdis.noaa.gov/owinds/winds_info_framed.htm
NOAA National Ocean Service (NOS) Water Temperature Data	Obtained and used to drive SSATS. *Not used in 4-km evaluation.*
NOAA Physical Oceanography Real-Time System (PORTS)	Data for Aug/Sep 1998 requested from NOAA but not delivered.
NOAA Polar Orbiting Satellite (POES) "Coastwatch" SST Data	Data obtained and processed, but geo-registration problems resulted in large uncertainties. *Not used in 4-km evaluation.*
NEXRAD WSR88D Volume Azimuth Display (VAD) Data from League City Texas	None obtained.

The table shows that there were two primary data sources used for evaluating the 4-km runs. The first was the set of hourly surface observations processed by the NOAA Techniques Development Lab (TDL). These data contain objective shelter-level observations of winds (speed and direction), temperature, and relative humidity. The second, provided by TNRCC, was a set of radar wind profiler (RWP) half-hourly time-height observations from Ellington Field, Houston.

Many other potential data sources were considered. For example, NCEP Global Upper Air and surface observations were used in combination with NCEP Global tropospheric analyses (for S1) and NCEP Eta tropospheric analyses (for S2) to develop MM5-system-based objective tropospheric analyses to drive MM5. Hypothetically, portions of these datasets could have been used for evaluation, but were not because of (1) potential redundancies at the surface with the TDL dataset and (2) resource constraints. The first factor was also a consideration in not using the EPA AIRS data, in addition to the fact that the meteorological data in the AIRS datasets tend to be less-well quality assured. No source of NOAA-based RWP data was located, though an attempt was made. TNRCC provided some very low-level acoustic sounder data (Galveston Airport and Wharton Power Plant), but the backscatter data were not deemed useful beyond about 10:30 a.m. LDT, since acoustic sounding does not normally provide any information about mixing heights during summer high ozone days (per e-mail note from B. Lambeth, TNRCC, November, 2000).

TNRCC Continuous Air Monitoring Station (CAMS) data were available, some of which were incorporated as surface observations to drive TOPLATS (Peters-Lidard, 2001a). Uncertainties about shelter conditions in the CAMS (and HRM) data resulted in these data not being used for the evaluation. The availability of various high-resolution (< 10 km) land-surface data types was investigated, and none was located, with the exception of station-based RSD data, discussed in Section 3. These data were not appropriate for the evaluation effort. The disposition of other kinds of data considered, including Cloud Drift Winds, various Defense Meteorological Satellite Program (DMSP) datasets, NOAA National Ocean Service (NOS), NOAA Physical Oceanography Real-Time System (PORTS), NOAA Polar Orbiting Earth Satellite (POES), and Volume Azimuth Display (VAD) datasets is provided in Table 6.3.

Quantitative evaluation followed a fairly standard approach. Time-series statistics from individual observing stations were produced, along with spatial-aggregate time-series plots. To construct the time-series plots, MM5 data were bi-linearly interpolated from the latitudes and longitudes of the grid-cell centers to the latitudes and longitudes of the stations, using the four nearest surrounding cells. Wind components were rotated from map-north and map-east to true north and east, respectively.

Table 6.3 provides the location and name of the observing stations by grid cell, while Figure 6.1.1 shows the location of the surface stations within the domain.

Table 6.3. Observation stations, ID's, and locations by grid cell (col, row) in the MM5 4-km MM5/TOPLATS/SSATS domain.

Map ID	COL	ROW	Reference Name
BTP	55	44	Beaumont/Port Arthur Jefferson County Airport
CXO	21	54	Conroe, Montgomery County Airport
DWH	18	46	Houston, Hooks Memorial Airport
EFD	28	34	Houston/Ellington
GLS	35	24	Galveston, Scholes Field
HOU	25	35	Houston, Houston Hobby Airport
IAH	23	43	Houston, Houston Intercontinental Airport
LBX	21	20	Angelton/Lake Jackson, Brazoria County Airport
PSX	2	8	Palacios Municipal Airport
SRG	16	34	Houston, Sugar Land Municipal/Hull Field Airport
UTS	17	65	Huntsville, Huntsville Municipal Airport

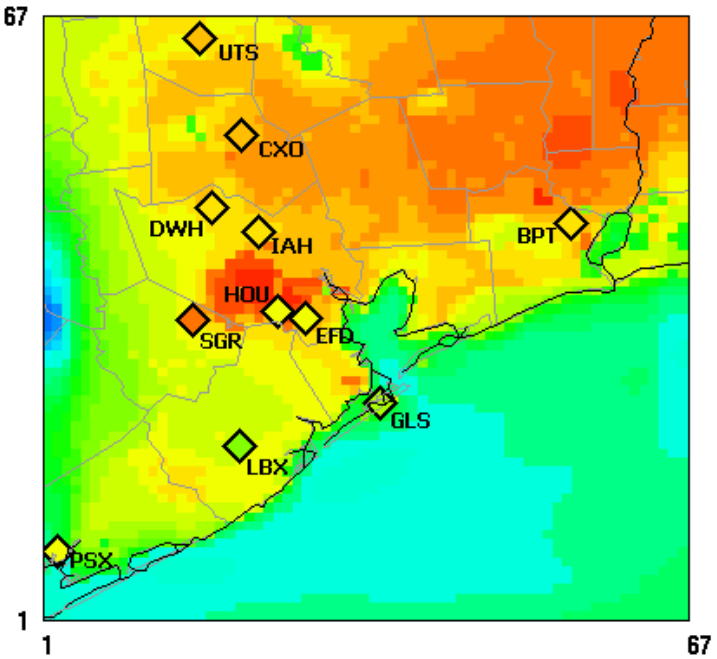

Figure 6.1.1. Observation station locations and ID's within the 4-km domain.

Sections 6.2 and 6.3 discuss the time-series plots. Section 6.4 discusses the episodic mean results, constructed by calculating the bias and root-mean-square errors (RMSEs) over all data pairs in space and time. These data are presented in both tabular and bar-graph form. The bar graphs are particularly useful for discerning the overall, gross performance of the runs.

Sections 6.5 through 6.8 provide the qualitative part of the evaluation. The modeled surface sensible and latent heat fluxes are compared, and then the models' representation of the sea breeze as depicted in satellite imagery and surface station data are discussed. An analysis of cloud representation is provided that compares model results against satellite observations, and boundary-layer depth and evolution are described along with their key similarities and differences. The qualitative comparisons are presented with a view toward the effects the various processes (surface fluxes, PBL, sea-bay-land breezes, and clouds) have on air quality and on air quality model simulations that would be driven by the 4-km runs.

6.2 Time-series Plots at Individual Surface Observing Stations

Even for the small number of stations evaluated, the amount of data and number of time-series plots is significant. Six stations were selected as representative of different locations in the domain. These six are (1) Conroe (CXO), a northern rural location; (2) Houston Hobby (HOU), a central urban location; (3) Ellington Field (EFD), a Bay-proximate location; (4) Galveston (GLS), a gulf-coast location; (5) Brazoria County Airport (LBX), a rural coastal plain location; and (6) Palacios Municipal Airport (PSX), a far south-west gulf-coast location.

Each of these locations represents a somewhat distinct regional climatology in that they differ in land-use types and in proximity to significant bodies of water. For each of these locations, 10-m wind speed and direction (Figures a and b), 2-m mixing ratio (Figures c), and 2-m temperature (Figures d) time-series plots are provided. Other variables, such as west-to-east (U) and south-to-north (V) wind components and dew-point temperature were plotted but are not presented because of their similarity to the above four parameters. In all cases, the "wspd" coupled runs are compared with the uncoupled runs. In the plots, the ordinate labels designate which parent 36 km–12 km run was used to provide boundary conditions for the 4-km run being evaluated; i.e., either "van," "kf5.2w," or "kf5.2w.c2." The blue and red time-series depict the uncoupled ("van") versus coupled ("wspd.c2") runs being compared, and the black lines show the observations. By appending the time-series labels to each of the ordinate labels, the full **boldface** run designation shown in Table 6.1 is obtained.

6.2.1 CXO (Conroe) - rural north

Figure 6.2.1a shows the 10-m wind speed time-series plots at Conroe. Just after 0000 UTC on August 30, both "kf5" run sets miss the 10-kt peak, whereas the "van" runs are more realistic. Wind speed is seen to have a diurnal signal, becoming calm and/or light and variable on many nights. The models capture this well after 0000 UTC on August 26, but only the "kf5.2w.c2" run captures it on August 27.

Figure 6.2.1b shows wind direction. Since the wind-direction plots fluctuate when the wind changes between the northwest and northeast quadrants, caution is advised in interpreting the directional plots. The modeled wind direction tracks reasonably well at Conroe, particularly between 1200 UTC on August 26 and 1200 UTC on August 27.

Mixing ratio time-series plots are presented in Figure 6.2.1c. The models are fairly consistent with the observations through 0000 UTC on August 27. After 1200 UTC on August 28, when the models were re-initialized, a phase lag is seen, most notably in the coupled runs. The "van" runs appear to reproduce the observed signal more faithfully during this period, and the uncoupled "kf5" runs appear to be too moist from about 1200 UTC on August 29 until the end of the episode (this is the only one of the six stations discussed where a significant moist bias was observed). In contrast, the two "kf5" coupled runs become driest near sunrise with a moisture peak thereafter, especially after 1200 UTC on August 28.

Figure 6.2.1d shows the 2-m temperature time-series plots. Immediately evident is the weak diurnal amplitude in the uncoupled model. In contrast, the coupled models' amplitudes are much more consistent with the observations.

6.2.2 HOU (Houston Hobby) - central urban

Figure 6.2.2a shows the 10-m wind speed time-series plots at Houston. Both sets of "kf5" runs seem to capture the speed amplitude better than the "van" run on August 25, 26, and 27, when clear afternoon maximum values and overnight minimum values are observed. Later in the period, from about 0000 UTC on August 28 onward, the speed does not contain a clear diurnal signal. All of the models miss the peak in wind speed before sunrise on August 30. It is not known whether this feature was real or not, nor what physical process was responsible. Generally, the speed traces are fairly consistent between coupled and uncoupled models, with mostly minor differences.

Figure 6.2.2b shows wind-direction. For the most part, the directional differences between the models and the observations are minor prior to about 1800 UTC on August 28. At that point, especially in the "kf5.2w" run (middle panel), the uncoupled models predict wind with a more easterly component, more consistent with the observations, than do the coupled models. Toward the end of the episode, both uncoupled and coupled models have too much northerly component, especially in the "van" runs.

Mixing ratio time-series plots are presented in Figure 6.2.2c. In contrast to the data at Conroe, these time-series plots reveal that all of the runs are essentially too dry, and that they become drier over time. However, both "van" runs are somewhat better, especially through about 0000 UTC on August 27. Interestingly, the models all recover at 1200 UTC on August 28, when they were re-initialized. This suggests that MM5 has some difficulty maintaining the proper level of moisture near the surface, whence it may be mixing down too much dry air from aloft, or not evaporating enough from the surface.

Figure 6.2.2d shows the 2-m temperature time-series plots. As at Conroe, the coupled runs are somewhat better than the uncoupled runs, with the latter being too warm at night. The uncoupled runs also exhibit a phase "lead," warming too quickly in the early morning. This is consistent with the observation, discussed below, that the uncoupled models tend to "kick on" the boundary layer earlier than do the coupled models, probably in response to more rapidly increasing surface sensible heat fluxes.

6.2.3 EFD (Ellington Field) - Bay proximate

Ellington Field is the surface station most proximate to the Bay and the major emission sources of concern to the TNRCC. Figure 6.2.3a shows the 10-m wind speed time-series plots, Figure 6.2.3b the wind-direction, Figure 6.2.3c the mixing ratio, and Figure 6.2.3d the temperature. In contrast to Houston and Conroe, Ellington Field reports a positive wind speed most of the time, suggesting that its proximity to the Bay may not allow a true surface-based inversion at night. If so, some downward mixing of momentum to the surface would occur nocturnally. The time-series plots show that, from a magnitude point of view, there is not much difference between the runs: the two "kf5" coupled runs overestimate the wind-speed slightly between 1800 UTC and 2300 UTC on August 30. For both wind speed and direction, there are more data gaps (e.g., between 0001 UTC and 1600 UTC on August 26) than for other stations. Near 1800 UTC on August 27, there are significant discrepancies between model runs and observations, but there are not enough data to fully confirm significant model errors during this period. Both uncoupled and coupled models have too much northerly component between 0006 UTC and 1500 UTC on August 29, but the uncoupled model is somewhat better directionally (depending on the run) between 1800 UTC on August 28 and 0006 UTC on August 29. The "van" runs do a poor job in capturing wind direction on August 30: after 1500 UTC, modeled wind direction is nearly opposite that observed. A sub-tropical complex was moving northeast toward the region and the observed wind shifted from easterly to southwesterly around 1600 UTC on August 30 but the models did not capture this shift.

Modeled mixing ratios are not as dry as at Houston Hobby, relatively speaking. The model re-initialization at 1200 UTC on August 28 is still noticeable, however. Also, the trend toward drying out as the simulation progresses, especially during the first segment, is still clearly present. Both "van" runs appear to be less dry-biased than the two "kf5" run sets. The driest periods in the two "kf5" run sets are overnight, with the models' observed mixing ratios dropping (briefly) near sunrise. Toward the end of the episode, the dry-bias is least offensive in the "kf5.2w.c2" runs.

The temperature data at Ellington Field suggest increasingly warm daytime highs (with the exception of August 30) throughout the episode. As at Houston Hobby and Conroe, the coupled models again outperform the uncoupled models both in amplitude and temperature phase, although the phase-lead noted at Houston Hobby in the uncoupled models is not as obvious here. This phase-lead is also apparent in the uncoupled models' Conroe time-series plots, discussed above.

6.2.4 GLS (Galveston) - Gulf coast

Galveston is a coastal station that exhibits a distinctly different regional climatology than the other stations. Influenced by both the Bay and near-shore Gulf, the winds tend to blow much more steadily than at interior rural sights. Further, the temperature amplitude may not be as great due to near-shore effects.

Both sets of "kf5" runs outperform the "van" runs with respect to wind-speed, shown in Figure 6.2.4a. In particular, the "van" runs underestimate wind speeds between

1800 UTC on August 28 and 1200 UTC on August 29, and then overestimate its magnitude on much of August 30. The "kf5" run sets track much more smoothly with the observations. There is not a notable difference between the uncoupled and coupled runs for any of the runs in this figure.

However, in a manner similar to the Ellington Field data, wind direction tracks better in the "van" runs (top panel, Figure 6.2.4b). The observed wind veers (clockwise) from about 100^0 to about 270^0 between 0000 UTC on August 27 and 1800 UTC on August 28, probably in association with the approach of the weak, dry trough on that day. However, the two "kf5" runs back the wind counterclockwise, finally arriving at the same direction around 1800 UTC on August 28. This would lead to significantly different parcel trajectories. All models fail profoundly on August 30, with modeled winds in near opposition to observed winds through much of that day.

Mixing ratio time-series plots are presented in Figure 6.2.4c. Galveston's proximity to the water allows for a nearly constant moist environment. MM5's dry bias is obvious. However, on average, the coupled models appear to be somewhat less biased. The coupled "van" run in particular is moister during the daytime, a good example being the period from 1200 UTC to 2300 UTC on August 27.

Figure 6.2.4d shows the 2-m temperature time-series plots, which reveal that none of the models capture the observed diurnal temperature amplitude. Nonetheless, each of the coupled models is clearly superior to its uncoupled counterpart, in most cases reaching daily maxima closer to that observed, as well as many nocturnal minima. This is no doubt a reflection of the careful land-water mask developed for the coupled model.

6.2.5 LBX (Brazoria County Airport) - rural southwest

Figure 6.2.5a shows the 10-m wind speed time-series plots at Brazoria County Airport, a site located in the coastal plain southwest of metropolitan Houston. This area is often subject to the passage of high ozone plumes that form in metropolitan Houston and are transported down the coast on weak northeasterly winds. Much like Conroe, Brazoria exhibits a diurnal speed cycle, in which winds die off at night and re-develop during the day, in accordance with more classic land-based PBL behavior. For the most part, the models capture this, though they have trouble capturing the calm winds overnight on August 26.

There were not a lot of useful directional wind data at Brazoria (Figure 6.2.5b). Mixing ratio time-series plots are presented in Figure 6.2.5c. The coupled model shows a clear propensity to recover during the day, but is significantly drier than the uncoupled model at night.

Figure 6.2.5d shows the 2-m temperature time-series plots. Again, the uncoupled model exhibits two features: a warm bias at night and a phase-lead in the morning. While the coupled models are in phase, their diurnal amplitude is slightly too wide: the nocturnal minimum is a little cool, and the daytime maximum a little warm. This is likely a reflection of MM5's dry bias. Without the dry bias, the uncoupled model would not

warm as much during the daytime, and would not cool as much at night, i.e., the weak diurnal temperature amplitude would be weaker. Together with the phase-leads already noted, the combined warm-dry biases in the model suggest a fundamental problem in the surface-flux physics in the uncoupled models, at least with the parameterizations explored in this study.

6.2.6 PSX (Palacios Municipal) - Gulf Coast southwest

Palacios is near the southwest border of the 4-km domain and is located on Matagorda Bay. Of the six stations selected for review, Palacios is expected to be most influenced by the boundary conditions, and thus show greater differences between the "van" runs and the two sets of "kf5" runs. Figure 6.2.6a shows the 10-m wind-speed time-series plots. During the day on August 29—the day when spurious KF convection was a significant problem—the wind speed appears to be better represented in the two sets of "kf5" runs. All model-runs underestimate the wind-speed maximum during the afternoon of August 26; the wind-speed maximum may have been sea-breeze related (e.g., Figure 6.2.6a).

Interestingly, Palacios exhibits a rather constant wind direction (Figure 6.2.6b), out of the east-southeast, through most of the first 72 hours of the episode, and this is tracked exceedingly well by all the models. This may be a reflection of good boundary-condition winds at this point in the domain. The wind changes direction, veering to the south, west, and northwest after 0000 UTC on August 28, and this is captured very effectively by the "van" runs (top panel). Large swings in direction around 360^0 after 0000 UTC make it difficult to interpret the rest of the time-series plots.

Mixing ratio time-series plots are presented in Figure 6.2.6c. Both uncoupled and coupled models perform similarly, but again, the "van" runs outperform the two sets of "kf5" runs, the latter being much too dry during the daylight hours on August 26 and 27. Again, at the beginning of S2, the mixing ratios return to match the observations. This recovery at model re-initialization, present in most mixing ratio time-series plots, strongly suggests that model processes, rather than initial conditions, are responsible for the various dry-biases noted.

Figure 6.2.6d shows the 2-m temperature time-series plots. Both models overpredict the daytime maxima, especially for the second half of the episode. It is likely that Palacios was influenced more from Matagorda Bay and the Gulf than was captured by the models. The boundary conditions may also play a role. The "van" models show the most error, with a lessening of the errors in the two sets of "kf5" runs, supporting the latter argument. Only at Palacios and Galveston did the uncoupled models not exhibit a phase-lead in early morning temperature rise. This is likely due to Palacios' and Galveston's proximity to the water.

This page intentionally left blank.

6.2.7 Figures for Section 6.2

6.2.7.1 Conroe Time-Series Plots

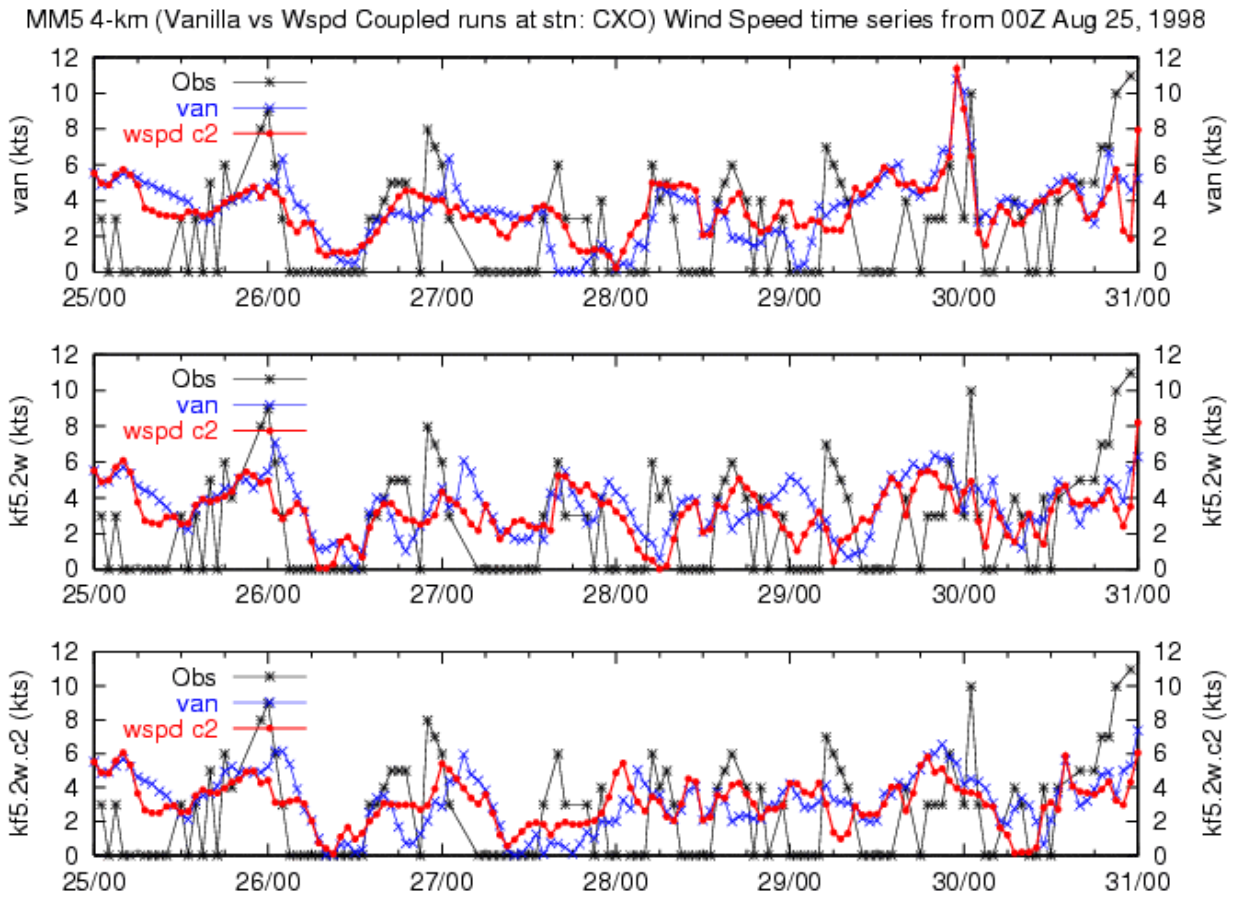

Figure 6.2.1a. Conroe 10-m wind speed time-series plots comparing three sets of coupled runs (red), uncoupled runs (blue), and observations (black) from August 25 at 0000 UTC to August 31 at 0000 UTC.

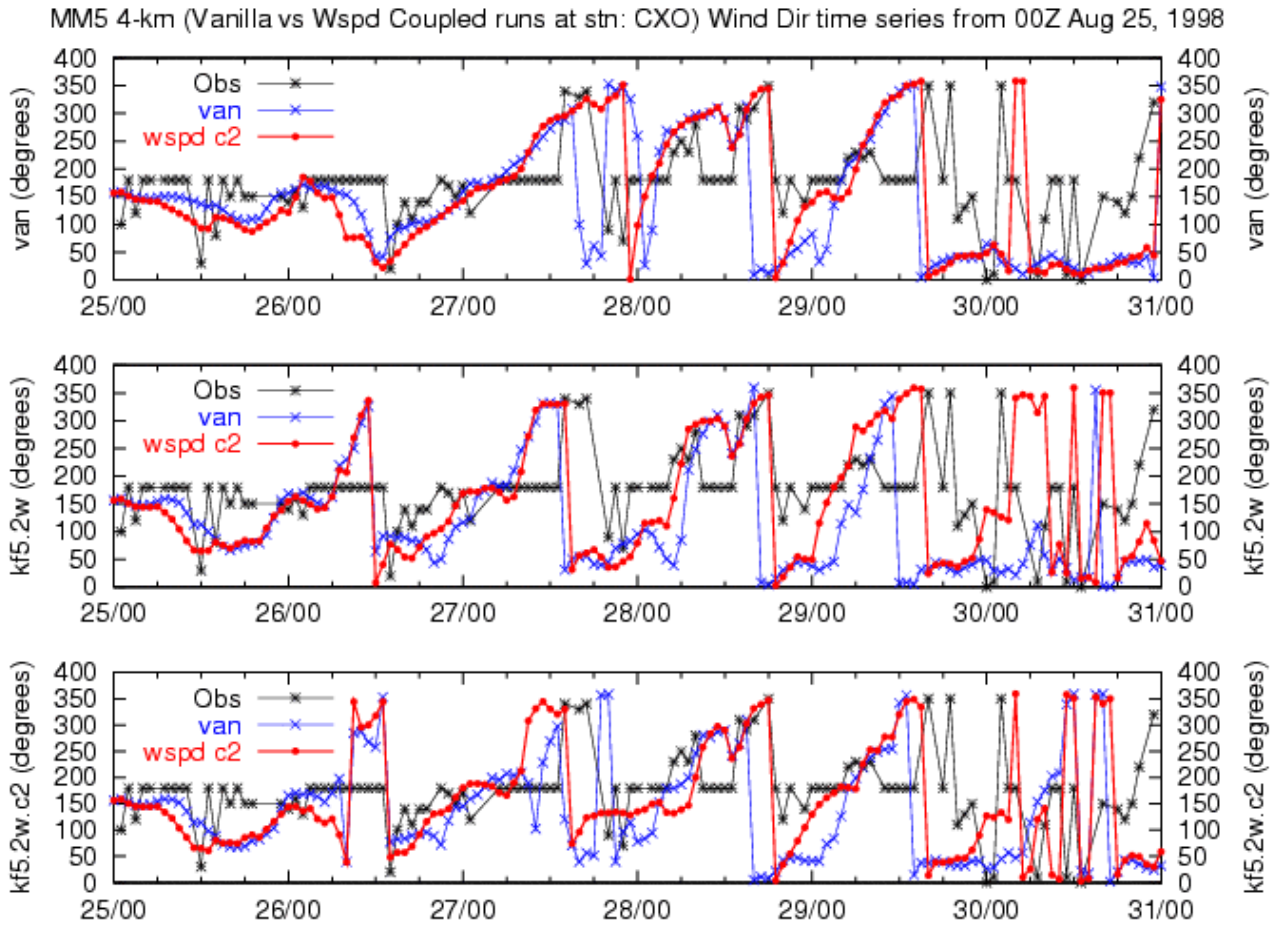

Figure 6.2.1b. Conroe 10-m wind direction time-series plots comparing three sets of coupled runs (red), uncoupled runs (blue), and observations (black) from August 25 at 0000 UTC to August 31 at 0000 UTC.

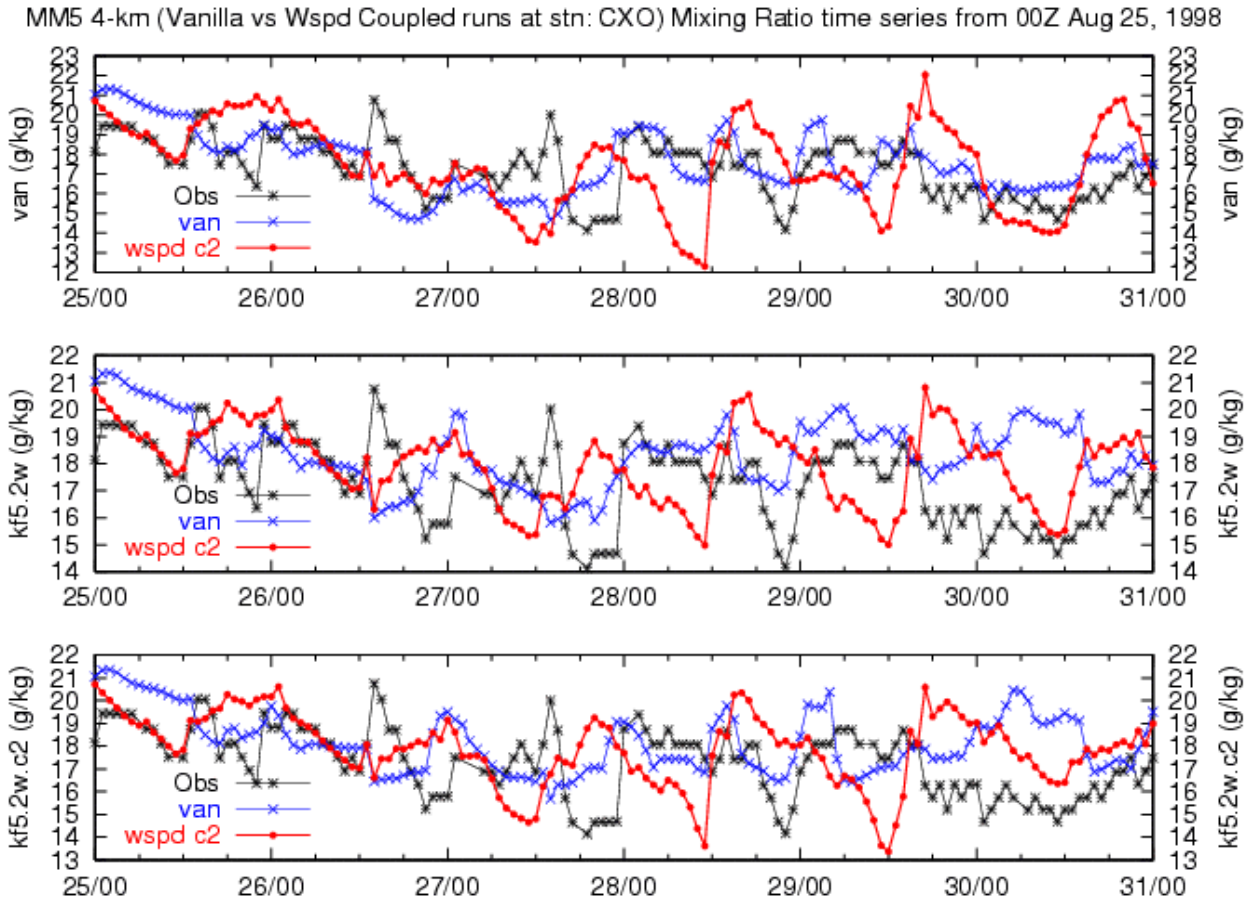

Figure 6.2.1c. Conroe 2-m mixing ratio time-series plots comparing three sets of coupled runs (red), uncoupled runs (blue), and observations (black) from August 25 at 0000 UTC to August 31 at 0000 UTC.

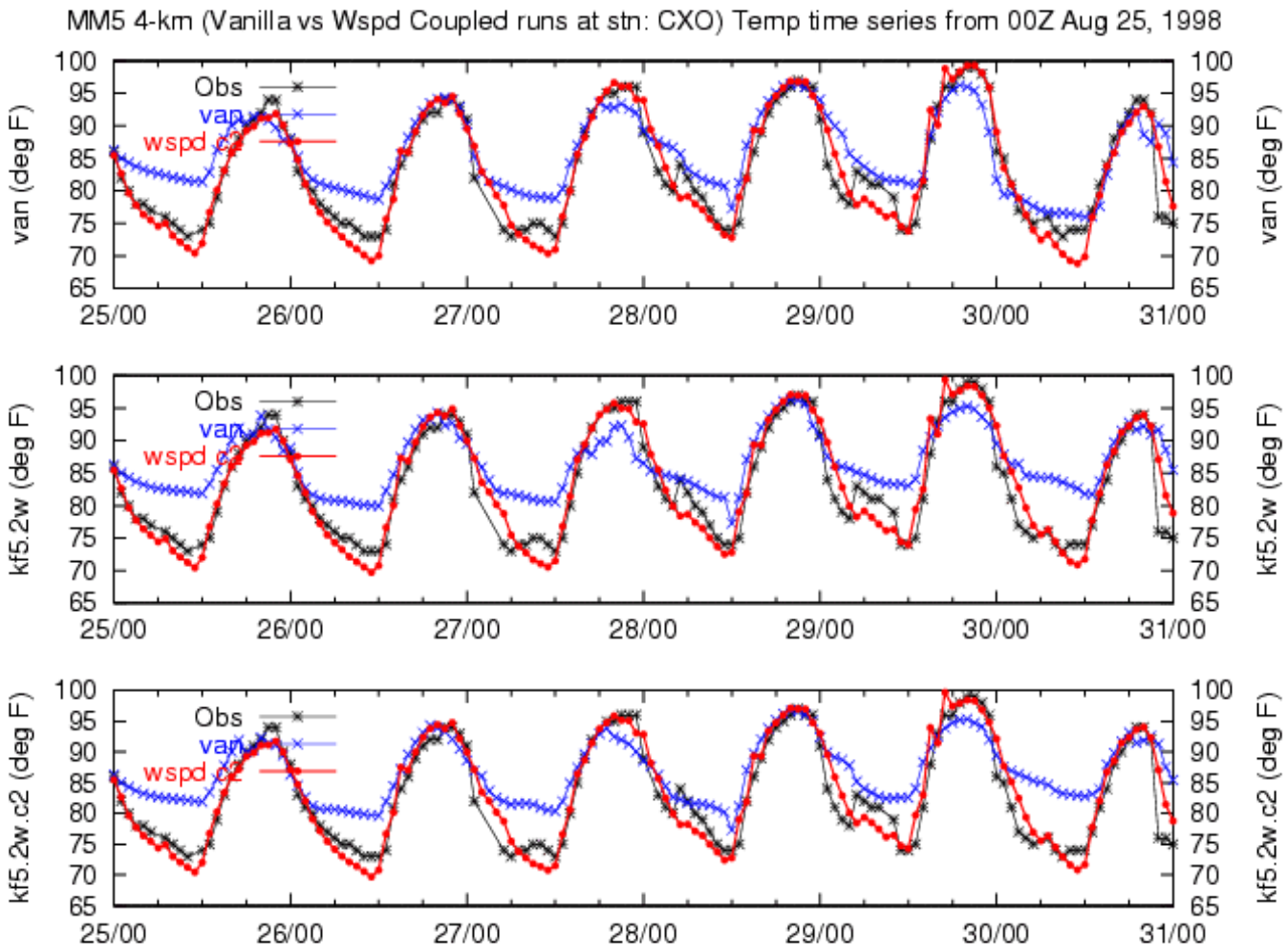

Figure 6.2.1d. Conroe 2-m temperature time-series plots comparing three sets of coupled runs (red), uncoupled runs (blue), and observations (black) from August 25 at 0000 UTC to August 31 at 0000 UTC.

6.2.7.2 Houston (Hobby) Time-Series Plots

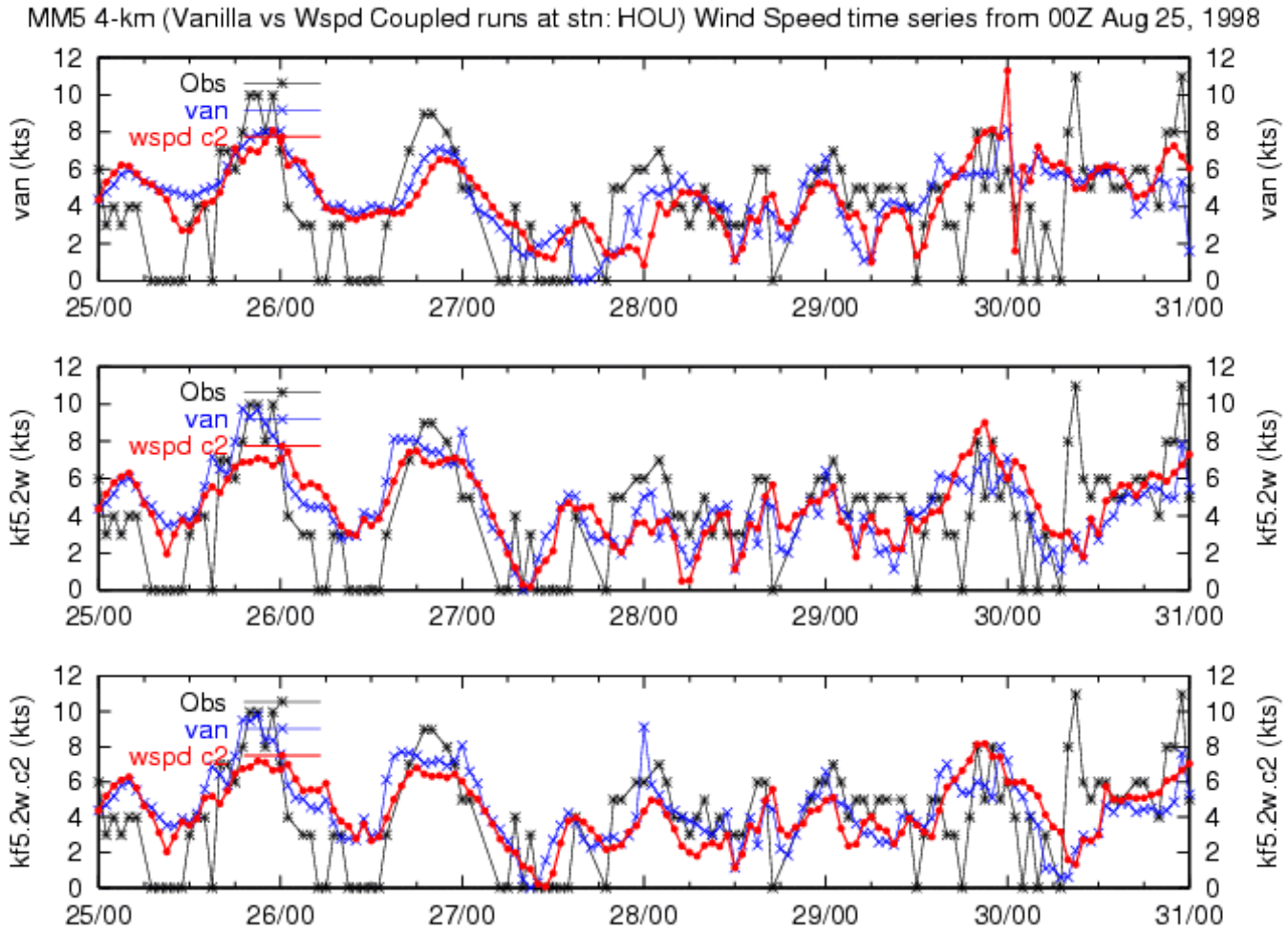

Figure 6.2.2a. Houston Hobby 10-m wind speed time-series plots comparing three sets of coupled runs (red), uncoupled runs (blue), and observations (black) from August 25 at 0000 UTC to August 31 at 0000 UTC.

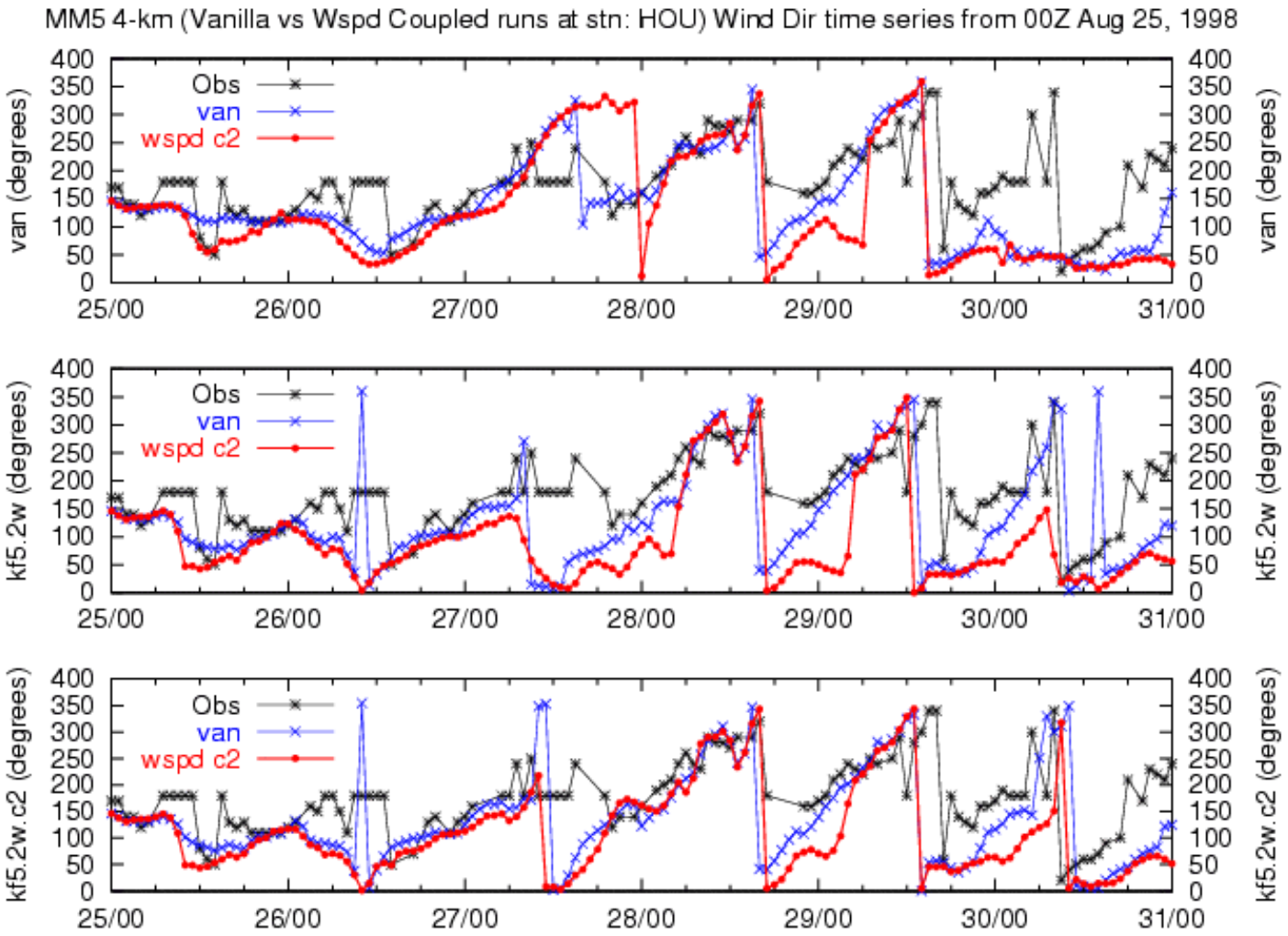

Figure 6.2.2b. Houston Hobby 10-m wind direction time-series plots comparing three sets of coupled runs (red), uncoupled runs (blue), and observations (black) from August 25 at 0000 UTC to August 31 at 0000 UTC.

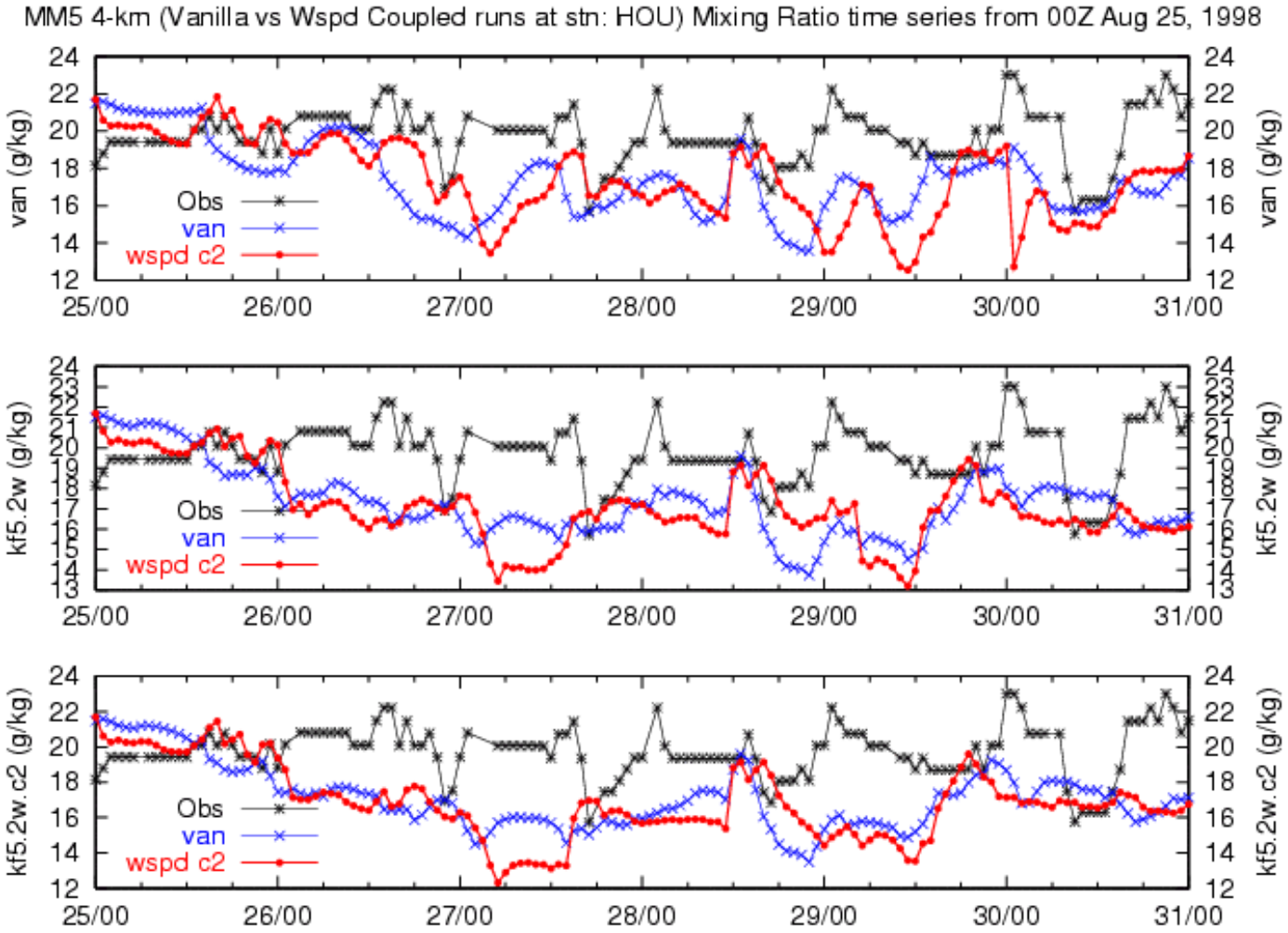

Figure 6.2.2c. Houston Hobby 2-m mixing ratio time-series plots comparing three sets of coupled runs (red), uncoupled runs (blue), and observations (black) from August 25 at 0000 UTC to August 31 at 0000 UTC.

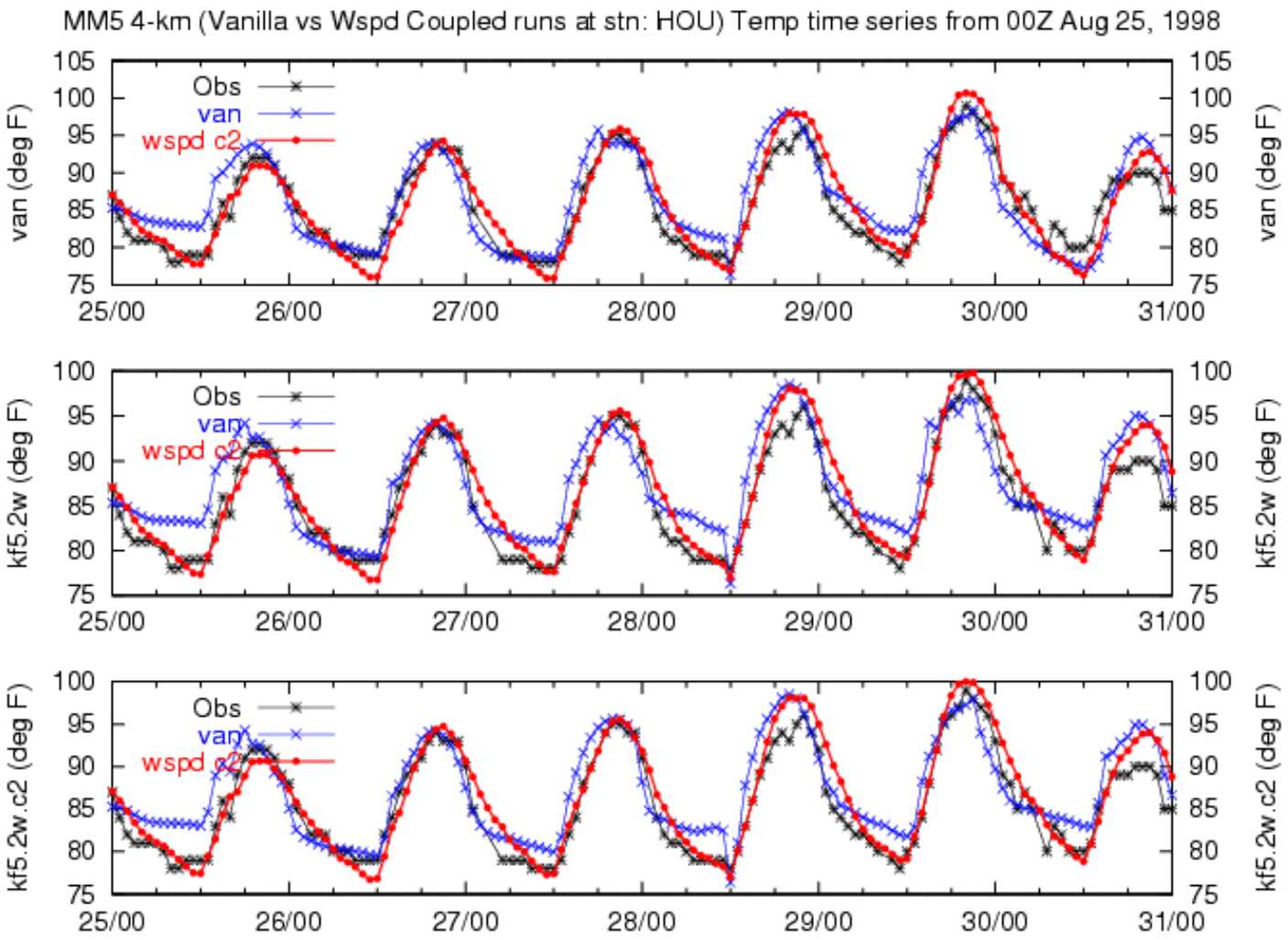

Figure 6.2.2d. Houston Hobby 2-m temperature time-series plots comparing three sets of coupled runs (red), uncoupled runs (blue), and observations (black) from August 25 at 0000 UTC to August 31 at 0000 UTC.

6.2.7.3 Ellington Field Time-Series Plots

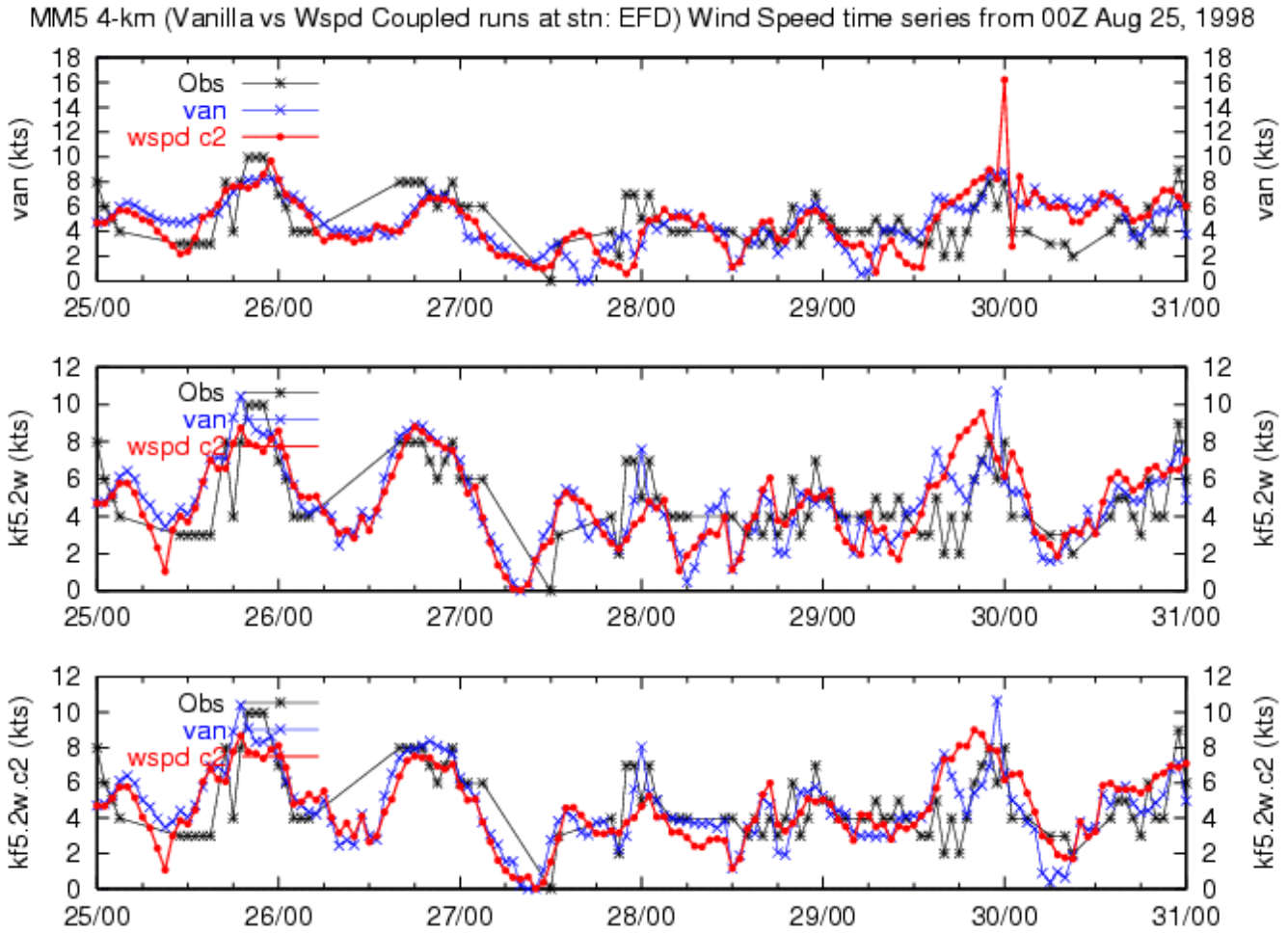

Figure 6.2.3a. Ellington Field 10-m wind speed time-series plots comparing three sets of coupled runs (red), uncoupled runs (blue), and observations (black) from August 25 at 0000 UTC to August 31 at 0000 UTC.

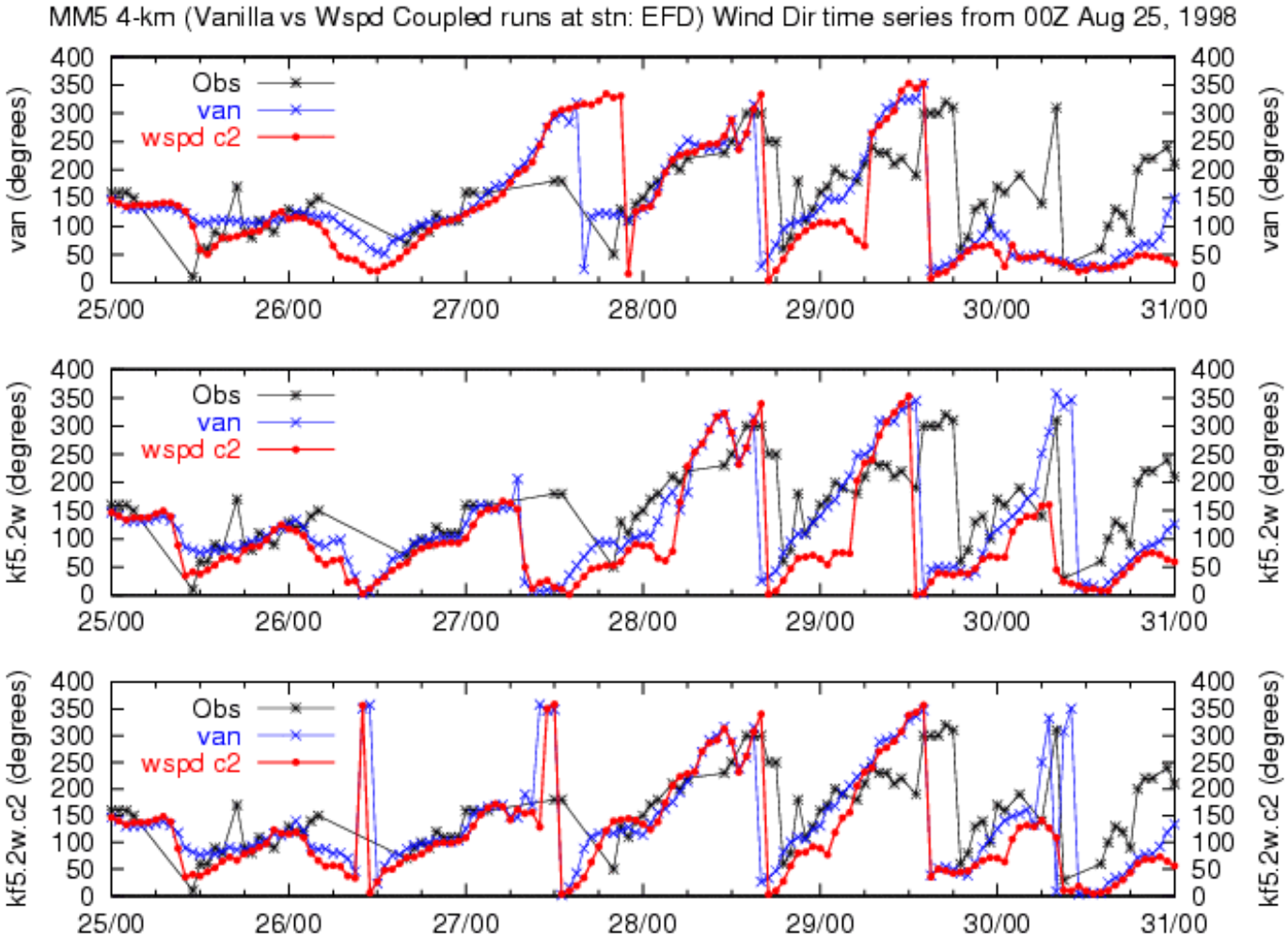

Figure 6.2.3b. Ellington Field 10-m wind direction time-series plots comparing three sets of coupled runs (red), uncoupled runs (blue), and observations (black) from August 25 at 0000 UTC to August 31 at 0000 UTC.

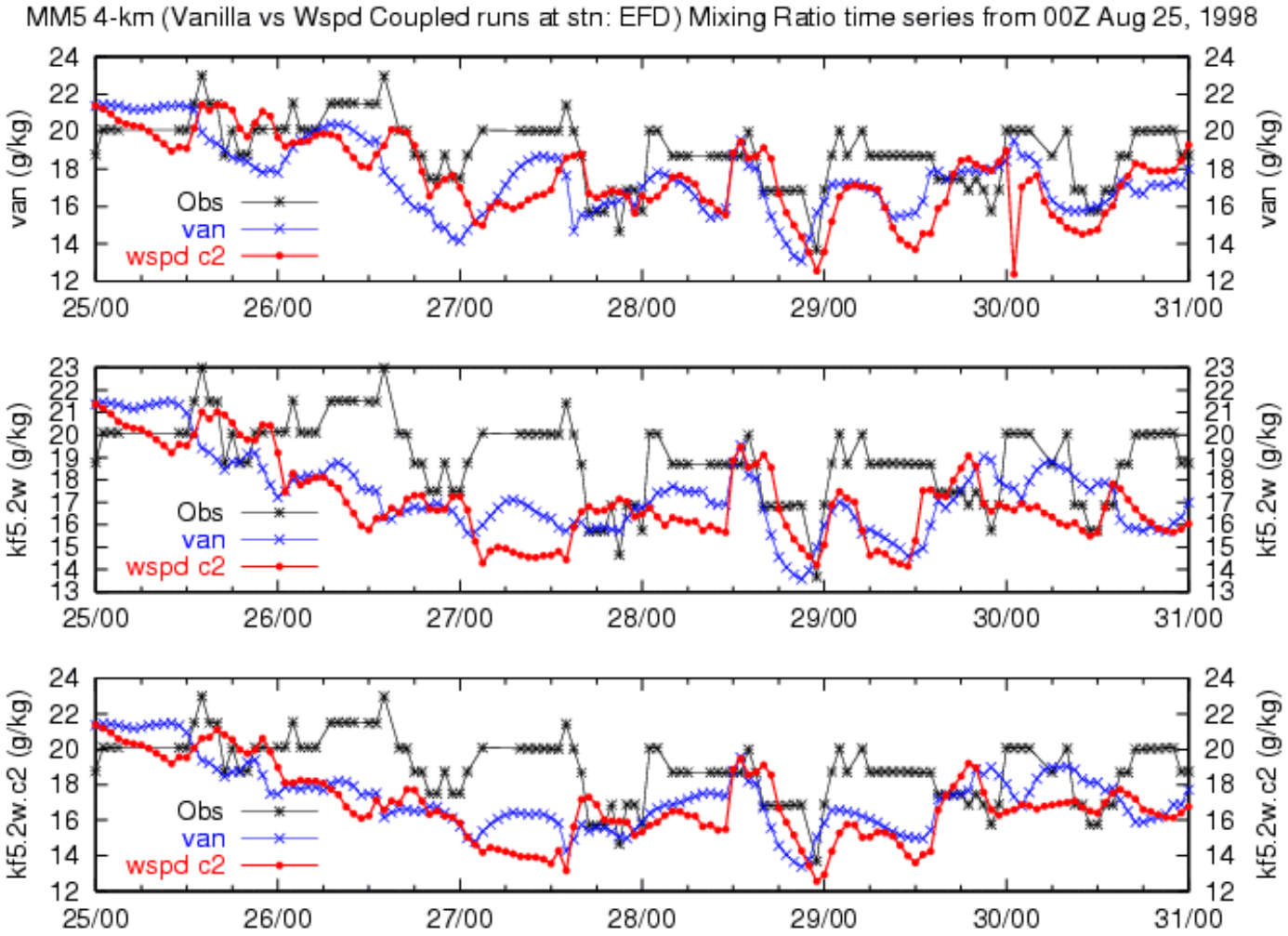

Figure 6.2.3c. Ellington Field 2-m mixing ratio time-series plots comparing three sets of coupled runs (red), uncoupled runs (blue), and observations (black) from August 25 at 0000 UTC to August 31 at 0000 UTC.

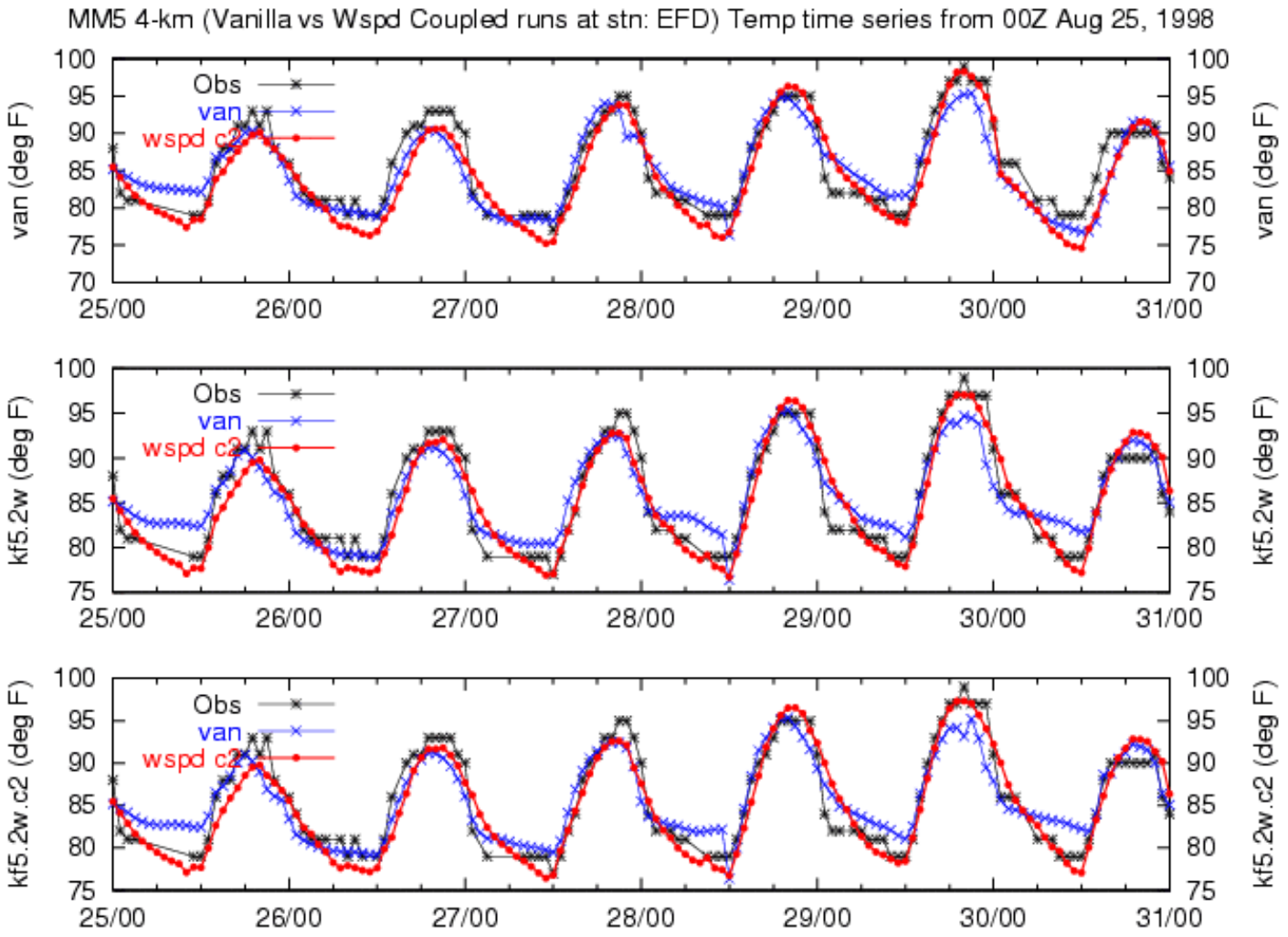

Figure 6.2.3d. Ellington Field 2-m temperature time-series plots comparing three sets of coupled runs (red), uncoupled runs (blue), and observations (black) from August 25 at 0000 UTC to August 31 at 0000 UTC.

6.2.7.4 Galveston Time-Series Plots

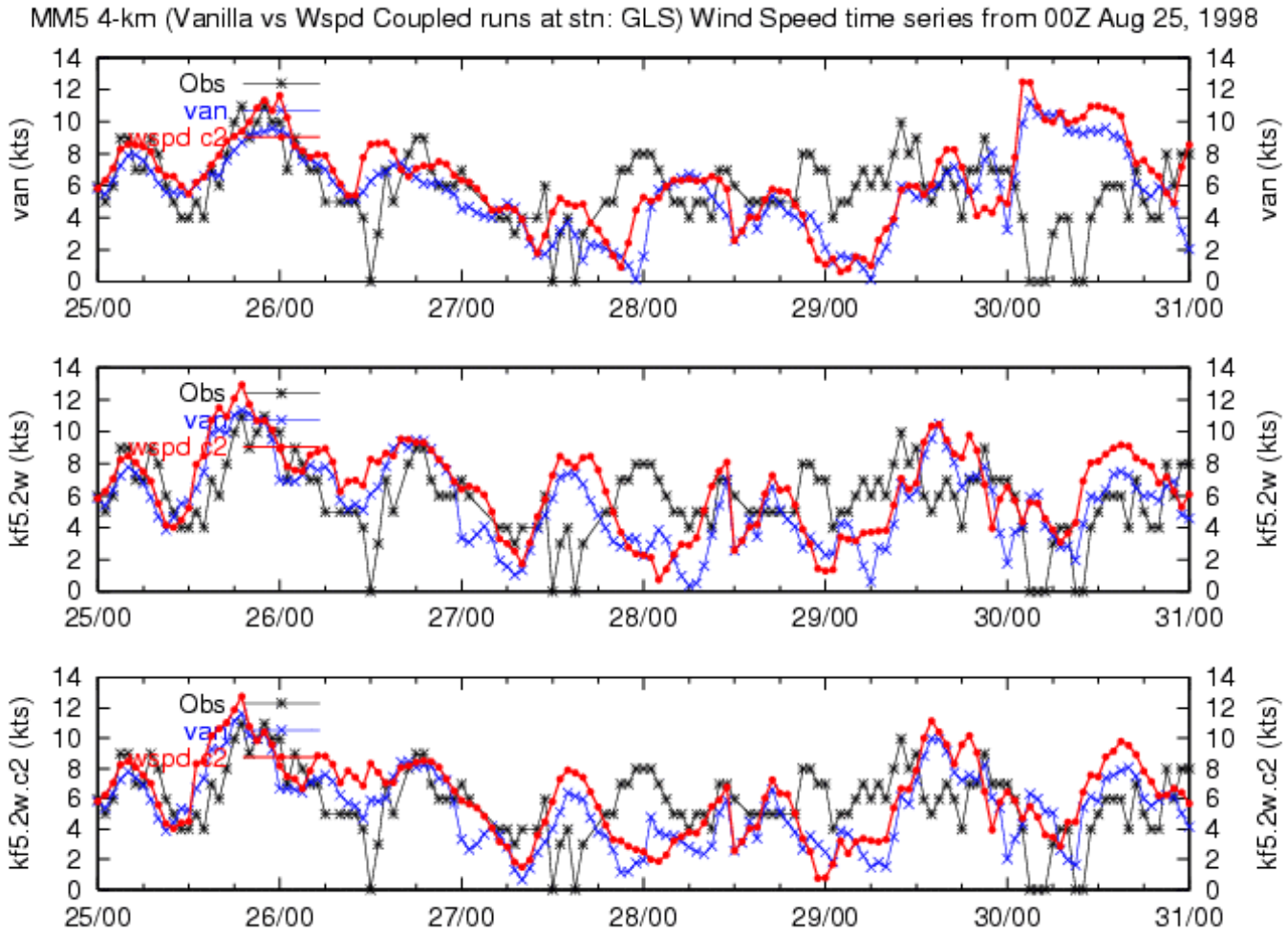

Figure 6.2.4a. Galveston 10-m wind speed time-series plots comparing three sets of coupled runs (red), uncoupled runs (blue), and observations (black) from August 25 at 0000 UTC to August 31 at 0000 UTC.

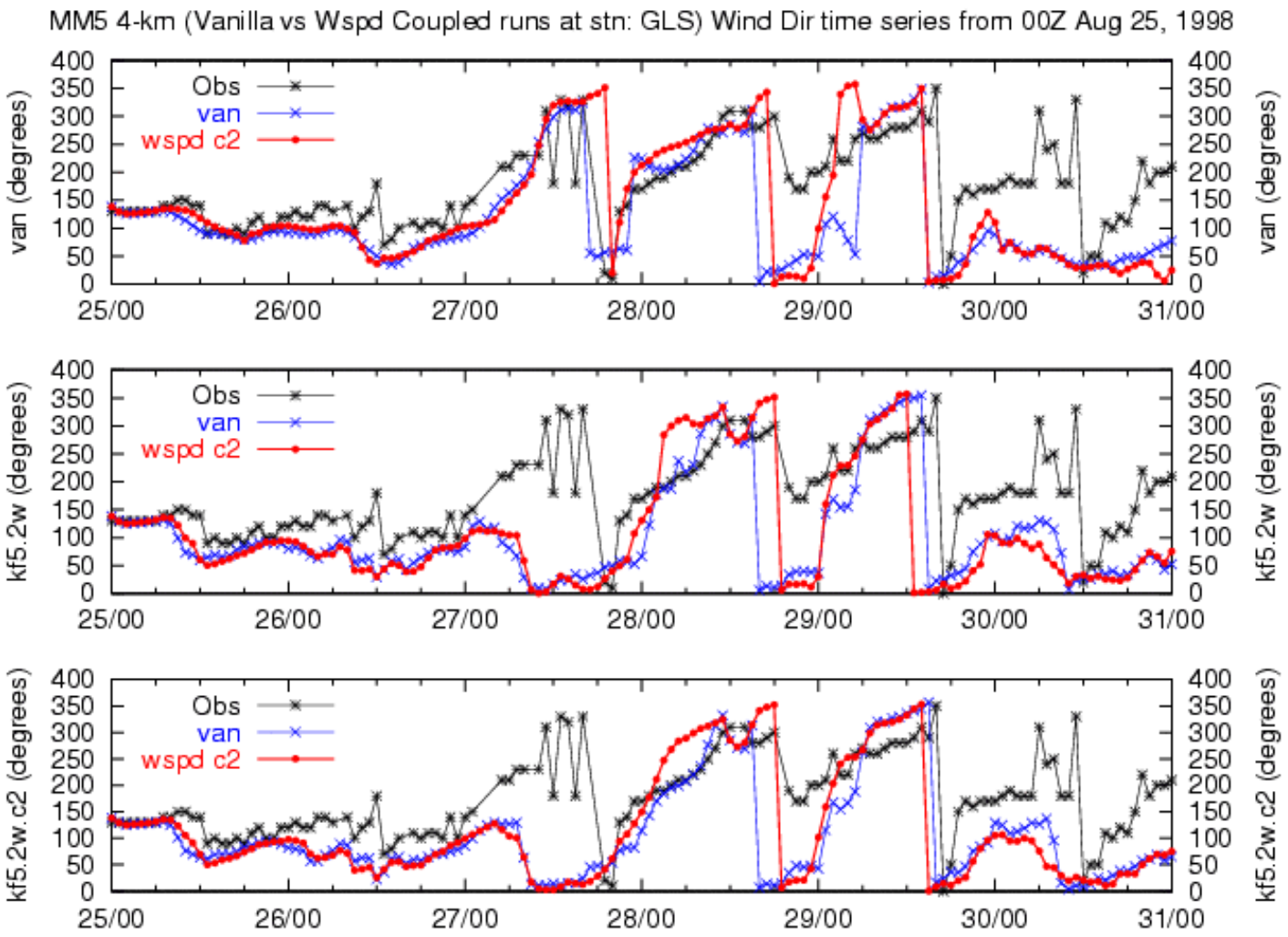

Figure 6.2.4b Galveston 10-m wind direction time-series plots comparing three sets of coupled runs (red), uncoupled runs (blue), and observations (black) from August 25 at 0000 UTC to August 31 at 0000 UTC.

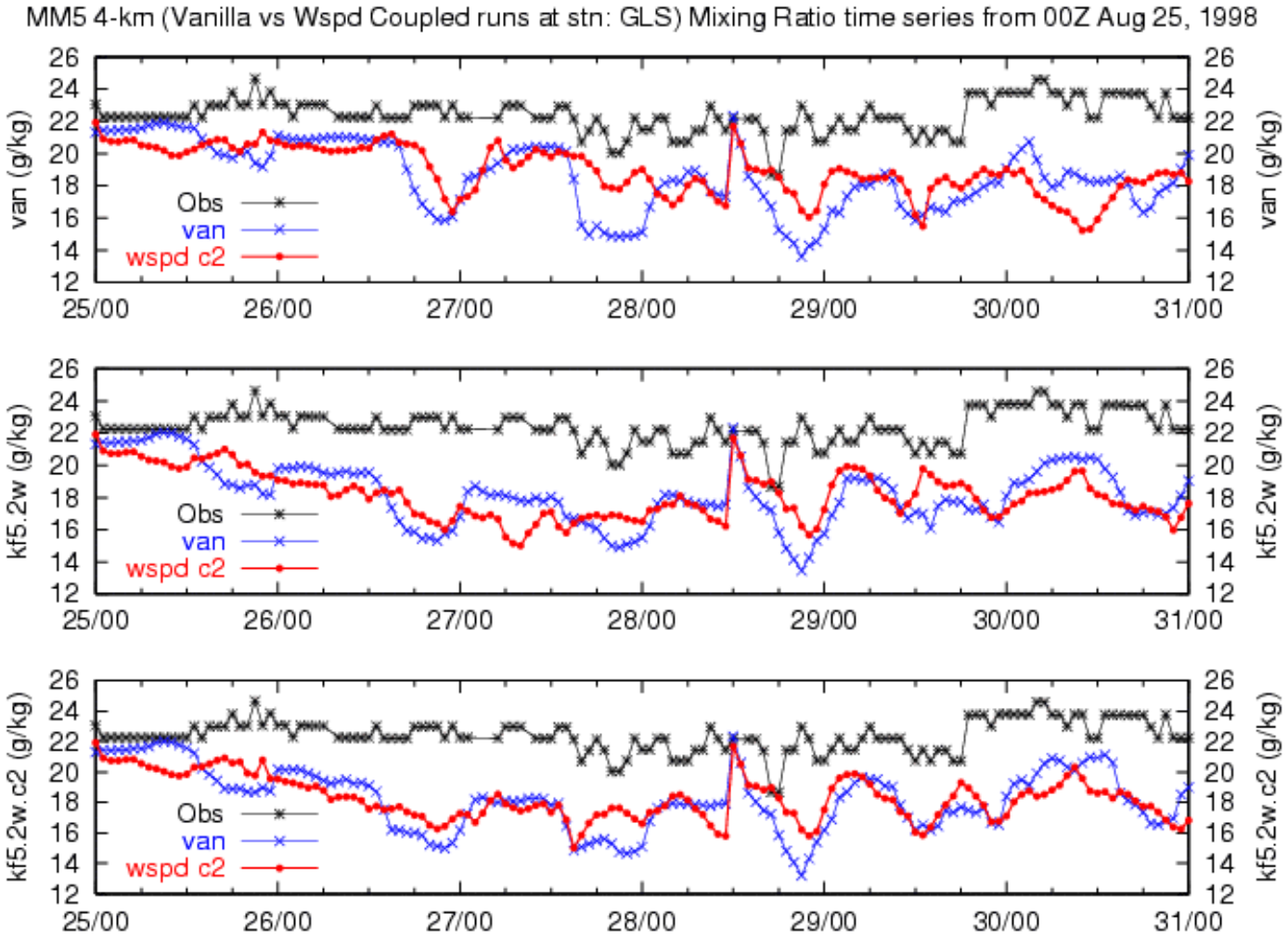

Figure 6.2.4c. Galveston 2-m mixing ratio time-series plots comparing three sets of coupled runs (red), uncoupled runs (blue), and observations (black) from August 25 at 0000 UTC to August 31 at 0000 UTC.

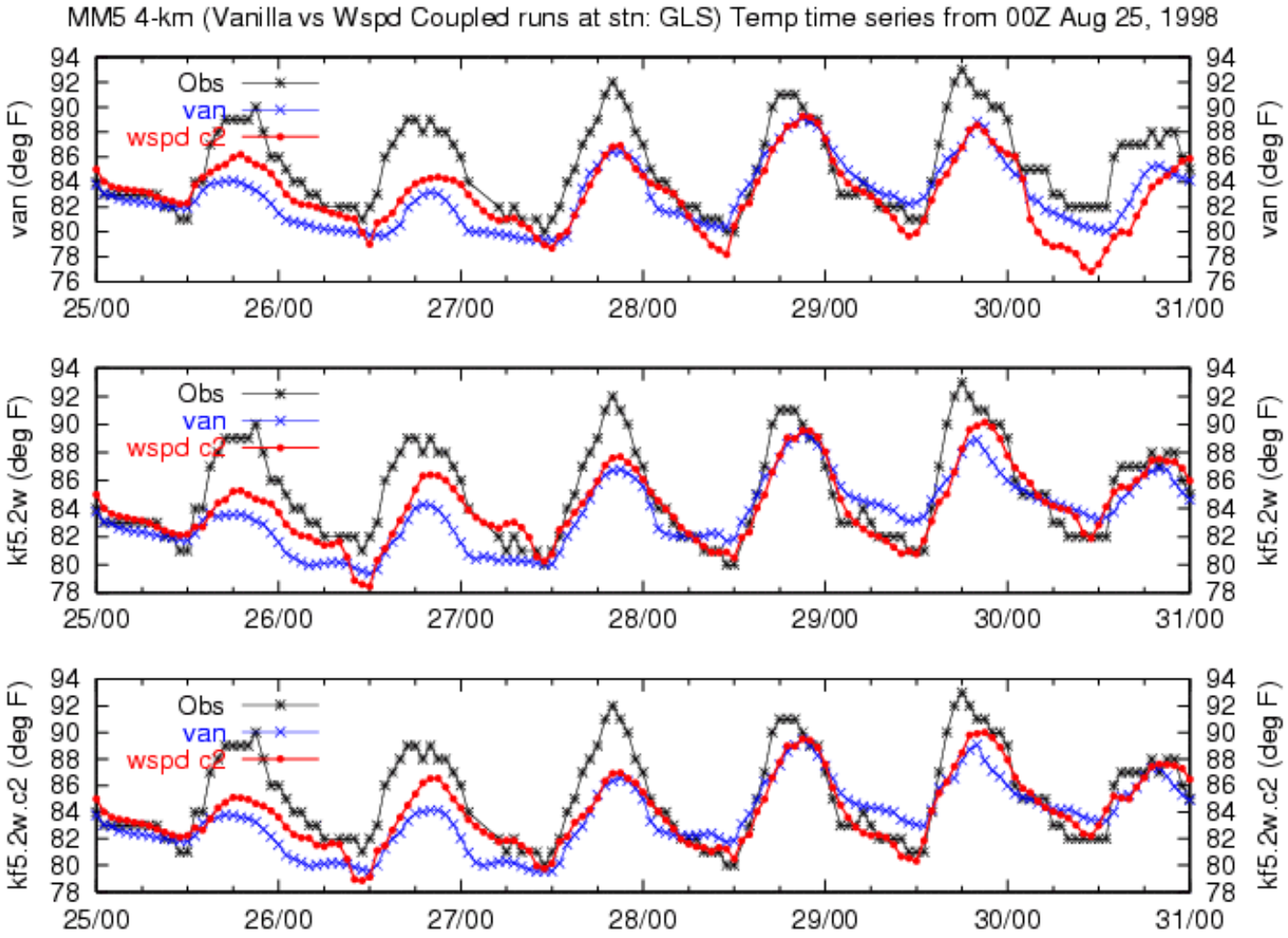

Figure 6.2.4d. Galveston 2-m temperature time-series plots comparing three sets of coupled runs (red), uncoupled runs (blue), and observations (black) from August 25 at 0000 UTC to August 31 at 0000 UTC.

6.2.7.5 Brazoria County Airport Time-Series Plots

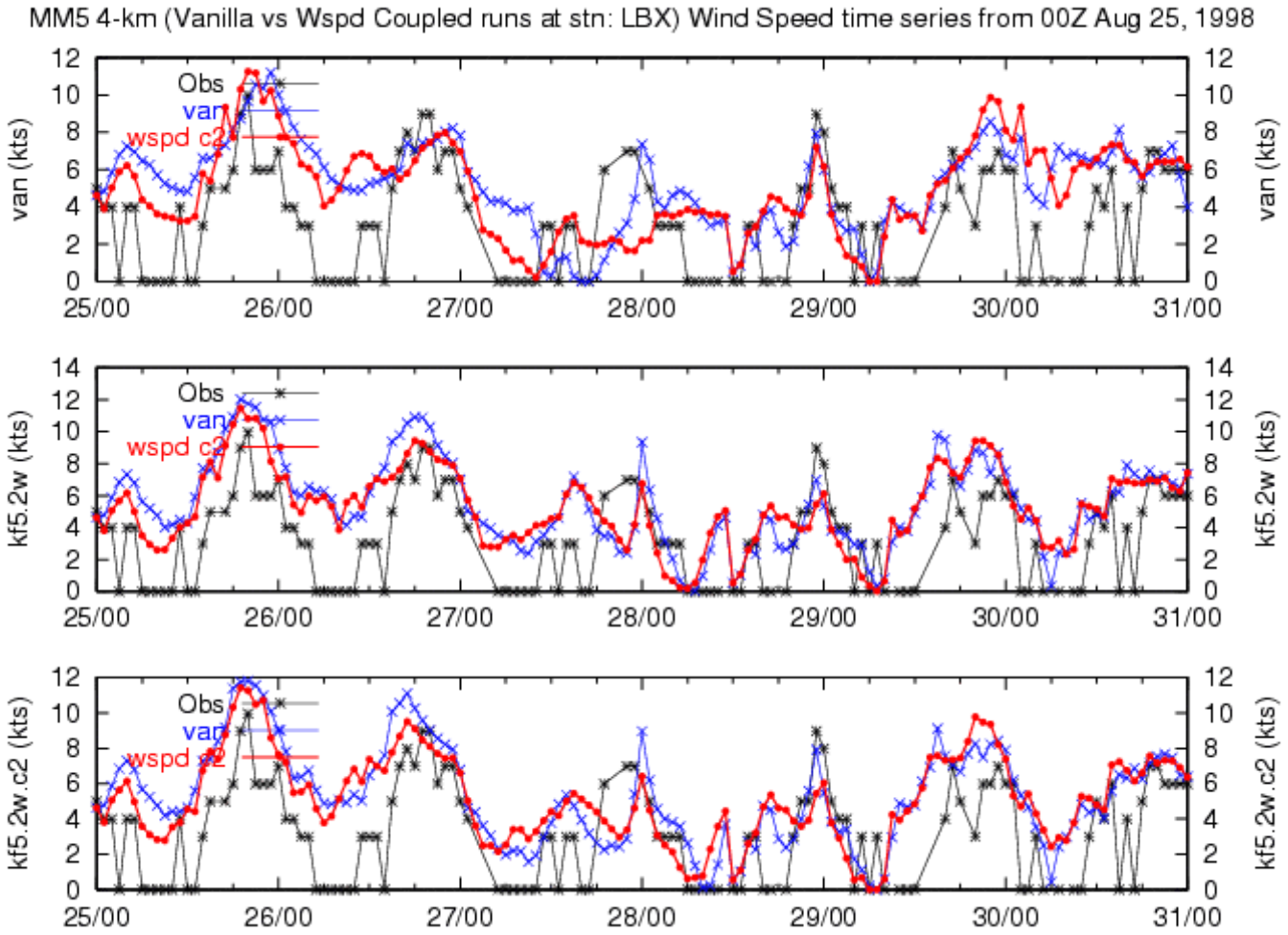

Figure 6.2.5a. Brazoria County Airport 10-m wind speed time-series plots comparing three sets of coupled runs (red), uncoupled runs (blue), and observations (black) from August 25 at 0000 UTC to August 31 at 0000 UTC.

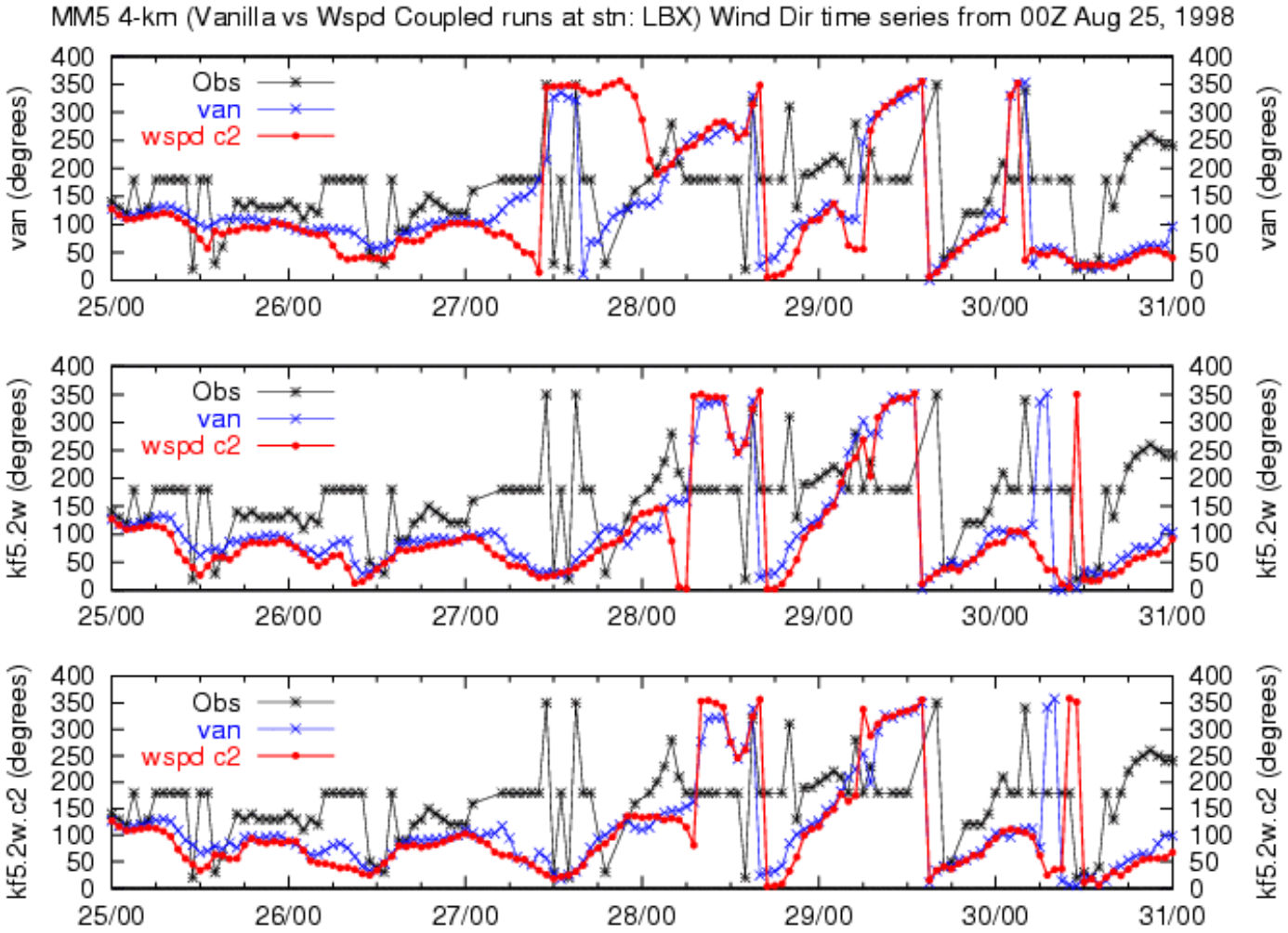

Figure 6.2.5b. Brazoria County Airport 10-m wind direction time-series plots comparing three sets of coupled runs (red), uncoupled runs (blue), and observations (black) from August 25 at 0000 UTC to August 31 at 0000 UTC.

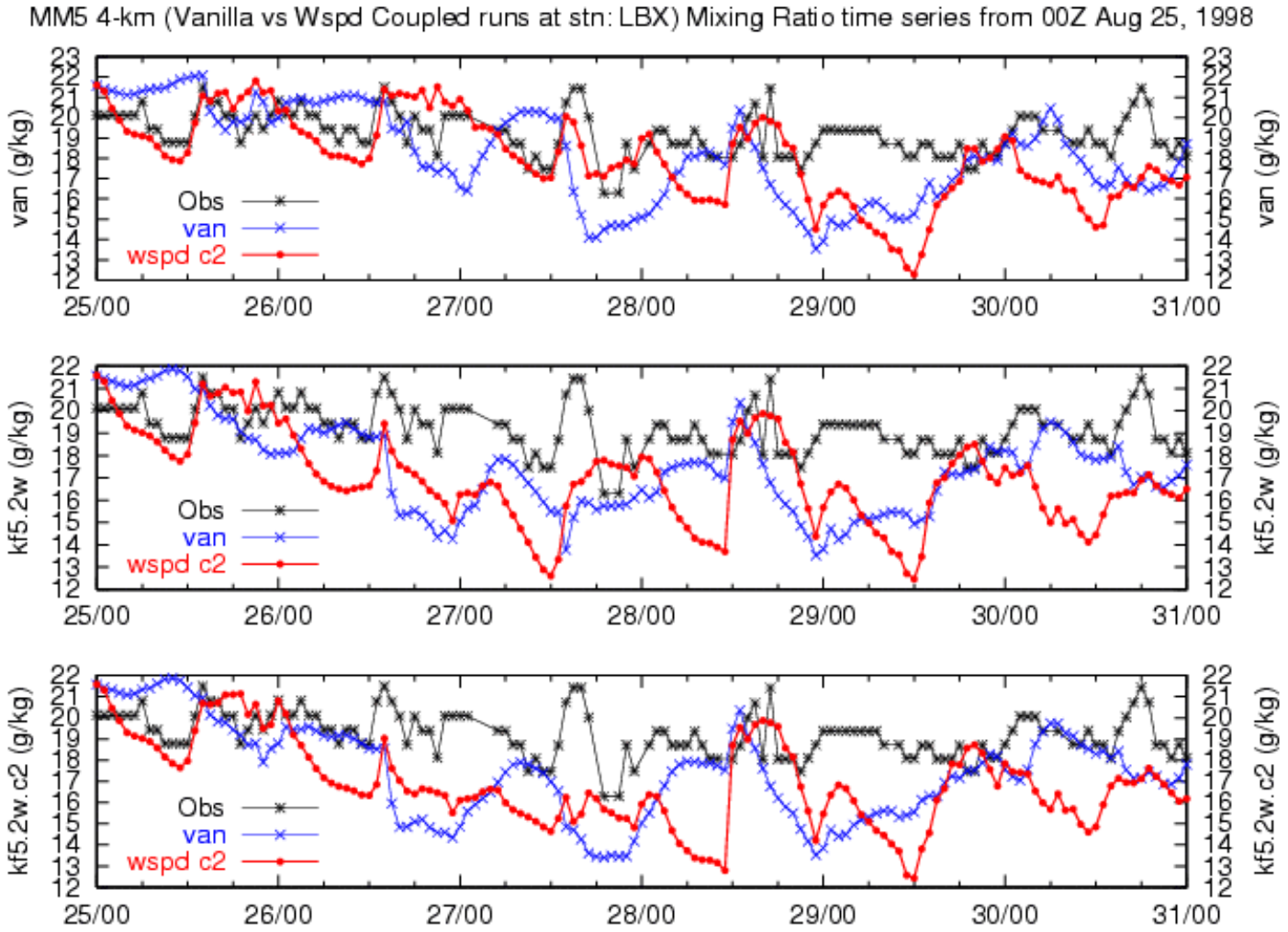

Figure 6.2.5c. Brazoria County Airport 2-m mixing ratio time-series plots comparing three sets of coupled runs (red), uncoupled runs (blue), and observations (black) from August 25 at 0000 UTC to August 31 at 0000 UTC.

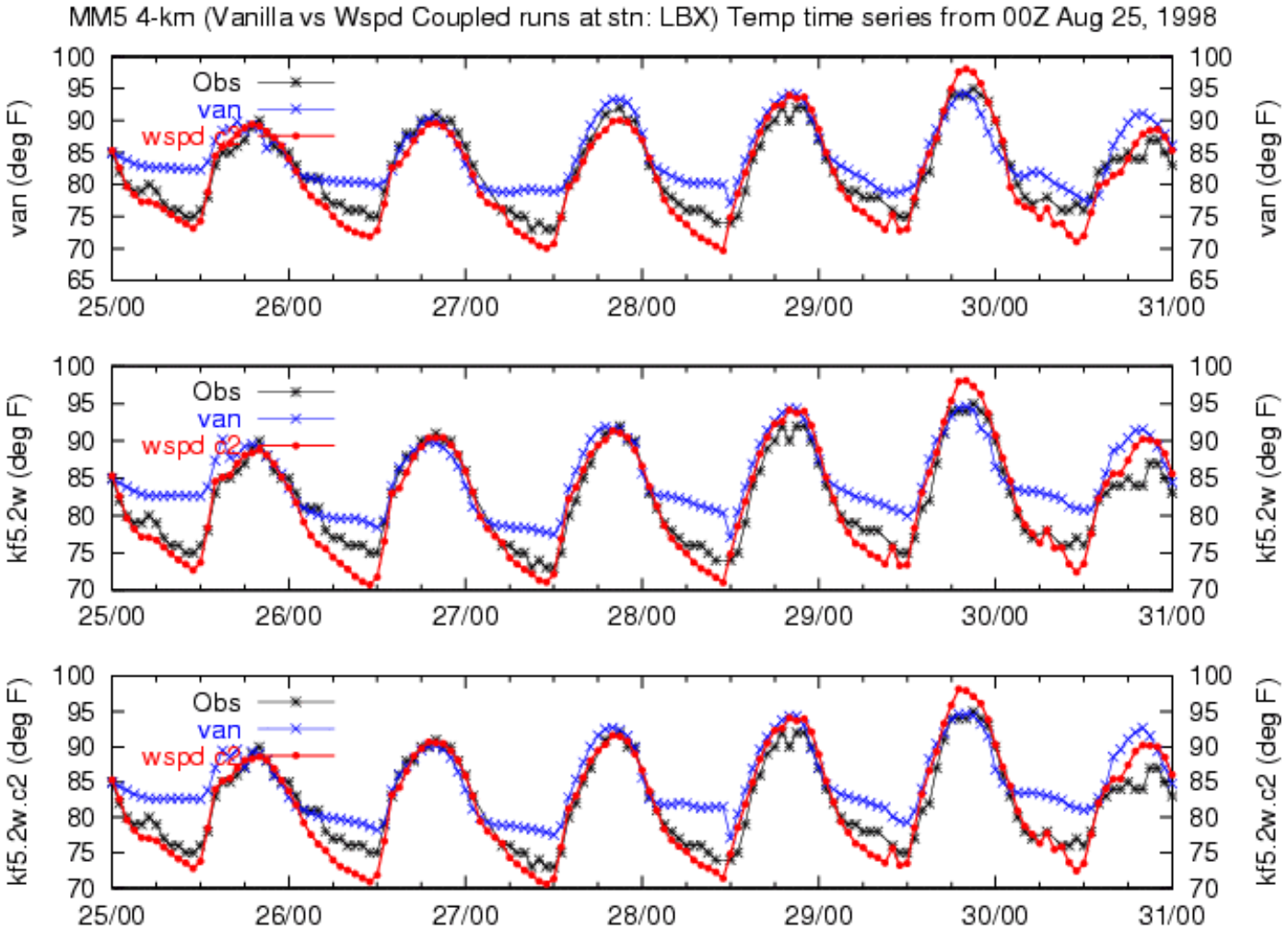

Figure 6.2.5d. Brazoria County Airport 2-m temperature time-series plots comparing three sets of coupled runs (red), uncoupled runs (blue), and observations (black) from August 25 at 0000 UTC to August 31 at 0000 UTC.

6.2.7.6 Palacios Municipal Airport Time-Series Plots

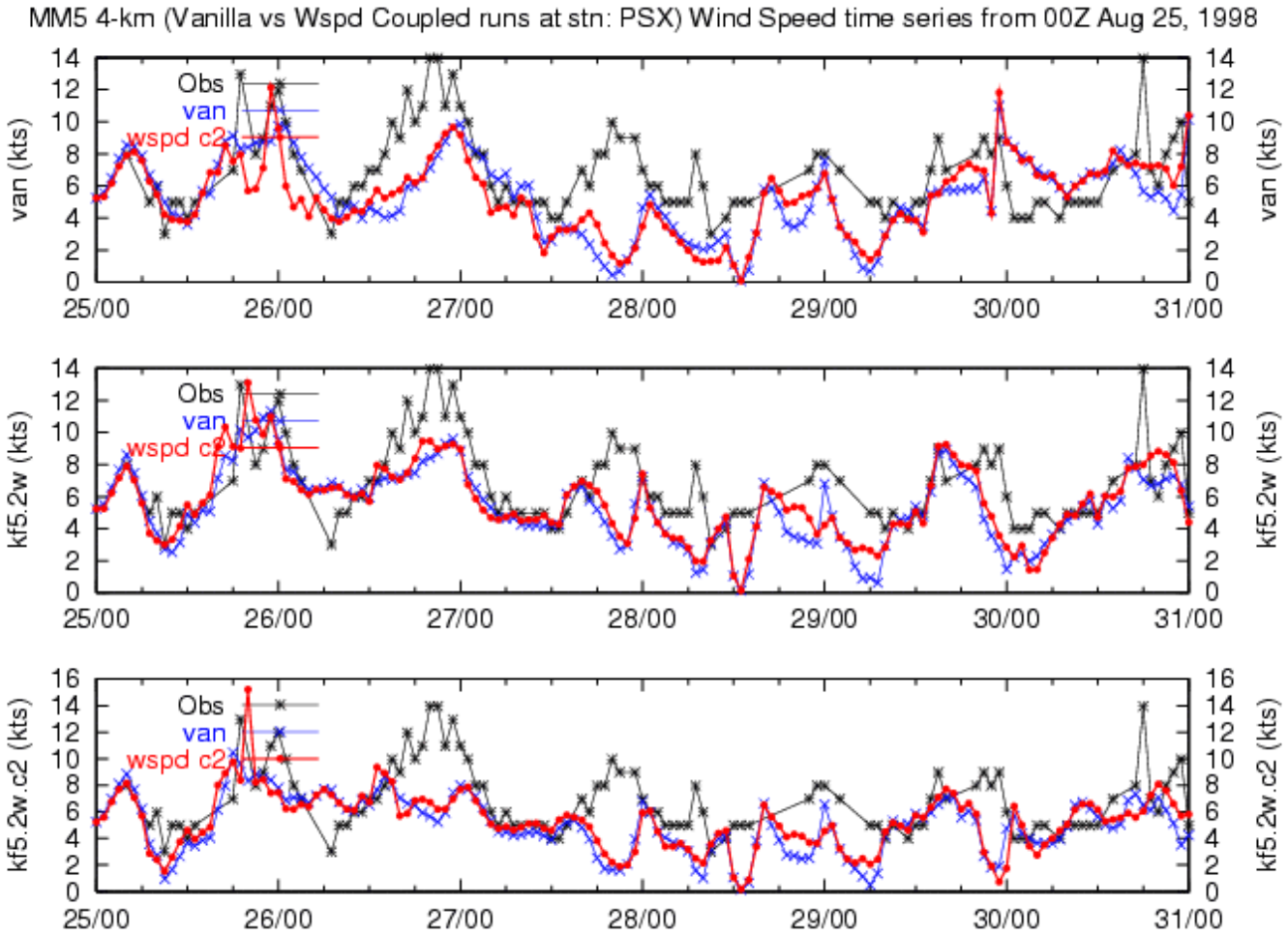

Figure 6.2.6a Palacios 10-m wind speed time-series plots comparing three sets of coupled runs (red), uncoupled runs (blue), and observations (black) from August 25 at 0000 UTC to August 31 at 0000 UTC.

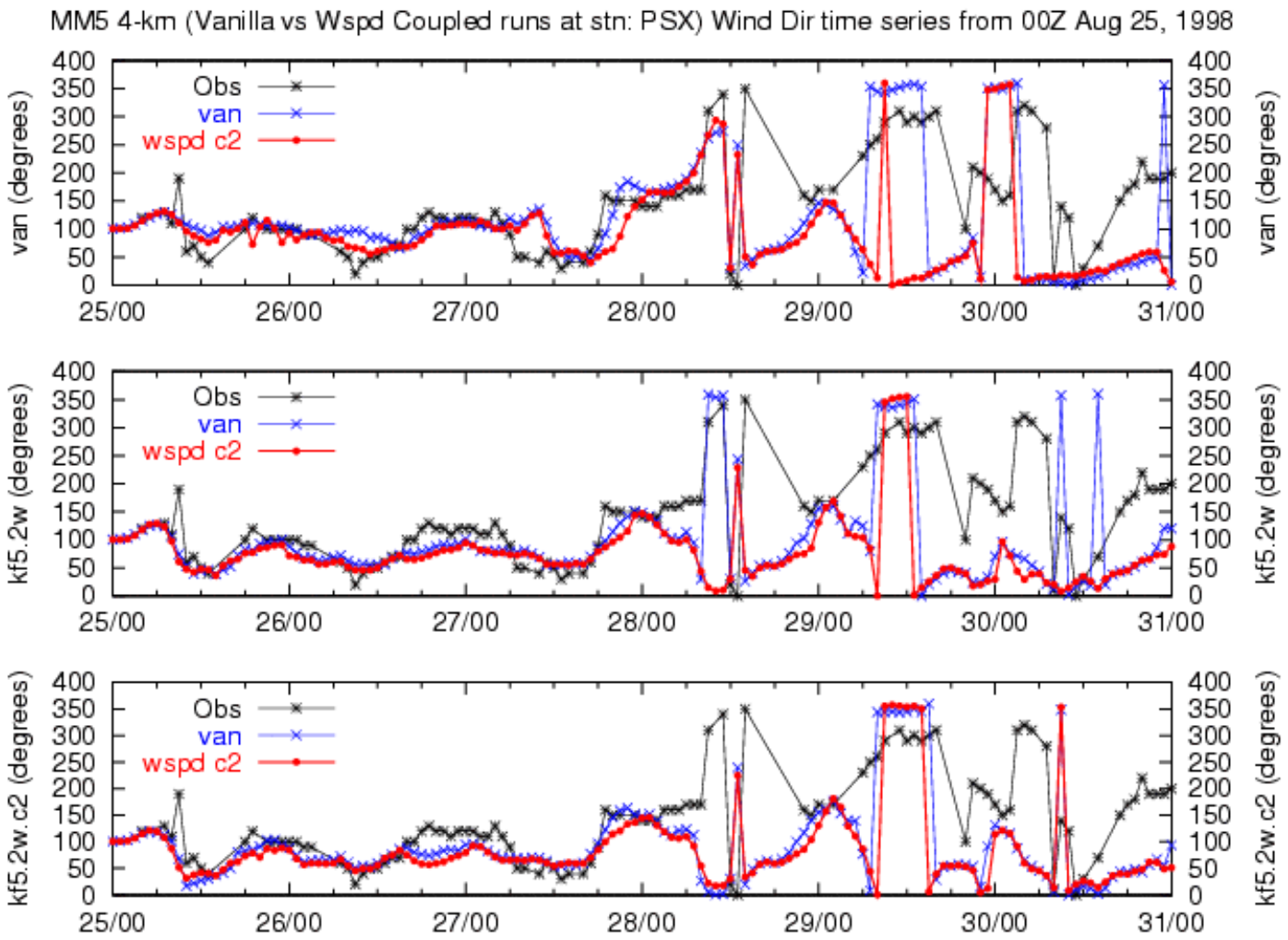

Figure 6.2.6b. Palacios Municipal Airport 10-m wind direction time-series plots comparing three sets of coupled runs (red), uncoupled runs (blue), and observations (black) from August 25 at 0000 UTC to August 31 at 0000 UTC.

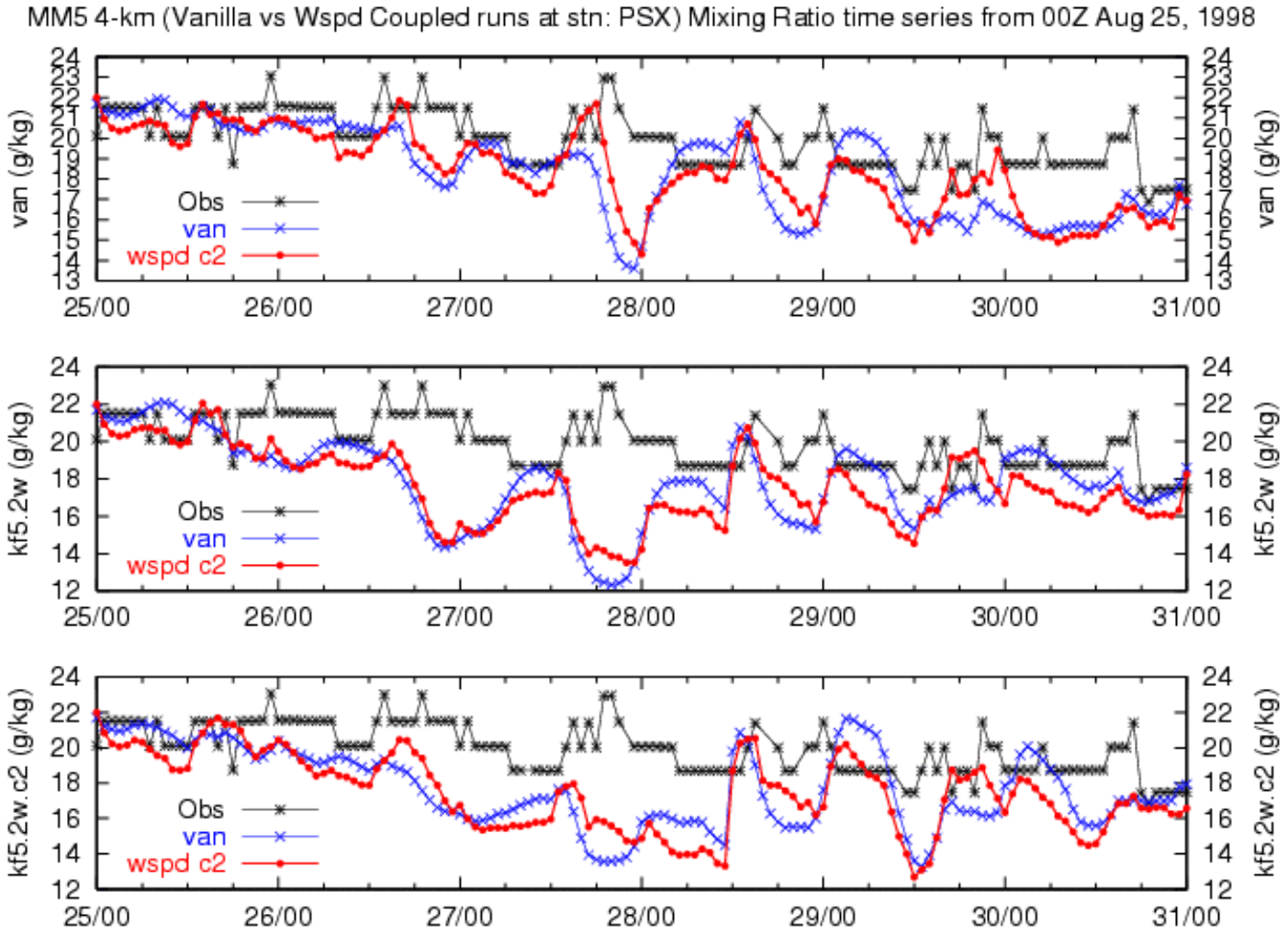

Figure 6.2.6c. Palacios Municipal Airport 2-m mixing ratio time-series plots comparing three sets of coupled runs (red), uncoupled runs (blue), and observations (black) from August 25 at 0000 UTC to August 31 at 0000 UTC.

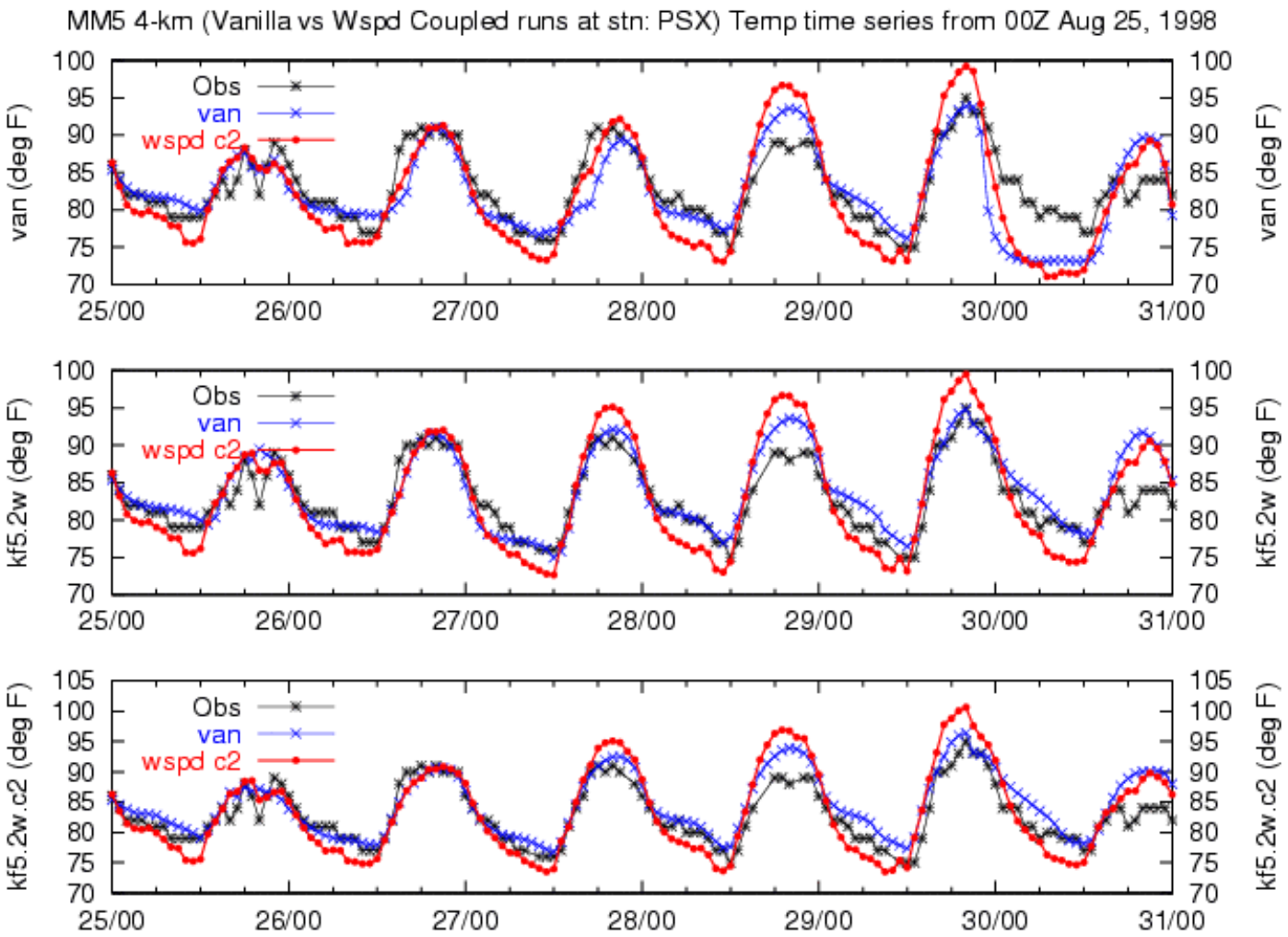

Figure 6.2.6d. Palacios Municipal Airport 2-m temperature time-series plots comparing three sets of coupled runs (red), uncoupled runs (blue), and observations (black) from August 25 at 0000 UTC to August 31 at 0000 UTC.

6.3 Spatial Aggregate Time-Series Plots for Mean, Bias, and Error

Spatial aggregate, bias, and error time-series plots are discussed in this section. These time-series plots smooth out the station-to-station differences and reveal the spatial-mean signal, spatial-mean bias, and spatial-mean absolute errors as functions of time. For each of the three 36 km-12 km cases ("van", "kf5.2w", and "kf5.2w.c2") four figures are presented, one for each of the four variables (wind speed, wind direction, mixing ratio, and temperature) discussed in Section 6.2. The upper panel of each figure shows the spatial-mean observed and modeled (in all cases coupled versus uncoupled) values, the middle panel compares the uncoupled versus coupled spatial-mean biases, and the bottom panel compares the uncoupled versus coupled mean-absolute error. The number of observations is also presented in the bottom panel of each figure.

6.3.1 Wind Speed

For parent case "van" (Figure 6.3.1a), the wind speed mean time-series, bias, and error plots are remarkably similar. The most notable exception occurs the afternoon of August 27, when the coupled model is clearly superior. The bias is variable and changes sign, typically being positive (too windy) at night and negative (too calm) during the day. This is especially true for S1. Between 1200 UTC on August 29 and 0000 UTC on August 30, the models perform well, though they overestimate the wind speed slightly. After 0000 UTC on August 30, both models significantly overestimate wind speed (4-5 kts). This period had the worst statistics of the runs.

For parent case "kf5.2w" (Figure 6.3.1b), two features stand out in contrast to parent case "van." The first is the significant improvement in the coupled model on the afternoon of August 25. The overestimate by the uncoupled model is likely related to its vigorous cloud production (see also Figures 6.7.3 and 6.8.10), which tends to generate wind. The second feature is the improvement starting near 0000 UTC on August 30. This is thought to be a result of the boundary condition improvement in the "kf5" versus "van" 36 km-12 km parent runs.

As in the first two cases, there is not a substantial difference between the coupled and uncoupled models in parent case "kf5.2w.c2" (Figure 6.3.1c). There are a couple of short periods where one outperforms the other, but these are relatively brief and balanced, and reflected in both bias and error time-series plots. Overall, the two "kf5" cases appear to outperform case "van." The better performance is dominated by improvements during and after late afternoon on August 29. Neither the coupled nor uncoupled models are clearly superior with respect to wind speed. Both would result in about the same amount of ventilation if used to drive an air quality model for this episode.

6.3.2 Wind Direction

As Neilson-Gammon has described, wind hodographs tend to precess about a mean wind vector with a rotational frequency tied to the phase equivalency of both the diurnal and inertial periods at about 30° north (Neilson-Gammon, 2001a, 2001b). Though no hodographs were plotted, the mean observed time-series plots for the parent case "van"

reveal such a precession on most days of the episode (Figure 6.3.2a). This is most clearly seen between 1200 UTC August 26 and 1200 UTC August 27, when the wind veered steadily between 50^0 (east-northeast) and 270^0 (west); and between 1200 UTC August 27 and 1200 UTC August 28, when the wind first exhibited about an 8-hour light-and-variable period followed by a "reset" to around 120^0 (east-southeast) and then veered steadily to about 320^0 (west-northwest).

Parcel trajectories tend to follow precessing spirals which "blow" along the mean wind vector. Under a scenario in which the mean wind is light and doesn't change direction, parcels can approximate a circle in 24 hours. Both coupled and uncoupled models do a remarkable job following this directional precession through the beginning of the "reset" period at 1200 UTC on August 27. During this time, the coupled model has a bit more trouble adjusting, until it recovers at around 0000 UTC on August 28. Note that this was one of the two highest ozone days, and, further, that the calm-followed-by reset was associated with the strengthening High and its weak anticyclonic flow over Houston. The mean observed wind speed during the calm period was about 2 kts.

Another reset occurs during the afternoon of August 28, with the approaching trough, when the mean wind shifts from about 300^0 (west-northwest) to 150^0 (south-southeast). Here, the timing of the coupled model "reset" is better than the uncoupled, the uncoupled adjusting much too soon. In general, the directional bias and errors are remarkably low through about 1800 UTC on August 27, during the middle of the calm. From after the second reset on the afternoon of August 28 through the end of the episode, statistics for both models degrade, retaining their similarity in this regard too. Since the land-surface formulation was the only difference between the runs, and they are so similar, almost none of the bias/error can be attributed to the land-surface formulation in either model after 0000 UTC on August 29. Rather, boundary condition/large-scale forcing is thought to be the most important factor here. It is possible that the switch to the EDAS analysis data at 1200 UTC on August 28 played a role in the poorer directional performance after that time. For large blocks of time on August 30, both models predicted winds blowing in opposition to those observed.

Prior to the first "reset," statistics for parent case "kf5.2w" (Figure 6.3.2b) are similar to those for case "van." The first notable difference occurs during the first reset on August 27, when both coupled and uncoupled models shift the wind first to the north-northeast and then gradually "catch up" over the next 18 hours.

Parent case "kf5.2w.c2" (Figure 6.3.2c) adjusts more quickly after the first reset than does case "kf5.2w". Both "kf5" cases are similar following the second "reset" during the afternoon of August 28. Case "kf5.2w.c2" and case "van" appear superior during the reset on August 27. Because case "van" is superior in wind speed, it would be expected to produce the optimal surface mean flow characteristics during S1. Further, there is not a lot of difference in bias/error statistics between the two "kf5" cases and the "van" case during most of S2. For S2, speed statistics were better in the "kf5" runs, with no clear winner between the two directionally, nor between coupled and uncoupled models. Because speeds were similar, one would expect similar ventilation effects during S2 from

either coupled or uncoupled "kf5" runs. Directional differences in the mean appear minor, with both models continuing to do poorly on the afternoon of August 30. Because the "kf5" cases were superior to case "van" for wind speed, they should be better choices for S2, from a wind perspective.

6.3.3 Mixing Ratio

For parent case "van," mixing ratio mean, bias, and error reveal that MM5 output is, on average, too dry (Figure 6.3.3a). This is most true for the uncoupled model; the coupled model recovers during the afternoons of most days, whereas the uncoupled model's dryness persists. The dry errors are larger at night for the uncoupled model, likely because of its dew formation capability. On average, errors range up to 3.5 - 4.0 g/kg, but return to nominal at model initialization. This suggests a fundamental surface moisture problem, especially in the uncoupled model which does not allow dew formation.

Both parent case "kf5.2w" (Figure 6.3.3b) and parent case "kf5.2w.c2" (Figure 6.3.3c) reveal increases in moisture on August 30 when compared to the "van" runs. Correction of the KF-induced boundary condition being the only difference, this illustrates the importance of boundary conditions for scalar moisture variables. Overall, it appears that the "kf5" run sets handled S2 better than the "van" run sets, whereas, case "van" appears slightly better for S1 moisture. Finally, the coupled model appears to do a better job than the uncoupled model during the day, but is drier at night.

6.3.4 Temperature

In all cases, the coupled model outperforms the uncoupled model with respect to 2-m temperature. The two are closest for case "van" (Figure 6.3.4a), less close for case "kf5.2w" (Figure 6.3.4b), and farthest apart (the coupled model is better) for case "kf5.2w.c2" (Figure 6.3.4c). Both models are warmer on August 30 for the "kf5" cases, with the coupled model bias near zero, and the uncoupled model bias near +3.0°F. Temperature appears improved in the "kf5" run sets compared to the "van" case for S2.

The uncoupled model temperature bias is worst (warm) at night and somewhat better, though still too cool, during the day. Given that photochemical reactions are extremely sensitive to temperature, negative biases on August 27 and 29 during daylight hours could retard reaction rates.

In the mean, the phase-lead in morning temperature rise in the uncoupled models is barely discernable. The TOPLATS-coupled runs follow the observed mean temperature curves with no discernable phase difficulty.

The coupled model reveals a modest cold bias at night and warm bias during the day. The latter is likely a reflection of its somewhat warmer surface temperatures, and the former a reflection of the model's nocturnal dry bias. As mentioned above, increasing the moisture in the coupled model would further improve its temperature performance, but further degrade the uncoupled model's performance. This suggests that the coupled model provides a fundamental correction to problems related to the surface physics formulation in the uncoupled model.

6.3.5 Figures for Section 6.3

6.3.5.1 Wind Speed

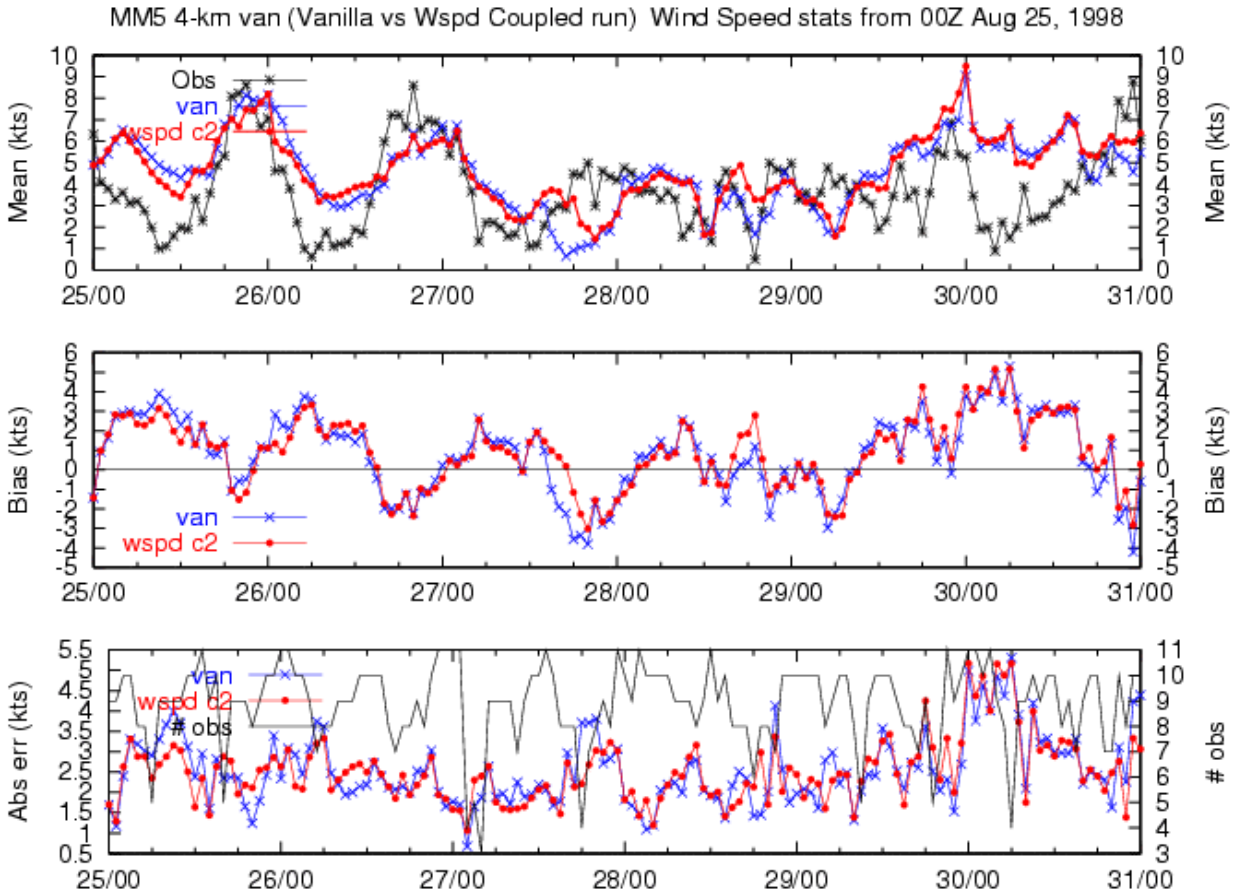

Figure 6.3.1a. Domain average 10-m wind speed time-series plot (top), bias time-series plot (middle), and absolute error time-series plot (bottom) for case "van". The number of observations is shown in the bottom panel.

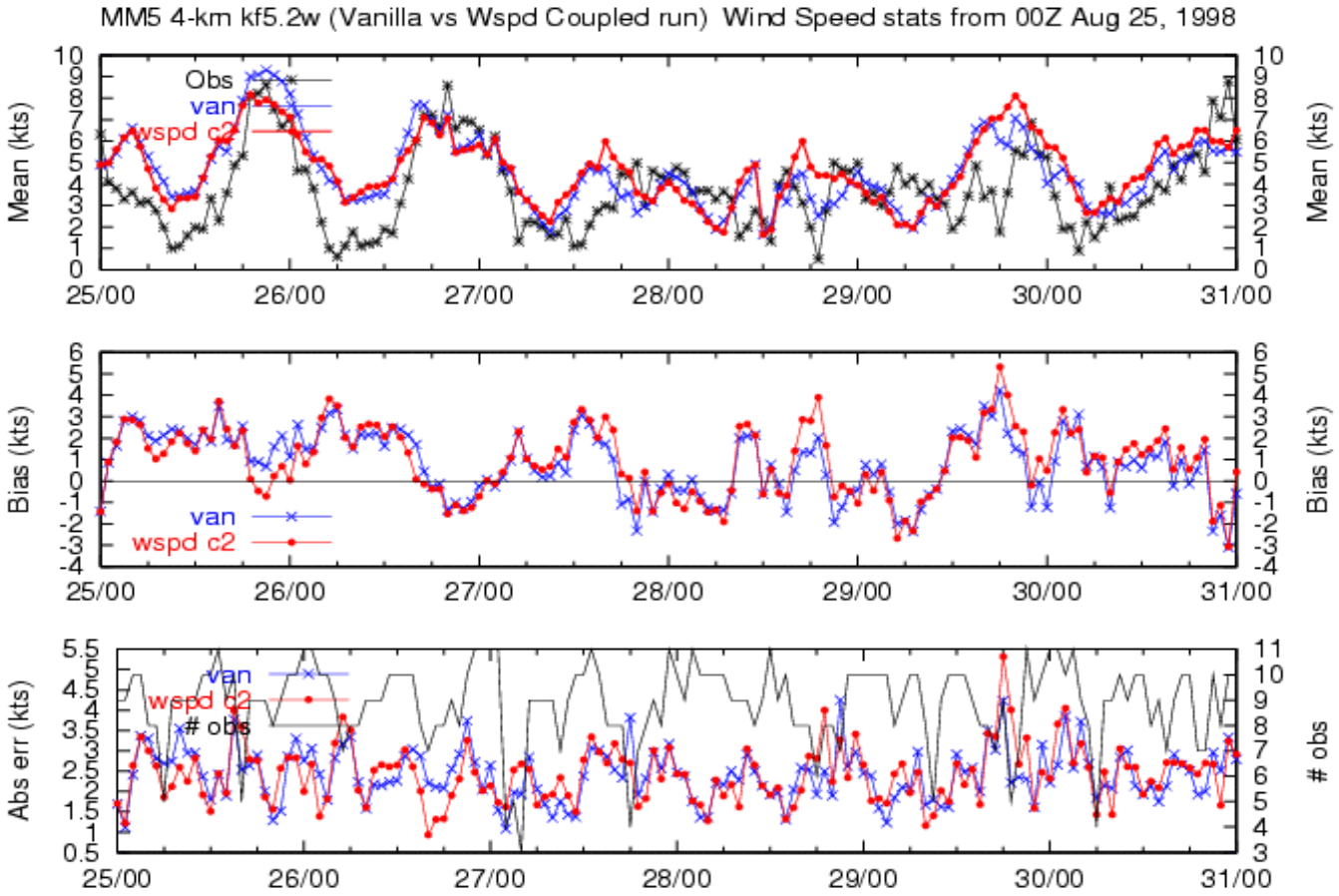

Figure 6.3.1b. Domain average 10-m wind speed time-series plot (top), bias time-series plot (middle), and absolute error time-series plot (bottom) for case "kf5.2w".

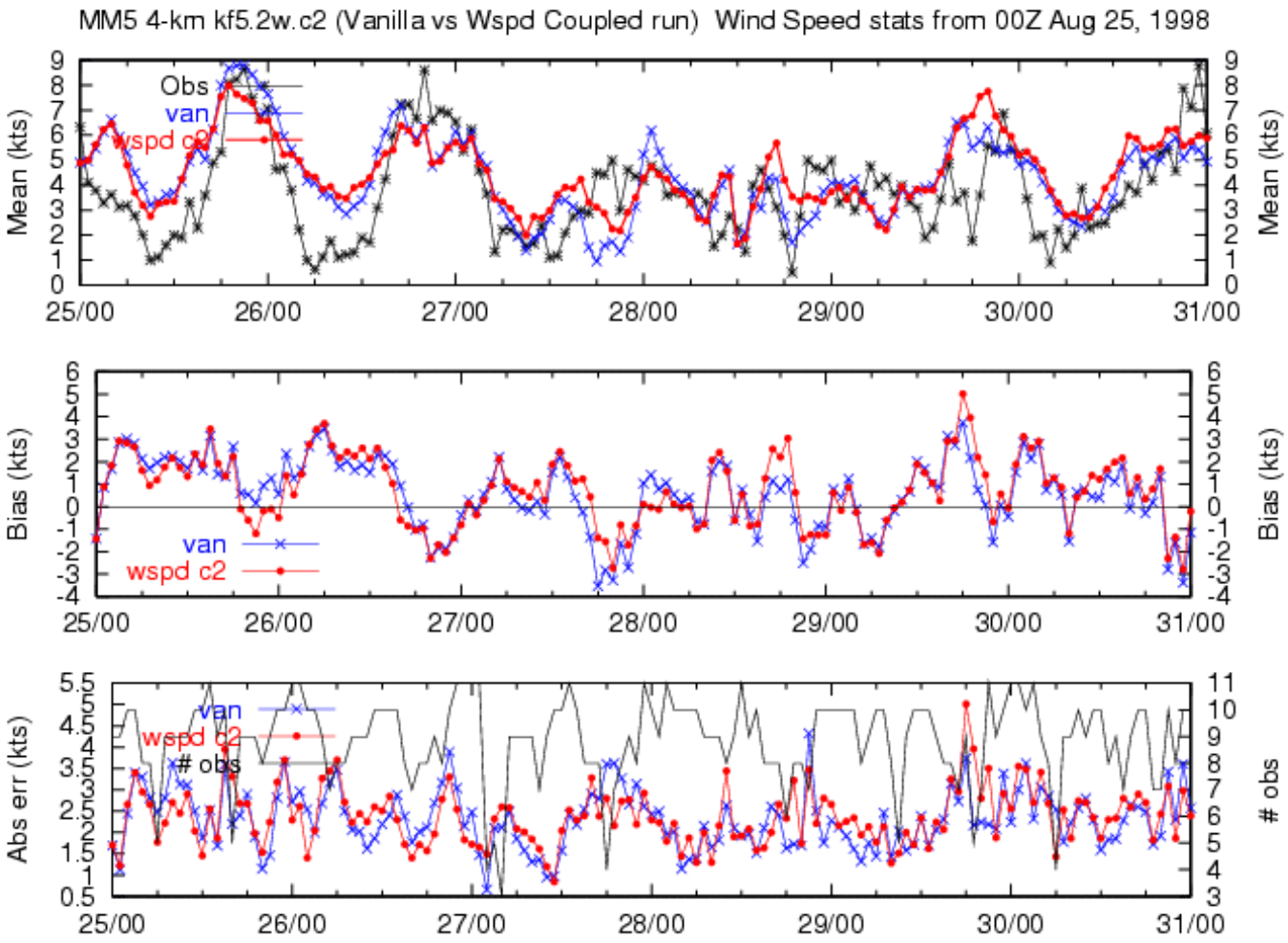

Figure 6.3.1c. Domain average 10-m wind speed time-series plot (top), bias time-series plot (middle), and absolute error time-series plot (bottom) for case "kf5.2w.c2".

6.3.5.2 Wind Direction

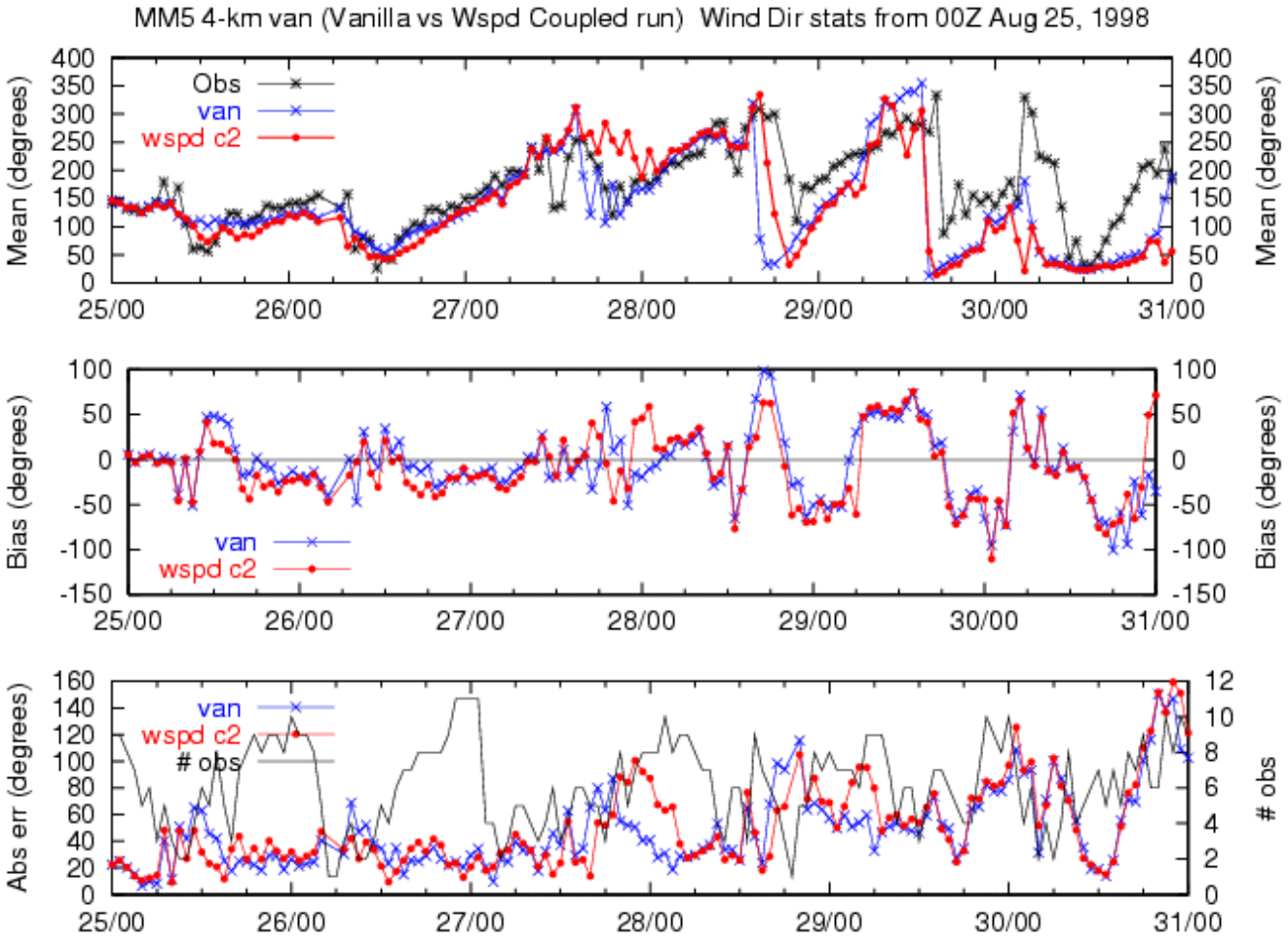

Figure 6.3.2a. Domain average 10-m wind direction time-series plot (top), bias time-series plot (middle), and absolute error time-series plot (bottom) for case "van". The number of observations is shown in the bottom panel.

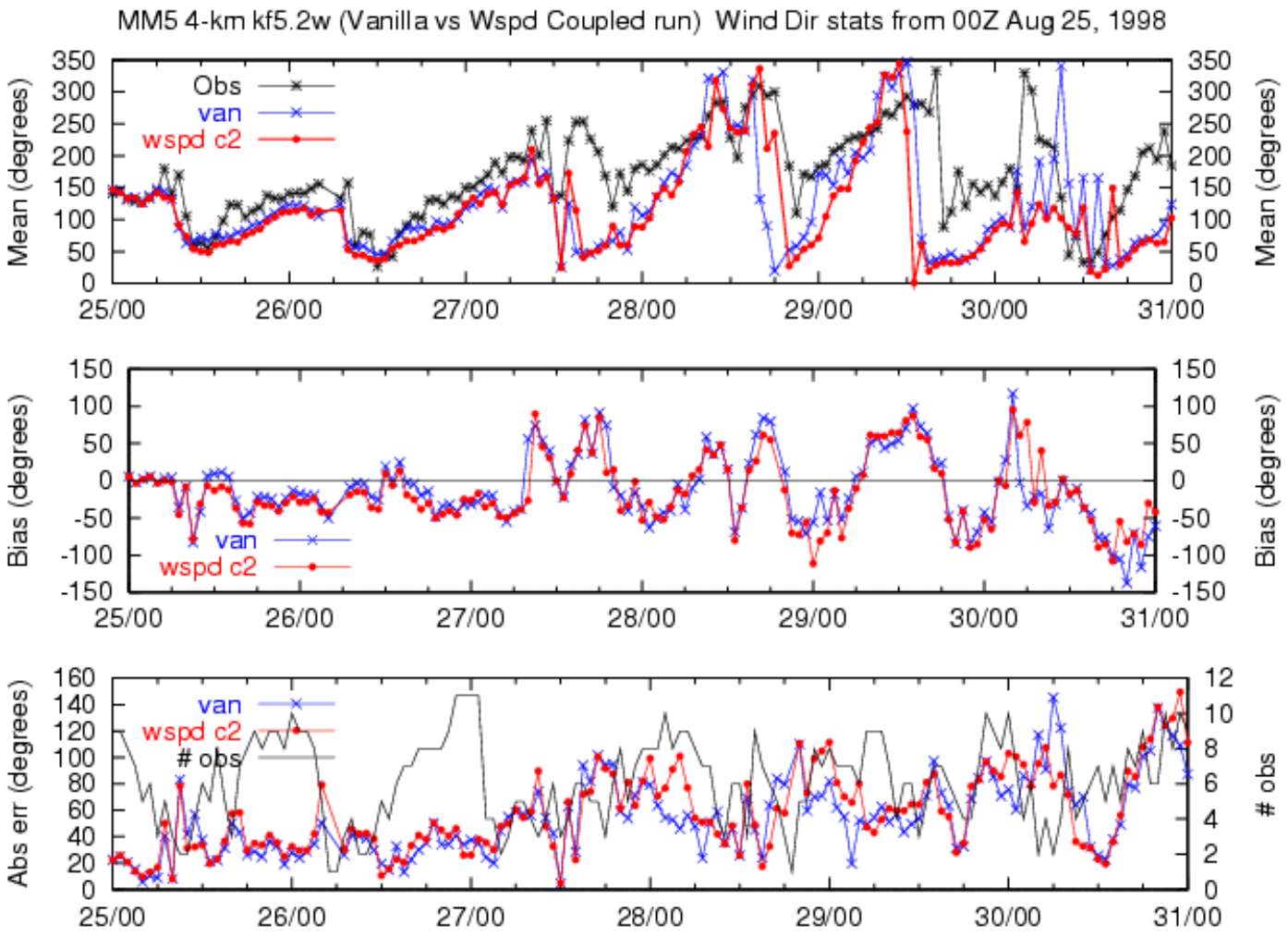

Figure 6.3.2b. Domain average 10-m wind direction time-series plot (top), bias time-series plot (middle), and absolute error time-series plot (bottom) for case "kf5.2w".

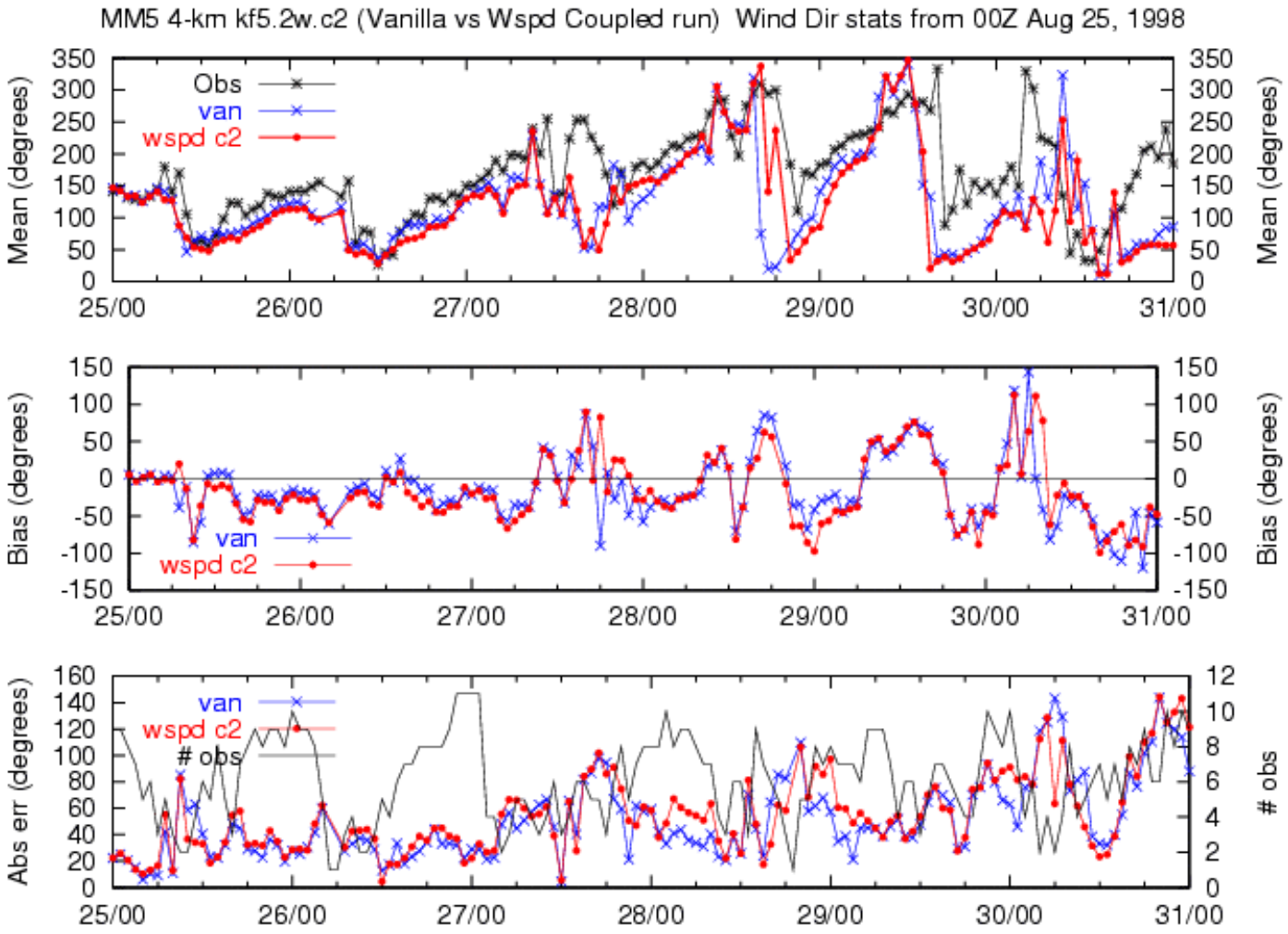

Figure 6.3.2c. Domain average 10-m wind direction time-series plot (top), bias time-series plot (middle), and absolute error time-series plot (bottom) for case "kf5.2w.c2".

6.3.5.3 Mixing Ratio

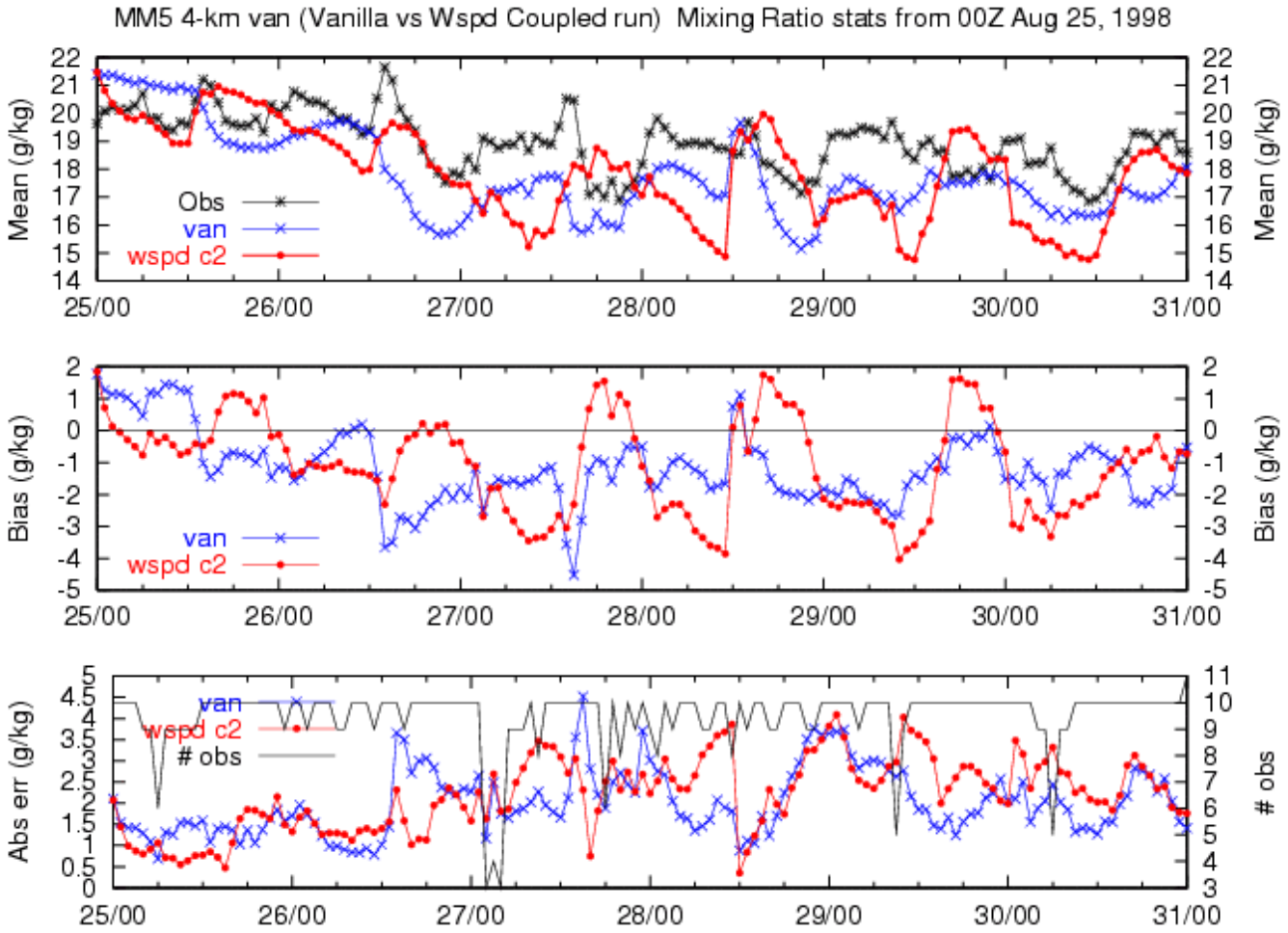

Figure 6.3.3a. Domain average 2-m mixing ratio time-series plot (top), bias time-series plot (middle), and absolute error time-series plot (bottom) for case "van". The number of observations is shown in the bottom panel.

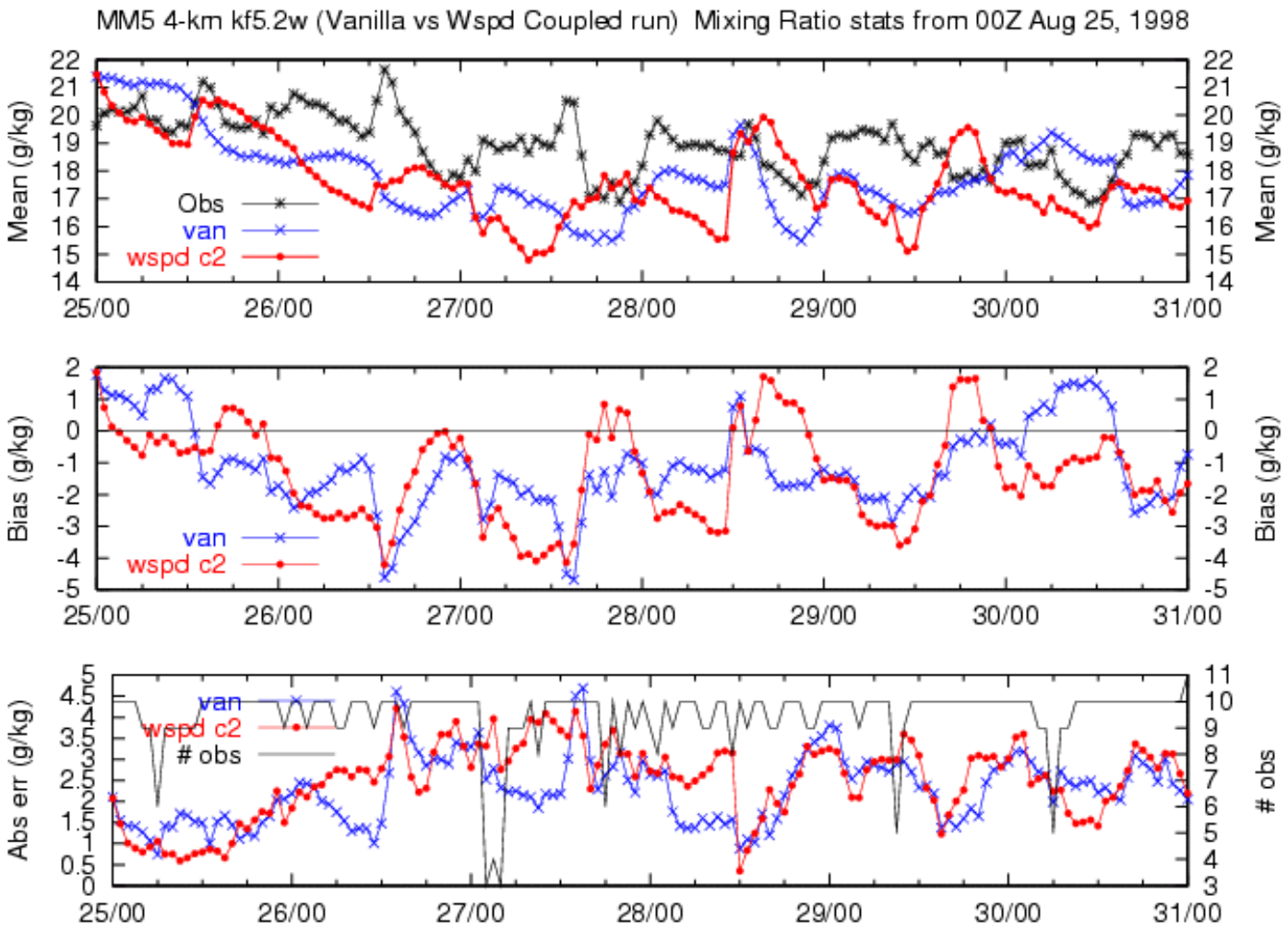

Figure 6.3.3b. Domain average 2-m mixing ratio time-series plot (top), bias time-series plot (middle), and absolute error time-series plot (bottom) for case "kf5.2w".

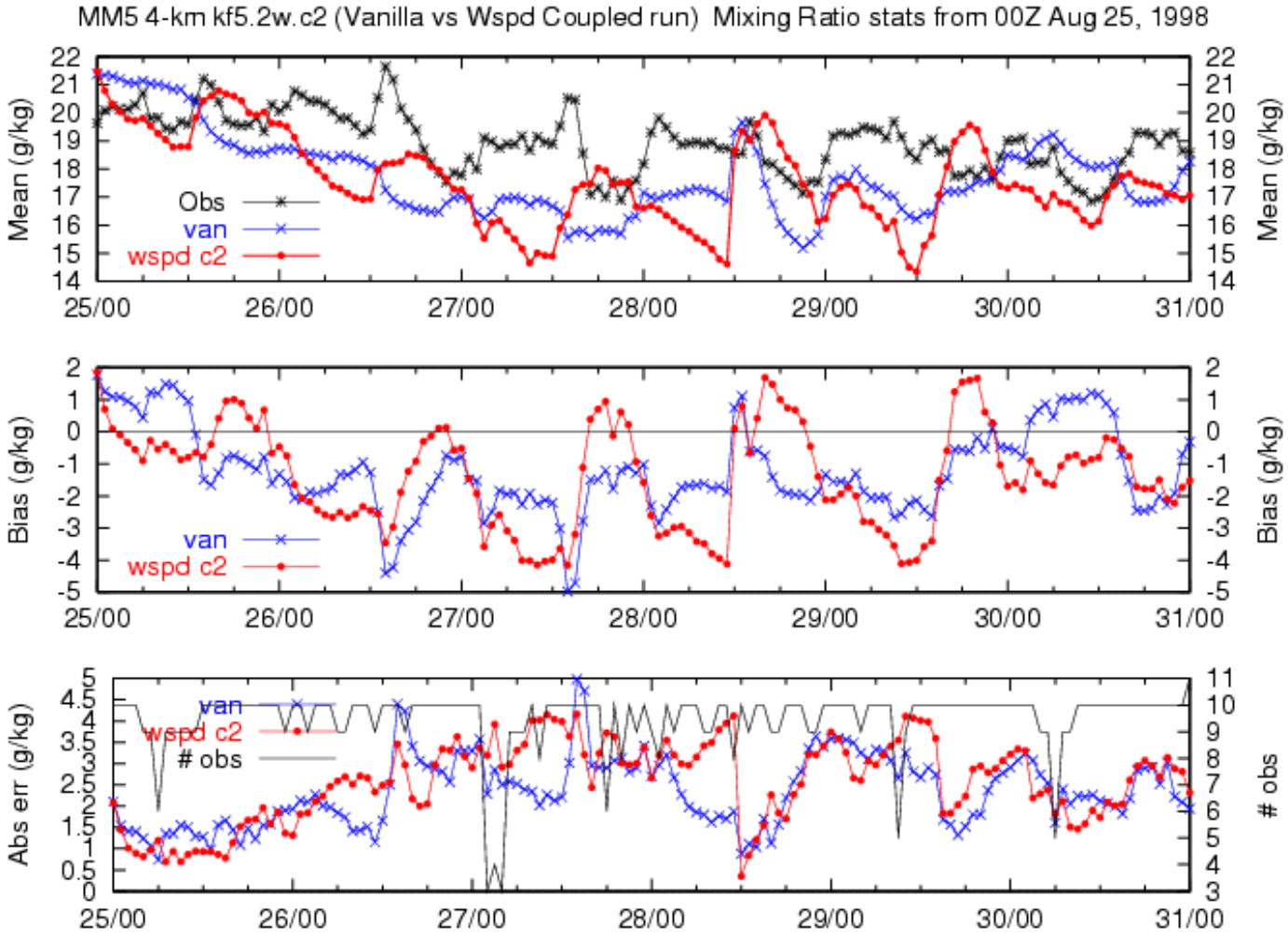

Figure 6.3.3c. Domain average 2-m mixing ratio time-series plot (top), bias time-series plot (middle), and absolute error time-series plot (bottom) for case "kf5.2w.c2".

6.3.5.4 Temperature

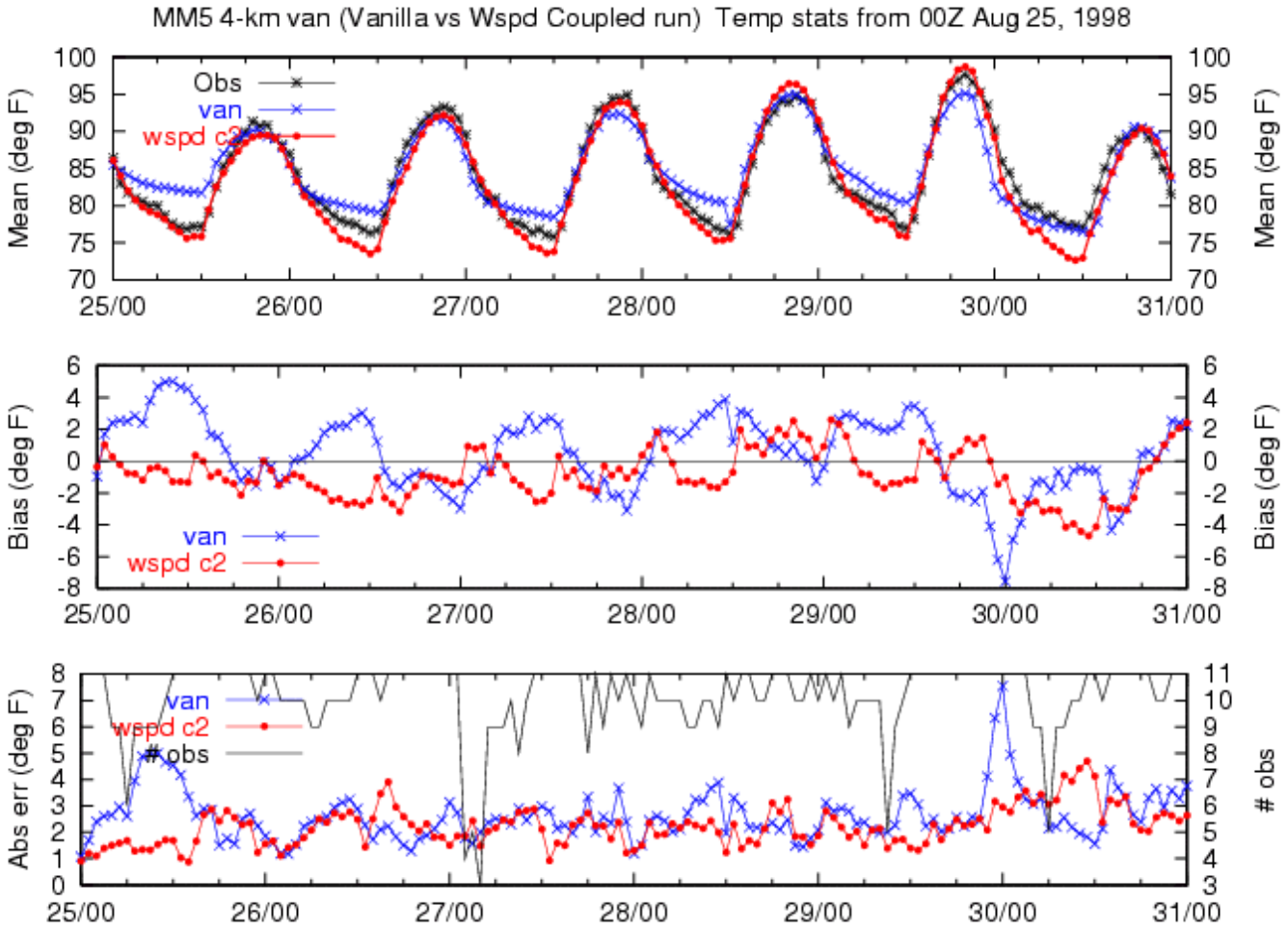

Figure 6.3.4a. Domain average 2-m temperature time-series plot (top), bias time-series plot (middle), and absolute error time-series plot (bottom) for case "van". The number of observations is shown in the bottom panel.

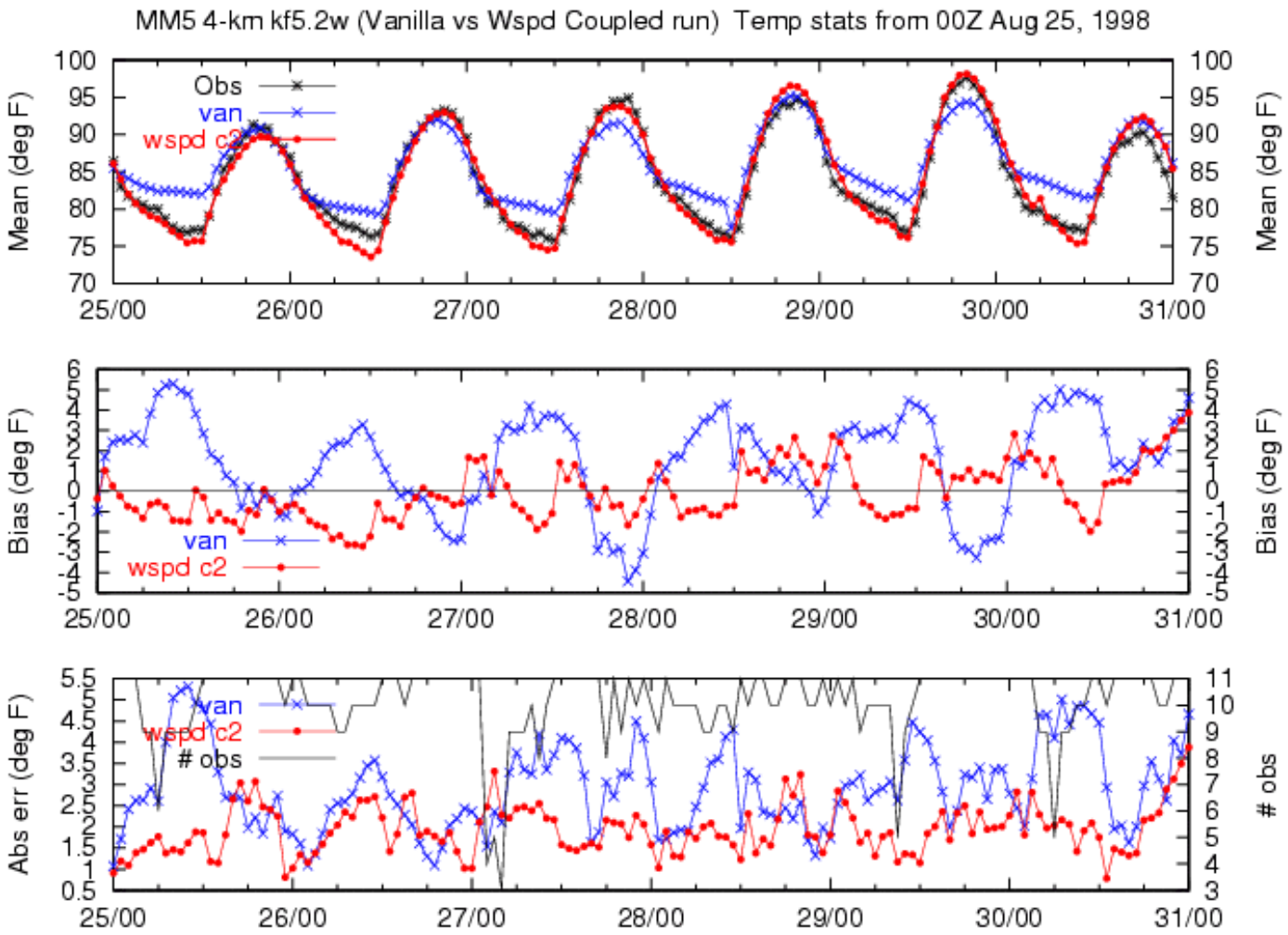

Figure 6.3.4b. Domain average 2-m temperature time-series plot (top), bias time-series plot (middle), and absolute error time-series plot (bottom) for case "kf5.2w".

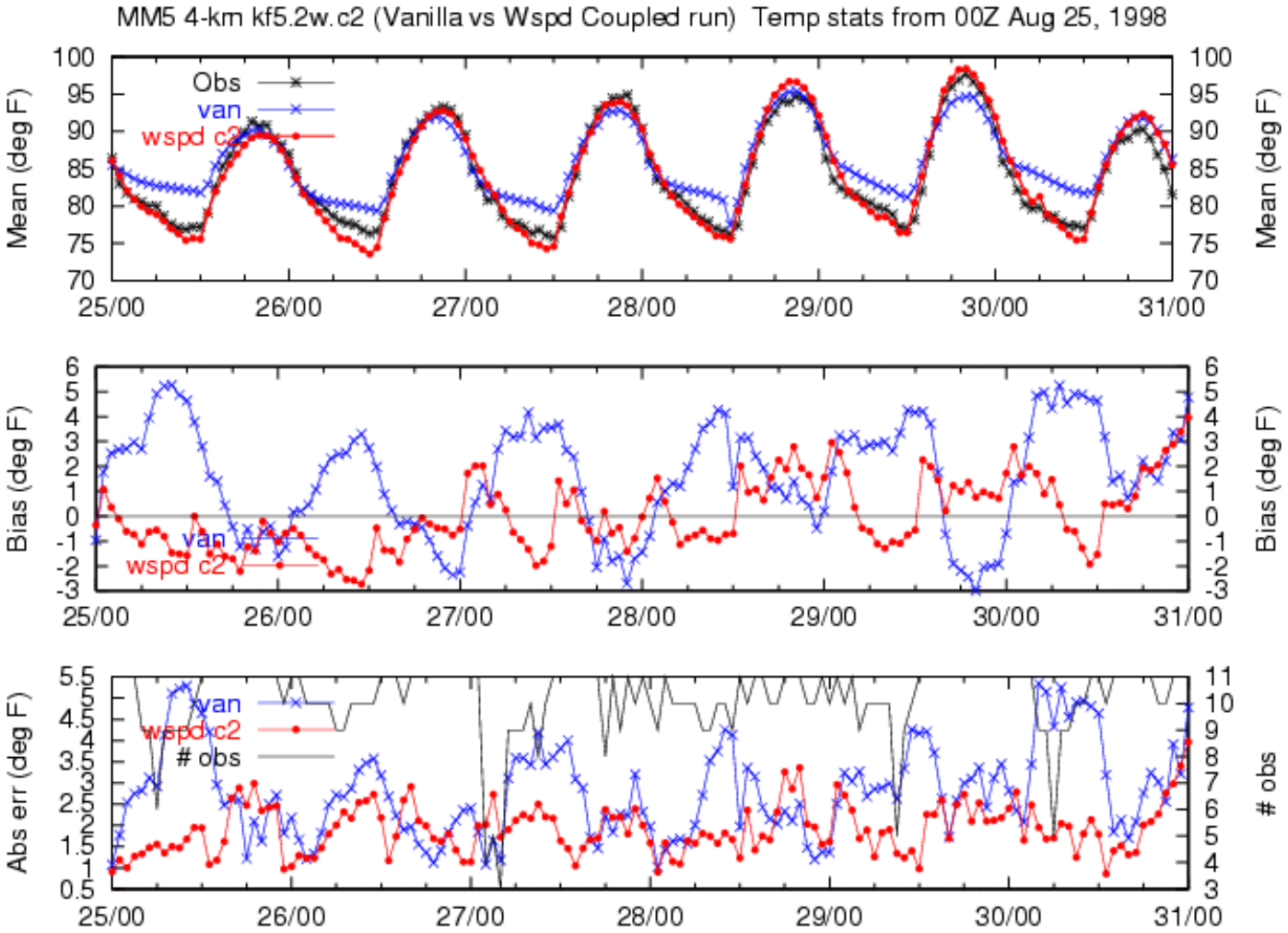

Figure 6.3.4c. Domain average 2-m temperature time-series plot (top), bias time-series plot (middle), and absolute error time-series plot (bottom) for case "kf5.2w.c2".

6.4 Episode Mean Statistics over the 4-km Domain

This section discusses the episodic mean results, constructed by calculating the bias and RMSEs over all data pairs in space and time. These data are presented in both tabular and bar-graph form. The bar graphs are particularly useful for discerning the overall, gross performance of the runs.

Bias and error statistics are calculated as follows:

Absolute Bias: $Bias(t) = \frac{1}{N}\sum_{i=1}^{N}\{V_m(x_i,t) - V_o(x_i,t)\}$;

Mean Absolute Error: $MAE(t) = \frac{1}{N}\sum_{i=1}^{N}\left|V_m(x_i,t) - V_o(x_i,t)\right|$;

Root Mean Square Error: $RMSE(t) = \sqrt{\frac{1}{N}\sum_{i=1}^{N}\{V_m(x_i,t) - \{V_o(x_i,t)\}^2}$;

where $V_m(x_i,t)$ is any model variable at the i^{th} surface-station-location x, $V_o(x_i,t)$ is the observation of that same variable at the same time, N=11 is the number of surface stations, and t is time (on the hour). For the episodic statistics, N is the total number of data pairs over all stations and time, and the statistics are no longer time functions.

Because of distinct differences in nocturnal versus daytime behavior as revealed in the time-series plots in the previous sections, these statistics were broken down into daytime (1200-0000 UTC) and nighttime (0000-1200 UTC) components, as well as the episode mean.

6.4.1 Tables

Tables 6.4 through 6.12 show the episode, daytime, and nighttime mean bias, mean RMSE, and mean absolute error for the temperature (T), dew-point temperature (Td), and mixing ratio (Q) at 2 m, and for the wind-speed (Spd), west-to-east wind component (U), and south-to-north wind component (V) at 10 m. For completeness, both the wind-speed corrected coupled runs and the standard u_* coupled runs have been included, even though the authors believe the coupled results with the standard formula would not be suitable for application in an air quality model (because of the overly-light daytime winds over land). Further, wind statistics for the coupled standard-u_* runs can be counter-intuitive: nearly calm modeled winds can result in smaller daytime errors and biases in some cases. Nevertheless, this type of wind field, which is also observed in many 4-km runs using the standard GSPBL scheme, would promote over-stagnation and over-production of ozone in an air quality model.

Table 6.4. Episodic statistics for case blk.van.van (uncoupled).

	T (°F)	Td (°F)	Q (g/kg)	Spd (kts)	U (kts)	V (kts)
Episode average bias	0.414	-2.184	-1.151	0.843	-1.293	-1.171
Episode average RMSE	3.385	4.211	2.567	3.220	3.369	3.808
Episode average abs error	2.667	3.296	2.017	2.548	2.562	2.868
Daytime average bias	-0.328	-2.395	-1.291	0.124	-1.286	-1.941
Daytime average RMSE	3.388	4.515	2.737	3.176	3.599	4.328
Daytime average abs error	2.625	3.518	2.134	2.485	2.684	3.227
Nighttime average bias	1.426	-1.908	-0.968	1.711	-1.302	-0.241
Nighttime average RMSE	3.381	3.780	2.328	3.272	3.070	3.065
Nighttime average abs error	2.724	3.006	1.865	2.625	2.416	2.436

Table 6.5. Episodic statistics case for blk.van.c2 (coupled).

	T (°F)	Td (°F)	Q (g/kg)	Spd (kts)	U (kts)	V (kts)
Episode average bias	-0.381	-2.540	-1.329	-0.947	-0.325	-1.336
Episode average RMSE	2.710	4.688	2.786	3.786	3.263	3.630
Episode average abs error	2.144	3.686	2.179	2.961	2.498	2.668
Daytime average bias	0.087	-1.628	-0.792	-2.522	0.443	-1.725
Daytime average RMSE	2.669	4.369	2.673	4.306	3.483	4.131
Daytime average abs error	2.076	3.397	2.080	3.410	2.642	2.999
Nighttime average bias	-1.026	-3.727	-2.027	0.951	-1.250	-0.868
Nighttime average RMSE	2.765	5.073	2.926	3.044	2.976	2.913
Nighttime average abs error	2.239	4.061	2.307	2.421	2.324	2.270

Table 6.6. Episodic statistics for case blk.wspd.van.c2 (coupled with u_* correction).

	T (°F)	Td (°F)	Q (g/kg)	Spd (kts)	U (kts)	V (kts)
Episode average bias	-0.822	-2.090	-1.040	0.907	-1.261	-2.069
Episode average RMSE	2.799	4.680	2.800	3.184	3.413	4.216
Episode average abs error	2.224	3.652	2.185	2.526	2.606	3.154
Daytime average bias	-0.523	-0.828	-0.296	0.442	-1.166	-3.063
Daytime average RMSE	2.789	4.274	2.671	3.156	3.562	4.977
Daytime average abs error	2.191	3.342	2.101	2.479	2.650	3.791
Nighttime average bias	-1.233	-3.733	-2.007	1.468	-1.376	-0.870
Nighttime average RMSE	2.813	5.162	2.959	3.218	3.223	3.057
Nighttime average abs error	2.270	4.055	2.293	2.582	2.553	2.387

Table 6.7. Episodic statistics for case blk.kf5.2w.van (uncoupled).

	T (°F)	Td (°F)	Q (g/kg)	Spd (kts)	U (kts)	V (kts)
Episode average bias	1.421	-2.091	-1.107	0.795	-1.759	-1.645
Episode average RMSE	3.629	4.634	2.843	3.009	3.473	3.742
Episode average abs error	2.910	3.723	2.291	2.426	2.625	2.896
Daytime average bias	0.505	-2.484	-1.353	0.687	-2.141	-2.598
Daytime average RMSE	3.467	5.019	3.053	3.165	4.045	4.306
Daytime average abs error	2.740	3.973	2.414	2.539	3.052	3.373
Nighttime average bias	2.682	-1.580	-0.786	0.925	-1.298	-0.495
Nighttime average RMSE	3.842	4.078	2.545	2.810	2.622	2.922
Nighttime average abs error	3.145	3.397	2.130	2.290	2.110	2.321

Table 6.8. Episodic statistics for case blk.kf5.2w.c2 (coupled).

	T (°F)	Td (°F)	Q (g/kg)	Spd (kts)	U (kts)	V (kts)
Episode average bias	0.217	-2.595	-1.398	-0.989	-0.623	-1.715
Episode average RMSE	2.466	4.986	3.025	3.611	3.170	3.693
Episode average abs error	1.930	4.010	2.417	2.866	2.434	2.801
Daytime average bias	0.566	-1.971	-1.020	-2.255	0.124	-2.138
Daytime average RMSE	2.537	5.089	3.122	4.139	3.483	4.186
Daytime average abs error	1.946	3.998	2.454	3.313	2.622	3.190
Nighttime average bias	-0.265	-3.408	-1.890	0.537	-1.523	-1.205
Nighttime average RMSE	2.363	4.849	2.895	2.846	2.746	2.993
Nighttime average abs error	1.909	4.025	2.368	2.327	2.206	2.332

Table 6.9. Episodic statistics for case blk.wspd.kf5.2w.c2 (coupled with u_* correction).

	T (°F)	Td (°F)	Q (g/kg)	Spd (kts)	U (kts)	V (kts)
Episode average bias	-0.020	-2.425	-1.293	0.896	-1.811	-2.535
Episode average RMSE	2.456	5.020	3.062	3.021	3.468	4.333
Episode average abs error	1.933	4.094	2.485	2.418	2.615	3.411
Daytime average bias	0.256	-1.496	-0.731	0.881	-1.958	-3.614
Daytime average RMSE	2.534	4.999	3.116	3.183	3.913	5.111
Daytime average abs error	1.956	3.992	2.493	2.525	2.873	4.176
Nighttime average bias	-0.400	-3.634	-2.023	0.914	-1.634	-1.235
Nighttime average RMSE	2.344	5.048	2.990	2.813	2.841	3.150
Nighttime average abs error	1.902	4.227	2.475	2.288	2.304	2.489

Table 6.10. Episodic statistics for case blk.kf5.2w.c2.van (uncoupled).

	T (°F)	Td (°F)	Q (g/kg)	Spd (kts)	U (kts)	V (kts)
Episode average bias	1.530	-2.266	-1.206	0.595	-1.509	-1.171
Episode average RMSE	3.519	4.722	2.883	2.963	3.326	3.555
Episode average abs error	2.800	3.843	2.351	2.324	2.509	2.686
Daytime average bias	0.638	-2.557	-1.390	0.202	-1.691	-2.190
Daytime average RMSE	3.248	5.040	3.057	3.125	3.802	4.096
Daytime average abs error	2.548	4.004	2.426	2.443	2.840	3.127
Nighttime average bias	2.759	-1.886	-0.965	1.070	-1.290	0.057
Nighttime average RMSE	3.861	4.273	2.640	2.755	2.641	2.767
Nighttime average abs error	3.148	3.634	2.255	2.180	2.111	2.154

Table 6.11. Episodic statistics for case blk.kf5.2w.c2.c2 (coupled).

	T (°F)	Td (°F)	Q (g/kg)	Spd (kts)	U (kts)	V (kts)
Episode average bias	0.322	-2.644	-1.411	-1.064	-0.486	-1.412
Episode average RMSE	2.494	5.057	3.045	3.705	3.256	3.582
Episode average abs error	1.929	4.093	2.459	2.884	2.491	2.673
Daytime average bias	0.667	-1.890	-0.958	-2.524	0.371	-2.003
Daytime average RMSE	2.620	4.974	3.046	4.326	3.560	4.115
Daytime average abs error	1.988	3.959	2.430	3.401	2.654	3.096
Nighttime average bias	-0.152	-3.626	-2.001	0.698	-1.519	-0.699
Nighttime average RMSE	2.310	5.163	3.044	2.779	2.845	2.809
Nighttime average abs error	1.848	4.268	2.496	2.260	2.295	2.163

Table 6.12. Episodic statistics for case blk.wspd.kf5.2w.c2.c2 (coupled with u_* correction).

	T (°F)	Td (°F)	Q (g/kg)	Spd (kts)	U (kts)	V (kts)
Episode average bias	0.026	-2.538	-1.338	0.712	-1.586	-2.029
Episode average RMSE	2.448	5.219	3.142	2.963	3.339	4.090
Episode average abs error	1.916	4.236	2.558	2.371	2.556	3.144
Daytime average bias	0.280	-1.461	-0.691	0.433	-1.559	-3.116
Daytime average RMSE	2.585	5.028	3.119	3.107	3.687	4.849
Daytime average abs error	1.993	4.020	2.505	2.467	2.715	3.869
Nighttime average bias	-0.324	-3.939	-2.179	1.049	-1.618	-0.719
Nighttime average RMSE	2.247	5.457	3.171	2.780	2.864	2.924
Nighttime average abs error	1.811	4.517	2.627	2.255	2.363	2.270

Bar charts showing the bias and RMSE corresponding to the above tables are presented in Figures 6.4.1 through 6.4.6. These figures facilitate interpretation of the tabular numbers and serve as the basis for the following discussion.

6.4.2 Discussion

Temperature: Figures 6.4.1a through 6.4.1f

The episode-mean temperature bias is clearly best for the two "kf5" coupled runs. The "van" coupled run is biased slightly cold. The best uncoupled run was case "van." Both during the day and at night, the coupled "kf5" runs outperformed the uncoupled runs.

Though the uncoupled "van" temperature bias may be slightly better than the coupled "van" bias, the RMSEs reveal that the TOPLATS-coupled runs are better for all cases, with an average RMSE difference approaching 1.0°F. This means that there are more large temperature errors, in addition to the mean errors, in the uncoupled model. Both SRB and NEXRAD which drive TOPLATS, along with TOPLATS' superior spatial land-use and land-surface physics, no doubt play a major role in this improvement.

Moisture: Figures 6.4.2a through 6.4.2f

Overall, the coupled model case "van" performs best in the mean, improving over the uncoupled model significantly during daylight hours when photochemistry is active. Of less significance is the dry bias at night, which is worse in the coupled model. The two "kf5" coupled runs are marginally worse in the mean, but are still better during the critical daytime hours. The daytime RMSEs are essentially equivalent; thus, given better mean daytime biases, the coupled models will give a better overall estimate of absolute daytime moisture.

Wind Speed: Figures 6.4.3a through 6.4.3f

All six coupled and uncoupled runs reveal episodic mean positive speed biases of between 0.5 kts and 1.0 kts. Over a 10-hour daytime period, when four of the six biases are under 0.5 kts, a parcel will travel two to four miles farther than it would in nature. This may be an unavoidable consequence of scale: it is hard not to overestimate the wind slightly in a mesoscale model. At night, the speed biases are greatest, with the uncoupled "van" case exceeding 1.5 kts. RMSEs are virtually identical between the uncoupled and coupled models. Thus, from a purely ventilation/dispersion viewpoint, neither coupled nor uncoupled model would be expected to outperform the other.

Wind Direction: Figures 6.4.4a through 6.4.5f

Both U-components and V-components were evaluated. The episodic mean U-component biases are nearly identical between all coupled and uncoupled runs, averaging around –1.5 kts. For a mean wind blowing out of the southeast, this suggests a counterclockwise bias (more out of the east). During the day, this bias is slightly smaller

for the coupled model than for the uncoupled model and slightly larger at night. There is no significant U-component RMSE difference in the mean at night or during the day.

The uncoupled model is clearly better at replicating the observed V-component of the wind, with a mean negative bias of around –1.3 kts, as opposed to a mean negative bias of around –2.2 kts for the coupled model. This again suggests a counterclockwise bias for a mean wind blowing out of the southeast. During the day, the coupled model performance is worst, with biases of around –3.3 kts (versus –2.3 kts for the uncoupled model). At night, the biases decrease to less than –1.0 kts for all models; the coupled model is, on average, about .5 kts worse. RMSEs are slightly worse for the coupled model, averaging around 4.2 kts as opposed to 3.6 kts for the uncoupled model. Both night and day RMSEs are worse in the coupled than in the uncoupled model for the V component.

Overall, the U- and V-component biases suggest a counterclockwise model bias, with the coupled model showing a slightly greater bias than the uncoupled model. This is shown in Figure 6.4.6, which presents the observed episode mean wind vectors compared to modeled episode mean wind vectors for all nine cases evaluated. The mean U and V components were calculated and then the mean wind vectors were resolved, where the U- and V-component means were obtained over all observing stations throughout the duration of the episode.

The mean observed wind vector blew out of the southeast. During the day, the counterclockwise bias was not as large as it was at night, when the mean observed wind was southerly, despite land-breeze forcing. As indicated in Section 6.3, much of the mean directional forcing was likely due to boundary conditions/large-scale forcing, i.e., the synoptic competence of the outer-domain model. However, differences in the mean direction between the coupled and uncoupled model simulations within the 4-km domain are due to the different land surface models and can be explained simply by noting that the coupled model simulations contain less daytime sea-breeze forcing due to warmer (observed) coastal waters, and more nighttime land-breeze forcing due to cooler land surfaces (also observed). By contrast, the uncoupled model simulations display a band of "too cold" SSTs (Figures 6.5.9, 6.5.10, and 6.8.9) which hug the Gulf shore, creating greater daytime sea-breeze forcing. Notwithstanding, anomalies in modeled mean wind direction do not alter the ability of the models to simulate the precession of the wind vector around the diurnal/inertial period. As indicated in the directional time-series plots presented in Section 6.3, both models capture diurnal wind vector rotation adequately.

6.4.3 Figures for Section 6.4

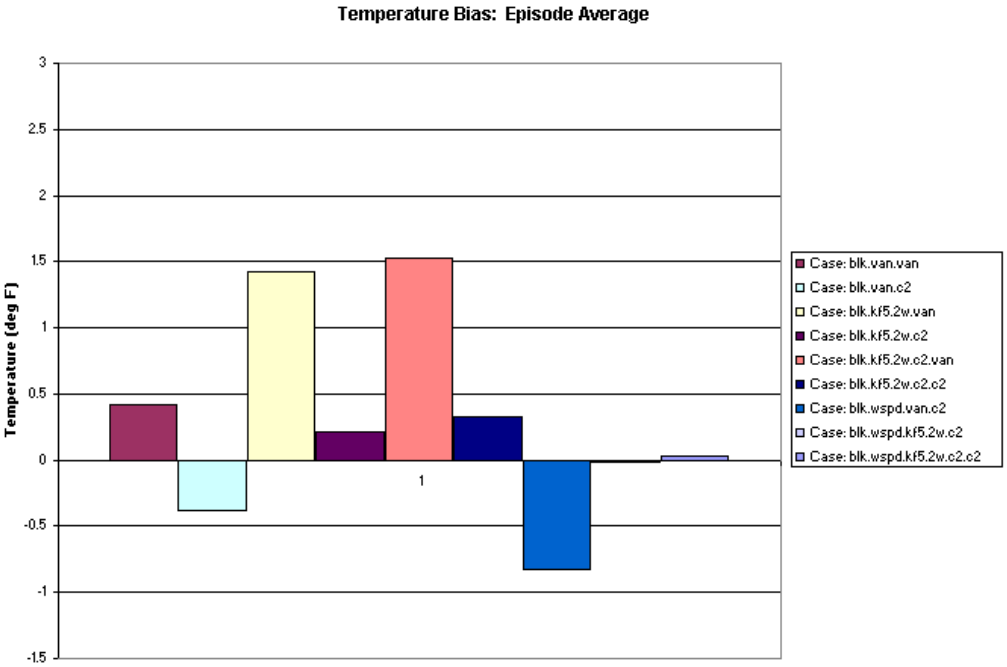

Figure 6.4.1a. Episodic-mean 2-m temperature performance comparison: overall bias (all hours).

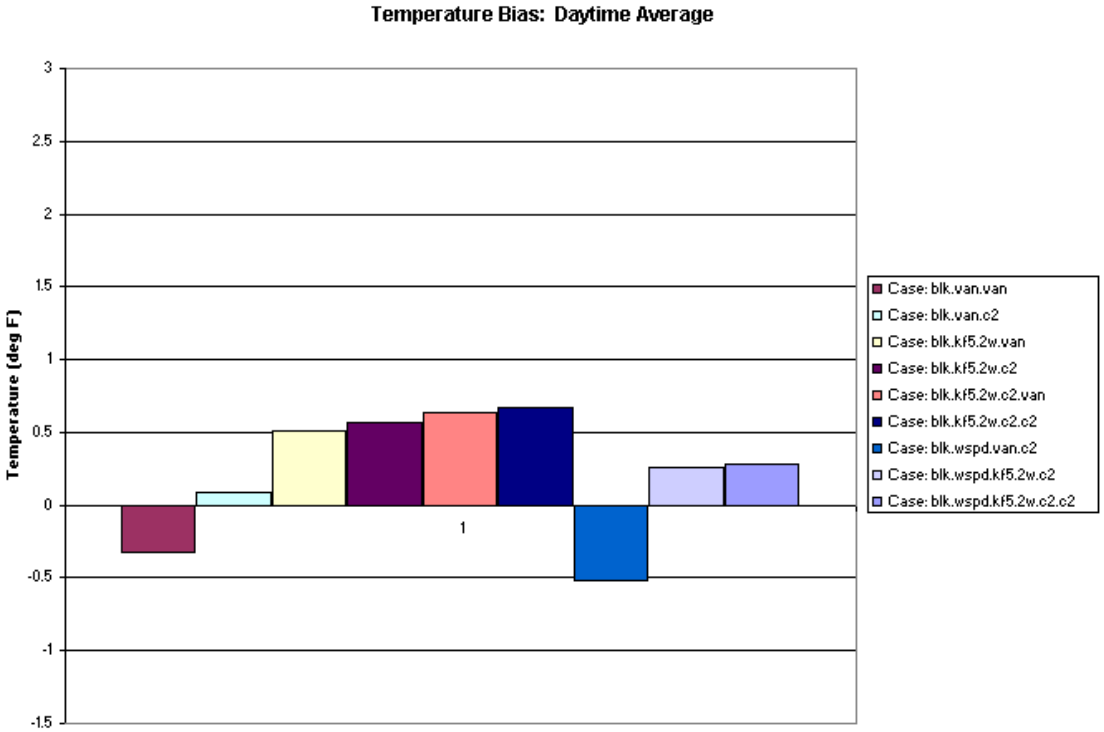

Figure 6.4.1b. Mean 2-m temperature performance comparison: daytime bias.

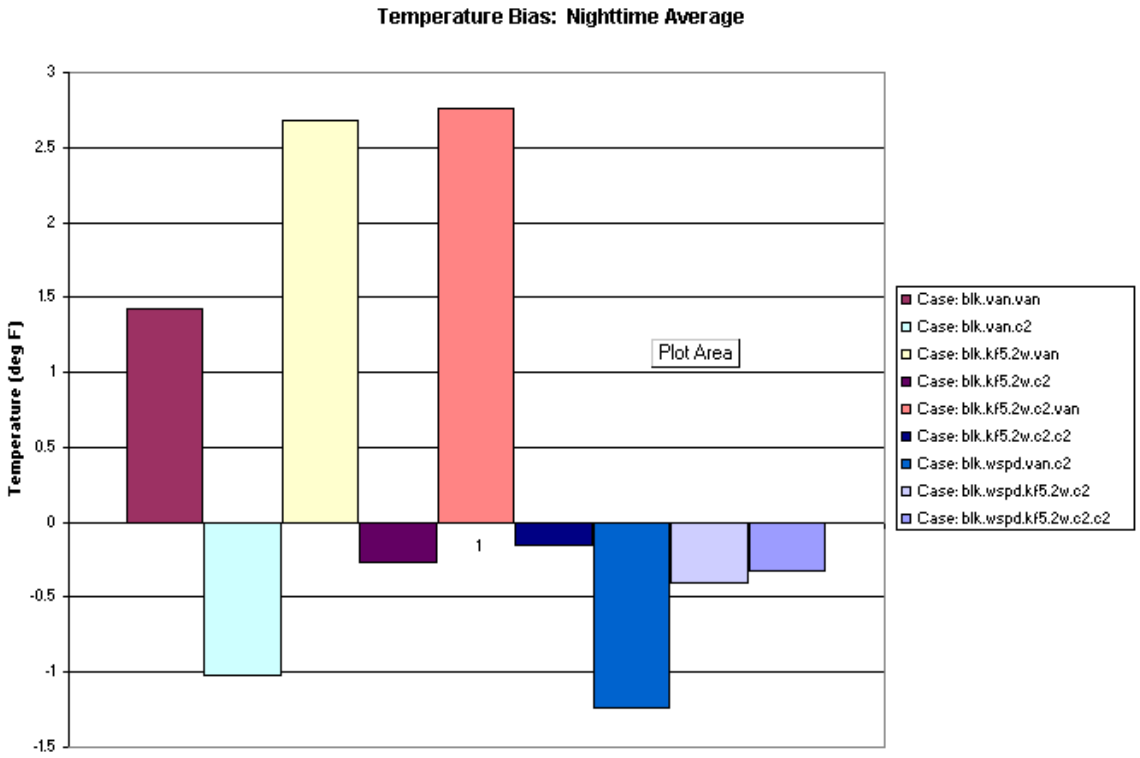

Figure 6.4.1c. Mean 2-m temperature performance comparison: nighttime bias.

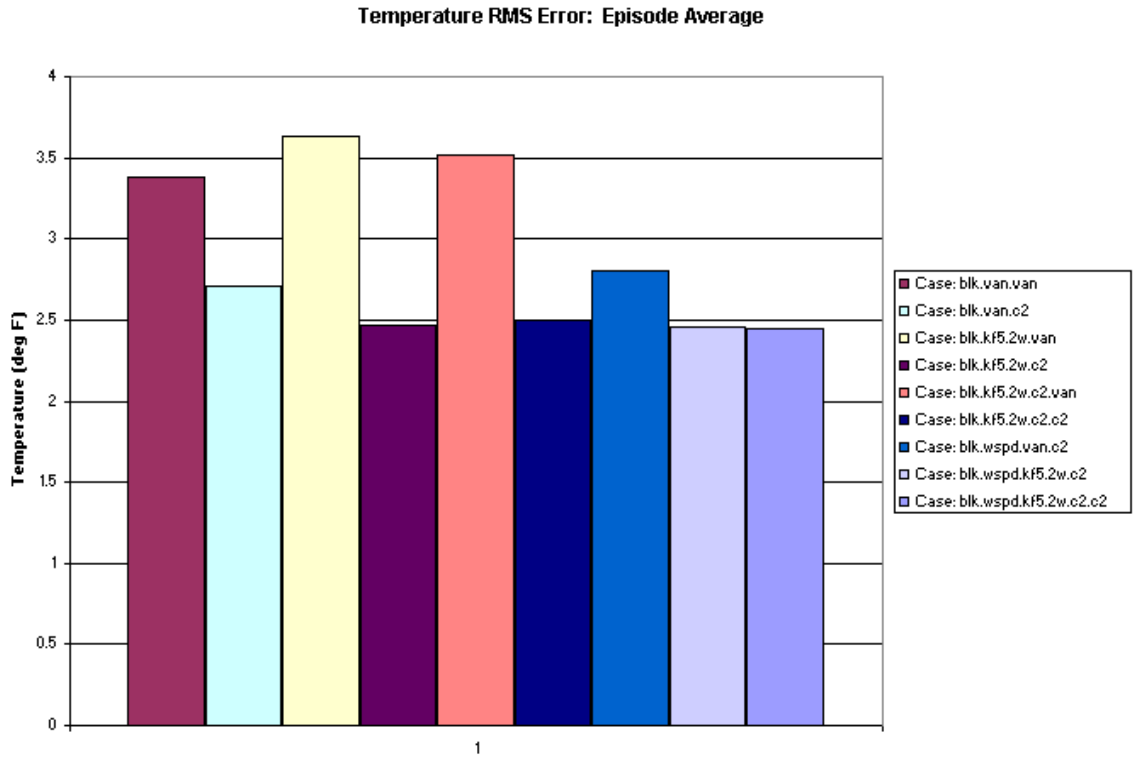

Figure 6.4.1d. Episodic-mean 2-m temperature performance comparison: overall RMSE (all hours).

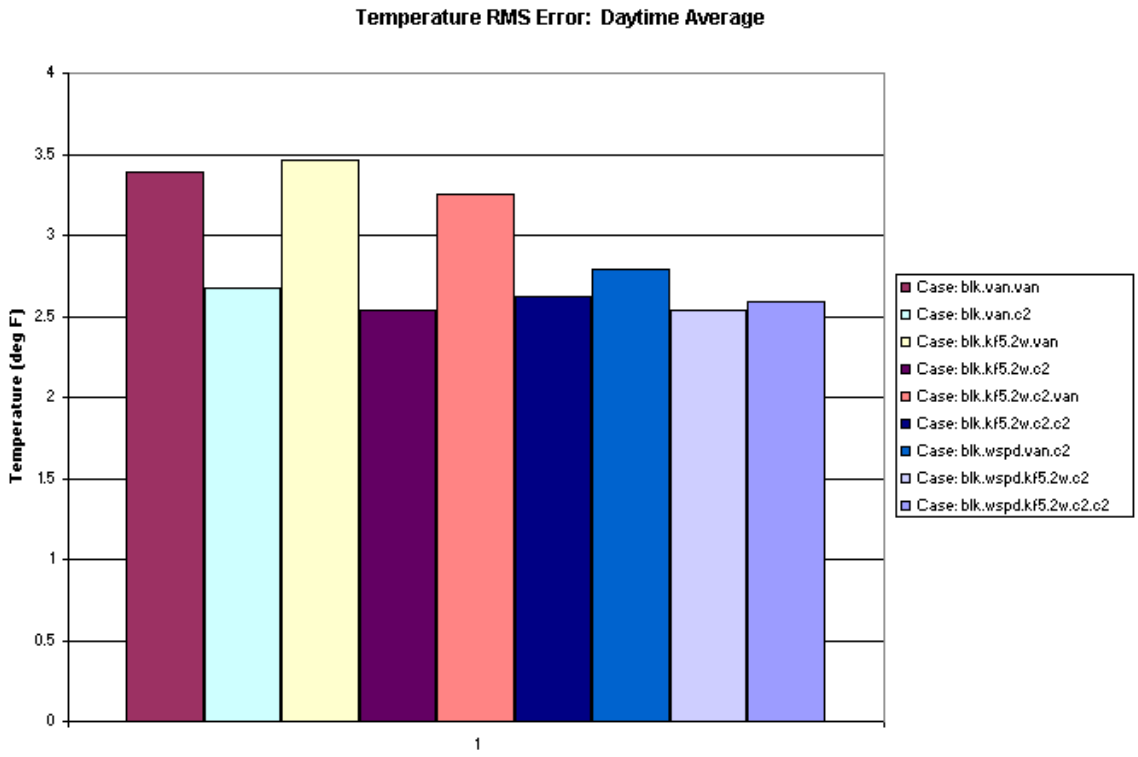

Figure 6.4.1e. Episodic-mean 2-m temperature performance comparison: daytime RMSE.

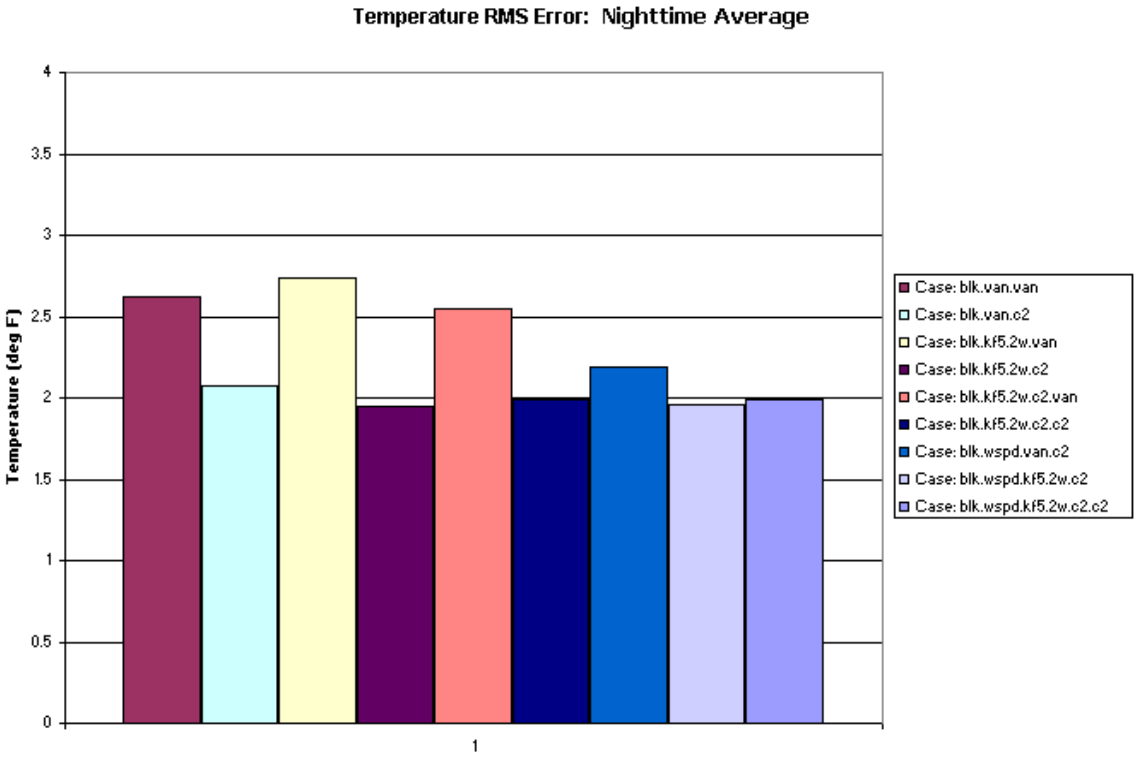

Figure 6.4.1f. Episodic-mean 2-m temperature performance comparison: nighttime RMSE.

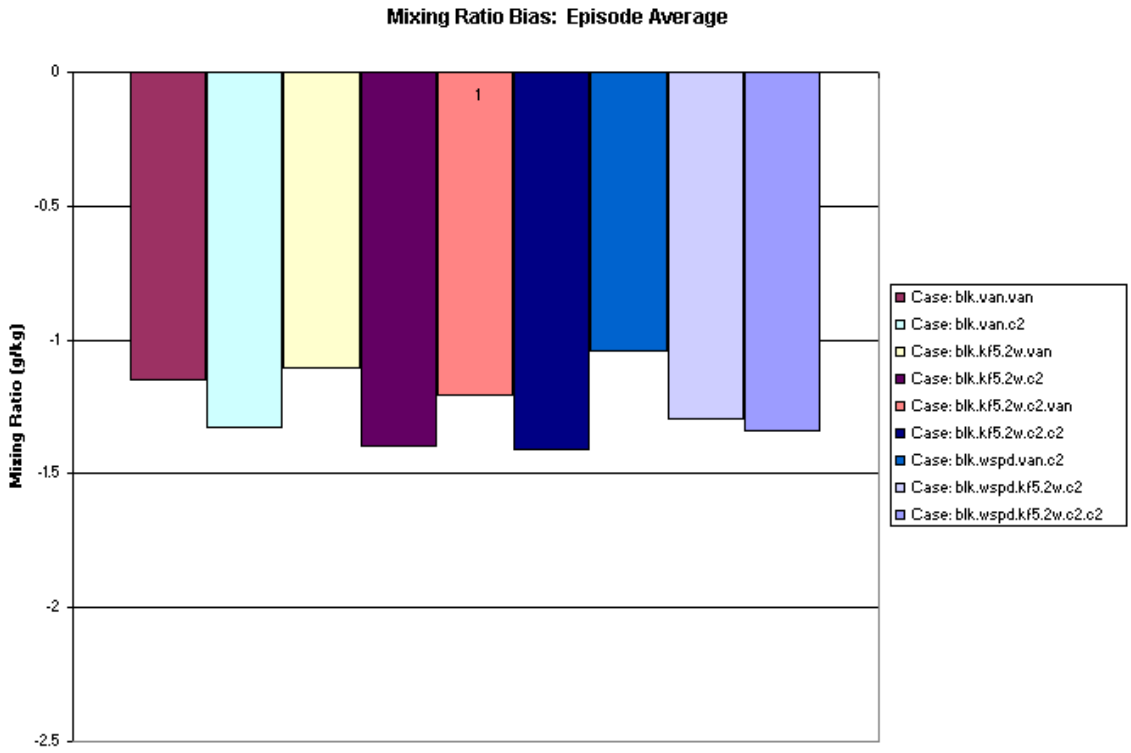

Figure 6.4.2a. Episodic-mean 2-m mixing ratio performance comparison: overall bias (all hours).

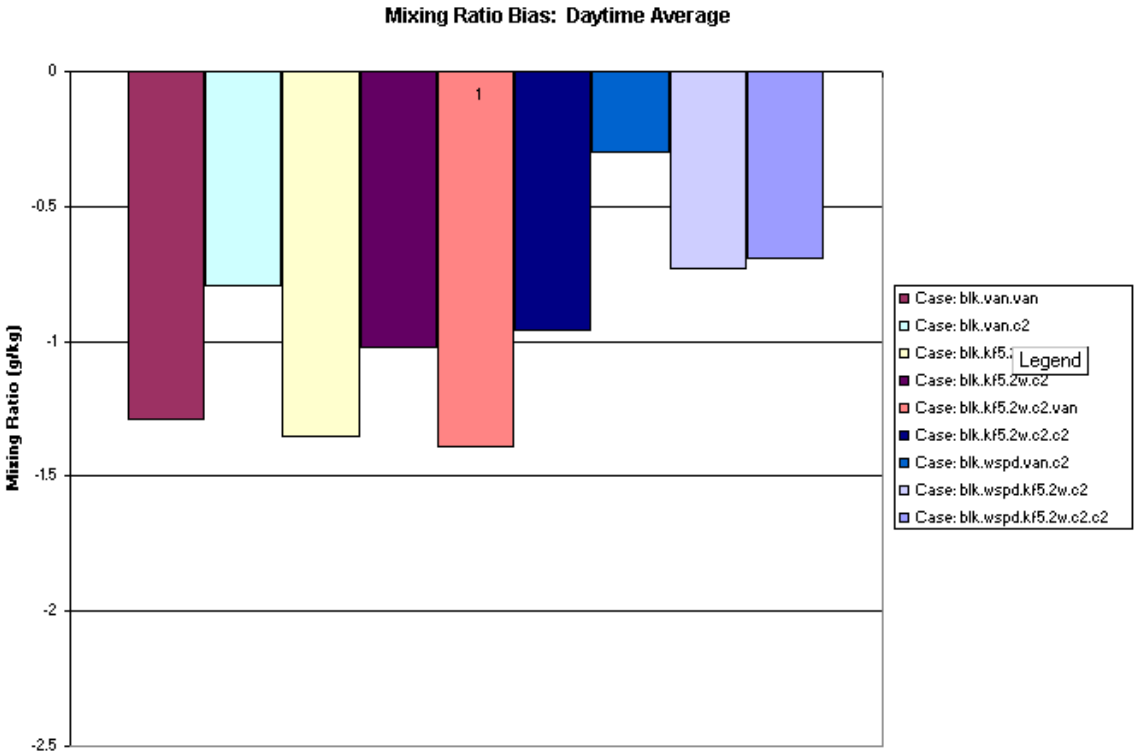

Figure 6.4.2b. Episodic-mean 2-m mixing ratio performance comparison: daytime bias.

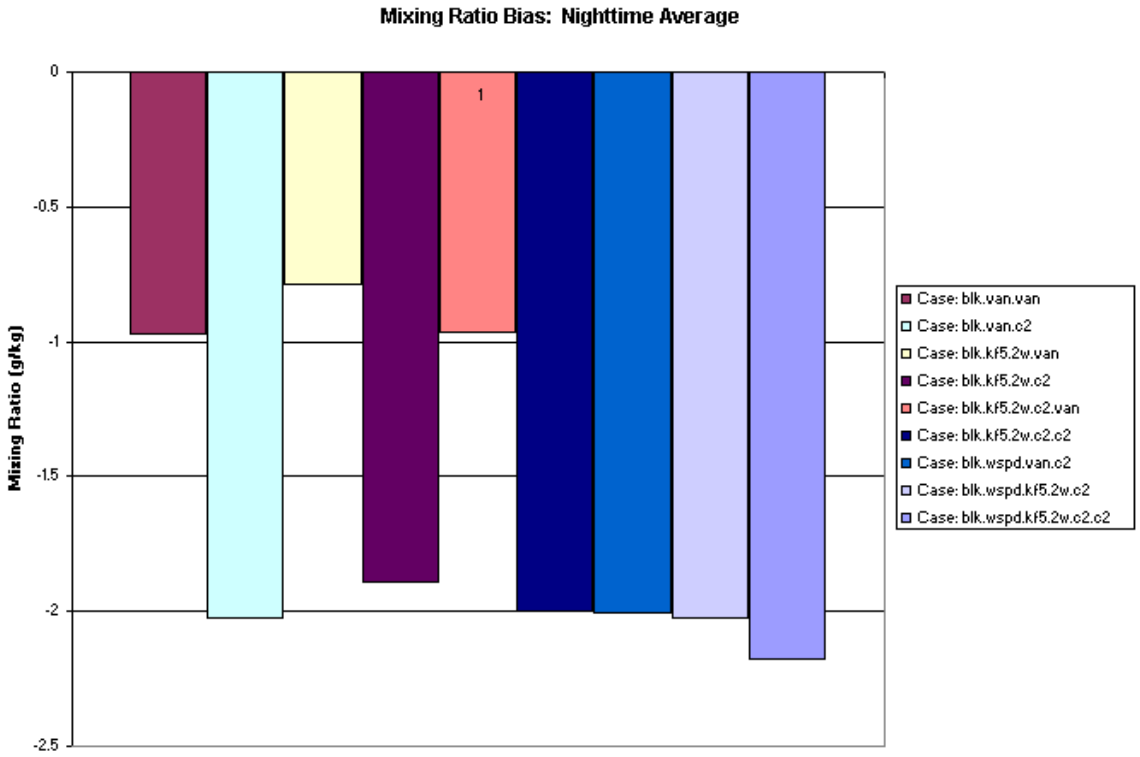

Figure 6.4.2c. Episodic-mean 2-m mixing ratio performance comparison: nighttime bias.

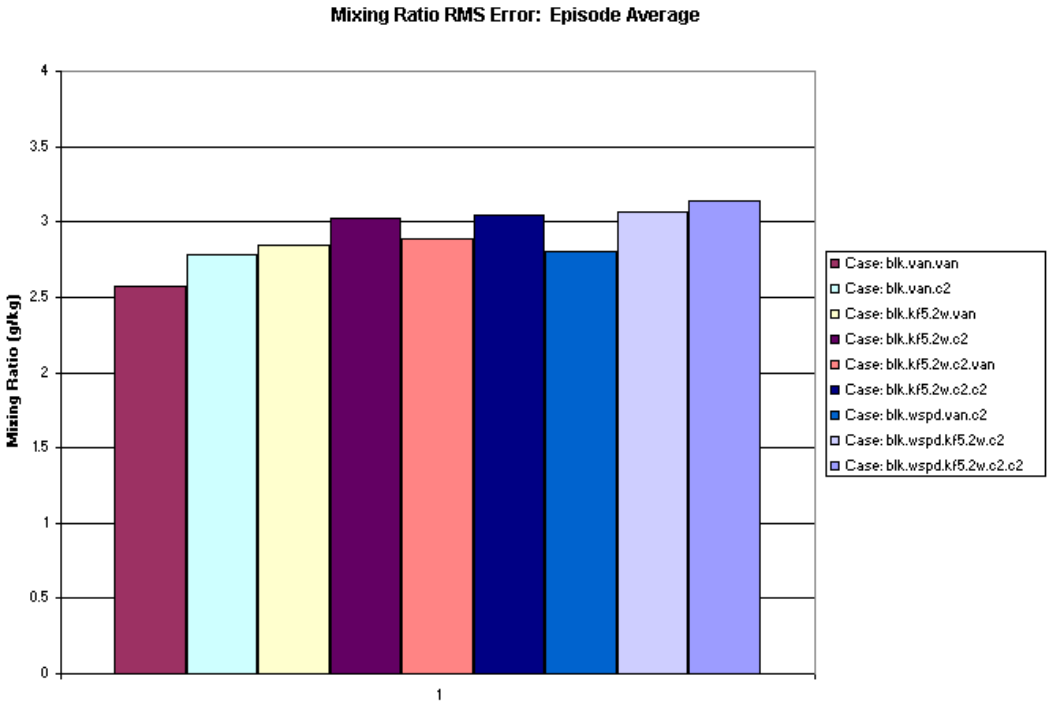

Figure 6.4.2d. Episodic-mean 2-m mixing ratio performance comparison: overall RMSE (all hours).

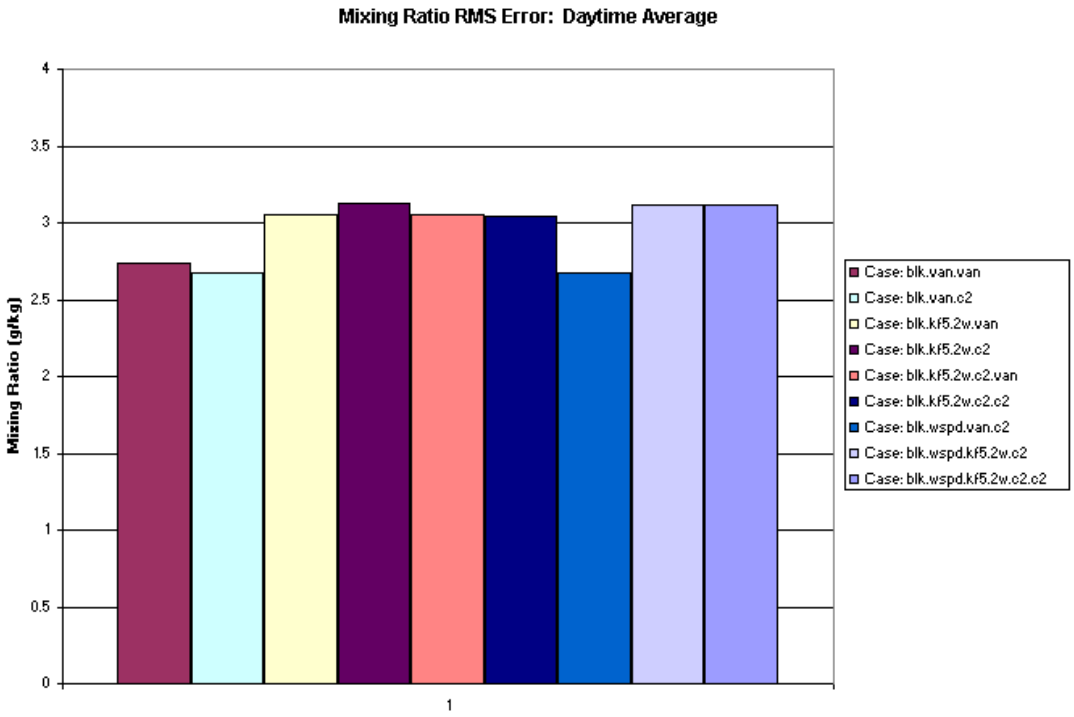

Figure 6.4.2e. Episodic-mean 2-m mixing ratio performance comparison: daytime RMSE.

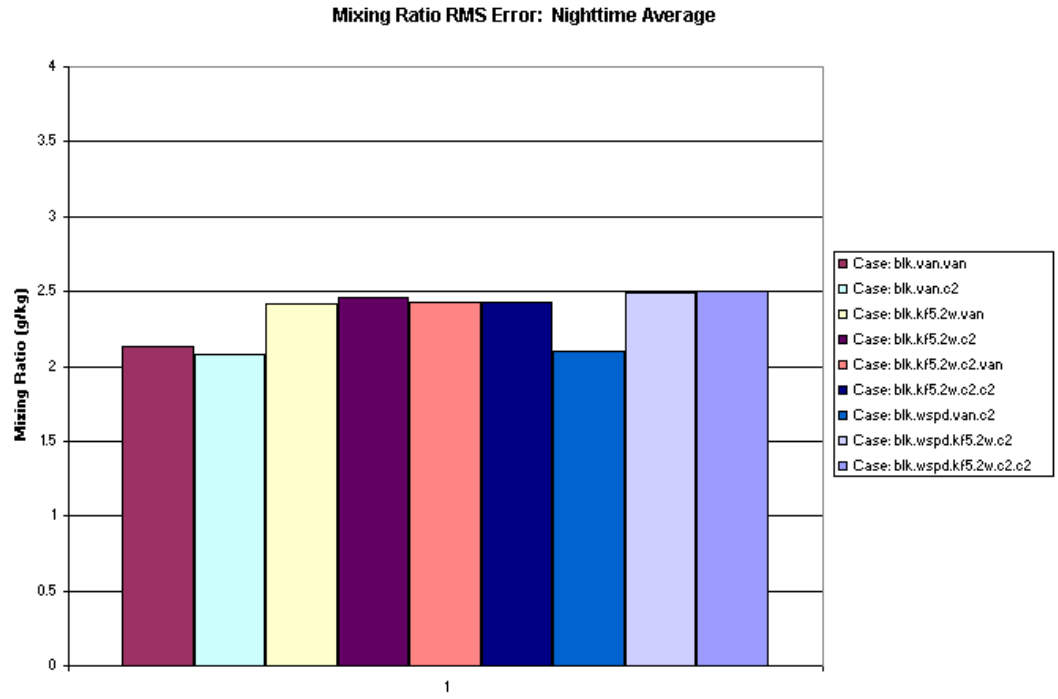

Figure 6.4.2f. Episodic-mean 2-m mixing ratio performance comparison: nighttime RMSE.

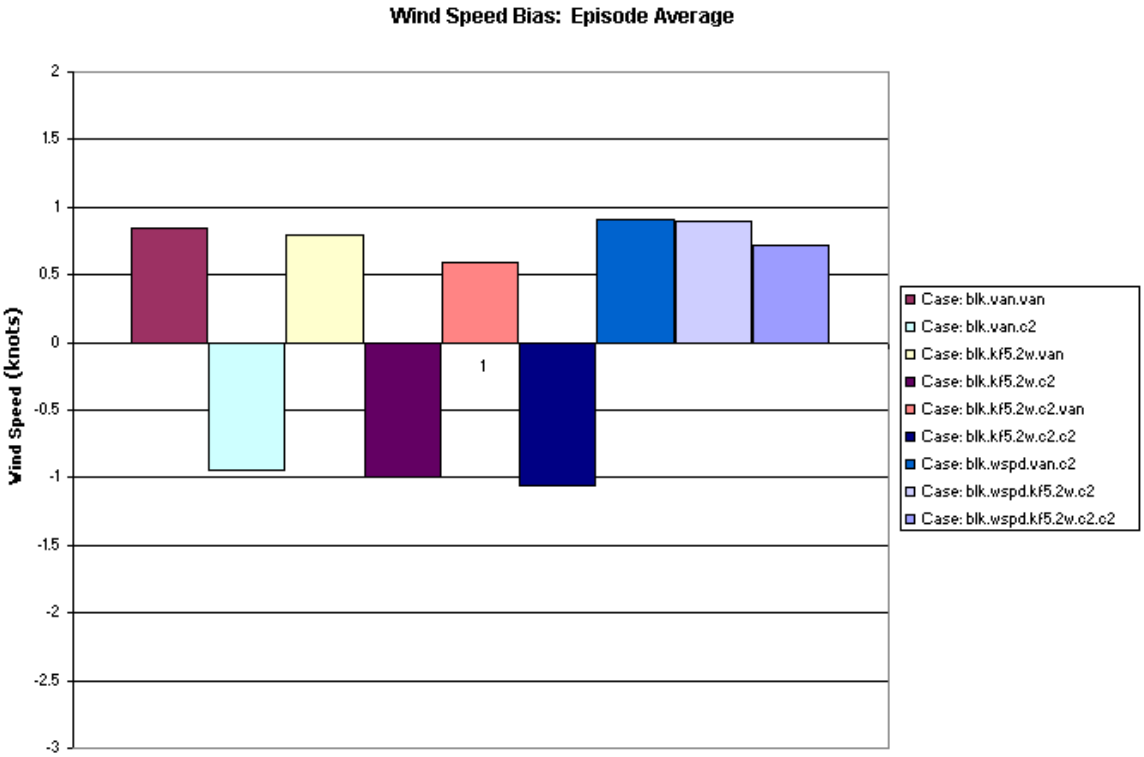

Figure 6.4.3a. Episodic-mean 10-m wind speed performance comparison: overall bias (all hours).

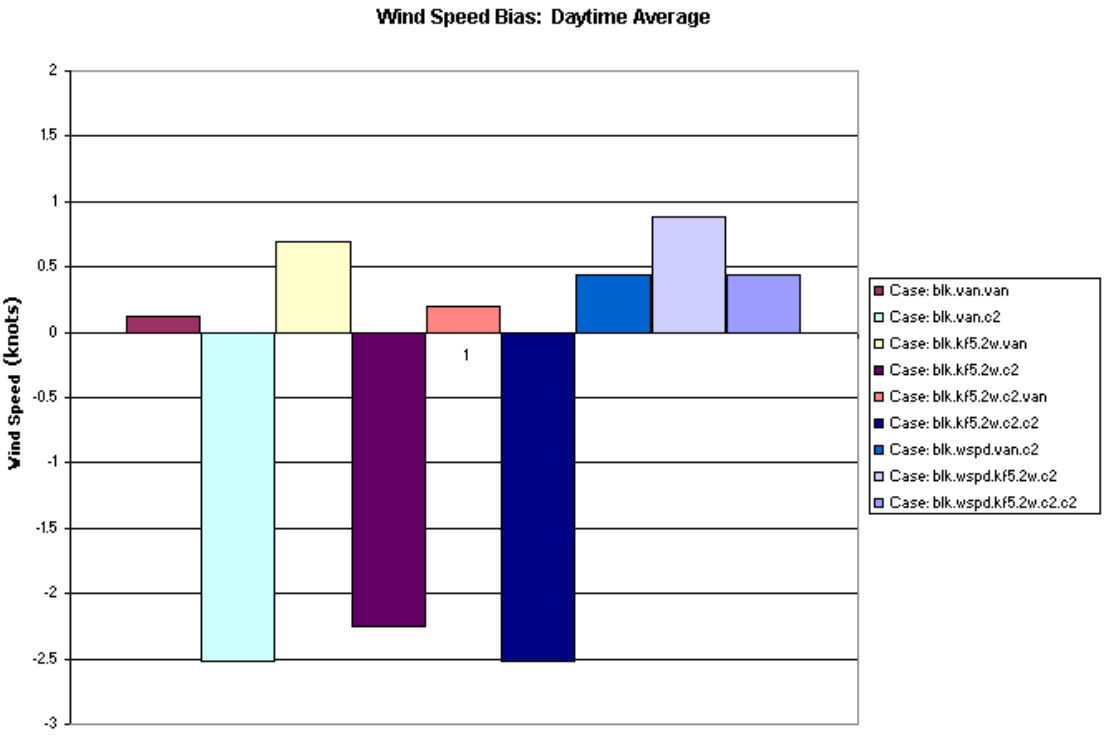

Figure 6.4.3b. Episodic-mean 10-m wind speed performance comparison: daytime bias.

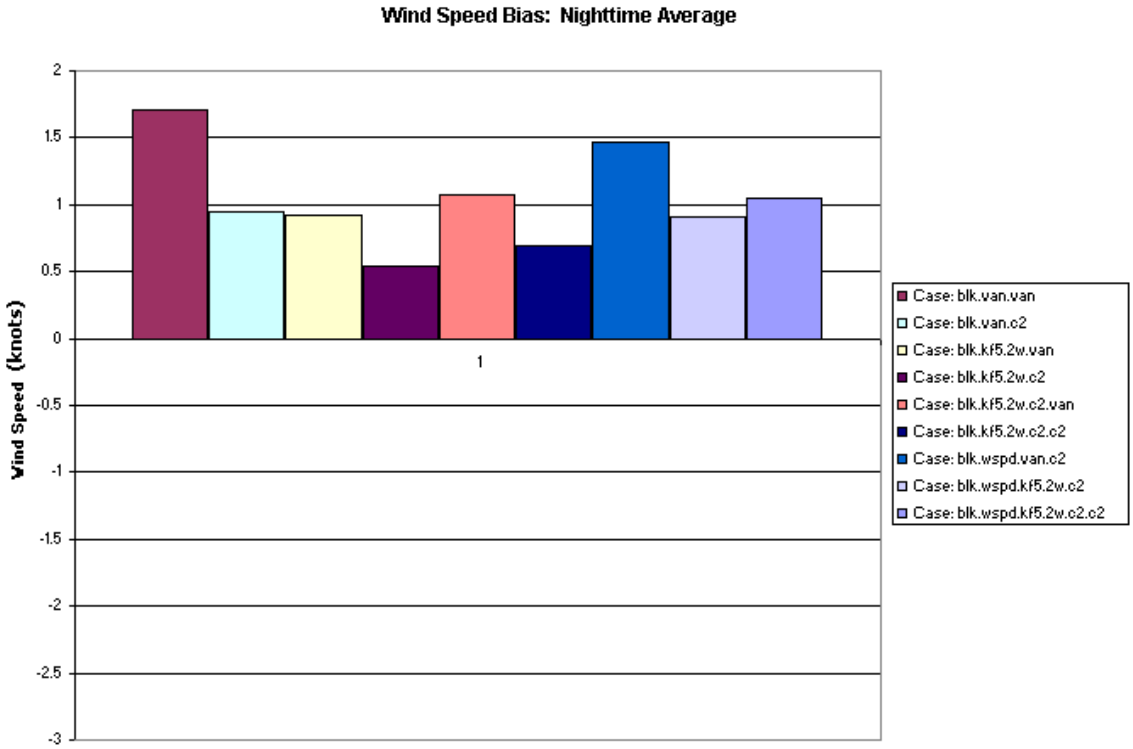

Figure 6.4.3c. Episodic-mean 10-m wind speed performance comparison: nighttime bias.

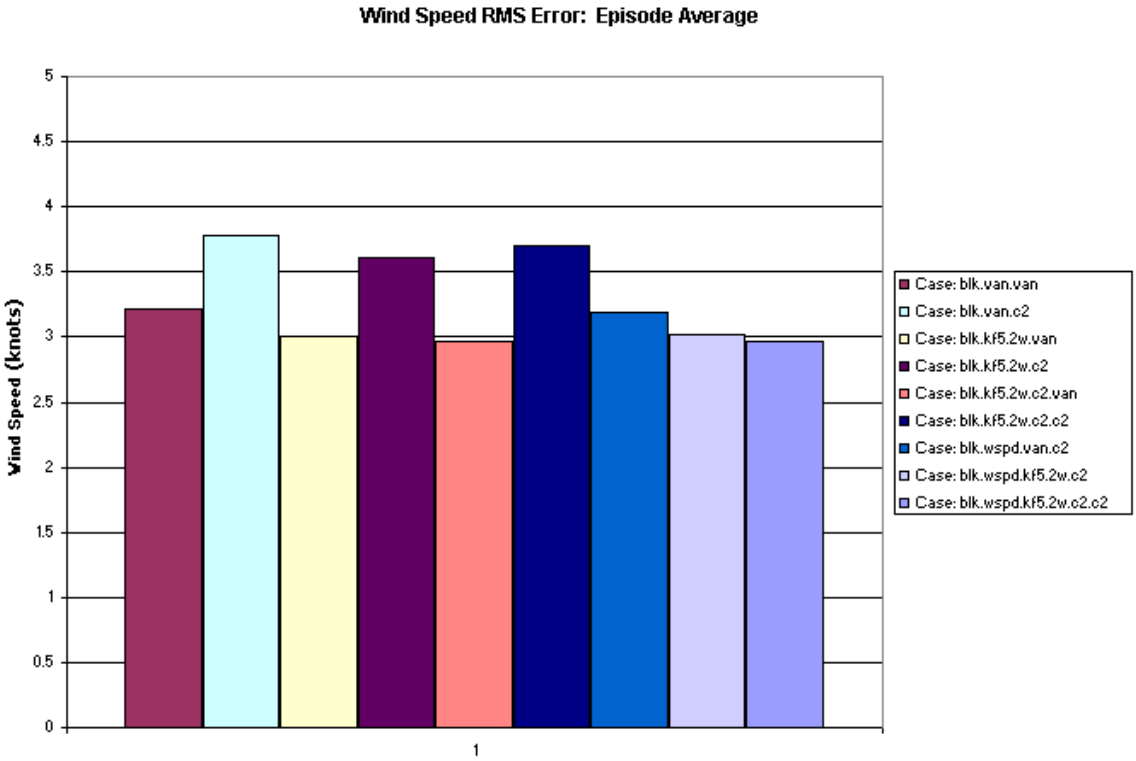

Figure 6.4.3d. Episodic-mean 10-m wind speed performance comparison: overall RMSE (all hours).

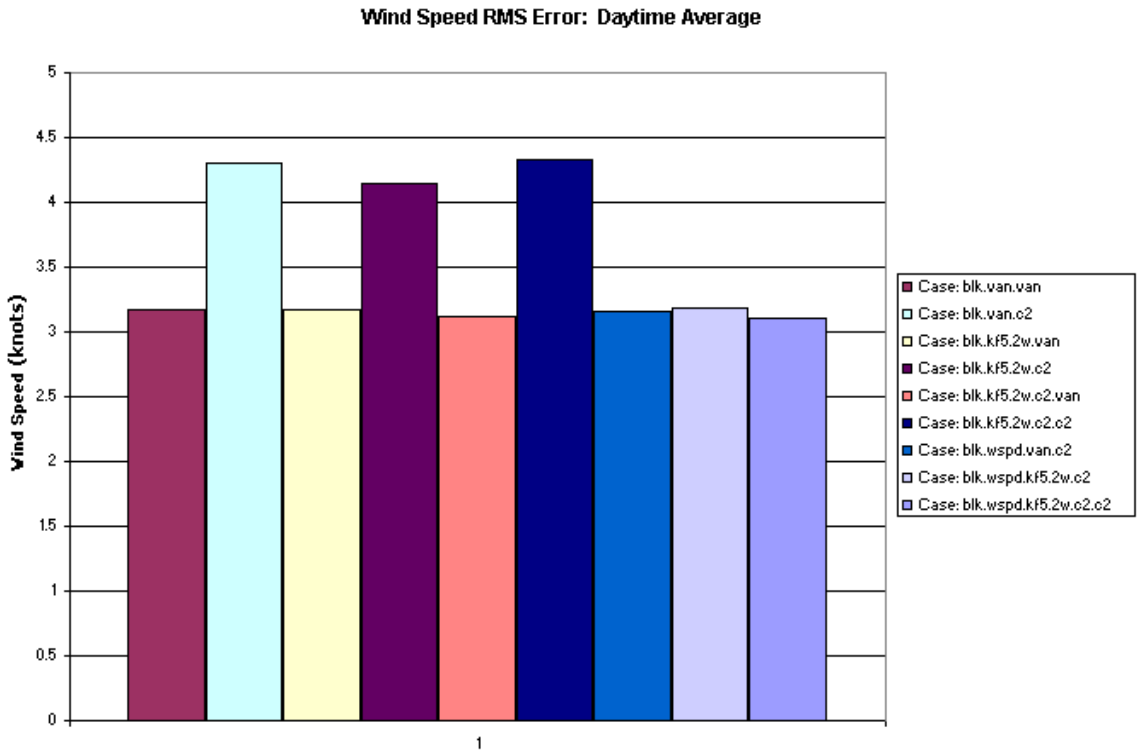

Figure 6.4.3e. Episodic-mean 10-m wind speed performance comparison: daytime bias.

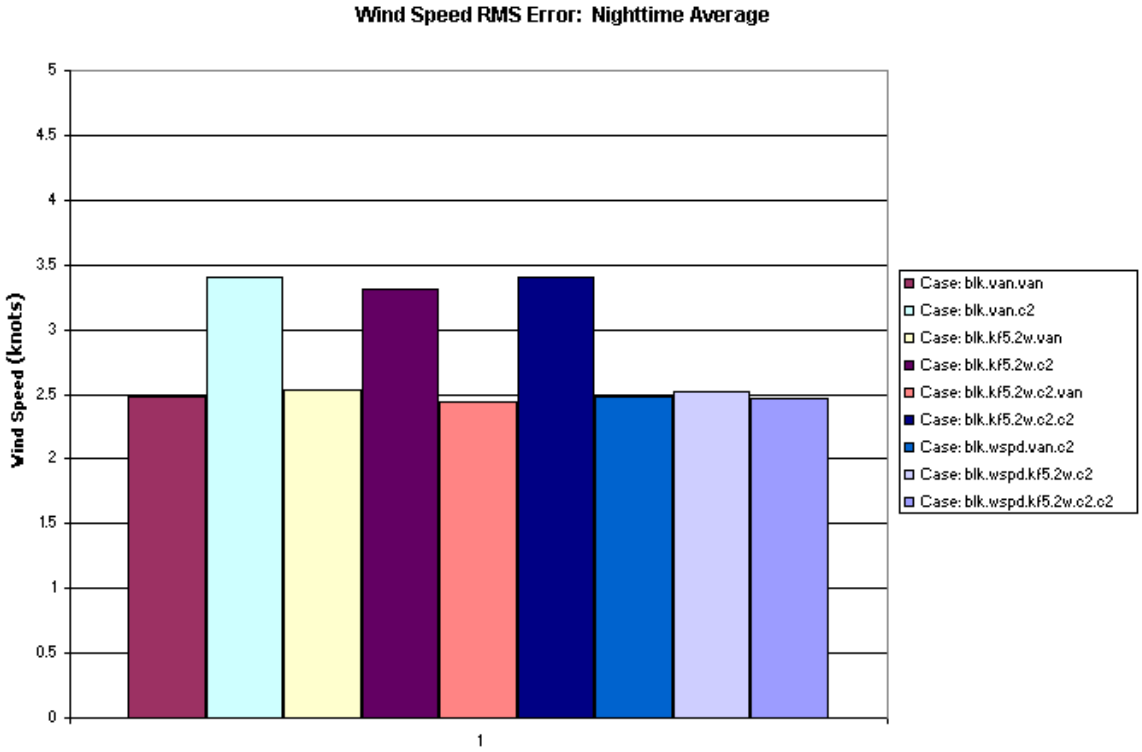

Figure 6.4.3f. Episodic-mean 10-m wind speed performance comparison: nighttime bias.

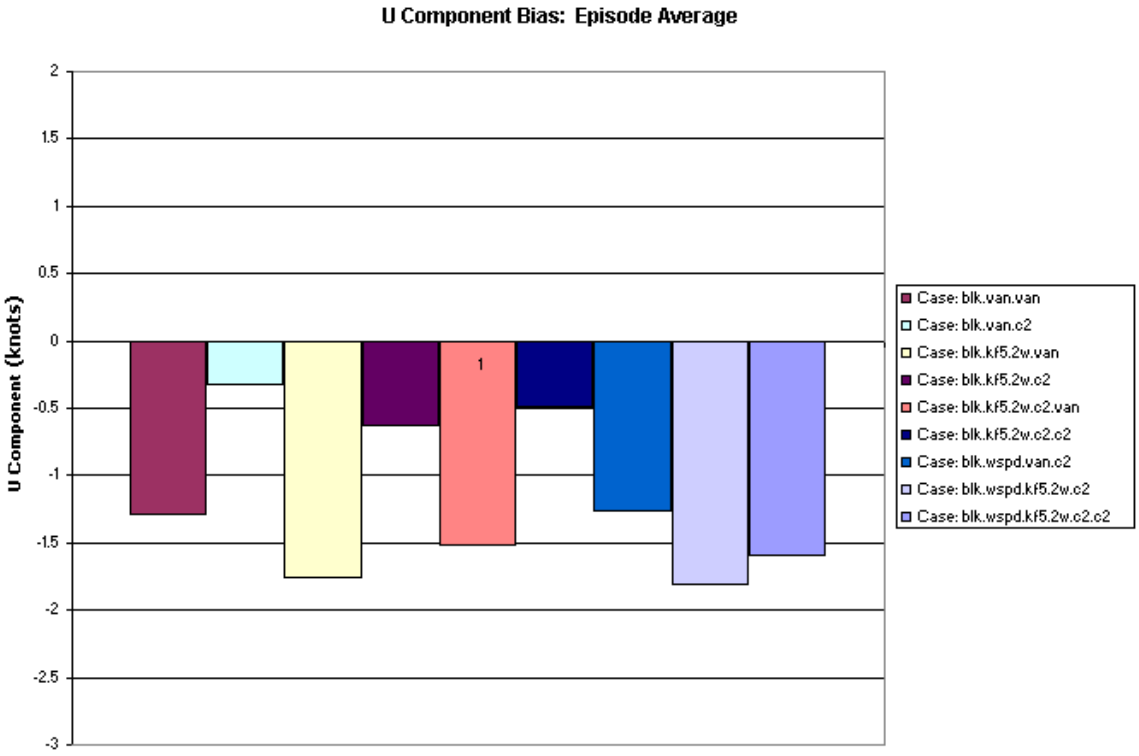

Figure 6.4.4a. Episodic-mean 10-m U-component performance comparison: overall bias (all hours).

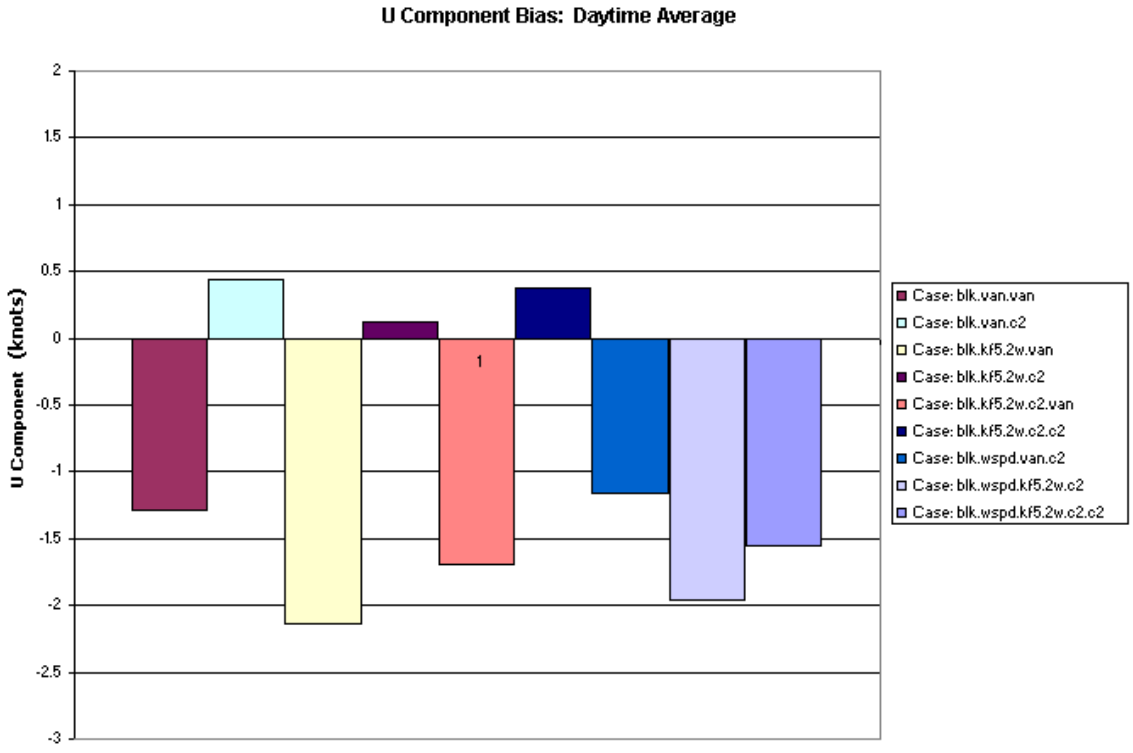

Figure 6.4.4b. Episodic-mean 10-m U-component performance comparison: daytime bias.

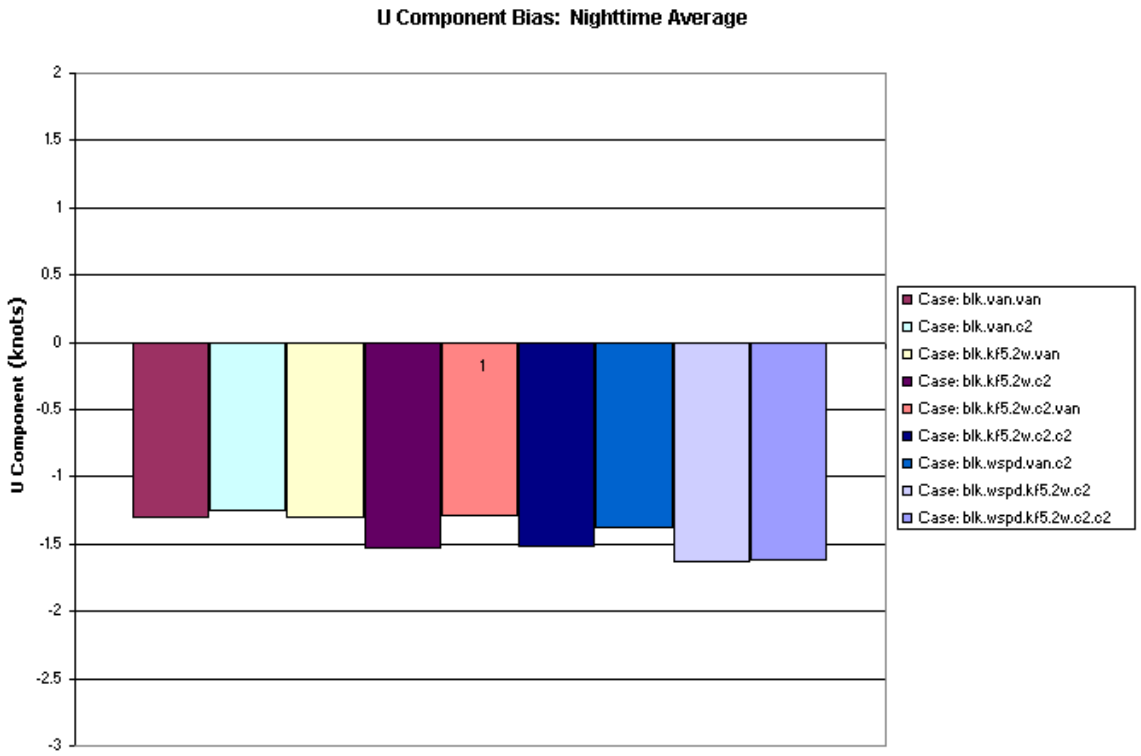

Figure 6.4.4c. Episodic-mean 10-m U-component performance comparison: nighttime bias.

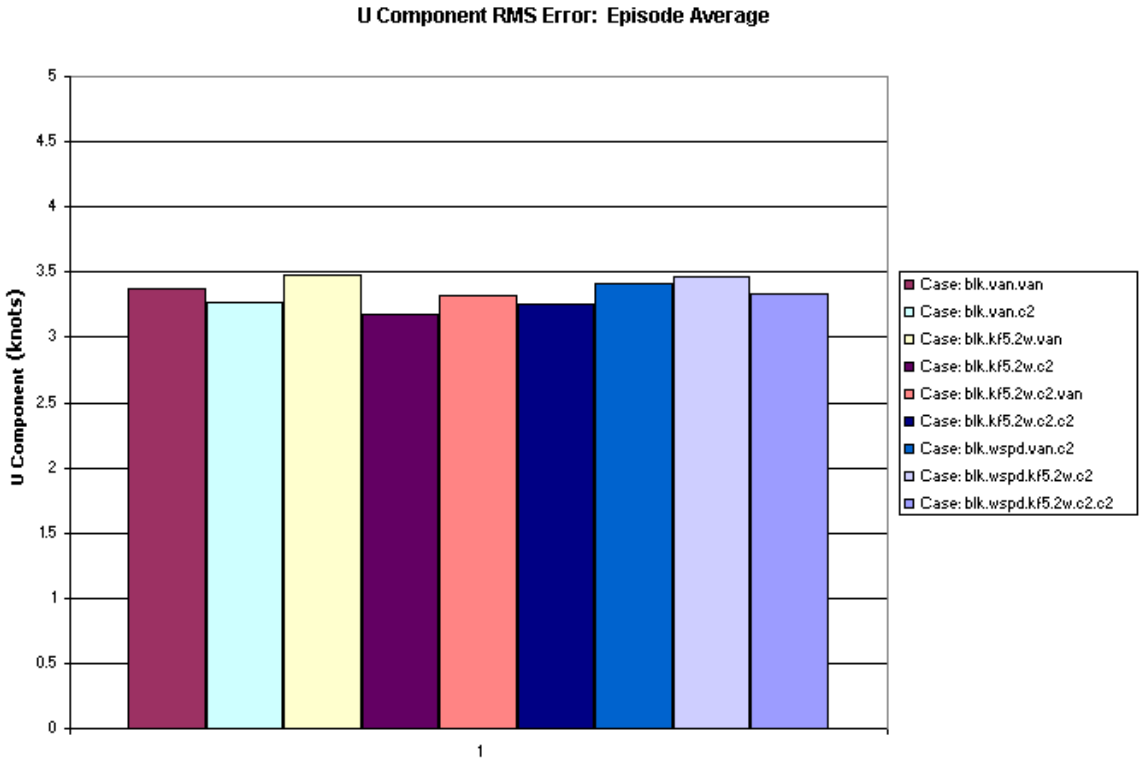

Figure 6.4.4d. Episodic-mean 10-m U-component performance comparison: overall RMSE (all hours).

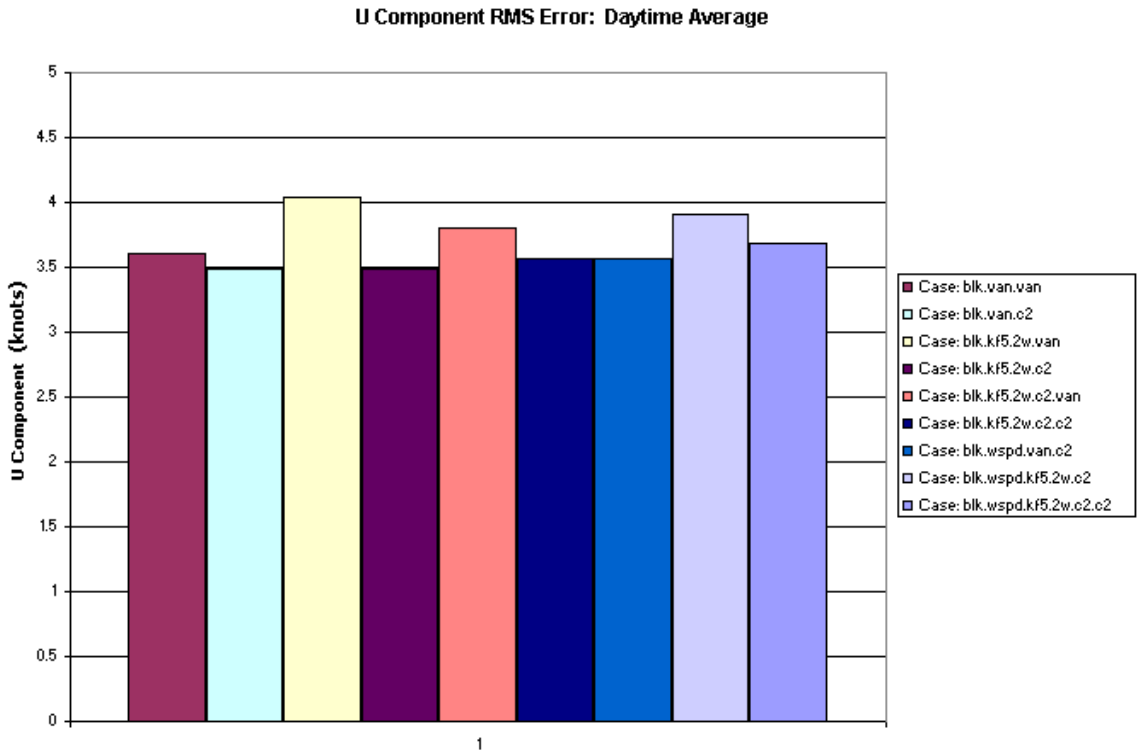

Figure 6.4.4e. Episodic-mean 10-m U-component performance comparison: daytime bias.

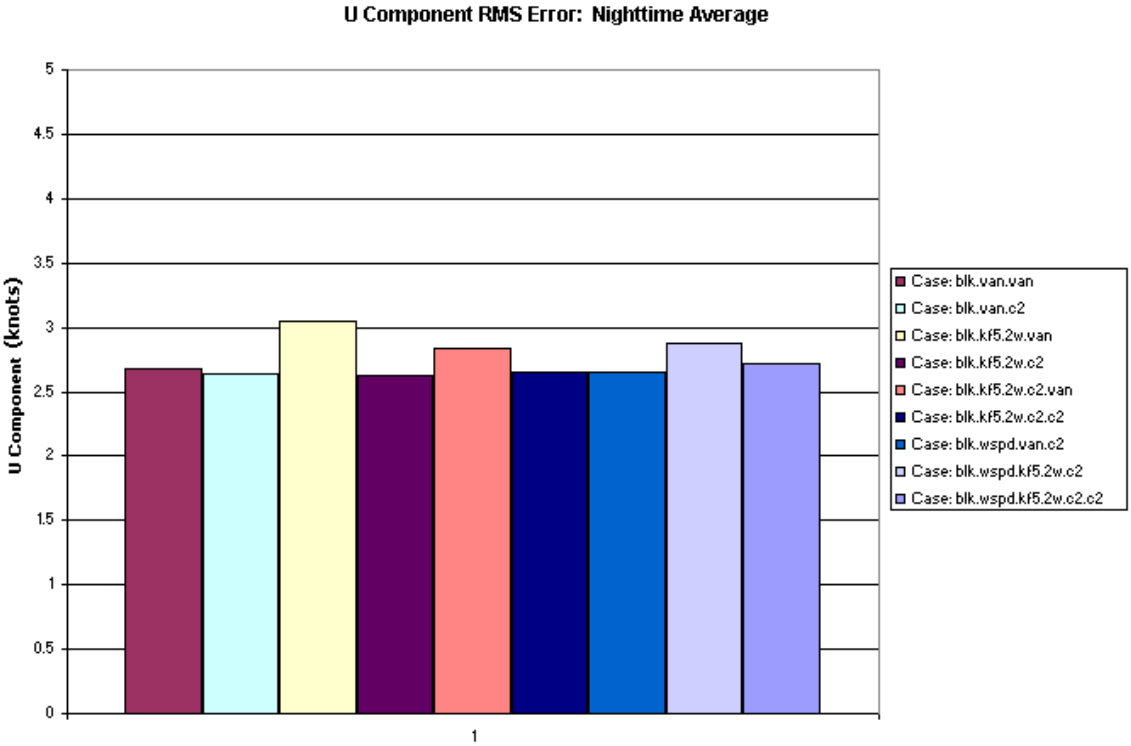

Figure 6.4.4f. Episodic-mean 10-m U-component performance comparison: nighttime bias.

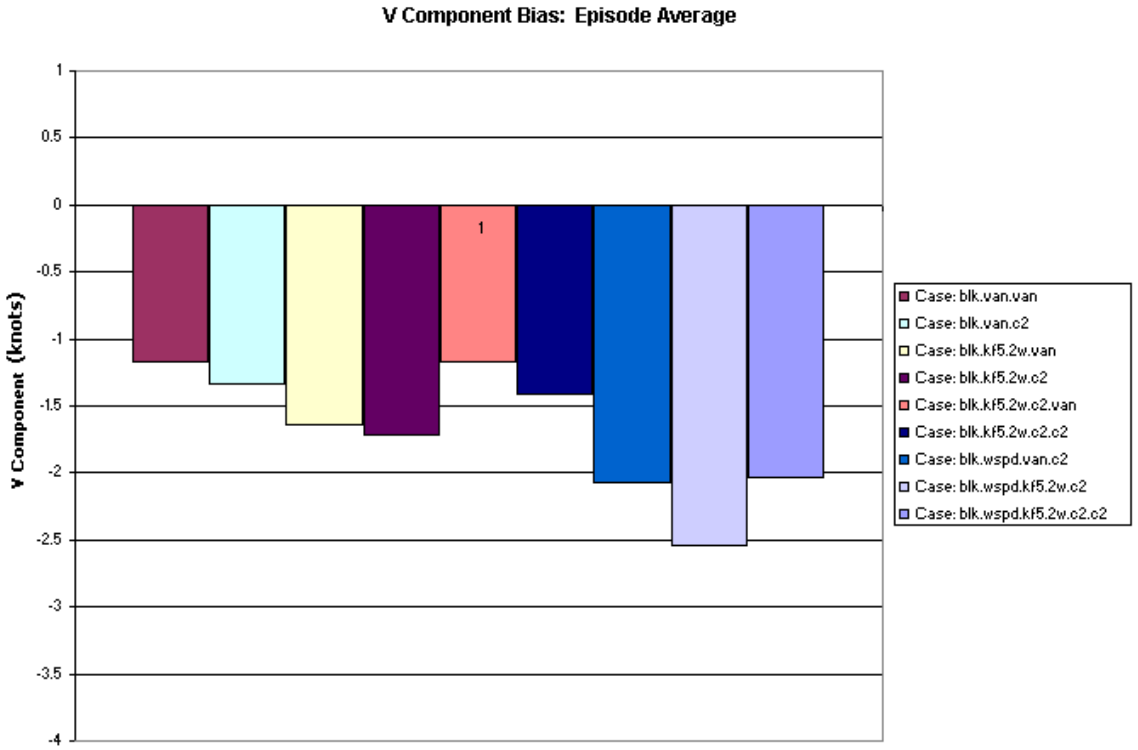

Figure 6.4.5a. Episodic-mean 10-m V-component performance comparison: overall bias (all hours).

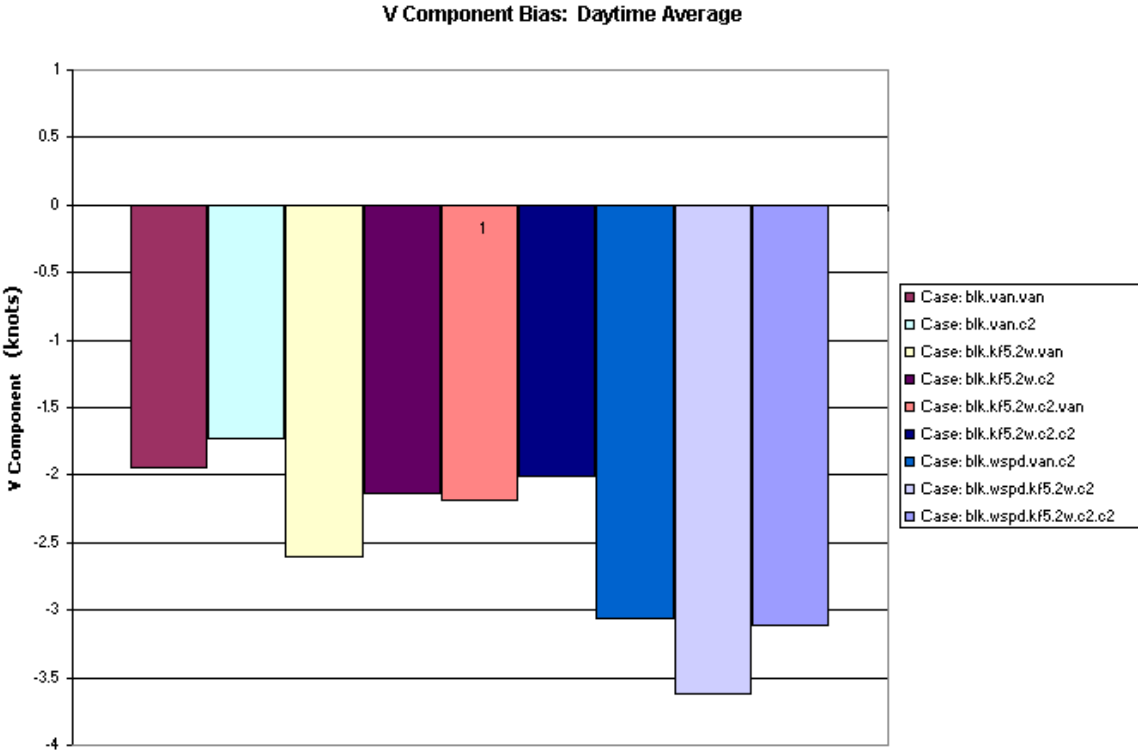

Figure 6.4.5b. Episodic-mean 10-m V-component performance comparison: daytime bias.

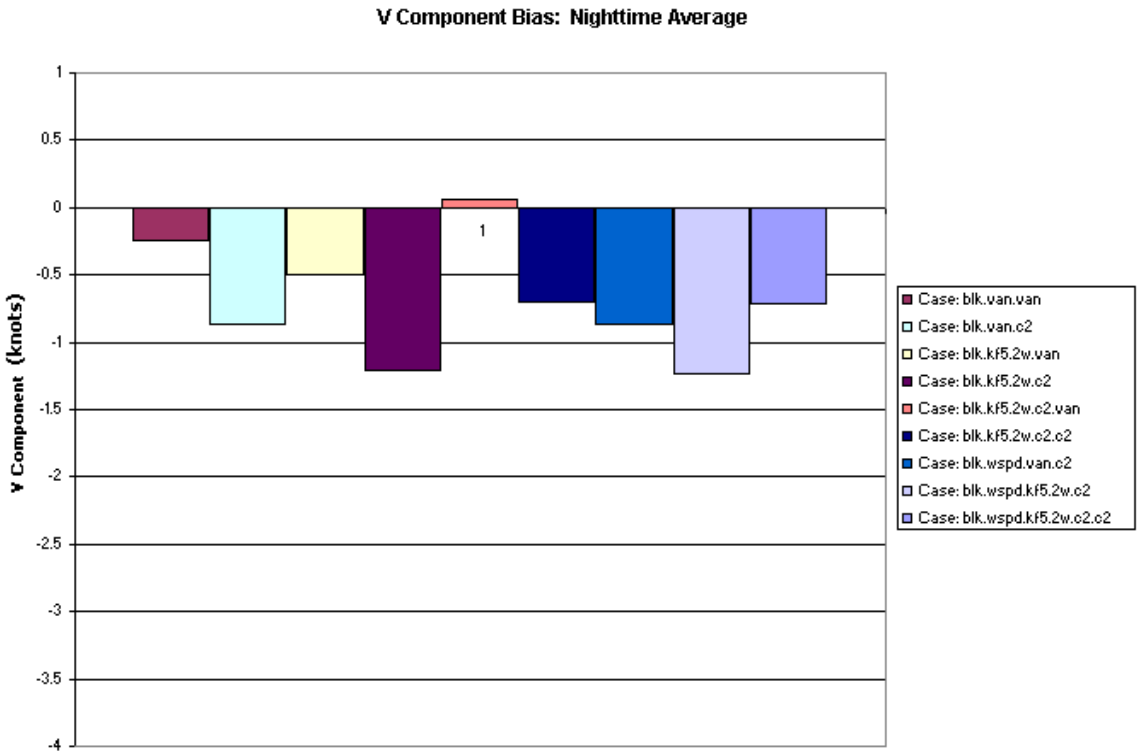

Figure 6.4.5c. Episodic-mean 10-m V-component performance comparison: nighttime bias.

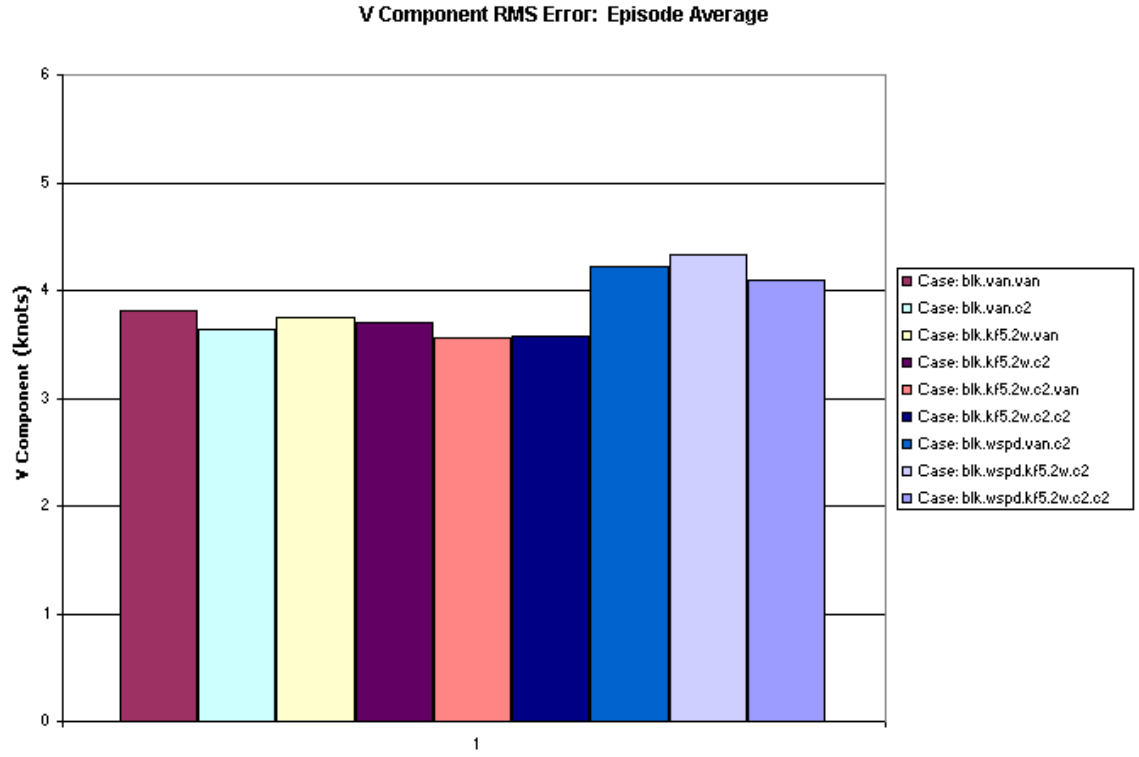

Figure 6.4.5d. Episodic-mean 10-m V-component performance comparison: overall RMSE (all hours).

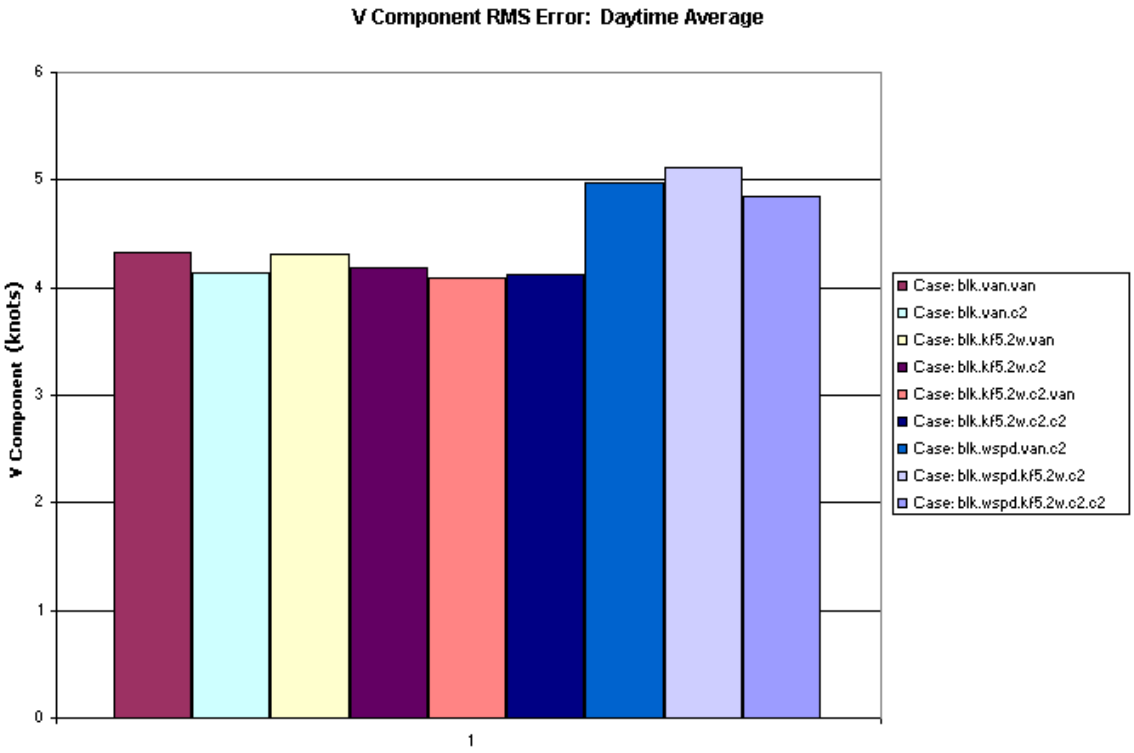

Figure 6.4.5e. Episodic-mean 10-m V-component performance comparison: daytime bias.

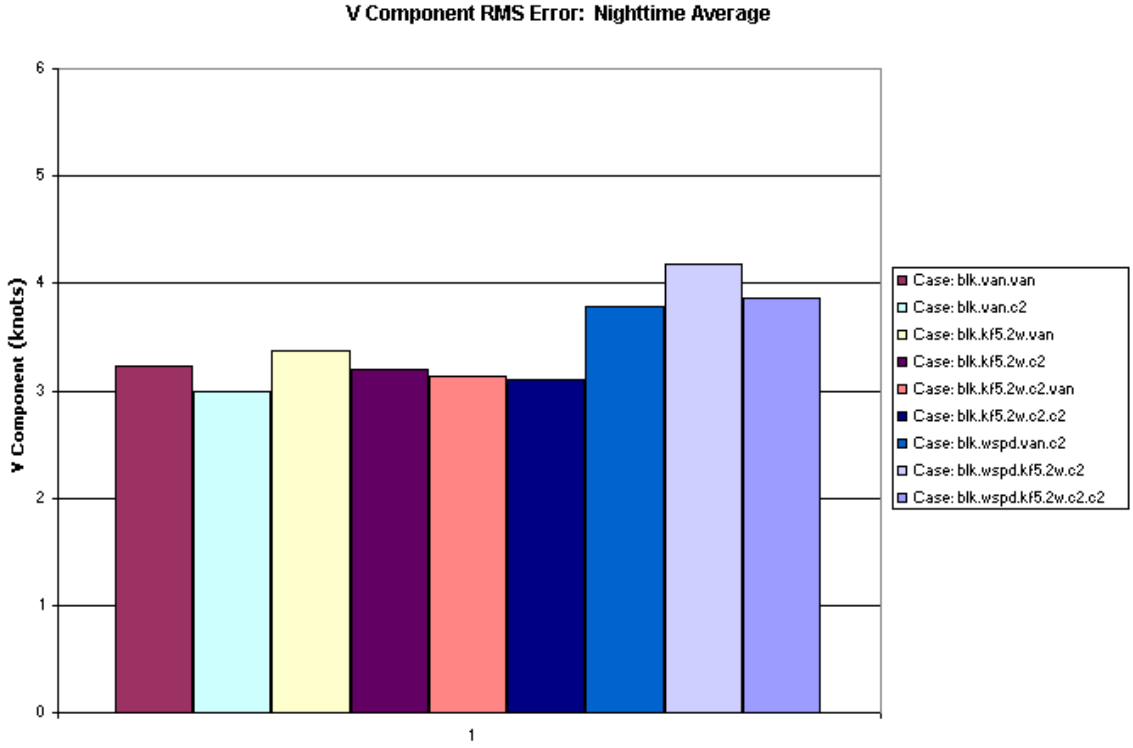

Figure 6.4.5f. Episodic-mean 10-m V-component performance comparison: nighttime bias.

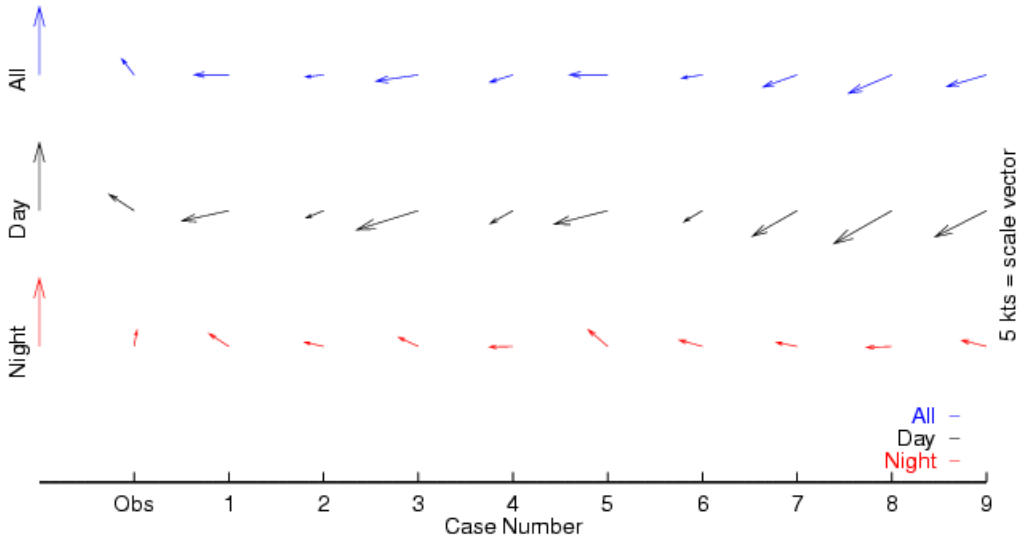

Figure 6.4.6. Observed mean wind vectors (Obs) and mean wind vectors for the nine cases, numbered as follows:

1) blk.van.van
2) blk.van.c2
3) blk.k5f.2w.van
4) blk.kf5.2w.van.c2
5) blk.kf5.2w.c2.van
6) blk.kf5.2w.c2.c2
7) blk.wspd.van.c2
8) blk.wspd.kf5.2w.c2
9) blk.wspd.kf5.2w.c2.c2

6.5 Earth Surface Flux Comparison: Uncoupled Versus Coupled

This section presents qualitative comparisons of the surface fluxes, with a focus on sensible heat flux (HFX) in the uncoupled versus coupled runs. The subsections below provide examples of flux differences for the entire domain. Issues related to sea-surface flux differences are also discussed.

6.5.1 Land-Surface Flux Comparison

There are two primary controls on differences between coupled and uncoupled land surface fluxes. The first control is the ingestion of SRB solar insolation products, as described in Section 2. This yields differences in available energy for partitioning into sensible, latent, and ground heat fluxes. The second control is due to inherent differences in the TOPLATS model versus MM5's SLAB model, particularly with regard to land cover, soils, and topographic data and the time-varying moisture content in TOPLATS. These controls yield substantial differences in the diurnal cycle of sensible and latent heat fluxes predicted by the two modeling systems. In particular, the most important flux differences influencing the coupled model dynamics appear to fall into the following three general areas: (1) Houston heat island representation; (2) nocturnal dew formation; and (3) flux spatial variability due to land cover, soil, topographic, and moisture variation.

6.5.1.1 Heat-Island Representation

One of the major features observed in the coupled runs but not in the uncoupled runs is the Houston "heat island", which is reflected as a positive HFX value that persists into the evening, and therefore modifies the boundary layer in the coupled runs, as illustrated in Figure 6.5.1. This effect is hypothesized to be a function of the higher heat capacity for urban areas in TOPLATS. The most significant impact of a persistent positive HFX value into the evening would likely be a delay in the collapse of the boundary layer, which in turn could have implications for circulations and transport in the vicinity of Houston. The impact of HFX differences for August 29 (shown in Figure 6.5.1) on predicted boundary layer heights in the coupled model is shown in Figure 6.8.45, with differences ranging from 500-1000 m.

6.5.1.2 Dew Formation

A second major feature observed in the coupled runs but not in the uncoupled runs is the formation of dew at night, which is reflected as negative latent heat flux (QFX) values, illustrated in Figure 6.5.2 for August 26 at 0900 UTC. The sign of the latent heat flux in TOPLATS is determined entirely by the specific humidity gradient (Peters-Lidard, 2001e), whereas in the SLAB model, negative gradients are effectively prohibited. Differences in this gradient result from at least two factors: (1) differences in surface or "skin" specific humidity (calculated in both models using the saturation vapor pressure at the skin temperature); and (2) differences in surface-layer (observation height or MM5 lowest-model-layer) specific humidity between internal MM5 calculations and the surface-station observations used to drive TOPLATS.

Later in the episode, it appears that TOPLATS' dew formation is decreased, but still present, in most of the domain, as shown in Figure 6.5.3 for August 30, 1998. In the uncoupled MM5, the positive latent heat fluxes increase (nocturnal evaporation). In general, both effects could occur in the models due to drying of the overlying air (see Figure 3.5) between August 26 and early morning on August 30. But the lack of dynamic soil moisture in SLAB prohibits the interaction of dew with the earth's surface, and thus the latent flux is entirely controlled by the lowest-model-layer specific humidity and the moisture "availability" parameter. Clearly, strong nocturnal evaporation over land is unrealistic. However, the statistics show that the impact of TOPLATS' dew formation may have been to extract too much moisture from the atmosphere at night, leading to the large nocturnal dry biases. Implementation of scaling considerations in a more complex coupling scheme might be needed to both preserve TOPLATS' dew formation capability and restrict its impact on the overlying modeled air at the 4-km scale.

In this light and with reference to the discussions under Sections 6.2.5, 6.3.3, and 6.3.4 above, it appears that the standard MM5 has a significant surface thermodynamic (temperature and moisture) process-representation problem. It is both too warm and too dry at night, and too cool and too dry during the daytime. Improving the moisture representation would further degrade the temperature performance, by further restricting the already poor diurnal temperature cycle. Since photochemistry is sensitive to temperature (and somewhat less so to moisture), the coupled model's ability to correct this fundamental problem is an important result.

6.5.1.3 Flux Spatial Variability

The third important difference between the uncoupled and TOPLATS-coupled runs is indicated by differences in flux spatial patterns. These differences reflect a combination of differences in available energy due to the SRB data, and the detailed (90-m) representation of land cover, soil, topographic, and moisture variations by TOPLATS as described in Peters-Lidard (2001a). The results shown below reflect the 4-km grid-average fluxes derived from the 90-m fluxes predicted by TOPLATS, so that they can be compared directly with the 4-km fluxes predicted by the uncoupled model. The expected impacts of differences in spatial flux patterns would be differences in near-surface temperature, humidity, and local circulations, in addition to differences in PBL depth. Specific examples of these differences are discussed in the following paragraphs.

The episode began following a relatively wet period, and, therefore, one would expect that more available energy would initially partition into latent heat as compared to sensible heat. As shown in the Figure 6.5.4, the sensible heat fluxes for the uncoupled run are considerably higher than those for the TOPLATS-coupled run, even in the morning at 1500 UTC on August 25. (Note that the heat-flux heterogeneity present in the coupled model run—right hand panel of Figure 6.5.4—is not well-represented in the figure due to the range of scale necessary for comparison with the uncoupled model.) Given approximately equal solar insolation (not shown), the differences are likely due to a combination of soil moisture and land-cover effects. Later in the day (at 1900 UTC, approximately solar noon), the flux differences are greater in magnitude (Figure 6.5.5), due largely to differences in solar insolation driven by spurious clouds in the uncoupled model, shown in Figure 6.7.1.

The response of the PBL depth to the flux pattern differences on August 25 at 1500 UTC is illustrated in Figure 6.8.6. As the figure shows, the uncoupled model reveals a collapsed boundary layer over Lake Livingston in the north central part of the domain, and a growing boundary layer over the city of Houston. The coupled model modifies this typical MM5 behavior, revealing more uniformity over the Lake and a more depressed morning urban boundary layer. This is a result of correcting the too-cold water in Lake Livingston and correcting the urban heat-capacity formulation. Further, spatial structure in the PBL, particularly in the eastern half of the domain over land, appears to be more heterogeneous in the coupled model, even though the plot-scale in Figure 6.5.4 is too coarse to reveal the corresponding HFX heterogeneity.

A second illustration is shown in Figure 6.5.6, at about 1900 UTC on August 27. Especially in the southwest part of the domain, where solar insolation was reasonably equivalent, differences in land-surface characteristics probably play a role. The effect is shown in Figure 6.7.9, where these differences lead to much greater thermal heterogeneity in the 2-m coupled model temperature at 2000 UTC.

On August 30, the heat flux differences between the two models are quite small (Figure 6.5.7). However, more significant differences are seen in the latent heat flux (Figure 6.5.8), particularly for the lakes in the north-central portion of the domain, and in the northeastern part of the domain.

6.5.2 Sea-Surface Flux Comparison

Figure 6.5.9 shows the climatological SSTs in the vicinity of Galveston Bay as used by the uncoupled MM5. These data are derived from either the GDAS or EDAS initialization discussed above. They are time-independent, and for near-shore areas, may be subject to interpolation biases inherent in MM5's pre-processing. In contrast, the SSATS model used observed Physical Oceanographic Real-Time System (PORTS) SST data for both the Bay and near-shore Gulf (Peters-Lidard, 2001b).

Figure 6.5.10 shows gridded SSTs on the 4-km MM5 grid for August 29, 1998, at 2300 UTC. A comparison of this figure with Figure 6.5.9 shows that there are significant differences between these temperatures and the climatological values derived from the EDAS. Based on theory, these differences will lead to large differences in sensible and latent heat fluxes in the vicinity of Galveston Bay.

Figure 6.5.11 illustrates the differences in sensible heat flux arising from the SST differences discussed. The sensible heat flux resulting from the climatological SSTs is quite small (approximately 0-10 Wm^{-2}). That predicted by SSATS is larger, ranging, from about 5-42 Wm^{-2}, with a significant spatial gradient corresponding exactly to the SST field. These differences in sensible heat flux over the Bay can lead to substantial differences in PBL heights and near-surface winds, as discussed in Section 6.8. For example, the modeled boundary layer heights and surface winds in the vicinity of the Bay shown in Figure 6.8.53 (August 29, 2100 UTC) and Figure 6.8.55 (August 30, 0000 UTC), illustrate how the PBL predicted by the uncoupled model using

climatological SST's collapses earlier and has significantly different wind-flows than the coupled model.

This illustrates the importance of obtaining accurate spatial SST information capable of resolving the spatial pattern within the Bay. It is anticipated that more recent remotely-sensed data (such as those collected during TXAQS2000) would be even better suited for application in this context. This would represent a significant advance over the climatological values currently available for use in simulating episodes of interest using the standard MM5.

6.5.3 Figures for Section 6.5

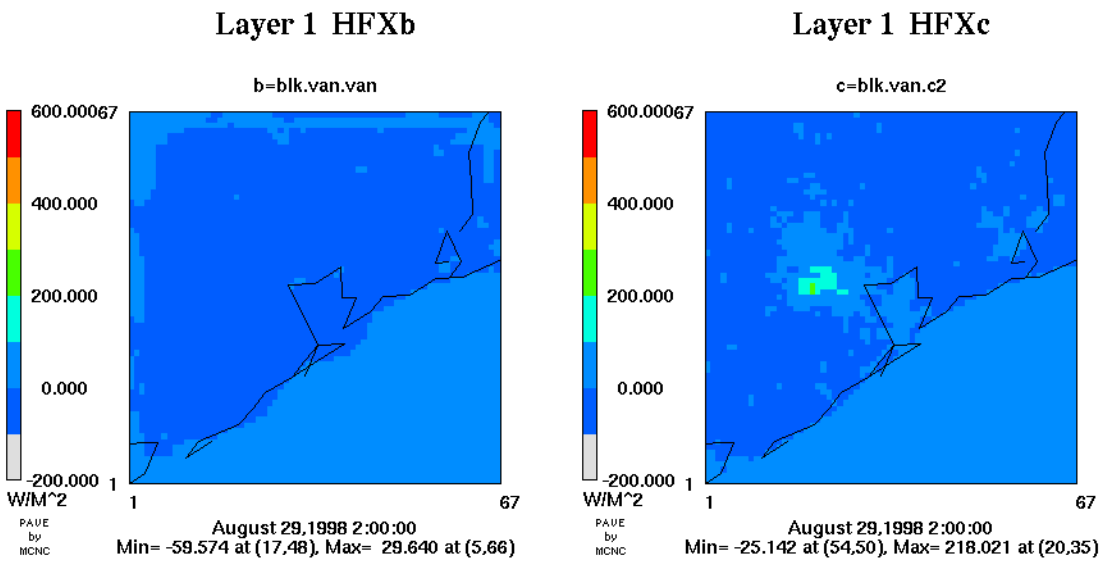

Figure 6.5.1. Sensible heat flux at 0200 UTC on August 29, 1998, illustrating the representation of the Houston heat island in the TOPLATS-coupled run and not in the uncoupled run, both for case "van."

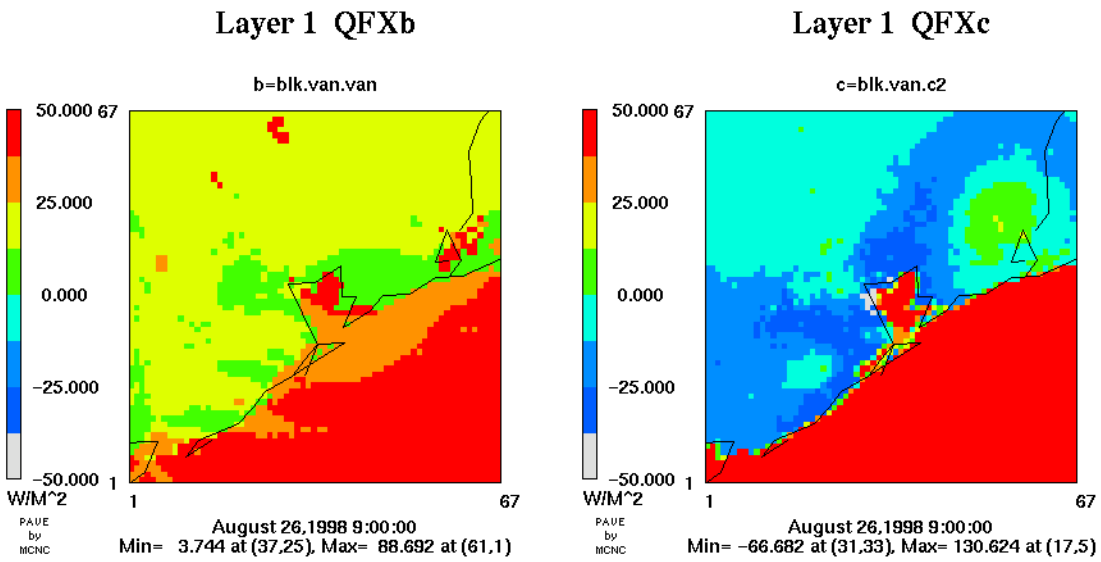

Figure 6.5.2. Latent heat flux at 0900 UTC on August 26, 1998, illustrating the formation of dew in the TOPLATS-coupled run and not in the uncoupled run, for case "van."

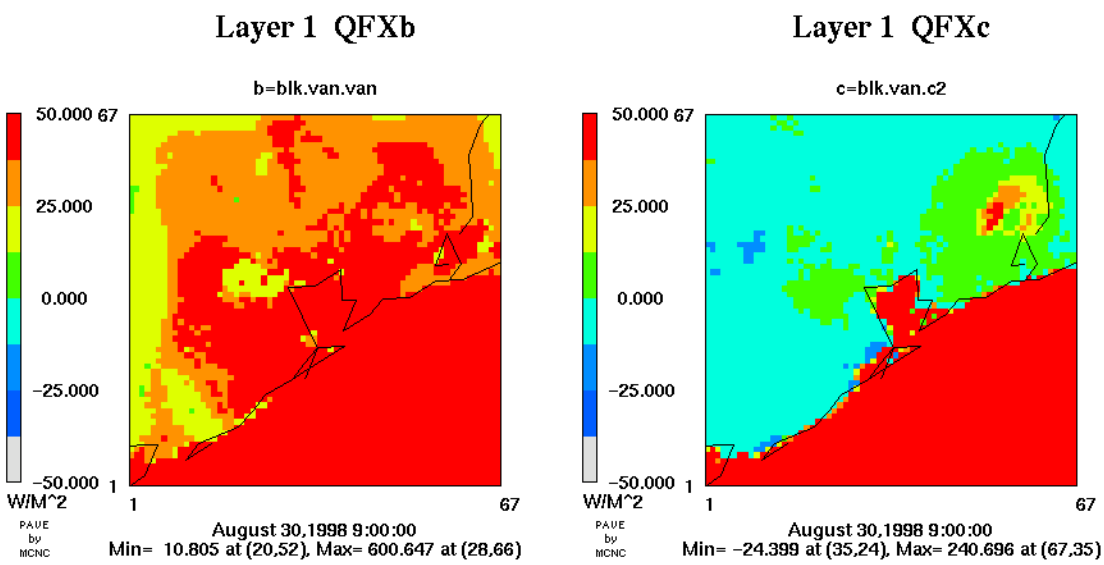

Figure 6.5.3. Latent heat flux at 0900 UTC on August 30, 1998. Dew formation in the TOPLATS coupled simulation (right) appears to decrease during the episode, presumably due to drying of the overlying air. Case "van."

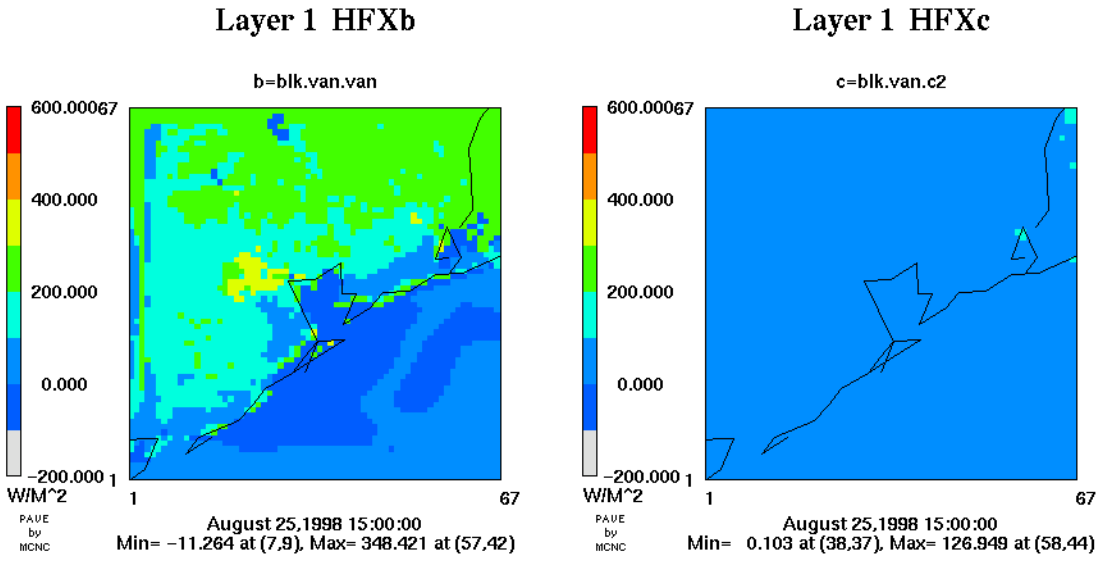

Figure 6.5.4. Sensible heat flux at 1500 UTC on August 25, 1998, illustrating differences in spatial patterns between the TOPLATS-coupled run and the uncoupled run, both for case "van."

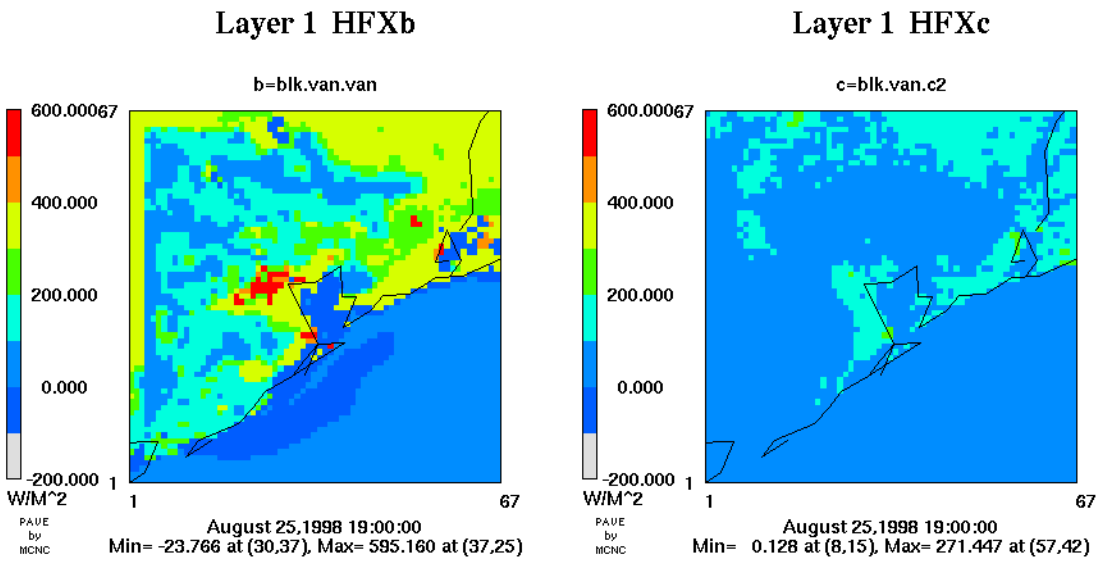

Figure 6.5.5. Sensible heat flux at 1900 UTC on August 25, 1998, illustrating differences in spatial patterns between the TOPLATS-coupled run (right) and the uncoupled run (left), for case "van."

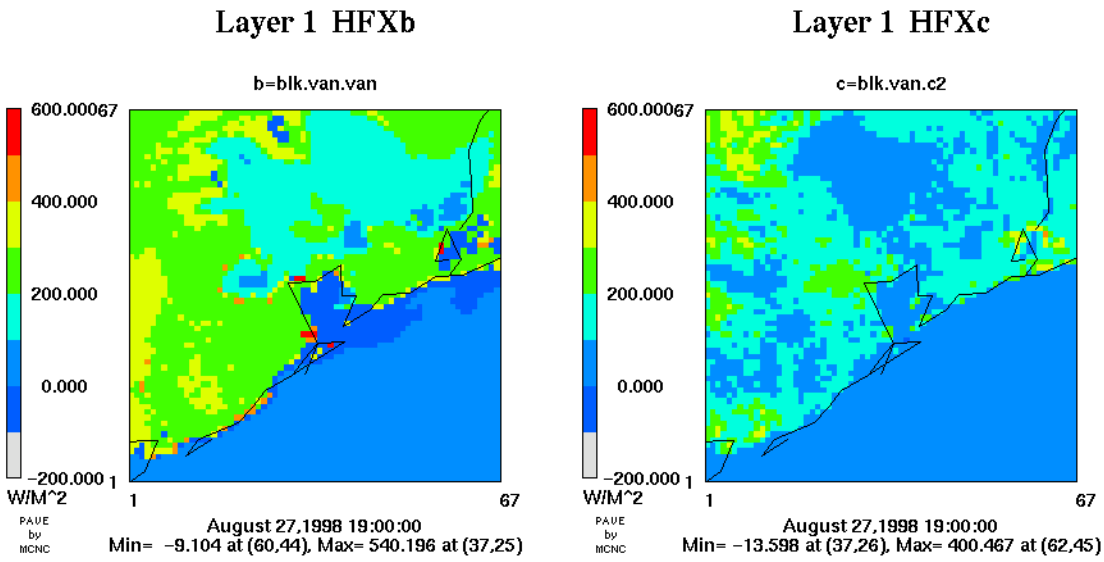

Figure 6.5.6. Sensible heat flux at 1900 UTC on August 27, 1998, illustrating differences in spatial patterns between the TOPLATS-coupled run and the uncoupled run for case "van."

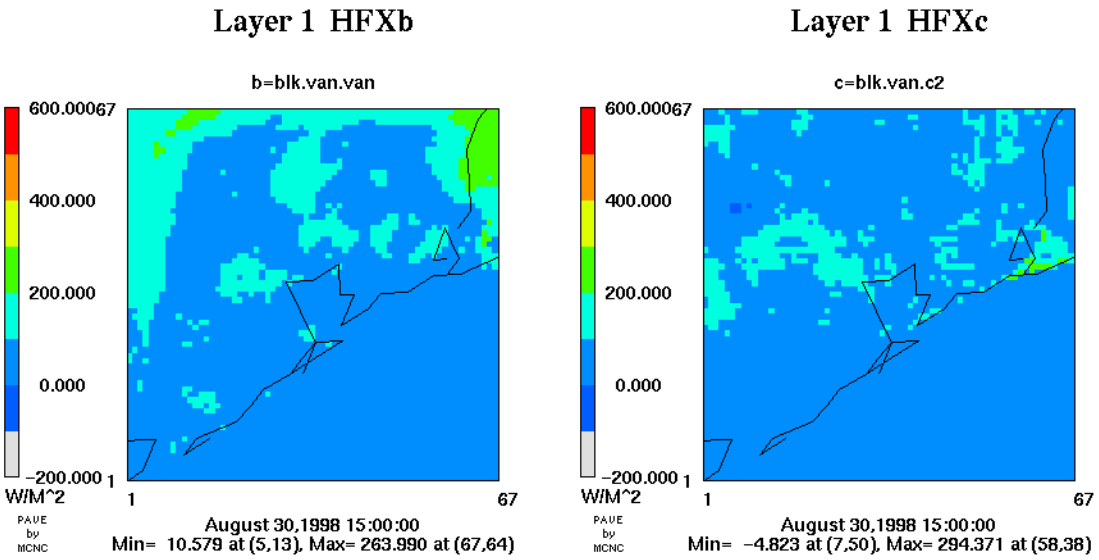

Figure 6.5.7. Sensible heat flux at 1500 UTC on August 30, 1998, illustrating only minor differences in spatial patterns between the TOPLATS-coupled run (right, blk.van.c2) and the uncoupled run (left, blk.van.van).

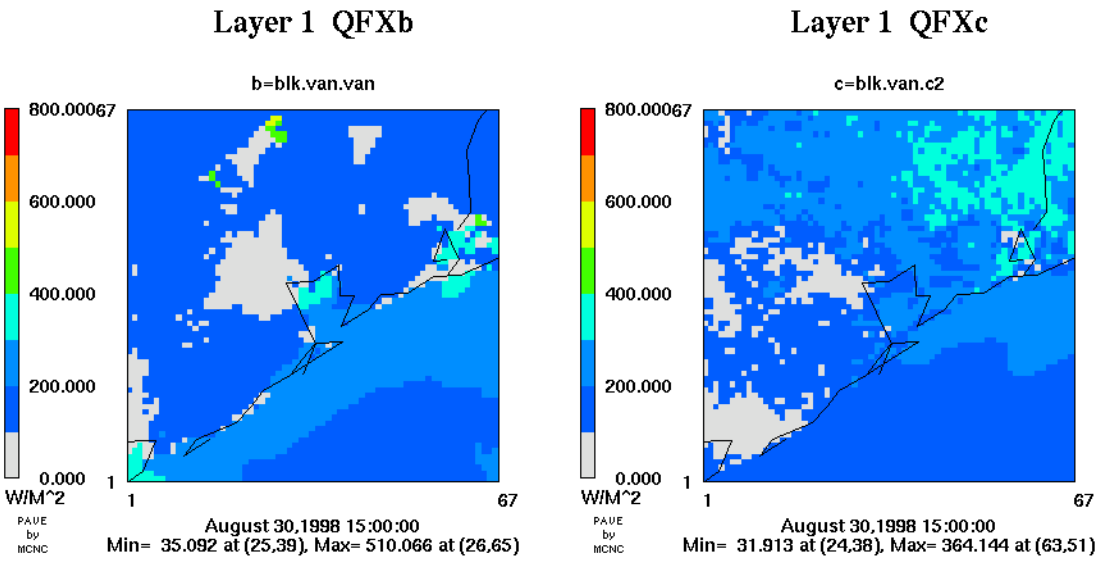

Figure 6.5.8. Latent heat flux at 1500 UTC on August 30, 1998, illustrating only minor differences in spatial patterns between the TOPLATS-coupled run (right, blk.van.c2) and the uncoupled run (left, blk.van.van). This indicates that differences in latent heat flux are due to land surface representation.

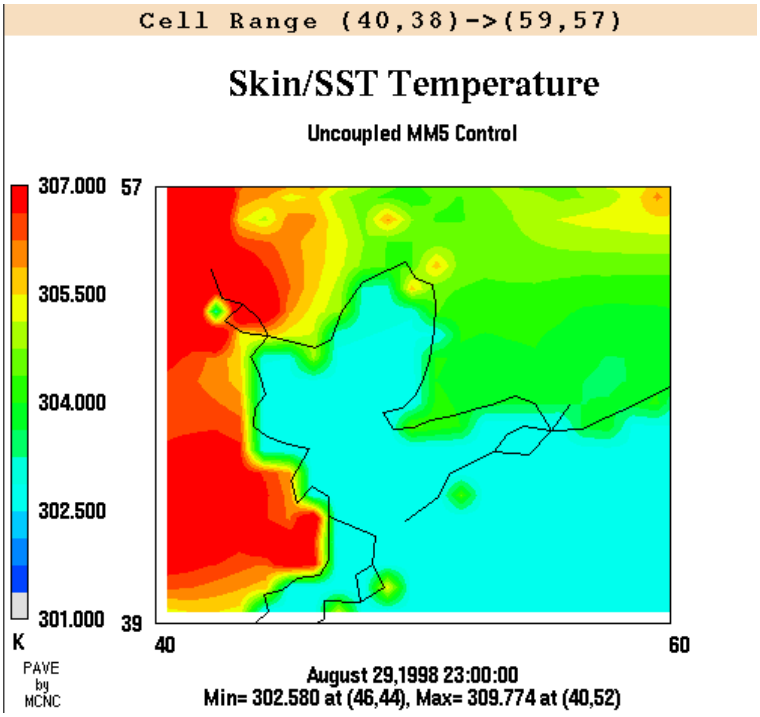

Figure 6.5.9. Climatological skin and Sea Surface Temperatures (SST) in the vicinity of Galveston Bay for August 29, 2300 UTC.

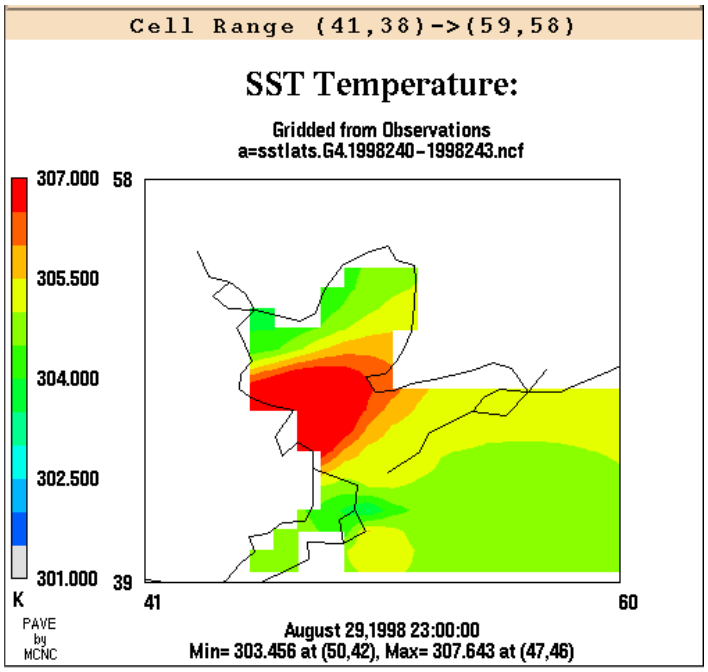

Figure 6.5.10. Gridded sea-surface temperatures on the 4-km MM5 grid for August 29, 1998, at 2300 UTC.

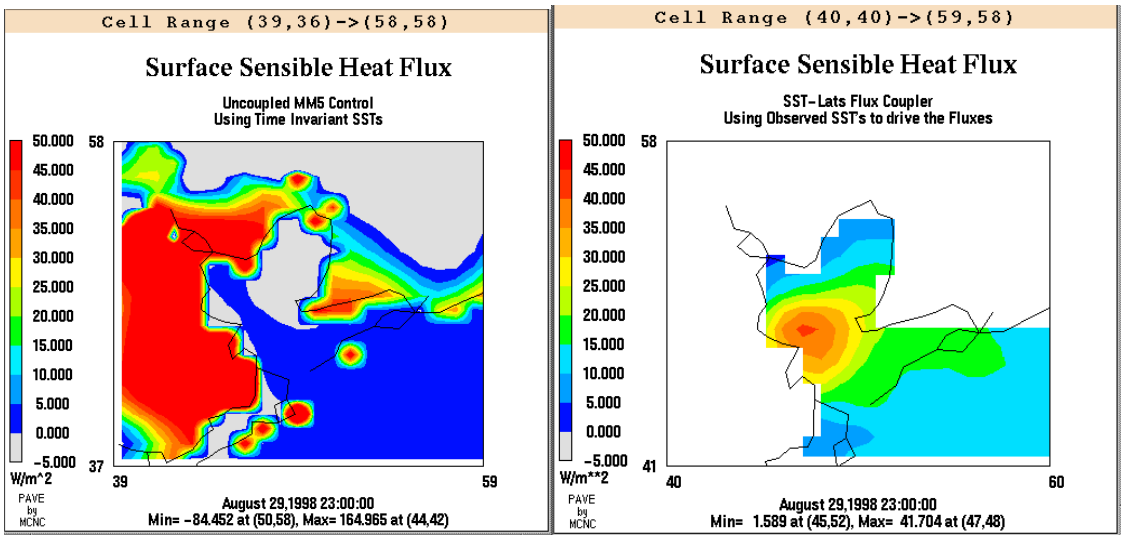

Figure 6.5.11. Surface sensible heat flux (HFX) predicted by MM5 using its climatological SST data from the EDAS (left) and predicted by SSATS using SST gridded data (right). Note the strong correspondence between the SST and HFX using SSATS.

6.6 Surface Sea-breeze Intrusion Analysis

6.6.1 Discussion

Figures 6.6.1 through 6.6.10 present an analysis of the daytime sea-breeze representation in the models, starting with August 25, using both satellite imagery and surface observed winds. Cases "van" and "kf5.2w" are used to compare coupled versus uncoupled models.

The sea breeze was well established on August 25, as shown in Figures 6.6.1 and 6.6.2. Observed surface vectors are plotted in blue on the model vector plots. At 1800 UTC, the sea breeze was light but beginning to advance. Both models were biased counterclockwise at this time, with the coupled model slightly more biased, consistent with the discussions in Sections 6.3 and 6.4. By 2100 UTC, both coupled and uncoupled model outputs were are similar, with mean wind vectors in reasonable agreement with the observations. The coupled model appears to represent the wind vector at BPA slightly better.

Figures 6.6.3 and 6.6.4 portray August 26, when the retrograding eastern High produced a mean northeast flow. At 1500 UTC, a sea breeze began to form near Corpus Christi, well southwest of the HGA. By 2000 UTC, the sea breeze expanded up the coast, and the uncoupled model featured a slightly more shore-perpendicular component, in better accordance with the observations.

August 27 was a relatively calm day as the High expanded and settled over Houston. Winds slowly "reset" from the south late in the day (Figures 6.6.5 and 6.6.6). At 2100 UTC, the sea breeze was weak to non-existent, except immediately along the coast. By 2300 UTC, a modest sea breeze approached metropolitan Houston, and the uncoupled model did better with this feature, the exception being the vector at Brazoria (lower left panel, Figure 6.6.6).

On August 28, the approach of a weak trough from the west allowed development of a more organized sea breeze along the Gulf coast. At 2000 UTC (Figure 6.6.7), the sea breeze had not yet reached Houston, and model winds were generally light and variable. The uncoupled model induced more sea-breeze forcing than was observed at Brazoria at the time. By 2200 UTC, the wind (Figure 6.6.8) had switched directions at Brazoria but there was not a domain-wide sea breeze. Weak onshore flow was reported, however, at GLS. Both models were similar at this time.

On August 29 at 2100 UTC (Figure 6.6.9), observed wind vectors indicated that a sea breeze had formed, moving inland at least as far as the city of Houston. The models do not replicate this very well. In the top panels, wind vectors along the northern boundary reveal the KF-caused boundary condition problem.

On August 30, convective sub-tropical moisture approached from the southwest and the observed mean winds shifted nearly 180 degrees from northeast to southwest during

the day. Model winds remained generally easterly. Additional convective outflow approached the HGA from the north, a result of the proximity of the east-west axis airmass boundary to the north. Central Gulf of Mexico low pressure contributed to observed offshore east-to-northeast winds throughout the day. This complexity apparently led to the poor wind performance on that day by both uncoupled and coupled models.

Figures 6.6.10a through 6.6.10e depict the evolution of the observed winds and visible cloud patterns compared to modeled winds on August 30. Through about 1400 UTC (Figure 6.6.10a) , both modeled and observed winds were in general agreement (out of the northeast), consistent with the synoptic forcing between the central Gulf-of-Mexico low pressure and the weak high pressure over east-central Texas. By about 1600 UTC (Figure 6.6.10b), observed surface winds veered into the southeast. This is not consistent with the timing of the sea breeze on other days, and in addition, there is no evidence of a sea breeze on the cloud imagery. The models do not reflect this change in observed wind, maintaining their east-northeasterly direction.

By 2000 UTC (Figure 6.6.10c), the mean observed winds have veered further to the southwest, whereas the models continue to maintain the east-northeast flow consistent with the synoptic pressure gradient. The counter-gradient observed flow may be explained by the proximity of the convective complex to the southwest, which may have provided low-level outflow propagating toward the northeast. Alternatively, the proximity of the complex to the southwest could have resulted in enough subsidence aloft to generate a weak, unanalyzed meso-high sandwiched between the synoptic low in the central Gulf and the convective axis to the north of the HGA. High quality four-dimensional meso-analyses might be necessary to fully determine the cause(s) of the observed wind behavior; since it is rather complex.

At 2200 UTC (Figure 6.6.10d), radar imagery indicates the presence of convection to the north and to the south, with a small shower over Galveston Bay. The shower may have erupted from surface convergence caused by the proximity of the convective complex to the southwest and the developing line to the north. By 2300 UTC (Figure 6.6.10e), the observed wind vectors indicate convergence near central Houston. At this time the difference in boundary conditions appears to make the most difference in model results, with the “van” runs revealing KF-generated outflow propagating inward from the north and west, a feature not found in the “kf5.2w” runs. However, the outflow propagation effect is too strong in the “van” runs. Overall, Figures 6.6.10a through 6.6.10e reveal that neither the coupled nor the uncoupled model captures the counter-synoptic-gradient flow reversal that occurred during the day on August 30.

In general, the analysis suggests that the uncoupled model simulations handle a relatively weak sea breeze slightly better than the coupled model simulations. On August 25, the coupled model’s sea breeze began about an hour later than the uncoupled model’s (slightly slow). Again on August 26, the coupled model was biased a little farther left (counterclockwise) than the uncoupled model. On August 27, both models replicated the light winds but the uncoupled model appears to better represent the sea

breeze at 2300 UTC. On August 28, the uncoupled model seems to induce a weak sea breeze too early. On August 29, the models are similar. Finally, on August 30, both coupled and uncoupled models maintain an east-northeast wind direction consistent with the larger-scale low-level synoptic forcing, failing to capture the surface flow reversal that accompanied a convective complex moving northeastward under weak southwesterly 500-mb flow. There is no evidence of a true sea breeze on August 30.

A seemingly simple phenomenon such as the sea breeze is actually the result of several superimposed processes. Therefore, analyzing why a model has difficulty representing the sea breeze is more difficult than might be expected. There are at least two interrelated mechanisms, described above in relationship to inertial oscillations and low-level jets, that also contribute to the overall model winds and representation of the sea breeze. These include (1) diurnal surface-frictional de- and re-coupling (night/day) and (2) uneven (land-sea) heating effects. The uncoupled model does a poorer job representing the second of these two processes, evidenced by too-cold near-shore water (Figures 6.5.9, 6.5.10, and 6.8.9) and unrealistically uniform nocturnal land-sea skin temperatures (Figure 6.8.26). This latter effect is related to a fundamental surface thermodynamic problem in the uncoupled model, where the near-surface atmosphere has a weak diurnal temperature cycle while also being too dry. This would be expected to induce stronger-than-realistic daytime sea-breeze forcing and weaker-than-realistic nighttime land-breeze forcing, suggesting that the uncoupled model should exhibit an overly strong daytime sea breeze and an overly weak nighttime land breeze. Why then, does the uncoupled model perform slightly better, overall, with the sea breeze?

It is hypothesized that the uncoupled land-sea thermal forcing error compensates for a larger-scale misrepresentation of coast-normal frictional differences (combining both land-sea and day-night surface stress representation), which act in an abnormal out-of-phase manner, with the overly-forced land-sea heating effects. This larger-scale forcing error would manifest itself particularly in the boundary conditions produced by the outer-domain model, used by the 4-km model. The hypothesized frictional (surface-stress) deficiency produces the fundamental mean counterclockwise directional bias (Figure 6.4.6) described above. Upon improving the scalar flux representation in the coupled model, which weakens (as compared to the standard uncoupled model) the daytime sea-breeze forcing and strengthens (as compared to the standard uncoupled model) the nocturnal land-breeze forcing, the actual coupled model wind-directional results become somewhat more biased in the counterclockwise direction, because a compensating error has been eliminated.

There is some evidence in the literature for an inappropriate surface stress formulation over water in the default MM5. Pagowski and Moore (1998) note that the so-called Charnock formula, given by

$$z_0 = a_c u_*^2 / g + 1.0E - 4;$$

where z_0 is roughness length over water, g is the gravitational acceleration, and a_C is the Charnock constant equal to 0.032, may overestimate the over-water roughness length.

This is because observations suggest over-water values for a_C between one-half and one-third that amount (Smith, 1988; Garratt, 1992). Overestimating the over-water roughness length would effectively overestimate the surface stress (given by $t = ru_*^2$) and thus the frictional force depicted in Figure 4.8. The effect would be to inordinately increase the ageostrophic wind vector shown in panel "b" of that figure, resulting in a counterclockwise wind direction bias, consistent with what the model simulations produced. Sensitivity studies with the surface stress formulation, in particular the Charnock constant over water, would be needed to firmly confirm this hypothesis.

One other possibility, discussed in the caption describing Figure 6.8.9, is that the 4-km scale simply does not respond correctly to the proper thermal forcing, requiring too-large thermal forcing to produce an adequate sea breeze. This could occur if the energetics of the sea breeze are at significantly sub-4-km spatial scales. Although idealized sea-breeze simulations would be needed to rule this out, this is a less-likely explanation, since coast-normal land-sea contrasts extend for tens of kilometers both directions during the daytime heating period.

6.6.2 Figures for Section 6.6

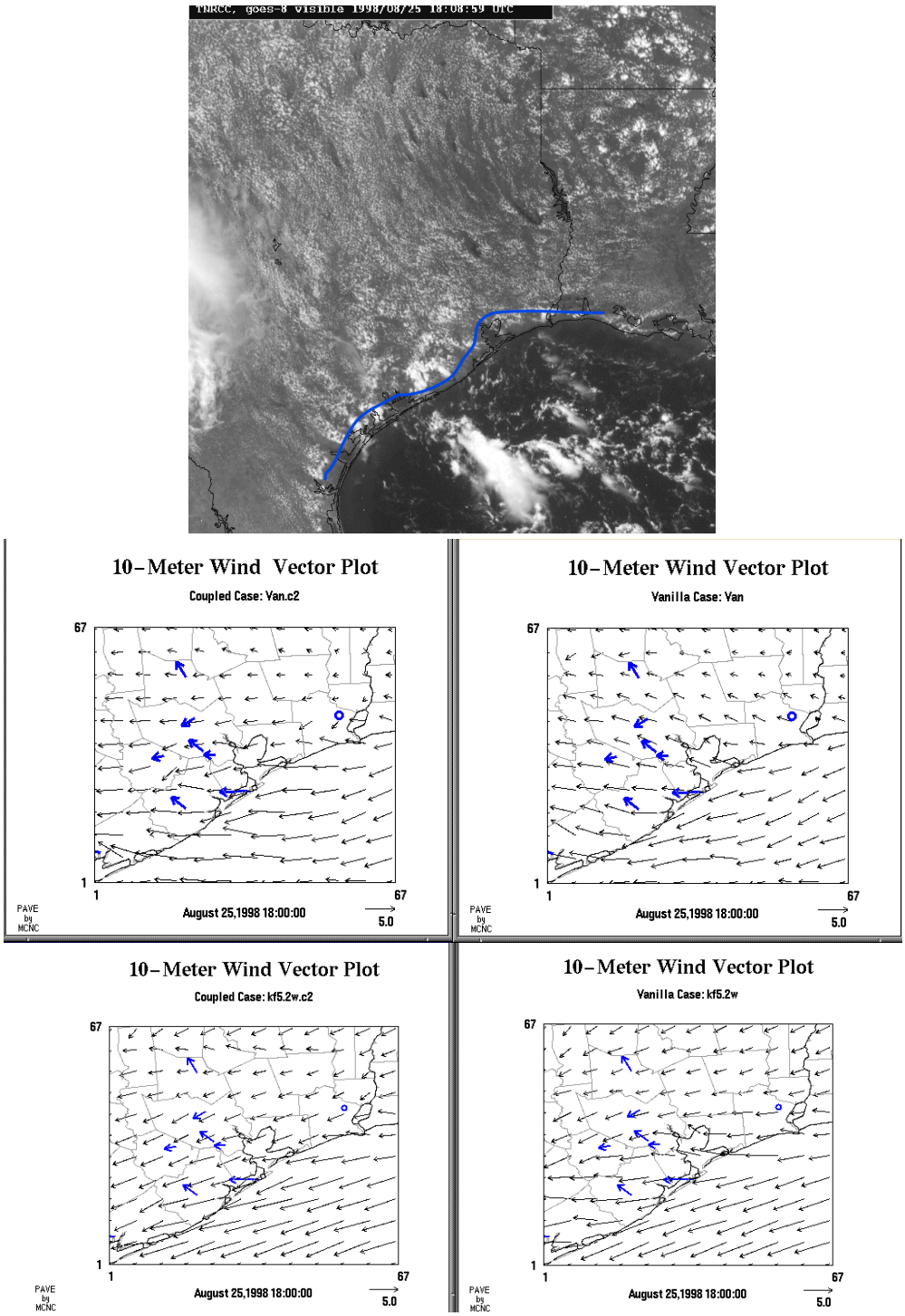

Figure 6.6.1. The sea breeze as observed from GOES satellite at 1800 UTC on August 25, 1998, compared to model simulations. Two coupled model cases are shown on the left; equivalent uncoupled model cases are shown on the right. Observed surface wind vectors are plotted in blue. Note that the uncoupled model supports a slightly more shore-perpendicular wind component.

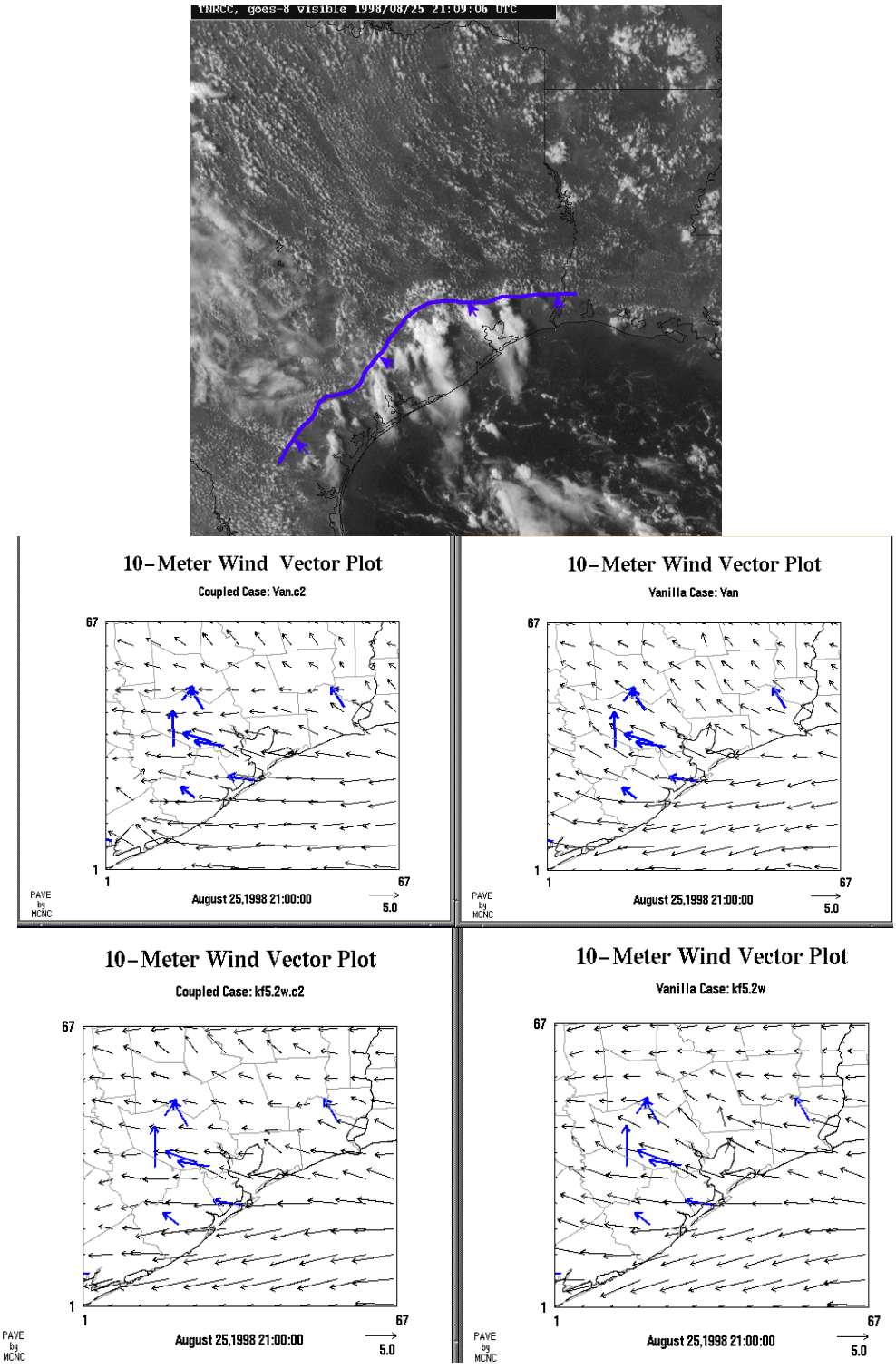

Figure 6.6.2. The sea breeze as observed from GOES satellite at 2100 UTC on August 25, 1998, compared to model simulations. Two coupled model cases are shown on the left; equivalent uncoupled model cases are shown on the right. Observed surface wind vectors are plotted in blue. Both coupled and uncoupled models are similar, with mean vectors in reasonable agreement with the observations. The coupled models predict slightly more accurate wind-vector data at Beaumont-Port Arthur.

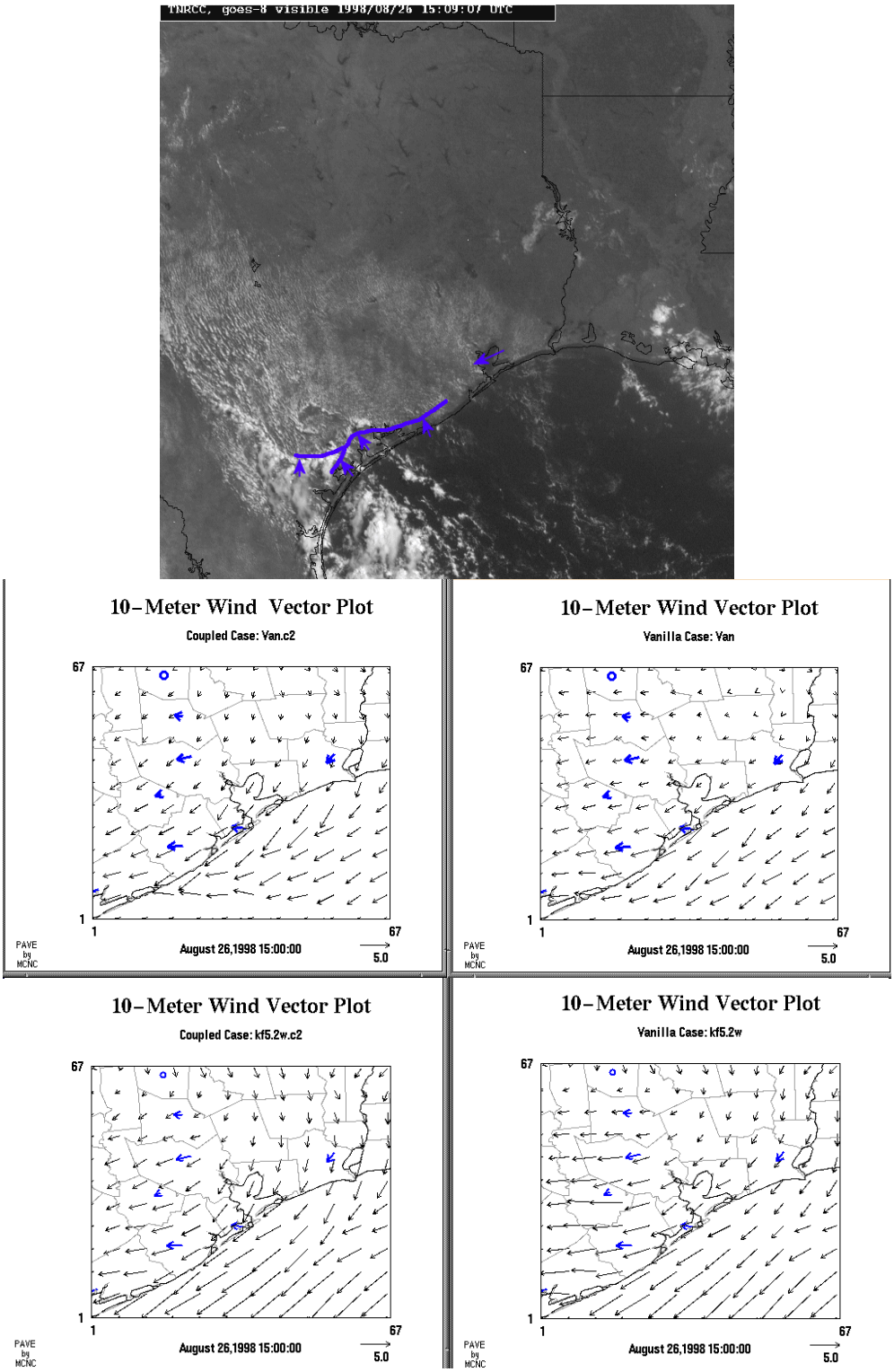

Figure 6.6.3. The sea breeze as observed from GOES satellite at 1500 UTC on August 26, 1998, compared to model simulations. Two coupled model cases are shown on the left; equivalent uncoupled model cases are shown on the right. Both models capture the northeasterly surface flow due to the retrograding Eastern High. At the time, a sea breeze was beginning to form near Corpus Christi.

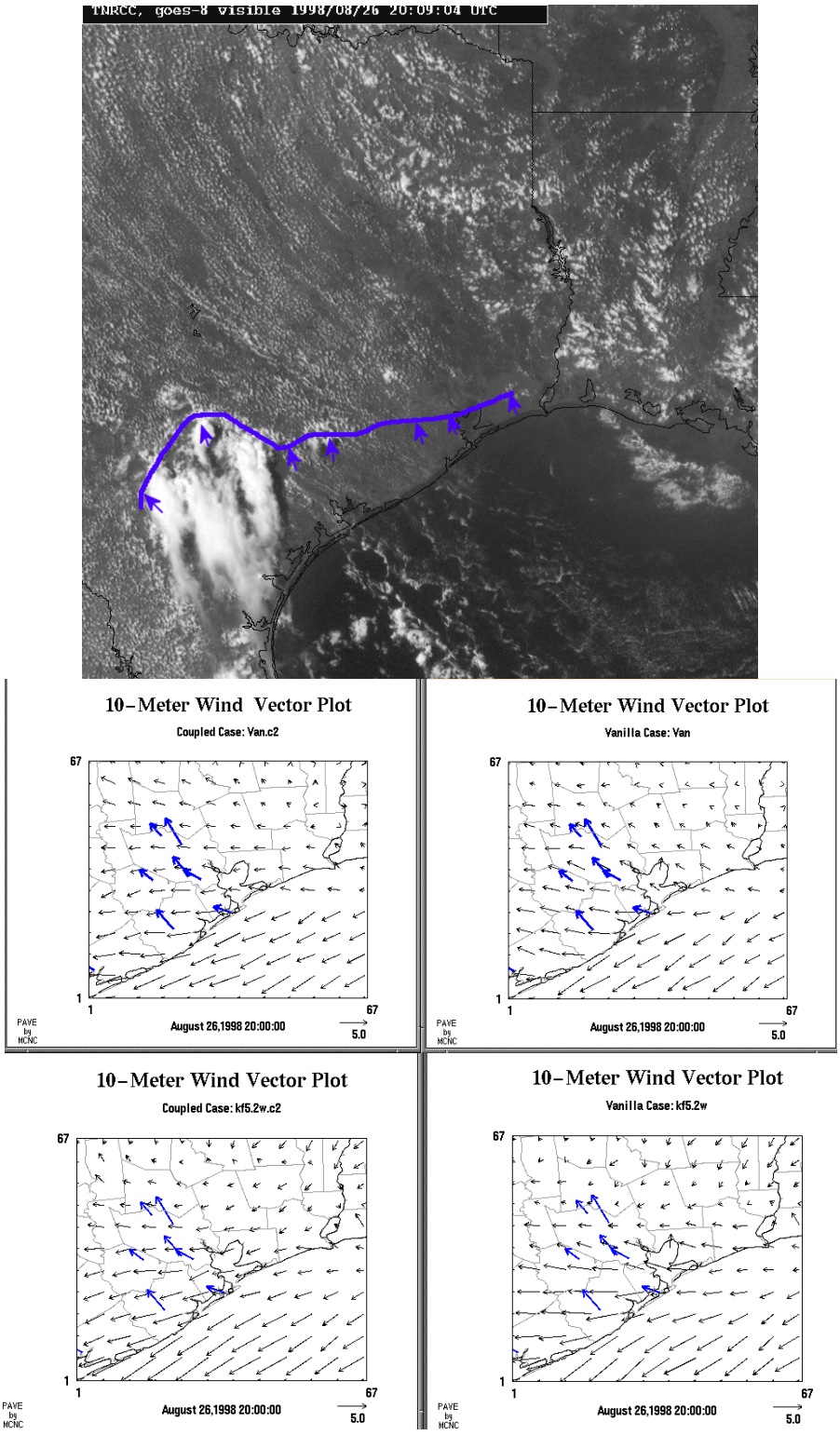

Figure 6.6.4. The sea breeze as observed from GOES satellite at 2000 UTC on August 26, 1998, compared to model simulations. Two coupled model cases are shown on the left; equivalent uncoupled model cases are shown on the right. As indicated in blue on the satellite image, the sea breeze has expanded up the coast toward Houston, validated by the plotted observed vectors. The uncoupled model features a slightly more shore-perpendicular component, in better accordance with the observations.

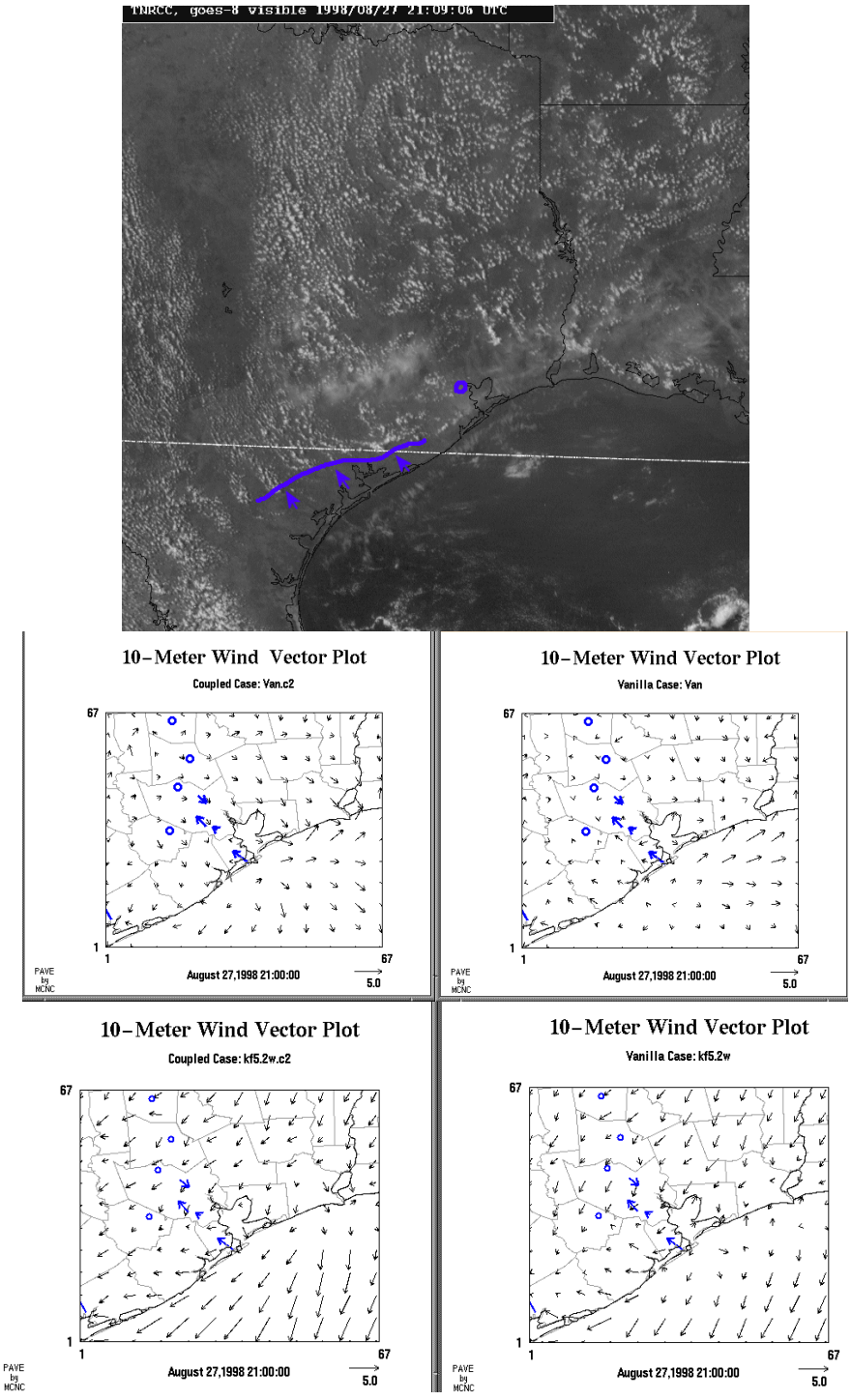

Figure 6.6.5. The sea breeze as observed from GOES satellite at 2100 UTC on August 27, 1998, compared to model simulations. Two coupled model cases are shown on the left; equivalent uncoupled model cases are shown on the right. The sea breeze was weak to non-existent at this time, with the immediate coast being the exception. Differences in the position of the High centered near Houston between the "van" runs and the "kf5.2w" runs explain the differences in the position of the surface anticyclonic flow centers between the top and bottom sets of panels.

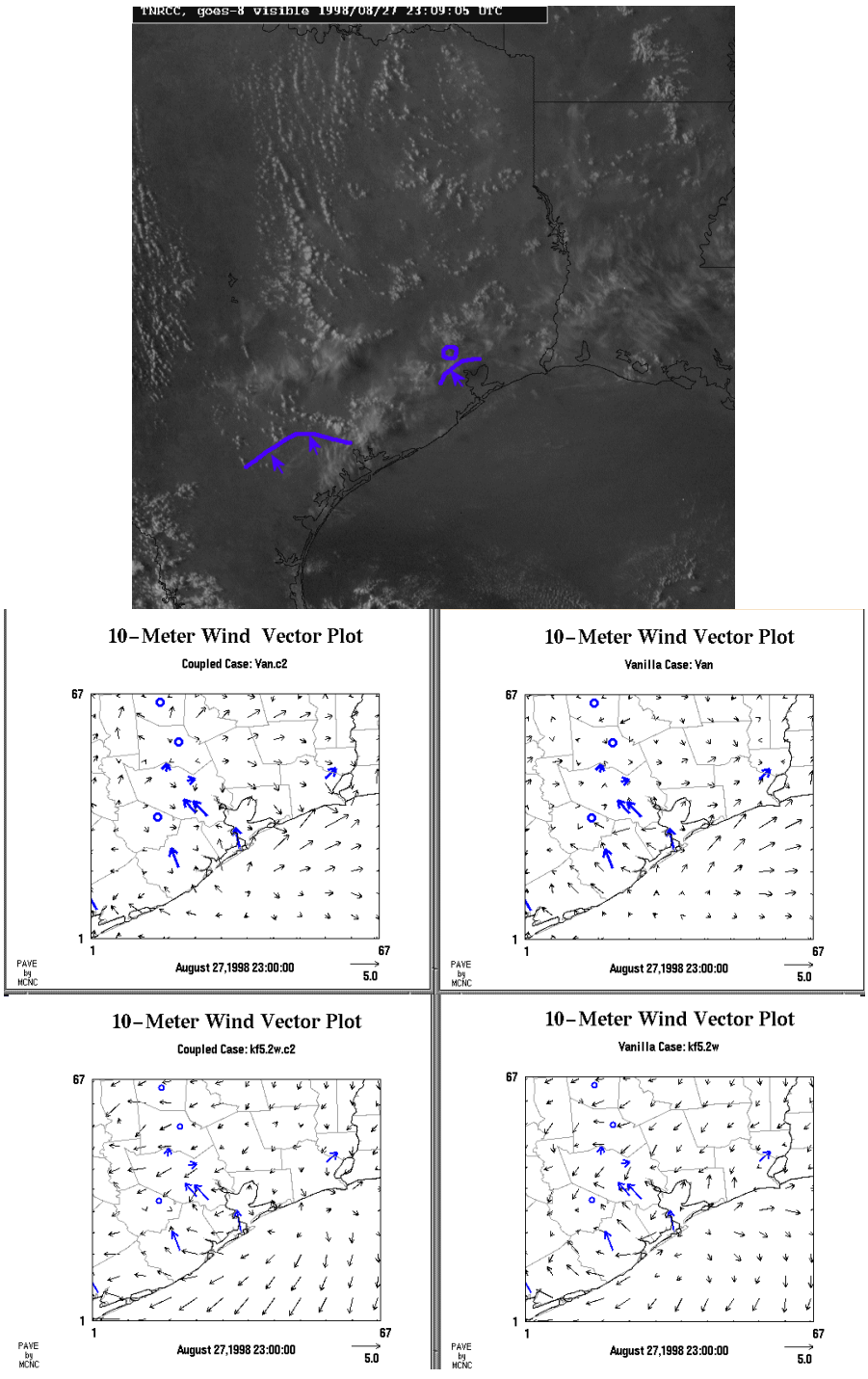

Figure 6.6.6. The sea breeze as observed from GOES satellite at 2300 UTC on August 27, 1998, compared to model simulations. Two coupled model cases are shown on the left; equivalent uncoupled model cases are shown on the right. By this time, a modest sea breeze was approaching metropolitan Houston. The uncoupled models are slightly better depicting this feature.

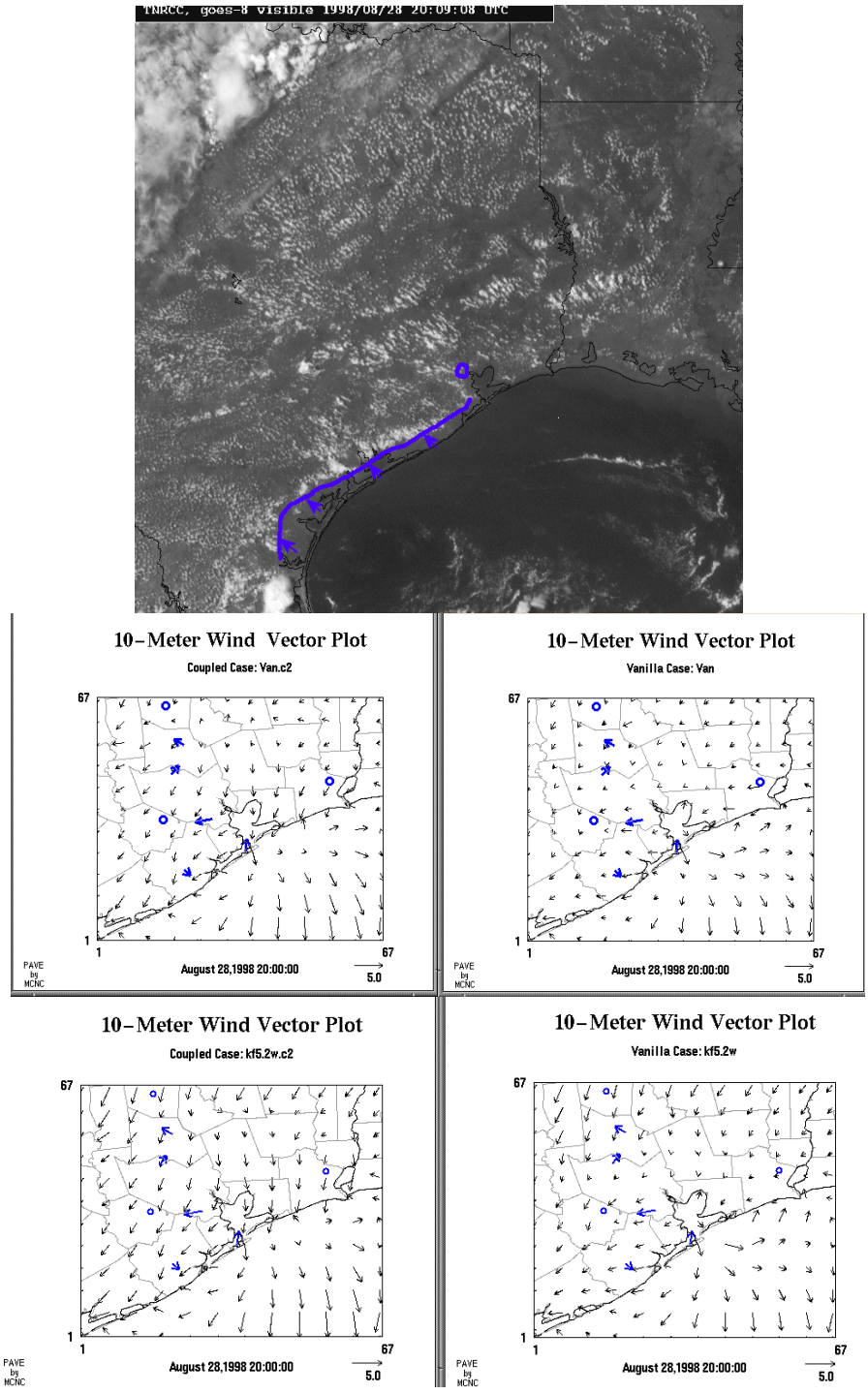

Figure 6.6.7. The sea breeze as observed from GOES satellite at 2000 UTC on August 28, 1998, compared to model simulations. Two coupled model cases are shown on the left; equivalent uncoupled model cases are shown on the right. Approach of a weak trough allowed development of a more organized sea breeze south along the coast at this time.

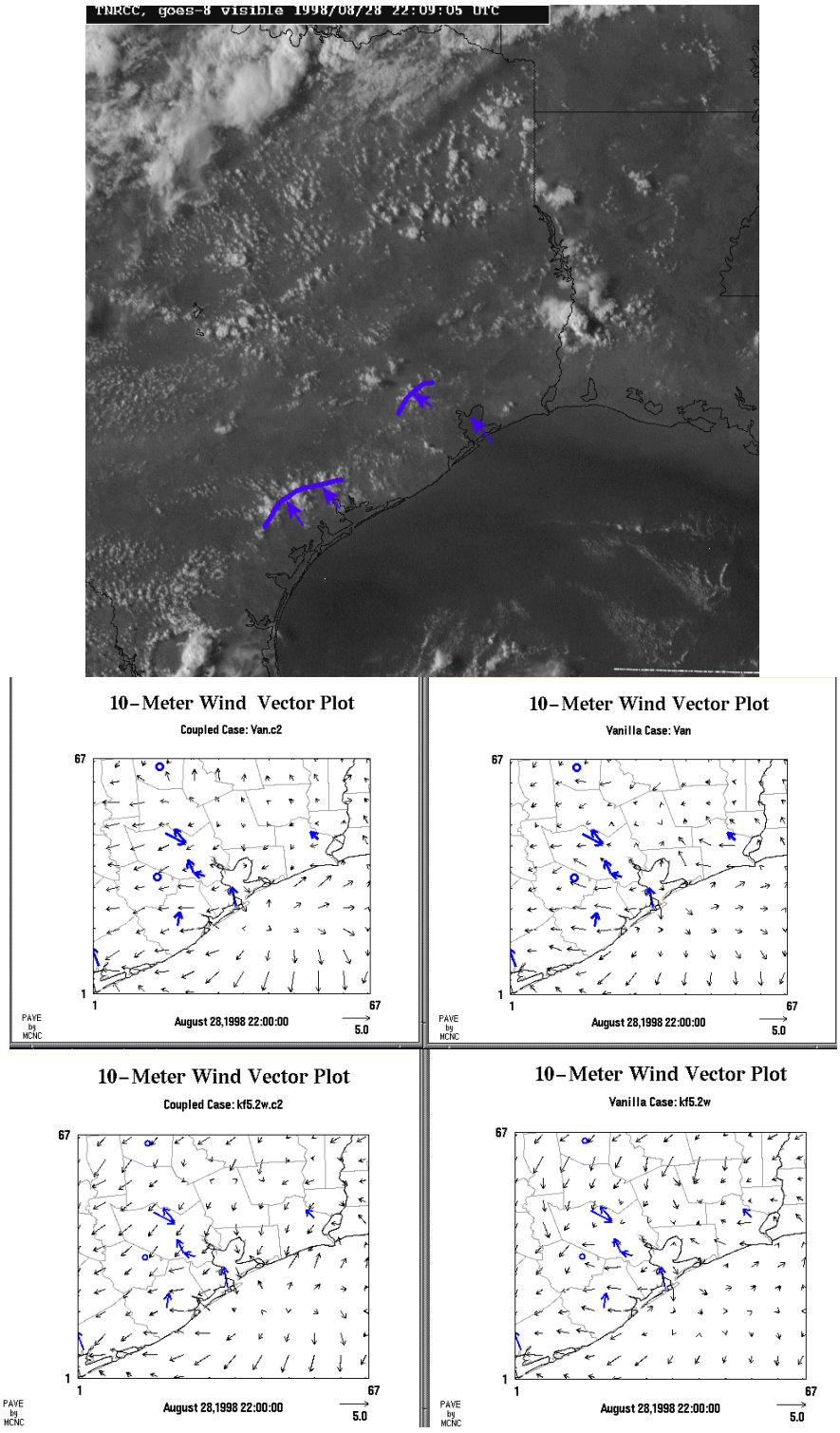

Figure 6.6.8. The sea breeze as observed from GOES satellite at 2200 UTC on August 28, 1998, compared to model simulations. Two coupled model cases are shown on the left; equivalent uncoupled model cases are shown on the right. Though there is no widely organized sea breeze within the domain, Galveston and several other stations indicated weak onshore (toward the coast) flow.

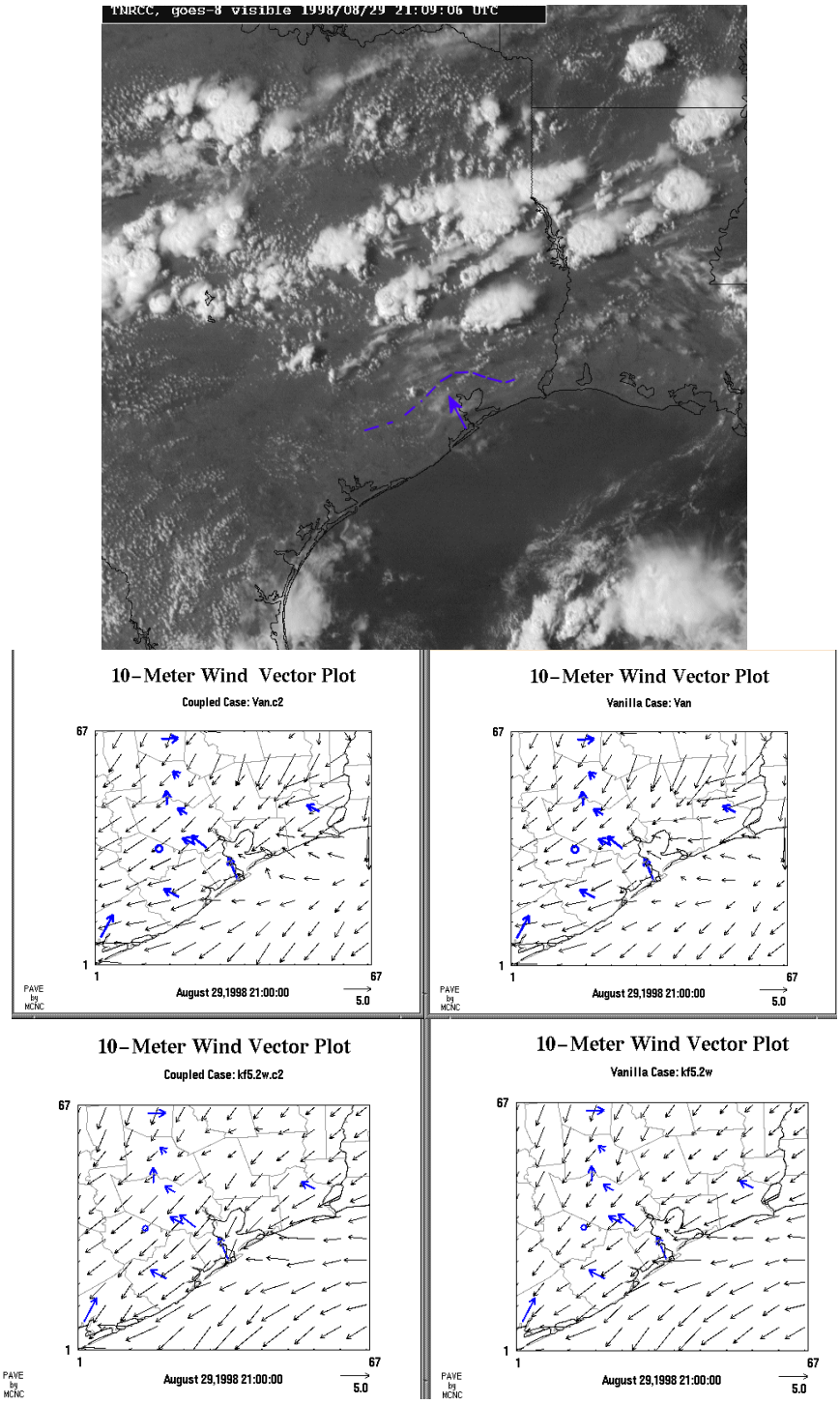

Figure 6.6.9. The sea breeze as observed from GOES satellite at 2100 UTC on August 29, 1998, compared to model simulations. Two coupled model cases are shown on the left; equivalent uncoupled model cases are shown on the right. At this time, observed vectors indicate that a sea breeze formed, moving inland at least as far as the city of Houston. The models do not replicate this very well. In the top panels, the wind vectors along the northern boundary reveal the KF-caused boundary condition problem, discussed in the text as the reason for adding cases "kf5.2w" and "kf5.2w.c2." Figure 4.3 shows the KF-outflow winds dominating the domain by 2300 UTC for the "van" runs.

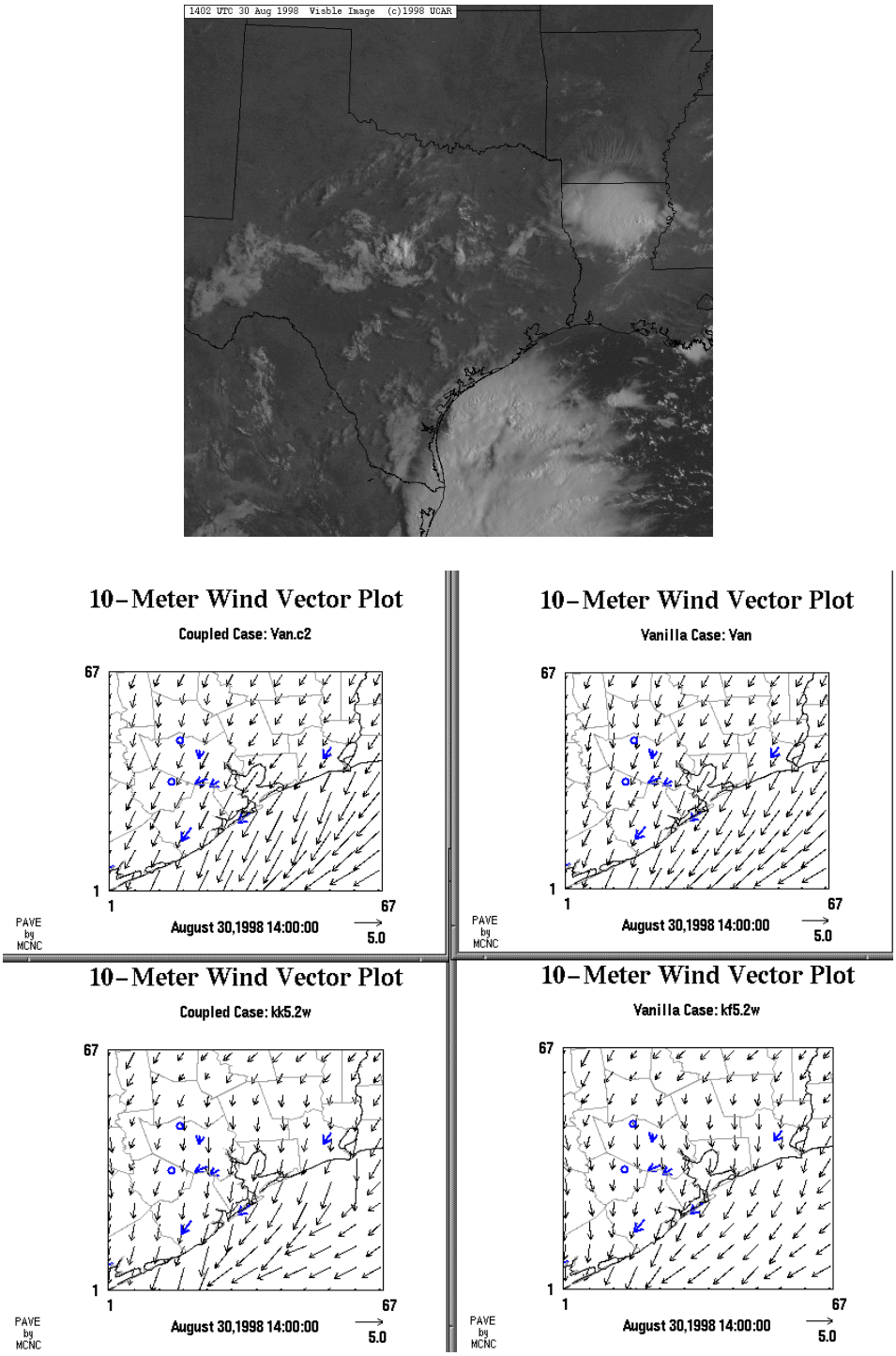

Figure 6.6.10a. Observed GOES visible satellite imagery at 1400 UTC on August 30, 1998, compared to model simulations. Two coupled model cases are shown on the left; equivalent uncoupled model cases are shown on the right. No sea breeze is evident at this time. Both modeled and observed winds are consistent directionally.

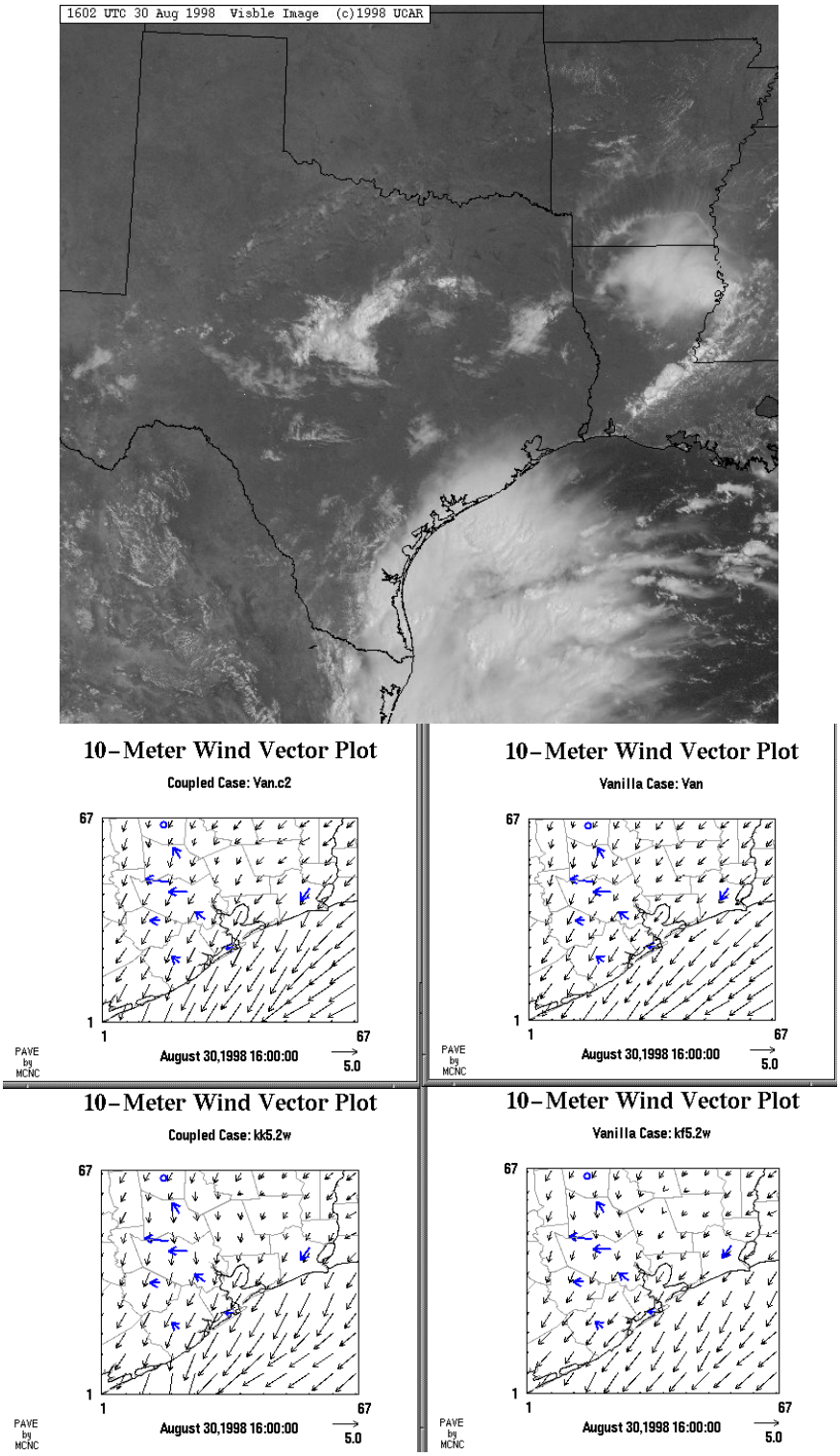

Figure 6.6.10b. Observed GOES visible satellite imagery at 1600 UTC on August 30, 1998, compared to model simulations. Two coupled model cases are shown on the left; equivalent uncoupled model cases are shown on the right. Though it is only 11 a.m. local time, observed winds in the western half of the domain are now southeasterly; however, *no sea-breeze is evident on the imagery*. Model winds remain northeasterly. Outflow from the large convective complex to the southwest may have helped turn the winds.

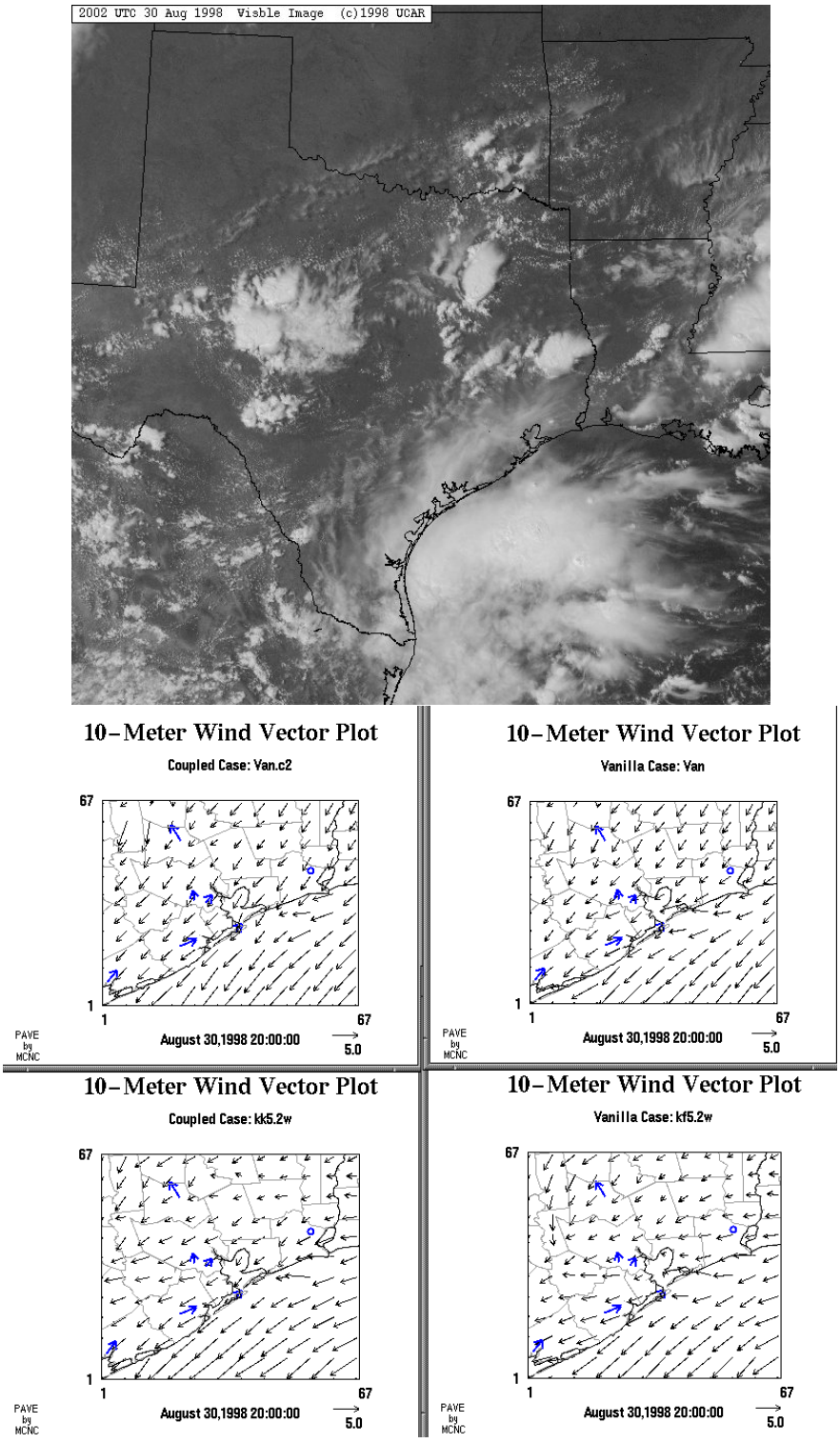

Figure 6.6.10c. Observed GOES visible satellite imagery at 2000 UTC on August 30, 1998, compared to model simulations. Two coupled model cases are shown on the left; equivalent uncoupled model cases are shown on the right. Observed winds are now mostly southwesterly; *no sea-breeze is evident on the imagery*. Model winds remain northeasterly. Outflow from the large convective complex to the southwest may have helped turn the winds.

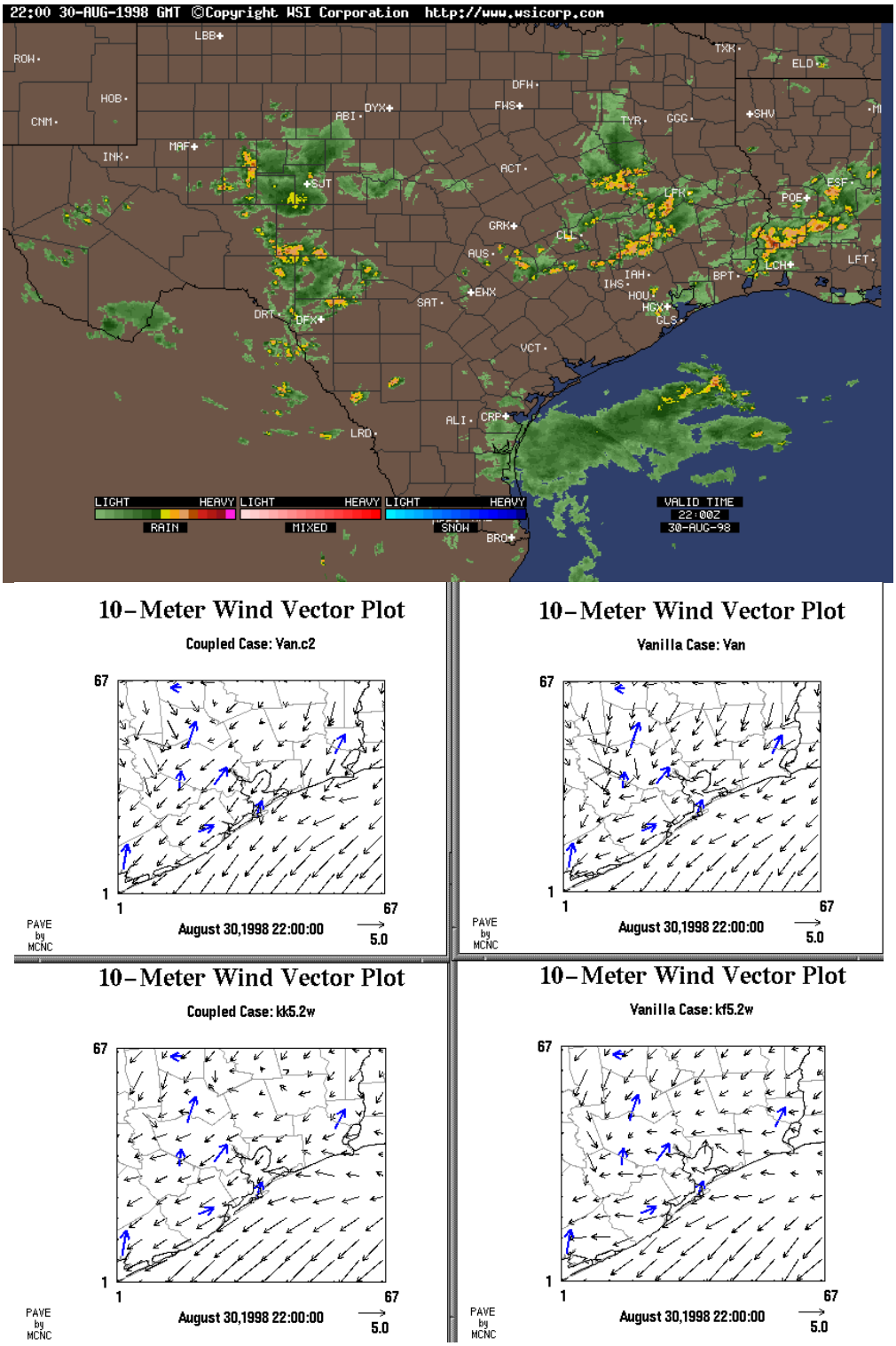

Figure 6.6.10d. NEXRAD radar imagery (courtesy of WSI Corporation) at 2200 UTC on August 30, 1998, compared to model simulations. Two coupled model cases are shown on the left; equivalent uncoupled model cases are shown on the right. Observed winds are southwesterly. Model winds remain generally out of the northeast. The imagery shows the proximity of the convective complex to the SW and the convection breaking out to the NE.

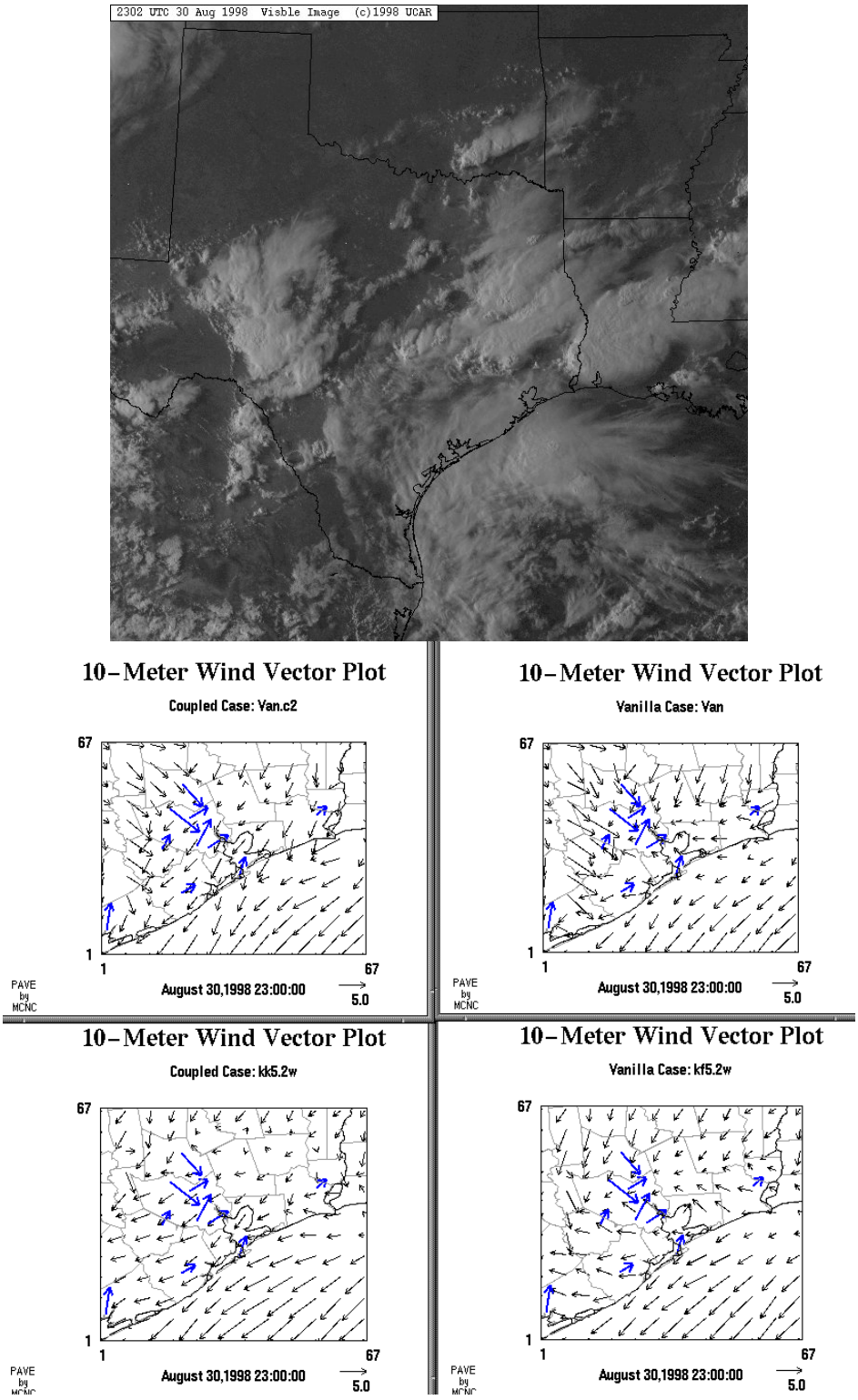

Figure 6.6.10e. Observed GOES visible satellite imagery at 2300 UTC on August 30, 1998, compared to model simulations. Two coupled model cases are shown on the left; equivalent uncoupled model cases are shown on the right. Observed winds are now a mixed bag with apparent outflow now coming from both the northwest and the southwest. Although overdone, the top two "van" runs reveal KF-generated outflow advecting inward from the northern and western boundaries. The "kf5.2w" runs do not have this outflow.

6.7 Accuracy of Cloud Representation

6.7.1 Discussion

Clouds play a major role in the evolution of weather and air quality. Most ozone exceedance episodes are relatively cloud free. However, clouds in proximity can create environments conducive-to or destructive-of incipient events. Along with the models' known difficulties in handling clouds, these characteristics make the importance of cloud processes critical in ozone-producing environments.

Figures 6.7.1 through 6.7.21 describe and compare uncoupled versus coupled model performance for case "van" during the day when photochemistry is active. At 1800 UTC on August 25, satellite imagery shows mostly shallow cumulus along the coast and inland from a weak sea breeze. The uncoupled run has produced extensive spurious grid-scale clouds, as shown by the (green) reduction in solar insolation (RSD) in the top-left panel of Figures 6.7.1 through 6.7.21. Surface solar insolation patterns are the best surface surrogates for grid-scale clouds. The coupled MM5 calculates this variable internally but does not use it in the surface energy balance, thus, it can be used to indicate the presence of clouds, but shouldn't be confused with the driving RSD derived from the SRB data, which may be very different from the RSD output from MM5.

The coupled model, by contrast, is far better at depicting both the coverage and location of the clouds. The evolution of these cloud fields and their associated below-cloud temperature (which may be reduced by cool downdrafts or changes in surface fluxes) are shown in Figures 6.7.2 and 6.7.3. At 2000 UTC, the convective cells (shown in the satellite images) over Galveston Bay and to the south are well represented in the coupled run, whereas the cloud pattern in the uncoupled run (too much coverage, not organized) does not resemble the imagery. By 2200 UTC, the models have not moved the clouds inland as much as the sea breeze has actually carried them; nonetheless, cloud amount is still overestimated in the uncoupled run. Areas of associated surface temperature reduction are well-correlated.

August 26 was essentially a clear day. At 1500 UTC (Figure 6.7.4), a thin area of small shallow cumulus can be seen on the GOES image appearing like a milky sheath over much of the modeling domain. Lake Conroe and other inland bodies of water are void of these clouds. Additional thin clouds are present over the near-shore Gulf. Both models pick up on the Gulf cloudiness, but overestimate it. More surface temperature detail is evident in the coupled model than in the uncoupled model. By 2000 UTC (Figure 6.7.5), both models are similar in the relatively small coverage amounts, though it is spurious. By 2200 UTC (Figure 6.7.6), a large spurious cloud has formed in the northeast quadrant of the uncoupled model. Of note is the classic sea-breeze "cooling pattern," not associated with the aforementioned cloud, in the uncoupled run. Data from GLS confirm that this was erroneous: the uncoupled model air temperature was nearly 6°F too cold. This likely results from overly cold near-shore SSTs in the uncoupled model—a problem corrected in the coupled model.

On August 27 (Figures 6.7.8 through 6.7.10), the uncoupled model produced a large spurious cloud by 2000 UTC, causing widespread temperature reductions. By 2200 UTC, this cloud expanded further. The widely scattered clouds in the coupled model are consistent with satellite imagery. By 2200 UTC on August 28, a large spurious cloud has again formed in the uncoupled model (Figure 6.7.12), reducing surface temperatures northwest of Galveston Bay.

Spurious clouds, depending on their thickness and extent, will likely affect PBL structure by reducing sensible heat fluxes below the cloud. This is shown in Section 8 (Figure 6.8.34), where spurious clouds may suddenly reduce PBL height. Since clouds are grid-scale in the 4-km simulations, this can leave a cloud suddenly "trapped" above the top of the PBL, with no access to the vertical mixing that induces evaporative turnover in natural fair weather clouds. Thus, these spurious clouds may just "sit there" and grow in the model. Since the coupled model's surface fluxes are not influenced by model cloud formation of any type, natural evaporative turnover at the top of the PBL is much more likely to suppress spurious cloud growth and keep the PBL elevated as it should be on fair weather cloudy days.

August 29 (Figures 6.7.13 through 6.7.17) begins clear in models and observations. By 2000 UTC, a thick convective cell has formed in the uncoupled model, too close to Houston, and by 2200 UTC, it has expanded southwestward, in disagreement with satellite imagery. Note that the figures presented depict case "van," which was negatively affected by the KF-boundary problem about this time. Despite this, the cloud pattern in the coupled model is far better throughout August 29, which featured the highest hourly ozone concentration of the episode.

On August 30 (Figures 6.7.18 through 6.7.21) by 2000 UTC, both coupled and uncoupled models' RSD patterns were similar: the interior greens in the figures suggest approach of the subtropical moisture from the southwest and the patchy light blues indicate convective formation in good agreement with satellite imagery. At 2300 UTC, as the subtropical moisture arrived from the south, convection flanked the northern Houston suburbs. For case "van", this convection is better represented in the uncoupled model. By contrast, the coupled model produced too little of the northern flanking convective cloud. Compared with case "kf5.2w.c2" in Figure 6.7.21, the coupled model produced some, but not a lot, more convective cloud than in case "van." Interestingly, the accompanying temperature plots reveal a second possible boundary condition problem, not before noticed, with the "van" case that is not seen in case "kf5.2w.c2."

In summary, comparison of cloud development and evolution suggests that, with the exception of August 30, the coupled model is superior in its ability to develop and properly locate grid-scale clouds for this exceedance episode than the uncoupled model. This is likely a result of superior solar and precipitation inputs in the coupled model, resulting in superior flux outputs. Since the cloud-flux feedback is turned off in the coupled model, it appears to be much more difficult to form and maintain spurious clouds than in the uncoupled model. This could have a significant impact on the model's potential for improving photochemical simulations.

6.7.2 Figures for Section 6.7

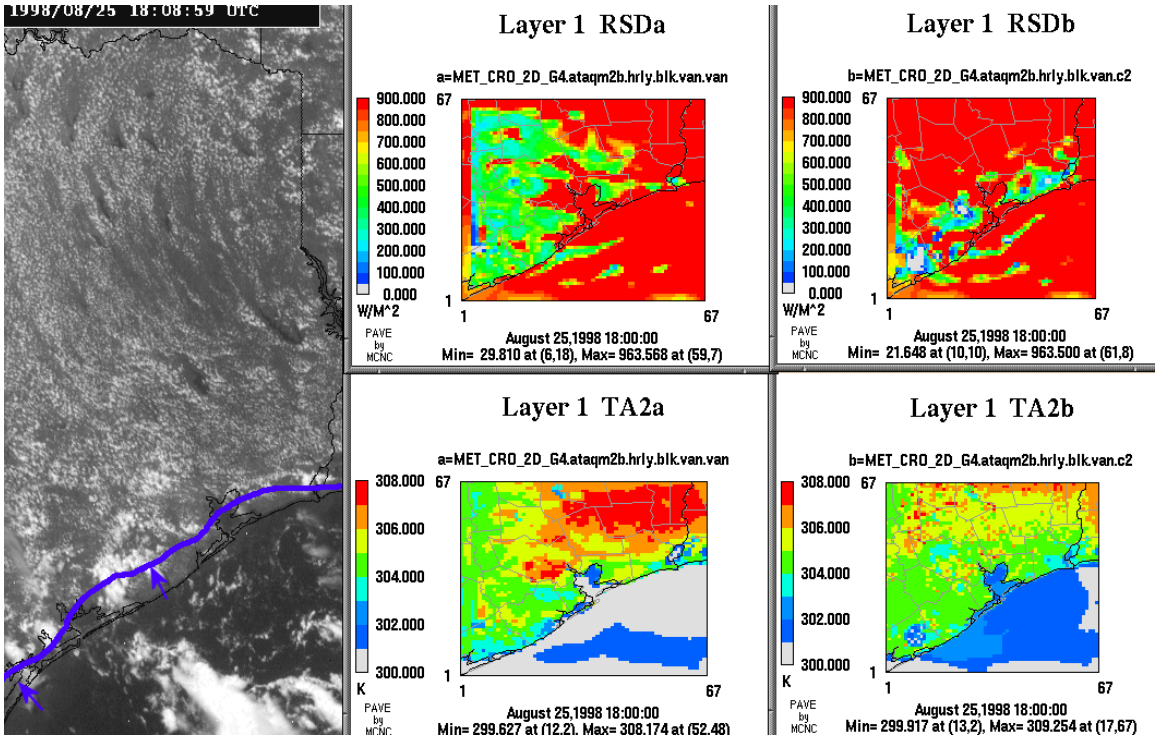

Figure 6.7.1. GOES satellite image (left) contrasted with MM5-calculated downward shortwave solar radiation (RSD, top panels) and 2-m temperature (bottom panels) at 1800 UTC on August 25. Case "van" is shown as representative of all three sensitivity runs, with the uncoupled run on the left and the coupled run on the right. Areas of reduction in RSD (top, green) represent the position of MM5 grid-scale clouds. These areas are often correlated with reductions in modeled surface temperature, clearly seen in green (western sections of uncoupled run) and in light blue (coupled run). Note that the coupled run depicts both the amount and location of clouds better than the uncoupled run. Note the absence of a daytime Houston heat island in the coupled run.

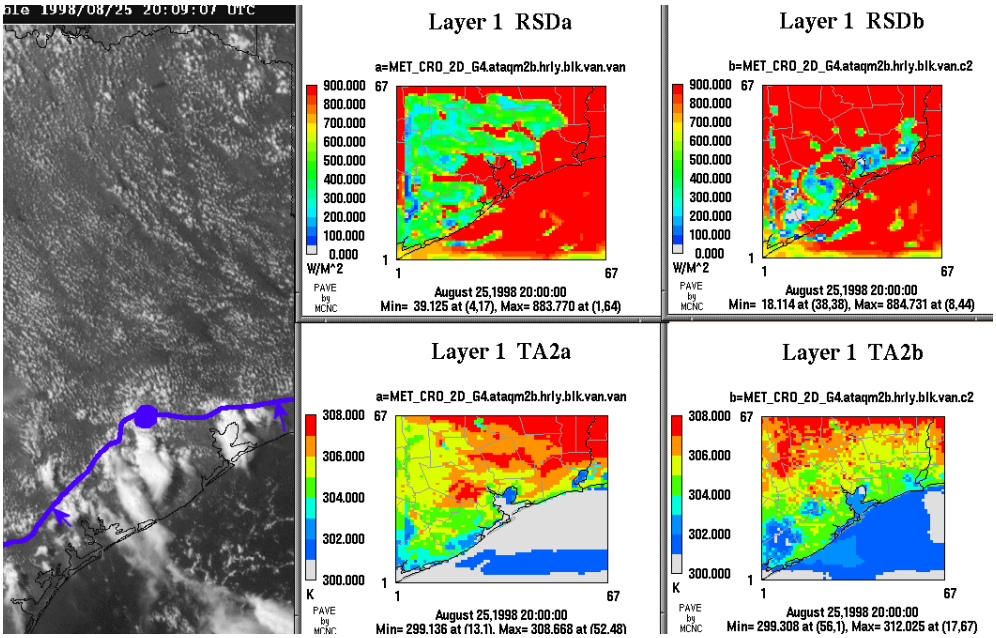

Figure 6.7.2. GOES satellite image (left) contrasted with MM5-calculated downward shortwave solar radiation (RSD, top panels) and 2-m temperature (bottom panels) at 2000 UTC on August 25. Case "van" is shown as representative of all three sensitivity runs, with the uncoupled run on the left and the coupled run on the right. The convective cells over Galveston Bay and to the south are well represented in the coupled run, whereas the cloud patterns in the uncoupled run do not resemble the satellite imagery.

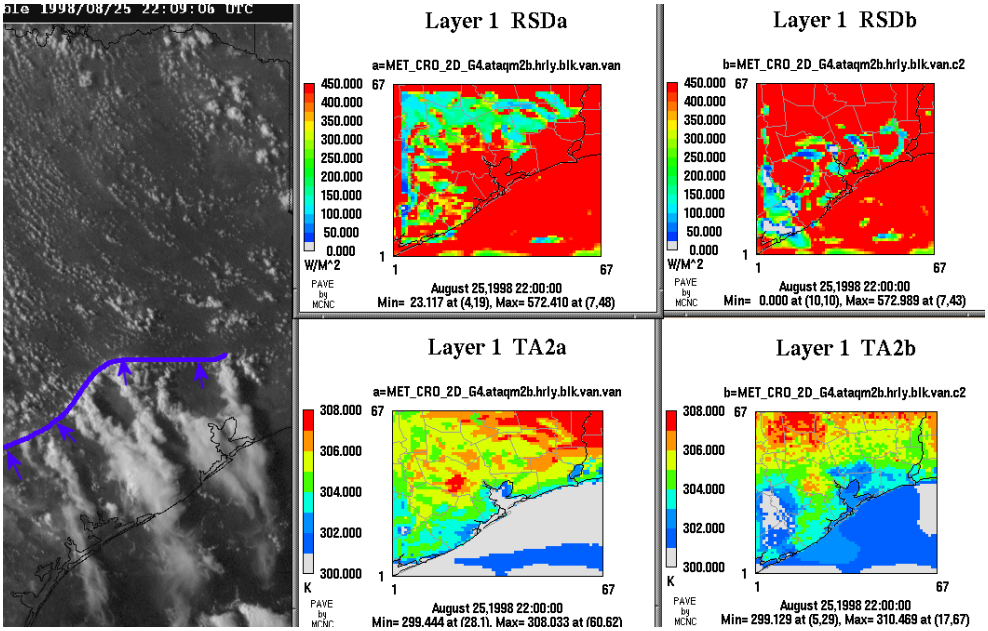

Figure 6.7.3. GOES satellite image (left) contrasted with MM5-calculated downward shortwave solar radiation (RSD, top panels) and 2-m temperature (bottom panels) at 2200 UTC on August 25. Case "van" is shown as representative of all three sensitivity runs, with the uncoupled run on the left and the coupled run on the right. The convective cells have moved inland on the leading edge of the sea breeze. By contrast, the clouds in the models have not moved much, in agreement with the left-biased mean vectors noted in Figure 6.6.2. Cloud amount is still overestimated in the uncoupled run (left), well-correlated with its areas of temperature reduction.

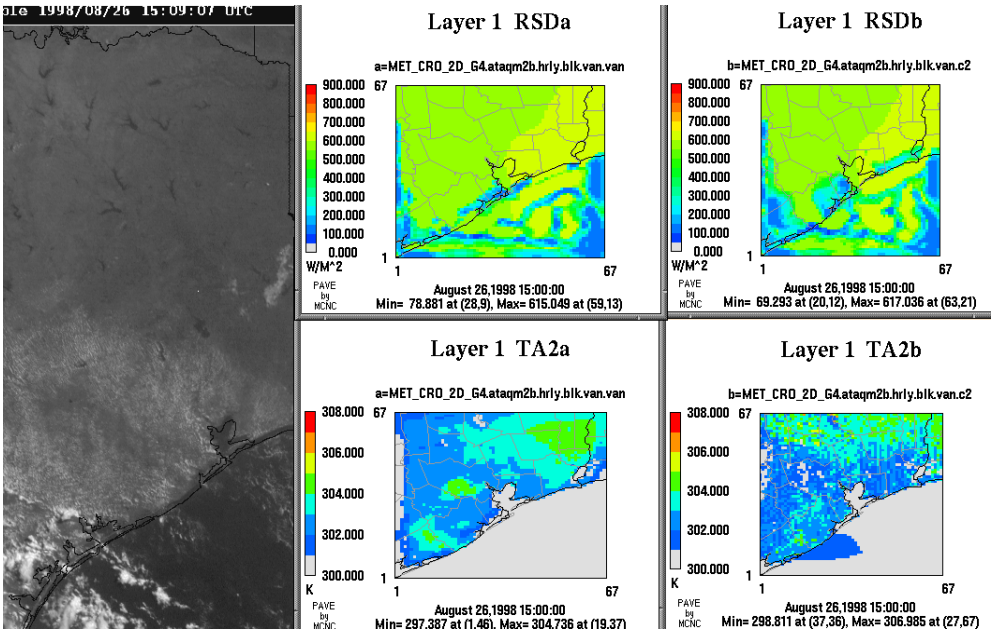

Figure 6.7.4. GOES satellite image (left) contrasted with MM5-calculated downward shortwave solar radiation (RSD, top panels) and 2-m temperature (bottom panels) at 1500 UTC on August 26. Case "van" is shown as representative of all three sensitivity runs, with the uncoupled run on the left and the coupled run on the right. A thin area of small shallow cumulus can be seen on the GOES image appearing like a milky sheath over much of the modeling domain. Lake Conroe and other inland bodies of water are void of these clouds. Additional thin cloud is present over the near-shore Gulf. Both models pick up on the Gulf cloudiness, but overdo it. More surface temperature detail is evident in the coupled model than in the uncoupled model.

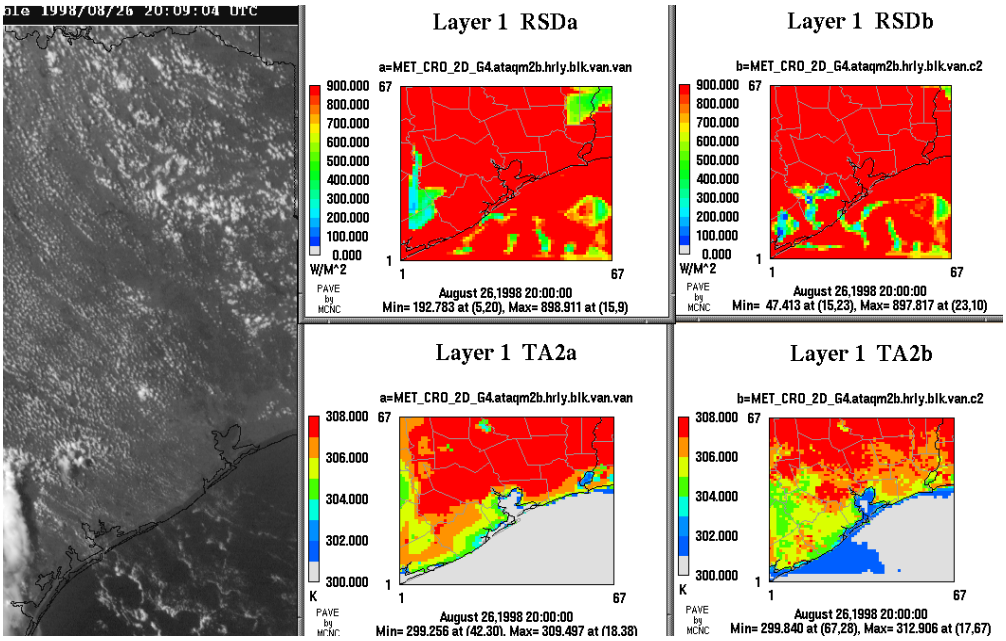

Figure 6.7.5. GOES satellite image (left) contrasted with MM5-calculated downward shortwave solar radiation (RSD, top panels) and 2-m temperature (bottom panels) at 2000 UTC on August 26. Case "van" is shown as representative of all three sensitivity runs, with the uncoupled run on the left and the coupled run on the right. The northern extent of the sea breeze depicted in Figure 6.6.4 has swept through Houston, bringing clear skies. Both models are similar in their cloud coverage amounts, which are essentially all spurious.

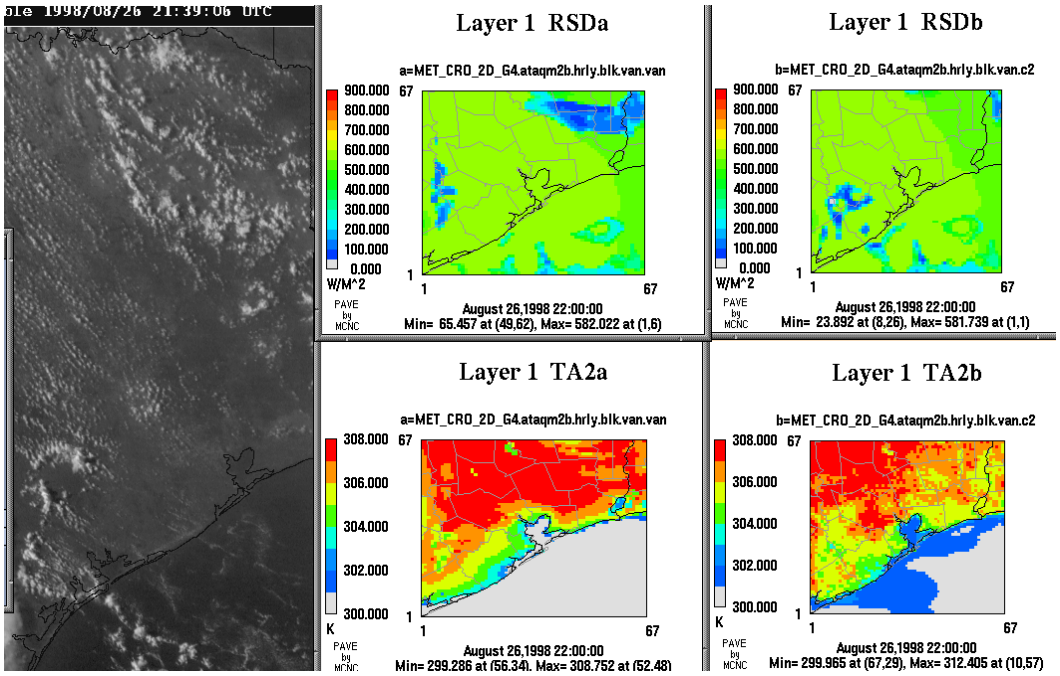

Figure 6.7.6. GOES satellite image (left) contrasted with MM5-calculated downward shortwave solar radiation (RSD, top panels) and 2-m temperature (bottom panels) at 2200 UTC on August 26. Case "van" is shown as representative of all three sensitivity runs, with the uncoupled run on the left and the coupled run on the right. By this time, a large spurious cloud has formed in the northeastern quadrant in the uncoupled model. The effects of the sea-breeze front on near-shore 2-m temperatures are clear in both models, with a more uniform, classic pattern showing up in the uncoupled model. Not enough data were available to validate these patterns.

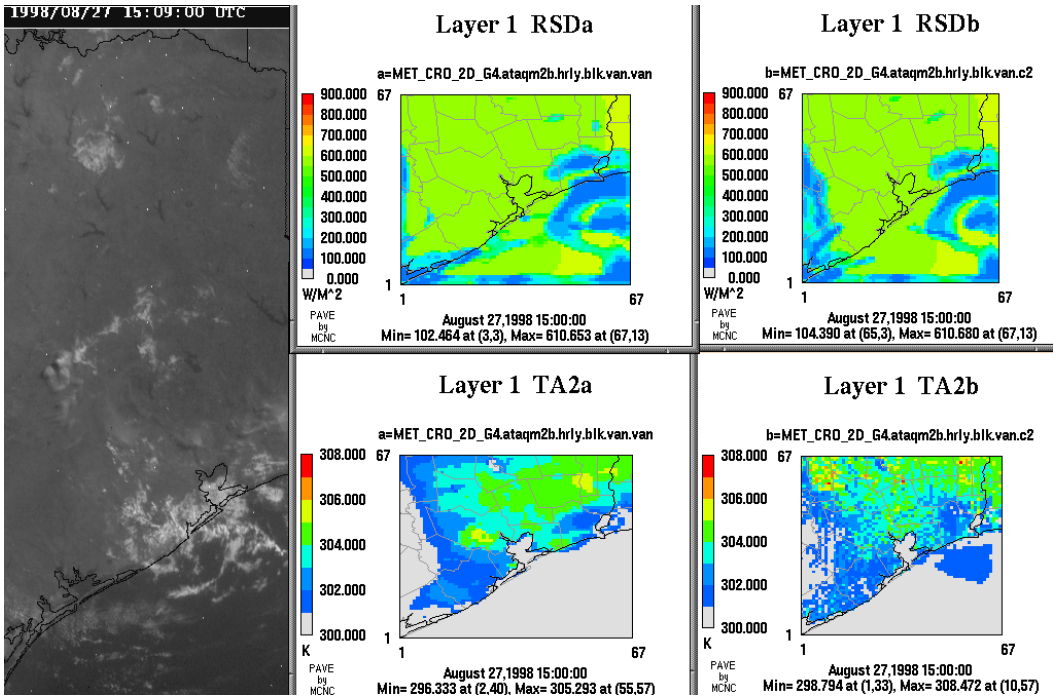

Figure 6.7.7. GOES satellite image (left) contrasted with MM5-calculated downward shortwave solar radiation (RSD, top panels) and 2-m temperature (bottom panels) at 1500 UTC on August 27. Case "van" is shown as representative of all three sensitivity runs, with the uncoupled run on the left and the coupled run on the right. The remnant cloud over Houston is circulating anticyclonically under the influence of a meso-High. Cloud patterns in both models suggest displacement of the High too far southeast at 1500 UTC.

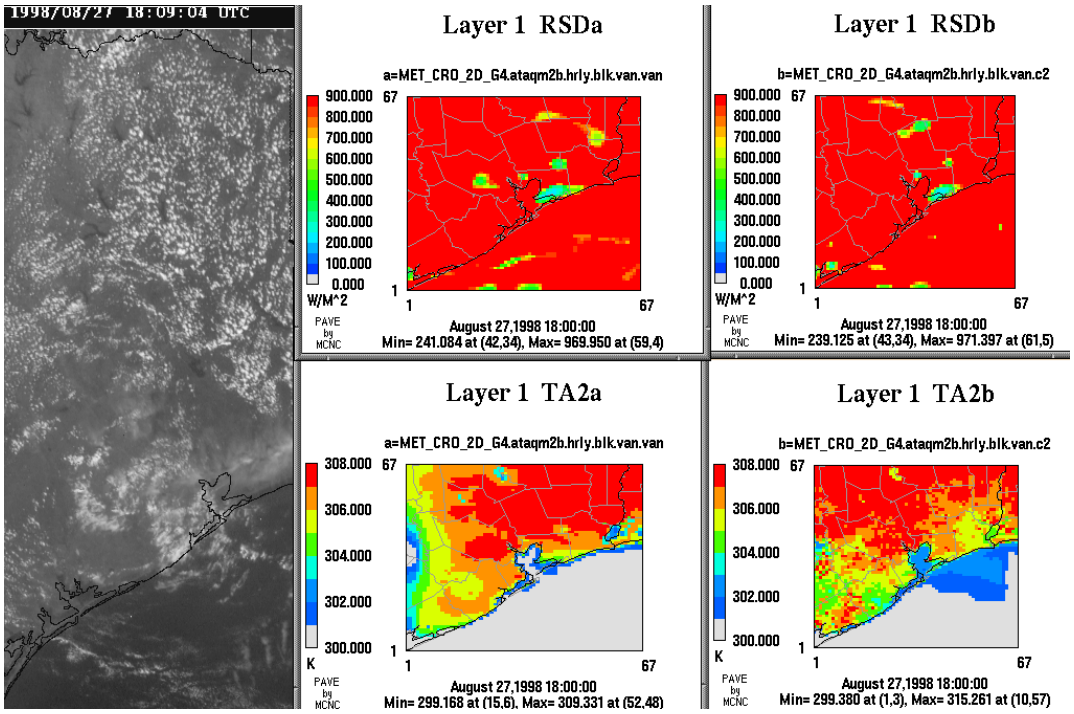

Figure 6.7.8. GOES satellite image (left) contrasted with MM5-calculated downward shortwave solar radiation (RSD, top panels) and 2-m temperature (bottom panels) at 1800 UTC on August 27. Case "van" is shown as representative of all three sensitivity runs, with the uncoupled run on the left and the coupled run on the right. Anti-cyclonic flow is still evident over Houston. Cloud patterns are consistent with observations in both models.

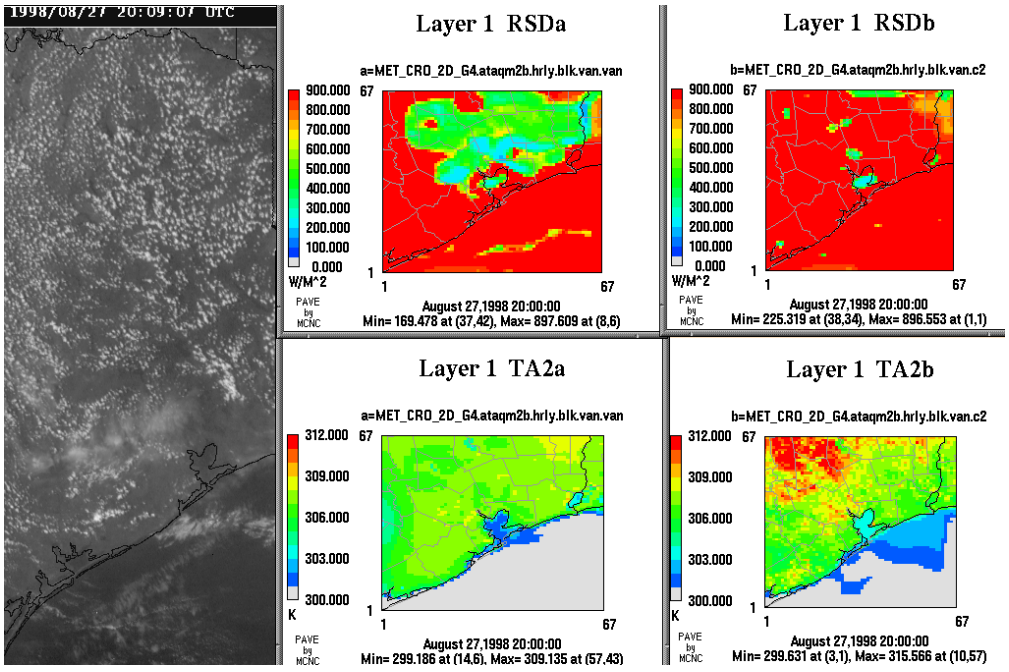

Figure 6.7.9. GOES satellite image (left) contrasted with MM5-calculated downward shortwave solar radiation (RSD, top panels) and 2-m temperature (bottom panels) at 2000 UTC on August 27. Case "van" is shown as representative of all three sensitivity runs, with the uncoupled run on the left and the coupled run on the right. The uncoupled model has formed a large spurious cloud, causing widespread temperature reductions.

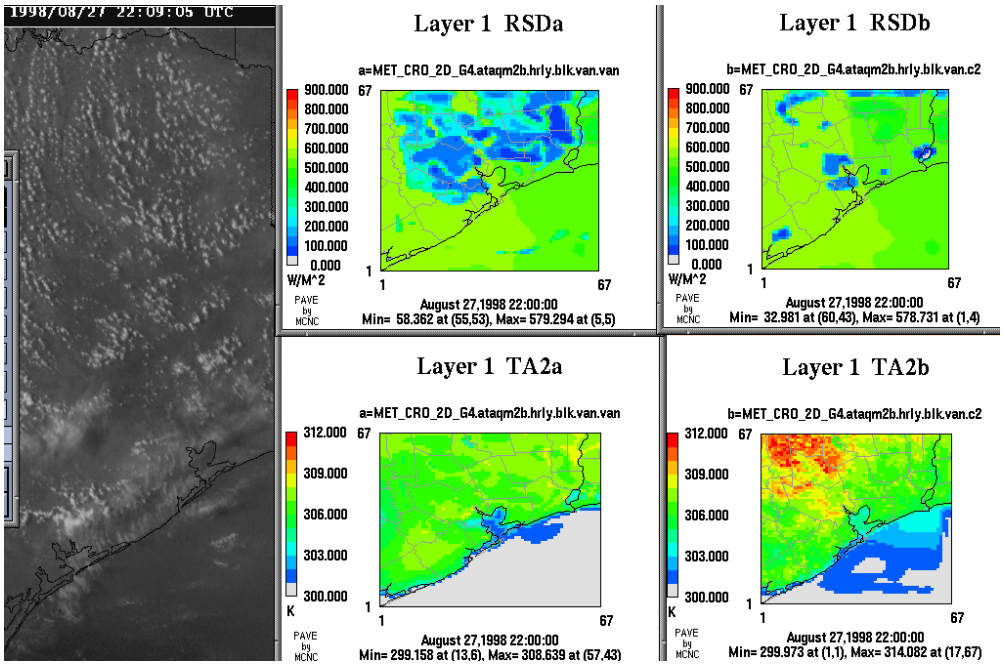

Figure 6.7.10. GOES satellite image (left) contrasted with MM5-calculated downward shortwave solar radiation (RSD, top panels) and 2-m temperature (bottom panels) at 2200 UTC on August 27. Case "van" is shown as representative of all three sensitivity runs, with the uncoupled run on the left and the coupled run on the right. The spurious cloud in the uncoupled model has expanded further. The widely scattered clouds in the coupled model are consistent with satellite imagery.

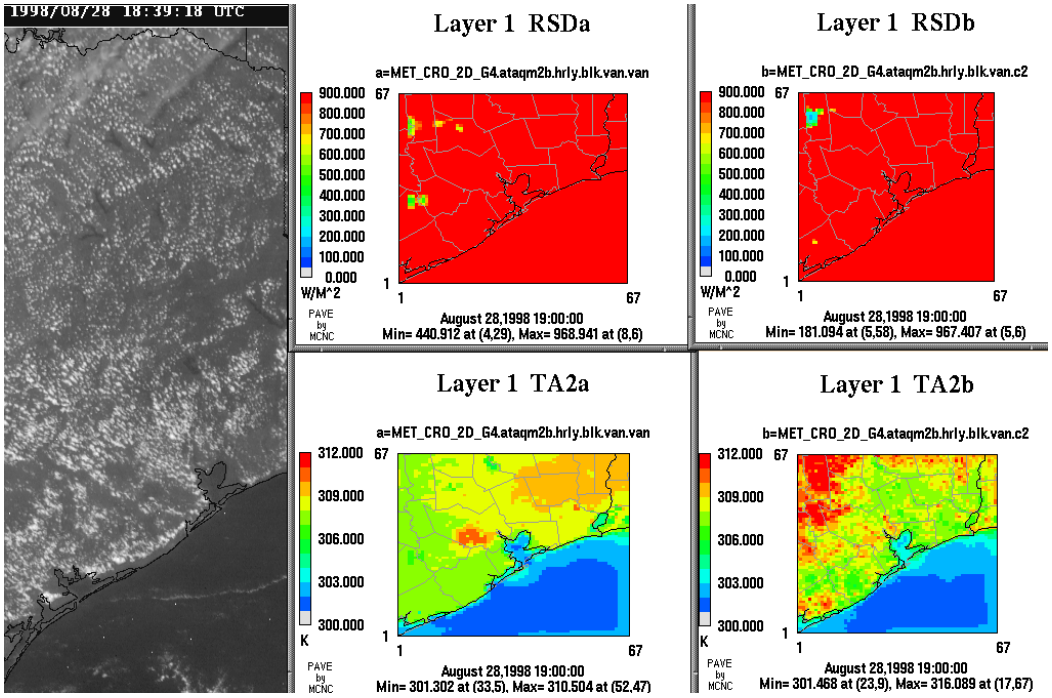

Figure 6.7.11. GOES satellite image (left) contrasted with MM5-calculated downward shortwave solar radiation (RSD, top panels) and 2-m temperature (bottom panels) at 1900 UTC on August 28. Case "van" is shown as representative of all three sensitivity runs, with the uncoupled run on the left and the coupled run on the right. Neither model predicts the shallow cloud fields with cyclonic curvature ahead of the weak trough.

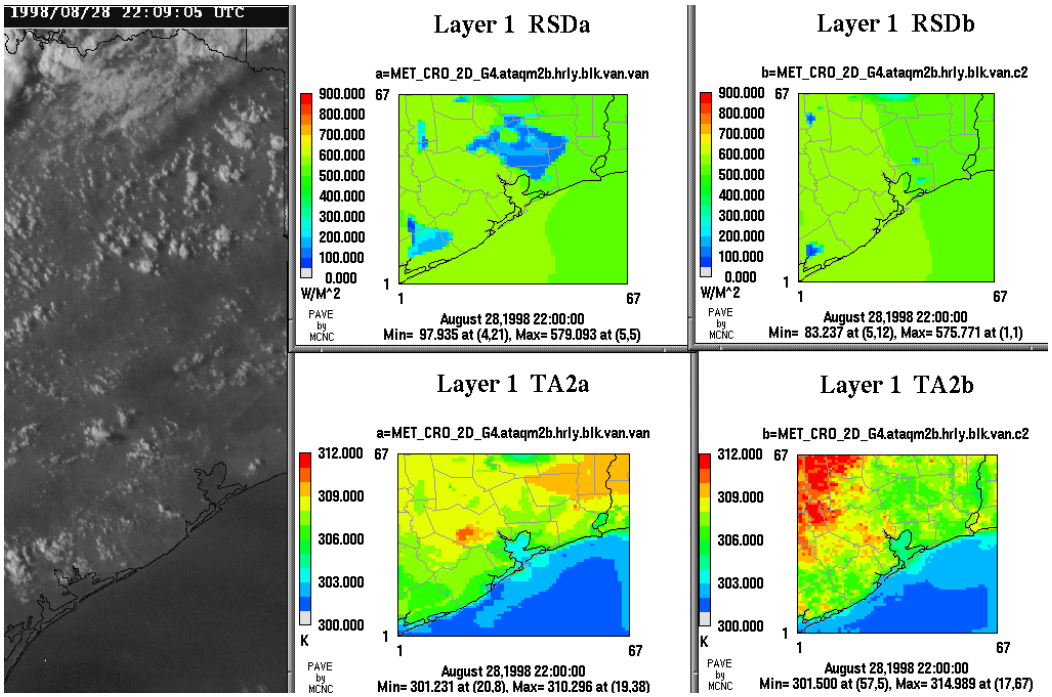

Figure 6.7.12. GOES satellite image (left) contrasted with MM5-calculated downward shortwave solar radiation (RSD, top panels) and 2-m temperature (bottom panels) at 2200 UTC on August 28. Case "van" is shown as representative of all three sensitivity runs, with the uncoupled run on the left and the coupled run on the right. A large spurious cloud has formed in the uncoupled model, reducing surface temperatures northwest of Galveston Bay. Note that the orange-yellow temperature line (bottom left panel) running northwest-southeast toward BPA is precisely correlated with the northeastern flank of the spurious cloud.

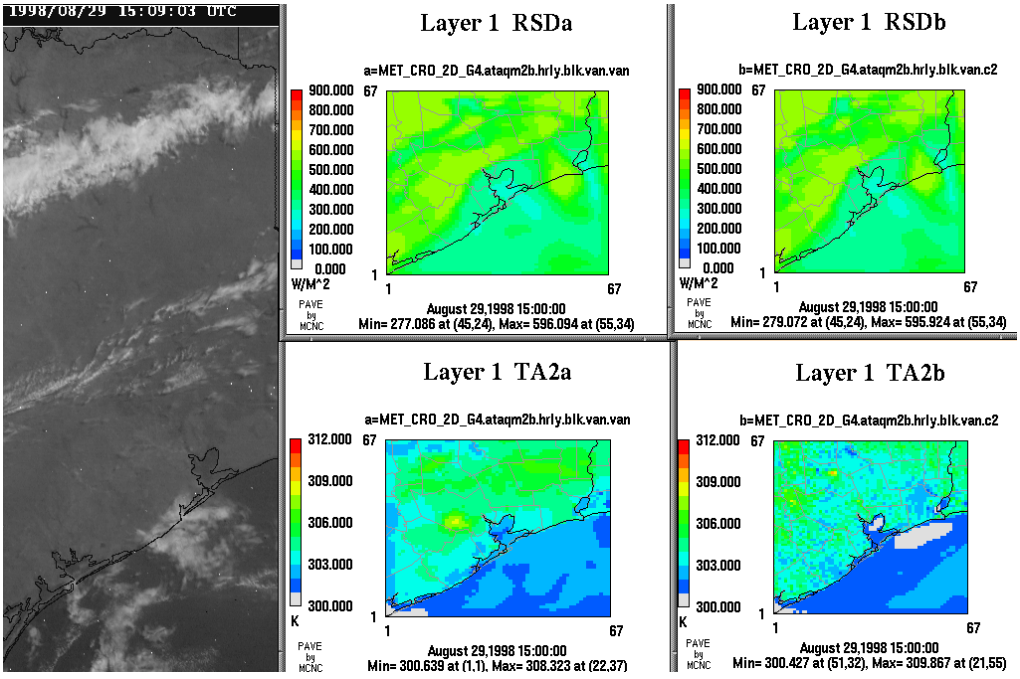

Figure 6.7.13. GOES satellite image (left) contrasted with MM5-calculated downward shortwave solar radiation (RSD, top panels) and 2-m temperature (bottom panels) at 1500 UTC on August 29. Case "van" is shown as representative of all three sensitivity runs, with the uncoupled run on the left and the coupled run on the right. Neither model reveals any clouds of significance, in accordance with the GOES imagery. The convergence zone that will produce significant convection lies about 120 km north of Houston, extending southwest-northeast.

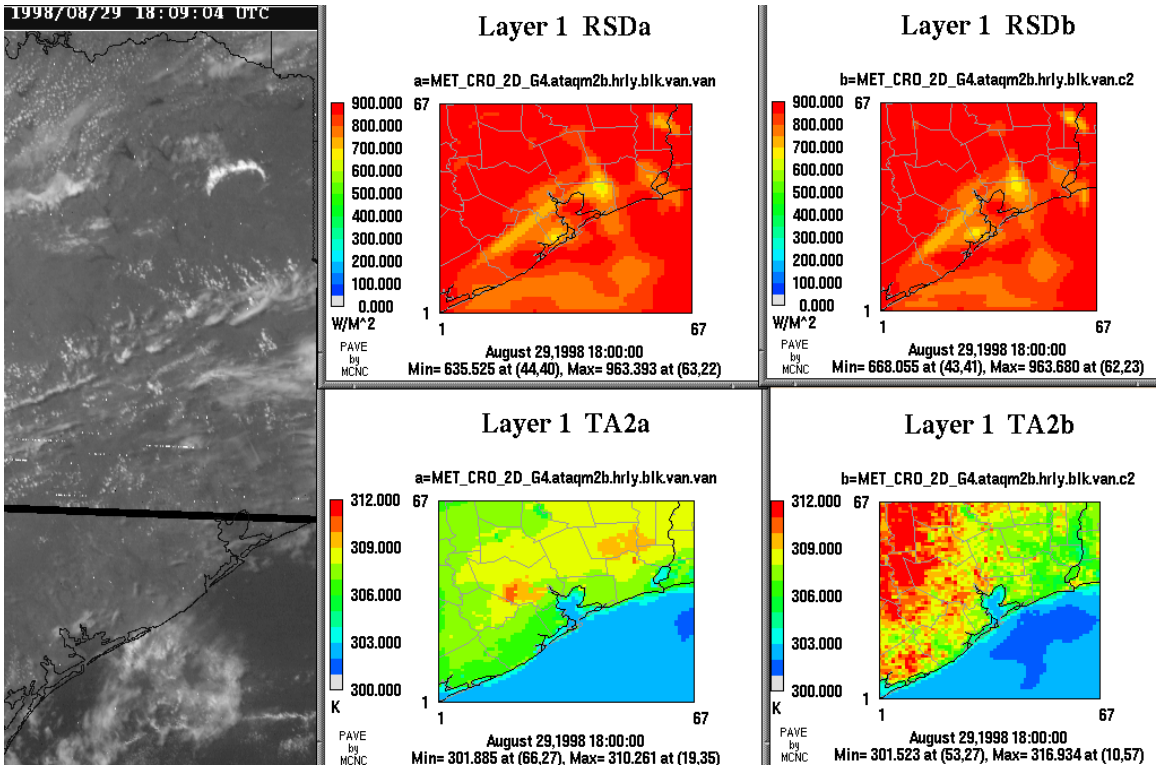

Figure 6.7.14. GOES satellite image (left) contrasted with MM5-calculated downward shortwave solar radiation (RSD, top panels) and 2-m temperature (bottom panels) at 1800 UTC on August 29. Case "van" is shown as representative of all three sensitivity runs, with the uncoupled run on the left and the coupled run on the right. Again, neither model reveals significant clouds.

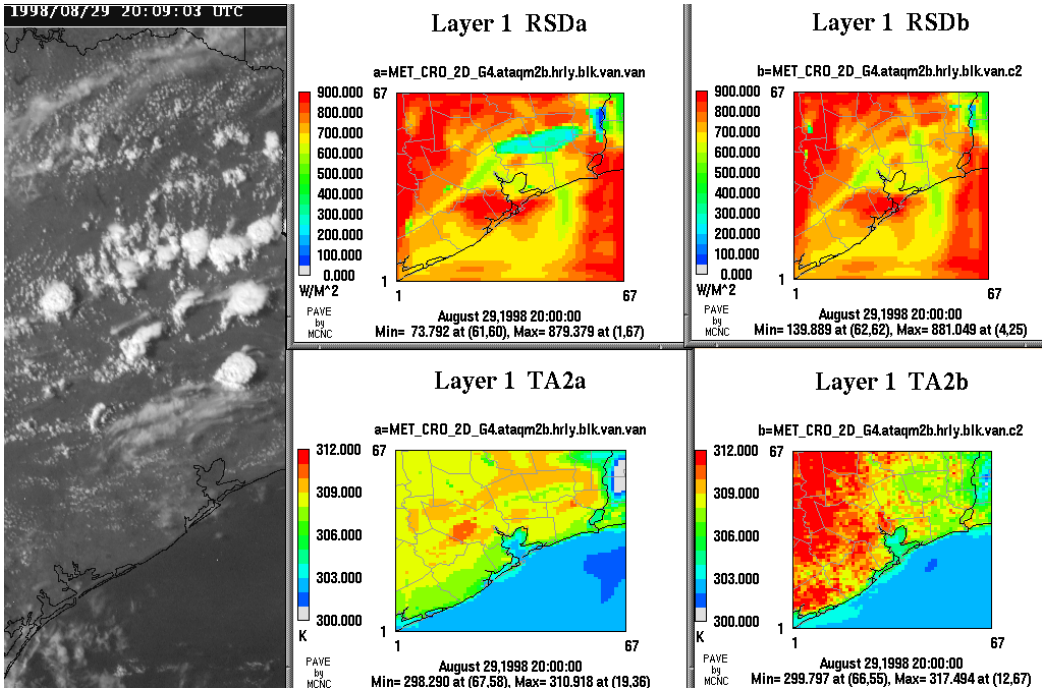

Figure 6.7.15. GOES satellite image (left) contrasted with MM5-calculated downward shortwave solar radiation (RSD, top panels) and 2-m temperature (bottom panels) at 2000 UTC on August 29. Case "van" is shown as representative of all three sensitivity runs, with the uncoupled run on the left and the coupled run on the right. A thick convective cell forms in the uncoupled model, too close to Houston.

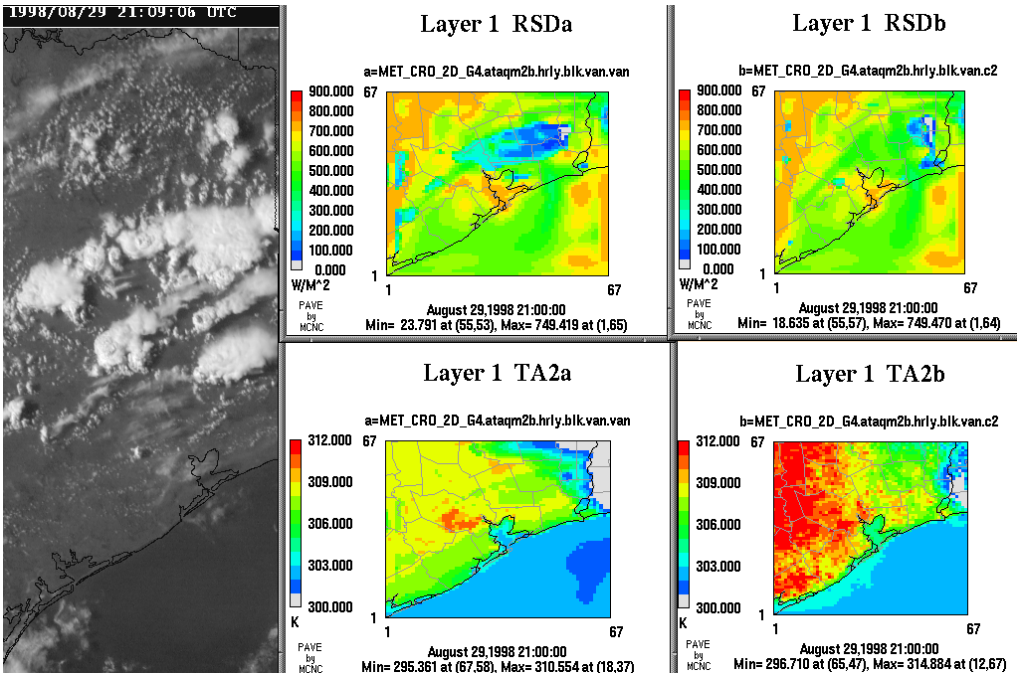

Figure 6.7.16. GOES satellite image (left) contrasted with MM5-calculated downward shortwave solar radiation (RSD, top panels) and 2-m temperature (bottom panels) at 2100 UTC on August 29. Case "van" is shown as representative of all three sensitivity runs, with the uncoupled run on the left and the coupled run on the right. The uncoupled model cell which formed at 2000 UTC is now expanding toward the south and west. A smaller cell is also forming in the coupled model.

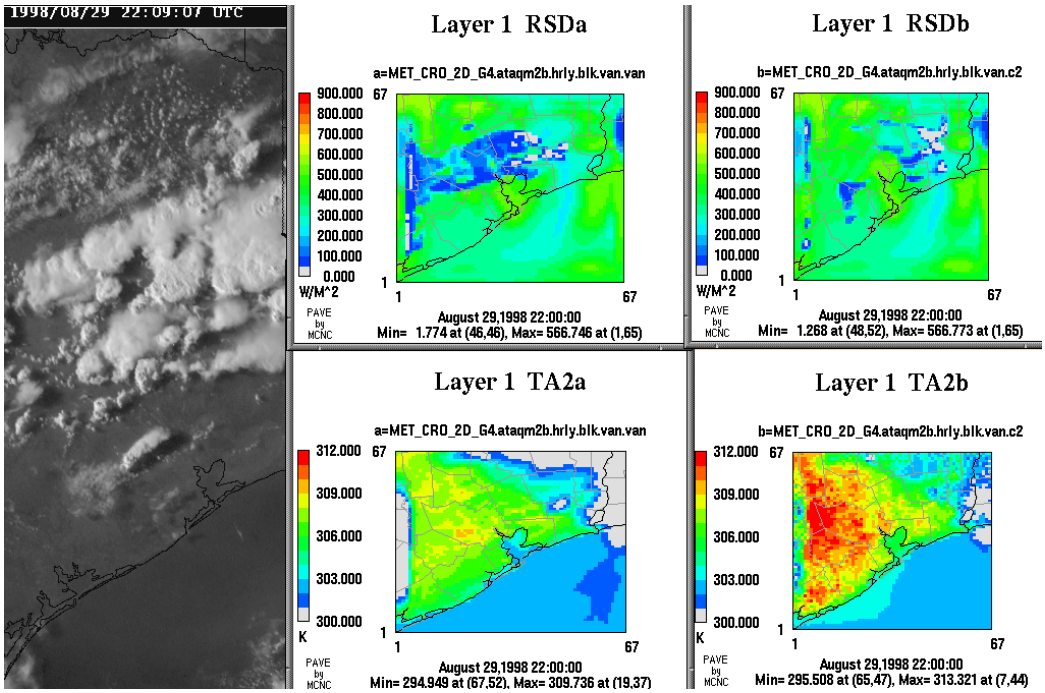

Figure 6.7.17. GOES satellite image (left) contrasted with MM5-calculated downward shortwave solar radiation (RSD, top panels) and 2-m temperature (bottom panels) at 2200 UTC on August 29. Case "van" is shown as representative of all three sensitivity runs, with the uncoupled run on the left and the coupled run on the right. The uncoupled model cell has expanded southwestward, covering much of metropolitan Houston, not verified by satellite. The coupled model has formed a small cell just southwest of metropolitan Houston, similar to the satellite imagery (which shows this cell more to the west). Cloud cover amount, placement, and expansion are erroneous in the uncoupled model.

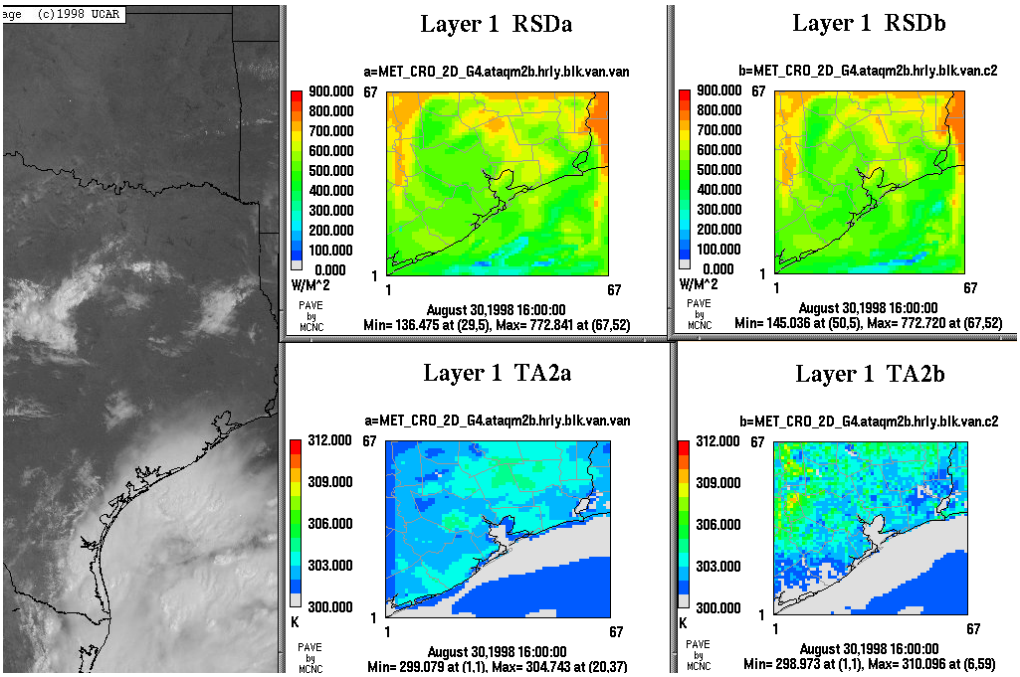

Figure 6.7.18. GOES satellite image (left) contrasted with MM5-calculated downward shortwave solar radiation (RSD, top panels) and 2-m temperature (bottom panels) at 1600 UTC on August 30. Case "van" is shown as representative of all three sensitivity runs, with the uncoupled run on the left and the coupled run on the right. The GOES imagery reveals the approach of subtropical moisture from the southwest. The models' RSD patterns are similar.

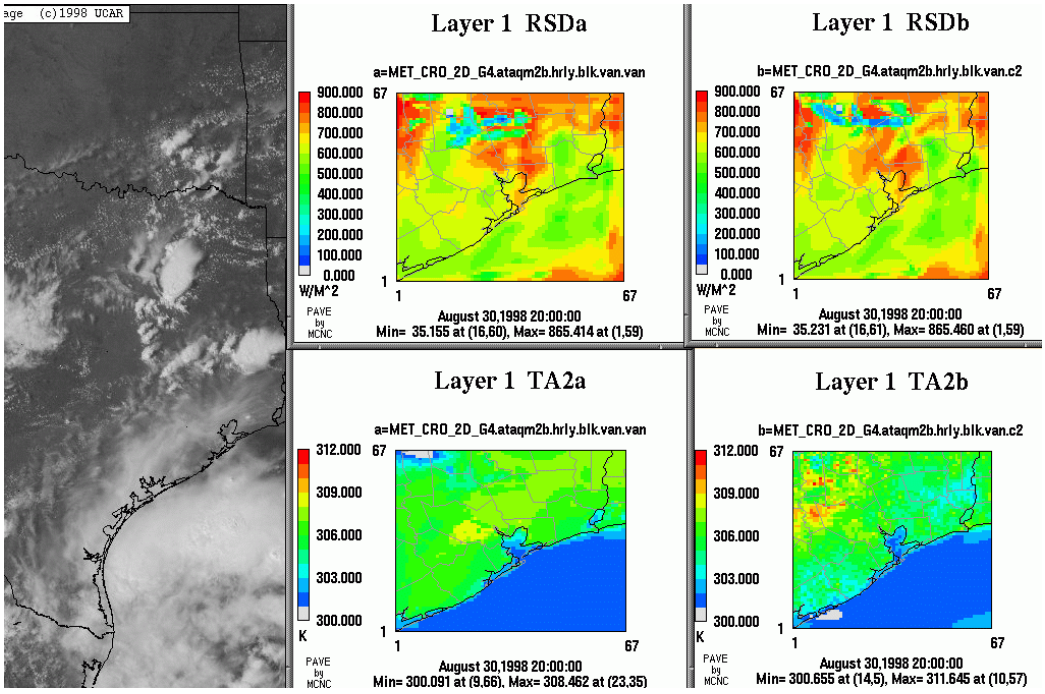

Figure 6.7.19. GOES satellite image (left) contrasted with MM5-calculated downward shortwave solar radiation (RSD, top panels) and 2-m temperature (bottom panels) at 2000 UTC on August 30. Case "van" is shown as representative of all three sensitivity runs, with the uncoupled run on the left and the coupled run on the right. The GOES imagery reveals the approach of subtropical moisture from the southwest. The models' RSD patterns remain similar: the interior greens suggest the approach of the subtropical moisture, and the light blues indicate convection forming in good agreement with the satellite imagery.

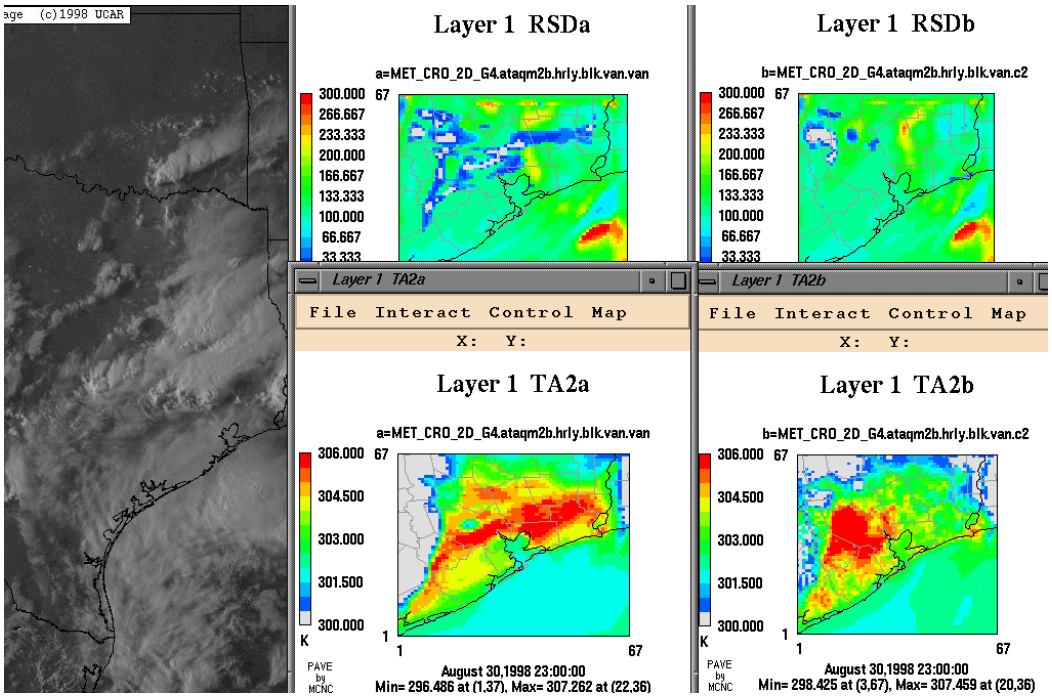

Figure 6.7.20. GOES satellite image (left) contrasted with MM5-calculated downward shortwave solar radiation (RSD, top panels) and 2-m temperature (bottom panels) at 2300 UTC on August 30. Case "van" is shown as representative of all three sensitivity runs, with the uncoupled run on the left and the coupled run on the right. As the subtropical moisture arrives from the south, the convection flanks the northern Houston suburbs. The convection is better represented in the uncoupled model, with cloud extent and location matching the satellite imagery fairly well.

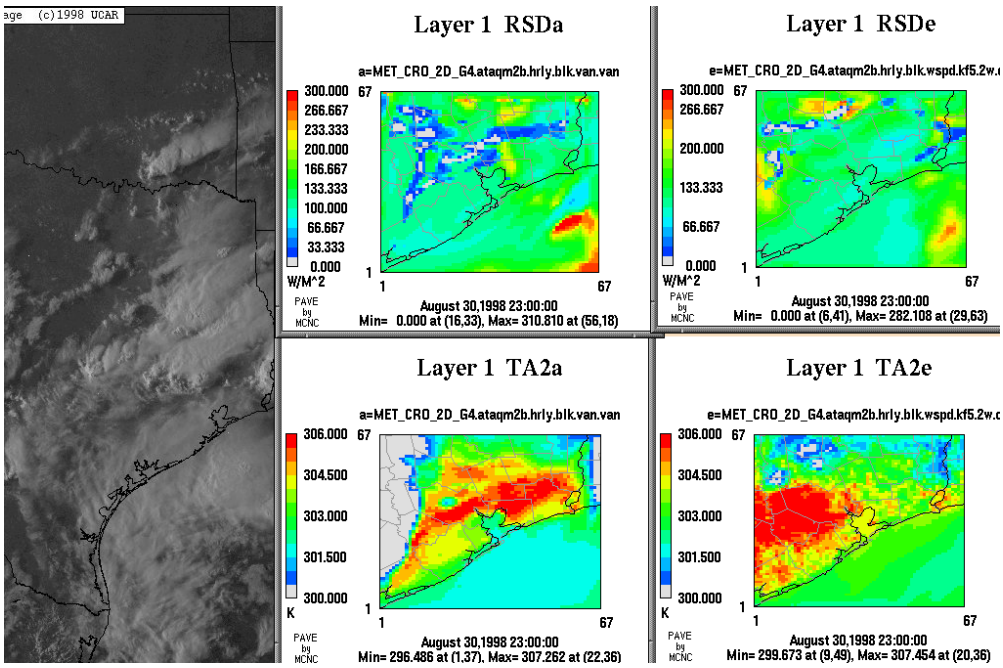

Figure 6.7.21. GOES satellite image (left) contrasted with MM5-calculated downward shortwave solar radiation (RSD, top panels) and 2-m temperature (bottom panels) at 2300 UTC on August 30. The case "van" uncoupled runs are shown on the left and case "kf5.2w.c2" coupled runs are shown on the right. The coupled model for case "kf5.2w.c2" produces more convective clouds than it does for case "van," however, their extent is still too small.

6.8 Boundary-Layer Depth and Evolution Comparison

6.8.1 Discussion

Because the evolution of the PBL plays such an important role in photochemical modeling, Figures 6.8.1 through 6.8.65 are provided as an "evolutionary record" of the uncoupled and coupled model runs' PBL performance. The figures are in 3-hourly or 6-hourly sequence, and include three-panel comparisons of PBL heights, comparisons of skin-temperature—a critical driving parameter related to PBL heights—and close-up panels comparing PBL heights and winds overlaid in the vicinity of Galveston Bay.

The available Radar Wind Profiler (RWP) data did not contain enough information to determine PBL depth. Therefore, no comparison of RWP wind and modeled PBL heights were made. Further, 00z and 12z standard upper-air observations (RAOBS) are generally not useful because the observation times occur during morning and evening transition. Hence, this section addresses specific qualitative model features that are pertinent to photochemical modeling. This section focuses specifically on (1) land-sea PBL contrasts, (2) the Houston heat-island effect, (3) episodic (day-to-day) PBL differences, (4) intra-day PBL differences, (5) nocturnal surface inversions, and (6) Bay-scale wind effects related to PBL evolution.

1. Land-Sea Contrasts

Figures 6.8.3, 6.8.5, 6.8.12, 6.8.19, 6.8.23, and others document model differences in land-sea contrasts. Of particular note are two factors. (1) The uncoupled model contains a strangely homogeneous skin temperature across the land-Gulf boundary at night. A good example is shown in Figure 6.8.26. Because of the documented warm bias at night in the uncoupled model it seems unlikely that this process is accurately represented in the uncoupled model. More feasible is the coupled model's behavior, shown in Figure 6.8.26, where the land temperature has cooled and the winds have a more offshore component over land. (2) The uncoupled model contains a slice of "cold" Gulf water along-shore (Figure 6.8.23). Both of these effects (lack of land-breeze forcing at night; stronger forcing during the day) contribute to the "better actual" sea-breeze performance in the uncoupled model. This suggests that the uncoupled model outperforms the coupled model through a confluence of two errors rather than better surface physics.

2. Houston Heat-Island Effects

Figures 6.8.3, 6.8.13, 6.8.25, 6.8.40, and others document diurnally-out-of-phase heat island effects between the coupled and uncoupled models. As noted in Section 6.5, the high heat capacity for urban areas is generally what drives urban heat islands—urban areas cool more slowly in the evening and warm more slowly in the morning. Because they absorb and store heat, they can become hotter than surrounding environs by mid-afternoon, and fail to cool off much at night. In the uncoupled model, the heat island produces a PBL "bubble" fairly early in the morning, certainly by 1500 UTC on August 28. (In Figure 6.8.40, the PBL is greater than 1700 m with the uncoupled model

and less than half that with the coupled model.) In the coupled model, the effect is slower to develop, and thus can be seen in the early evening, when the PBL remains elevated due to the lingering heat-source below. This may result in profound local modeled wind differences in and proximate to Houston.

3. Episodic (day-to-day) PBL Differences

Figures 6.8.10, 6.8.20, 6.8.33, 6.8.42, 6.8.52, and 6.8.64 show a daily progression in modeled PBL heights throughout the episode, at 2100 UTC each day. The mean PBL height over land appears to rise in the coupled model from about 1250 m on August 25 to over 2200 m on August 29. This trend is closely correlated with TOPLATS' increasing HFX, as shown in Figure 3.4. By contrast, the mean PBL height is much more constant in the uncoupled model, increasing only slightly day-to-day, averaging between 1900 and 2300 m through the episode. The dynamic range in the coupled model is largely explained by its capturing of the soil dry-down and repartitioning of the sensible and latent heat budgets as the episode progresses.

Day-to-day differences in synoptic-scale subsidence, which helps to entrain free tropospheric air into the top of the growing daytime PBL, may have also played a role in the modeled differences. Given strengthening high pressure essentially through August 29, episodically strengthening subsidence would also be expected. This would lead to a concomitant rise in PBL heights over the course of the episode, and could help explain the uncoupled model's results, especially in light of its static land-surface soil moisture. Hence, the range in day-to-day PBL heights in the coupled model likely occurs because of a combination of its dynamic soil moisture and increasing subsidence effects, with the dynamic soil moisture being the larger of the two forcings.

4. Intra-day PBL Differences

Figure 6.8.42 provides a good example of the spatial variability in PBL heights on a clear (model) afternoon at 2100 UTC. Mean land-based heights well exceed 2000 m in the uncoupled model, but remain somewhat lower over forested areas northwest of Houston in the coupled model. This is consistent with the coupled model's ability to handle differences in evapo-transpiration, and thus flux partitioning, between different land-use types in the domain. Unfortunately, the available RWP data did not contain enough information to diagnose PBL heights, and so could not be used to augment the intra-day PBL difference analysis.

5. Nocturnal Surface Inversions

Figure 6.8.14 shows modeled PBL heights at 0900 UTC on August 26. The cooler land-surface leads to a truer surface inversion than is observed in the uncoupled model. Such a surface inversion would support a stronger low-level jet, hypothesized by Neilson-Gammon, 2001b, to be an important mechanism for lateral nocturnal redistribution of elevated ozone. The surface inversion differences are also shown for 0300 UTC on August 29 in Figure 6.8.45. In the coupled model, the PBL is elevated over

the Bay, and metropolitan Houston, due to the relative Bay warmth and lingering heat island. This leads to a much more complex flow regime in the coupled model.

6. Bay-scale Wind Effects

The combination of spatial differences in urban, rural, Bay, and near-shore Gulf nocturnal cooling leads to much greater flow variability at night in the coupled model. During the day, these spatial differences may also create flow differences between the two models at the Bay scale. To isolate this, consider Figure 6.6.2, which shows that at 2100 UTC on August 25, the coupled and uncoupled models wind patterns were similar and in reasonable agreement with the observations. Figure 6.8.11 shows that despite good regional agreement, the flow patterns through the Bay can be quite different. With fixed-in-time "cold" Bay water, a very depressed, if not collapsed, PBL has formed over the Bay in the coupled model. This results in a wind channeling effect, whereby mass flows as if through a squeezed pipe as it enters the Bay. Winds accelerate and curve through the Bay before exiting. Figures 6.8.21, 6.8.24 (a very good example), 6.8.35, 6.8.44 (large scale view), 6.8.51, 6.8.53, 6.8.55, and 6.8.62 show various effects on the winds caused by a heat-of-the-afternoon collapse of the PBL in the uncoupled model. In the coupled model, the PBL does not collapse during the day, and winds follow a more straight-line pattern consistent with the regional-scale wind.

Because SSATS uses time-varying, observed (warmer) Bay temperatures, it does not induce MM5 to collapse the PBL during the daytime over the Bay. Further, the spatial variability in heat fluxes in the Bay area induces more complex nocturnal flows when different proximate land-use types interact with the Bay. These features of the coupled model system are believed to be more realistic, but high resolution data are needed in order to validate this.

Unfortunately, no three- or four-dimensional Bay-scale wind measurement data were available for this project. The only surface sites were Ellington Field and Galveston and the only profiler site was Ellington Field. Assuming that the hypothesis about the counterclockwise wind bias, discussed in Section 6.1.1, is correct, actual improvement of modeled flows will depend on elimination of biases and physical deficiencies at the synoptic scale. Since Bay-scale flows can be considered non-linear modifications to the more general forcing that creates the land-sea breeze, improvements in Bay-scale fluxes could actually degrade the overall statistical wind performance. Thus, it is essential that follow-on projects conduct the surface-stress sensitivity studies suggested in order to isolate and correct possible large-scale deficiencies. This would allow a more complete understanding of the complex interrelationships that occur at multiple scales. Application to a case in which high resolution four-dimensional wind data are available would result in the capacity for more quantitative conclusions as well.

6.8.2 Figures for Section 6.8

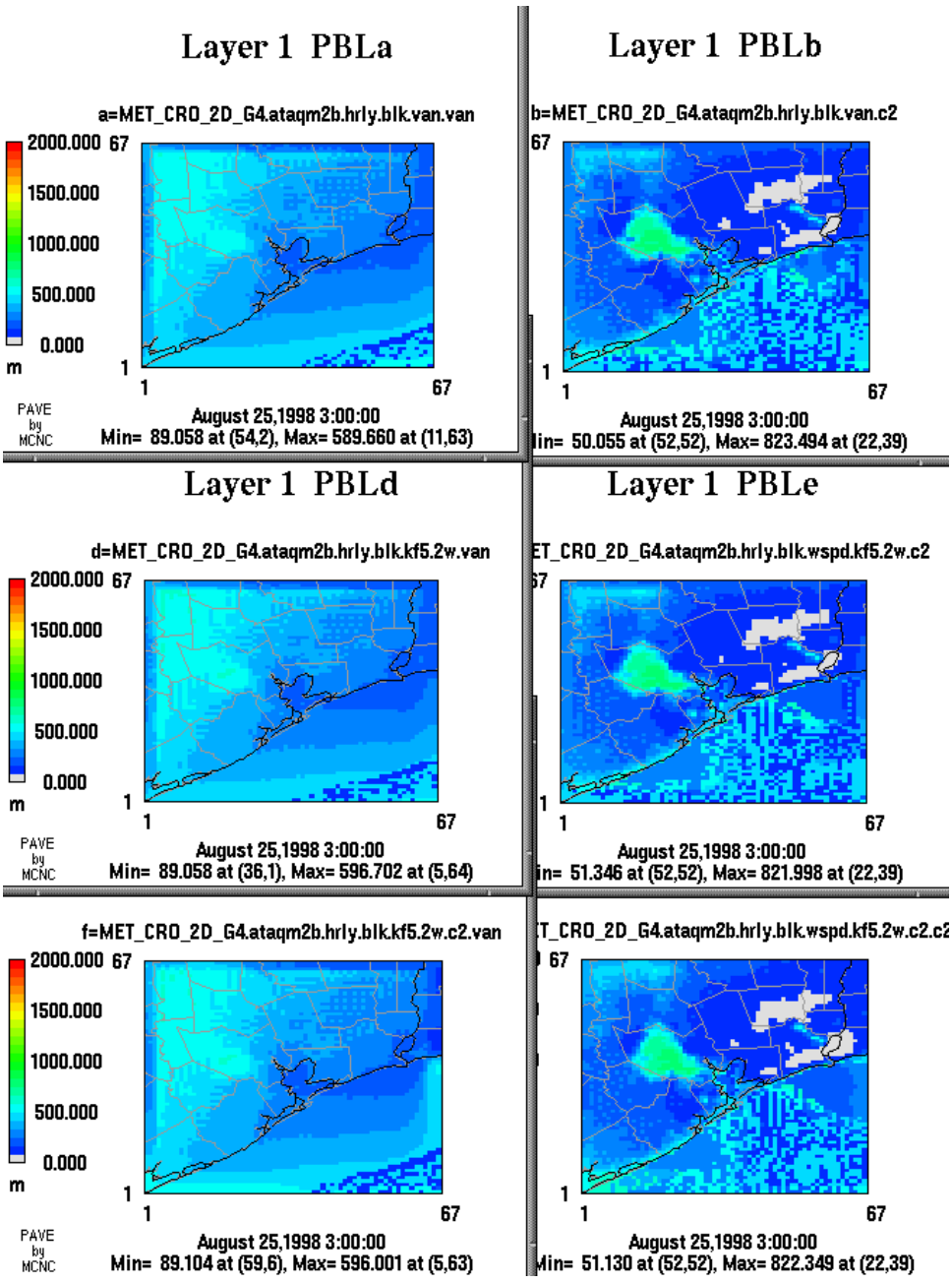

Figure 6.8.1. Modeled boundary layer heights at 0300 UTC on August 25. The uncoupled model is on the left and the coupled model is on the right. The top two panels are case "van", the middle panels are case "kf5.2w", and the bottom panels are case "kf5.2w.c2". A nocturnal Houston heat-island effect is evident in the coupled model runs, with nocturnal PBL instability trailing in plume-like fashion to the southeast (all right-hand panels).

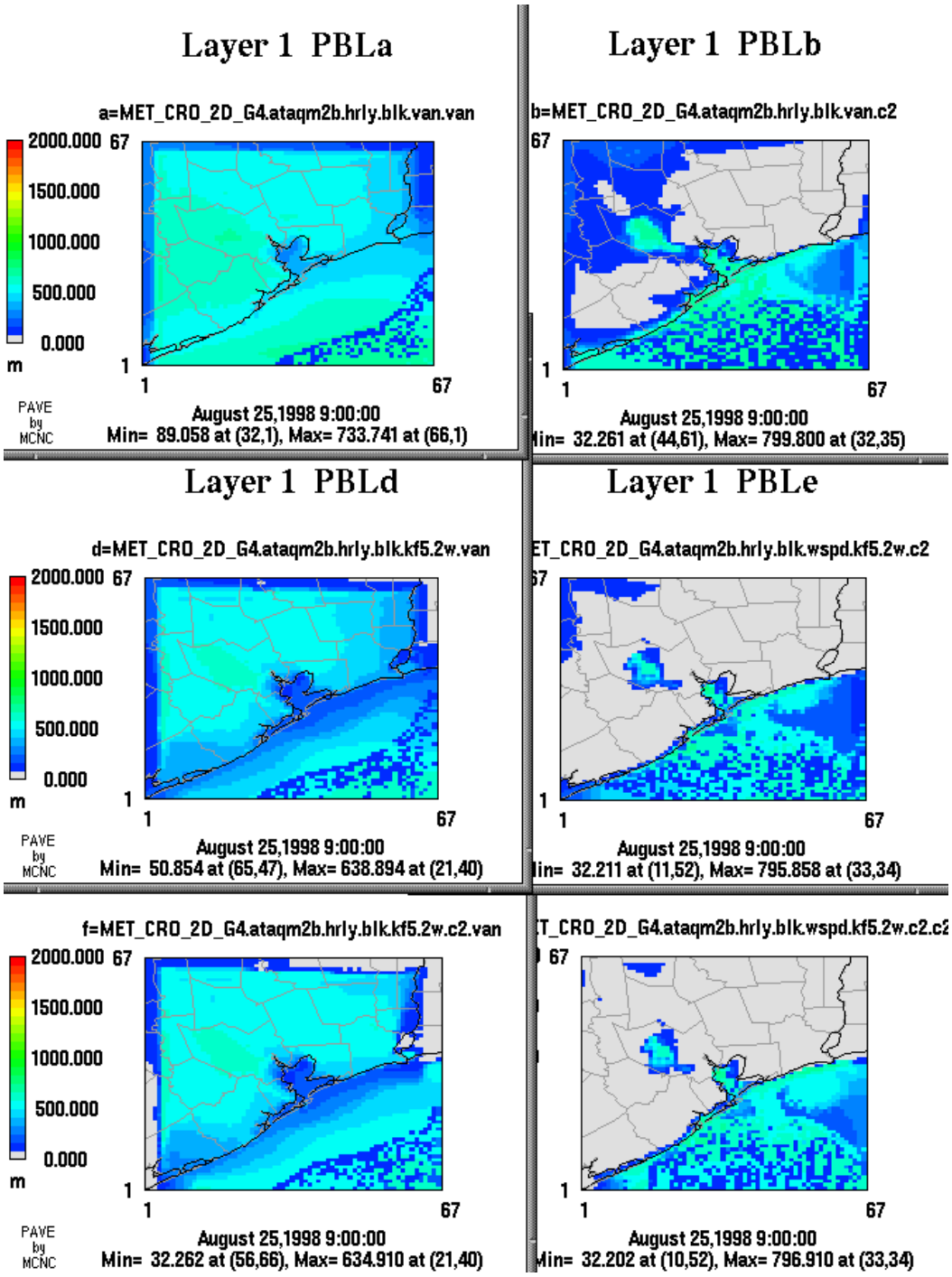

Figure 6.8.2. Modeled boundary layer heights at 0900 UTC on August 25. The uncoupled model is on the left and the coupled model is on the right. The top two panels are case "van", the middle panels are case "kf5.2w", and the bottom panels are case "kf5.2w.c2". Again, the nocturnal Houston heat-island effect is seen in the coupled models. Some sort of PBL instability is present in the uncoupled runs (left), probably due to an abrupt change in SSTs.

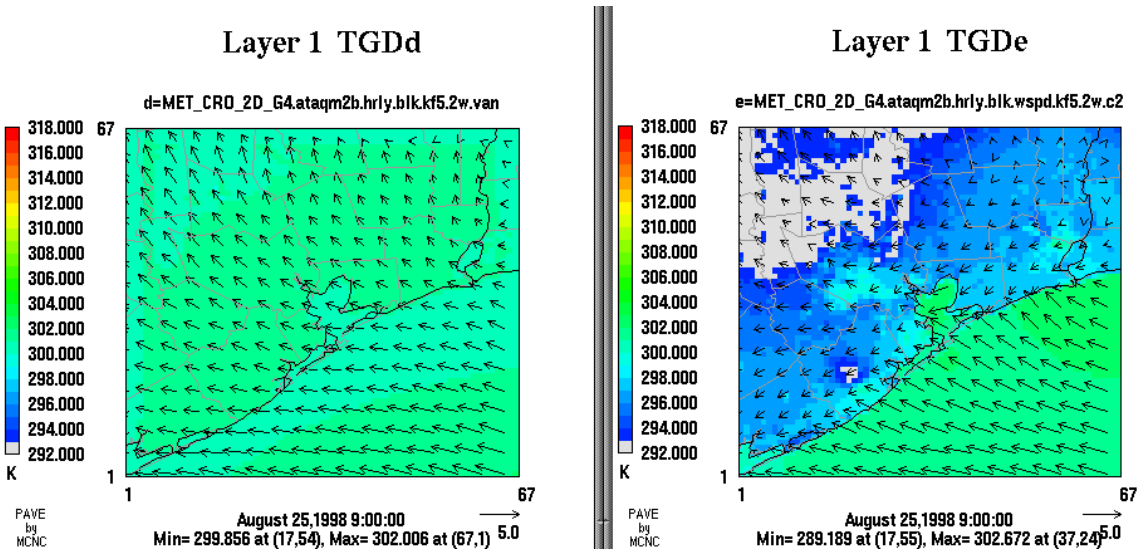

Figure 6.8.3. Modeled skin temperature at 0900 UTC on August 25 for case "kf5.2w." The uncoupled model is on the left. Note the broadly uniform nocturnal skin temperature between land and sea. More realistic is the cooler land/warmer water scenario portrayed by the coupled model (right). Under a strong inversion, winds have died over land at night in the coupled model, but continue to blow in the uncoupled model. The warmth of the city of Houston is clearly seen in the coupled model.

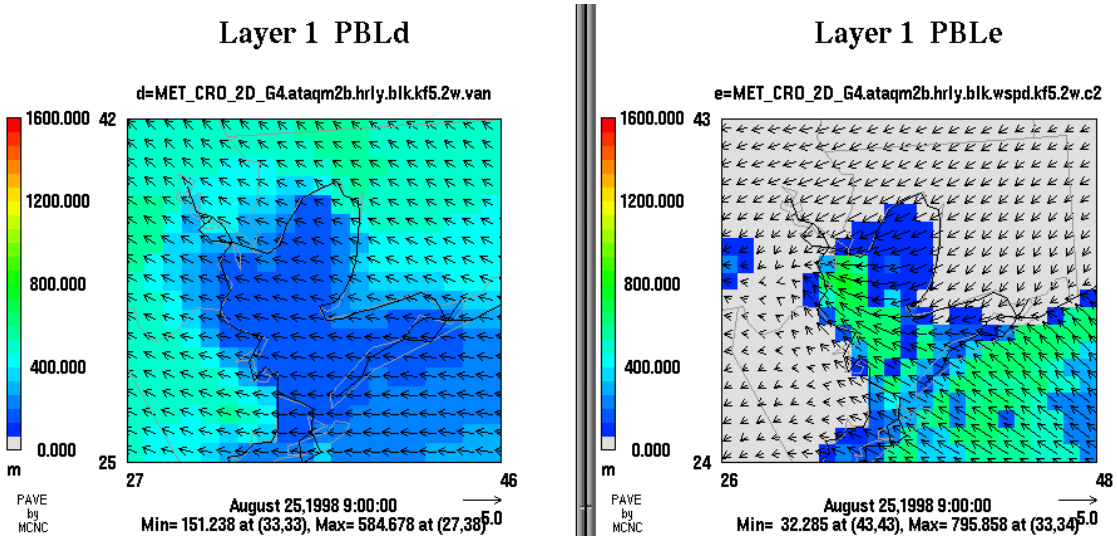

Figure 6.8.4. Modeled boundary layer heights at 0900 UTC on August 25. The uncoupled model is on the left and the coupled model is on the right. Case "kf5.2w" is shown, with wind vectors overlaid. Note that there are nocturnal differences in PBL heights between the two models. Uncoupled model heights are lower over the Bay and higher over land. Coupled model heights are the opposite.

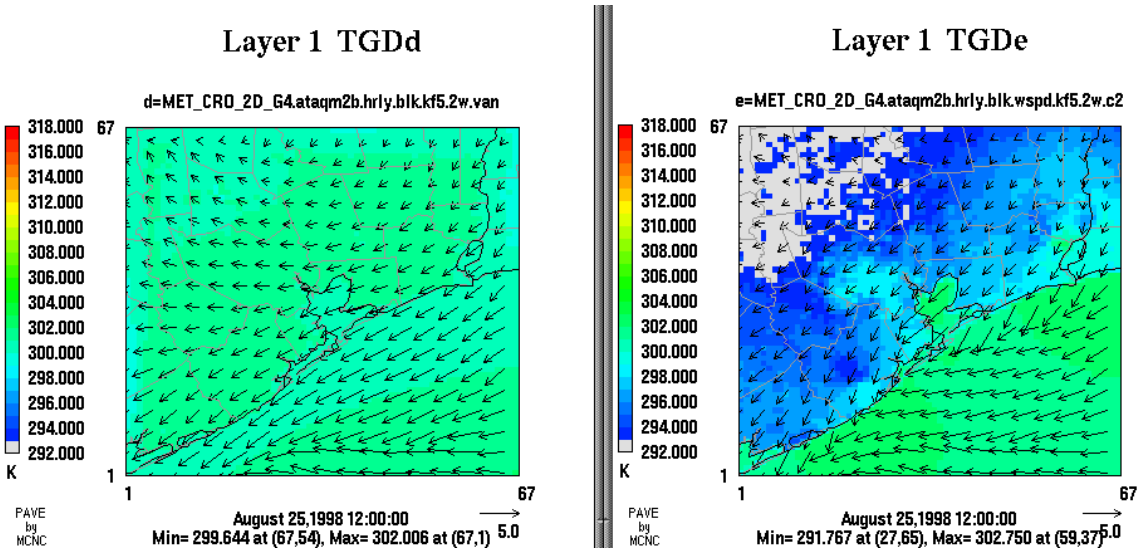

Figure 6.8.5. Modeled skin temperature at 1200 UTC on August 25 for case "kf5.2w." The uncoupled model is on the left. The expected land breeze is better defined in the coupled model, particularly from Brazoria County southwestward. Lack of a contrast between land-surface and water temperatures in the uncoupled model does not provide adequate forcing for the land breeze in this case (left).

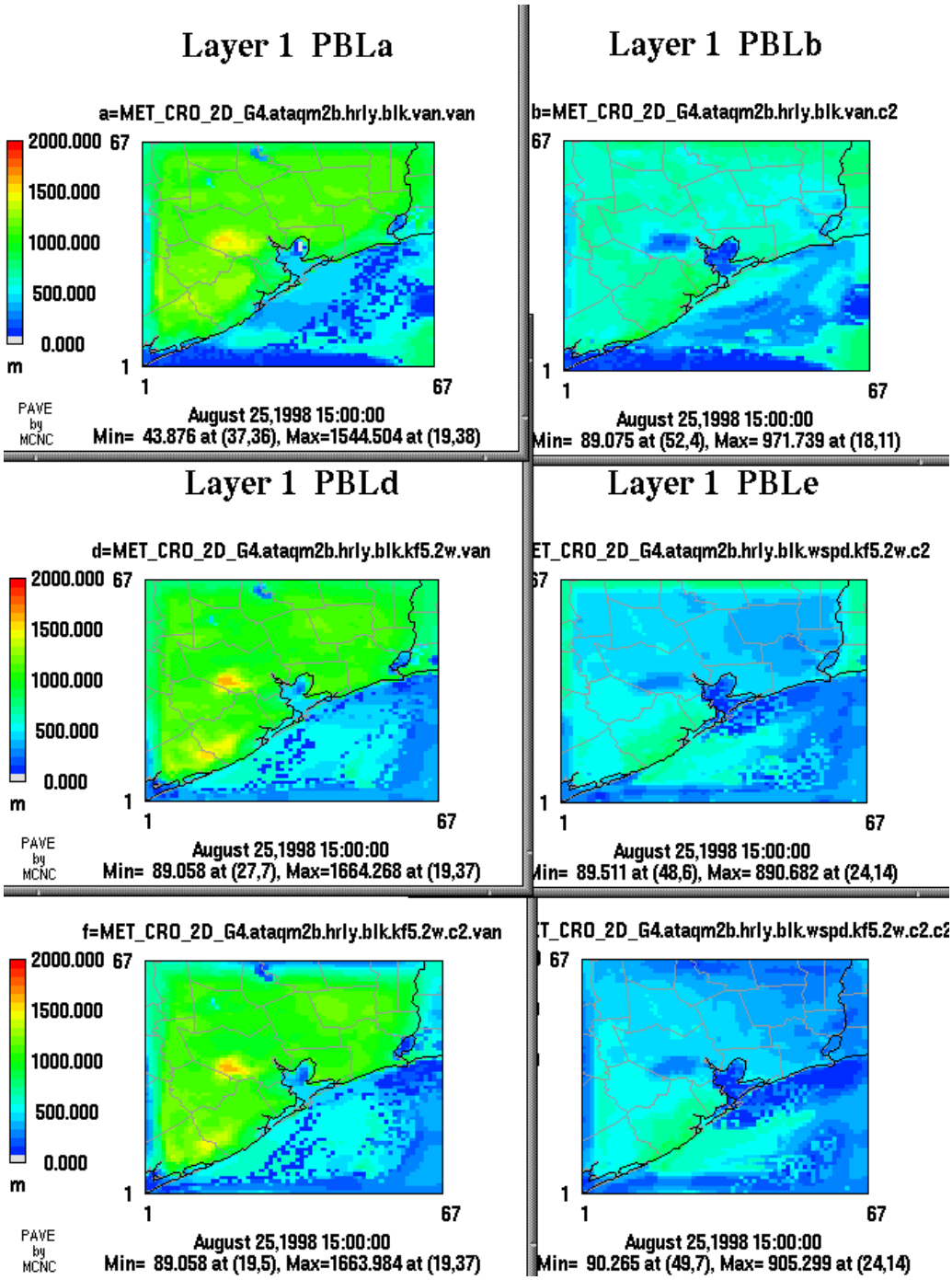

Figure 6.8.6. Modeled boundary layer heights at 1500 UTC on August 25. The uncoupled model is on the left and the coupled model is on the right. The top two panels are case "van", the middle panels are case "kf5.2w", and the bottom panels are case "kf5.2w.c2". Note the phase lag in PBL development between the two models over Houston: urban land-use types in the uncoupled MM5 heat quickly, whereas the surrounding land heats more quickly when driven by TOPLATS (right). Further, the PBL in the uncoupled model is generally deeper, suggesting a quicker sensible heat flux response following sunrise (left).

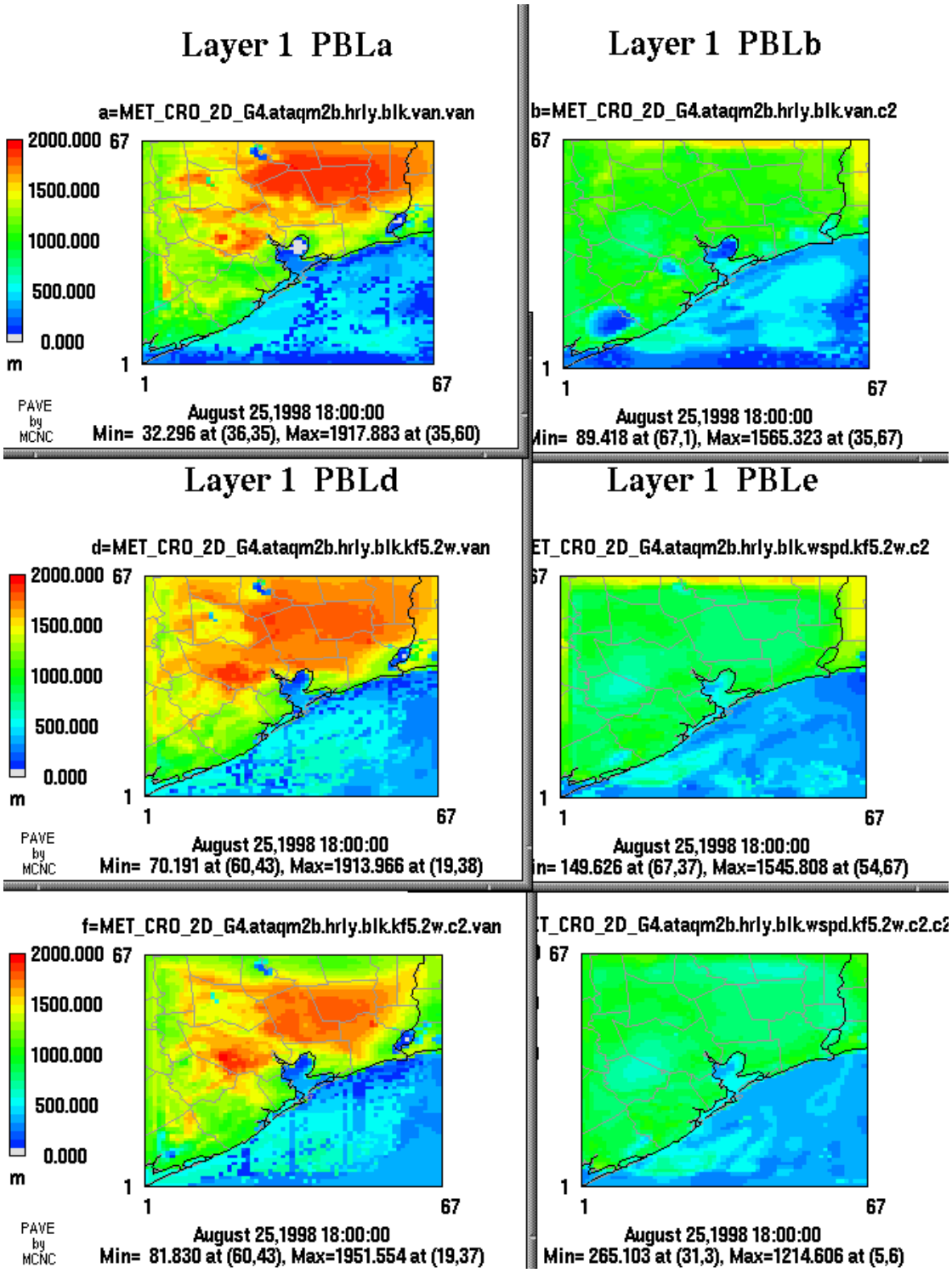

Figure 6.8.7. Modeled boundary layer heights at 1800 UTC on August 25. The uncoupled model is on the left and the coupled model is on the right. The top two panels are case "van", the middle panels are case "kf5.2w", and the bottom panels are case "kf5.2w.c2". On August 25, the PBL was notably shallower in the coupled model. In contrast, the PBL over Galveston Bay is not as depressed in the coupled model (see Figure 6.8.8).

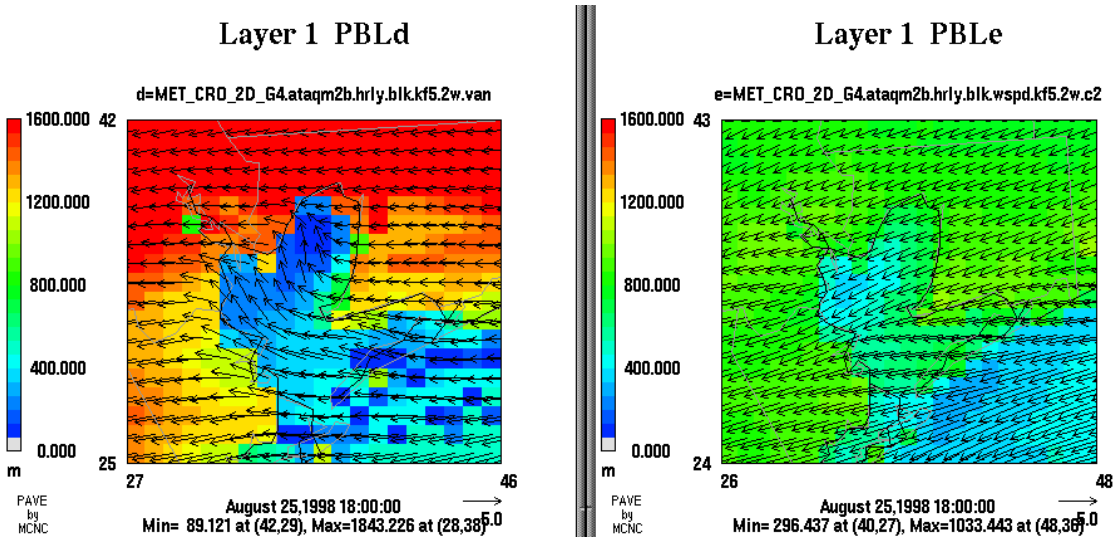

Figure 6.8.8. Modeled boundary layer heights at 1800 UTC on August 25. The uncoupled model is on the left and the coupled model is on the right. Case "kf5.2w" is shown, with wind vectors overlaid. The very depressed PBL in the uncoupled model—characteristic of many standard MM5 simulations conducted over Galveston Bay—leads to "channeling" of the wind as it gets ducted under a nocturnal-like cap. Modeled—and perhaps unrealistic—negative heat fluxes over the Bay cause the Blackadar scheme to respond this way. In the coupled model, the underlying SSATS produces positive fluxes and only modest depression, but not collapse, of the PBL. Thus, no channeling flow is seen.

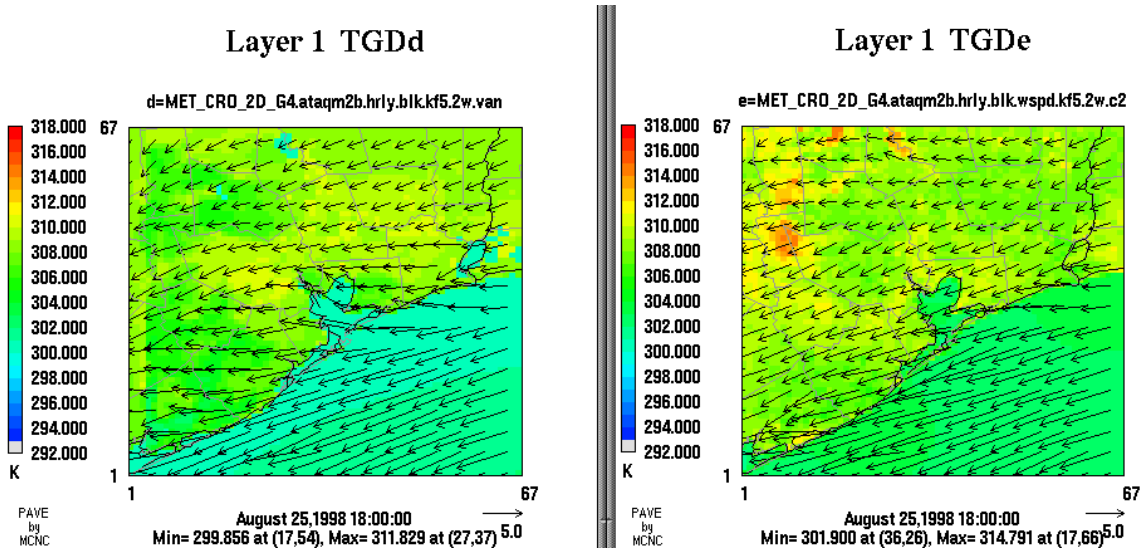

Figure 6.8.9. Modeled skin temperature at 1800 UTC on August 25 for case "kf5.2w." The uncoupled model is on the left. Key to this figure is the colder near-shore SSTs in the uncoupled model. The authors hypothesize that this leads to a somewhat stronger shore-perpendicular sea-breeze component during the afternoons. Because the coupled model used observed SSTs, it is not certain whether the "sea-breeze improvement" seen in the uncoupled model occurs for the right physical reasons. It is plausible that the 4-km scale doesn't respond to more modest land-sea thermal contrasts that, in nature, are sufficient to force the sea breeze.

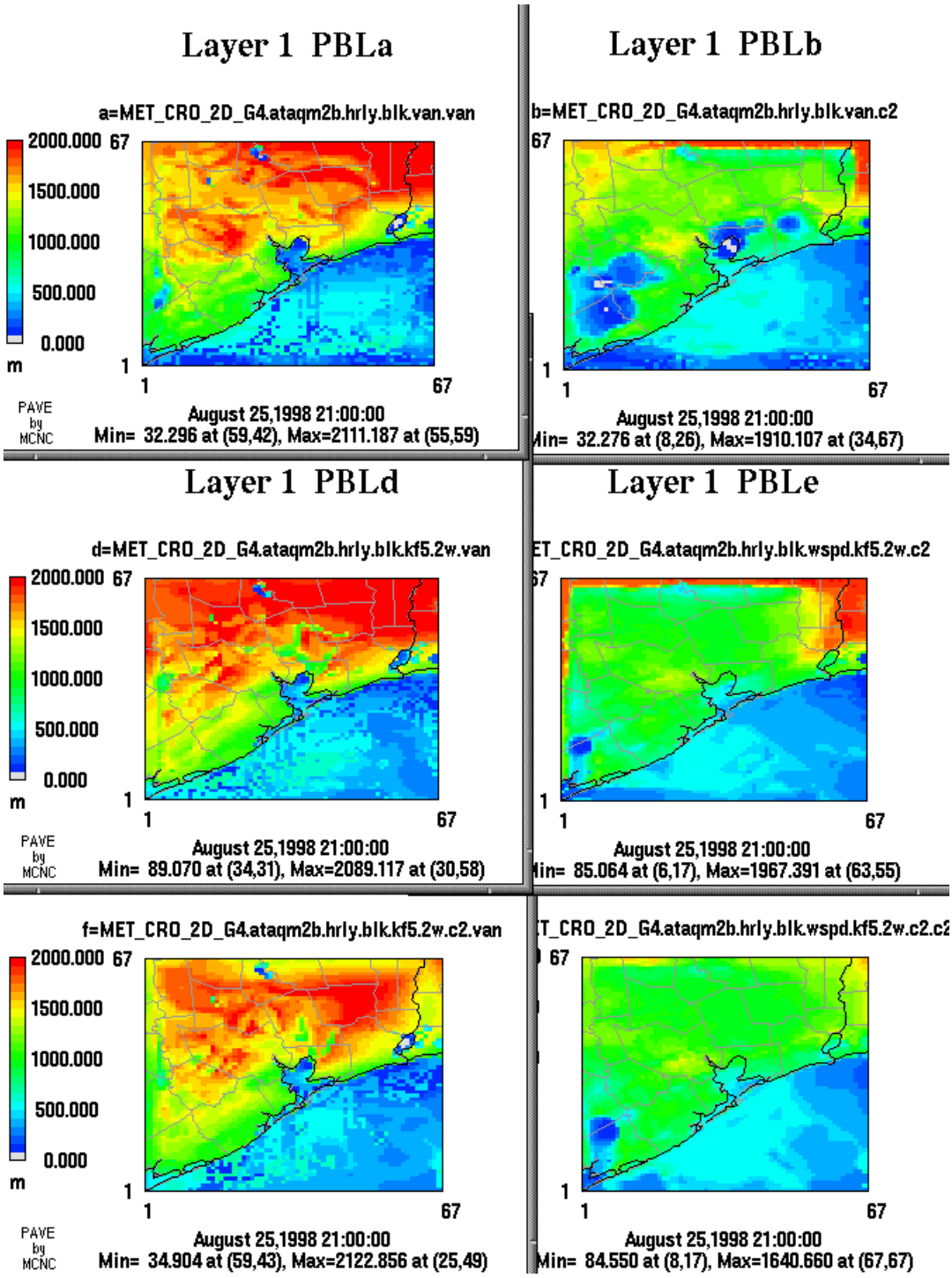

Figure 6.8.10. Modeled boundary layer heights at 2100 UTC on August 25. The uncoupled model is on the left and the coupled model is on the right. The top two panels are case "van", the middle panels are case "kf5.2w", and the bottom panels are case "kf5.2w.c2". PBL heights are on the order of 500 m higher in the uncoupled case. In the coupled case, soil was moister at the episode beginning, leading to lower sensible fluxes and lower PBL heights. No dynamic soil moisture is possible in the uncoupled model.

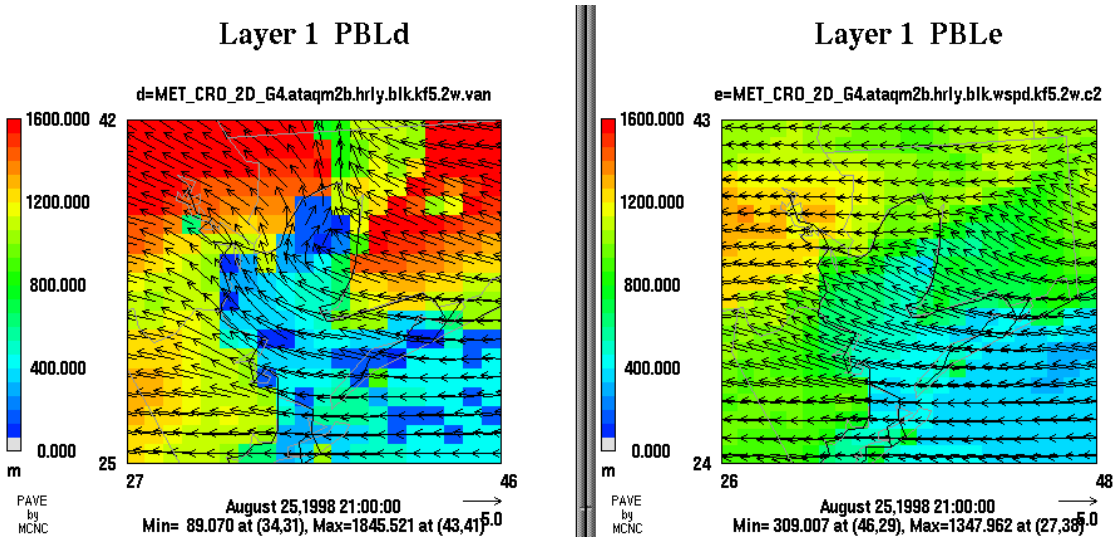

Figure 6.8.11. Modeled boundary layer heights at 2100 UTC on August 25. The uncoupled model is on the left and the coupled model is on the right. Case "kf5.2w" is shown, with wind vectors overlaid. The very depressed PBL continues in the uncoupled model, as in Figure 6.8.8. The sea breeze has established itself in the coupled model, but the channeling effect is not present (right).

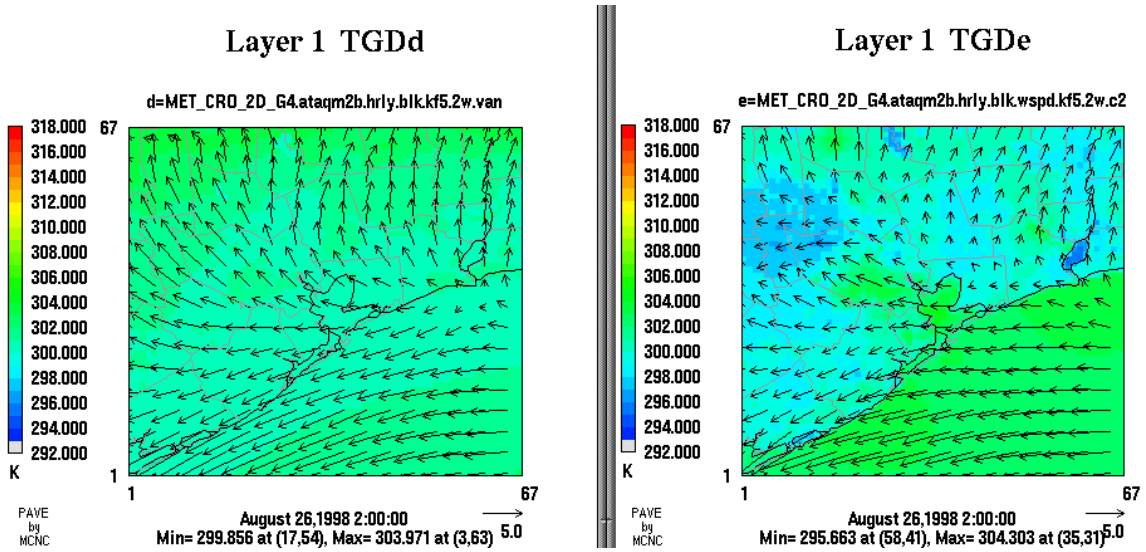

Figure 6.8.12. Modeled skin temperature at 0200 UTC on August 26 for case "kf5.2w." The uncoupled model is on the left. The land-surface is already cooling in the coupled model, with winds accelerating into and out of the Houston heat-island as the nocturnal inversion sets in. This effect is absent in the uncoupled model.

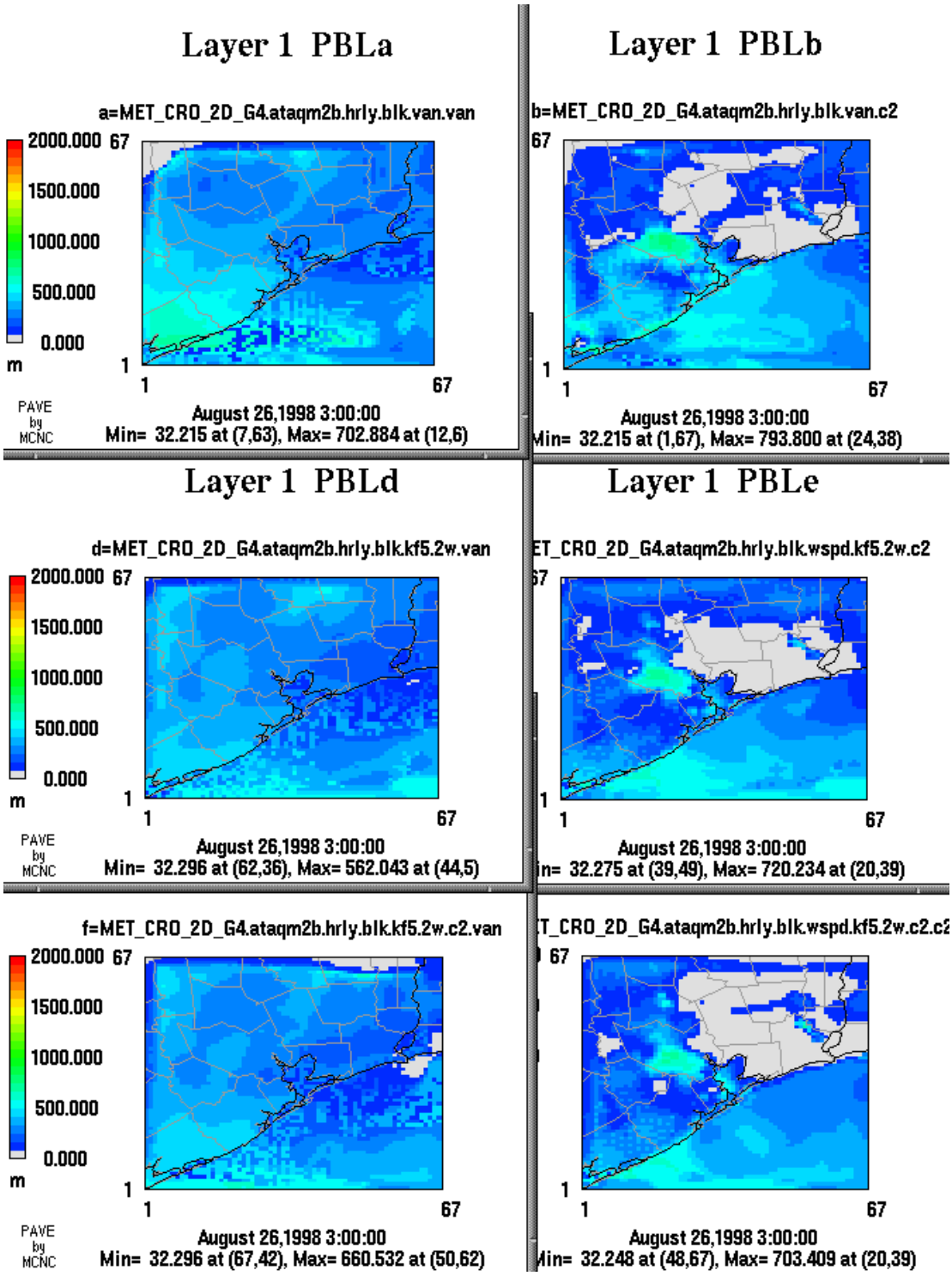

Figure 6.8.13. Modeled boundary layer heights at 0300 UTC on August 26. The uncoupled model is on the left and the coupled model is on the right. The top two panels are case "van", the middle panels are case "kf5.2w", and the bottom panels are case "kf5.2w.c2". The heat island is again seen in the coupled runs.

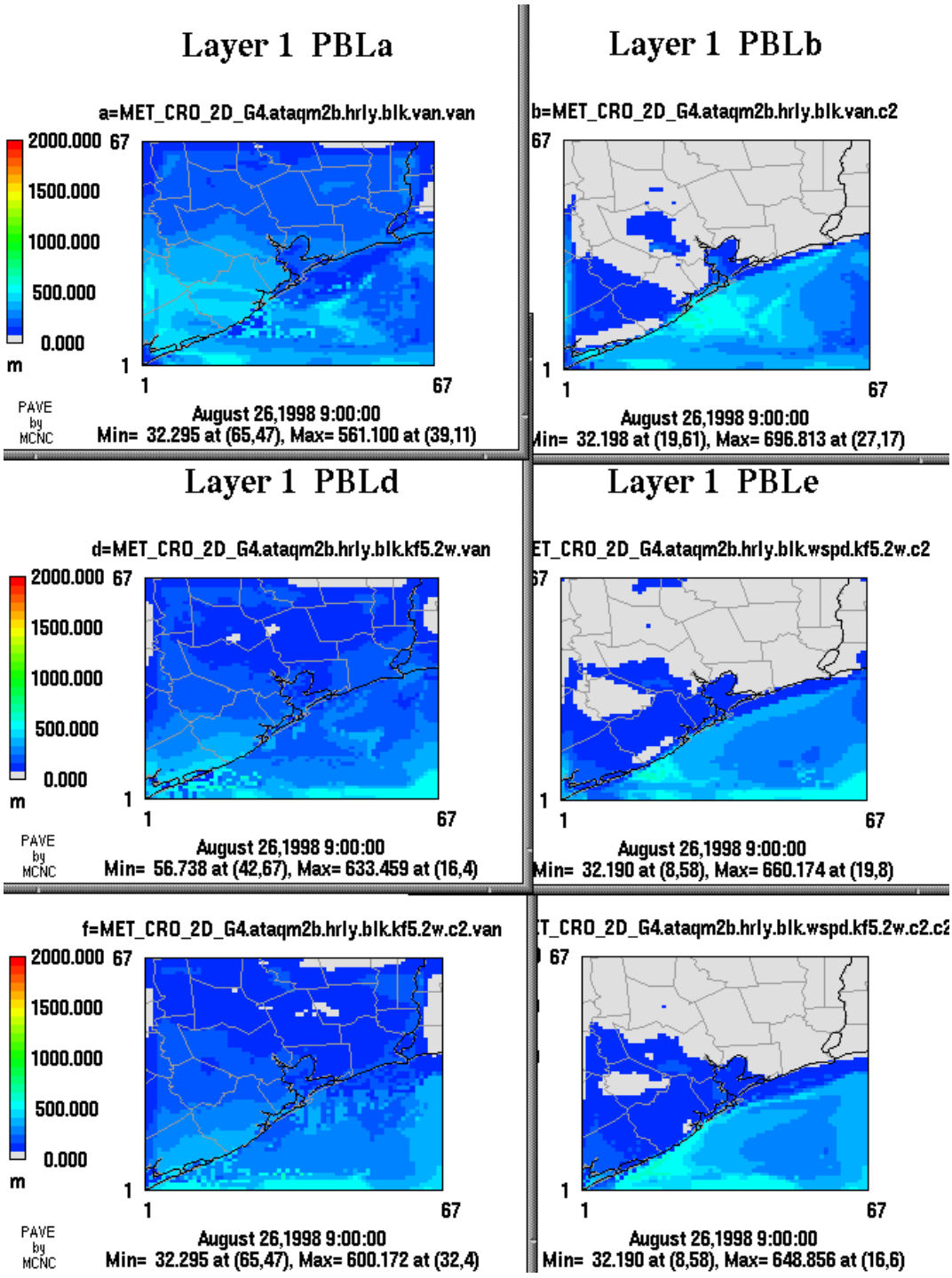

Figure 6.8.14. Modeled boundary layer heights at 0900 UTC on August 26. The uncoupled model is on the left and the coupled model is on the right. The top two panels are case "van", the middle panels are case "kf5.2w", and the bottom panels are case "kf5.2w.c2". The cooler land-surface leads to a true surface inversion in much of the coupled model domain. This is not seen in the uncoupled run. Surface inversions play a large role in the dynamics of the low-level jet.

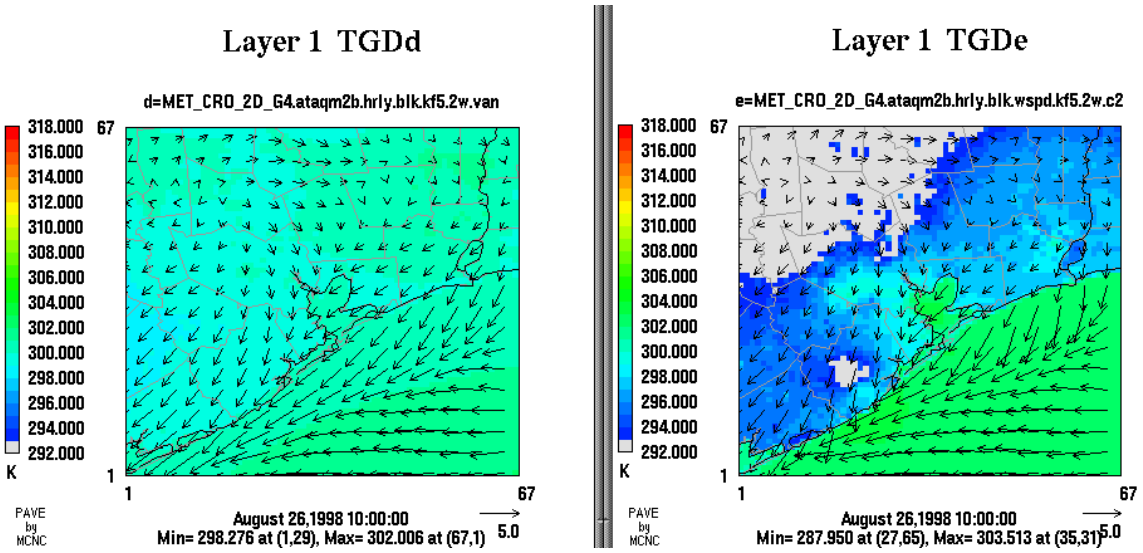

Figure 6.8.15. Modeled skin temperature at 1000 UTC on August 26 for case "kf5.2w." The uncoupled model is on the left. Again, the uncoupled model skin temperatures are homogeneous across the land-Gulf interface, whereas the much more realistic contrast allows an offshore breeze to develop in the coupled model.

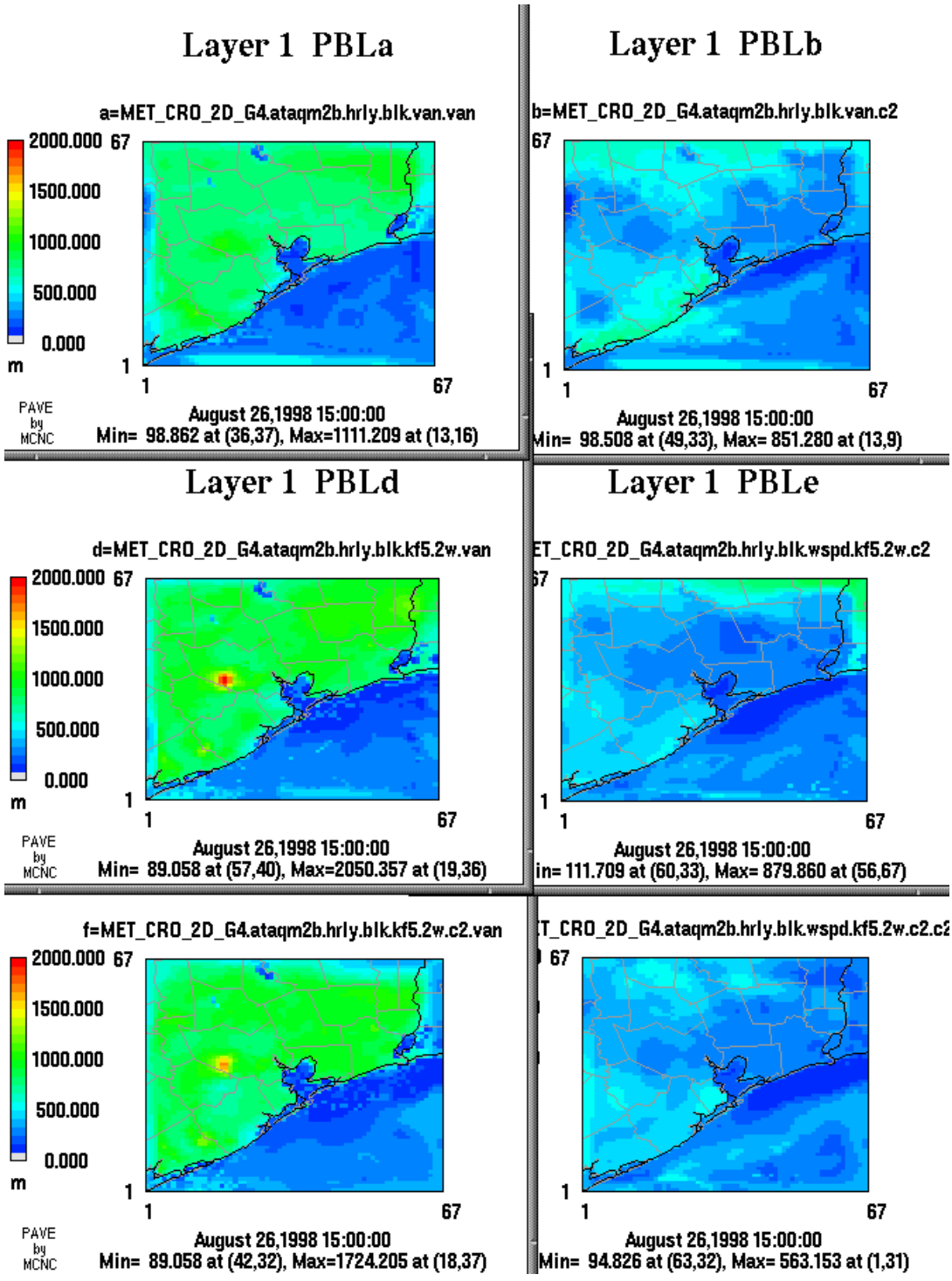

Figure 6.8.16. Modeled boundary layer heights at 1500 UTC on August 26. The uncoupled model is on the left and the coupled model is on the right. The top two panels are case "van", the middle panels are case "kf5.2w", and the bottom panels are case "kf5.2w.c2". For this day, PBL heights grow much more rapidly in the uncoupled model than in the coupled model.

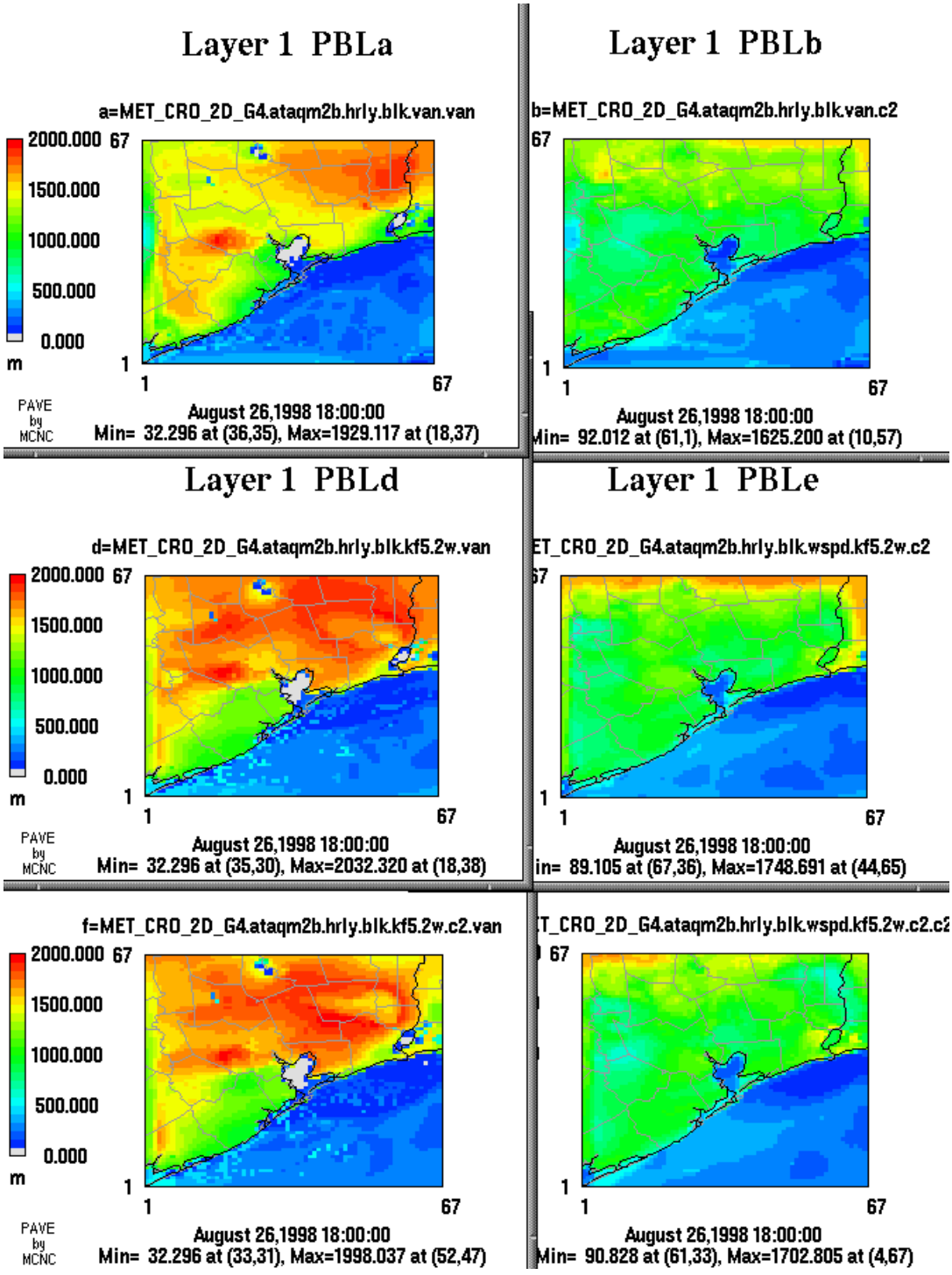

Figure 6.8.17. Modeled boundary layer heights at 1800 UTC on August 26. The uncoupled model is on the left and the coupled model is on the right. The top two panels are case "van", the middle panels are case "kf5.2w", and the bottom panels are case "kf5.2w.c2". Mean depths are near 1000 m (~3000 ft) in the coupled model and above 1500 m (~4500 ft) in the uncoupled model by noon LST. Note the complete collapse of the PBL over Galveston Bay in the uncoupled model (see Figure 6.8.18).

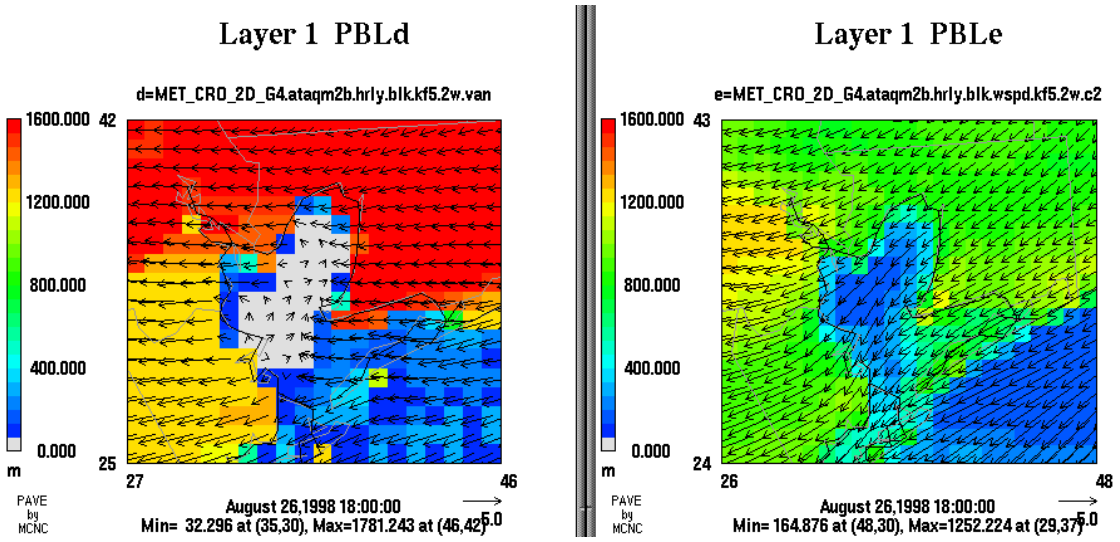

Figure 6.8.18. Modeled boundary layer heights at 1800 UTC on August 26. The uncoupled model is on the left and the coupled model is on the right. Case "kf5.2w" is shown, with wind vectors overlaid. The PBL has collapsed in the uncoupled model, with winds becoming calm at the surface but apparently blowing over the top of the cold dome hugging Galveston Bay. In the coupled model, the winds penetrate the Bay at the surface, continuing out of the northwest.

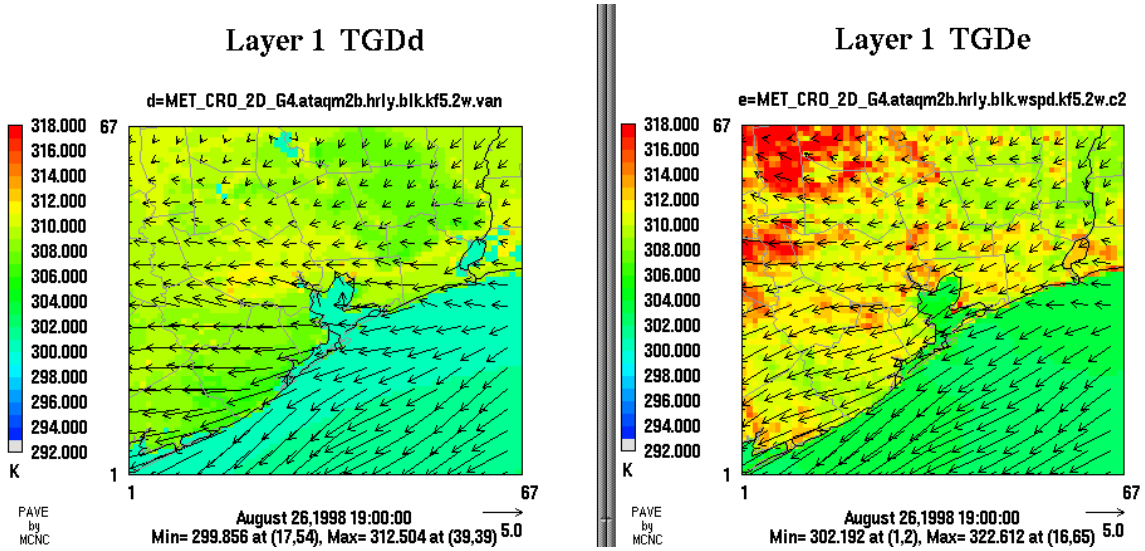

Figure 6.8.19. Modeled skin temperature at 1900 UTC on August 26 for case "kf5.2w." The uncoupled model is on the left. The slice of near-shore cold Gulf water temperatures is again seen in the uncoupled model. Replacement with SSATS in the coupled model corrects this problem.

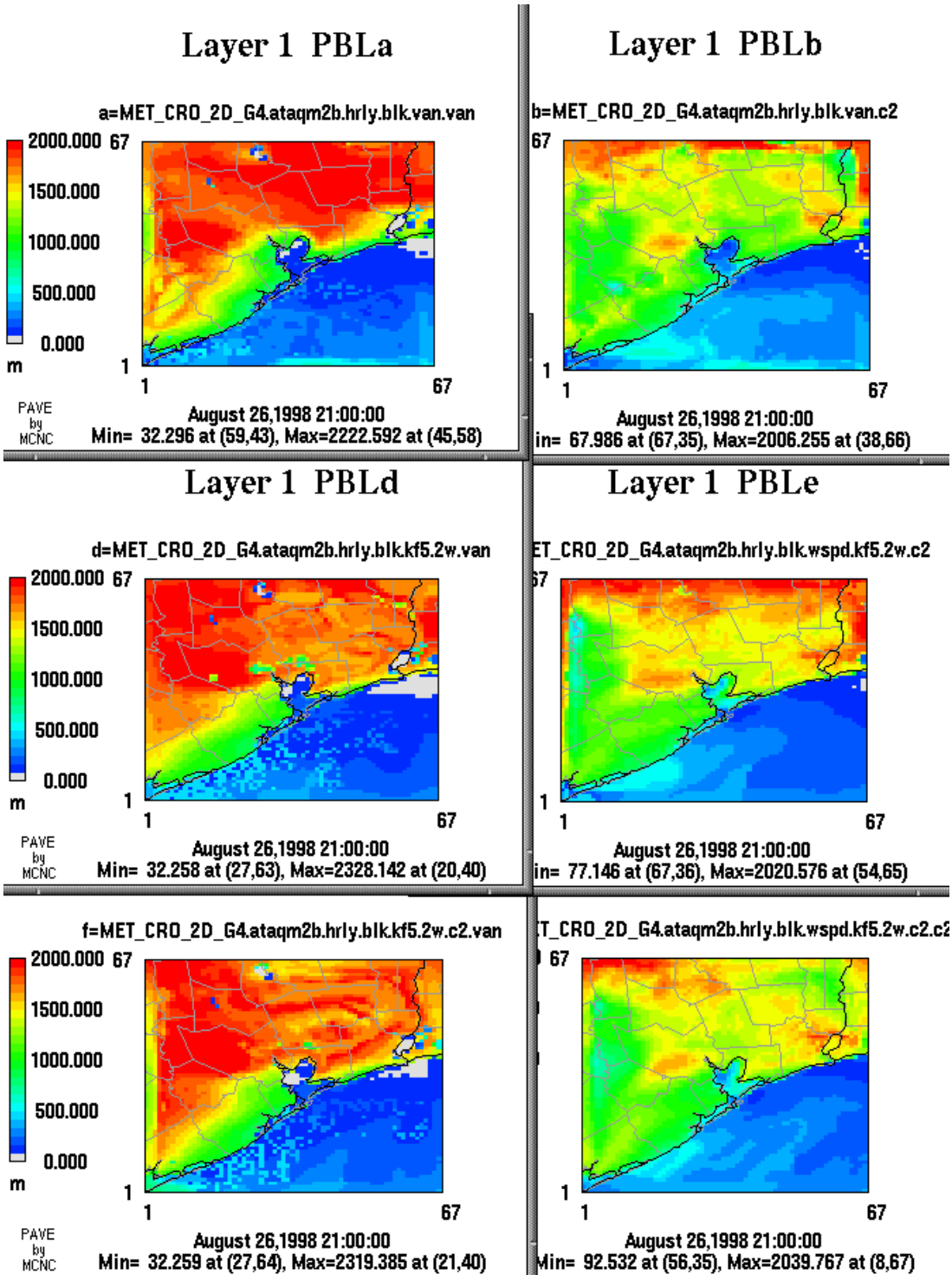

Figure 6.8.20. Modeled boundary layer heights at 2100 UTC on August 26. The uncoupled model is on the left and the coupled model is on the right. The top two panels are case "van", the middle panels are case "kf5.2w", and the bottom panels are case "kf5.2w.c2". PBL heights have collapsed over the two lakes northwest of Houston which is often a problem for air quality models. Better treatment of lake temperatures and fluxes in TOPLATS avoids this problem in the coupled model.

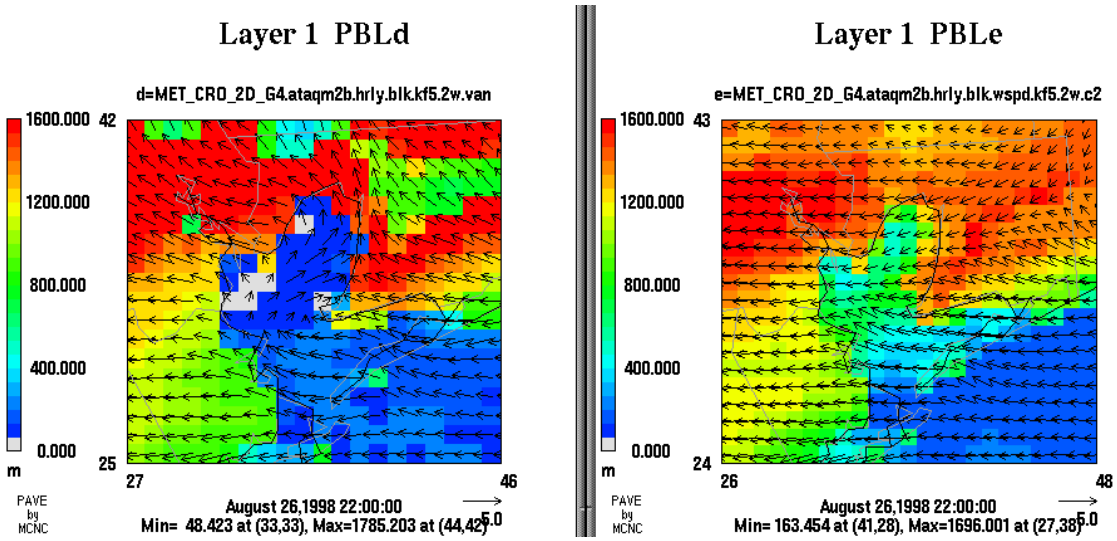

Figure 6.8.21. Modeled boundary layer heights at 2200 UTC on August 26. The uncoupled model is on the left and the coupled model is on the right. Case "kf5.2w" is shown, with wind vectors overlaid. With onset of the sea breeze, the channeling effect sets-in in the uncoupled model. In the coupled model, a hint of channeling is also present.

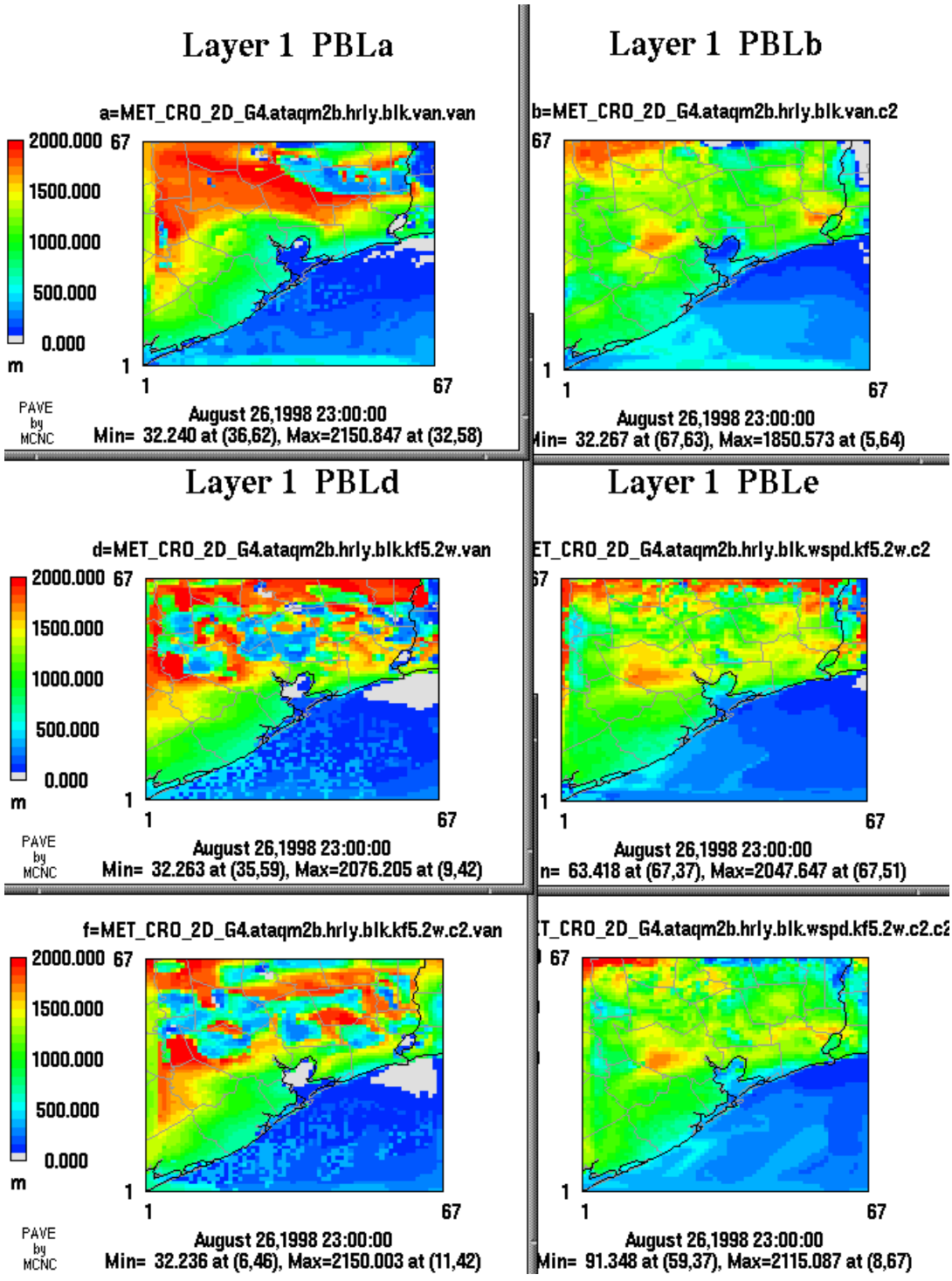

Figure 6.8.22. Modeled boundary layer heights at 2300 UTC on August 26. The uncoupled model is on the left and the coupled model is on the right. The top two panels are case "van", the middle panels are case "kf5.2w", and the bottom panels are case "kf5.2w.c2". Here, the influence of spurious clouds in the uncoupled model (left) is evident (see Figure 6.7.6). No clouds were observed in nature.

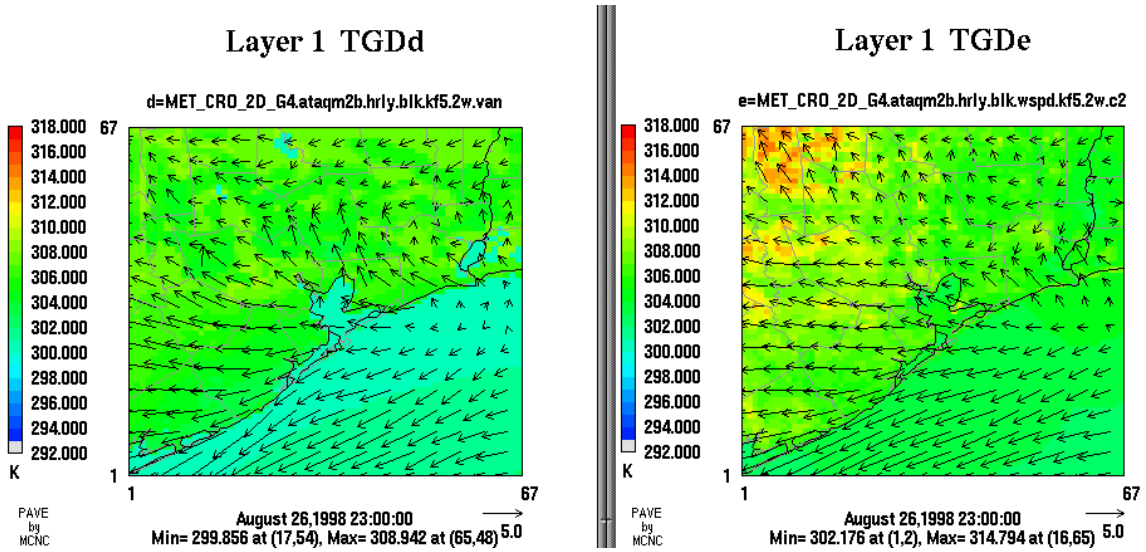

Figure 6.8.23. Modeled skin temperature at 2300 UTC on August 26 for case "kf5.2w." The uncoupled model is on the left. The stronger sea-breeze effect is noted in the uncoupled model. This may be due to a combination of model effects: the earlier development of the PBL together with the (anomalously) cold near-shore SSTs. The noted surface temperature phase lead in the uncoupled model, however, suggests that the PBL may be growing a bit too early. Thus, though the uncoupled model seems to capture the sea-breeze effect better than the coupled model, it may be "getting the right answer for the wrong reasons."

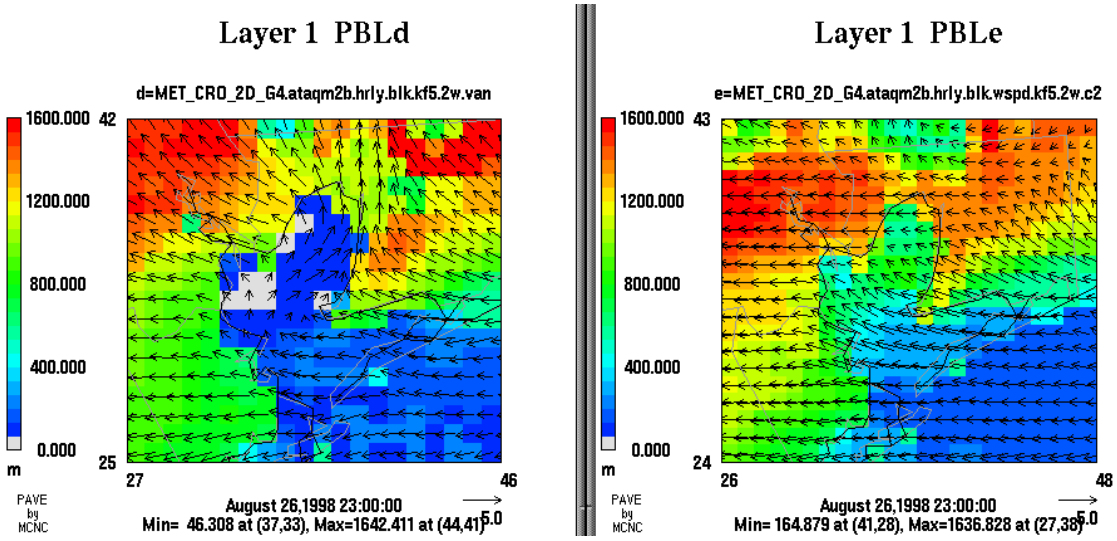

Figure 6.8.24. Modeled boundary layer heights at 2300 UTC on August 26. The uncoupled model is on the left and the coupled model is on the right. Case "kf5.2w" is shown, with wind vectors overlaid. At this time, the channeling effect reaches its peak with winds blowing strongly out of the duct near the northeast corner of the Bay, after taking a sharp right turn (left, uncoupled model).

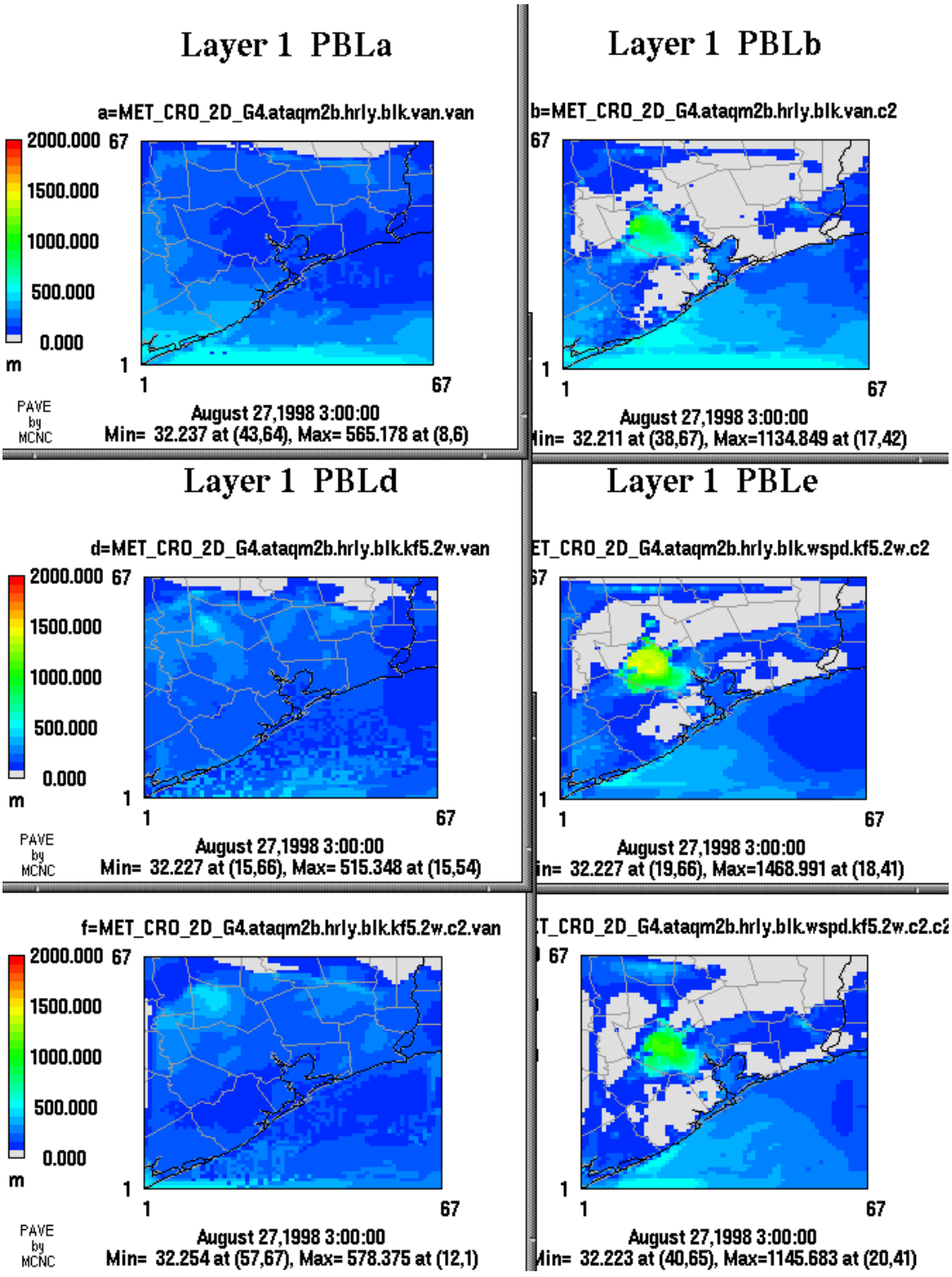

Figure 6.8.25. Modeled boundary layer heights at 0300 UTC on August 27. The uncoupled model is on the left and the coupled model is on the right. The top two panels are case "van", the middle panels are case "kf5.2w", and the bottom panels are case "kf5.2w.c2". The nocturnal heat island is visible in the coupled model.

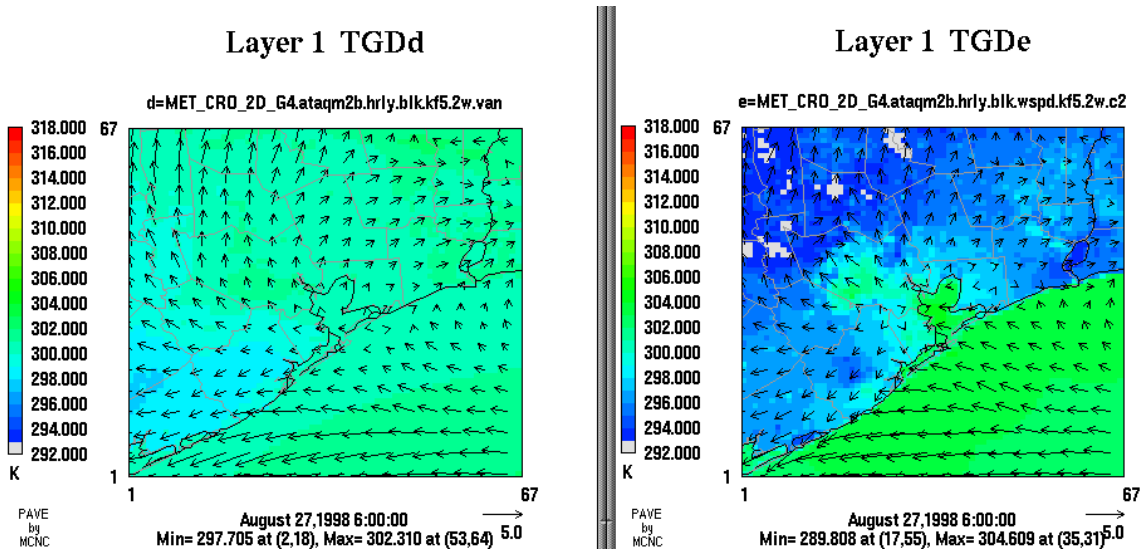

Figure 6.8.26. Modeled skin temperature at 0600 UTC on August 27 for case "kf5.2w." The uncoupled model is on the left, the coupled model is on the right.

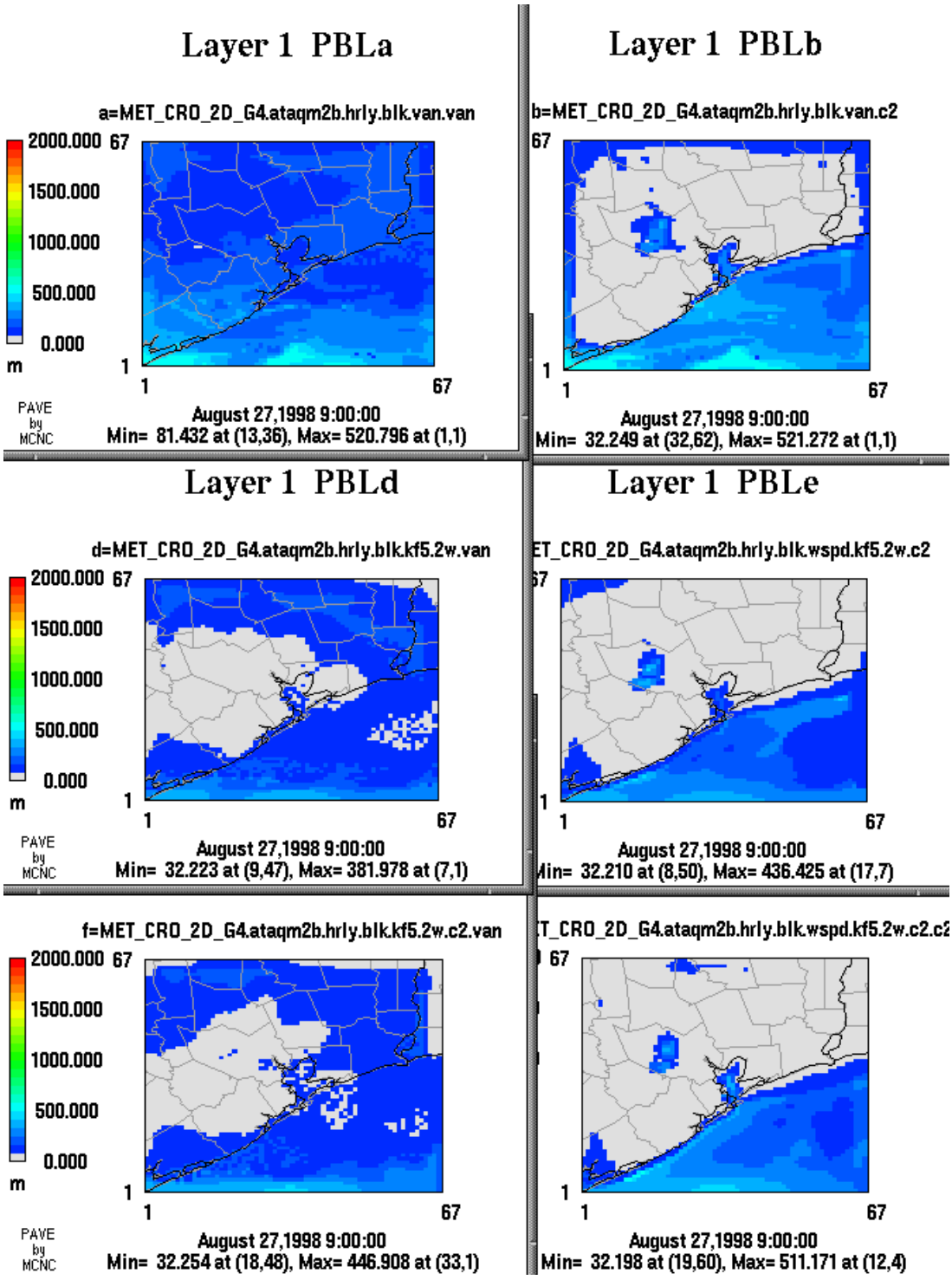

Figure 6.8.27. Modeled boundary layer heights at 0900 UTC on August 27. The uncoupled model is on the left and the coupled model is on the right. The top two panels are case "van", the middle panels are case "kf5.2w", and the bottom panels are case "kf5.2w.c2". As above, a true land-surface inversion is entrenched in the coupled model over the entire domain. By contrast, about half of the land surface reveals a surface inversion in the two "kf5.2w" runs for the uncoupled model.

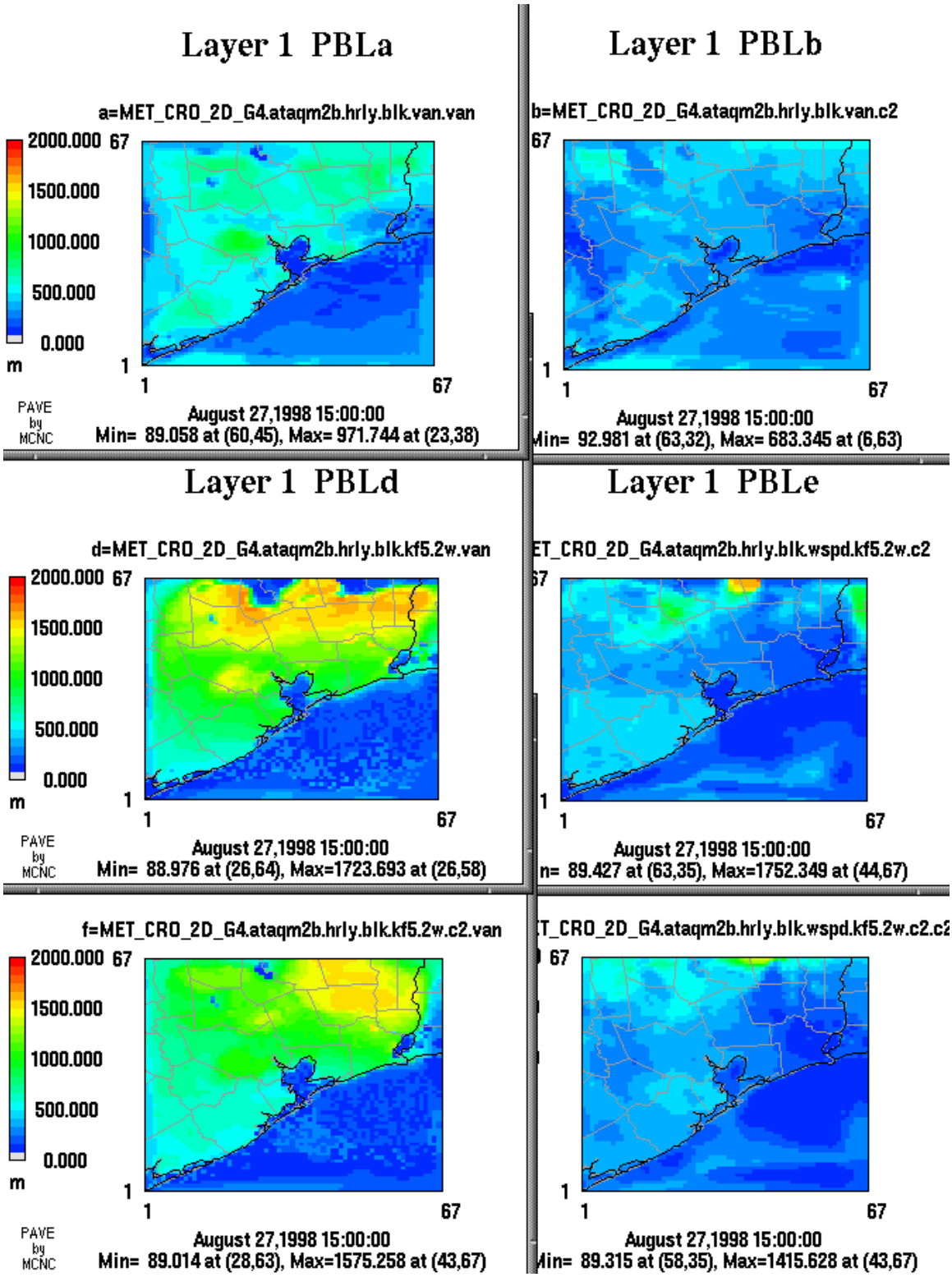

Figure 6.8.28. Modeled boundary layer heights at 1500 UTC on August 27. The uncoupled model is on the left and the coupled model is on the right. The top two panels are case "van", the middle panels are case "kf5.2w", and the bottom panels are case "kf5.2w.c2". The PBL has grown somewhat more rapidly in the uncoupled model than in the coupled model.

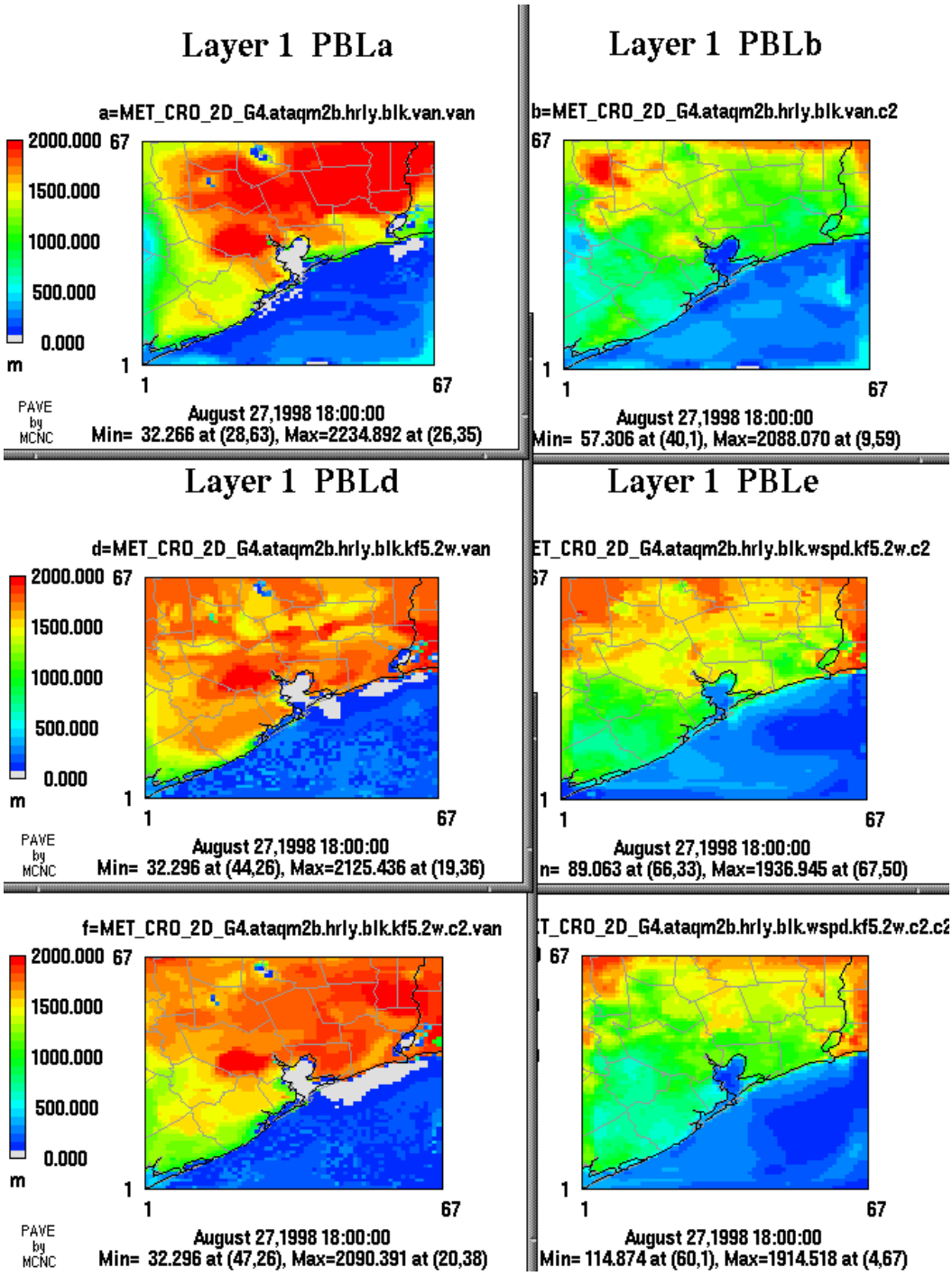

Figure 6.8.29. Modeled boundary layer heights at 1800 UTC on August 27. The uncoupled model is on the left and the coupled model is on the right. The top two panels are case "van", the middle panels are case "kf5.2w", and the bottom panels are case "kf5.2w.c2". Mean PBL heights are around 1400 m in the coupled model and near 2000 m in the uncoupled model. This difference could result in much lower ozone levels in an air quality model driven by the uncoupled model, due to the deeper mixed layer. This was the first of the two highest ozone days of the episode.

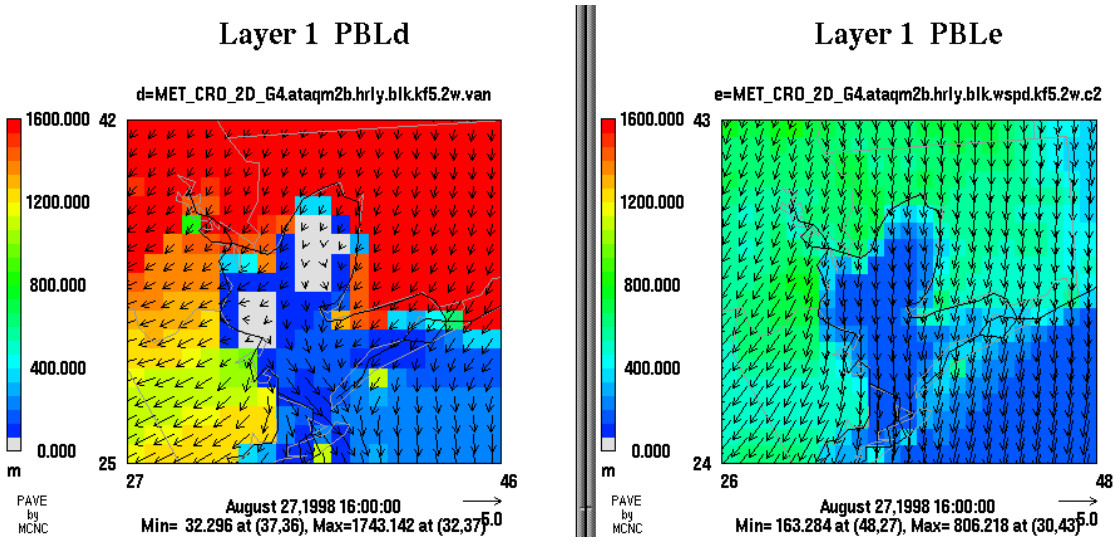

Figure 6.8.30. Modeled boundary layer heights at 1600 UTC on August 27. The uncoupled model is on the left and the coupled model is on the right. Case "kf5.2w" is shown, with wind vectors overlaid. Characteristic offshore flow has a channeling effect in the uncoupled model, as air mass flows out through the Bay inlet, forced through a shallow duct. The Bay PBL is deep enough in the coupled model to avoid this effect.

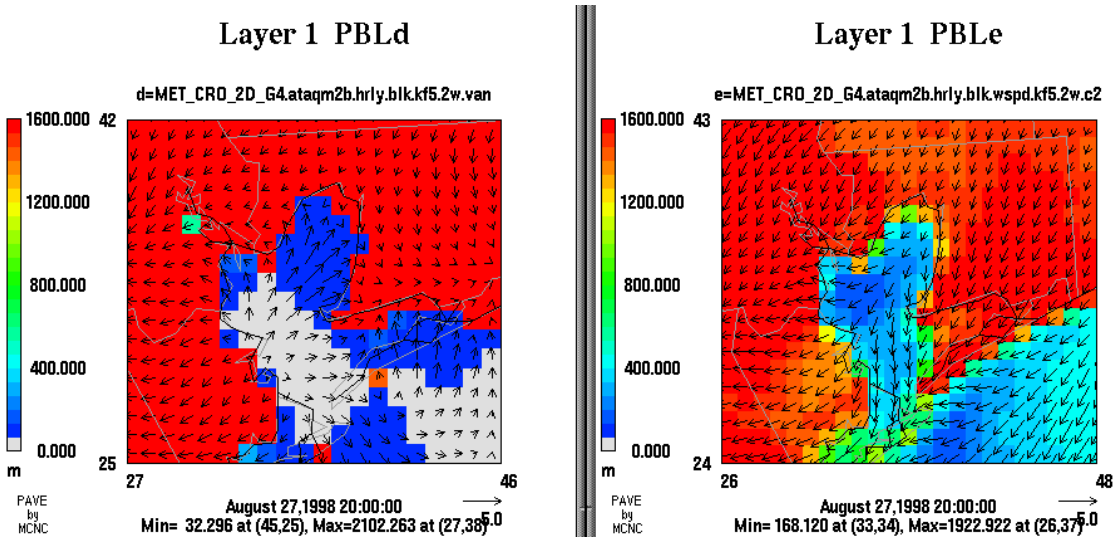

Figure 6.8.31. Modeled boundary layer heights at 2000 UTC on August 27. The uncoupled model is on the left and the coupled model is on the right. Case "kf5.2w" is shown, with wind vectors overlaid. By 2000 UTC, air is sinking rapidly near the western shore of the Bay in the coupled model and spreading out like a fan. In the uncoupled model, the PBL has become depressed but has not collapsed, and some outward channeling flow has set in.

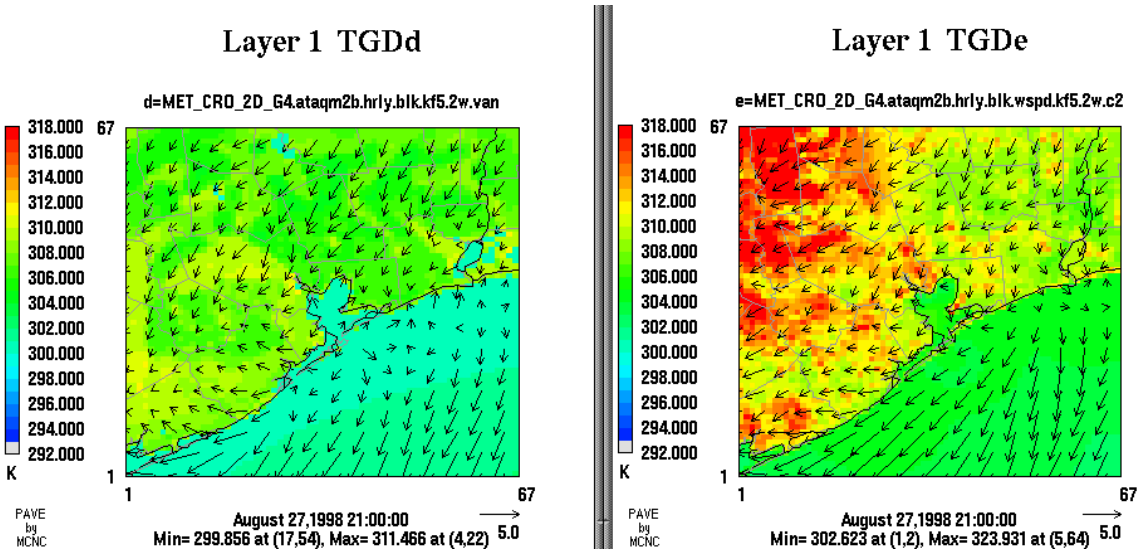

Figure 6.8.32. Modeled skin temperature at 2100 UTC on August 27 for case "kf5.2w." The uncoupled model is on the left. Under light winds, the land surface heats rapidly in the coupled model, with a maximum of 50°C. The uncoupled skin surface maximum is 12°C cooler than that for the coupled model.

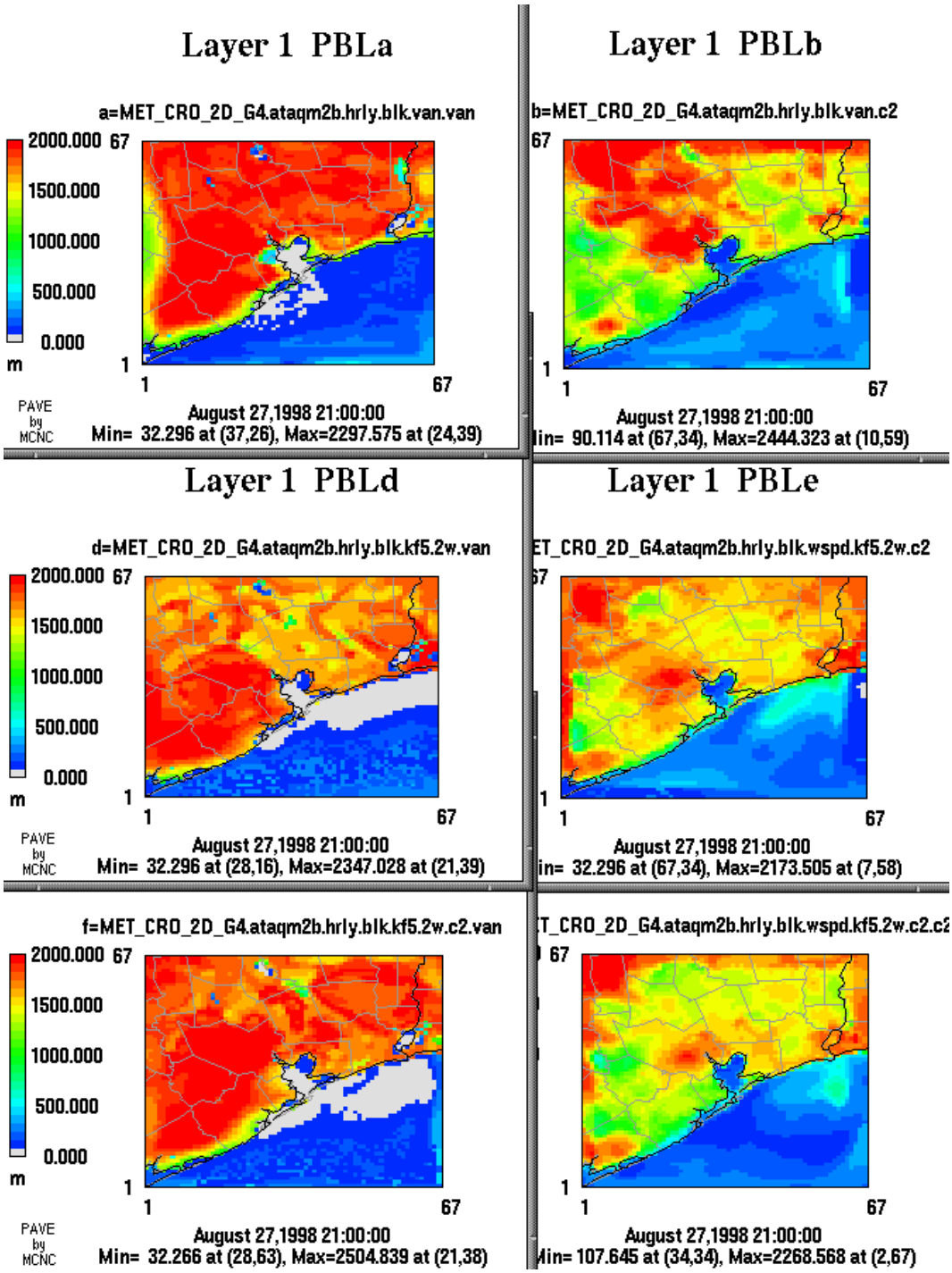

Figure 6.8.33. Modeled boundary layer heights at 2100 UTC on August 27. The uncoupled model is on the left and the coupled model is on the right. The top two panels are case "van", the middle panels are case "kf5.2w", and the bottom panels are case "kf5.2w.c2". Mean PBL heights are fairly comparable by this time. The underlying SSATS prevents the PBL from collapsing over either the Bay or near-shore Gulf in the coupled model.

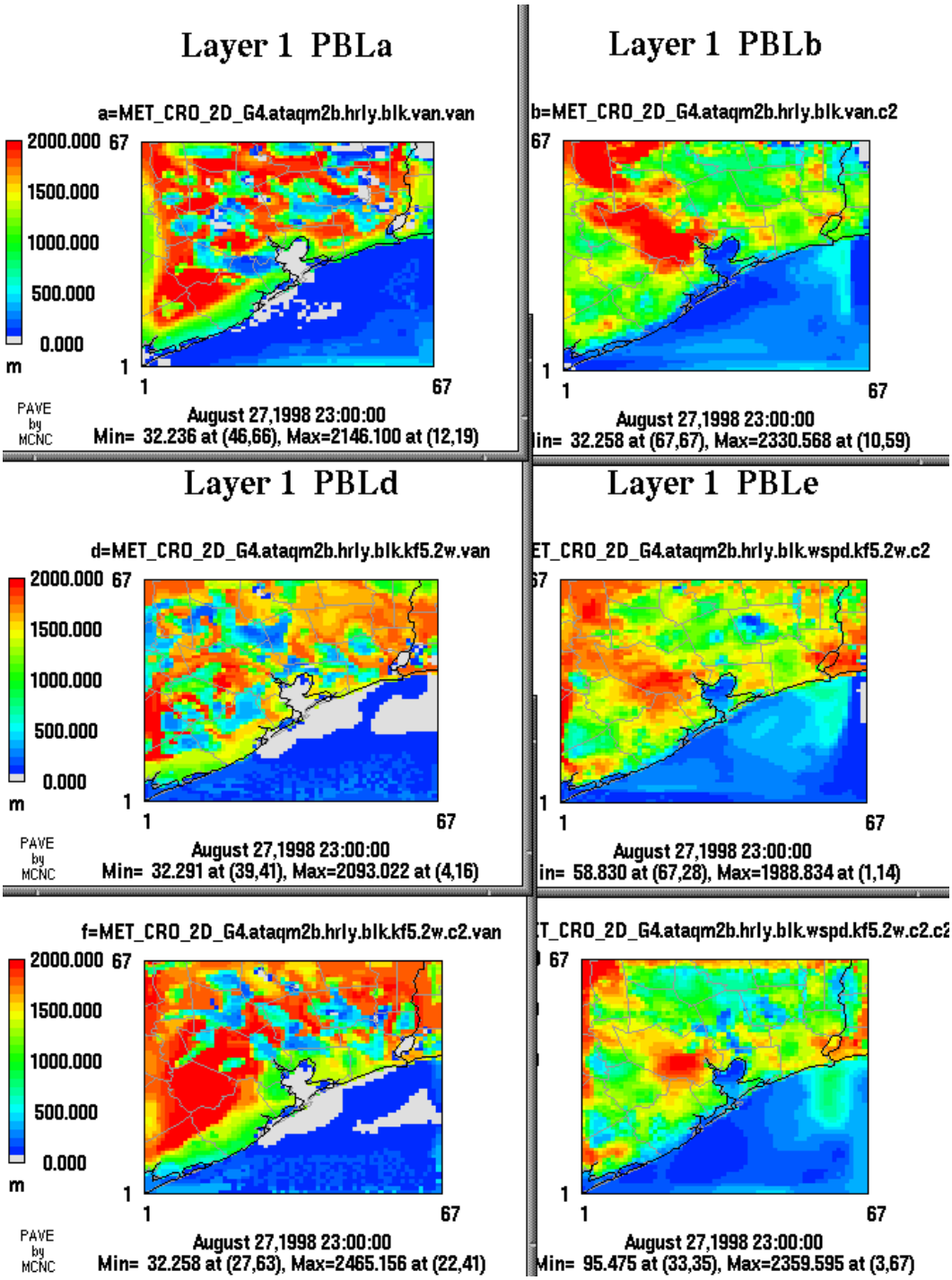

Figure 6.8.34. Modeled boundary layer heights at 2300 UTC on August 27. The uncoupled model is on the left and the coupled model is on the right. The top two panels are case "van", the middle panels are case "kf5.2w", and the bottom panels are case "kf5.2w.c2". Spurious clouds have again formed in the uncoupled model, reducing PBL heights in a patchwork fashion.

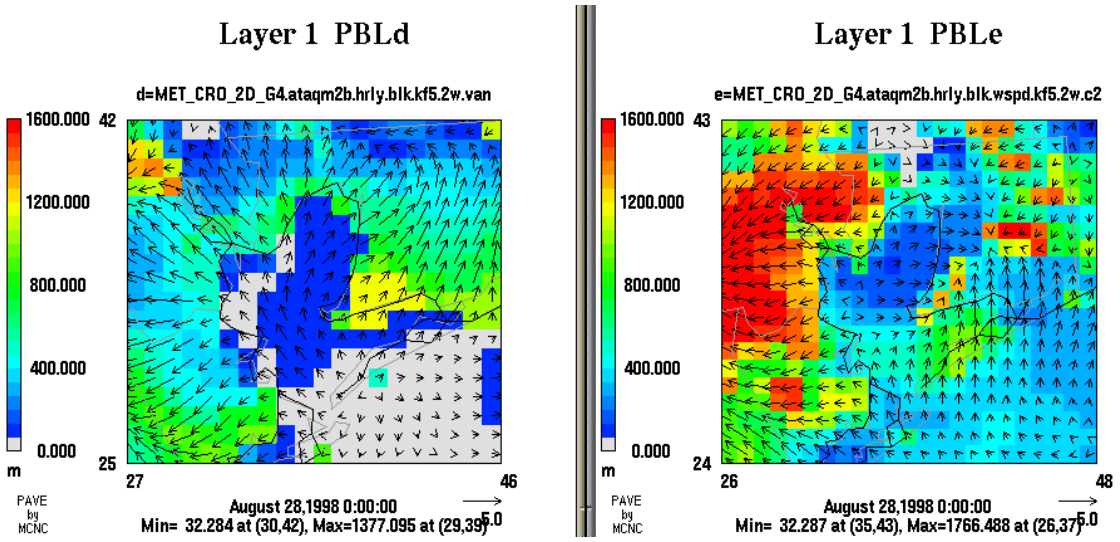

Figure 6.8.35. Modeled boundary layer heights at 0000 UTC on August 28. The uncoupled model is on the left and the coupled model is on the right. Case "kf5.2w" is shown, with wind vectors overlaid. A strongly divergent surface wind out of the Bay is driving strong Bay breezes in the uncoupled model. Onshore Bay flows do exist in the coupled model, but they are weaker.

.

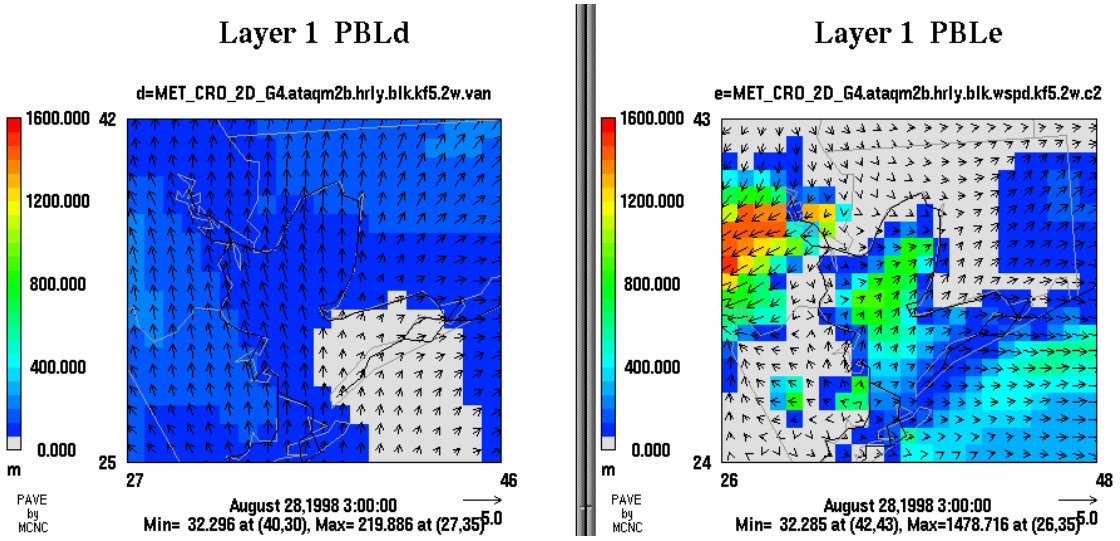

Figure 6.8.36. Modeled boundary layer heights at 0300 UTC on August 28. The uncoupled model is on the left and the coupled model is on the right. Case "kf5.2w" is shown, with wind vectors overlaid. With the collapse of the daytime PBL in the uncoupled model (left), the flow has become rather uniform and onshore. The relative warmth of the Bay has induced a nocturnal PBL in the coupled model, which together with the nocturnal Houston heat-island effect, lead to a much more complex flow regime (right).

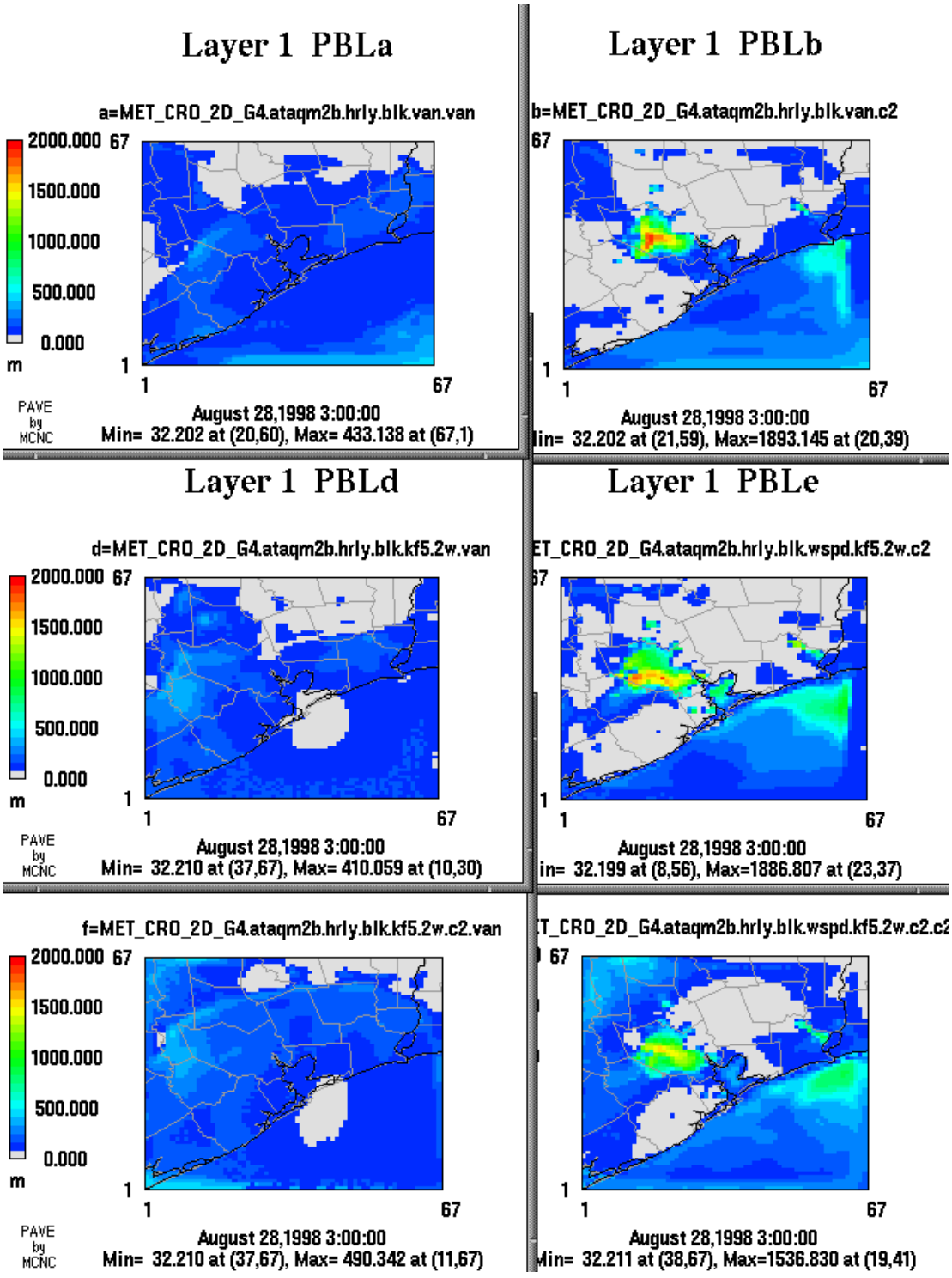

Figure 6.8.37. Modeled boundary layer heights at 0300 UTC on August 28. The uncoupled model is on the left and the coupled model is on the right. The top two panels are case "van", the middle panels are case "kf5.2w", and the bottom panels are case "kf5.2w.c2".

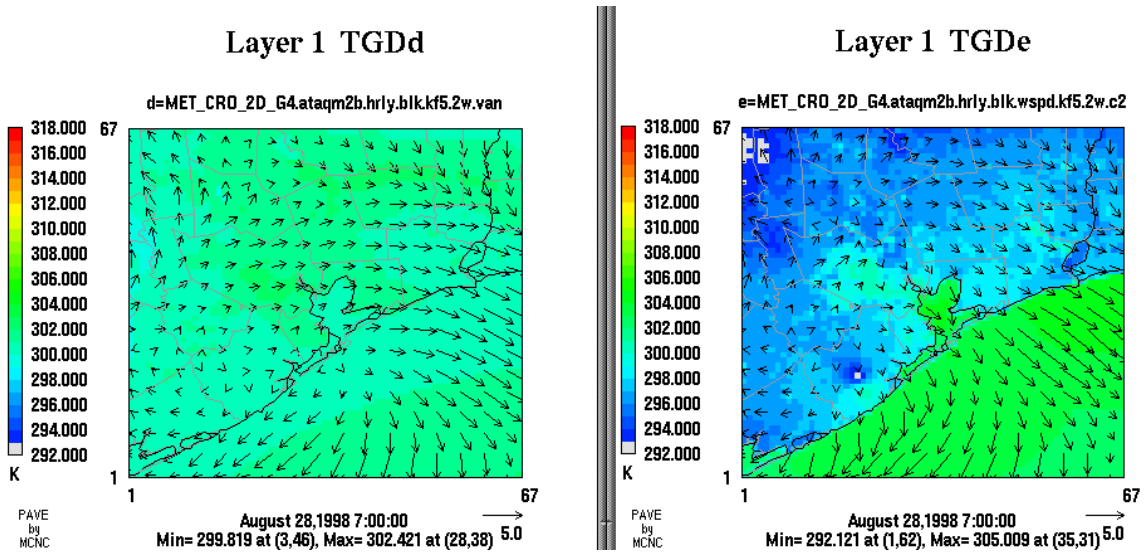

Figure 6.8.38. Modeled skin temperature at 0700 UTC on August 28 for case "kf5.2w." The uncoupled model is on the left. This figure is similar to Figures 6.8.26 and 6.8.15.

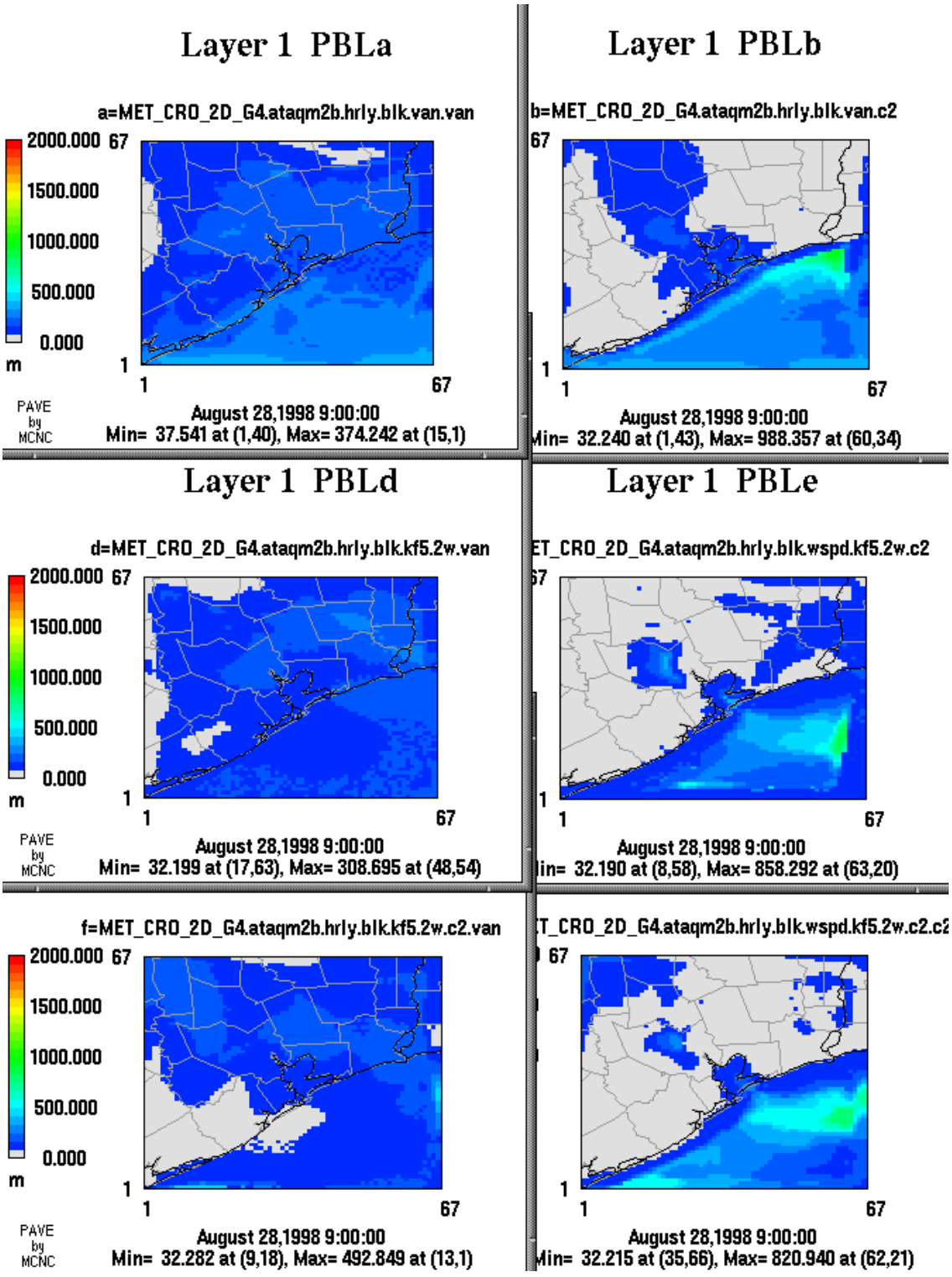

Figure 6.8.39. Modeled boundary layer heights at 0900 UTC on August 28. The uncoupled model is on the left and the coupled model is on the right. The top two panels are case "van", the middle panels are case "kf5.2w", and the bottom panels are case "kf5.2w.c2". The modeled character of the nocturnal PBL closely resembles the previous four nights for both the coupled and uncoupled models.

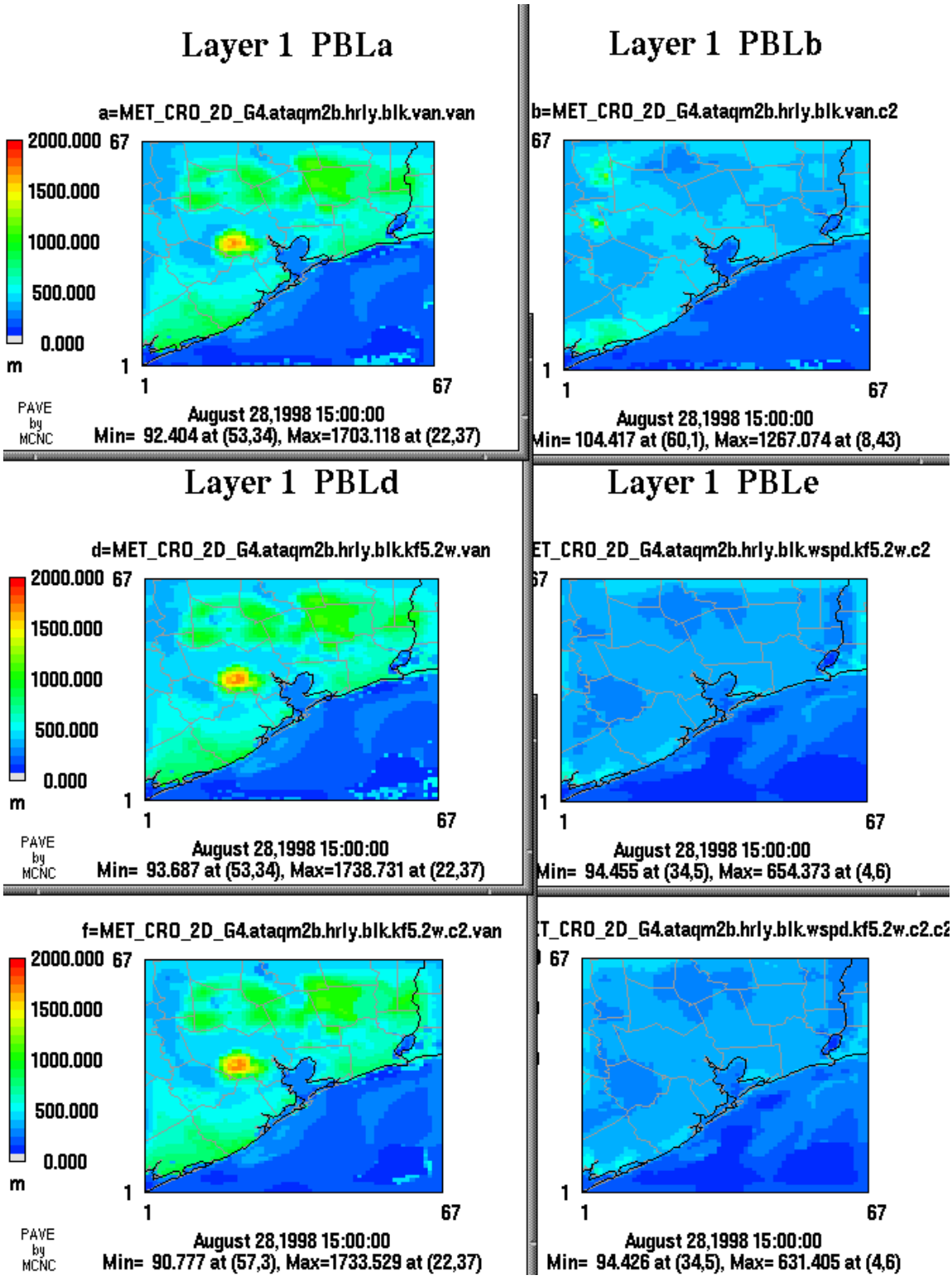

Figure 6.8.40. Modeled boundary layer heights at 1500 UTC on August 28. The uncoupled model is on the left and the coupled model is on the right. The top two panels are case "van", the middle panels are case "kf5.2w", and the bottom panels are case "kf5.2w.c2". Compared with the morning of August 27 (Figure 6.8.28), the coupled model PBL is somewhat closer in depth to that of the uncoupled model.

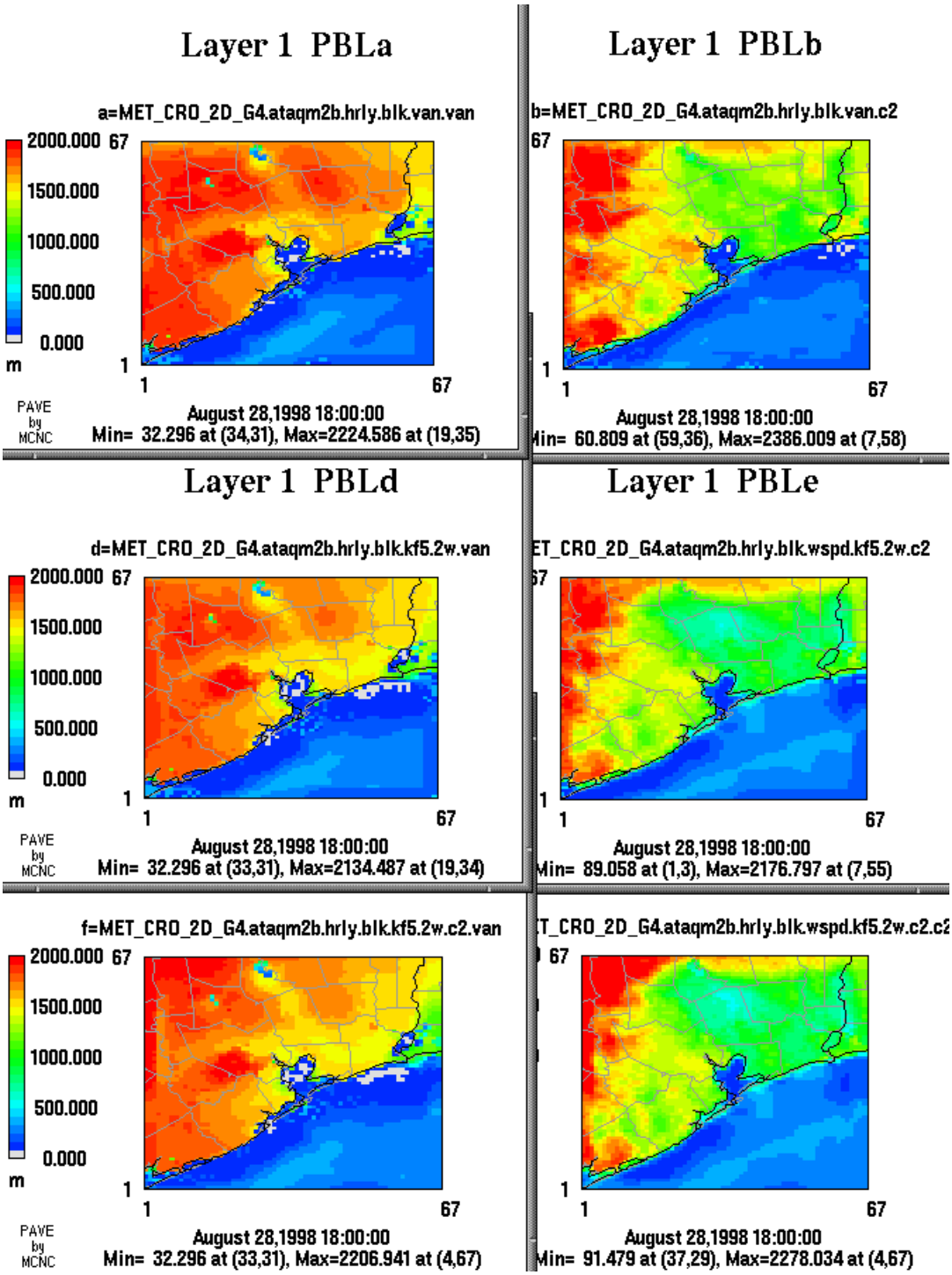

Figure 6.8.41. Modeled boundary layer heights at 1800 UTC on August 28. The uncoupled model is on the left and the coupled model is on the right. The top two panels are case "van", the middle panels are case "kf5.2w", and the bottom panels are case "kf5.2w.c2". In the coupled model, the highest PBL heights are restricted to the western half of the domain, in stark contrast to the uncoupled model. In addition, the uncoupled model reveals a "daytime" Houston heat-island whose plume appears to be advecting weakly southwestward.

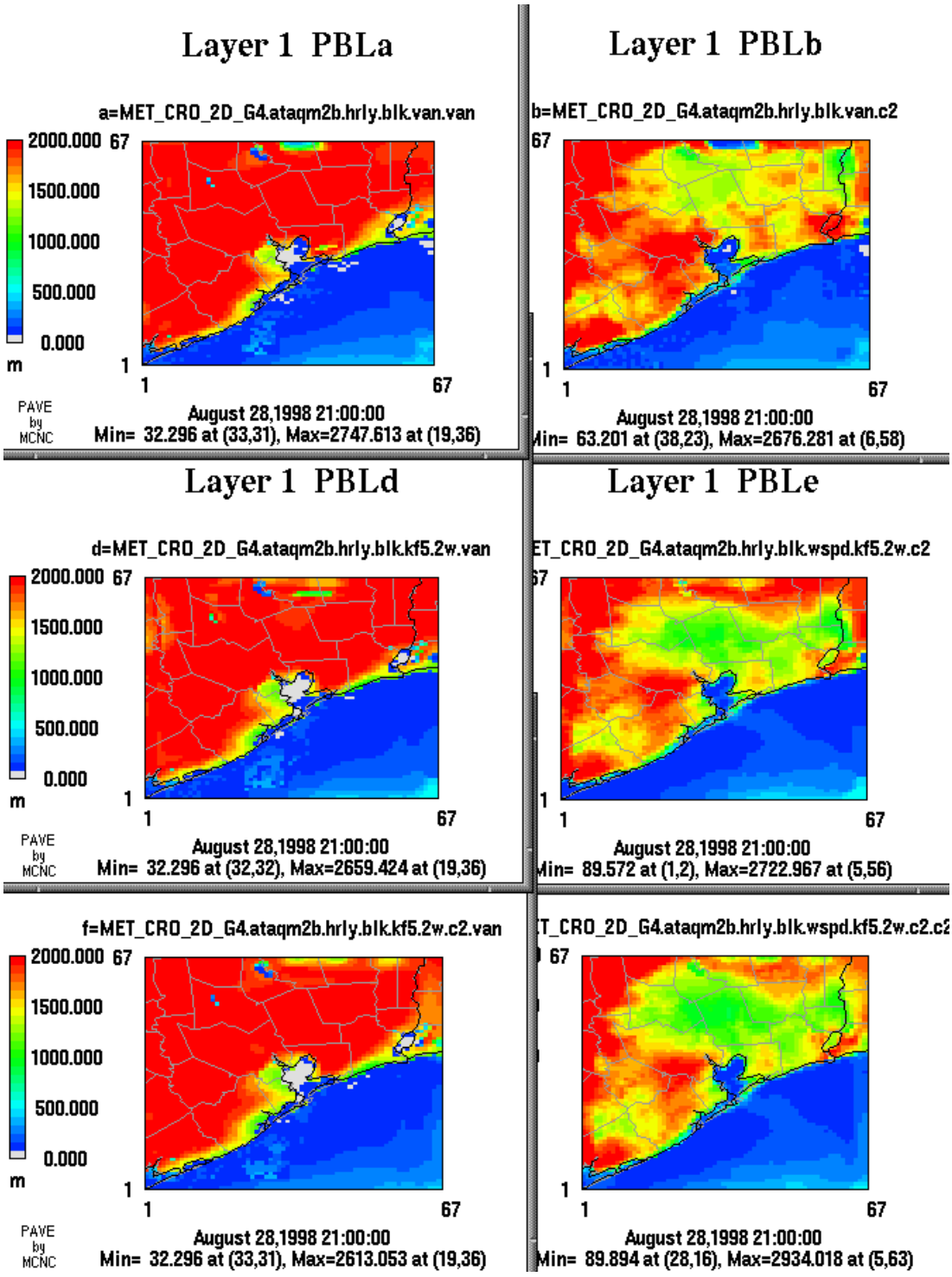

Figure 6.8.42. Modeled boundary layer heights at 2100 UTC on August 28. The uncoupled model is on the left and the coupled model is on the right. The top two panels are case "van", the middle panels are case "kf5.2w", and the bottom panels are case "kf5.2w.c2". Mean heights well exceed 2000 m in the uncoupled model (left), but remain somewhat lower over the forested areas northwest of Houston in the coupled model.

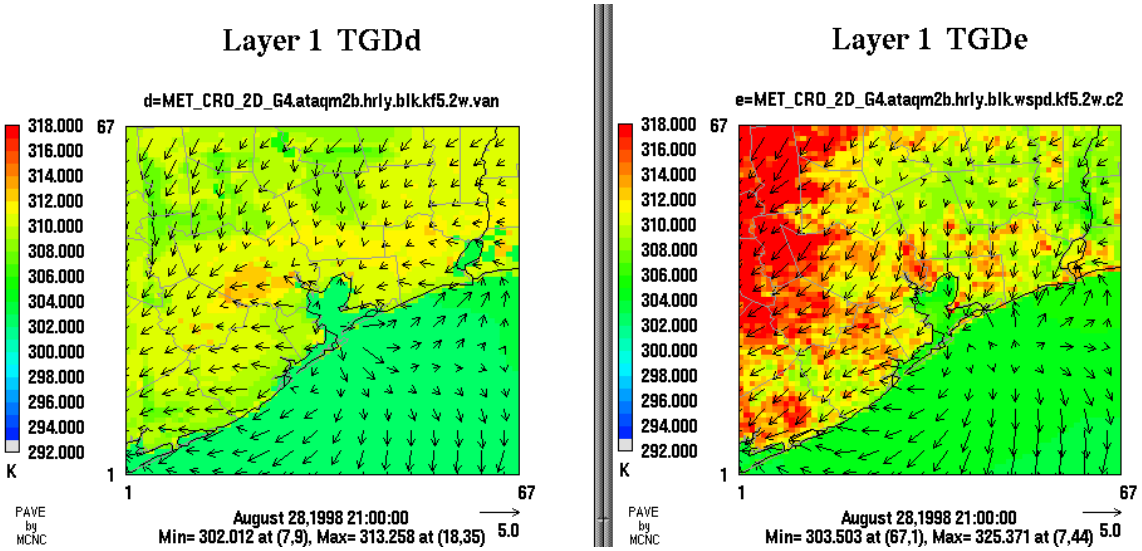

Figure 6.8.43. Modeled skin temperature at 2100 UTC on August 28 for case "kf5.2w." The uncoupled model is on the left. The coupled model skin temperature correlates well in space with its PBL heights (right panels, this figure and Figure 6.8.42).

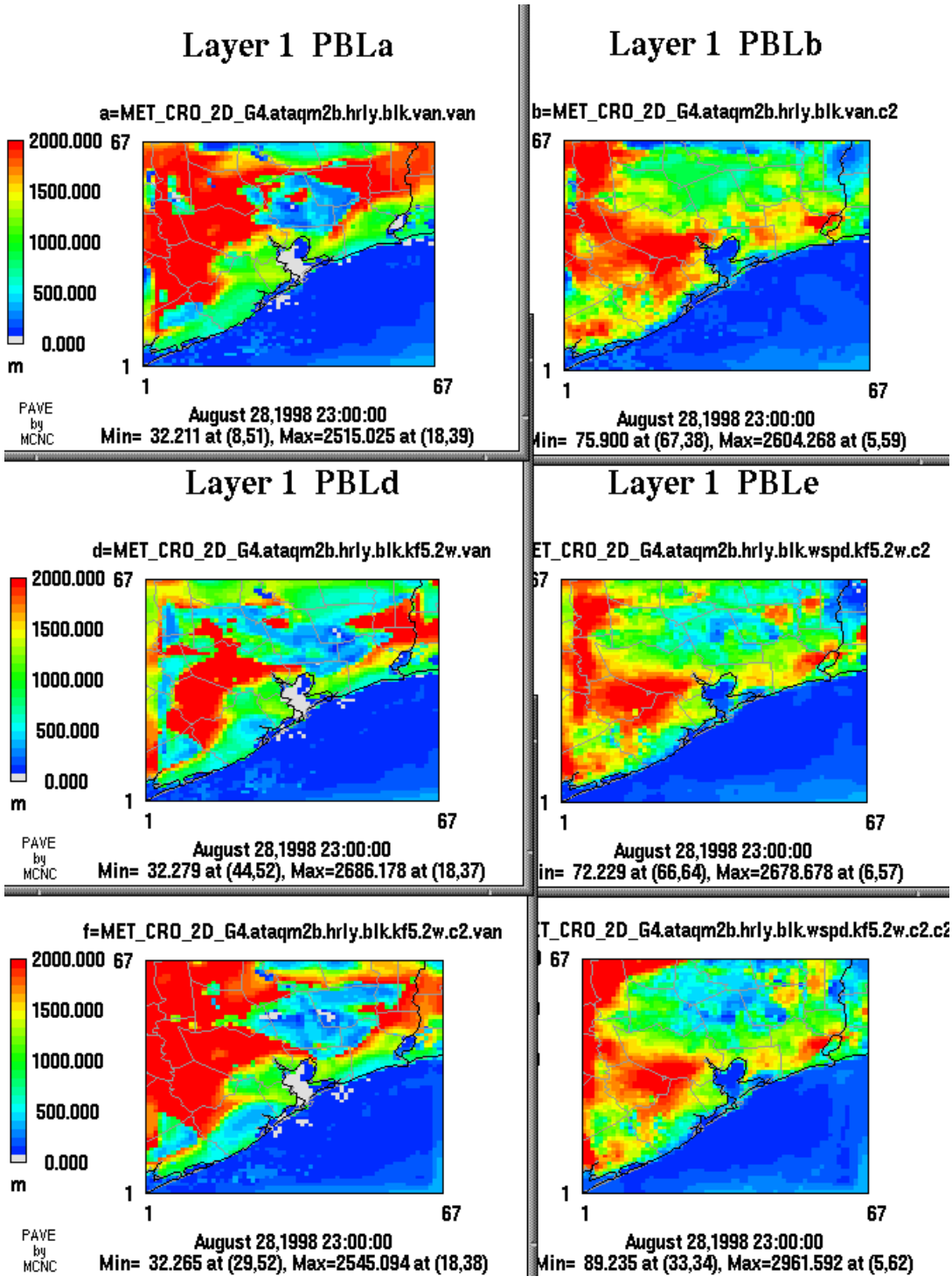

Figure 6.8.44. Modeled boundary layer heights at 2300 UTC on August 28. The uncoupled model is on the left and the coupled model is on the right. The top two panels are case "van", the middle panels are case "kf5.2w", and the bottom panels are case "kf5.2w.c2". Spurious clouds are again present in all of the uncoupled runs and in the "kf5.2w.c2" coupled run.

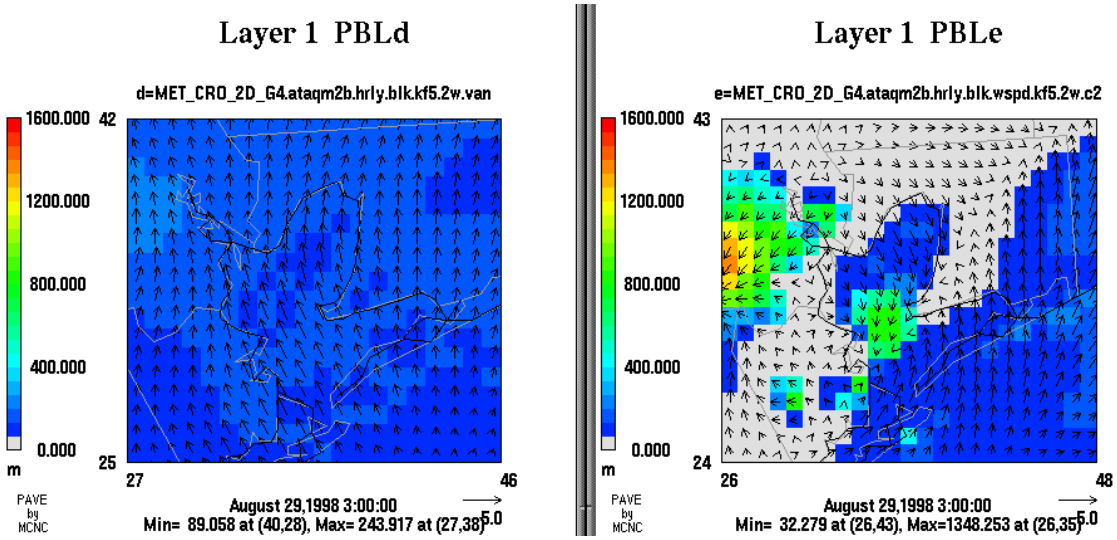

Figure 6.8.45. Modeled boundary layer heights at 0300 UTC on August 29. The uncoupled model is on the left and the coupled model is on the right. Case "kf5.2w" is shown, with wind vectors overlaid. Similar to this time on August 28 (Figure 6.8.36), the relative warmth of the Bay has induced a nocturnal PBL in the coupled model, which together with the nocturnal Houston heat-island effect lead to a much more complex flow regime (right).

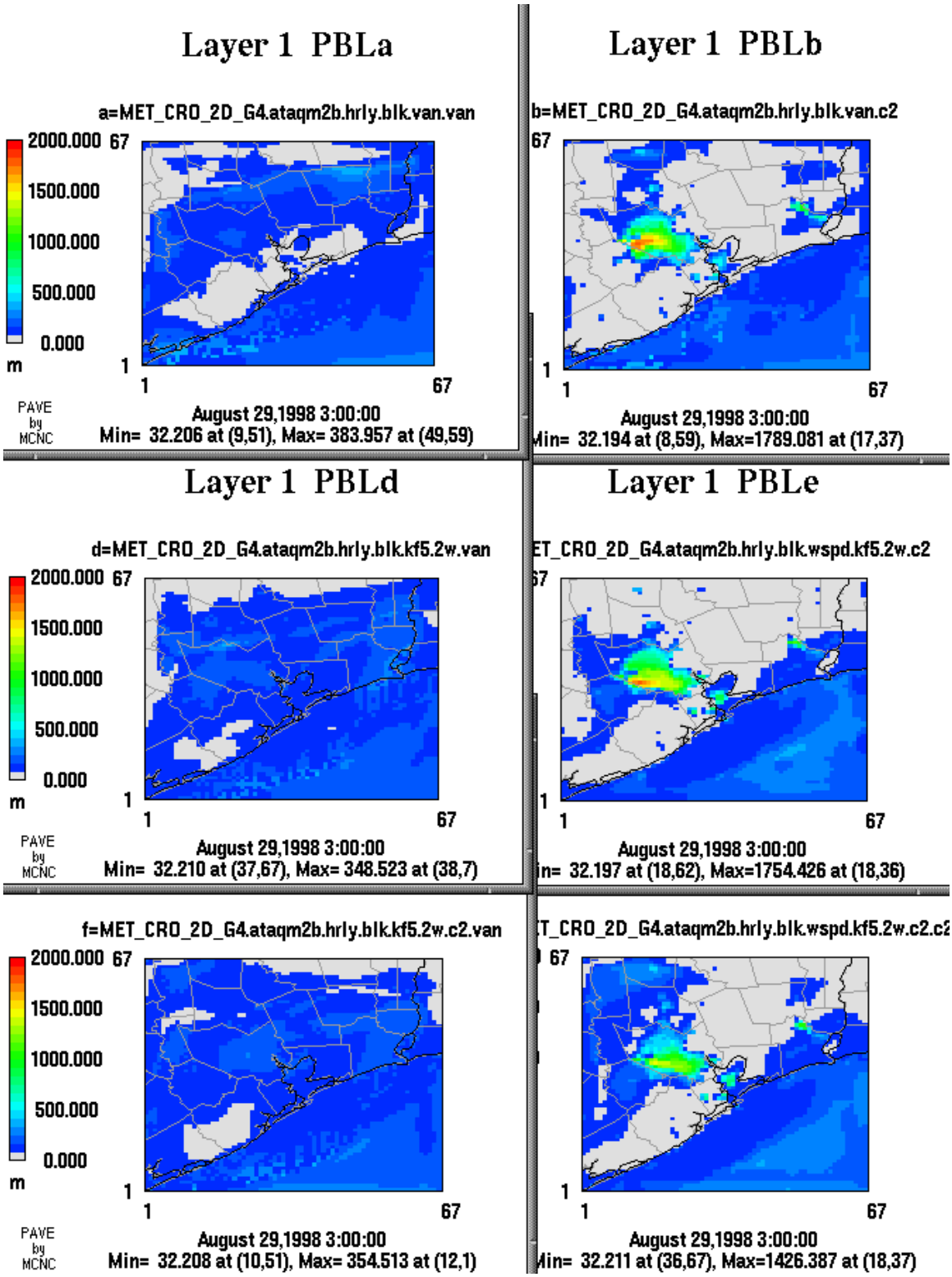

Figure 6.8.46. Modeled boundary layer heights at 0300 UTC on August 29. The uncoupled model is on the left and the coupled model is on the right. The top two panels are case "van", the middle panels are case "kf5.2w", and the bottom panels are case "kf5.2w.c2".

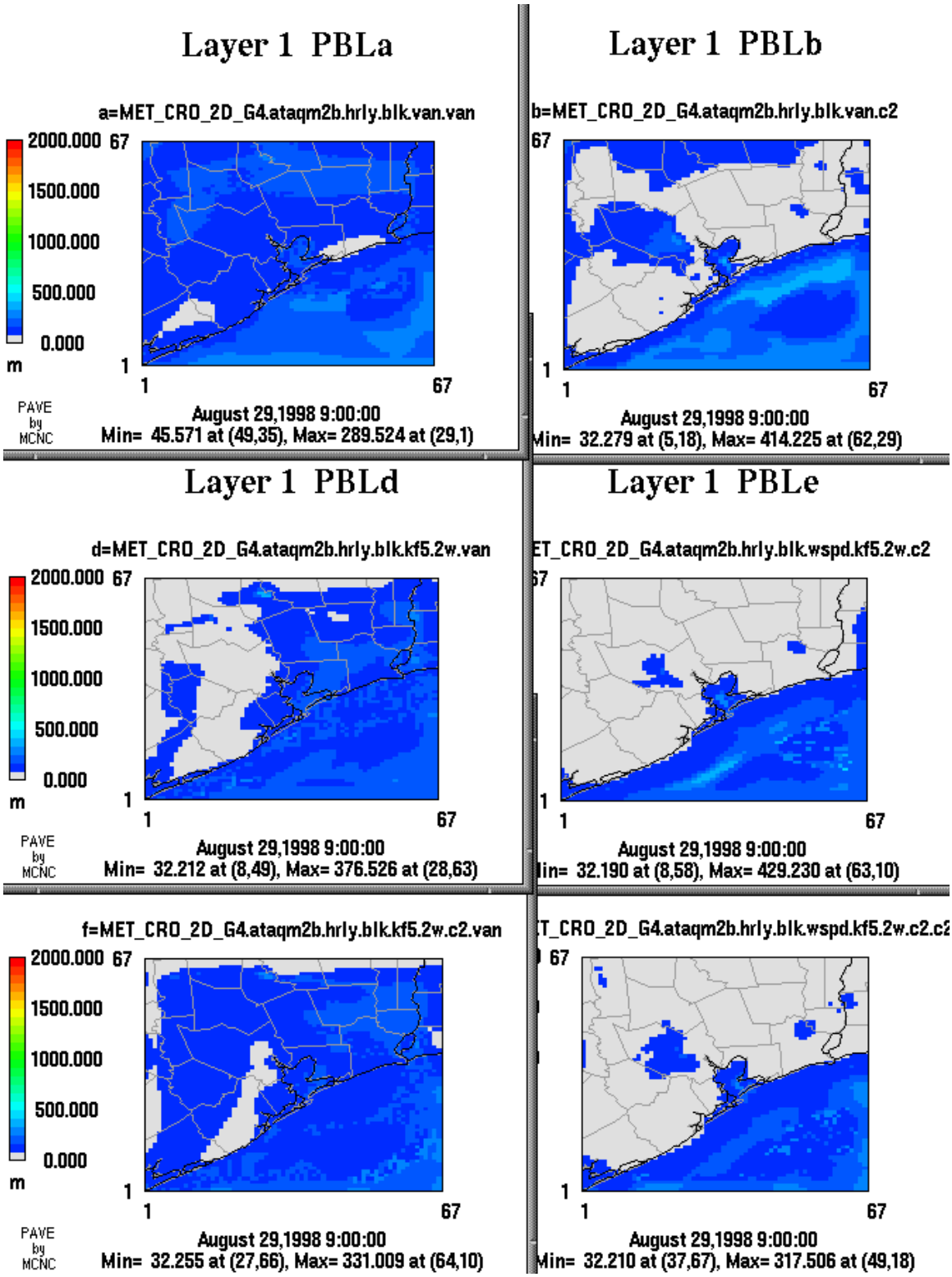

Figure 6.8.47. Modeled boundary layer heights at 0900 UTC on August 29. The uncoupled model is on the left and the coupled model is on the right. The top two panels are case "van", the middle panels are case "kf5.2w", and the bottom panels are case "kf5.2w.c2".

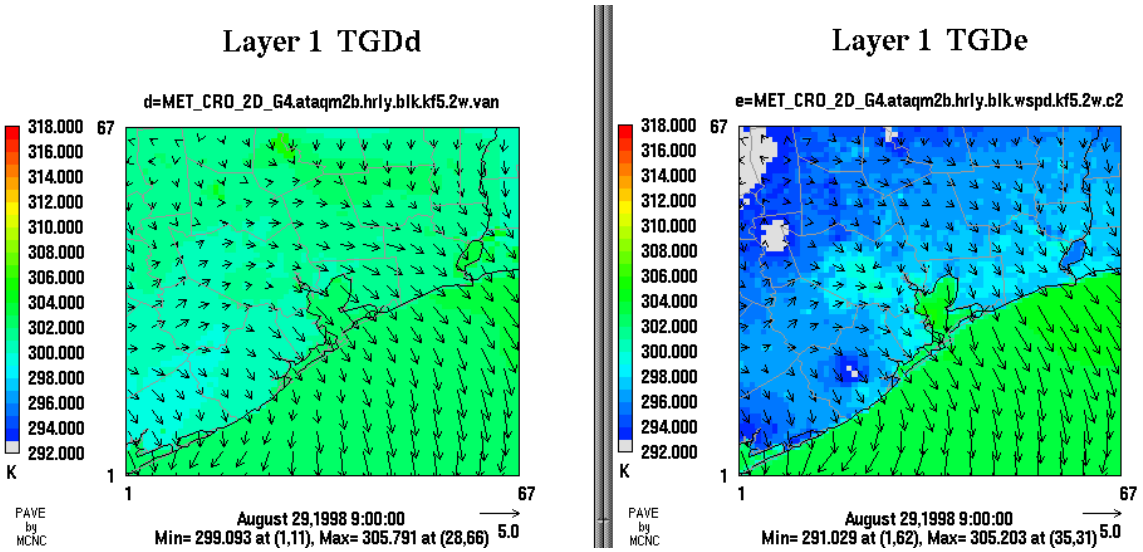

Figure 6.8.48. Modeled skin temperature at 0900 UTC on August 29 for case "kf5.2w." The uncoupled model is on the left.

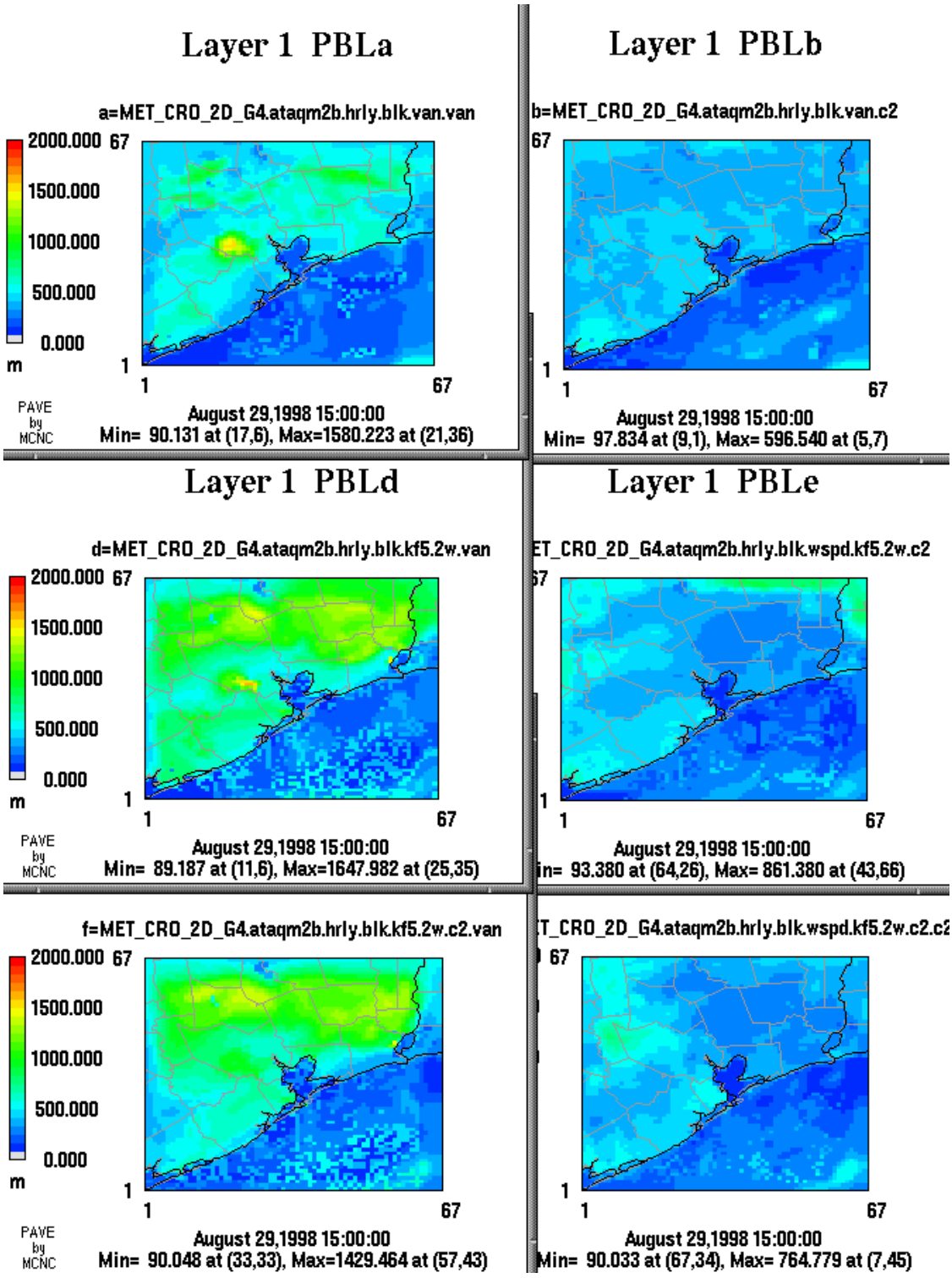

Figure 6.8.49. Modeled boundary layer heights at 1500 UTC on August 29. The uncoupled model is on the left and the coupled model is on the right. The top two panels are case "van", the middle panels are case "kf5.2w", and the bottom panels are case "kf5.2w.c2".

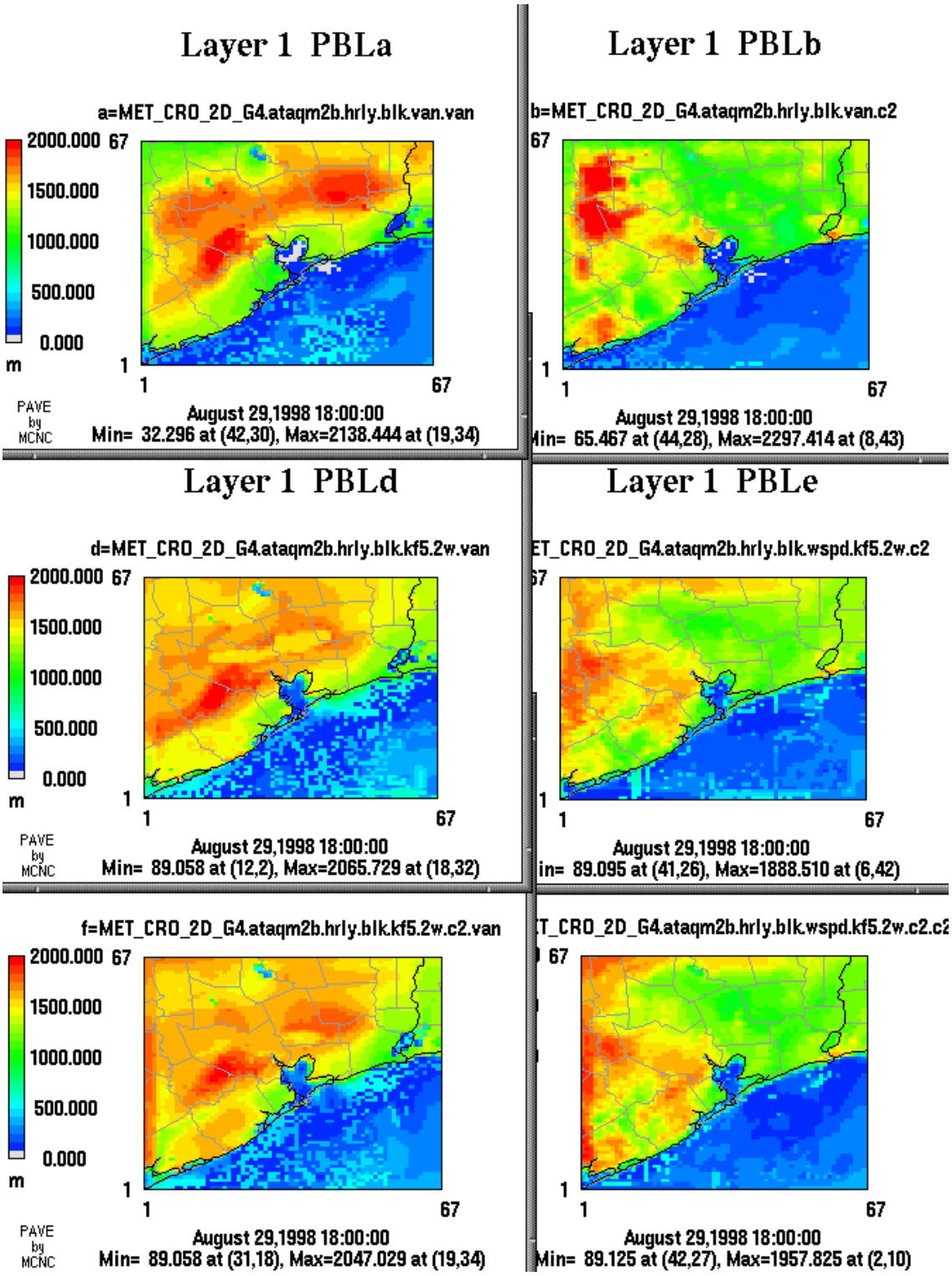

Figure 6.8.50. Modeled boundary layer heights at 1800 UTC on August 29. The uncoupled model is on the left and the coupled model is on the right. The top two panels are case "van", the middle panels are case "kf5.2w", and the bottom panels are case "kf5.2w.c2". Similar to previous days, the coupled model PBL heights are somewhat lower over the forested areas to the northwest of Houston.

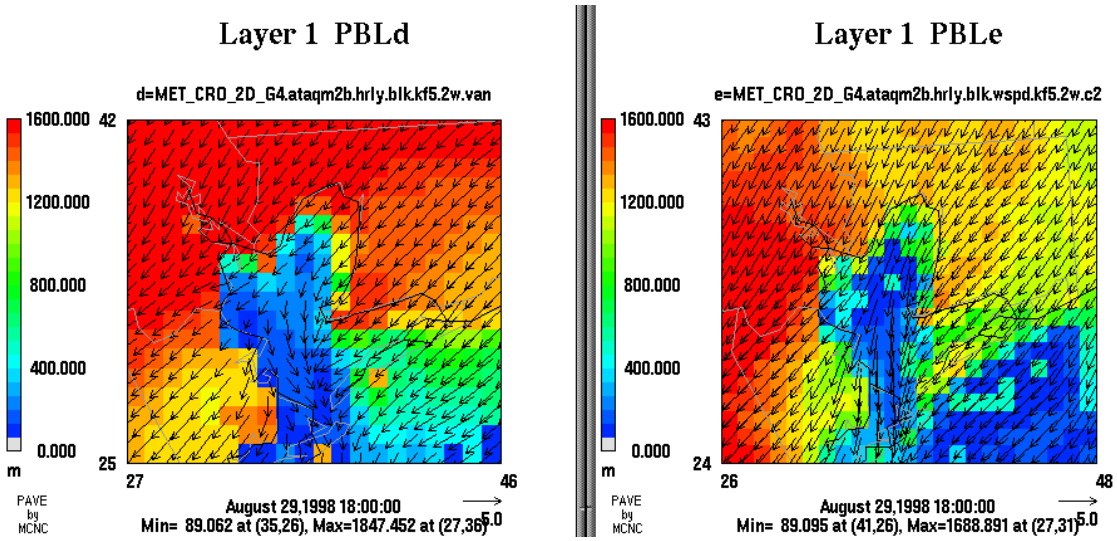

Figure 6.8.51. Modeled boundary layer heights at 1800 UTC on August 29. The uncoupled model is on the left and the coupled model is on the right. Case "kf5.2w" is shown, with wind vectors overlaid. Channeling outflow from the Bay is again evident in the uncoupled model, whereas the flow is more uniform in the coupled model.

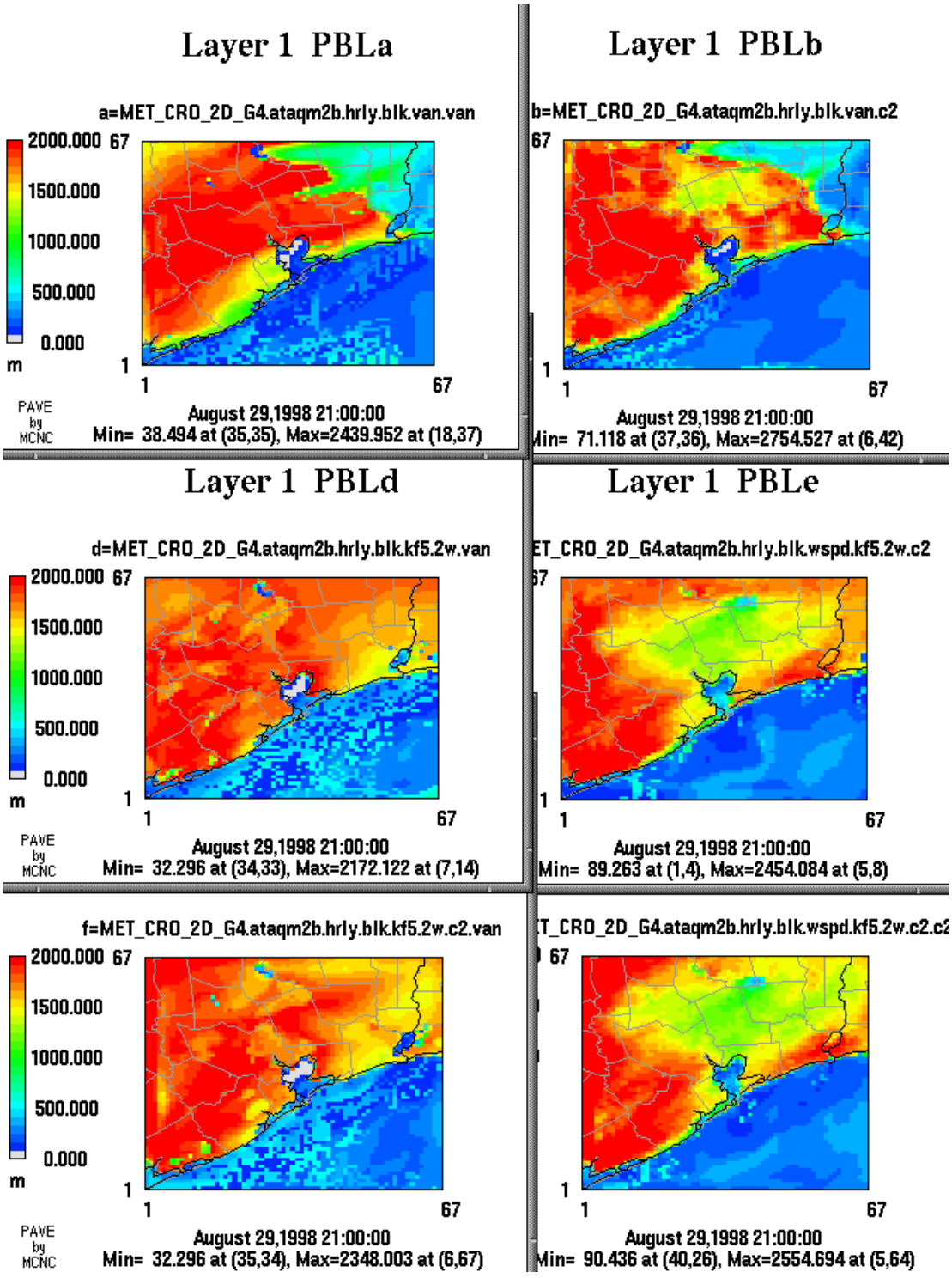

Figure 6.8.52. Modeled boundary layer heights at 2100 UTC on August 29. The uncoupled model is on the left and the coupled model is on the right. The top two panels are case "van", the middle panels are case "kf5.2w", and the bottom panels are case "kf5.2w.c2". The effects of the 36 km-12 km spurious KF-cloud boundary condition problem can be seen in the top panels, as air rapidly advances southwestward. (This was not observed in nature).

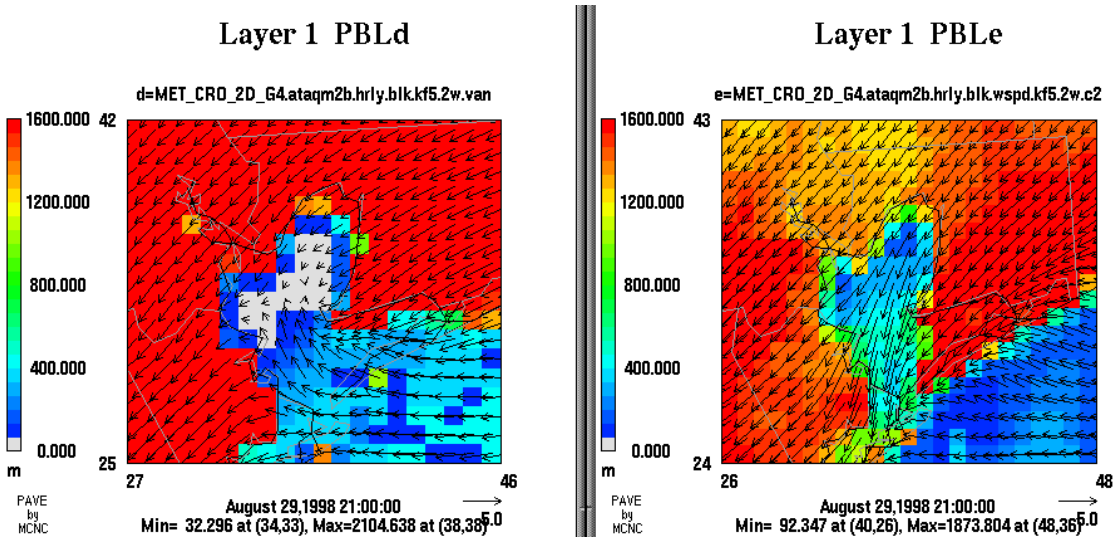

Figure 6.8.53. Modeled boundary layer heights at 2100 UTC on August 29. The uncoupled model is on the left and the coupled model is on the right. Case "kf5.2w" is shown, with wind vectors overlaid. The PBL has again collapsed under the influence of negative sensible heat fluxes in the uncoupled model.

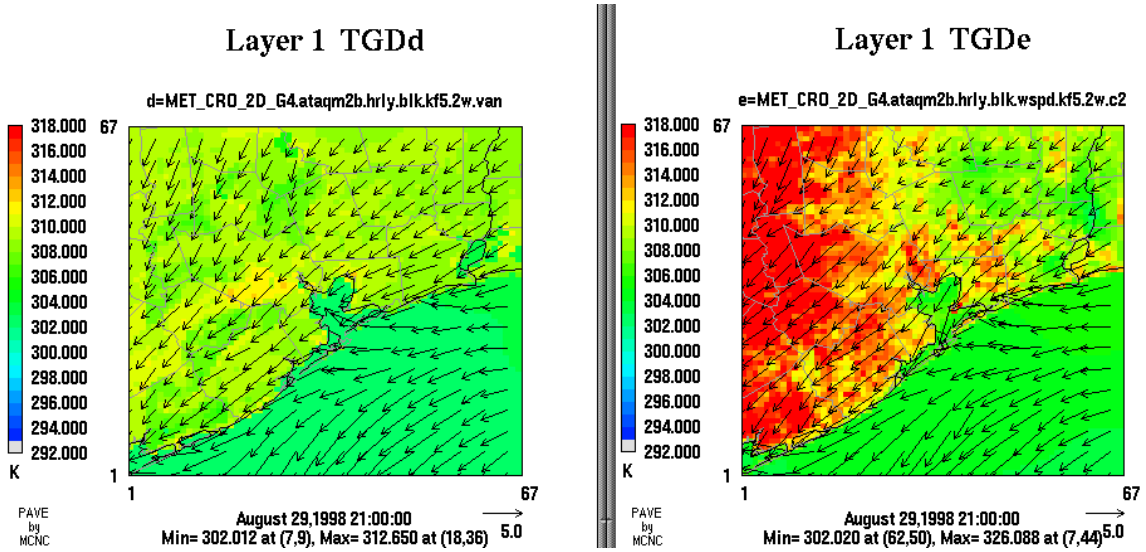

Figure 6.8.54. Modeled skin temperature at 2100 UTC on August 29 for case "kf5.2w." The uncoupled model is on the left. This was the highest ozone day of the episode.

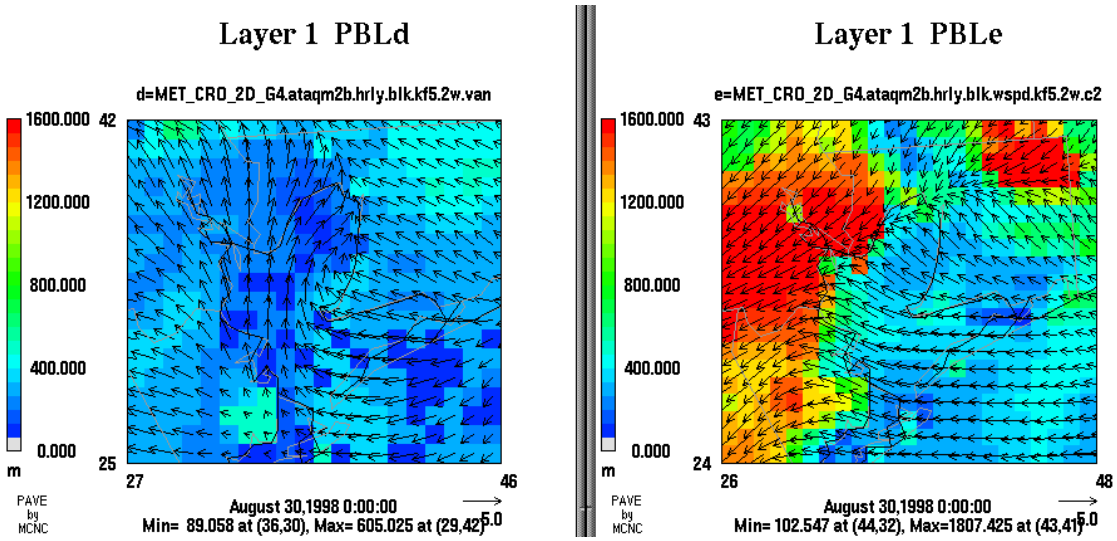

Figure 6.8.55. Modeled boundary layer heights at 0000 UTC on August 30. The uncoupled model is on the left and the coupled model is on the right. Case "kf5.2w" is shown, with wind vectors overlaid. The sea-breeze front has progressed farther inland in the uncoupled model (see Figure 6.6.9).

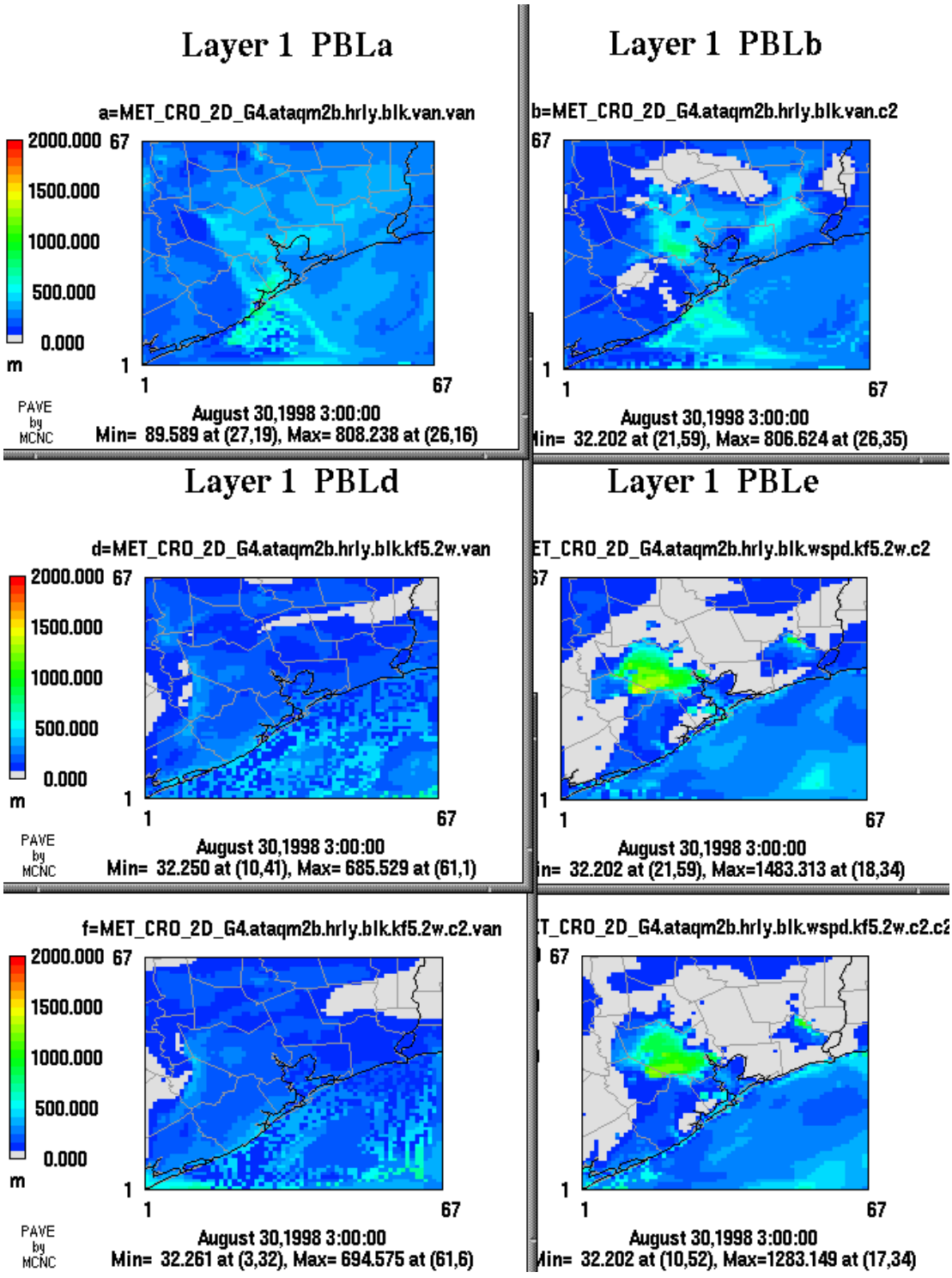

Figure 6.8.56. Modeled boundary layer heights at 0300 UTC on August 30. The uncoupled model is on the left and the coupled model is on the right. The top two panels are case "van", the middle panels are case "kf5.2w", and the bottom panels are case "kf5.2w.c2". In case "van", the convergence of the spurious KF-generated boundary conditions is evident in both models. The nocturnal heat island stands out in the bottom two panels for the coupled model (right).

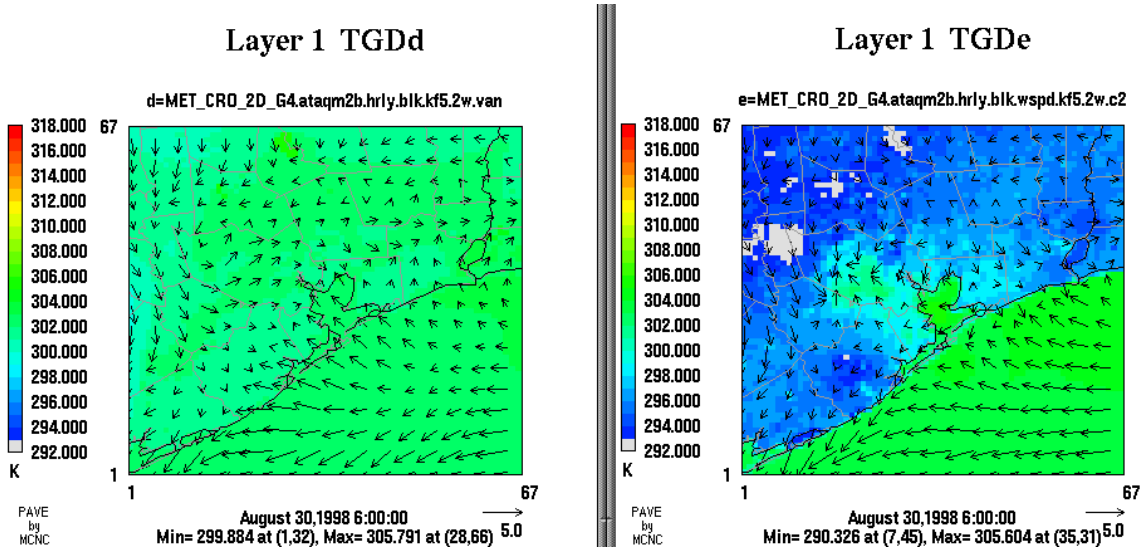

Figure 6.8.57. Modeled skin temperature at 0600 UTC on August 30 for case "kf5.2w." The uncoupled model is on the left.

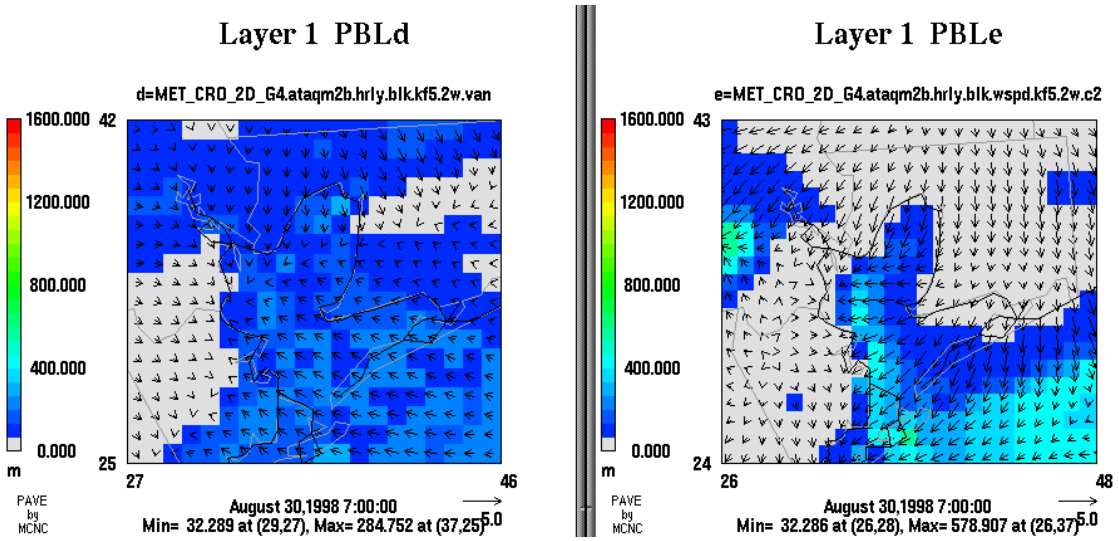

Figure 6.8.58. Modeled boundary layer heights at 0700 UTC on August 30. The uncoupled model is on the left and the coupled model is on the right. Case "kf5.2w" is shown, with wind vectors overlaid. Variability in Bay and sea-surface temperatures in the coupled model play a role in the nocturnal PBL and low-level flow structure as shown in the right panel.

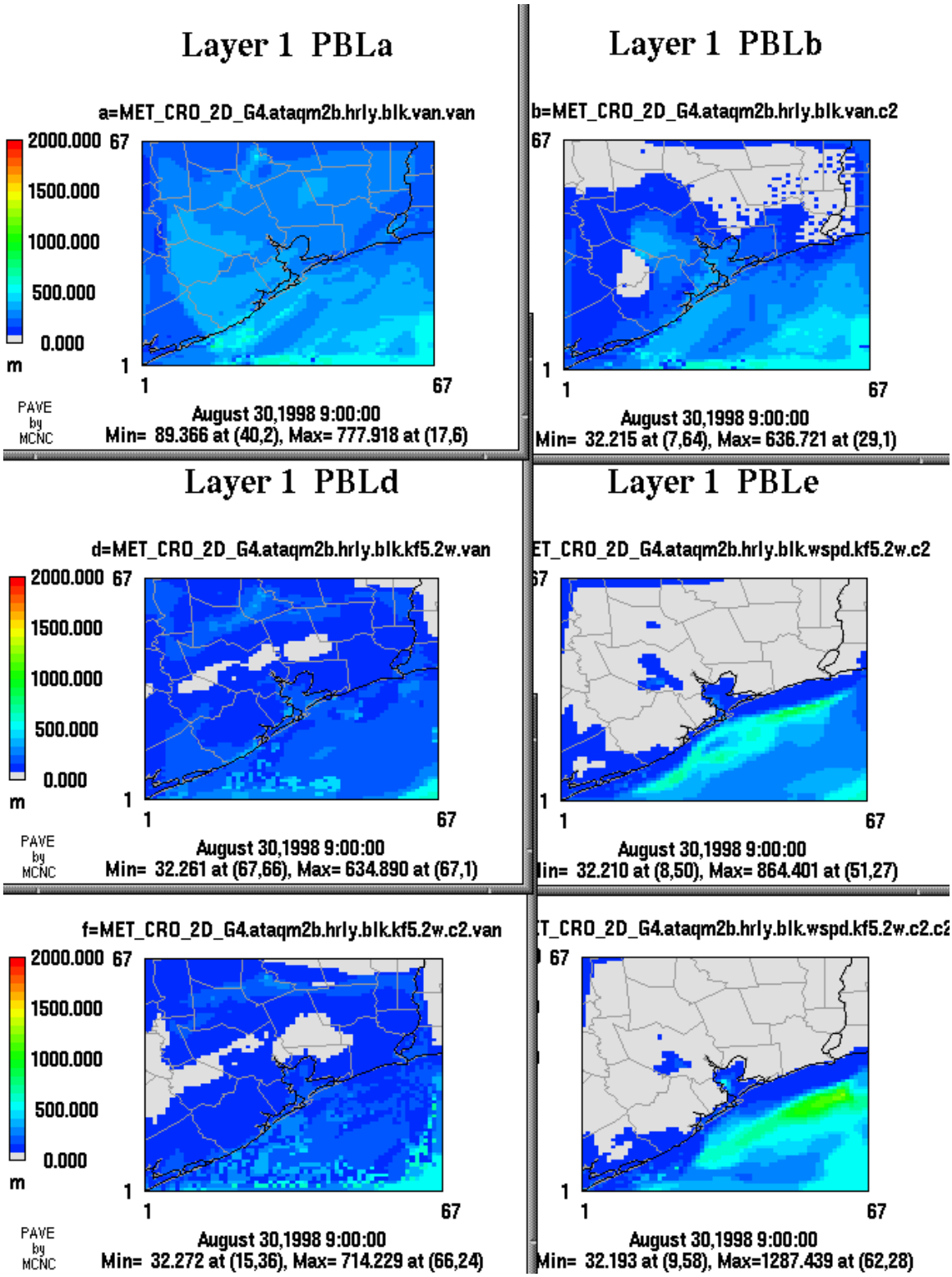

Figure 6.8.59. Modeled boundary layer heights at 0900 UTC on August 30. The uncoupled model is on the left and the coupled model is on the right. The top two panels are case "van", the middle panels are case "kf5.2w", and the bottom panels are case "kf5.2w.c2".

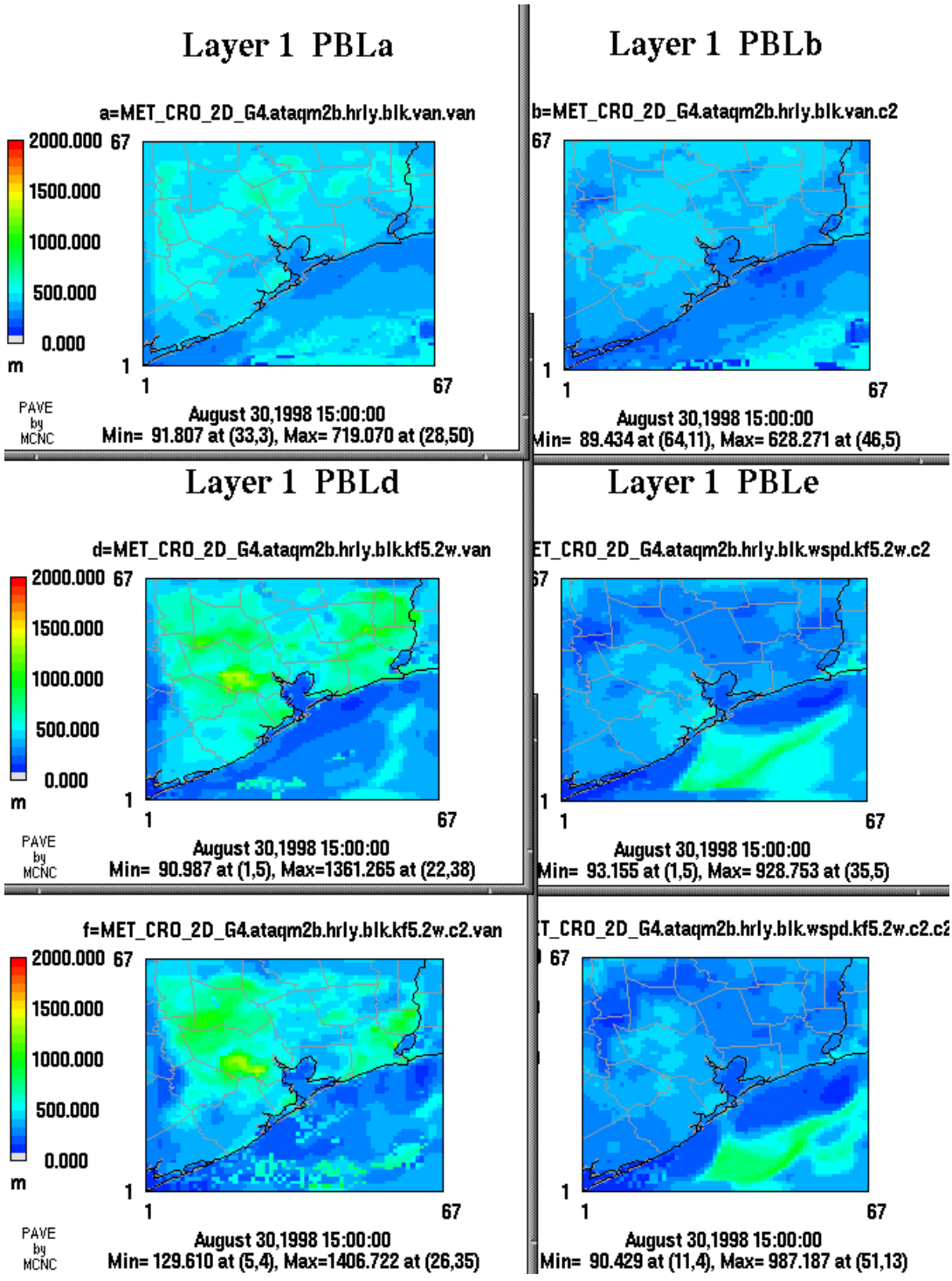

Figure 6.8.60. Modeled boundary layer heights at 1500 UTC on August 30. The uncoupled model is on the left and the coupled model is on the right. The top two panels are case "van", the middle panels are case "kf5.2w", and the bottom panels are case "kf5.2w.c2".

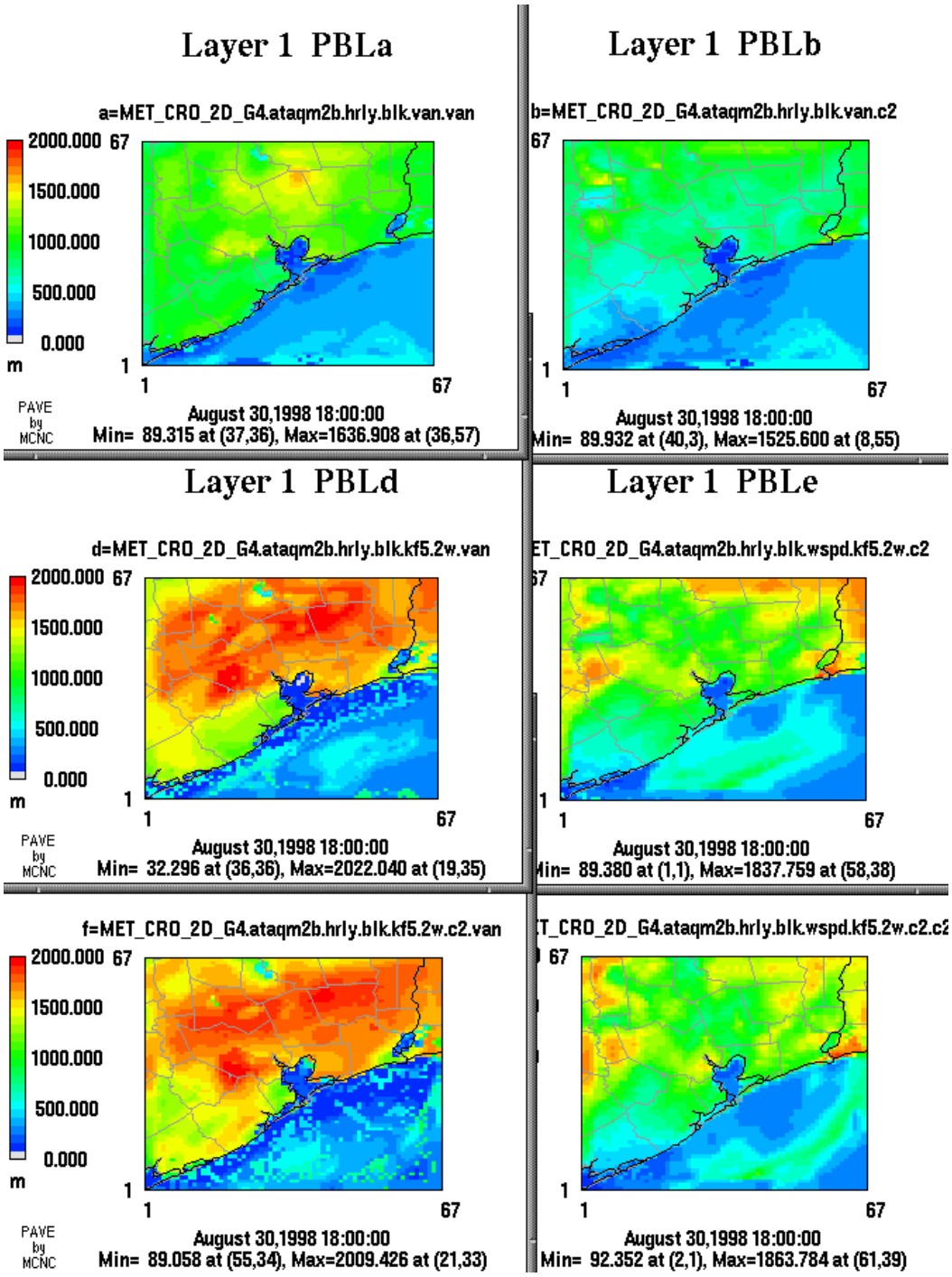

Figure 6.8.61. Modeled boundary layer heights at 1800 UTC on August 30. The uncoupled model is on the left and the coupled model is on the right. The top two panels are case "van", the middle panels are case "kf5.2w", and the bottom panels are case "kf5.2w.c2". In the left-hand panels, the differences in boundary conditions between the "van" case and the "kf5.2w" case result in differences in PBL heights. In the right-hand panels, the same boundary conditions appear to advect lower (top panel)/higher (bottom panel) PBL air into the domain.

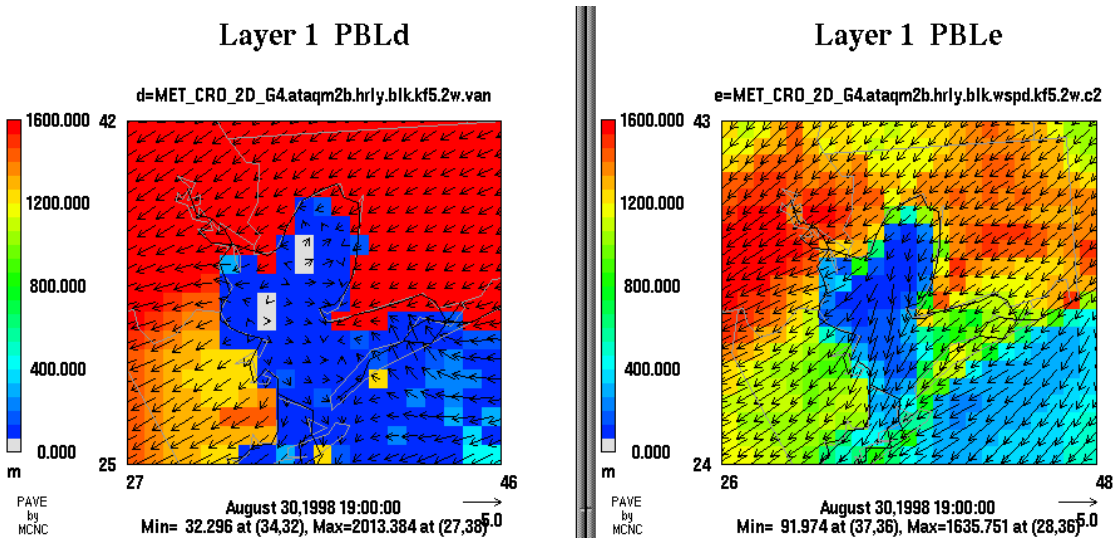

Figure 6.8.62. Modeled boundary layer heights at 1900 UTC on August 30. The uncoupled model is on the left and the coupled model is on the right. Case "kf5.2w" is shown, with wind vectors overlaid. The flow is again stagnant under a nearly collapsed PBL in the uncoupled model.

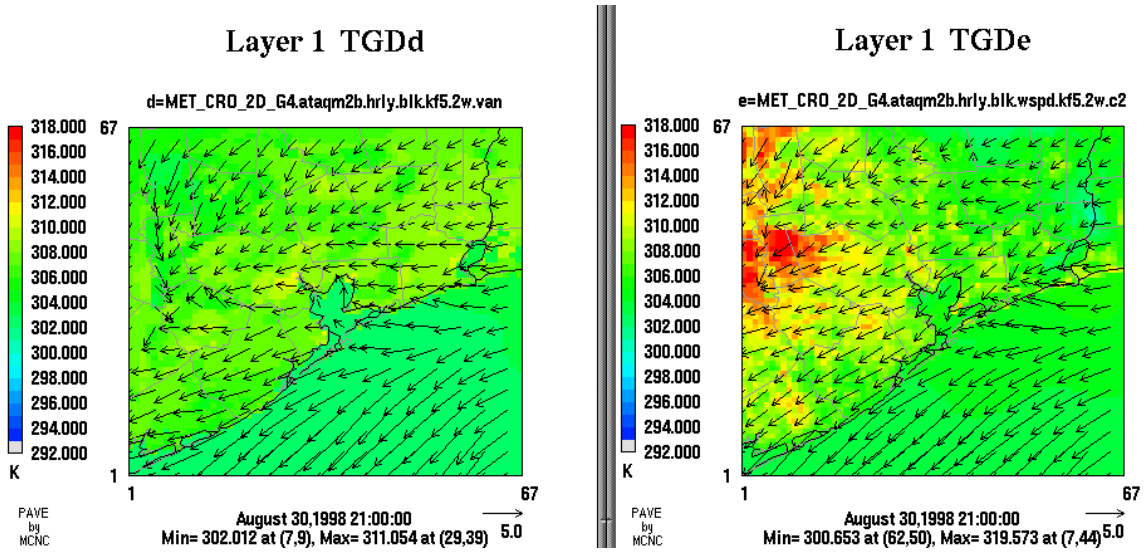

Figure 6.8.63. Modeled skin temperature at 2100 UTC on August 30 for case "kf5.2w." The uncoupled model is on the left. The skin temperature is not nearly as warm in the coupled model as in the uncoupled model on this day. Observed ozone levels were also significantly lower.

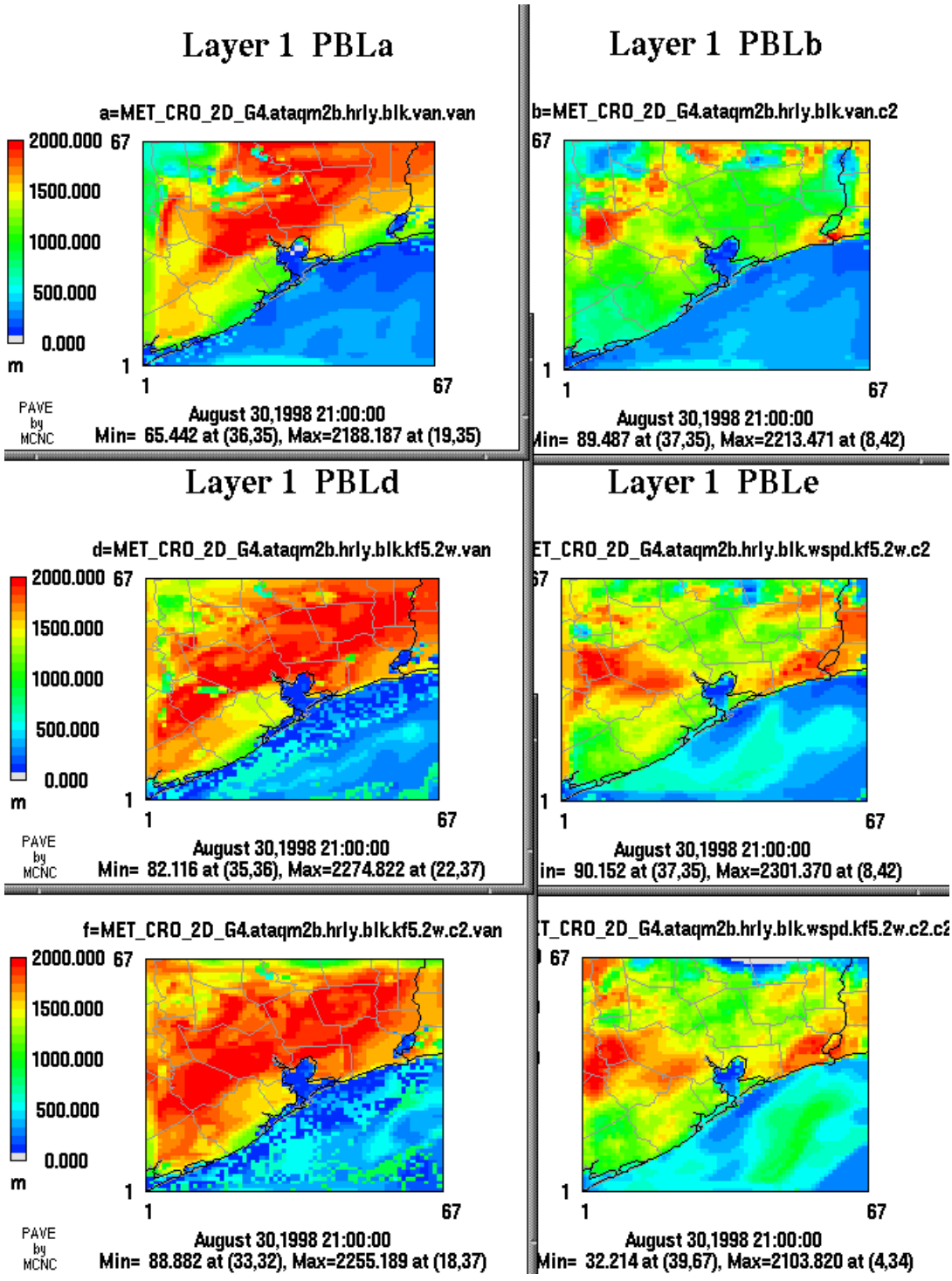

Figure 6.8.64. Modeled boundary layer heights at 2100 UTC on August 30. The uncoupled model is on the left and the coupled model is on the right. The top two panels are case "van", the middle panels are case "kf5.2w", and the bottom panels are case "kf5.2w.c2".

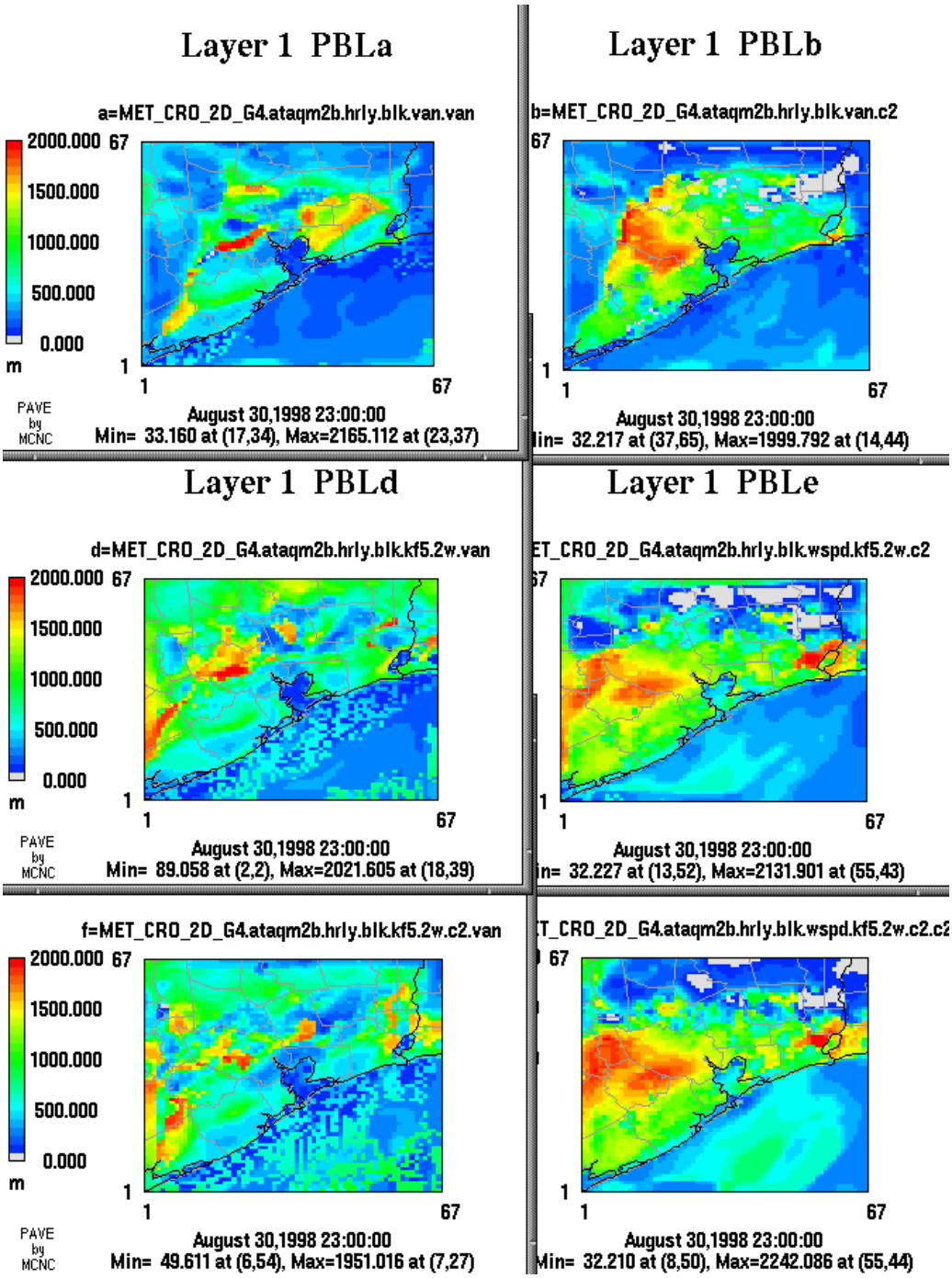

Figure 6.8.65. Modeled boundary layer heights at 2300 UTC on August 30. The uncoupled model is on the left and the coupled model is on the right. The top two panels are case "van", the middle panels are case "kf5.2w", and the bottom panels are case "kf5.2w.c2". Again, differences between the "van" runs and the "kf5.2w" runs reveal surprising boundary effects. In the top panels, more stable air appears to be advecting in from the north, whereas in the other two runs, it does not. Darker blue areas in the northern part of the domain in the "kf5.2w" runs, for the coupled model (right) are due to clouds. Clouds have also cut away the previously high PBL heights in the uncoupled model.

6.9 Radar Wind Profile Analysis

Radar Wind Profiler (RWP) data at Ellington Field (EFD) were obtained from TNRCC (Lambeth, 2002) for the August 25-30, 1998, period. Only one hour of data was available on August 30, 1998, so no analysis for that day was performed. These data provide half-hourly wind speed and direction profiles to support analysis of the time-height performance of the coupled and uncoupled models. The RWP data necessary to analyze PBL heights were not available. Therefore, no comparisons between RWP and modeled PBL heights were made.

This section focuses on comparisons between the vertical wind structure observed at the EFD RWP and that predicted by the coupled and uncoupled model runs, as described in Section 6.1. In the subsections below, the RWP data and model output are organized by the day of the episode, and are presented in Central Standard Time (CST) to match the time convention of the provided RWP data. Only two days of the episode (August 27 and 29) have complete RWP coverage, although discussion is included for the August 25-29 period.

All RWP plots have been prepared with a half-hourly time step (17 and 47 minutes past each hour) and a 192-m vertical spacing up to a maximum altitude of 2828 m MSL. Winds from the 4-km MM5 simulations were extracted from the model output, rotated to real earth coordinates, and estimated at EFD using bilinear interpolation from the four nearest grid cells. The plots for the MM5 winds were also prepared with half-hourly time steps (on the hour and 30 minutes past the hour). The plotted MM5 winds extend to 2997 m MSL with the vertical spacing varying with height. The spacing between the lowest two model layers is approximately 44 m and increases to 210 m for the highest two layers on the plots.

Although the RWP data have undergone automated QA (Lambeth, 2002), they are subject to sporadic contamination that may not be removed by the automated QA process, possibly including, for example, the effects of birds, aircraft, or poor signal strength. Therefore, point-by-point comparisons are not provided, and instead the discussion focuses on general circulation features, including flow transitions/separations and the timing of onshore and offshore flows.

Figures 6.9.1 through 6.9.5 provide day-by-day comparison of the RWP data with the model predictions. These figures are organized with the observed RWP wind plots displayed at the top of the figure. Below the observed winds are six plots showing the modeled winds. The modeled winds plotted on the left side of the figure are for the uncoupled model cases and those on the right side of the figure are for the coupled cases. The three rows of modeled winds represent the three different 36-km 12-km MM5 cases used to establish the lateral boundary conditions for the 4-km simulations. The upper row of wind plots is for the default lateral boundary condition case, “van”, which used one-way nesting between the 36-km and 12-km domains. The middle row is for the two-way nesting simulations with the modified KF downdraft formulation, “kf5.2w”. The lower row is for case “kf5.2w.c2” where TOPLATS/SSATS was coupled with the 12-km domain of the “kf.52w”. The plots shown in Figures 6.9.1 through 6.9.5 are provided in Appendix D as enlargements for added clarity.

6.9.1 August 25

August 25 featured a synoptic-scale flow from the south-southeast, followed by the development of deep convective cells and clusters in the afternoon. As shown in Figure 6.9.1, south-southeasterly flow is observed at EFD between 0000 and 0600 CST, followed by a transition to a weaker easterly flow until the data end at 0900 CST.

The results indicate that between 0000 and 0400 CST, both coupled and uncoupled models are generally in good agreement with the RWP data from 192 m MSL to about 1500 m MSL. Above 1500 m MSL, both models indicate a more easterly flow, in contrast to the south-southeasterly flow indicated by the RWP.

After 0400 CST, all model results indicate a flow transition beginning at the surface and rising over the course of the daytime heating. For the upper model plots (the default boundary conditions; i.e. case "van"), this transition is clearly more distinct and occurs at about the right time (near 0600 CST) in the coupled model (upper right of the six plots in Figure 6.9.1). For the two-way coupled runs, the transition initiates earlier (near 0400 CST) and contains a sharper surface-based wind shift in the coupled runs (lower two right hand plots).

The largest model-to-model differences on this day appear to result from the lateral boundary conditions. The default boundary conditions shown in the upper model plots of Figure 6.9.1 indicate that the area of flow separation is confined to the first 1000 m MSL, with what appears to be a somewhat faster decay in the uncoupled model versus the coupled model. All results using the two-way nested lateral boundary conditions indicate not only an earlier development of this flow separation, but also a much greater depth—approximately 2000 m MSL. The differences between the coupled and uncoupled model for the two-way nested cases do not appear to be significant.

6.9.2 August 26

On August 26, the flow was generally weaker and less southerly than on August 25. This resulted from changes in the synoptic flow pattern discussed previously. As shown in Figure 6.9.2, the EFD RWP indicates a generally southeasterly flow below 1000 m MSL from 0000 CST until about 0600 CST, at which time the flow becomes weaker and more easterly, until the data end at 1100 CST. Above 1000 m MSL, the flow is much stronger and from the east-northeast until about 0300 CST, at which time it becomes southeasterly until 1100 CST.

As with Figure 6.9.1, the upper model plots of Figure 6.9.2 indicate the default lateral boundary conditions for the uncoupled (left) and coupled (right) cases. At the surface, the uncoupled run retains an onshore wind component through about 0400 CST, where the coupled run, is offshore (a land-breeze) for the 12-hour overnight period. The RWP data do not appear to contain surface vectors, so this difference cannot be analyzed. Above 1000 m MSL, neither result reflects the flow from the east-northeast (observed until about 0300 CST), although after 0300 CST, the modeled winds above 1000 m MSL are consistent with the observations.

The middle and lower model plots in Figure 6.9.2 illustrate results of the two-way nested lateral boundary condition tests. These results indicate that the simulated flow below 1000 m MSL is generally too strong and more easterly than that observed at the

EFD RWP. This in turn, seems to result in a shallower area of flow separation from 0300 CST until about 1100 CST, at which time the area of flow separation appears to reach the 1000 m MSL level in all two-way nested simulations.

6.9.3 August 27

August 27 is one of the two dates for which a complete day of RWP data is available. August 27 featured anticyclonic circulation and weak daytime flow in the boundary layer, which contributed to a maximum 1-hour ozone concentration of 203 ppb (at CAMS 35), with four monitors exceeding 124 ppb (CAMS 10, 34, 35, and 53). As shown in Figure 6.9.3, the flow indicated by the EFD RWP below 1000 m MSL is generally south to southwesterly between 0000 and 0600 CST, and becomes weaker and indicates a rotation from westerly to northerly to easterly to southerly between 0600 and 2100 CST. By 2300 CST, the flow is again south to southwesterly and somewhat stronger than during the daytime. Above 1000 m MSL, the flow is generally northeasterly to easterly, with the exception of flow from the southeast between 0000 and 1300 CST above 2000 m MSL. The flow is lighter and more northerly between 1300 and 1800 CST from 1000 m MSL to 2200 m MSL. These direction changes and associated areas of flow separation reflect the growth of the atmospheric boundary layer and its interaction with the sea-land breeze.

As with the previous results, Figure 6.9.3 indicates the results for case "van" in the upper model plots, followed by the two-way nested boundary condition results without and with TOPLATS coupling on the 12-km grid in the middle and bottom model plots. The default lateral boundary condition results in Figure 6.9.3 indicate that neither model is reflective of the RWP observed southwesterly flow below 1000 m MSL between 0000 and 0600 CST, although the magnitudes are consistent. Both default boundary condition model results above 2000 m MSL are consistent with the EFD RWP observations. The most striking improvements due to the coupled model shown by these results are (1) the representation of the northerly flow from 1000 to 2000 m MSL between 1400 and 1800 CST and (2) the representation of the southerly flow from 100 to 800 m MSL between 1700 to 2000 CST.

6.9.4 August 28

On August 28, a very weak, dry, surface trough approached from the northwest, although the flow above 1000 m MSL continued to be fairly strong (10 to 15 m/s) from the northeast, as indicated by the EFD RWP data in Figure 6.9.4.

As shown in Figure 6.9.4, the model results for all configurations are very similar on this day, particularly during daytime hours. The largest differences are seen between the uncoupled (left) and coupled (right) model results in terms of the height of the flow separation area (i.e., the boundary layer height), which is about 200 m higher and more temporally persistent in the coupled model than in the uncoupled model. The other significant difference is the models' behavior between 0000 and 0600 CST. For example, the EFD RWP indicates southwesterly to westerly flow below 1000 m MSL between these hours, which is well-represented in the default lateral boundary condition runs (upper model plots), while the two-way runs reflect either northeasterly or southeasterly flows that are also too weak.

6.9.5 August 29

The highest ozone values of the episode developed on August 29, which featured weak surface flow and a diurnal flow pattern similar to that on August 27, the other high ozone day. As shown in Figure 6.9.5, the EFD RWP winds below 1000 m MSL are generally light and somewhat variable, and seem to organize along the same rotating westerly to northerly to easterly to southerly pattern observed on August 27 during the daytime.

Overall, the model results shown in Figure 6.9.5 reasonably capture the rotating flow observed in the RWP data; however, it appears that only the models with the two-way nested lateral boundary conditions are able to capture the southerly flow observed after 1900 CST, and even so are generally late in capturing this feature. In addition, no model runs reflect the higher wind speeds observed in the early morning and late evening hours between 1800 and 2600 m MSL.

Comparisons between the coupled and uncoupled model results in Figure 6.9.5 reveal that the coupled model seems to capture the observed flow separation area from 0000 to 0600 CST better than the uncoupled model; otherwise, the results are generally similar for this day.

6.9.6 Figures for Section 6.9 (also see Appendix D)

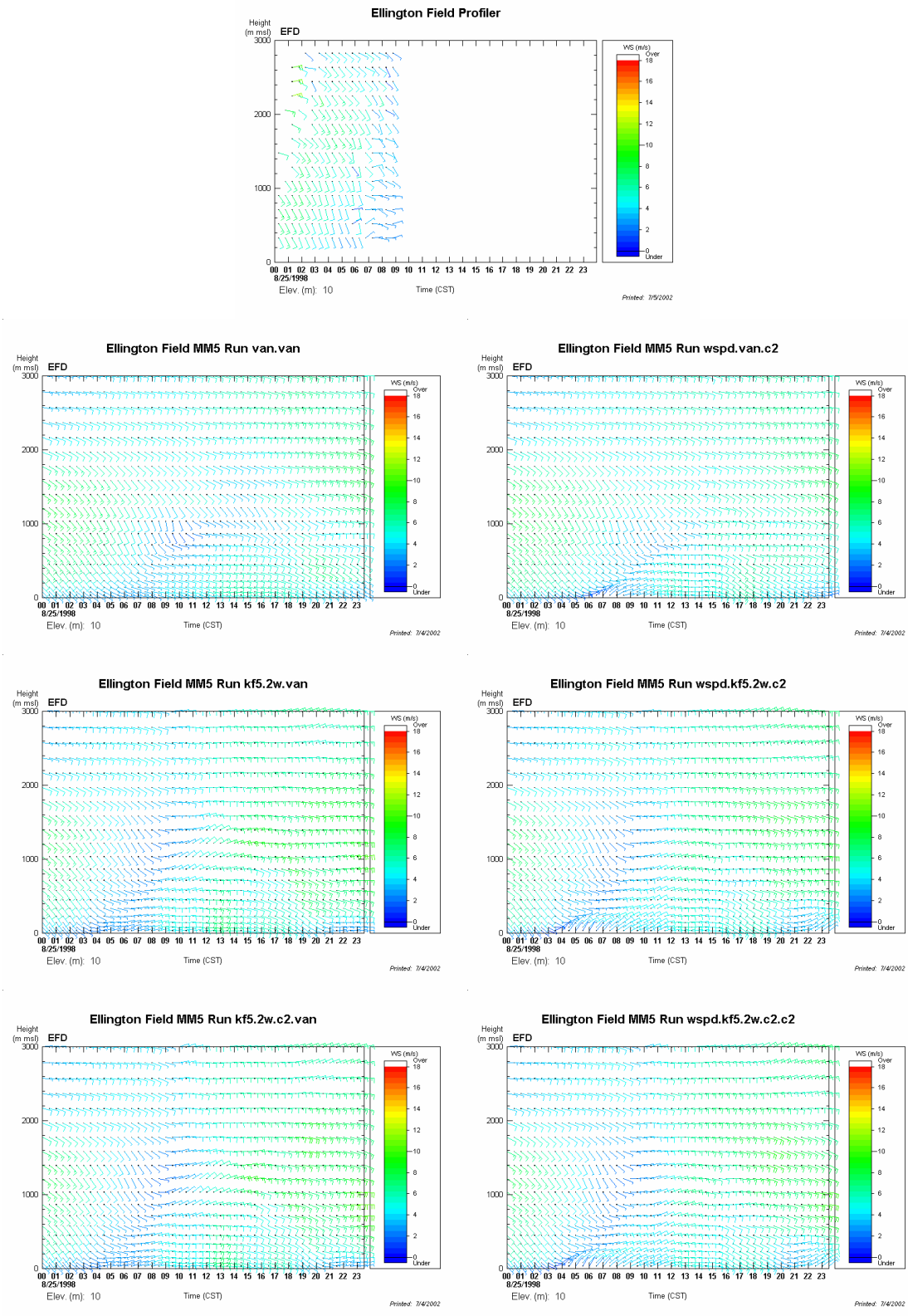

Figure 6.9.1. August 25, 1998, time-height cross sections at Ellington Field. The top panel shows Radar Wind Profiler data. Uncoupled model results are shown on the left; coupled model results are shown on the right. The rows correspond to the three different lateral boundary conditions for the 4-km domain.

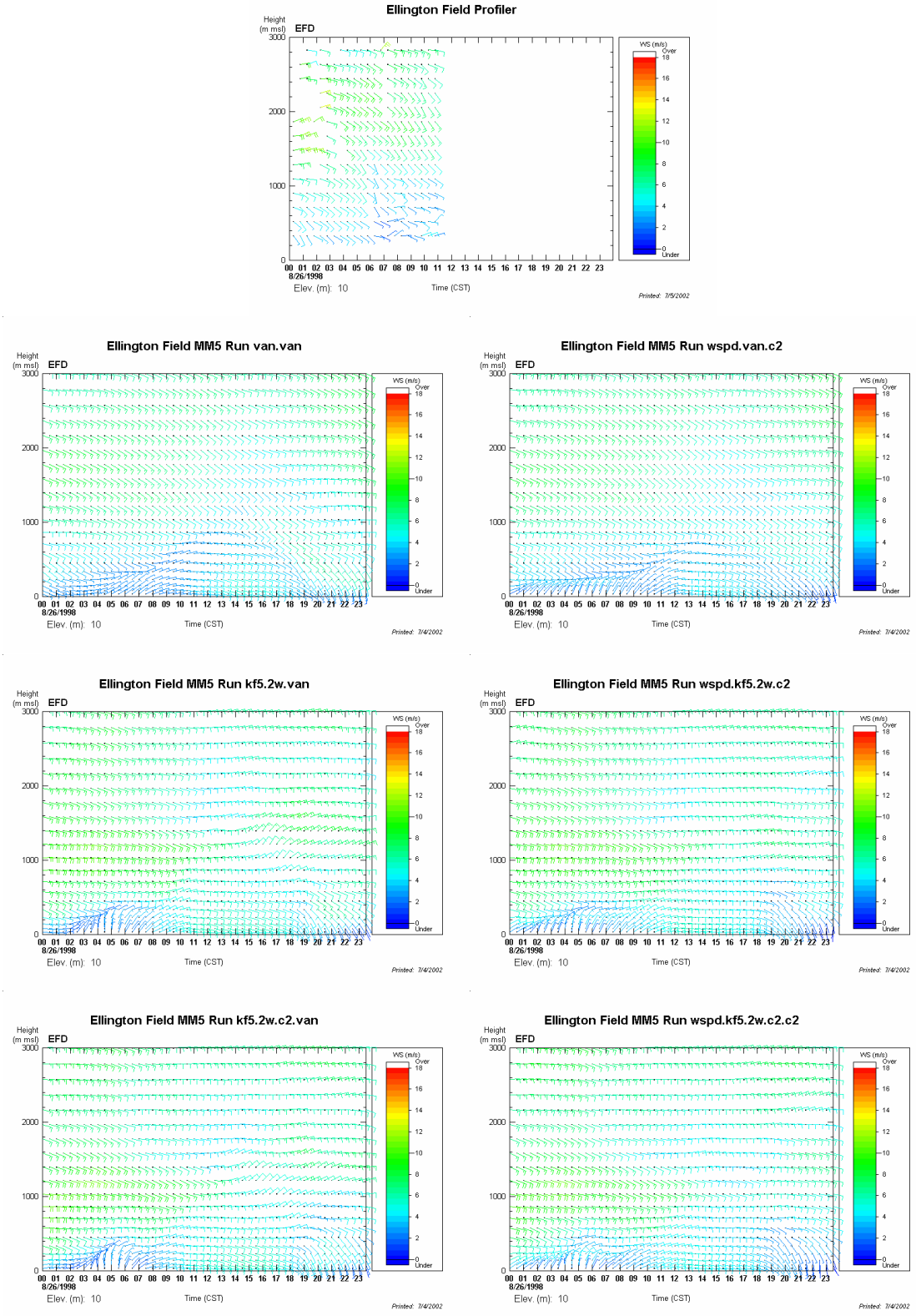

Figure 6.9.2. August 26, 1998, time-height cross sections at Ellington Field. The top panel shows Radar Wind Profiler data. Uncoupled model results are shown on the left; coupled model results are shown on the right. The rows correspond to the three different lateral boundary conditions for the 4-km domain.

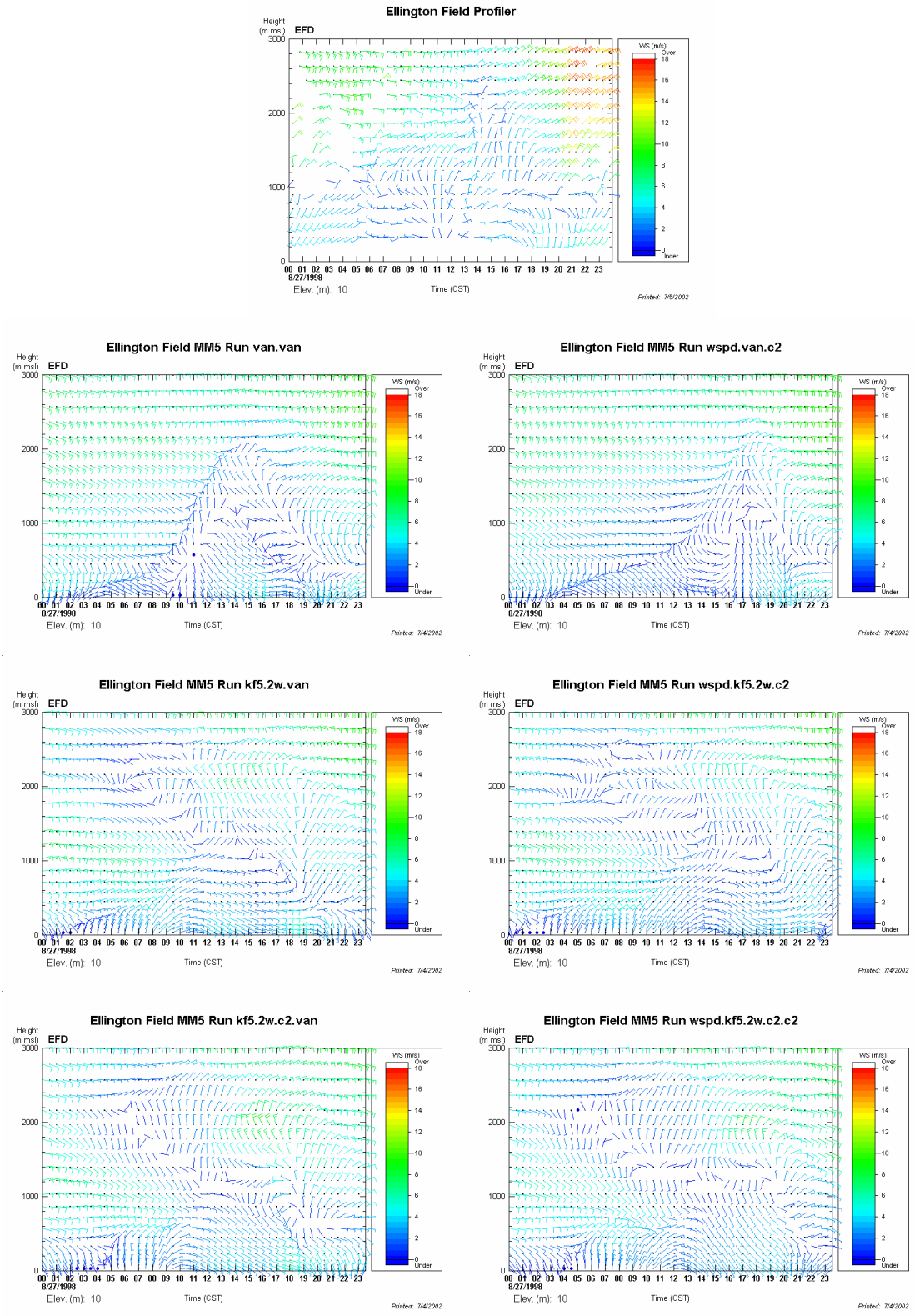

Figure 6.9.3. August 27, 1998, time-height cross sections at Ellington Field. The top panel shows Radar Wind Profiler data. Uncoupled model results are shown on the left; coupled model results are shown on the right. The rows correspond to the three different lateral boundary conditions for the 4-km domain.

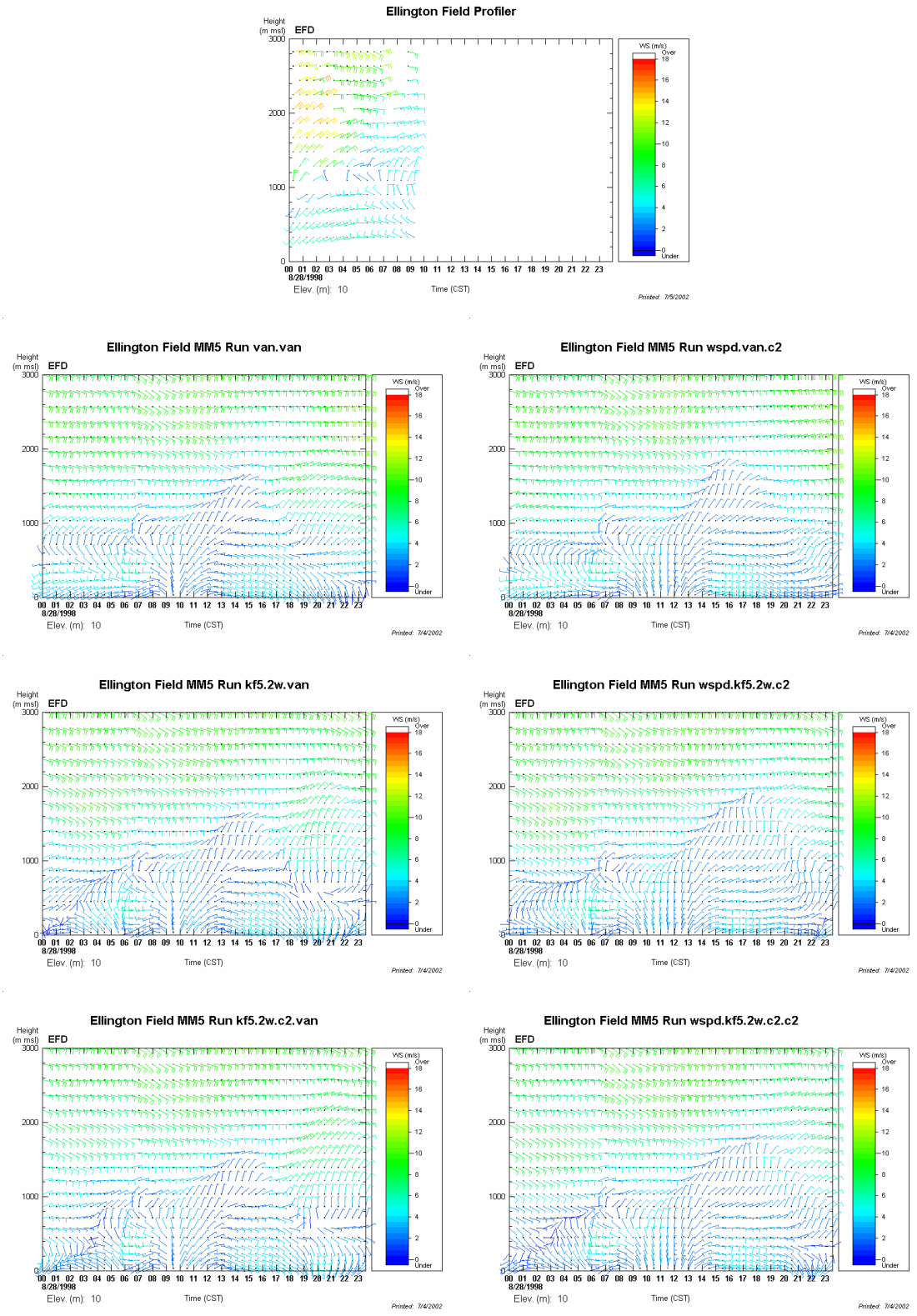

Figure 6.9.4. August 28, 1998, time-height cross sections at Ellington Field. The top panel shows Radar Wind Profiler data. Uncoupled model results are shown on the left; coupled model results are shown on the right. The rows correspond to the three different lateral boundary conditions for the 4-km domain.

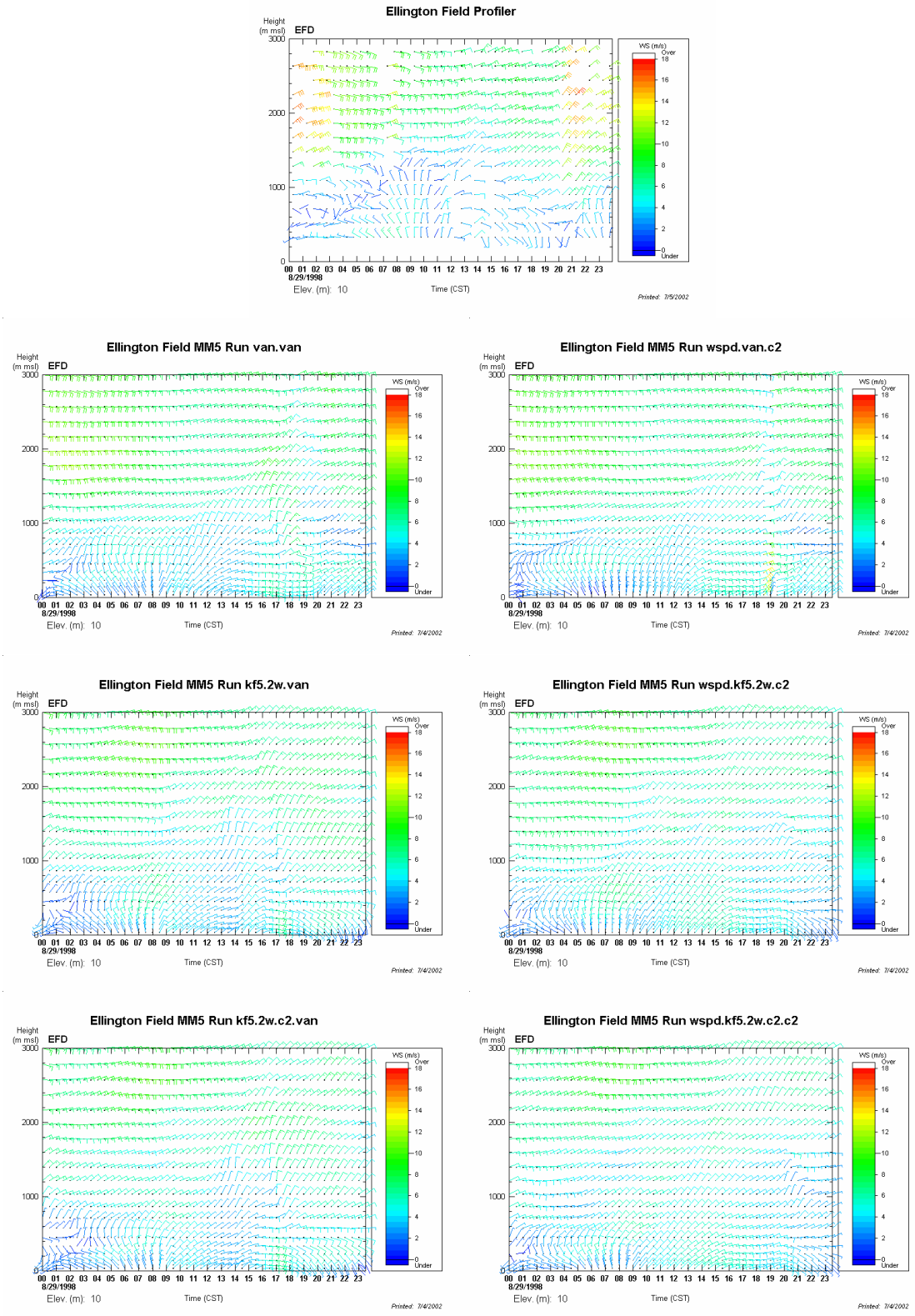

Figure 6.9.5. August 29, 1998, time-height cross sections at Ellington Field. The top panel shows Radar Wind Profiler data. Uncoupled model results are shown on the left; coupled model results are shown on the right. The rows correspond to the three different lateral boundary conditions for the 4-km domain.

7. Conclusions

This report describes the successful application of the MM5/TOPLATS/SSATS modeling system to an ozone episode that occurred in August 1998, completing the ATAQM Phase 2 work. The coupled model was evaluated by comparing it to an uncoupled counterpart through isolation of the land-surface differences in a 4-km hypothetical photochemical model domain. The evaluation used both quantitative and qualitative methods to assess model performance for August 25-30, 1998.

To summarize the evaluations performed, a simple rating system was devised for the coupled model ranging from -2 (performed much worse than the uncoupled model), through 0 (performed about the same as the uncoupled model) to +2 (performed much better than the uncoupled model). The scale applies to case "van" for segment S1 (since it outperformed both of the "kf5" cases for the first segment) and either of the two "kf5" cases for S2 (since they both outperformed case "van" for the second segment). The scale was used to summarize model performance by summing the ranking scores for each variable or process evaluated. The summary score provides a measure of overall model performance, assuming the variables or processes evaluated are equally important.

Table 7.1 shows the rankings based on the quantitative statistical evaluation of episode mean winds, mixing ratios, and temperatures. The models are essentially equal in their abilities to predict wind speed. The uncoupled model is better at predicting mean wind direction, due to the slightly greater counterclockwise bias in the coupled model discussed in Section 6.4, and the coupled model is better at predicting mixing ratio, due to its better daytime performance. The coupled model outperforms the uncoupled model for predicting mean 2-m temperature. Summing the individual scores in Table 7.1 results in a net quantitative score of +2 for the coupled model.

Table 7.1. Quantitative ranking based on episode mean statistics.

Evaluated Variable	Coupled Score				
	-2	-1	0	+1	+2
10-m Wind Speed			X		
10-m Wind Direction		X			
2-m Mixing Ratio				X	
2-m Temperature					X

-2 = Coupled model performed much worse than the uncoupled model
0 = Coupled model performed about the same as the uncoupled model
+2 = Coupled model performed much better than the uncoupled model

Table 7.2 shows the ranking of the same variables as in Table 7.1 based on a qualitative evaluation of the time-series plots of mean bias and error statistics discussed in Section 6.3. The resulting qualitative rankings are identical to the quantitative rankings for these variables.

Table 7.2. Qualitative ranking based on a review of time-series plots of mean bias and error statistics.

Evaluated Variable	Coupled Score				
	-2	-1	0	+1	+2
10-m Wind Speed			X		
10-m Wind Direction		X			
2-m Mixing Ratio				X	
2-m Temperature					X

-2 = Coupled model performed much worse than the uncoupled model
0 = Coupled model performed about the same as the uncoupled model
+2 =Coupled model performed much better than the uncoupled model

Underlying these results are two fundamental corrections manifest in the coupled model:

(1) The coupled model corrects the standard MM5 surface thermodynamic deficiency by jointly improving the diurnal temperature range and daytime water vapor mixing ratio. This is no doubt a result of improved surface fluxes. Since photochemistry is critically sensitive to temperature (and somewhat less so to moisture), the coupled model's ability to correct this fundamental problem is an extremely important result.

(2) The coupled model corrects the standard MM5 land-sea contrast deficiency through a combination of the use of near-shore SSTs (used by SSATS) and the improved surface diurnal temperature range. In the standard MM5, the nocturnal contrasts are too weak and the daytime contrasts are negatively affected by too-cold near-shore water temperatures.

Table 7.3 shows the rankings based on the qualitative evaluations of 17 physical processes that were assessed and discussed in this report. Many of these processes were evaluated without the support of observational data. The seventh column of Table 7.3 indicates whether data were available and used in the assessment. Adding the scores for each process evaluated results in a net qualitative score of +11 for the coupled model.

The following list summarizes the basis for the qualitative rankings given:

- *Sea-Surface Temperatures.* The coupled model ingests observed Bay/Gulf Coast SSTs so it replicates those temperatures more accurately.
- *Sea-Surface Fluxes.* The coupled model revealed flux patterns with strong correlations to ingested observed SSTs.
- *Land-sea Thermal Contrast.* The coupled model handles land-sea thermal contrast better (especially at night) due to its realistic Bay/Gulf SSTs. This supports the larger negative V-wind bias overall (compared to the uncoupled model), leading to a somewhat poorer actual sea-breeze representation as measured against the data. Compensating errors may lead to better sea-breeze performance in the uncoupled model, whereby imbalanced land-sea forcing may compensate a deficient surface-stress formulation.

Table 7.3. Qualitative ranking based on process evaluations.

Process Evaluated	Coupled Score					
	-2	-1	0	+1	+2	Data Available (Y/N)
Sea-Surface Temperatures				X		Y
Sea-Surface Fluxes				X		N
Land-sea Thermal Contrast				X		Y
Daytime Sea-breeze Performance		X				Y
Spurious Cloud Avoidance				X		Y
Observed Cloud Representation				X		Y
PBL evolution: episodic				X		N
PBL evolution: diurnal			X			N
PBL: morning transition			X			Y
PBL: daytime Bay behavior				X		N
Nocturnal Surface Inversions				X		N
Houston Heat-Island Effects				X		N
Dew Formation				X		N
Heat Flux Spatial Variability				X		N
Land-Sea Mask Effects				X		Y
Wind Precession			X			Y
Bay-scale Wind Flows			X			N

-2 = Coupled model performed much worse than the uncoupled model
0 = Coupled model performed about the same as the uncoupled model
+2 =Coupled model performed much better than the uncoupled model

- *Daytime Sea-breeze Performance.* The uncoupled model slightly outperforms the coupled model for predicting surface observations, but the "too cold" near-shore Gulf water temperatures in the uncoupled model may result in anomalous over-forcing, which may compensate for a bias in wind direction boundary conditions. A weaker but more accurate land-sea contrast in the coupled model does not compensate as much, and thus the uncoupled model has a larger negative V-wind bias during the daytime.
- *Spurious Cloud Avoidance.* The uncoupled model produces more spurious grid-scale clouds than the coupled model does. This is attributed to ingestion of observed RSD in the coupled model.
- *Observed Cloud Representation.* The coupled model represents the timing and location of observed clouds better than the uncoupled model. This is attributed to ingestion of observed RSD in the coupled model.
- *PBL Evolution: Episodic.* The coupled model's time-varying soil moisture and RSD result in a PBL that adjusts more dynamically day-to-day. The uncoupled PBL does not show this kind of response.

- *PBL Evolution: Diurnal.* Spatially distributed flux differences in the coupled model result in lower PBL heights over the forested areas northwest of Houston, due to better evapo-transpiration processes.
- *PBL: Morning Transition.* The uncoupled PBL grows more rapidly in the early morning. It is not known what effect this has on the photochemistry.
- *PBL: Daytime Bay Behavior*. The collapse of the PBL during the heat of the day over the Bay is unreasonable, and may promote undesirable flow effects in the uncoupled model. This does not occur in the coupled model.
- *Nocturnal Surface Inversions.* The coupled model cools the land surface more efficiently than the uncoupled model does, in close agreement with observations. Over land, it predicts surface-based inversions over a larger portion of the domain than does the uncoupled model.
- *Houston Heat-Island Effects.* Urban areas warm and cool slowly, exhibiting a phase lag in the diurnal temperature cycle. They retain heat through the evening, and warm slowly through the morning. The coupled model captures this better than the uncoupled model does.
- *Dew Formation.* Though dew formation accentuates a dry/cold bias at night in the coupled model, the uncoupled model appears to have a more fundamental problem—a dry bias with a weak diurnal temperature cycle.
- *Heat Flux Spatial Variability.* Over land, the spatially-distributed TOPLATS appears to promote greater variability, in accordance with land-use patterns, ingested solar radiation, and ingested precipitation, than does the uncoupled model. This appears to be realistic.
- *Land-Sea Mask Effects.* Improved temperature prediction at Galveston demonstrated the effect of carefully preparing land-water masks between TOPLATS and SSATS.
- *Wind Precession.* Both models capture the diurnal rotation of the wind.
- *Bay-scale Wind Flows.* These flows can be significantly different between the models, and behave differently at night than during the day. No data were available to investigate these differences.

Based on these evaluations, it is concluded that for both quantitative and qualitative metrics, the coupled MM5/TOPLATS/SSATS model outperforms the uncoupled model at the 4-km scale.

The qualitative conclusions suggest that the coupled model contains many desirable features—time-varying SSTs, time-varying soil moisture, high resolution land use, use of remotely-sensed data—and that it produces results that may not be achievable or even testable with any other version of MM5 available. The quantitative results suggest that the model performs better than its uncoupled counterpart for the parameterizations tested, revealing two fundamental deficiencies in the standard MM5: a poor surface thermodynamic representation and a poor land-sea thermal contrast.

It is recommended that future work involve sensitivity studies that explore the potential surface stress formulation deficiencies hypothesized, particularly over water. For truly accurate wind-field representation in an episodic case such as this one, systematic biases need correction. The counterclockwise wind bias appears to be larger-scale than the 4-km domain in which the coupled model was applied. Since the coupled model does not aggregate the surface stress from TOPLATS, surface stress modifications could be easily tested. Further, it is believed that additional benefits would be gained by applying and evaluating the model for a case that includes an intensive field program, such as TXAQS2000. This would allow further exploration and validation of the many qualitative advantages of the coupled model system, particularly at the urban and bay scales.

8. References

Dudhia, J., 1989: Numerical study of convection observed during the winter monsoon experiment using a mesoscale two dimensional model. *J. Atmos. Sci*., **46**, 3077-3107

Famiglietti, J.S. and E.F. Wood, 1994: Application of multiscale water and energy balance models on a tallgrass prairie. *Water Res. Rsch.*, **30(11)**: 3061-3078.

Garratt, J.R., 1992: The atmospheric boundary layer. Cambridge Univ. Press, 316 pp.

Grell, G.A., J. Dudhia, and D.R. Stauffer, 1995: A Description of the fifth-generation Penn State/NCAR Mesoscale Model. NCAR/TN-398 + STR.

Holtslag, A.A.A., E.I.F. de Bruijn, and H.-L. Pan, 1990: A high resolution air mass transformation model for short-range weather forecasting. *Mon. Wea. Rev.*, **118**, 1561-1575.

Lambeth, B., 2002: Texas Natural Resource Conservation Commission, Austin, TX. Personal communication July 2, 2002.

McHenry, J.N., C.D. Peters-Lidard, and C.J. Coats, 2001: TNRCC air quality modeling advanced Texas air quality model: study, progress, results: phase II final report. Delivered to TNRCC August 31, 2001, and available online at MCNC http://www.emc.mcnc.org/projects/TNRCC-projects/ATAQM/ataqmII.html

McHenry, J.N., C.D. Peters-Lidard, C.J. Coats, K. Alapaty, S. Fine, A. Trayanov, and F. Pan, 1999: Preliminary results of coupling a 1-D column version of the PSU/NCAR MM5 with a data-assimilating version of the TOPLATS Land-Surface Hydrology Model. *Preprint volume: 14th Conference on Hydrology, American Meteorological Society*, Dallas, Texas, January 10-15.

Moore, J.T., 2002: Evolution of the low-level jet. COMET/COMAP course presented at the Cooperative Institute for Precipitation Systems, St. Louis University.

Neilson-Gammon, J., 2001a: The subtropical sea breeze. Presented at the Texas Natural Resource Conservation Commission, August 2001. Dept. of Atmos. Sciences, 3150 TAMU, College Station, TX, 77843-3150.

Neilson-Gammon, J., 2001b: Initial modeling of the August 2000 Houston-Galveston ozone episode. Report prepared for the Technical Analysis Division, Texas Natural Resource Conservation Commission. Dept. of Atmos. Sciences, 3150 TAMU, College Station, TX, 77843-3150.

Pagowski, M, and K. Moore, 1998: Why MM5 overestimates fluxes over the sea? The Eighth PSU/NCAR Mesoscale Model Users' Workshop. June 15-16, 1998, Boulder, CO. pp 26-28.

Peters-Lidard, C.D., 2001a: TNRCC ATAQM Phase II Report 1: TOPLATS databases and parameters. Delivered to TNRCC August 31, 2001, and available online at MCNC http://www.emc.mcnc.org/projects/TNRCC-projects/ATAQM/ataqmII.html

Peters-Lidard, C.D., 2001b: TNRCC ATAQM Phase II Report 2: Lake/Bay Handler. Delivered to TNRCC August 31, 2001, and available online at MCNC http://www.emc.mcnc.org/projects/TNRCC-projects/ATAQM/ataqmII.html

Peters-Lidard, C.D., 2001c: TNRCC ATAQM Phase II Report 3: Generic diffusion solver. Delivered to TNRCC August 31, 2001, and available online at MCNC http://www.emc.mcnc.org/projects/TNRCC-projects/ATAQM/ataqmII.html

Peters-Lidard, C.D., 2001d: TNRCC ATAQM Phase II Report 4: River routing module. Delivered to TNRCC August 31, 2001, and available online at MCNC http://www.emc.mcnc.org/projects/TNRCC-projects/ATAQM/ataqmII.html

Peters-Lidard, C.D., 2001e: TNRCC ATAQM Phase II technology transfer: TOPLATS manual. Delivered to TNRCC August 31, 2001, and available online at MCNC http://www.emc.mcnc.org/projects/TNRCC-projects/ATAQM/ataqmII.html

Peters-Lidard, C.D., M.S. Zion and E.F. Wood, 1997: A soil-vegetation-atmosphere transfer scheme for modeling spatially variable water and energy balance processes, *J. Geophys. Res.*, **102(D4),** 4303-4324.

Pinker, 2001: Personal communication, November, 2001, University of Maryland.

Pinker, et al., 2001: GEWEX Continental Scale International Project (GCIP) and GEWEX Americas Prediction Project (GAPP) Surface Radiation Budget (SRB) Data. http://metosrv2.umd.edu/~srb/gcip

Pinker, R.T. and I. Laszlo, 1992: Modeling of surface solar irradiance for satellite applications on a global scale. *J. Appl. Meteor.* **31**, 194-211.

Reisner, J., R.J. Rasmussen, and R.T. Bruintjes, 1998: Explicit forecasting of supercooled liquid water in winter storms using the MM5 mesoscale model. *Quart. J. Roy. Meteor. Soc*., **124B**, 1071-1107.

Smith, S.D., 1988: Coefficients for sea-surface wind stress, heat flux, and wind-profiles as a function of wind speed and temperature. *J. Geophys. Res.* **93**, pp 15467-15472.

Appendix A.
Phase 2b Terrain Namelist

```
&MAPBG
 PHIC  =  39.0,
 XLONC =  -98.0,
 IEXP  =   .T.,
 AEXP  =  180.,
 IPROJ = 'LAMCON',
 &END
 &DOMAINS
 MAXNES =   4,
 NESTIX =  112,   121,  70,   61,    1,
 NESTJX =  140,   121,  70,   52,    1,
 DIS    = 36.,  12.,   4.,   1.333333,  1.0,
 NUMNC  =   1,    1,    2,    3,    4,
 NESTI  =   1,   11,   41,   23,    1,
 NESTJ  =   1,   56,   58,   26,    1,
 RID    = 1.5,  1.5,  1.5,  1.5,  2.3,
 NTYPE  =   4,    5,    6,    6,    6,
 NSTTYP=   2,  2,  1,  1,   1,
 &END
 &OPTN
 IFTER   = .TRUE.,
 DATASW  = .T.,
 IFANAL  = .F.,
 ISMTHTR =  2 ,
 IFEZFUG = .F.,
 IFTFUG  = .F.,
 IFFUDG  = .F.,
 IPRNTD  = .F.,
 IPRTHT  = .F.,
 IPRINT  =  1,
 FIN     = 200., 100., 10., 500., 100.,
 IFILL    = .TRUE.,
 LSMDATA  = .FALSE.,
 VEGTYPE  = 1,
 VSPLOT = .TRUE.,
 IEXTRA  = .TRUE.,
 &END
 &FUDGE
 IFFUG   = .F.,.F.,.F.,.F.,
 NDFUG   = 0,0,0,0
 IFUG(1,1)=  200*0,
 IFUG(1,2)=  200*0,
 JFUG(1,1)=  200*0,
 JFUG(1,2)=  200*0,
 LNDFUG(1,1)= 200*0,
 LNDFUG(1,2)= 200*0,
 &END
 &FUDGET
 NFUGBOX = 4
 STARTLAT=45.0,44.0,
 ENDLAT  =46.5,45.0,
 STARTLON=-95.0,-79.8,
 ENDLON  =-92.6,-78.5,
 &END
 &EZFUDGE
 HTPS(441) =  -.001
 HTPS(550) =  183.
 HTPS(587) =  177.
 HTPS(618) =  176.
 HTPS(613) =  174.
 HTPS(645) =   75.
 HTPS(480) = 1897.
 HTPS(500) = 1281.
 &END
 &DATANAME
```

```
 TERNAME = 'Data/DEM_60M_GLOBAL ',
         'Data/DEM_30M_GLOBAL ',
         'Data/DEM_10M_GLOBAL ',
         'Data/DEM_05M_GLOBAL ',
         'Data/DEM_02M_GLOBAL ',
         'Data/DEM_30S_GLOBAL ',
 LNDNAME = 'Data/LANDUSE.60     ',
         'Data/LANDUSE.30     ',
         'Data/LANDUSE.10     ',
         '                    ',
         '                    ',
         '                    ',
 LWNAME  = 'Data/LWMASK-USGS.60 ',
         'Data/LWMASK-USGS.30 ',
         'Data/LWMASK-USGS.10 ',
         'Data/LWMASK-USGS.05 ',
         'Data/LWMASK-USGS.02 ',
         'Data/LWMASK-USGS.30s',
 VGNAME  = 'Data/VEG-USGS.60    ',
         'Data/VEG-USGS.30    ',
         'Data/VEG-USGS.10    ',
         'Data/VEG-USGS.05    ',
         'Data/VEG-USGS.02    ',
         'Data/VEG-USGS.30s   ',
 SONAME  = 'Data/SOILCAT.60     ',
         'Data/SOILCAT.30     ',
         'Data/SOILCAT.10     ',
         'Data/SOILCAT.05     ',
         'Data/SOILCAT.02     ',
         'Data/SOILCAT.30s    ',
 VFNAME  = 'Data/VEG-FRACTION.10',
 TSNAME  = 'Data/SOILTEMP.60    ',
 &END
 &END
```

Appendix B.
MM5 Compile Options

```
#         3b. IRIX.6.X (SGI_Origin,SGI_R10000,SGI_R8000 which support OpenMP)
#       Use OpenMP directives for multi-processor runs.
#       - set RUNTIME_SYSTEM = SGI_Origin
#       - works with 7.2.1 and above compiler
#       - select appropriate XLOCAL0 macro for loader option
#
#    - For parallel execution of MM5 set the following environment variables:
# setenv OMP_NUM_THREADS <number_of_processors>
# setenv _DSM_PLACEMENT ROUND_ROBIN
#    - For parallel execution on a processor set without contention:
# setenv _DSM_WAIT SPIN
# setenv OMP_DYNAMIC FALSE
# setenv MPC_GANG OFF
#    - For parallel execution on a contented set of processors:
# setenv _DSM_WAIT YEILD
# setenv OMP_DYNAMIC TRUE
# setenv MPC_GANG OFF
#--------------------------------------------------------------------------
RUNTIME_SYSTEM = "DEC_ALPHA"
FC = f77
#ABI = -n32 # 2 GB address space
ABI = -64 # For 64-bit address space
IO = -mpio
#PREC = # default 32-bit floating-point presicion.
##PREC = -r8 # 64-bit floating-point precision.
##Conversion program between different precisions of mminput and bdyout available from wesley@sgi.com
MP = -mp -MP:old_mp=OFF
##MP = -mp -MP:open_mp=OFF # Use SGI multiprocessing directives
##OPT = -O3 -OPT:roundoff=3:IEEE_arithmetic=3 -OPT:reorg_common=OFF
OPT = -O3 -OPT:roundoff=3:IEEE_arithmetic=3 -OPT:Olimit=0
##debugging#OPT = -g -DEBUG:div_check:subscript_check=ON:trap_uninitialized=ON
##select appropriate XLOCAL loader
#XLOCAL0 =
### Burk-Thompson PBL (IBLTYP=3) option mp directives
##XLOCAL0 = -Wl,-Xlocal,bt1_,-Xlocal,blk1_,-Xlocal,blk2_
### OSU LSM (ISOIL=2) option mp directives
##XLOCAL0 = -Wl,-Xlocal,rite_,-Xlocal,abci_
### Gayno-Seaman PBL (IBLTYP=6) option mp directives
##XLOCAL0 = -Wl,-Xlocal,fog1d_,-Xlocal,surface1_,-Xlocal,surface2_,-Xlocal,surface3_,-Xlocal,comsurfslab_
LOCAL_DEFNS = -DDEC_ALPHA=1 -DAQM_VMM=1 -DAQMOUT=1 -DMCPL_ACTIVE=1 -
DAQM_SEAICE_IN_SNOWC=1
FCFLAGS = -I$(LIBINCLUDE) $(LOCAL_DEFNS) $(ABI) -mips4 $(MP) $(IO) $(OPT)
CFLAGS =
CPP = /usr/lib/cpp

CPPFLAGS = -I$(LIBINCLUDE) -C -P $(LOCAL_DEFNS)
LDOPTIONS = -I$(LIBINCLUDE) $(ABI) -mips4 $(MP) $(IO) $(OPT) $(XLOCAL0)
#LOCAL_LIBRARIES = -lfastm
LOCAL_LIBRARIES = -L/env/proj/ppar/IRIX64 -liocpl \
          -L/env/proj/ppar/IRIX64 -lioapi_new \
          -L/env/proj/ppar/IRIX64 -lnetcdf -lfastm \
          -L$(PVM_ROOT)/lib/SGI64 -lpvm3
MAKE = make -i –r
#--------------------------------------------------------------------------
5. Options for making ./include/parame.incl
#--------------------------------------------------------------------------
#
# FDDAGD (integer)          - "1" -> FDDA gridded run
FDDAGD = 1
#
# FDDAOBS (integer)         - "1" -> FDDA obs run
FDDAOBS = 0
#
# MAXNES (integer)          - Max Number of Domains in simulation
MAXNES = 2
```

```
#
# MIX,MJX (integer)          - Maximum Dimensions of any Domain
MIX = 121
MJX = 140
# MKX (integer)              - Number of half sigma levels in model
MKX = 43
#-----------------------------------------------------------------------
# 6. Physics Options
#     The first MAXNES values in the list will be used for the corresponding model nests; the rest in the list can be used to compile other options.
#       The exception is FRAD, of which only the first value is used in the model, (i.e., only one radiation option is used for all nests). The rest allow other options to be compiled.
#       Compilation of Arakawa-Schubert cumulus scheme requires imsl.
#-----------------------------------------------------------------------
# IMPHYS - for explicit moisture schemes (array,integer)
IMPHYS = "5,5,1,1,1,1,1,1,1"
#                    - Dry,stable,warm rain,simple ice,mix phase,
#                            - 1  ,2     ,3        ,4         ,5
#                    - graupel(gsfc),graupel(reisner2),schultz
#                            -,6           ,7               ,8
MPHYSTBL = 0
#                    - 0=do not use look-up tables for moist
#                       physics
#                    - 1=use look-up tables for moist physics
#                     (currently only simple ice and mix phase
#                             are available)
#
# ICUPA - for cumulus schemes (array,integer)
#                    - None,Kuo,Grell,AS,FC,KF,BM - 1,2,3,4,5,6,7
ICUPA  = "6,6,1,1,1,1,1,1,1"
#
# IBLTYP - for planetary boundary layer (array,integer)
#                    - 0=no PBL fluxes,1=bulk,2=Blackadar,
#                      3=Burk-Thompson,4=Eta M-Y,5=MRF,
#                      6=Gayno-Seaman,7=Pleim-Xiu
IBLTYP  = "2,2,1,1,1,0,0,0,0,0"
#
# FRAD - for atmospheric radiation (integer)
#                    - Radiation cooling of atmosphere
#                      0=none,1=simple,2=cloud,3=ccm2,4=rrtm
FRAD = "4,4,2,2,2"
#
# ISOIL - for multi-layer soil temperature model (integer)
#                     - 0=no,1=yes (only works with IBLTYP=2,4,5,6)
#                       2=OSU land-surface scheme (IBLTYP=5 only)
#                       3=Pleim-Xiu LSM (IBLTYP=7 only)
ISOIL = 1
#
# ISHALLO (array,integer)   - Shallow Convection Option
#                       1=shallow convection,0=No shallow convection
ISHALLO  = "0,0,0,0,0,0,0,0,0,0"
```

Appendix C.
MM5 Run-Time Namelist

```
cat > ./Run/lparam << EOF
&LPARAM
 ;
 ;      1. user-chosen options I
 ;
 RADFRQ    = 10.,  ;atmospheric radiation calculation frequency (in minutes)
 IMVDIF    = 1,    ;moist vertical diffusion in clouds - 0, 1 (IBLTYP=2,5 only)
 IVQADV    = 0,    ;vertical moisture advection uses log interpolation - 0, linear - 1
 IVTADV    = 0,    ;vertical temperature advection uses theta interpolation - 0, linear - 1
 ITHADV    = 1,    ;advection of temperature uses potential temperature - 1, standard - 0
 ITPDIF    = 1,    ;diffusion using perturbation temperature - 0,1
 ICOR3D    = 1,    ;3D Coriolis force - 0, 1
 IFUPR     = 1,    ;upper radiative boundary condition - 0, 1
 ;
 ;      2. do not change IBOUDY
 ;
 IBOUDY = 3, 2, 2, 2, 2, 2, 2, 2, 2, 2, ;boundary conditions
 ;       (fixed, time-dependent, relaxation -0,2,3)
 ;
 ;      3. keep the following 8 variables as they are
 ;        unless doing sensitivity runs
 ;
 IFDRY  = 0,                     ;fake-dry run (no latent heating) - 0, 1
 ;                               for IMPHYS = 2,3,4,5,6,7 (requires ICUPA = 1)
 ISSTVAR= 0,                     ;varying SST in time - 1, otherwise, 0
 IMOIAV = 0, 0, 0, 0, 0, 0, 0, 0, 0, 0, ;bucket soil moisture scheme. 0 - not used,
                                 ;1 - used w/o extra input, 2 - user w/ soil m input
 IFSNOW = 1, 1, 1, 1, 0, 0, 0, 0, 0, 0, ;SNOW COVER EFFECTS - 0, 1
 ;       (only if snow data are generated in DATAGRID)
 ISFFLX = 1, 1, 1, 1, 1, 1, 1, 1, 1, 1, ;surface fluxes - 0, 1
 ITGFLG = 1, 1, 1, 1, 1, 1, 1, 1, 1, 1, ;surface temperature prediction - 1:yes, 3:no
 ISFPAR = 1, 1, 1, 1, 1, 1, 1, 1, 1, 1, ;surface characteristics - 0, 1
 ICLOUD = 1, 1, 1, 1, 1, 1, 1, 1, 1, 1, ;cloud effects on radiation - 0, 1
 ;                               currently for IFRAD = 1,2
 IEVAP  = 1, 1, 1, 1, 1, 1, 1, 1, 1, 1, ;evap of cloud/rain water - <0, 0, >0
 ;                               (currently for IMPHYS=3,4,5 only)
 ISMRD  = 0,                     ;soil moisture initialization by PX LSM:
 ;                               =0, use moisture avail from LANDUSE.TBL;
 ;                               =2, use soil moisture from REGRID
 ;
EOF
cat > ./Run/nparam << EOF
 &NPARAM
 ;
 ;     ************** NEST AND MOVING NEST OPTIONS ***************
 ;
 LEVIDN =   0,1,2,3,1,1,1,1,1,1,              ; level of nest for each domain
 NUMNC  =   1,1,2,3,1,1,1,1,1,1,              ; ID of mother domain for each nest
 NESTIX = 112,  121,  100,  13,  46,  46,  46,  46,  46,  46,  ; domain size i
 NESTJX = 140,  121,  100,  13,  61,  61,  61,  61,  61,  61,  ; domain size j
 NESTI  =   1,  11,   36,   49,  1,   1,   1,   1,   1,   1,  ; start location i
 NESTJ  =   1,  56,   54,   42,  1,   1,   1,   1,   1,   1,  ; start location i
 XSTNES =   0.,   0.,   0.,1440., 0.,  0.,  0.,  0.,  0.,  0., ; domain initiation
 XENNES =5040.,5040.,1440.,720.,720.,720.,720.,720.,720.,720.; domain termination
 IOVERW =   1,   1,   1,   2,   0,   0,   0,   0,   0,   0,  ; overwrite nest input
 ;         0=interpolate from coarse mesh (for nest domains);
 ;         1=read in domain initial conditions
 ;         2=read in nest terrain file
 IACTIV =   1,   0,   0,   0,   0,   0,   0,   0,   0,   0,  ;
 ;         in case of restart: is this domain active?
 ;
 ;     ************** MOVING NEST OPTIONS *******************
 ;
 IMOVE  =   0,   0,   0,   0,   0,   0,   0,   0,   0,   0, ; move domain 0,1
 IMOVCO =   1,   1,   1,   1,   1,   1,   1,   1,   1,   1, ; 1st move #
```

```
 ;         imovei(j,k)=L, ; I-INCREMENT MOVE (DOMAIN J, MOVE NUMBER K) IS L
 IMOVEI =   0,   0,   0,   0,   0,   0,   0,   0,   0,   0, ; I move #1
            0,   0,   0,   0,   0,   0,   0,   0,   0,   0, ; I move #2
            0,   0,   0,   0,   0,   0,   0,   0,   0,   0, ; I move #3
            0,   0,   0,   0,   0,   0,   0,   0,   0,   0, ; I move #4
            0,   0,   0,   0,   0,   0,   0,   0,   0,   0, ; I move #5
 IMOVEJ =   0,   0,   0,   0,   0,   0,   0,   0,   0,   0, ; J move #1
            0,   0,   0,   0,   0,   0,   0,   0,   0,   0, ; J move #2
            0,   0,   0,   0,   0,   0,   0,   0,   0,   0, ; J move #3
            0,   0,   0,   0,   0,   0,   0,   0,   0,   0, ; J move #4
            0,   0,   0,   0,   0,   0,   0,   0,   0,   0, ; J move #5
 IMOVET =   0,   0,   0,   0,   0,   0,   0,   0,   0,   0, ; time of move #1
            0,   0,   0,   0,   0,   0,   0,   0,   0,   0, ; time of move #2
            0,   0,   0,   0,   0,   0,   0,   0,   0,   0, ; time of move #3
            0,   0,   0,   0,   0,   0,   0,   0,   0,   0, ; time of move #4
            0,   0,   0,   0,   0,   0,   0,   0,   0,   0, ; time of move #5
 IFEED  =  3,     ; no feedback; 9-pt weighted average; 1-pt feedback w/o smoothing /
                  ; light smoothing / heavy smoothing - 0,1,2,3, and 4
 &END
EOF
cat > ./Run/pparam << EOF
 &PPARAM
 ;
 ;     ************** MISCELLANEOUS OPTIONS ******************
 ;
 ; The values for the following 5 variables are only used if ISFPAR = 0
 ;    (i.e. only land/water surface catagories)
 ;
 ZZLND  = 0.1,          ; roughness length over land in meters
 ZZWTR  = 0.0001,       ; roughness length over water in meters
 ALBLND = 0.15,         ; albedo
 THINLD = 0.04,         ; surface thermal inertia
 XMAVA  = 0.3,          ; moisture availability over land as a decimal fraction of one
 ;
 CONF   = 1.0,          ; non-convective precipitation saturation threshold (=1: 100%)
 &END
EOF
cat > ./Run/fparam << EOF
 &FPARAM
 ;
 ;     ************** 4DDA OPTIONS ***********************
 ;
 ;    THE FIRST DIMENSION (COLUMN) IS THE DOMAIN IDENTIFIER:
 ;       COLUMN 1 = DOMAIN #1, COLUMN 2 = DOMAIN #2, ETC.
 ;
 ;      START TIME FOR FDDA (ANALYSIS OR OBS) FOR EACH DOMAIN
 ;      (IN MINUTES RELATIVE TO MODEL INITIAL TIME)
 FDASTA=0.,0.,0.,0.,0.,0.,0.,0.,0.
 ;      ENDING TIME FOR FDDA (ANALYSIS OR OBS) FOR EACH DOMAIN
 ;      (IN MINUTES RELATIVE TO MODEL INITIAL TIME)
 FDAEND=5040.,5040.,0.,0.,0.,0.,0.,0.,0.,
 ;
 ;     ***************** ANALYSIS NUDGING ******************
 ;
 ;    THE FIRST DIMENSION (COLUMN) OF THE ARRAYS DENOTES THE
 ;    DOMAIN IDENTIFIER:
 ;       COLUMN 1 = DOMAIN #1, COLUMN 2 = DOMAIN #2, ETC.
 ;    THE SECOND DIMENSION (ROW OR LINE) EITHER REFERS TO THE 3D VS
 ;    SFC ANALYSIS OR WHICH VARIABLE IS ACCESSED:
 ;       LINE 1 = 3D, LINE 2 = SFC   OR
 ;       LINE 1 = U, LINE 2 = V, LINE 3 = T, LINE 4 = Q
 ;
 ;      IS THIS A GRID 4DDA RUN? 0 = NO; 1 = YES
 I4D= 1,0,0,0,0,0,0,0,0,
    0,0,0,0,0,0,0,0,0,
 ;
 ;      SPECIFY THE TIME IN MINUTES BETWEEN THE INPUT (USUALLY
 ;      FROM INTERP) USED FOR GRID FDDA
 DIFTIM=180.,180.,0.,0.,0.,0.,0.,0.,0.,      ; 3D ANALYSIS NUDGING
       180.,180.,0.,0.,0.,0.,0.,0.,0.,      ; SFC ANALYSIS NUDGING
```

```
;
;       GRID NUDGE THE WIND FIELD? 0 = NO; 1 = YES
IWIND=1,1,0,0,0,0,0,0,0,0,    ; 3D ANALYSIS NUDGING
      0,0,0,0,0,0,0,0,0,0,    ; SFC ANALYSIS NUDGING
;
;       NUDGING COEFFICIENT FOR WINDS ANALYSES
GV=2.5E-4,1.0E-4,0.,0.,0.,0.,0.,0.,0.,       ; 3D ANALYSIS NUDGING
  2.5E-4,1.0E-4,0.,0.,0.,0.,0.,0.,0.,       ; SFC ANALYSIS NUDGING
;
;       GRID NUDGE THE TEMPERATURE FIELD? 0 = NO; 1 = YES
ITEMP=1,1,0,0,0,0,0,0,0,0,    ; 3D ANALYSIS NUDGING
      0,0,0,0,0,0,0,0,0,0,    ; SFC ANALYSIS NUDGING
;
;       NUDGING COEFFICIENT FOR TEMPERATURE ANALYSES
GT=2.5E-4,1.0E-4,0.,0.,0.,0.,0.,0.,0.,       ; 3D ANALYSIS NUDGING
  2.5E-4,1.0E-4,0.,0.,0.,0.,0.,0.,0.,       ; SFC ANALYSIS NUDGING
;
IMOIS=1,1,0,0,0,0,0,0,0,0,    ; 3D ANALYSIS NUDGING
      0,0,0,0,0,0,0,0,0,0,    ; SFC ANALYSIS NUDGING
;
;       NUDGING COEFFICIENT FOR THE MIXING RATIO ANALYSES
GQ=1.E-5,1.E-5,0.,0.,0.,0.,0.,0.,0.,        ; 3D ANALYSIS NUDGING
  1.E-5,1.E-5,0.,0.,0.,0.,0.,0.,0.,        ; SFC ANALYSIS NUDGING
;
;       GRID NUDGE THE ROTATIONAL WIND FIELD? 0 = NO; 1 = YES
IROT=0,0,0,0,0,0,0,0,0,0,     ; 3D ANALYSIS NUDGING
;
;       NUDGING COEFFICIENT FOR THE ROTATIONAL COMPONENT OF THE WINDS
GR=5.E6,5.E6,0.,0.,0.,0.,0.,0.,0.,          ; 3D ANALYSIS NUDGING
;
;       IF GRID NUDGING (I4D(1,1)=1) AND YOU WISH TO EXCLUDE THE
;       BOUNDARY LAYER FROM FDDA OF COARSE GRID THREE DIMENSIONAL
;       DATA (USUALLY FROM INTERP),
;            0 = NO,  INCLUDE BOUNDARY LAYER NUDGING
;            1 = YES, EXCLUDE BOUNDARY LAYER NUDGING
INONBL =0,0,0,0,0,0,0,0,0,0,         ; U WIND
       0,0,0,0,0,0,0,0,0,0,         ; V WIND
       0,0,1,1,1,1,1,1,1,1,         ; TEMPERATURE
       1,1,1,1,1,1,1,1,1,1,         ; MIXING RATIO
;
;       RADIUS OF INFLUENCE FOR SURFACE ANALYSIS (KM).
;       IF I4D(2,1)=1 OR I4D(2,2)=1, ETC, DEFINE RINBLW (KM) USED
;       IN SUBROUTINE BLW TO DETERMINE THE HORIZONTAL VARIABILITY
;       OF THE SURFACE-ANALYSIS NUDGING AS A FUNCTION OF SURFACE
;       DATA DENSITY.  OVER LAND, THE STRENGTH OF THE SURFACE-
;       ANALYSIS NUDGING IS LINEARLY DECREASED BY 80 PERCENT AT
;       THOSE GRID POINTS GREATER THAN RINBLW FROM AN OBSERVATION
;       TO ACCOUNT FOR DECREASED CONFIDENCE IN THE ANALYSIS
;       IN REGIONS NOT NEAR ANY OBSERVATIONS.
RINBLW=250.,
;
;       SET THE NUDGING PRINT FREQUENCY FOR SELECTED DIAGNOSTIC
;       PRINTS IN THE GRID (ANALYSIS) NUDGING CODE (IN CGM
;       TIMESTEPS)
NPFG=50,
;
;     ********** OBSERVATION NUDGING **********
;
;
;    INDIVIDUAL OBSERVATION NUDGING.  VARIABLES THAT ARE ARRAYS
;    USE THE FIRST DIMENSION (COLUMN) AS THE DOMAIN IDENTIFIER:
;         COLUMN 1 = DOMAIN #1, COLUMN 2 = DOMAIN #2, ETC.
;
;       IS THIS INDIVIDUAL OBSERVATION NUDGING? 0 = NO; 1 = YES
I4DI   =0,0,0,0,0,0,0,0,0,0,
;
;       OBS NUDGE THE WIND FIELD FROM STATION DATA? 0 = NO; 1 = YES
ISWIND =1,0,0,0,0,0,0,0,0,0,
;
;       NUDGING COEFFICIENT FOR WINDS FROM STATION DATA
```

```
 GIV  =4.E-4,4.E-4,0.,0.,0.,0.,0.,0.,0.,0.,
 ;
 ;      OBS NUDGE THE TEMPERATURE FIELD FROM STATION DATA? 0 = NO; 1 = YES
ISTEMP=1,0,0,0,0,0,0,0,0,0,
 ;
 ;      NUDGING COEFFICIENT FOR TEMPERATURES FROM STATION DATA
 GIT  =4.E-4,4.E-4,0.,0.,0.,0.,0.,0.,0.,0.,
 ;
 ;      OBS NUDGE THE MIXING RATIO FIELD FROM STATION DATA? 0 = NO; 1 = YES
ISMOIS=1,0,0,0,0,0,0,0,0,0,
 ;
 ;      NUDGING COEFFICIENT FOR THE MIXING RATIO FROM STATION DATA
 GIQ  =4.E-4,4.E-4,0.,0.,0.,0.,0.,0.,0.,0.,
 ;
 ;      THE OBS NUDGING RADIUS OF INFLUENCE IN THE
 ;      HORIZONTAL IN KM FOR CRESSMAN-TYPE DISTANCE-WEIGHTED
 ;      FUNCTIONS WHICH SPREAD THE OBS-NUDGING CORRECTION
 ;      IN THE HORIZONTAL.
 RINXY=240.,
 ;
 ;      THE OBS NUDGING RADIUS OF INFLUENCE IN THE
 ;      VERTICAL IN SIGMA UNITS FOR CRESSMAN-TYPE DISTANCE-
 ;      WEIGHTED FUNCTIONS WHICH SPREAD THE OBS-NUDGING
 ;      CORRECTION IN THE VERTICAL.
 RINSIG=0.001,
 ;
 ;      THE HALF-PERIOD OF THE TIME WINDOW, IN MINUTES, OVER
 ;      WHICH AN OBSERVATION WILL AFFECT THE FORECAST VIA OBS
 ;      NUDGING. THAT IS, THE OBS WILL INFLUENCE THE FORECAST
 ;      FROM TIMEOBS-TWINDO TO TIMEOBS+TWINDO.  THE TEMPORAL
 ;      WEIGHTING FUNCTION IS DEFINED SUCH THAT THE OBSERVATION
 ;      IS APPLIED WITH FULL STRENGTH WITHIN TWINDO/2. MINUTES
 ;      BEFORE OR AFTER THE OBSERVATION TIME, AND THEN LINEARLY
 ;      DECREASES TO ZERO TWINDO MINUTES BEFORE OR AFTER THE
 ;      OBSERVATION TIME.
 TWINDO=40.0,
 ;
 ;      THE NUDGING PRINT FREQUENCY FOR SELECTED DIAGNOSTIC PRINT
 ;      IN THE OBS NUDGING CODE (IN CGM TIMESTEPS)
 NPFI=20,
 ;
 ;      FREQUENCY (IN CGM TIMESTEPS) TO COMPUTE OBS NUDGING WEIGHTS
 IONF=2,
 IDYNIN=0,  ;for dynamic initialization using a ramp-down function to gradually
 ;         turn off the FDDA before the pure forecast, set idynin=1 [y=1, n=0]
 DTRAMP=60.,;the time period in minutes over which the
 ;         nudging (obs nudging and analysis nudging) is ramped down
 ;         from one to zero.  Set dtramp negative if FDDA is to be ramped
 ;         down BEFORE the end-of-data time (DATEND), and positive if the
 ;         FDDA ramp-down period extends beyond the end-of-data time.
 &END
EOF
```

Appendix D.
Enlarged Plots from Figures 6.9.1 through 6.9.5

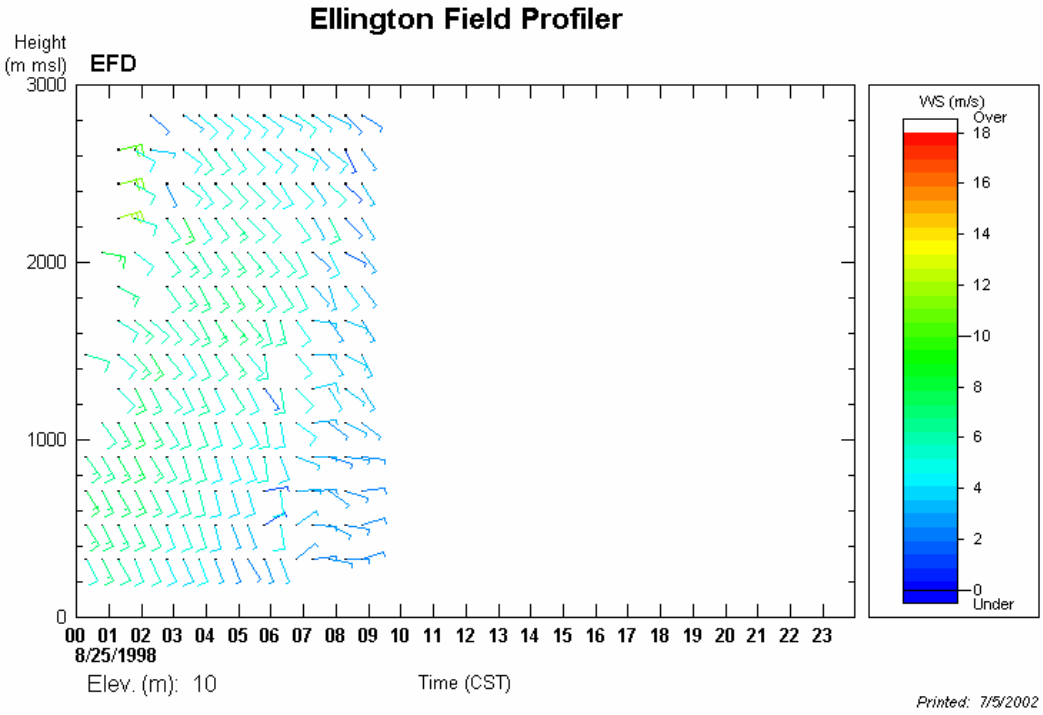

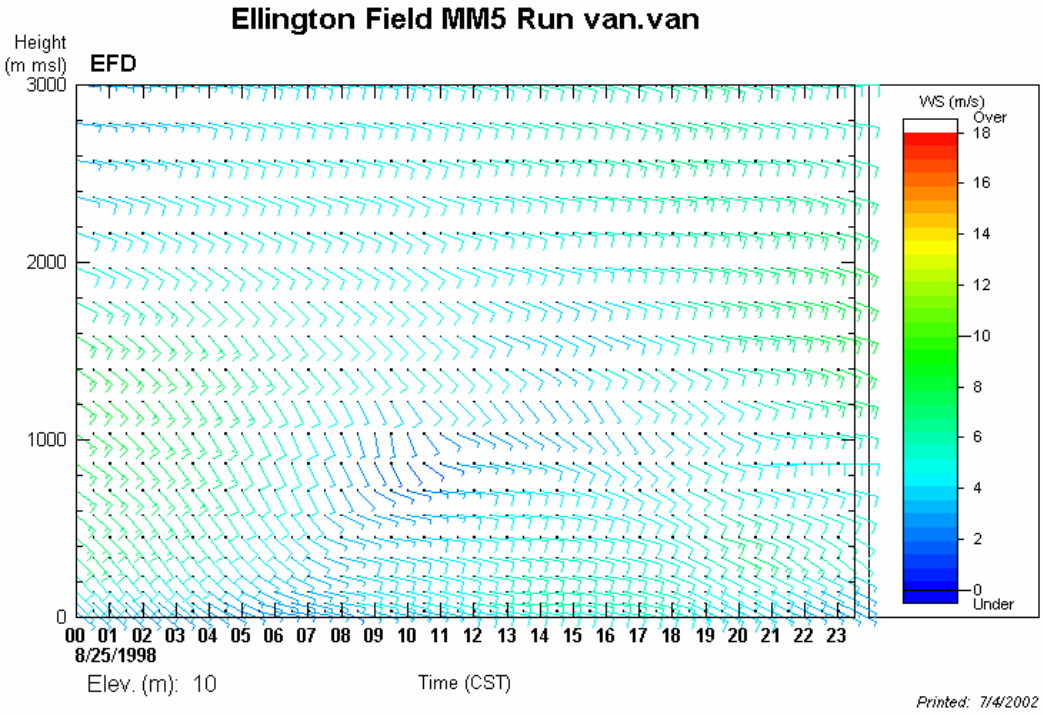

August 25, 1998, time-height cross sections at Ellington Field (from Figure 6.9.1).

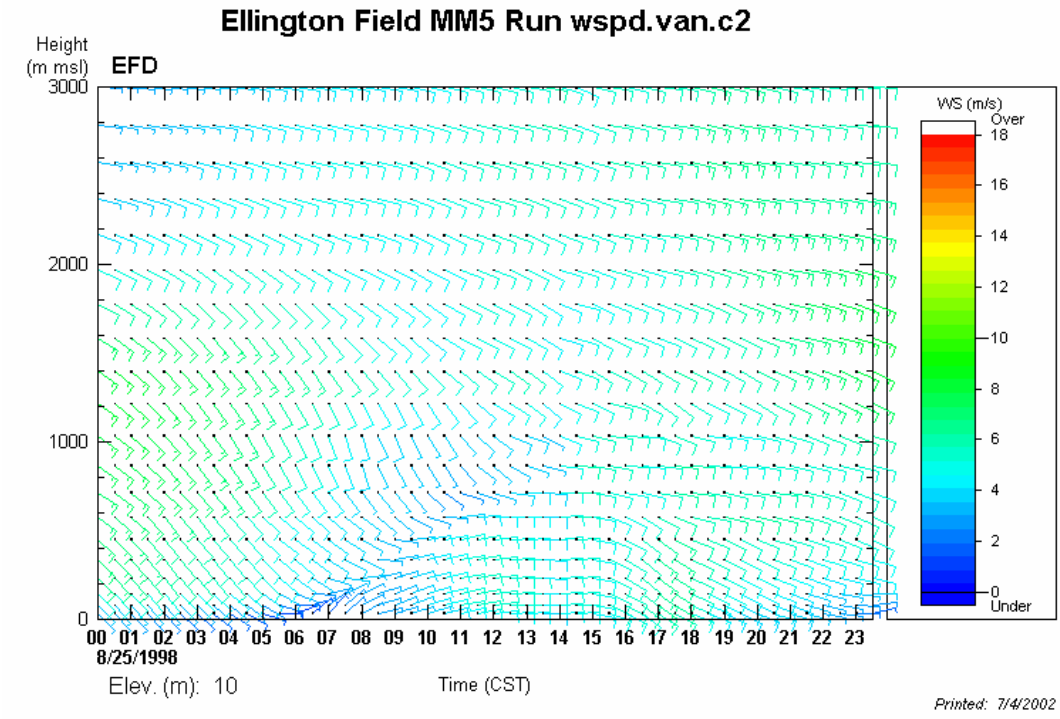

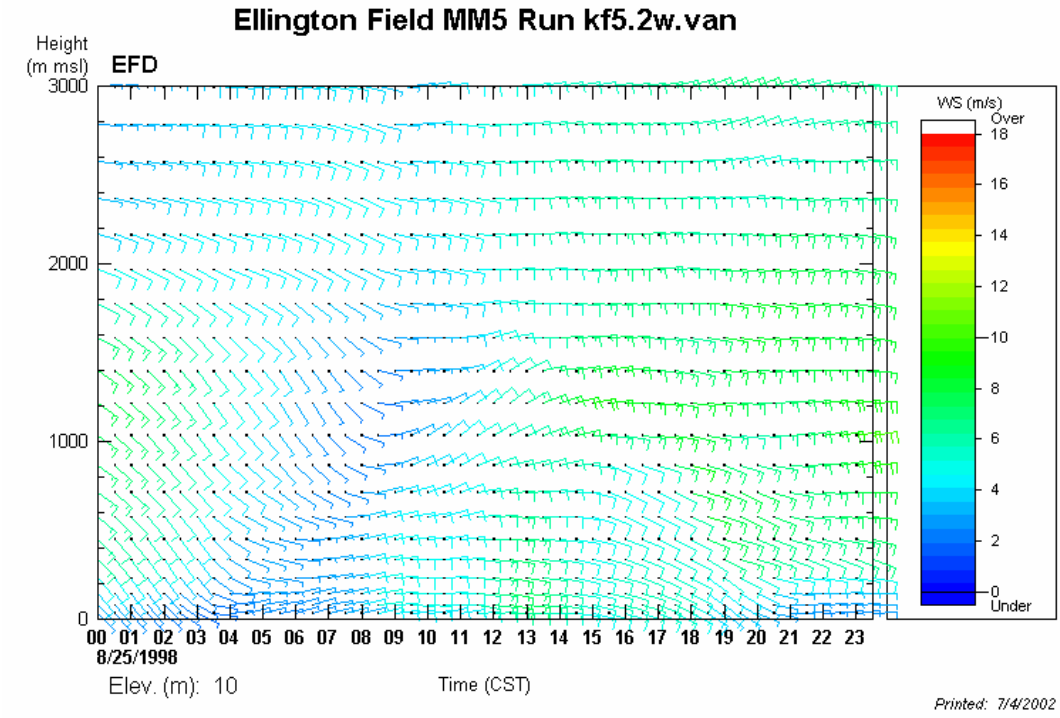

August 25, 1998, time-height cross sections at Ellington Field (from Figure 6.9.1).

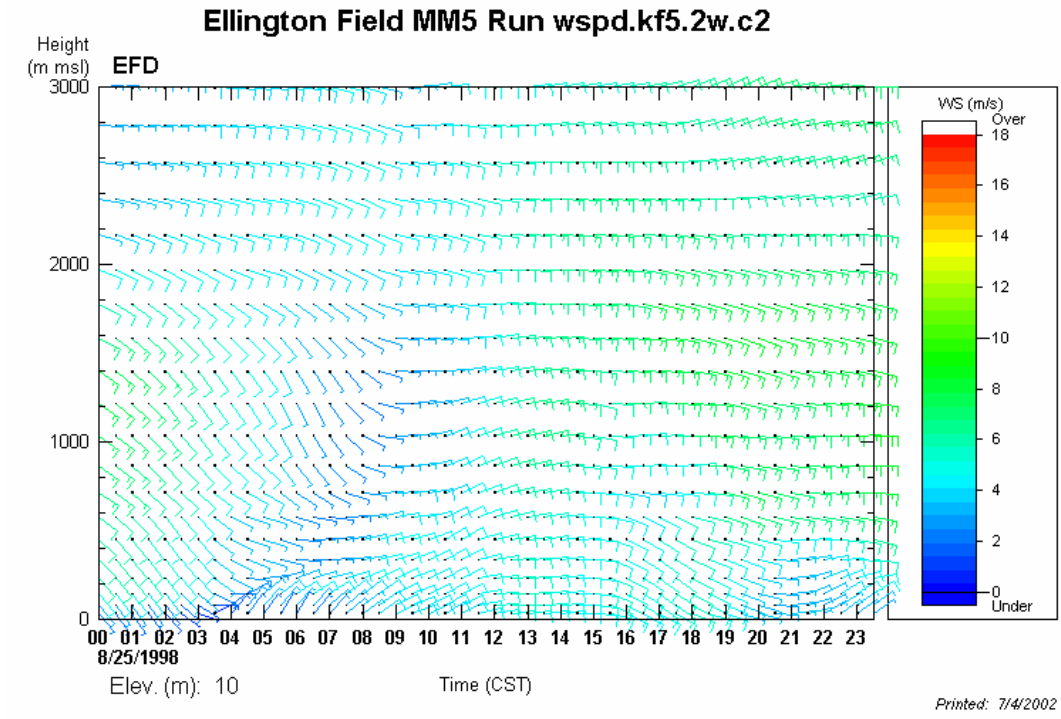

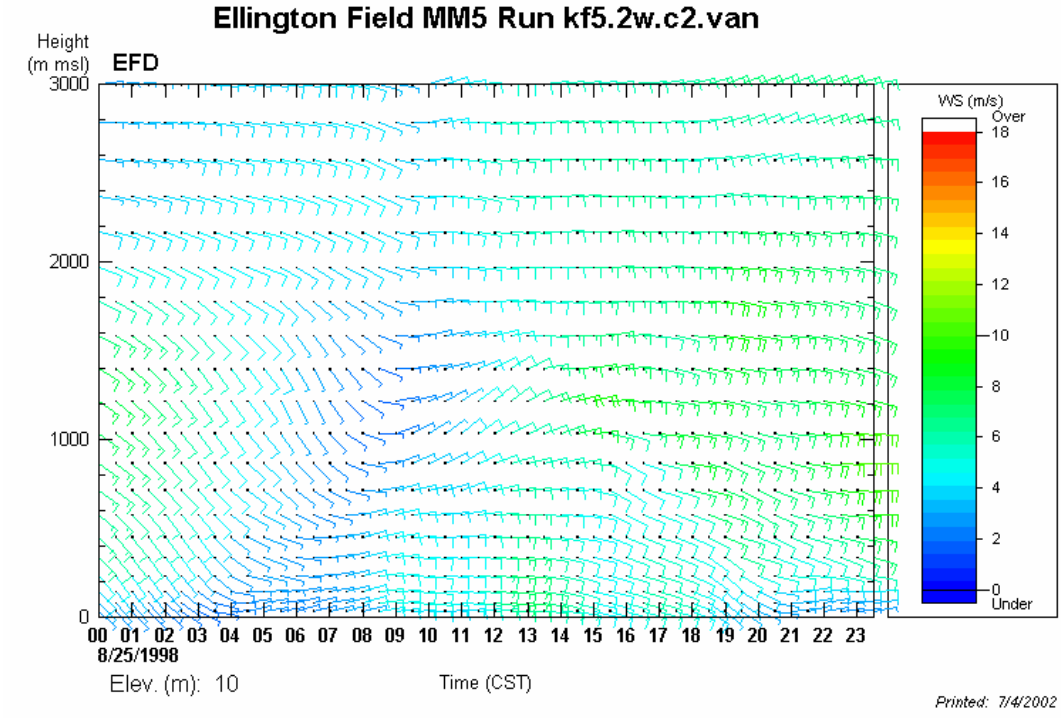

August 25, 1998, time-height cross sections at Ellington Field (from Figure 6.9.1).

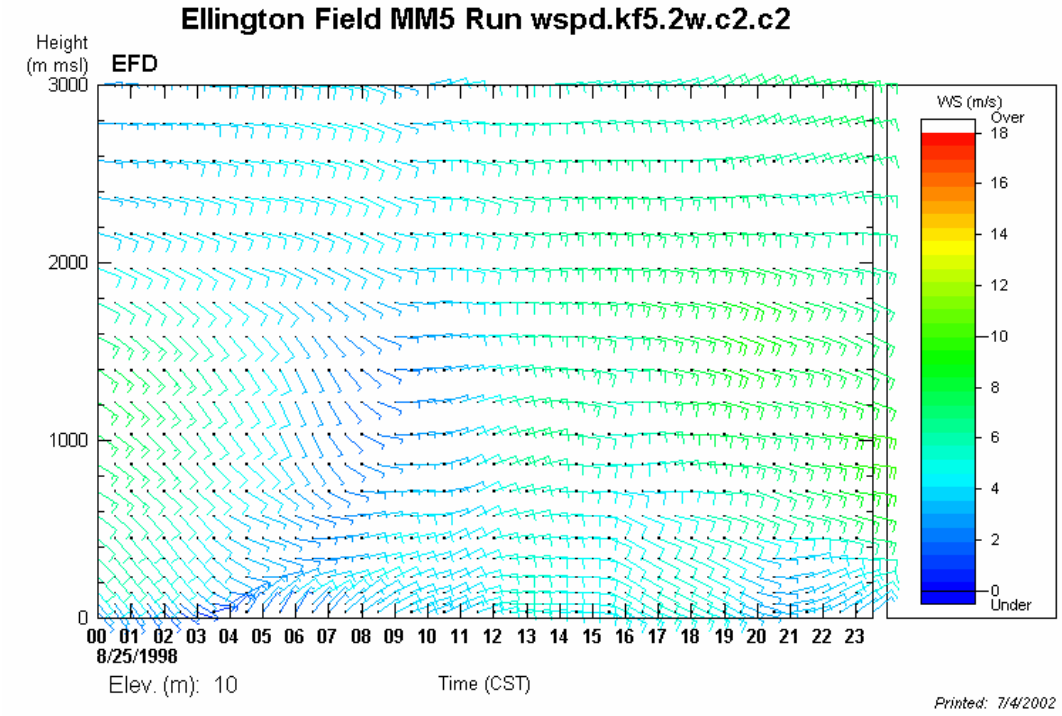

August 25, 1998, time-height cross sections at Ellington Field (from Figure 6.9.1).

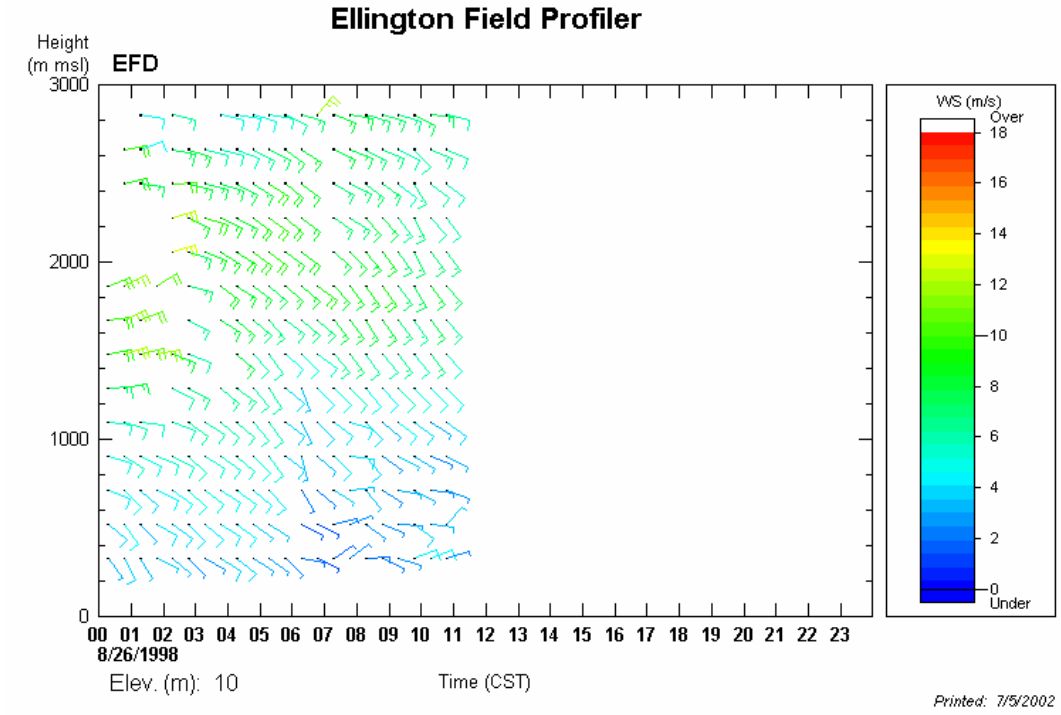

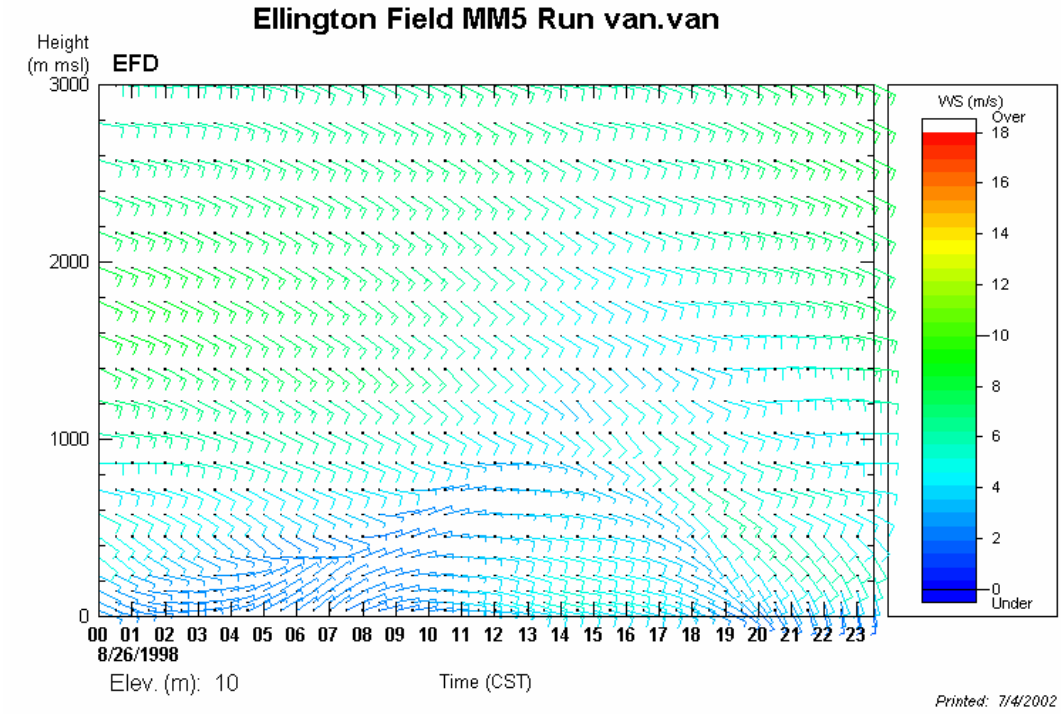

August 26, 1998, time-height cross sections at Ellington Field (from Figure 6.9.2).

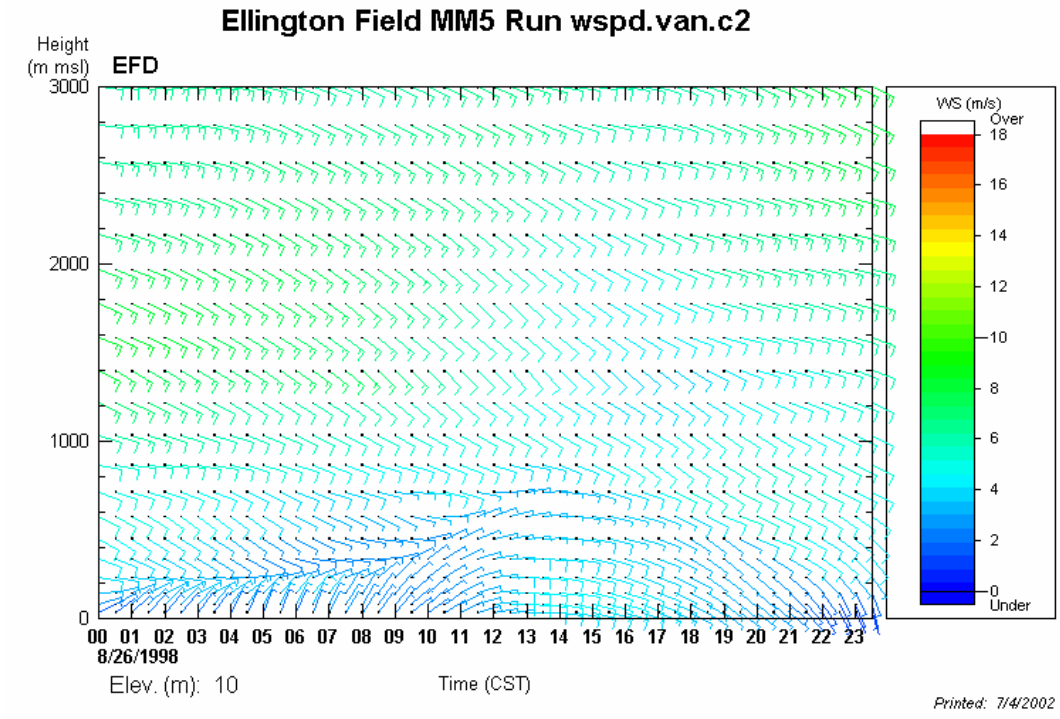

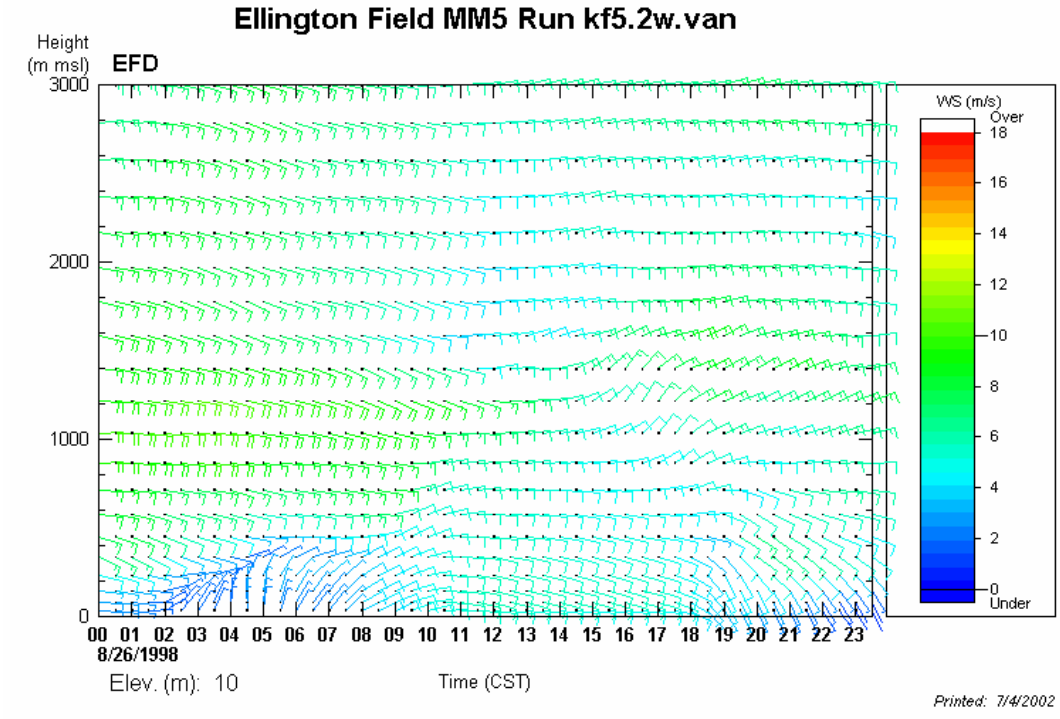

August 26, 1998, time-height cross sections at Ellington Field (from Figure 6.9.2).

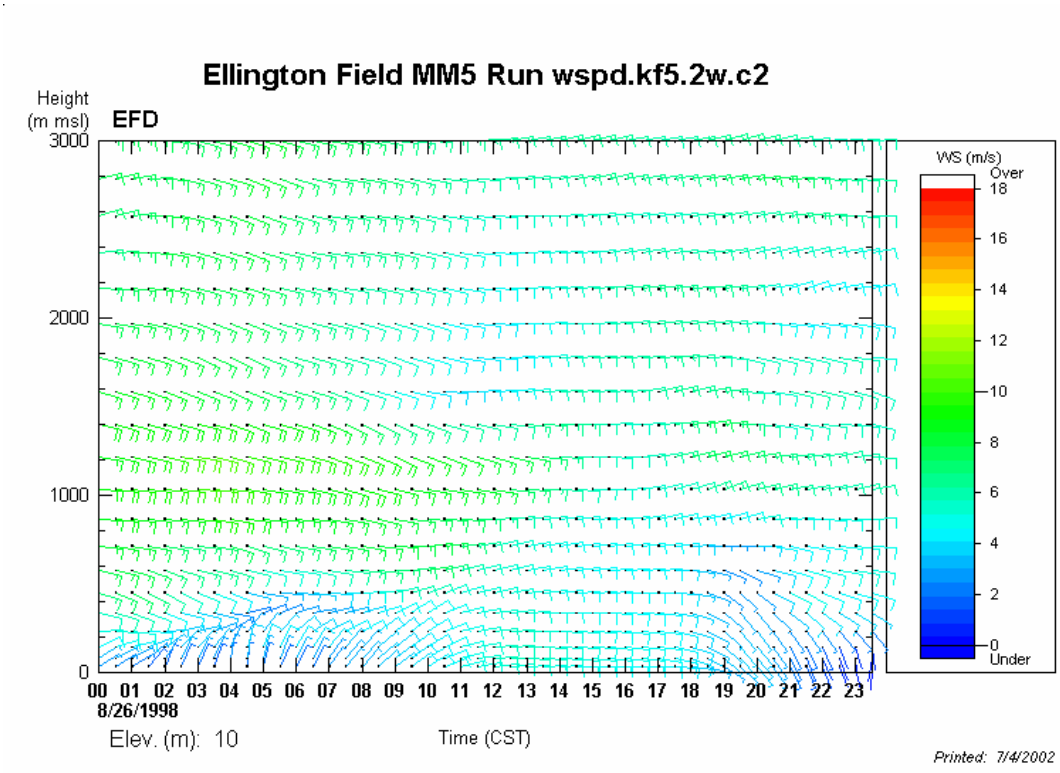

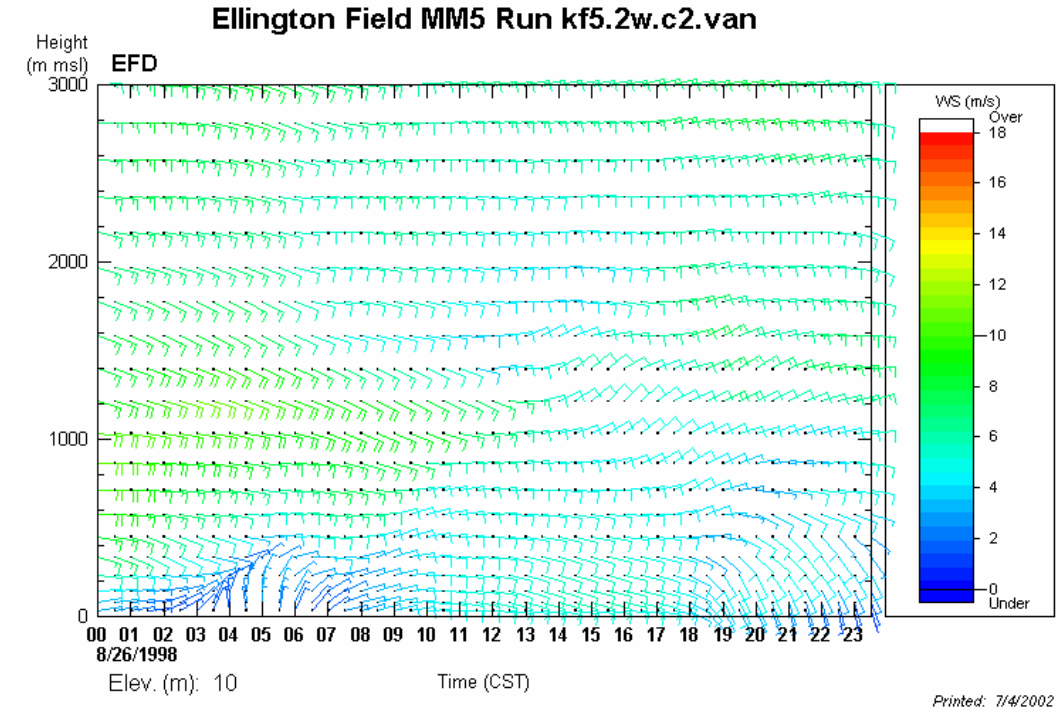

August 26, 1998, time-height cross sections at Ellington Field (from Figure 6.9.2).

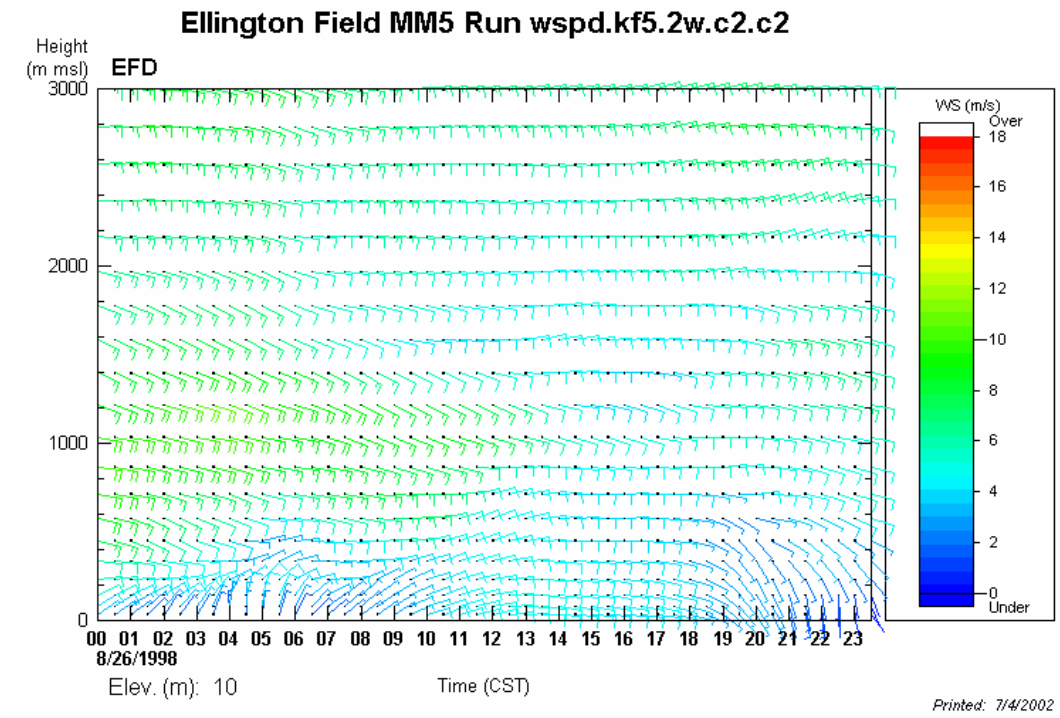

August 26, 1998, time-height cross sections at Ellington Field (from Figure 6.9.2).

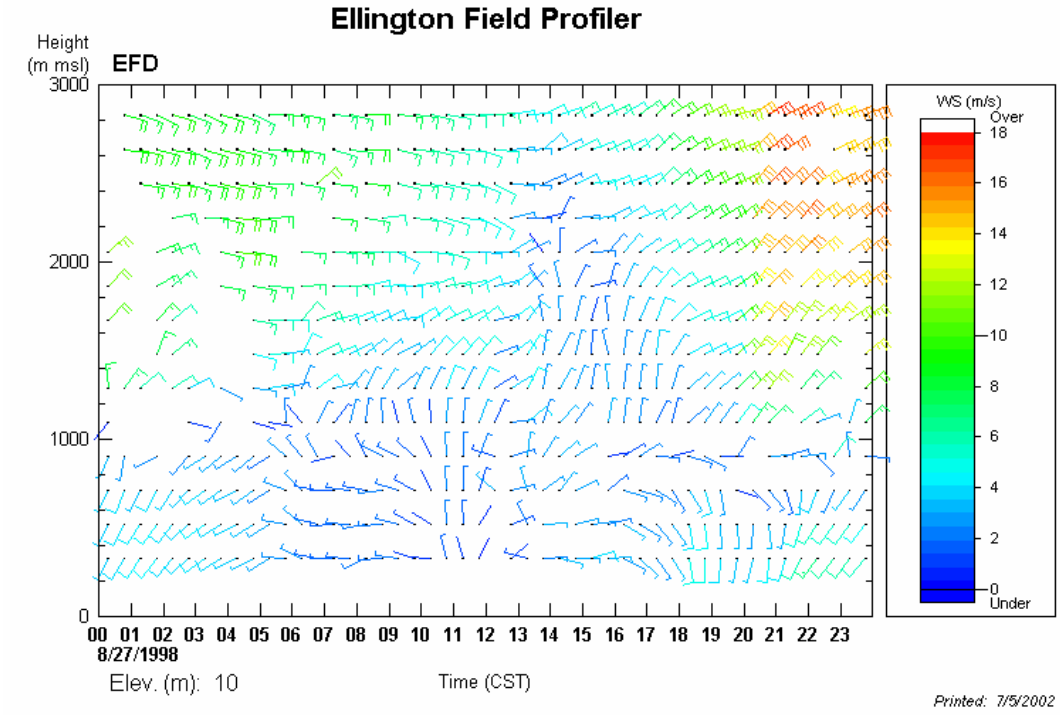

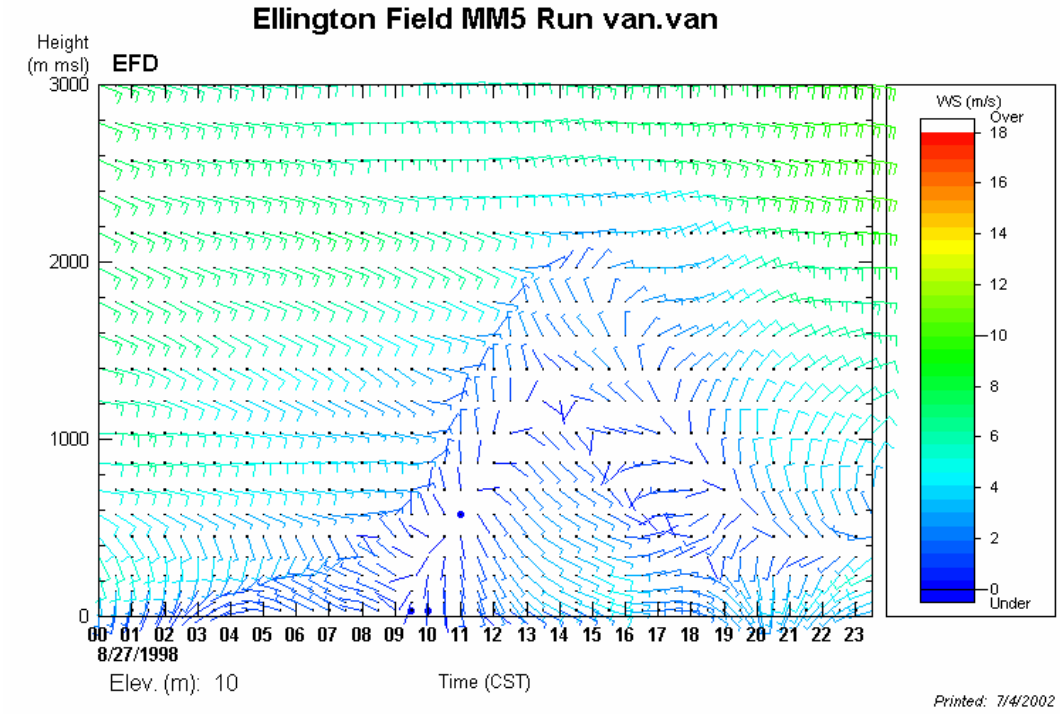

August 27, 1998, time-height cross sections at Ellington Field (from Figure 6.9.3).

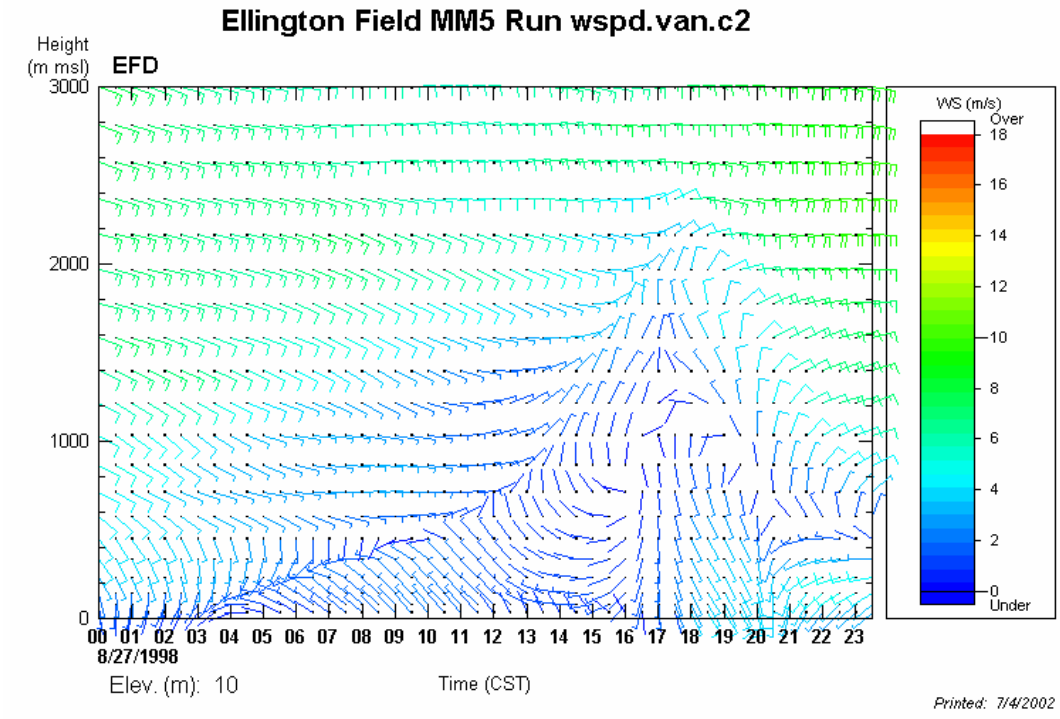

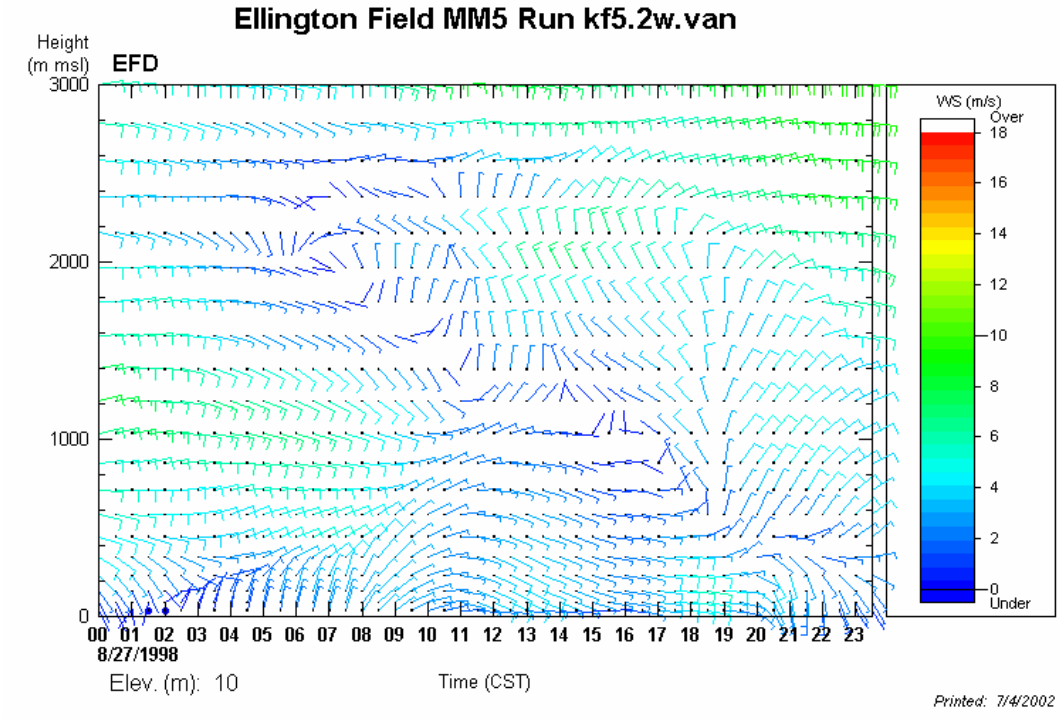

August 27, 1998, time-height cross sections at Ellington Field (from Figure 6.9.3).

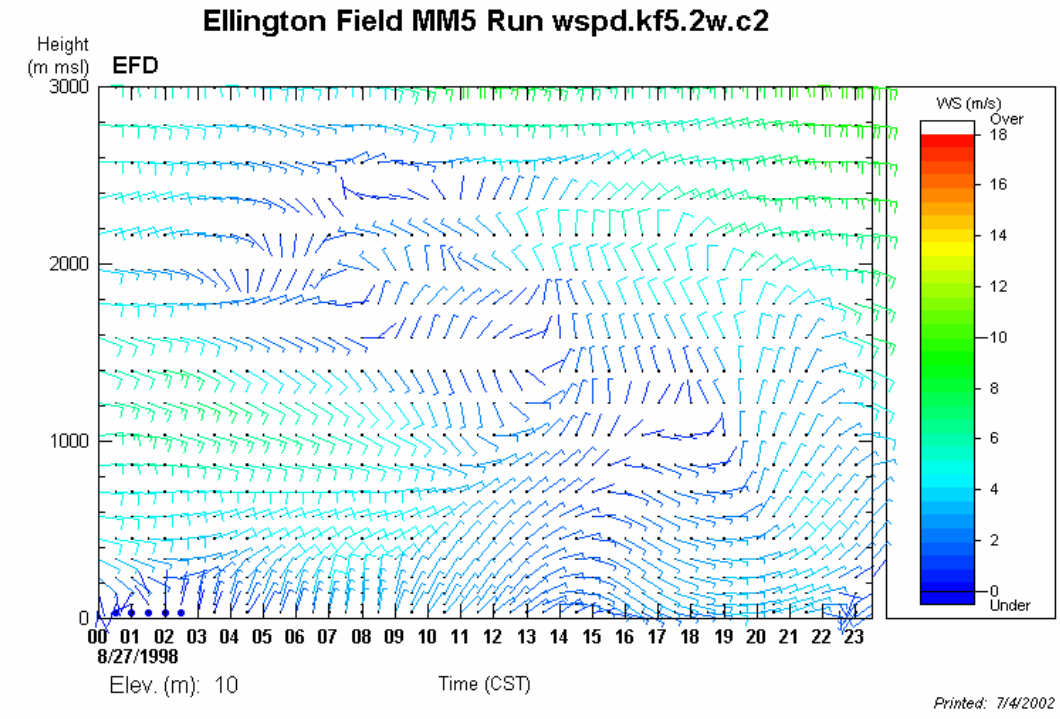

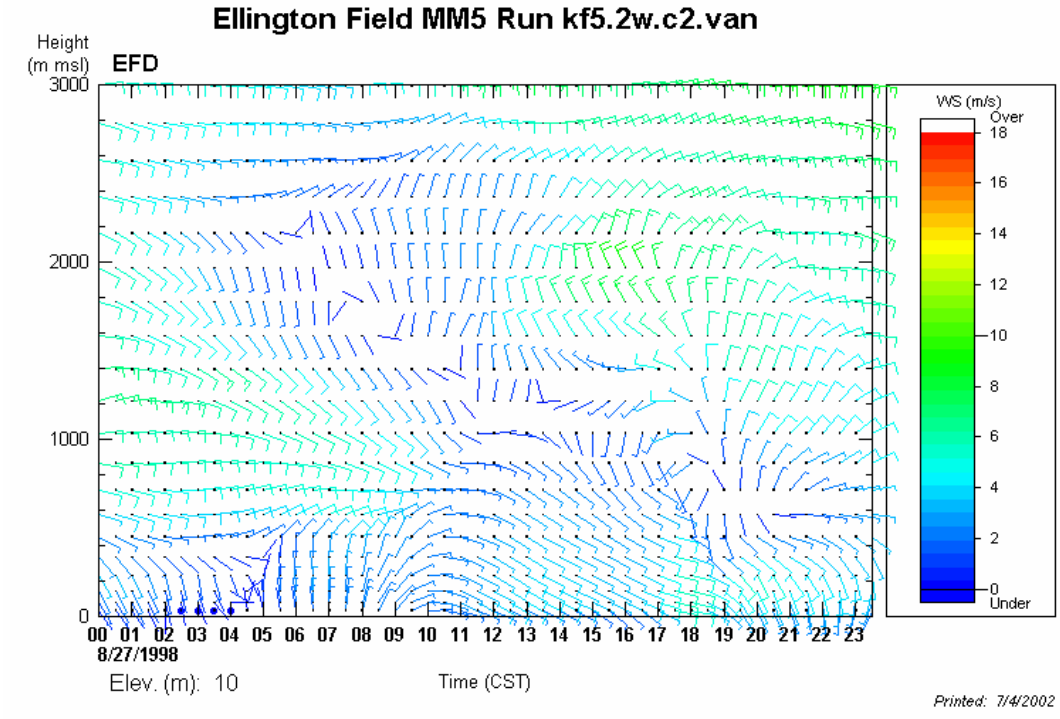

August 27, 1998, time-height cross sections at Ellington Field (from Figure 6.9.3).

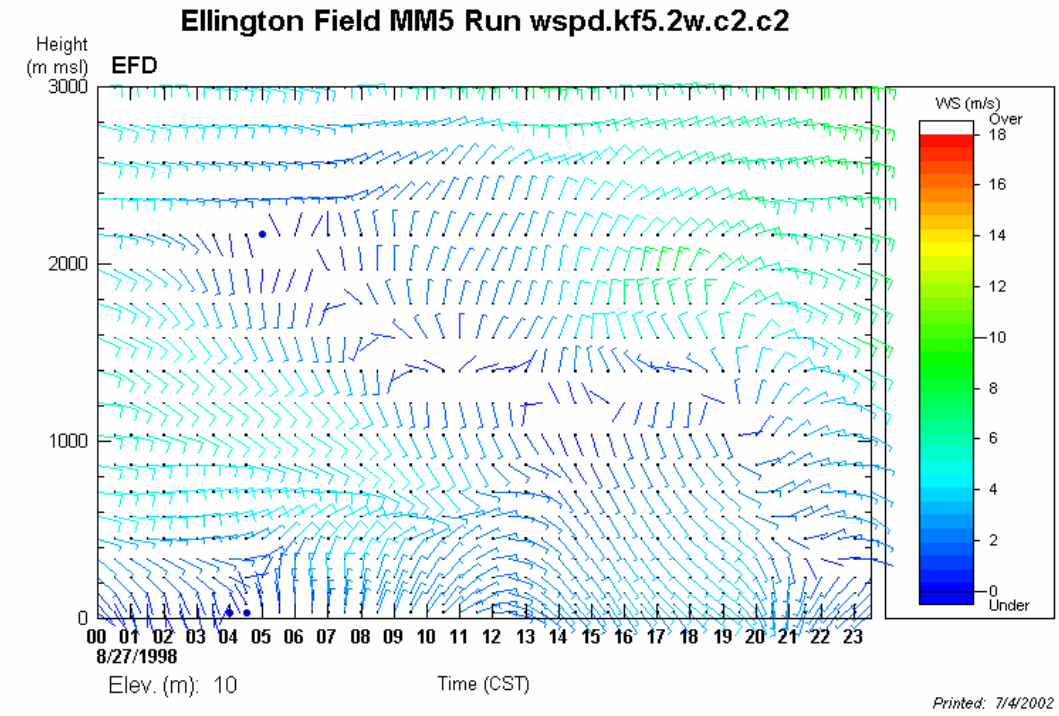

August 27, 1998, time-height cross sections at Ellington Field (from Figure 6.9.3).

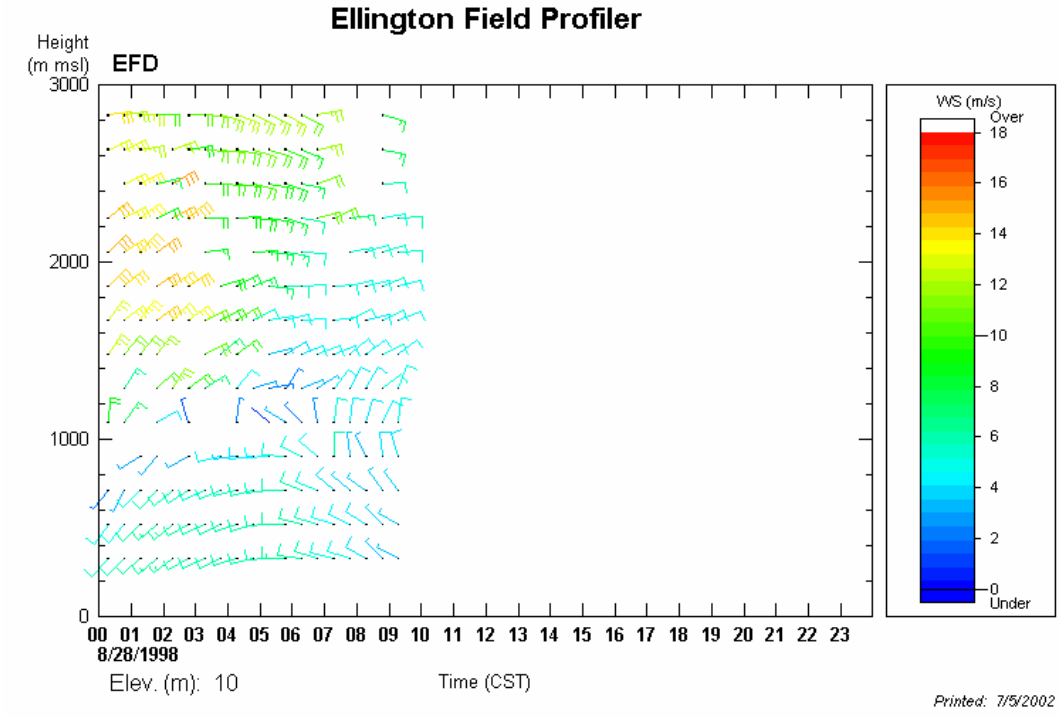

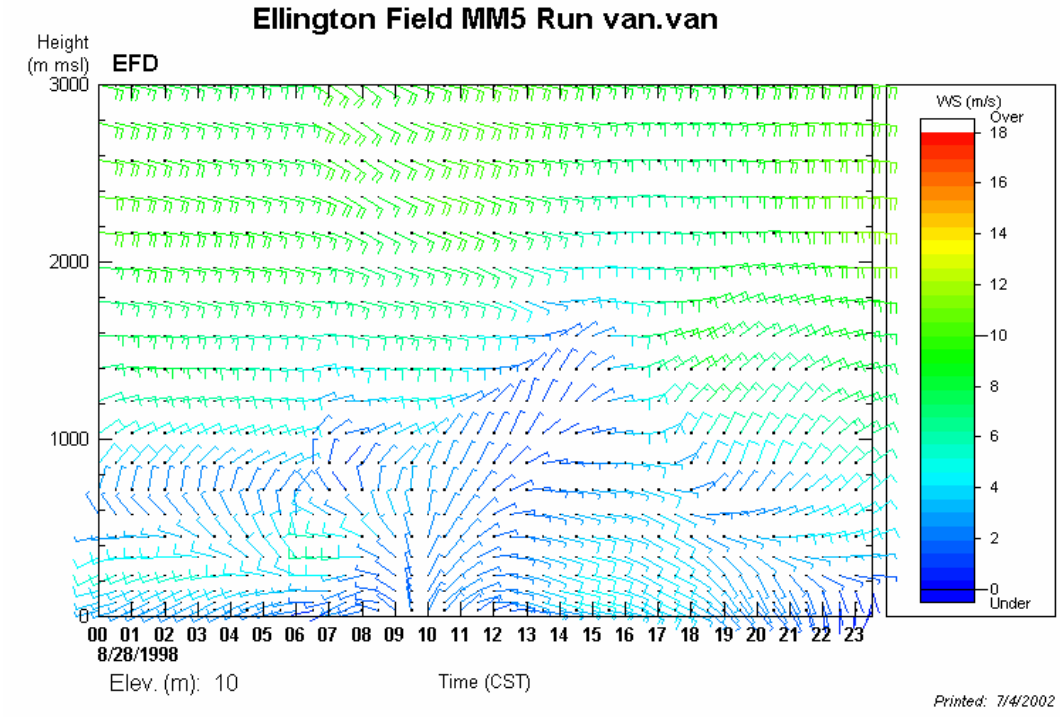

August 28, 1998, time-height cross sections at Ellington Field (from Figure 6.9.4).

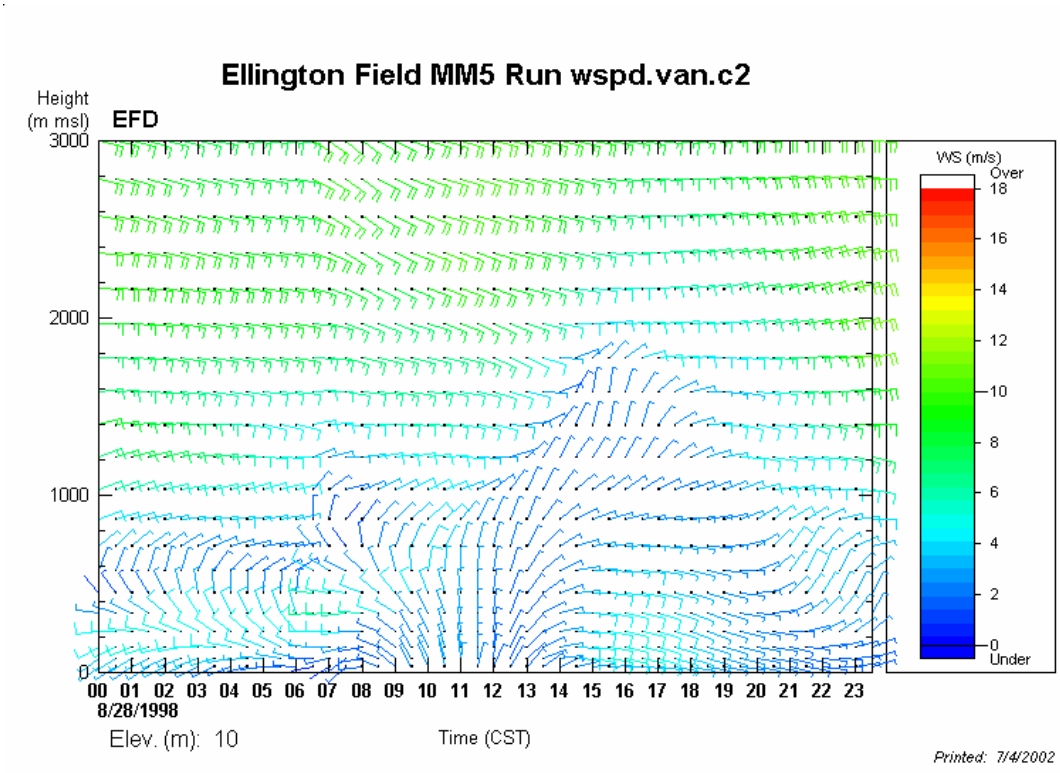

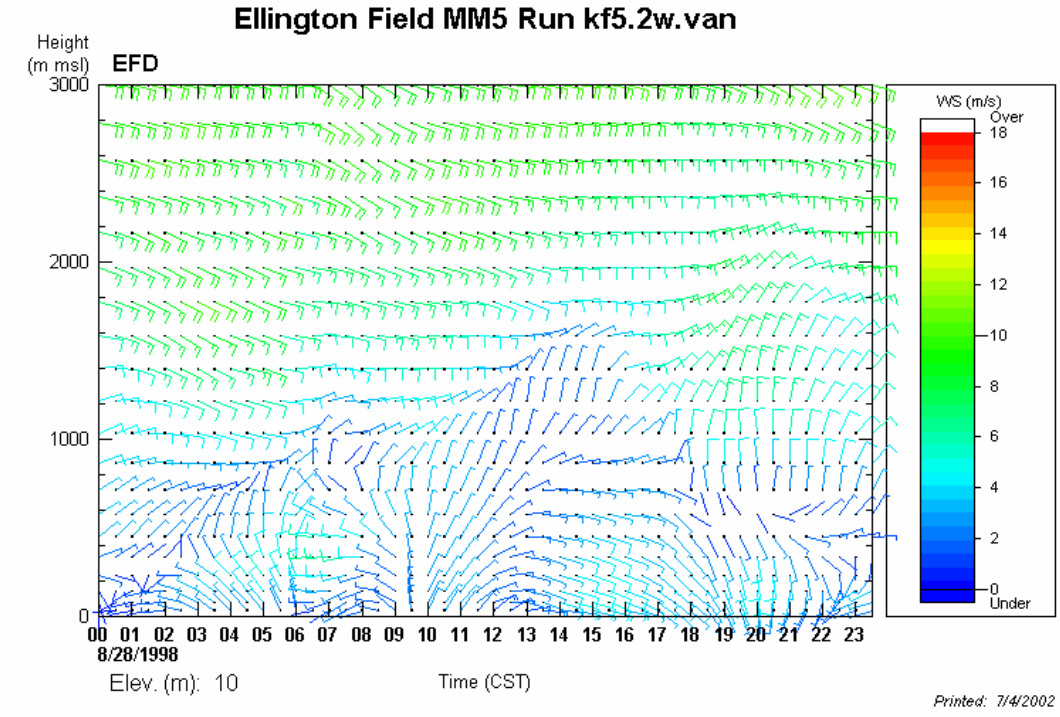

August 28, 1998, time-height cross sections at Ellington Field (from Figure 6.9.4).

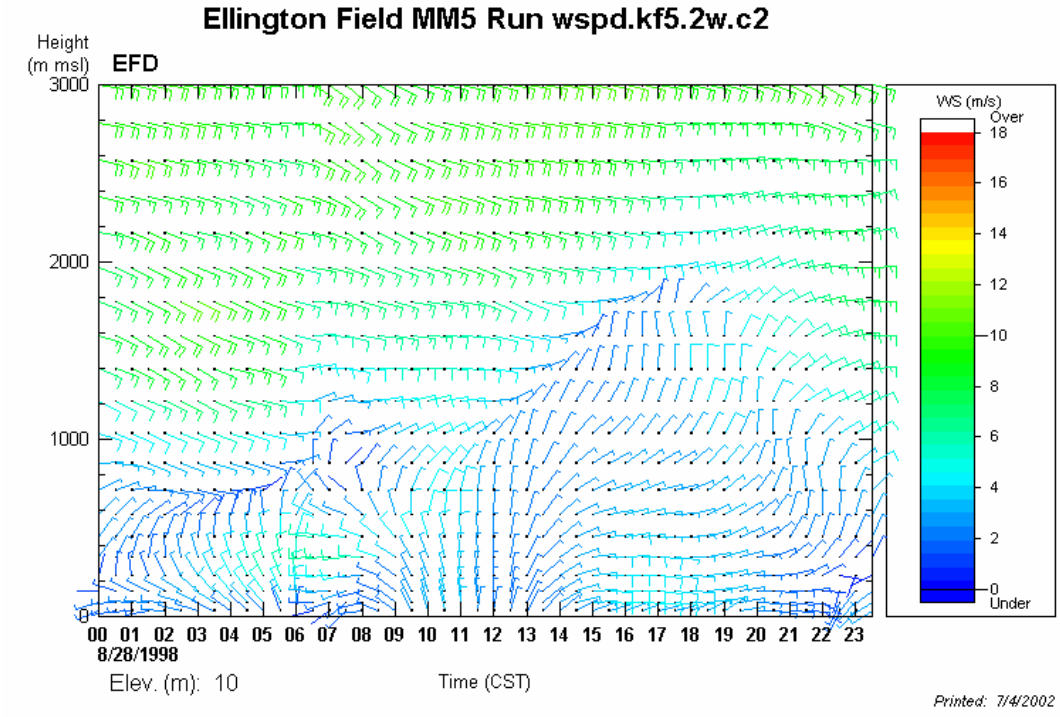

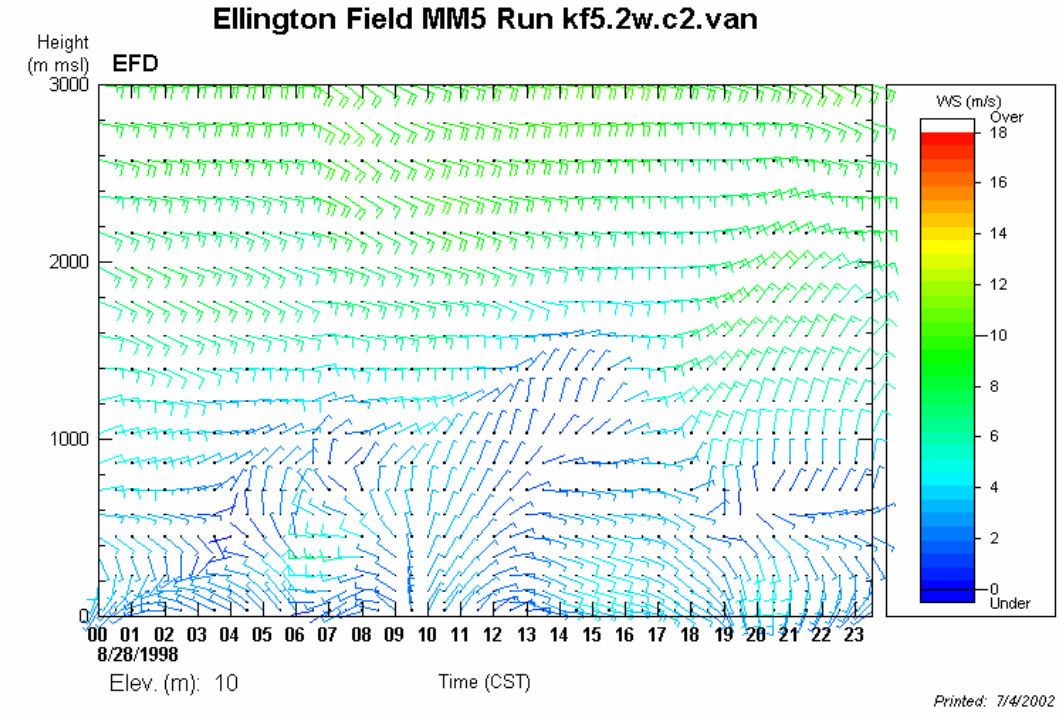

August 28, 1998, time-height cross sections at Ellington Field (from Figure 6.9.4).

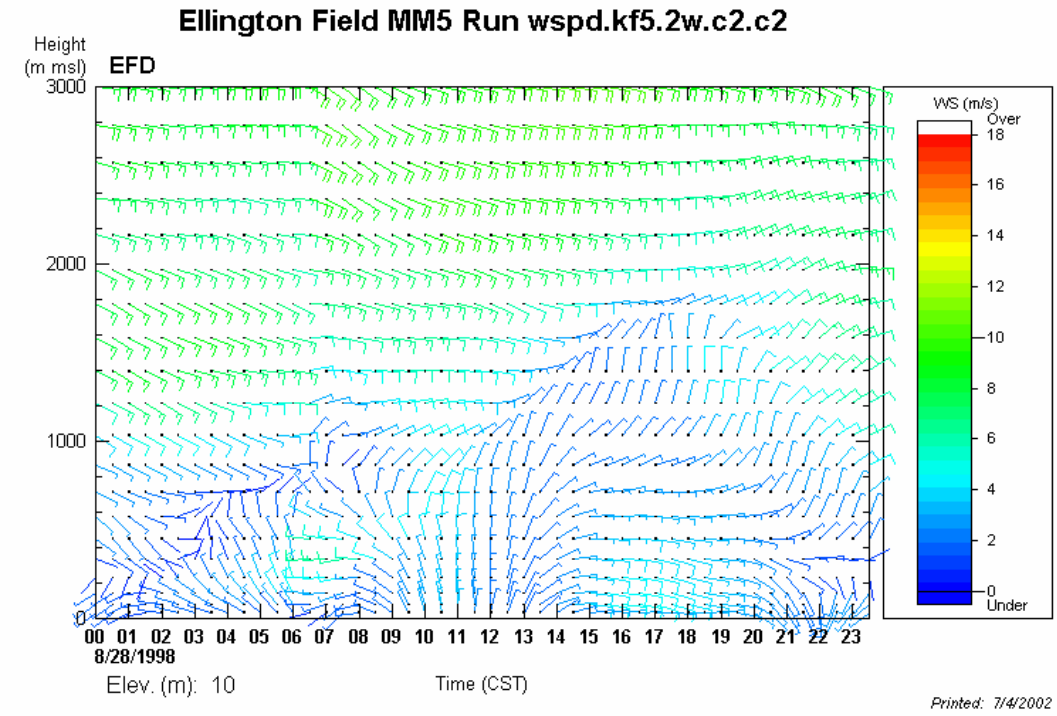

August 28, 1998, time-height cross sections at Ellington Field (from Figure 6.9.4).

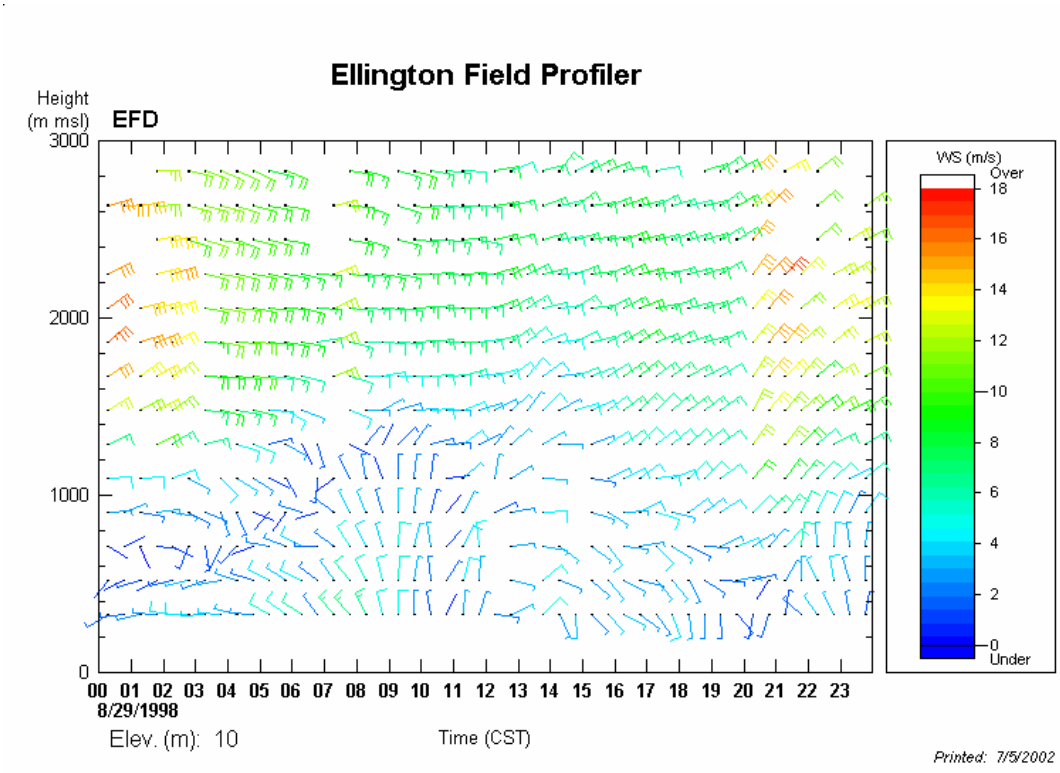

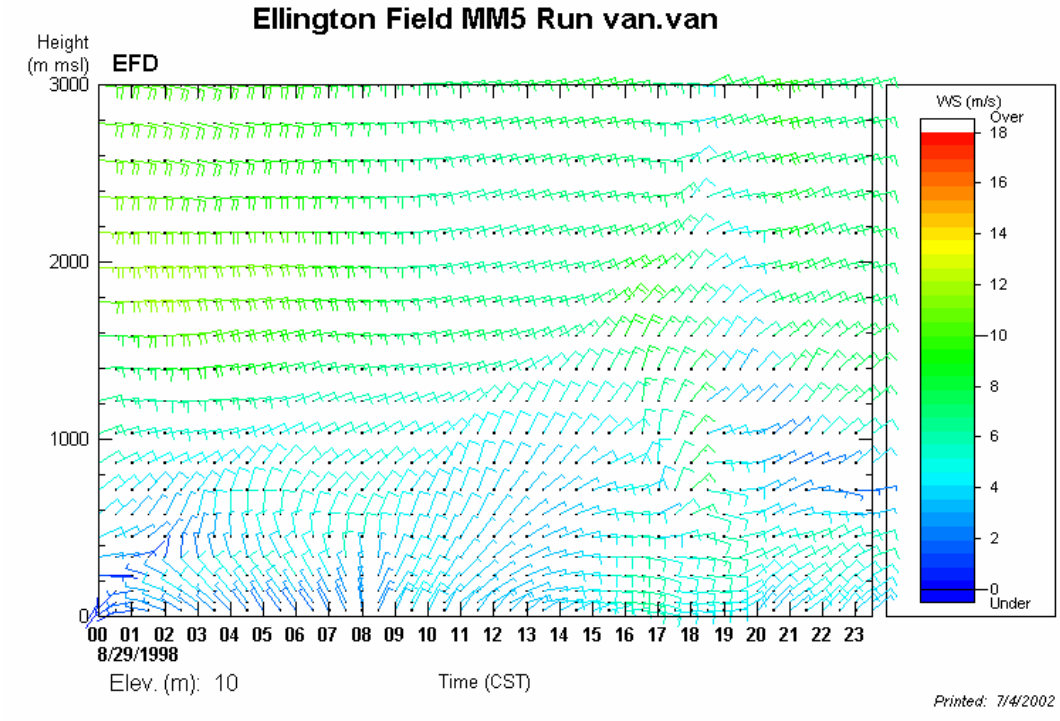

August 29, 1998, time-height cross sections at Ellington Field (from Figure 6.9.5).

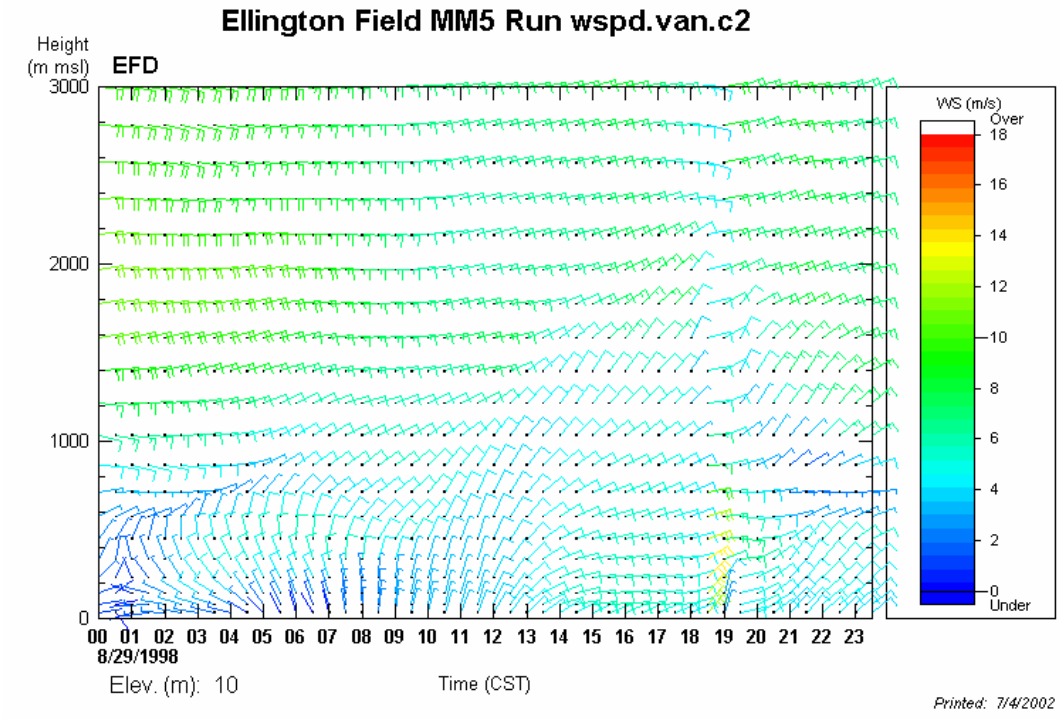

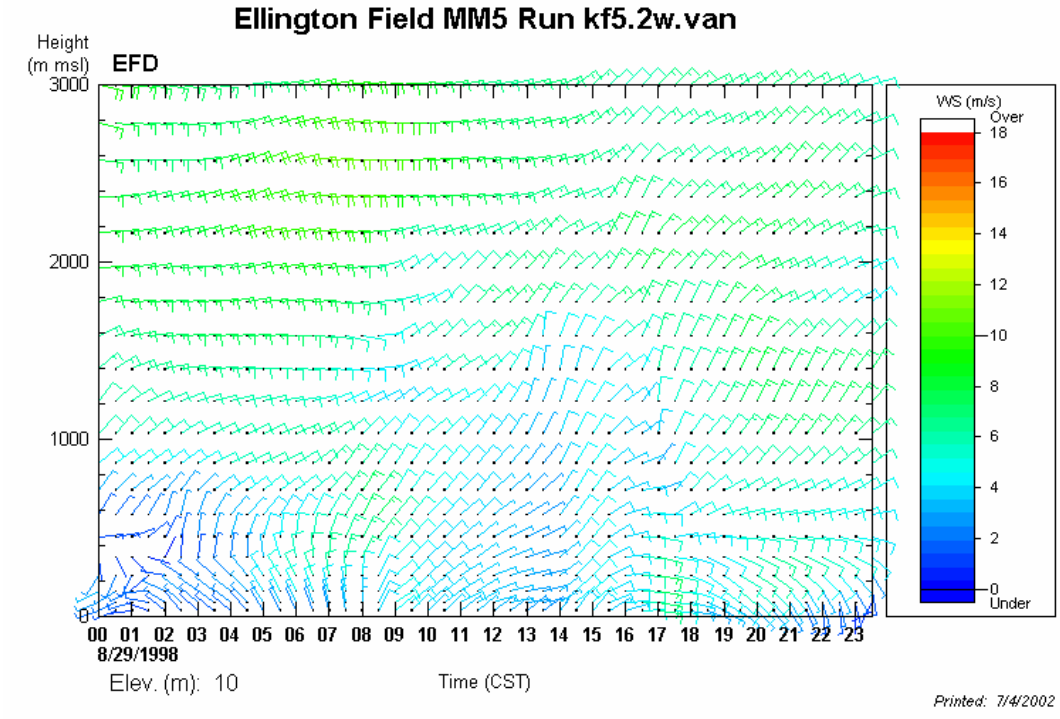

August 29, 1998, time-height cross sections at Ellington Field (from Figure 6.9.5).

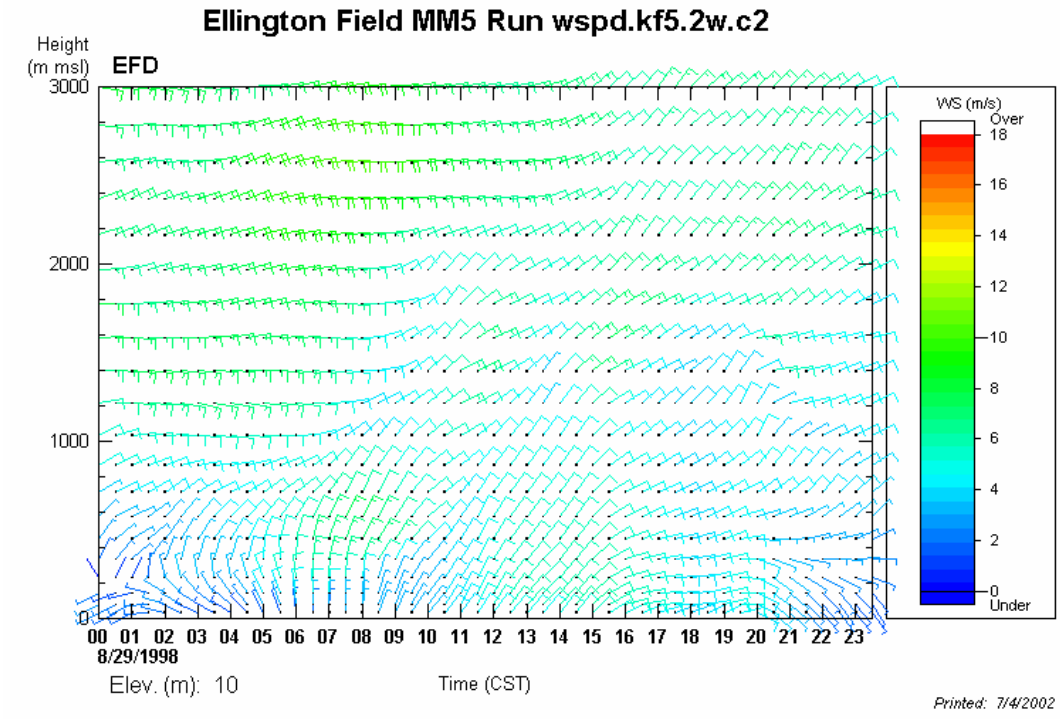

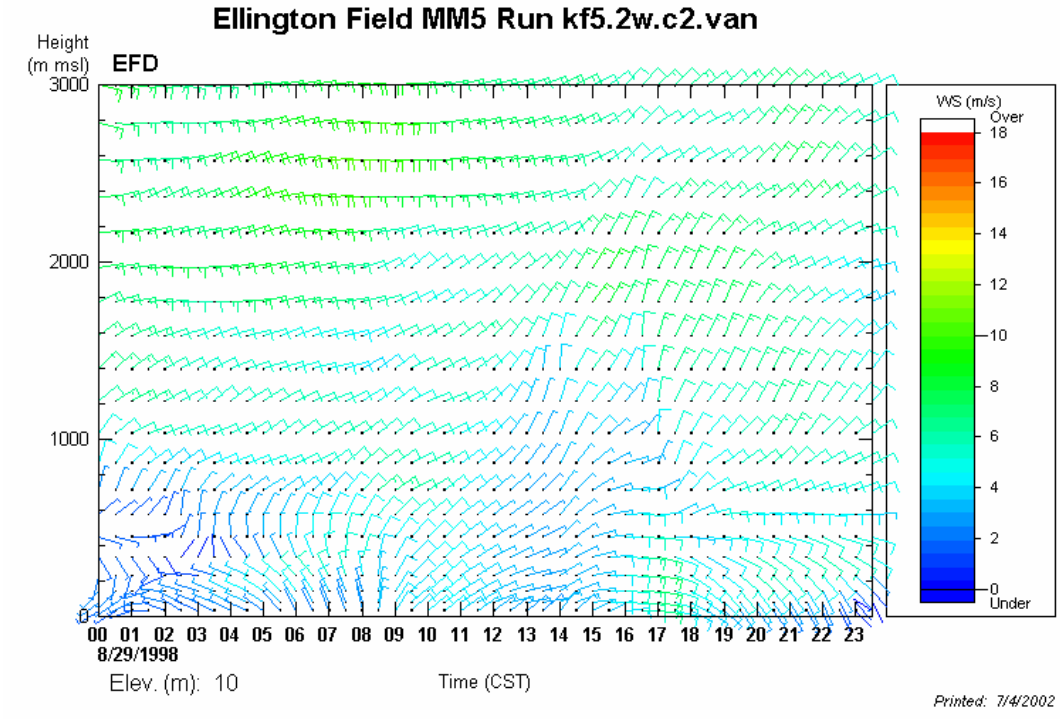

August 29, 1998, time-height cross sections at Ellington Field (from Figure 6.9.5).

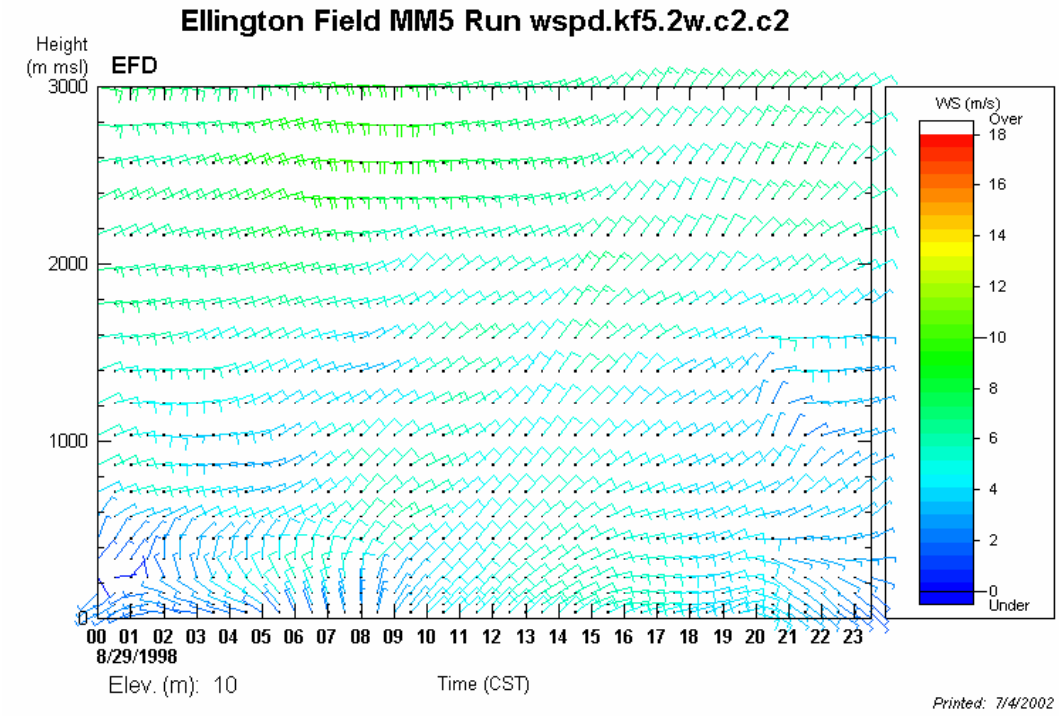

August 29, 1998, time-height cross sections at Ellington Field (from Figure 6.9.5).